



HAL
open science

Topology optimization of connections in mechanical systems

Lalaina Rakotondrainibe

► **To cite this version:**

Lalaina Rakotondrainibe. Topology optimization of connections in mechanical systems. Analysis of PDEs [math.AP]. Institut Polytechnique de Paris, 2020. English. NNT: 2020IPPAX101 . tel-03106332

HAL Id: tel-03106332

<https://theses.hal.science/tel-03106332>

Submitted on 11 Jan 2021

HAL is a multi-disciplinary open access archive for the deposit and dissemination of scientific research documents, whether they are published or not. The documents may come from teaching and research institutions in France or abroad, or from public or private research centers.

L'archive ouverte pluridisciplinaire **HAL**, est destinée au dépôt et à la diffusion de documents scientifiques de niveau recherche, publiés ou non, émanant des établissements d'enseignement et de recherche français ou étrangers, des laboratoires publics ou privés.



INSTITUT
POLYTECHNIQUE
DE PARIS

NNT : 2020IPPAX101

Thèse de doctorat



Optimisation topologique des liaisons dans les systèmes mécaniques

Thèse de doctorat de l'Institut Polytechnique de Paris
préparée à Ecole Polytechnique

École doctorale n°574 Ecole doctorale de mathématiques Hadamard (EDMH)
Spécialité de doctorat : Mathématiques Appliquées

Thèse présentée et soutenue à Montigny-Le-Bretonneux (visio-conférence), le 11 décembre 2020, par

LALAINA RAKOTONDRAINIBE

Composition du Jury :

Marc Bonnet Directeur de recherche, ENSTA	Président
Edouard Oudet Professeur, Université Grenoble Alpes	Rapporteur
Anca-Maria Toader Professeur, Université de Lisbonne	Rapporteur
Grégoire Allaire Professeur, Ecole Polytechnique	Directeur de thèse
Samuel Amstutz Professeur, Ecole Polytechnique	Examineur
Pierre Duysinx Professeur, Université de Liège	Examineur
François Jouve Professeur, Université de Paris	Examineur



GROUPE RENAULT



THÈSE DE DOCTORAT

Ecole doctorale de mathématiques Hadamard (EDMH, ED 574)

Etablissement d'inscription : Ecole Polytechnique

Laboratoire d'accueil : Centre de mathématiques appliquées de l'Ecole Polytechnique,
UMR 7641 CNRS

Spécialité du doctorat : Mathématiques appliquées

Optimisation topologique des liaisons dans les systèmes mécaniques

Topology optimization of connections in mechanical systems

Présentée par :

Mlle RAKOTONDRAINIBE Lalaina Anjanirina

M. ALLAIRE Grégoire
M. AMSTUTZ Samuel
M. BONNET Marc
M. DUYSINX Pierre
M. JOUVE François
M. ORVAL Patrick
M. OUDET Edouard
Mme TOADER Anca-Maria

Ecole Polytechnique
Ecole Polytechnique
ENSTA
Université de Liège
Université de Paris
Technocentre RENAULT
Université Grenoble Alpes
Université de Lisbonne

Directeur de thèse
Examineur
Examineur
Examineur
Examineur
Encadrant industriel
Rapporteur
Rapporteur

Remerciements

En premier lieu, je souhaite exprimer mes plus sincères remerciements à mon directeur de thèse, Grégoire Allaire, pour m'avoir accueillie dans son équipe d'optimisation de formes, pour sa confiance, ses remarques et conseils constructifs, sa disponibilité (malgré son agenda très chargé), sa patience, sa bienveillance et son soutien indéfectible. Je souhaite également remercier Patrick Orval, pour m'avoir introduite aux problématiques industrielles, pour son esprit critique, sa confiance, son engagement, son encadrement efficace et nos discussions enrichissantes.

Je remercie Anca-Maria Toader et Edouard Oudet pour avoir accepté de rapporter mon manuscrit avec enthousiasme. Je remercie également Marc Bonnet pour avoir présider le jury de thèse, ainsi que tous les examinateurs, Samuel Amstutz, Pierre Duysinx et François Jouve, pour l'intérêt qu'ils portent à mon travail.

Merci à l'ANRT pour le financement de cette thèse durant trois ans ainsi que la prolongation pour cause de Covid. Merci également à Antonin Chambolle de l'EDMH pour son soutien et à la direction de Renault pour l'accord de cette prolongation.

Je remercie les Optimistes de la DEA-TDS2 pour leur accueil chez Renault. Merci à Luc Dupin pour m'avoir aidé sur les installations en local sur les PC Renault (ça m'aura été très utile par la suite). Merci également à Christophe Buchou et Sonia Assou pour avoir essayé d'installer FreeFem sur les serveurs de Renault malgré l'échec cuisant... Merci à la communauté des Doctorants@Renault pour les repas sympathiques du vendredi, les pauses gâteaux et les chouettes discussions. Merci à Sylvain Maillot pour sa grande générosité et sa sympathie. Et enfin, merci du fond du cœur à Vanessa, Carlos et William pour avoir égayé mes semaines au rythme de leurs chorées (même en temps de confinement).

Je tiens à remercier Nasséra Naar, Alexandra Noiret et Maud Cadiz-Pena leur aide précieuse et leur grande patience face à mes incompréhensions administratives. Un grand merci également à Sylvain Ferrand et Pierre Straebler pour leur disponibilité et leur aide concernant mes déboires informatiques. Je remercie aussi Charles Dapogny pour son aide précieuse avec Advect. Merci à Alex, Matias, Perle, Florian, Mathilde, Jeet, Martin, Abdelhak, Beni et Alexis pour nos nombreuses expériences partagées (confs, groupe de travail, soirées soupe et fromage, pic-nics, discussions enthousiastes et enrichissantes). Une mention spéciale à Mathilde pour nos aventures en confs (on n'aura pas trouvé la rue des lanternes à Pékin...). Un merci particulier également à Jeet pour notre collaboration fructueuse.

Du côté de l'IRT, je remercie tous les membres du projet TOP pour leur accueil et leur sympathie lors que mes quelques passages sur le plateau. J'adresse un remerciement particulier à Chiara pour son aide précieuse concernant l'utilisation de MMG.

Enfin, je remercie ma famille et mes amis pour leur soutien et encouragements tout au long de ces trois années de thèse. Merci à tous !!!

Contents

Remerciements	i
Introduction (en français)	1
Introduction (in english)	8
I Mathematical tools and modelling	15
1 Background theory	16
1.1 Shape optimization	17
1.2 Mechanical connections optimization	25
2 Assembly model with an idealized bolt connection	27
2.1 Bolt idealization	28
2.2 Basis model : two elastic spheres linked by a pre-stressed spring	32
2.3 Variant model : two rigid spheres linked by a pre-stressed spring	37
2.4 Mechanical constraints specific to the bolt	42
2.5 Constraints integration in optimization problems	45
II Topological sensitivity analysis	50
3 The toy model of Laplace equation	51
3.1 Setting of the problem	52
3.2 Topological sensitivity analysis with respect to a high conducting inclusion . . .	53
3.3 Topological sensitivity analysis with respect to a thermal bridge	68
4 One rigid inclusion in elastic medium	91
4.1 Setting of the problem	92
4.2 Computation of the topological derivative	95
4.3 Numerical illustrations	110
5 Two elastic inclusions linked by a spring	118
5.1 Setting of the problem	119
5.2 Computation of the topological derivative	124
5.3 Numerical illustrations in 2d	137
5.4 Numerical illustrations in 3d	164
5.5 Conclusion of the chapter	168

6	Two rigid inclusions linked by a spring	170
6.1	Setting of the problem	171
6.2	Computation of the topological derivative	175
6.3	Numerical illustrations in 2d	191
6.4	Numerical illustrations in 3d	196
6.5	Conclusion of the chapter	200
7	Topological derivative of an idealized bolt	201
7.1	Setting of the problem	202
7.2	Computation of the topological derivative without contact	209
7.3	Computation of the topological derivative with sliding contact	224
III	Application to bolted assemblies with pre-tension and contact condition	238
8	Academic use cases with sliding contact condition	239
8.1	The small spring in 2d	240
8.2	The small 1 DOF idealized bolt	248
8.3	The 6 DOFs idealized bolt	250
9	Simplified industrial use case	268
9.1	Rigid supports	269
9.2	Idealized bolt connections	279
	Conclusion and perspectives	297
	Appendices	299
A	Simplified industrial use case	300
A.1	General information	300
A.2	Mechanical and geometric simplification	302
A.3	Summary of the simplified model	305

Introduction (en français)

Motivation et objectif

L'allégement dans l'industrie automobile

La masse d'un véhicule a un impact direct sur son coût et ses besoins énergétiques. Une petite voiture nécessite moins d'apport énergétique qu'un véhicule plus lourd. En d'autres termes, plus une voiture thermique est légère, moins elle consomme de carburant et produit du CO₂. De même, un véhicule électrique plus léger a une meilleure autonomie. Depuis les années 90, l'accroissement des normes de sécurité et de confort rend les véhicules plus lourds. En effet, la tenue de route et les performances de freinage sont inversement proportionnelles à la masse. De plus, l'électrification des véhicules implique des composants massifs tels que la batterie. Les véhicules modernes contiennent de plus en plus de capteurs et de calculateurs, ce qui augmente leur masse. Dans le domaine du Design, le diamètre des roues a été augmenté entre l'ancien modèle (Fig. 1) et le nouveau modèle (Fig. 2) du Scenic. Ce dernier tend alors à avoir des aspects de SUV. Cette amélioration esthétique conduit à une augmentation d'environ 40 kg de la masse totale. En conséquence, les dimensions des amortisseurs, de la caisse, des disques de frein, etc... sont réadaptées. Pour compenser, des matériaux et structures spécifiques sont choisis pour réduire la résistance au roulement des pneus. Tous ces ajouts augmentent la masse et le prix du véhicule. Pour intégrer ces nouvelles technologies, l'industrie automobile doit trouver les bons compromis technico-économiques. Pour cela, elle cherche à se doter de nouvelles approches.



Figure 1: Ancien Scenic



Figure 2: Nouveau Scenic

Deux familles de méthodes sont utilisées pour alléger les pièces mécaniques :

- Changement de matériaux
Par exemple, l'acier est remplacé par de l'aluminium. Des matériaux composites sont utilisés à la place du métal. L'acier non structural, tel que pour les ailes avant, peut être remplacé par un polymère adapté.

- Dimensionnement
La forme et la topologie d'une pièce sont optimisées afin de conserver la quantité de matière strictement utile.

Dans cette thèse, l'allègement des structures est réalisé à l'aide des méthodes d'optimisation de formes et d'optimisation topologique.

Optimisation de formes

L'optimisation de formes, géométrique et topologique, est un domaine d'étude bien établi (voir e.g. [4, 20]). De nombreuses méthodes ont été développées pour optimiser les structures. Les deux méthodes les plus connues sont la méthode SIMP (Solid Isotropic Material Penalization) [18, 20] et la méthode des lignes de niveaux [91, 90, 103]. La méthode SIMP optimise une fonction densité qui correspond à la présence ou à l'absence de matière. Cette méthode est aujourd'hui largement déployée dans les industries de transport, avec une position dominante du progiciel OptiStruct. Cette thèse s'appuie sur la méthode des lignes de niveaux. Les frontières de la structure sont explicitement définies par une fonction ligne de niveaux. Cette méthode s'allie à la méthode de variations de frontière d'Hadamard [59, 5, 94, 109] afin de réaliser les modifications de la forme. La plupart du temps, l'optimisation topologique est appliquée à une seule pièce. Son environnement n'est pas repris par l'étude mais est pris en compte au travers de conditions aux limites. De plus, ses liaisons mécaniques sont des données d'entrée qui ne seront pas modifiées dans le processus d'optimisation. Cette approche limite donc l'ensemble des formes optimales.

Objectif

Cette thèse est réalisée dans le cadre de l'optimisation topologique. Son objectif consiste à développer une méthode d'optimisation simultanée de la structure d'une pièce, d'une part, et des positions et du nombre de ses liaisons mécaniques, d'autre part.

Contributions

Modèle idéalisé de vis

Cette thèse se concentre sur les liaisons vissées. Le comportement des vis est complexe et requiert une modélisation raffinée à l'échelle locale, ce qui est coûteux en termes de temps de calcul. Dans le cadre d'une optimisation à l'échelle de la pièce, une telle modélisation n'est pas utile. On établit donc un modèle idéalisé au moyen d'une formulation analytique. La vis idéalisée conserve sa représentativité physique à l'ordre un. Ce modèle a pour objectif d'être facile d'utilisation pour le processus d'optimisation, peu coûteux en termes de temps de calcul et adapté aux développements de gradient topologique. Le modèle idéalisé s'accompagne de contraintes technologiques propres à la vis, pour assurer sa résistance mécanique.

Gradient topologique

L'analyse de sensibilité topologique permet de calculer une quantité que l'on appelle gradient topologique. Elle a tout d'abord été développée pour déterminer s'il est favorable ou non de créer un petit trou dans la structure au cours du processus d'optimisation [36, 86, 102, 107, 108].

Par la suite, cette méthode a été appliquée à un large éventail de modèles, tels que l'élasticité linéaire [51], un modèle de contact glissant dans les équations de l'élasticité [53], les équations de Navier-Stokes [12], l'équation de Poisson [56], l'équation de Helmholtz [100], la détection de fissures [13], le traitement d'images [15], les problèmes inverses [11], etc... Dans cette thèse, le gradient topologique est utilisé pour ajouter une nouvelle vis infinitésimale. Il est calculé pas à pas à partir des spécificités du problème mécanique : vis idéalisée, état de prétension, modèle de contact, etc... On obtient alors un résultat générique, valable pour tout critère, à condition de pouvoir calculer l'état adjoint qui lui correspond.

Optimisation couplée de la structure et des liaisons

La structure est représentée par une fonction lignes de niveaux [91, 90, 103] et est optimisée par la méthode de variations de frontière d'Hadamard [5, 94, 109]. On établit ensuite un gradient de descente paramétrique pour optimiser la position des liaisons. Le nombre de liaisons est géré par le gradient topologique. L'optimisation couplée est testée étape par étape sur de nombreux cas tests académiques en 2d et en 3d. Enfin, elle est capitalisée sur un cas test industriel simplifié. Toutes les illustrations numériques sont implémentées avec FreeFem++ [60].

Résumé des chapitres

Cette thèse comporte trois parties. La première présente les outils mathématiques d'optimisation de formes et établit un modèle idéalisé de la vis. La seconde partie est dédiée à plusieurs calculs de gradient topologique dont la finalité est l'ajout d'une petite vis idéalisée. La troisième partie contient des applications numériques.

Partie I : Outils mathématiques et modélisation

Chapitre 1 : Fondements théoriques

Ce chapitre introduit l'optimisation de formes au travers des méthodes les plus utilisées. Une attention particulière est apportée à la méthode de variations de frontière d'Hadamard pour modifier les formes. Les variations de la topologie sont réalisées à l'aide d'une analyse de sensibilité topologique, aussi appelée gradient topologique. La majorité des problèmes d'optimisation étudiés dans cette thèse sont des problèmes sous contraintes. Elles sont gérées par la méthode du Lagrangien Augmenté dont on expose les grandes lignes. Enfin, on présente un état de l'art non-exhaustif de l'optimisation des vis, ressorts, supports et des systèmes à composantes multiples.

Chapitre 2 : Modèle d'assemblage avec une vis idéalisée

Ce chapitre établit un modèle idéalisé de la vis longue en 3d. On considère un assemblage composé de deux pièces en contact qui seront assemblées par une vis idéalisée. Ce modèle est constitué de deux sphères représentant la tête et les filets de vis en connexion avec chacune des pièces et d'une poutre Euler-Bernoulli à 6 degrés de liberté représentant le comportement mécanique du noyau et sujette à un état de pré-tension (voir Fig. 3). Le modèle de référence utilise des sphères élastiques. Une variante de ce modèle utilise des sphères rigides. La procédure de serrage conduisant à un état de précontrainte et la mise en service du système sont décrits en deux étapes selon une formulation mécanique et mathématique rigoureuse. Des contraintes technologiques, propres à la tenue de la vis, sont établies pour le modèle idéalisé en vue de l'optimisation topologique.

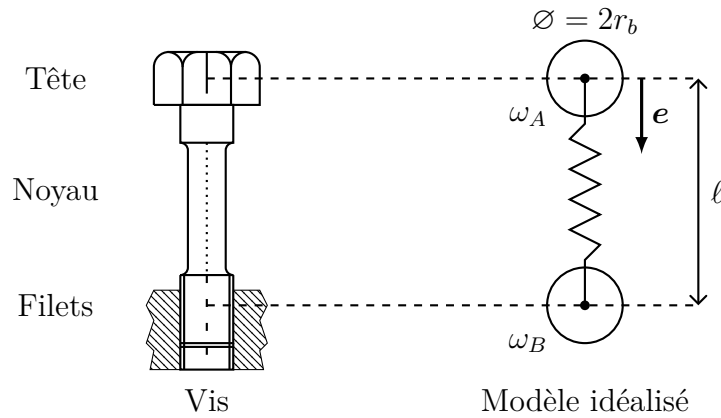


Figure 3: Idéalement d'une vis

Partie II : Analyse de sensibilité topologique

Chapitre 3 : Le modèle didactique de l'équation de Laplace

Ce chapitre contient des résultats techniques préliminaires en vue du calcul de gradients topologiques pour les problèmes de l'élasticité. Un modèle physique simple, gouverné par l'équation de Laplace pour la propagation de la chaleur, fournit une meilleure compréhension des techniques et astuces de l'analyse topologique. Ce chapitre ne concerne pas explicitement l'optimisation de structures et les liaisons mécaniques. Dans un premier temps, le gradient topologique est calculé pour une petite inclusion sur laquelle s'applique une température d'une valeur arbitraire. Cela correspond à une inclusion hautement conductrice. Cette perturbation correspondrait à une inclusion rigide pour le problème de l'élasticité. Par la suite, le gradient topologique est calculé par rapport à un pont thermique. Cette perturbation correspondrait à un ressort pour le problème de l'élasticité. Deux modèles de pont thermique sont développés. On gardera le modèle le plus pratique pour les calculs avec une vis idéalisée. Tous les gradients topologiques sont donnés en 2d et en 3d mais les preuves sont établies pour le problème 3d. Ils sont ensuite illustrés par des cas tests académiques en 2d et en 3d. La structure n'est pas optimisée.

Chapitre 4 : Une inclusion rigide dans un milieu élastique

On procède étape par étape et par niveau de difficulté. Ce chapitre établit le gradient topologique dans le cadre de l'élasticité linéaire pour l'ajout d'une petite inclusion rigide. Il est calculé à l'aide d'une approche variationnelle, comme développé au Chapitre 3. Les résultats principaux sont donnés en 2d et en 3d et les preuves sont établies pour le problème en 3d. Ils sont illustrés par des cas tests académiques simples en 2d et en 3d dans le but de tester l'efficacité du gradient topologique. La structure n'est pas optimisée.

Chapitre 5 : Deux inclusions élastiques reliées par un ressort

Ce chapitre est consacré au calcul du gradient topologique de la perturbation due à deux petites sphères élastiques reliées par un ressort de longueur fixe. Ce ressort n'est pas soumis à la pré-tension. Le modèle est adapté aux besoins de l'analyse de sensibilité topologique qui se base sur les techniques développées au Chapitre 3. Ainsi, le ressort travaille selon un seul degré de liberté. Les résultats principaux sont donnés en 2d et en 3d et les preuves sont établies pour le problème en 3d. Le gradient topologique est testé sur des cas tests académiques en 2d et en 3d. Puis, la liaison qui en résulte est mise en jeu dans diverses optimisations de formes (voir e.g. Fig 4).

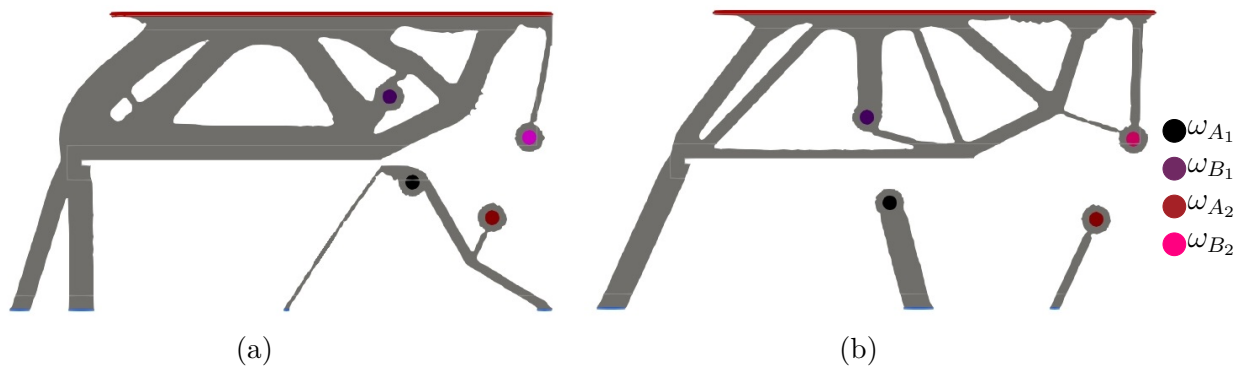


Figure 4: Formes optimales avec deux ressorts placés et orientés par le gradient topologique (a) et dont les positions sont optimisées par le gradient paramétrique (b) pour un problème de minimisation du volume sous une contrainte de compliance

Chapitre 6 : Deux inclusions rigides reliées par un ressort

On considère maintenant un mouvement de corps rigide sur les inclusions. Dans un souci de simplicité, l'état de pré-tension n'est toujours pas pris en compte. Ce chapitre étudie la sensibilité topologique de deux petites sphères rigides reliées par un ressort. Il mélange les outils des Chapitres 4 et 5. Ce chapitre a pour but de choisir le modèle le plus adapté au calcul du gradient topologique d'une petite vis idéalisée. Les résultats principaux sont donnés en 2d et en 3d et les preuves sont établies pour le problème en 3d. Le gradient topologique est testé sur le même cas test académique 2d que dans le Chapitre 5 et sur un autre cas test académique 3d.

Chapitre 7 : Gradient topologique d'une vis idéalisée

Ce chapitre calcule le gradient topologique d'une petite vis soumise à un état de précontrainte. La petite vis se compose de deux sphères élastiques reliées par un ressort à 1 degré de liberté de longueur fixe. La condition de précontrainte est appliquée dans une première étape, suivie d'une seconde étape pour l'application des conditions en service. L'analyse de sensibilité est tout d'abord réalisée sans condition de contact et est développée selon les problèmes de l'élasticité linéaire en deux étapes. Dans un second temps, l'analyse de sensibilité est complétée avec un modèle de contact glissant. Nous montrerons alors que le gradient topologique a la même expression, avec ou sans condition de contact. Ce chapitre est entièrement dédié au calcul de gradient topologique en 3d.

Partie III : Application aux assemblages vissés avec état de pré-tension et modèle de contact

Chapitre 8 : Cas tests académiques avec un modèle de contact glissant

Ce chapitre regroupe un ensemble de cas tests 2d et 3d utilisant le code de contact glissant de Jeet DESAI [44] dans le cadre du projet TOP (Topology Optimization Platform) hébergé à l'IRT System'X. Les problèmes d'optimisation du Chapitre 5 sont reproduits pour comparer les résultats avec et sans l'interface de contact en 2d. Ensuite, une rapide utilisation du gradient topologique d'une petite vis à un degré de liberté en 3d, calculé au Chapitre 7, illustre un cas particulier nécessitant une condition de non-chevauchement des vis. Enfin, on implémente le modèle de vis idéalisée à 6 degrés de liberté avec les contraintes technologiques établies au Chapitre 2.

Chapitre 9 : Cas test industriel simplifié

Ce chapitre concerne le cas test industriel simplifié d'une face accessoires assemblée d'un moteur thermique (voir Fig. 5). Dans la première partie, les liaisons entre le support accessoires et le carter-cylindres sont modélisées par des encastrement. Cette étude a pour but de montrer les gains substantiels qu'apporte l'optimisation couplée de la structure et de la position des liaisons sur un cas test industriel simplifié, même si le modèle de liaisons est basique. La seconde partie présente l'optimisation couplée de la structure et de la position et du nombre des vis. Elle regroupe tous les points clés développés dans cette thèse, à savoir : le modèle de vis idéalisée à 6 degrés de liberté complété par des contraintes technologiques, le gradient topologique pour optimiser le nombre de vis, l'algorithme de gradient paramétrique pour optimiser la position des vis et la méthodes des lignes de niveaux pour optimiser la structure du support accessoires.

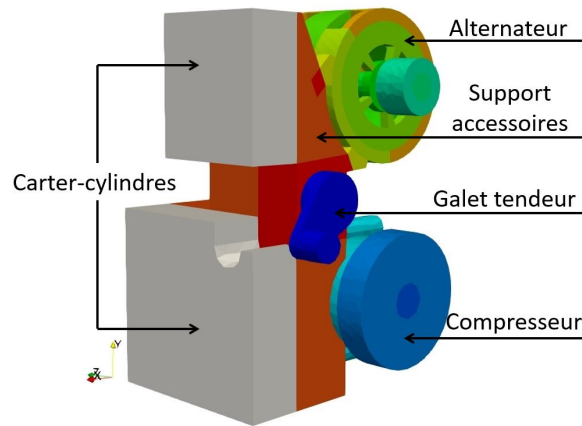


Figure 5: Face accessoires simplifiée utilisée avec le modèle de vis idéalisée

Annexe A : Cas test industriel simplifié

Cette annexe a pour but d'établir le modèle simplifié de la face accessoires utilisé au Chapitre 9. Le modèle simplifié dérive d'un modèle réel fourni par Renault. Il a été établi de telle sorte que la représentativité physique soit satisfaisante pour des analyses statiques et modales. On présente ici le modèle simplifié utilisé pour les encastrement. Il a été développé lors du stage précédent cette thèse. L'assemblage est ensuite légèrement revisité pour l'utilisation de vis idéalisées.

Communications scientifiques

Le travail présenté dans cette thèse a conduit aux communications suivantes

- **Articles de journal**

Coupled topology optimization of structure and connections in bolted mechanical systems, L. Rakotondrainibe, J. Desai, P. Orval, G. Allaire, en préparation, 2021

Topological sensitivity analysis with respect to a small idealized bolt, L. Rakotondrainibe, G. Allaire, P. Orval, en préparation, 2021

Topology optimization of connections in mechanical systems, L. Rakotondrainibe, G. Allaire, P. Orval, Structural and Multidisciplinary Optimization, 61:2253-2269, 2020

- **Communications orales**

Optimisation couplée de la structure et des liaisons vissées d'un assemblage mécanique, Congrès d'Analyse Numérique pour les jeunes, CAN-J 2020 - en ligne - Décembre 2020

Optimisation topologique couplée de la structure et des liaisons vissées d'un assemblage, ANR-SHAPO - en ligne - Octobre 2020

Coupled optimization of both structure and mechanical connections (location and number), Programme Gaspard Monge PGM Days - Saclay, France - Decembre 2019

Topology optimization of connections in mechanical systems, 13th World Congress on Structural and Multidisciplinary Optimization WCSMO 13 - Pékin, Chine - Mai 2019

- **Posters**

Optimisation topologique des liaisons dans les systèmes mécaniques, Journées Optimisation de Formes et Applications JOFA 4 - Palaiseau, France - Octobre 2019

Optimisation topologique des liaisons dans les systèmes mécaniques, 14ème Colloque national en calcul des structures CSMA 2019 - Giens, France - Mai 2019

Optimisation topologique des liaisons dans les systèmes mécaniques, 44ème Congrès National d'Analyse Numérique CANUM 2018 - Cap d'Adge, France - Mai 2018

Introduction (in english)

Motivation and objective

Weight reduction in the automotive industry

The weight of a vehicle has a direct impact on its cost and energy requirement. A small car requires less energy than a heavy one. In other words, the lighter a thermal car is, the less it consumes fuel and produces CO₂. Similarly, a lighter electric car has a better autonomy than a heavy one. Since the 90's, the increasing request of safety and comfort makes cars heavier as road handling and braking performance are inversely proportional to the mass. Furthermore, the electrification of vehicles implies weighty components such as the battery. Modern cars contain much more sensors and calculators that increase their weight. In the field of Design, the wheel diameter has been increased from the former (Fig. 1) to the latest (Fig. 2) Scenic model. The new model has then more a SUV aspect. This aesthetic improvement leads to an increase of about 40 kg of the car weight. As a consequence, this requires appropriate resized dampers, resized body shell, resized brake discs, etc. Besides, specific materials and structures has been chosen to reduce rolling resistance of tyres. All of that increases the weight and the cost of the vehicle. The automotive industry has to work on new approaches in order to integrate these technologies and find the right balance with cost saving.



Figure 1: Former Scenic



Figure 2: Latest Scenic

Two types of method are used to reduce the weight of mechanical parts :

- Change materials
For example, steel is replaced by aluminium. Composite material can be used instead of metal. Non structural steel plates, as front wings, are replaced by suitable polymer.

- Dimensioning
The shape and the topology of the part are optimized to keep useful material and remove the excess.

This thesis performs weight reduction with shape and topology optimization techniques.

Shape optimization

Shape and topology optimization of structures is a well-established field (see e.g. [4, 20]). Plenty of methods have been developed to optimize structures. The two most well-known approaches are the SIMP (Solid Isotropic Material Penalization) method [18, 20] and the level-set method [91, 90, 103]. The SIMP method consists in optimizing a density function that corresponds to the presence or the absence of material. Transport industry widely resorts to this method, with a predominance of the software package OptiStruct. This thesis relies on the level-set method. The boundaries of the structure are explicitly defined by a level-set function. This method is combined with Hadamard's boundary variation method [59, 5, 94, 109] to perform shape modifications. Most of the time, topology optimization is applied on a single piece. Its environment is not embodied in the study but is taken into account through boundary conditions. Moreover, its mechanical connections are input data and are not modified during the optimization process. Then, this classical approach bounds the set of optimal shapes.

Objective

This thesis is developed in the context of shape and topology optimization. Our purpose is to develop a method to optimize concurrently the structure of a part, on the one hand, and the locations and the number of its mechanical connections, on the other hand.

Contributions

Idealized model of bolt connection

This thesis focuses on bolt connection. Bolts behavior is complex and requires a fine modelling to obtain detailed local results, which is computationally costly. For the purpose of a system-level optimization, such fine modelling is useless and we would rather establish an idealized model of bolt connection. Based on an analytical formulation, the idealized bolt connection keeps physical representativeness at first order. This model aims to be easy to use for optimization process, computationally cheap and adapted to topological derivative developments. The idealized model is supplemented by mechanical constraints specific to the bolt, to insure bolt strength and resistance.

Topological sensitivity analysis

The topological sensitivity analysis computes a quantity called topological derivative. It was first developed to determine if it is favorable or not to add a small hole in the structure during the optimization process [36, 86, 102, 107, 108]. Thereafter, the method has been applied to a wide range of models, such as linear elasticity equations [51], sliding contact model for elasticity equations [53], Navier-Stokes equations [12], Poisson equation [56], Helmholtz equation [100], crack detection [13], image processing [15], inverse problems [11], etc... In this thesis,

the topological derivative is used to add a new bolt in the system. It is computed step by step with regards to specificities of the mechanical problem : idealized bolt, prestressed state, contact model, etc.. Then, we obtain a generic result, valid for all criteria, provided that the corresponding adjoint state is available.

Coupled optimization of both structure and connections

The structure is represented by a level-set function [91, 90, 103] and is optimized according to the Hadamard's boundary variation method [5, 94, 109]. Then, a parametric gradient-based algorithm is derived to optimize the location of connection. The number of connection is handled by the topological derivative. The coupled optimization is tested step by step on plenty of academic test cases in 2d and 3d. Finally, it is capitalized on a simplified industrial test case. All numerical illustrations are implemented with FreeFem++ [60].

Summary of chapters

This thesis is composed of three parts. The first one provides mathematical tools of shape optimization and draws up an idealized model of bolt connection. The second part is dedicated to various topological sensitivity analyses in order to nucleate a small idealized bolt. The third part contains numerical applications.

Part I : Mathematical tools and modelling

Chapter 1 : Background theory

This chapter introduces shape optimization through most commonly used methods. Then, we focus on the Hadamard's boundary variation method for shape modification. The framework of topological sensitivity analysis is given for topological variation of a structure. Most of the optimization problems investigated in this thesis are under constraints. They are handled by the Augmented Lagrangian method which general outline is given here. Finally, a non-exhaustive state of the art is drawn up for bolts, springs, supports and multi-component systems optimization.

Chapter 2 : Assembly model with an idealized bolt connection

This chapter establishes an idealized model of a long bolt in 3d. We consider here an assembly of two parts in contact linked by such an idealized bolt. This model contains two spheres, representing the head and the threads of the bolt in connection with each part, and a 6 degrees of freedom Euler-Bernoulli beam, representing the mechanical behavior of the root that is subjected to a prestressed state (see Fig. 3). The reference model deals with elastic spheres. A variant model dealing with rigid spheres is also studied. The tightening process provoking the prestress is described in two steps according to a mechanically and mathematically complete and rigorous formulation. For the purpose of topology optimization, technological constraints, specific to bolt strength and resistance, are derived with regards to the idealized model.

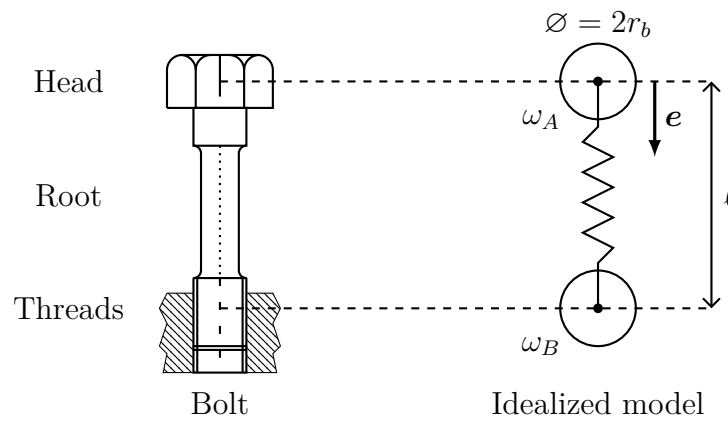


Figure 3: Idealization of a bolt

Part II : Topological sensitivity analysis

Chapter 3 : The toy model of Laplace equation

This chapter contains preliminary technical results for further topological sensitivity analysis for the purpose of elasticity problems. A simple physical model, ruled by Laplace equation for heat propagation, provides more pedagogical understanding of the analysis tricks and techniques, hence the term "toy model". This chapter does not explicitly concern structure optimization and mechanical connections. The topological derivative is first computed with regards to the creation of a small inclusion with a prescribed arbitrary temperature value. It corresponds to a high conducting inclusion. This perturbation shall correspond to a highly stiff or rigid inclusion for the elasticity problem. Then, the topological derivative is established with respect to a thermal bridge. This perturbation shall correspond to a linear spring for the elasticity problem. Two models of the thermal bridge are developed and the most convenient one is kept for the idealized bolt connection. All topological derivatives are given in 2d and 3d but proofs are carried out for the 3d problem. They are numerically illustrated with simple academic 2d and 3d test cases. The structure is not optimized.

Chapter 4 : One rigid inclusion in elastic medium

We proceed step by step and per level of difficulty. The present chapter investigates the topological derivative for the linear elasticity problem with respect to the nucleation of one small rigid inclusion. According to the techniques developed in Chapter 3, the topological derivative is established with a variational approach. Main results are given in 2d and 3d but the proof is carried out for the 3d problem. They are numerically illustrated with simple academic 2d and 3d test cases. These examples intend to test the topological derivative efficiency. The structure is not optimized.

Chapter 5 : Two elastic inclusions linked by a spring

This chapter is devoted to the sensitivity analysis of the perturbation due to a fixed-length spring linking two small elastic spheres. The spring is not under a pre-stressed state. The model is suited for the purpose of sensitivity analysis based on the techniques developed in Chapter 3. Then the spring works according to one degree of freedom. Main results are given in 2d and 3d but the proof is carried out for the 3d problem. The topological derivative is tested on 2d and 3d academic use cases. Thereafter, the resulting connection is involved in various structural optimizations (see e.g. Fig 4).

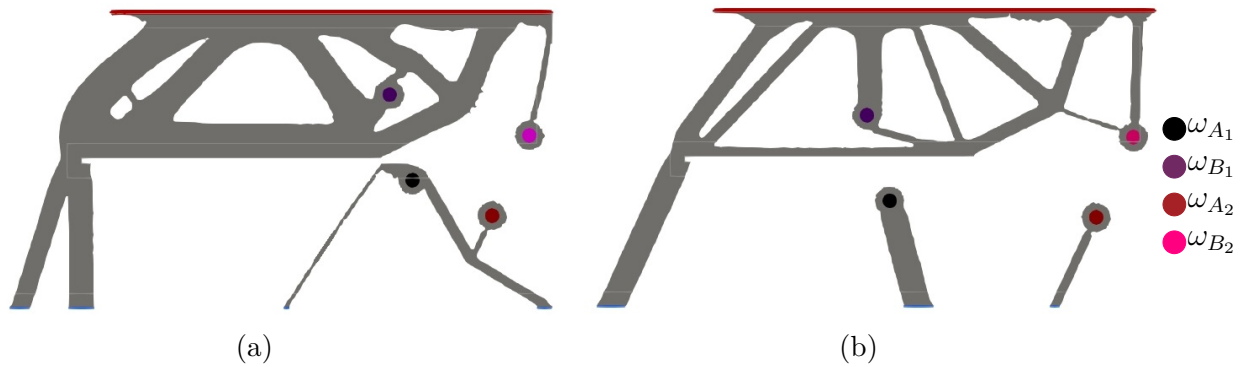


Figure 4: Optimal shapes with two springs placed and oriented by the topological derivative (a) and whose locations are optimized by the parametric gradient (b) for a problem of volume minimization under a compliance constraint

Chapter 6 : Two rigid inclusions linked by a spring

We consider the ingredient of rigid body motion on the inclusions. For the sake of simplicity, the pre-stressed state is still not taken into account. Then, the present chapter investigates the topological sensitivity analysis with regards to two small rigid inclusions linked by a spring. It mixes the tools of Chapters 4 and 5. This chapter aims at choosing the most suitable idealized bolt model for the purpose of topological sensitivity. Main results are given in 2d and 3d but the proof is carried out for the 3d problem. The topological derivative is tested on the same 2d academic use case as the one of Chapter 5 and on an other 3d academic use case.

Chapter 7 : Topological derivative of an idealized bolt

This chapter investigates the topological sensitivity analysis with respect to a small idealized bolt subjected to a pretension condition. The small bolt is made of two elastic spheres linked by a fixed-length 1 degree of freedom spring. The pretension condition is applied in a first step followed by a second step for application of in-service conditions. The sensitivity analysis is first carried out without contact condition and developed with regards to the two-steps linear elasticity problem. In a second part, the sensitivity analysis is complemented with a sliding contact condition. It will be shown that the topological derivative expression is the same with or without this contact condition. This chapter is fully about topological sensitivity analysis in 3d.

Part III : Application to bolted assemblies with pre-tension and contact condition

Chapter 8 : Academic use cases with sliding contact condition

This chapter exhibits a set of test cases in 2d and 3d using the sliding contact code of Jeet DESAI [44] in the framework of project TOP (Topology Optimization Platform) within IRT System'X. The optimization problems of Chapter 5 are reproduced to compare results with and without a contact interface in 2d. Then, a quick use of the topological derivative of small one degree of freedom idealized bolt in 3d, computed in Chapter 7, depicts a particular case where a non-overlapping condition between bolts is required. Finally, the 6 degrees of freedom idealized bolt model with the technological constraints set in Chapter 2 is implemented.

Chapter 9 : Simplified industrial use case

This chapter deals with the simplified industrial use case of a bracket and accessories assembly of a thermal engine (see Fig. 5). The first section models connections between the bracket and the crankcase by rigid supports. It aims to show that the optimization of both structure and connections locations brings substantial gain on a simplified industrial use case, even if the connection model is basic. The second section investigates a coupled optimization of the structure and the locations and number of bolts. It gathers all key points developed in this thesis, namely: the 6 degrees of freedom idealized bolt model complemented by specific mechanical constraints, the topological derivative to place new bolts, the parametric gradient-based algorithm to optimize bolts locations, and the level-set method to optimize the structure of the bracket.

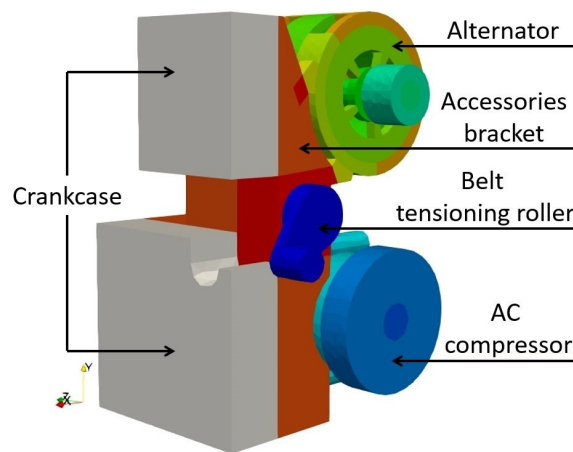


Figure 5: Simplified accessories and bracket assembly used with the idealized bolt model

Appendix A : Simplified industrial use case

The goal of this appendix is to establish the simplified model of an accessories and bracket assembly used in Chapter 9. The simplified model is based on a real assembly provided by Renault. It has to be representative enough for static and dynamic analysis. We present here the simplification for the use with rigid supports. It has been developed during the internship preceding this thesis. The assembly is then slightly revisited for the use with idealized bolts.

Scientific communications

The work presented in this thesis led to the following communications

- **Journal articles**

Coupled topology optimization of structure and connections in bolted mechanical systems, L. Rakotondrainibe, J. Desai, P. Orval, G. Allaire, in preparation, 2021

Topological sensitivity analysis with respect to a small idealized bolt, L. Rakotondrainibe, G. Allaire, P. Orval, in preparation, 2021

Topology optimization of connections in mechanical systems, L. Rakotondrainibe, G. Allaire, P. Orval, Structural and Multidisciplinary Optimization, 61:2253-2269, 2020

- **Talks**

Optimisation couplée de la structure et des liaisons vissées d'un assemblage mécanique, Congrès d'Analyse Numérique pour les jeunes, CAN-J 2020 - online - December 2020

Optimisation topologique couplée de la structure et des liaisons vissées d'un assemblage, ANR-SHAPO - online - October 2020

Coupled optimization of both structure and mechanical connections (location and number), Programme Gaspard Monge PGMO Days - Saclay, France - December 2019

Topology optimization of connections in mechanical systems, 13th World Congress on Structural and Multidisciplinary Optimization WCSMO 13 - Beijing, China - May 2019

- **Posters**

Optimisation topologique des liaisons dans les systèmes mécaniques, Journées Optimisation de Formes et Applications JOFA 4 - Palaiseau, France - October 2019

Optimisation topologique des liaisons dans les systèmes mécaniques, 14ème Colloque national en calcul des structures CSMA 2019 - Giens, France - May 2019

Optimisation topologique des liaisons dans les systèmes mécaniques, 44ème Congrès National d'Analyse Numérique CANUM 2018 - Cap d'Adge, France - May 2018

Part I

Mathematical tools and modelling

Background theory

Contents

1.1	Shape optimization	17
1.1.1	Generalities	17
1.1.2	Classical methods	18
1.1.3	Hadamard's method for shape sensitivity analysis	19
1.1.4	Topological sensitivity analysis	21
1.1.5	Constraints integration	22
1.2	Mechanical connections optimization	25
1.2.1	Bolts optimization	25
1.2.2	Embedded support connections	25
1.2.3	Multi-component systems	26

This chapter introduces shape optimization through most commonly used methods. Then, we focus on the Hadamard's boundary variation method for shape modification. The framework of topological sensitivity analysis is given for topological variation of a structure. Most of the optimization problems investigated in this thesis are under constraints. They are handled by the Augmented Lagrangian method which general outline is given here. Finally, a non-exhaustive state of the art is drawn up for bolts, springs, supports and multi-component systems optimization.

1.1 Shape optimization

1.1.1 Generalities

Shape optimization is a well-established mathematical theory. A shape optimization problem is defined with three ingredients :

- **a model** that describes the physical behavior of the structure to optimize. It is usually expressed by partial differential equations.
- **an objective function**, also named cost function and denoted J , to be minimized or maximized. It is generally a physical or a geometrical characteristic of the structure, such as the compliance or the volume.
- **a set of admissible shapes**, denoted \mathcal{U}_{ad} , evaluated by the model. It takes into account potential constraints imposed on design-variables.

The purpose of shape optimization is to find the best shape described by a given model in the set of admissible shapes. Its properties optimize an objective function and respect imposed constraints. The problem generally reads

$$\min_{\Omega \in \mathcal{U}_{ad}} J(\Omega). \quad (1.1)$$

Shape optimization is classified in three categories (cf. Fig. 1.1) :

- **parametric optimization** : shapes are modified according to a small set of variables such as thickness, diameter, height, etc...
- **geometric optimization** : boundaries of the structure are allowed to change but the topology is fixed.
- **topology optimization** : boundaries and topology of the structure are allowed to change. This approach has the largest set of admissible shapes.

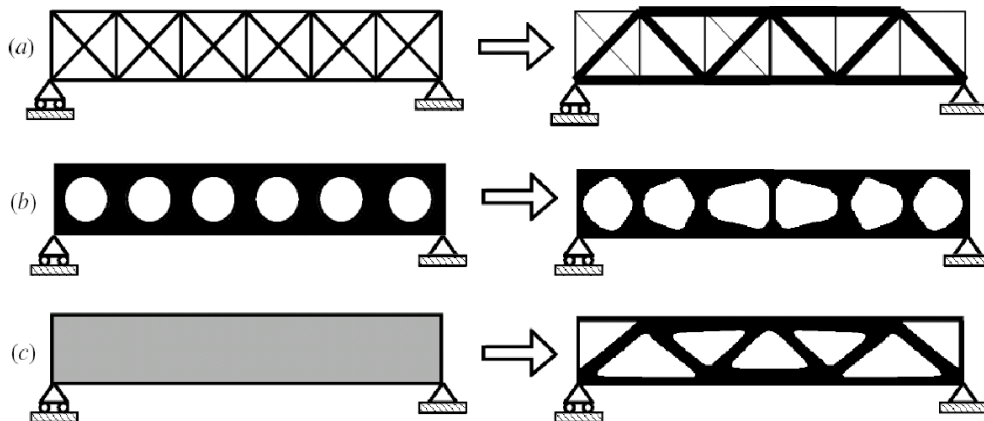


Figure 1.1: Truss structure from the initial design on the left hand-side to the optimal structure on the right using three categories of structural optimization : (a) size, (b) shape, (c) topology (figures from [20])

1.1.2 Classical methods

Shape optimization is a well-established field with a wide range of implemented methods. This section gives a short overview of the most popular ones.

Density and homogenization based methods

Density-based methods consist in optimizing a density function ρ that corresponds to the presence ($\rho = 1$) or the absence ($\rho = 0$) or intermediate cases ($0 < \rho < 1$) of material. These intermediate densities exhibit unclear contours. Some penalization scheme is required to interpret them and then get the convergence to real shapes. The Solid Isotropic Material Penalization method (commonly called SIMP method) is one of the simplest and most implemented methodology [18, 20]. This method is largely employed for the linear elasticity problem [98]. This is also the method used by the majority of commercial topology optimization softwares. Other density methods, close to the SIMP method, are the Rational Approximation of Material Properties (RAMP) [114], the SINH method [30], the Optimal Microstructure with Penalization (OMP) [97], etc...

The homogenization method was introduced by [67, 71, 82, 83] and popularized in mechanical engineering by [19]. It consists in finding the optimal varying microstructure to characterize a composite material. This method is related to density methods because the parameters of the microstructure are first optimized as material density. They are thus interpreted in a second phase. The reader can refer to [4] for more details.

Geometric optimization

Consider a shape with a given topology and boundaries. Geometric optimization consists in varying the boundaries location without changing the topology of the shape. It relies on the Hadamard's boundary variation method [59], detailed in Section 1.1.3. In addition, some geometrical regularity constraints are necessary to ensure existence of an optimal shape [38, 81, 10]. Mesh deformation algorithms have proved their efficiency to perform geometric optimization [9].

Level-set method

The level-set method was introduced by [91] (see also the textbooks [90, 103]). This method has been applied on a wide range of problems, such as Computational Fluid Dynamics [79, 104], solid-fluid coupling [37, 90], image analysis [73, 99], combustion [118, 133], structural optimization [7, 123], and many others. The level-set method offers a large flexibility in topological changes and the boundaries of the structure are explicitly defined. In the present work, structures are represented with the level-set method.

Let us outline the method. Consider a working domain $\mathcal{D} \subset \mathbb{R}^n$ that contains all admissible shapes. Structures are parameterized by a function ψ defined on \mathcal{D} such that

$$\begin{cases} \psi(\mathbf{x}) = 0 & \iff \mathbf{x} \in \partial\Omega \cap \mathcal{D} \\ \psi(\mathbf{x}) < 0 & \iff \mathbf{x} \in \Omega \\ \psi(\mathbf{x}) > 0 & \iff \mathbf{x} \in (\mathcal{D} \setminus \Omega) \end{cases} . \quad (1.2)$$

Then the boundaries of the structure are defined as the zeros of the level-set function. The shape is captured on a fixed mesh. In other words, the optimization does not require a

remeshing process. The boundary of the structure evolves in time with the transport equation of Hamilton-Jacobi

$$\begin{cases} \frac{\partial \psi}{\partial t} + V|\nabla \psi| = 0 \text{ on } [0, \infty[\times \mathbb{R}^n, \\ \psi(t = 0, \mathbf{x}) = \psi_0(\mathbf{x}) \end{cases}, \quad (1.3)$$

where $V(t, \mathbf{x})$, with $t \in \mathbb{R}^+$, is the velocity field. The level-set method is implemented here on one of the most famous topology optimization test case in linear elasticity (see Fig. 1.2). The problem is to minimize the volume of the structure (in black) with a compliance target. To avoid undefined tensor when the elasticity problem is solved, the void (in white) is replaced by an ersatz material.

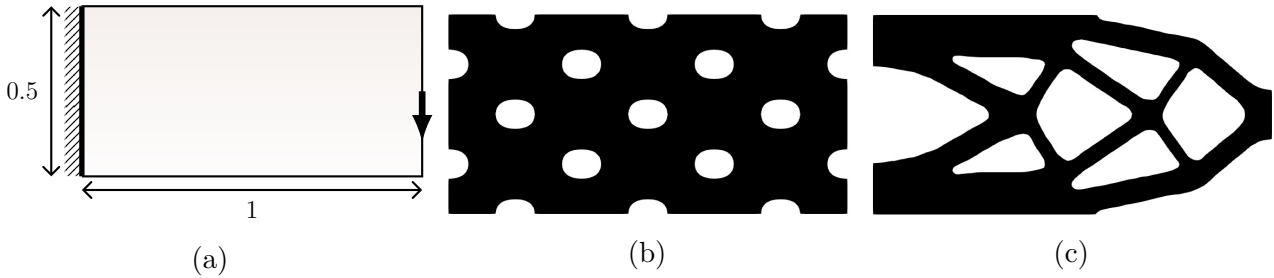


Figure 1.2: Cantilever 2d : the loading (a) from initial design (b) to final design (c)

Phase field method

The phase field method is a general interface tracking approach, close to the level-set method. It was introduced by [29] to handle perimeter constraints and represent phase transition phenomena on a given surface, such as solid-liquid transitions. Then phase field method has then been used to deal with local stress constraints or solid-void transitions [33, 117, 124]. The system is represented by a phase field function that has a constant value in one phase, the opposite value on the other phase and is zero on the interface.

Topological derivative method

Also known as the "bubble-method" [36, 47, 107] in the framework of shape optimization, the topological derivative method is one of the main issues of this thesis. Therefore, it is described properly in Section 1.1.4.

Evolutionary methods

Evolutionary Structural Optimization (ESO) is an heuristic-based approach using discrete variables [127, 128, 131]. The structure goes to an optimum by removing repetitively inefficient material by the means of "hard-kill" methods. Bidirectional Evolutionary Structural Optimization (BESO) is based on ESO but allows to add new elements [62, 95].

1.1.3 Hadamard's method for shape sensitivity analysis

Hadamard's boundary variation method was introduced by [59]. This method describes shape variations. It relies on the notion of differentiation with regards to the position of a shape Ω [5, 94, 109]. Thus, this method matches well with gradient-based algorithm and with the

level-set method. Let $\Omega \subset \mathbb{R}^n$ be a given reference shape. Assume that Ω is an open, smooth and bounded domain of \mathbb{R}^n . Let us introduce the space of Lipschitz bounded vector fields [31]

$$W^{1,\infty}(\mathbb{R}^n, \mathbb{R}^n) = \left\{ \boldsymbol{\theta} \in L^\infty(\mathbb{R}^n, \mathbb{R}^n), \nabla \boldsymbol{\theta} \in L^\infty(\mathbb{R}^n, \mathbb{R}^{n \times n}) \right\}. \quad (1.4)$$

Let $\boldsymbol{\theta} \in W^{1,\infty}(\mathbb{R}^n, \mathbb{R}^n)$ be a displacement field of small amplitude. In other words, it satisfies $\|\boldsymbol{\theta}\|_{W^{1,\infty}(\mathbb{R}^n, \mathbb{R}^n)} < 1$. Then, the transformation $\mathbf{Id} + \boldsymbol{\theta}$ is a diffeomorphism of \mathbb{R}^n . The purpose of Hadamard's boundary variation method is to transport the reference domain Ω into an admissible shape $\Omega_\theta = (\mathbf{Id} + \boldsymbol{\theta})(\Omega)$. The vector $\boldsymbol{\theta}$ moves slightly all points of Ω from a location \mathbf{x} to a deformed location $\mathbf{x} + \boldsymbol{\theta}(\mathbf{x})$ as displayed in Fig. 1.3.

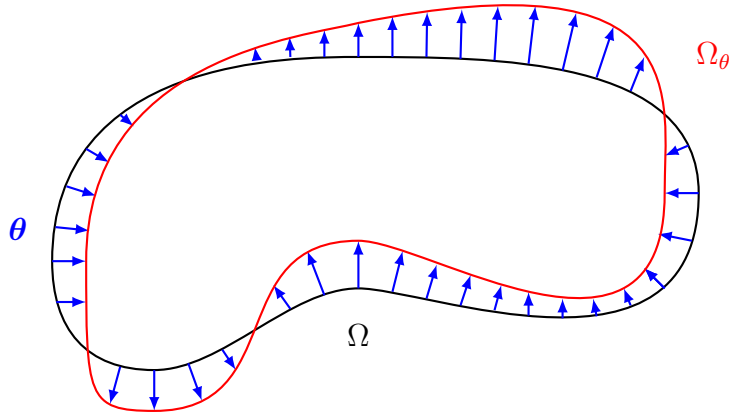


Figure 1.3: Transportation of a domain Ω to a domain Ω_θ with the Hadamard's boundary variation method

Definition 1. Let $J(\Omega)$ be a function from the set of admissible shapes \mathcal{U}_{ad} to \mathbb{R} . The shape function J is said to be shape differentiable if there exists a continuous linear form $J'(\Omega)$ acting on $W^{1,\infty}(\mathbb{R}^n, \mathbb{R}^n)$ such that

$$J((\mathbf{Id} + \boldsymbol{\theta})(\Omega)) = J(\Omega) + J'(\Omega)(\boldsymbol{\theta}) + o(\boldsymbol{\theta}), \text{ where } \lim_{\boldsymbol{\theta} \rightarrow \mathbf{0}} \frac{|o(\boldsymbol{\theta})|}{\|\boldsymbol{\theta}\|_{W^{1,\infty}(\mathbb{R}^n, \mathbb{R}^n)}} = 0. \quad (1.5)$$

The function $J'(\Omega)$ is called the shape derivative of the shape functional J . This notion of shape derivative is extensively discussed in [80, 81, 94, 109]. We give two basic examples of shape derivatives which are useful for the sequel.

Proposition 1. Let Ω be a smooth, bounded, open set of \mathbb{R}^n . Let $f \in W^{1,1}(\mathbb{R}^n, \mathbb{R}^n)$ and J a shape functional from \mathcal{U}_{ad} to \mathbb{R}^n defined by

$$J(\Omega) = \int_{\Omega} f dV.$$

Then, J is shape differentiable and it holds

$$J'(\Omega)(\boldsymbol{\theta}) = \int_{\Omega} \operatorname{div}(f\boldsymbol{\theta}) dV = \int_{\partial\Omega} f\boldsymbol{\theta} \cdot \mathbf{n} dS, \quad \forall \boldsymbol{\theta} \in W^{1,\infty}(\mathbb{R}^n, \mathbb{R}^n), \quad (1.6)$$

where \mathbf{n} is the outward normal to Ω .

Proposition 2. *Let Ω be a smooth, bounded, open set of \mathbb{R}^n . Let $f \in W^{2,1}(\mathbb{R}^n, \mathbb{R}^n)$ and J a shape functional from \mathcal{U}_{ad} to \mathbb{R}^n defined by*

$$J(\Omega) = \int_{\partial\Omega} f dS.$$

Then, J is shape differentiable and it holds

$$J'(\Omega)(\boldsymbol{\theta}) = \int_{\partial\Omega} \left(\frac{\partial f}{\partial \mathbf{n}} + Hf \right) \boldsymbol{\theta} \cdot \mathbf{n} dS, \quad \forall \boldsymbol{\theta} \in C^{1,\infty}(\mathbb{R}^n, \mathbb{R}^n), \quad (1.7)$$

where \mathbf{n} is the outward normal to Ω and H is the mean curvature of $\partial\Omega$ that reads $H = \operatorname{div}(\mathbf{n})$.

1.1.4 Topological sensitivity analysis

The main goal of topological sensitivity analysis is to compute a quantity called topological derivative, or topological gradient. As introduced in [36, 86, 102, 107, 108], the topological derivative indicates where it might be more interesting to introduce a small inclusion or a small hole with specific boundary conditions. Let Ω be a smooth bounded domain of \mathbb{R}^n , ($n = 2$ or 3). In [11, 51, 86, 107], the topological derivative is obtained by an asymptotic analysis of an objective function with respect to the creation of $\omega_\rho \subset \Omega$, a small hole or a small inclusion with suitable boundary conditions. This small perturbation (see Fig. 1.4) is centred at a point \mathbf{x}_0 in the domain and has a fixed shape ω that is rescaled by a small adimensional factor $\rho > 0$, namely

$$\omega_\rho = \left\{ \mathbf{x} \in \mathbb{R}^3, \frac{\mathbf{x} - \mathbf{x}_0}{\rho} \in \omega \right\}. \quad (1.8)$$

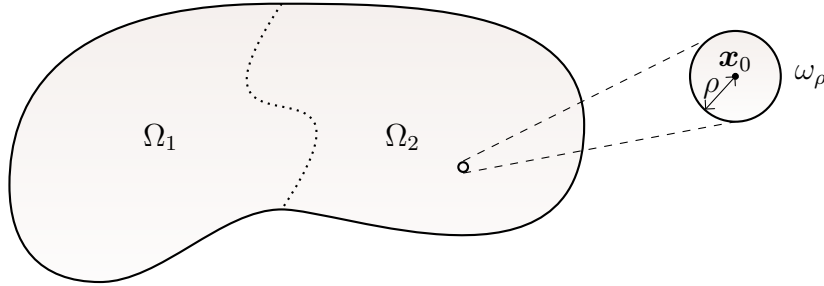


Figure 1.4: Perturbation of a domain Ω with a small inclusion or hole ω_ρ

Consider some objective function J to minimize and denote by $J_\rho(\Omega)$ its value in the domain Ω , perturbed by ω_ρ (thus, $J_0(\Omega)$ is its value in the unperturbed or background domain Ω).

Definition 2. *The objective function J_ρ is said to admit a topological derivative $DJ(\mathbf{x}_0)$ at the point \mathbf{x}_0 for an inclusion of shape ω , if the following asymptotic expansion holds for small $\rho > 0$*

$$J_\rho(\Omega) = J_0(\Omega) + s(\rho)DJ(\mathbf{x}_0) + o(s(\rho)), \quad (1.9)$$

where s is a positive scalar function of ρ satisfying $\lim_{\rho \rightarrow 0} s(\rho) = 0$. Then, the term $DJ(\mathbf{x}_0)$ is the topological derivative at the point \mathbf{x}_0 .

If the quantity $DJ(\mathbf{x}_0)$ is negative, it is then favorable to create a small hole or a small inclusion at the point \mathbf{x}_0 .

The topological derivative can be computed with an integral approach or layer potential techniques as in [11, 51, 56] or with a variational approach [8]. This notion has been deployed for a wide range of models, for various purposes : Navier-Stokes equations in [12] (for holes with Dirichlet boundary condition), Poisson equation in [56] (also for holes with Dirichlet boundary condition), Helmholtz equation for wave guide optimization in [100], crack detection in [13], image processing in [15], inverse problems in [11, 28], etc... The topological derivative has also been investigated in the framework of the elasticity problem, which is closer to the purpose of the present thesis. The influence of an arbitrary shaped hole with Neumann boundary condition for the linear elasticity problem is analyzed in [51]. This study relies on a generalized adjoint method and use a truncation domain technique. It allows to work with two domains independent of the size of the perturbation and provides suitable spaces for the asymptotic analysis. In [53], the authors study the asymptotic expansion of a shape functional with regards to the introduction of a small spherical hole, with homogeneous Neumann boundary condition, for an elastic problem with a frictionless contact model. The domain is under a sliding contact condition with a rigid foundation. The topological derivative is established in 3d using a domain decomposition method similarly to the method of [51]. This study provides a topological derivative of the same form as the one of the classic elasticity problem. The contact condition is implicitly expressed through the displacement and the adjoint fields. The topological derivative has also been computed for anisotropic elasticity problems [52]. In [8], the problem is to nucleate an infinitesimal damaged region inside a linear elastic domain. The material properties of the spherical inclusion differ from the unperturbed domain ones. The topological derivative is computed with variational techniques. The present thesis follows the same variational approach of topological sensitivity analysis. Table 1.1 gives a non-exhaustive list of the state of art of the topological sensitivity analysis.

1.1.5 Constraints integration

Consider an optimization set \mathcal{W} , a differentiable objective function $J : \mathcal{W} \rightarrow \mathbb{R}$ and the following standard constrained optimization problem

$$\begin{aligned} & \min_{\mathbf{x} \in \mathcal{W}} && J(\mathbf{x}), \\ & \text{s.t.} && \begin{cases} \mathbf{C}_1(\mathbf{x}) = \mathbf{0} \\ \mathbf{C}_2(\mathbf{x}) \leq \mathbf{0} \end{cases} \end{aligned} \tag{1.10}$$

where $\mathbf{C}_1 : \mathcal{W} \rightarrow \mathbb{R}^p$ and $\mathbf{C}_2 : \mathcal{W} \rightarrow \mathbb{R}^q$ are respectively differentiable functions accounting for p equality and q inequality differentiable constraints.

Generalities

Most popular iterative methods are : Penalty, Interior Point, Sequential Quadratic Programming (SQP) and Sequential Linear Programming (SLP), the Method of Moving Asymptotes (MMA) and the Method of Feasible Directions (MFD) [27, 49, 64, 70, 84, 111, 115, 119, 139].

Constrained optimization problems of this thesis are handled with a penalty method. Penalization is a line-search approach that measures the progress made from an iteration to the next

Physical model	Applications	Type of the perturbation	Shape	Boundary condition	References
Linear elasticity	Damage evolution modelling	Inclusion	Spherical	Change of the inclusion material properties	[8]
					[85]
Elasticity with sliding contact model	Vary the topology of a structure during the optimization process	Hole	Arbitrary	Neumann	[51, 107]
Anisotropic elasticity			Spherical		[53]
		Poisson equation	Inclusion	Arbitrary	Dirichlet
Navier-Stokes			Hole		
Helmholtz	Wave guide optimization	Hole	Spherical	Dirichlet	[12]
Laplace equation	Crack detection		Arbitrary		Neumann
Wave equation	Inverse problem	Inclusion		Arbitrary	
			Image processing		Hole

Table 1.1: Non-exhaustive overview of the state of the art of topological sensitivity analysis

one through an auxiliary function \mathcal{L} , called the merit function. This function is of the form

$$\mathcal{L}(\mathbf{x}) = J(\mathbf{x}) + P(\mathbf{x}),$$

where J is the objective function to be minimized and P is a function penalizing the constraint violation. This approach embraces Quadratic penalization, Lagrangian and Augmented Lagrangian methods. In the following, the Augmented Lagrangian method is exclusively used for all constrained optimization problems.

Augmented Lagrangian

The current section provides formulations of the Augmented Lagrangian method for equality and inequality constrained optimization problems. The reader can refer to [27, 40, 70, 84] for more details.

- **Equality constraints**

Consider the equality-constrained problem

$$\min_{\substack{\mathbf{x} \in \mathcal{W} \\ \text{s.t. } \mathbf{C}(\mathbf{x}) = \mathbf{0}}} J(\mathbf{x}), \quad (1.11)$$

where $C : \mathcal{W} \rightarrow \mathbb{R}^p$ is a differentiable function accounting for p equality constraints. Also called the method of multipliers, the Augmented Lagrangian method combines the Lagrangian function $\boldsymbol{\alpha} \cdot \mathbf{C}(\mathbf{x})$ and the quadratic penalty function $\frac{\beta}{2} |\mathbf{C}(\mathbf{x})|^2$. Thus the problem (1.11) is rewritten as

$$\min_{\mathbf{x} \in \mathcal{W}} \max_{\boldsymbol{\alpha} \in \mathbb{R}^p} \left\{ \mathcal{L}(\mathbf{x}) := J(\mathbf{x}) + \boldsymbol{\alpha} \cdot \mathbf{C}(\mathbf{x}) + \frac{\beta}{2} |\mathbf{C}(\mathbf{x})|^2 \right\}, \quad (1.12)$$

where $\boldsymbol{\alpha}$ are Lagrange multipliers and $\beta > 0$ is the penalty parameter. The Lagrange multiplier is updated at each iteration according to the optimality condition

$$\boldsymbol{\alpha}_{k+1} = \boldsymbol{\alpha}_k + \beta \mathbf{C}(\mathbf{x}_k). \quad (1.13)$$

The penalty parameter can be fixed or can be regularly increased during the optimization process.

- **Inequality constraints**

Consider now the inequality-constrained problem

$$\min_{\substack{\mathbf{x} \in \mathcal{W} \\ \text{s.t. } \mathbf{C}(\mathbf{x}) \leq \mathbf{0}}} J(\mathbf{x}), \quad (1.14)$$

where $C : \mathcal{W} \rightarrow \mathbb{R}^q$ is a differentiable function accounting for q inequality constraints. The problem (1.14) is converted to an equality-constrained problem by introducing slack variable \mathbf{s} and replacing the inequality $\mathbf{C}(\mathbf{x}) \leq \mathbf{0}$ by

$$\mathbf{C}(\mathbf{x}) + \mathbf{s} = \mathbf{0}, \quad \mathbf{s} \geq \mathbf{0}. \quad (1.15)$$

Then, the problem is rewritten as

$$\min_{\mathbf{x} \in \mathcal{W}, \mathbf{s} \geq \mathbf{0}} \max_{\boldsymbol{\alpha} \in \mathbb{R}^p} \left\{ \mathcal{L}(\mathbf{x}) := J(\mathbf{x}) + \boldsymbol{\alpha} \cdot (\mathbf{C}(\mathbf{x}) + \mathbf{s}) + \frac{\beta}{2} |\mathbf{C}(\mathbf{x}) + \mathbf{s}|^2 \right\}, \quad (1.16)$$

where $\boldsymbol{\alpha}$ are Lagrange multipliers and $\beta > 0$ is the penalty parameter. An analytical minimization of \mathcal{L} with respect to \mathbf{s} states that

$$\frac{\partial \mathcal{L}}{\partial \mathbf{s}} = 0 \iff \mathbf{s} = -\frac{\boldsymbol{\alpha}}{\beta} - \mathbf{C}(\mathbf{x}) \text{ if } \mathbf{s} \geq \mathbf{0}.$$

In other words, the optimal value of the slack variable is

$$\mathbf{s}_{opt} = \max \left(\mathbf{0}, -\frac{\boldsymbol{\alpha}}{\beta} - \mathbf{C}(\mathbf{x}) \right).$$

This optimal value is substituted into (1.14). The optimization problem is now

$$\min_{\mathbf{x} \in \mathcal{W}} \max_{\boldsymbol{\alpha} \in \mathbb{R}^p} \left\{ \mathcal{L}(\mathbf{x}) := J(\mathbf{x}) + \boldsymbol{\alpha} \cdot \max \left(\mathbf{C}(\mathbf{x}), -\frac{\boldsymbol{\alpha}}{\beta} \right) + \frac{\beta}{2} \left| \max \left(\mathbf{C}(\mathbf{x}), -\frac{\boldsymbol{\alpha}}{\beta} \right) \right|^2 \right\}. \quad (1.17)$$

1.2 Mechanical connections optimization

Shape optimization involves commonly a single part. Mechanical connections to other parts are assumed to be fixed. This section relates some works that intent to optimize jointly mechanical connections and structure. Connections are then allowed to be optimized with regards to their location, number and stiffness by adapting shape optimization methods. We present a non-exhaustive state of the art. It gathers some interesting works using, for instance, SIMP approach, the level-set method or a topological derivative formulation to manage mechanical connections optimization.

1.2.1 Bolts optimization

Complete bolt connection model provides a fine physical representativeness. Optimization studies of bolts are often investigated at the local scale of the bolt and concern properties such as load transfer, profile design, stress concentration factor or tightening process.

Bolts have standard characteristics (size, applied preload, material properties, etc...). A discrete selection in the database of bolt sizes is investigated in [22] to maximize the load carrying capability per unit mass by finding the optimal number and size of bolts. This work highlights the high importance of the pre-load in designing joints. The bolts profile (shape and rib space) is also a determinant factor of bonding capacity. Several laboratory experiments on a set of various bolts are carried out in [17] by push and pull testing to find the optimal bolt profile configuration to improve load transfer. The reader can refer to [35] for a more detailed study about bolt profile configuration and load transfer capacity optimization.

Threads design implies important stress concentrations that control bolt fatigue life. A reduction of the stress concentration factor improves the bolt performance. Such a study is investigated in [54, 92] with a finite element analysis and shape parametrization. A focus on the fillet under the head of the bolt also brings noticeable stress reduction [112].

Bolt tightening process enables the bonding between the joined parts. However, the pre-load may not be equally distributed in the bolts. This procedure is subjected to optimization in order to have uniform bolt load in [2, 42, 77].

This thesis does not focus on local optimization of bolts. Such a complete model of connection is irrelevant and we would rather use an idealized model described in Chapter 2, completed by technological constraints.

1.2.2 Embedded support connections

Embedded support is a simple and easy-to-use connection model. It is involved in many categories of structures and assemblies such as bar or frame structures. The bar properties and the supports features can be mutually optimized. For instance, a topological derivative approach is used in [26] to create new support in a coupled optimization problem of the cross-section area of bar structures and the location, number and stiffness of supports. In addition, [25, 78, 116, 93] investigate the optimization of location, number and stiffness of supports with the study of a bar or frame structure. This kind of structures often involves buckling or stability and free vibration problems. They were largely studied with regards to supports location, number and stiffness in [89, 3, 88, 24].

Concerning continuous structures, the level-set method is employed in [126] to optimize both structure and support. Supports have changing shapes and are rigid in this study. By contrast, supports are considered as elastic springs in [137]. Given a finite number of possible fixed

locations, the authors use a SIMP approach to find the optimal supports configuration. The springs are characterized by a penalization coefficient. Then, they are considered as inactive when the coefficient reaches the lower bound while they are fully active when the coefficient reaches the upper bound. A coupled optimization of both structure and supports, also with density approaches, is performed in [32], where the author puts springs in some identified support areas. An other example of supports modeled by elastic springs is investigated in [16]. The optimal locations and number of springs that support vibrating cantilever beam is determined to minimize the shear force of the support of the beam. In [110], supports are modeled by various boundary conditions delimited by separated segments. In [122], connections are successively modeled by elastic then by rigid supports. Geometric methods complete classical shape optimization techniques and provide satisfactory results for the optimization of supports components in [138]. Non-overlapping conditions are imposed through these geometric methods.

1.2.3 Multi-component systems

Classically, shape or topology optimization isolates the part to be optimized from a mechanical assembly and boundary conditions are adapted accordingly. Actually, the modeling of the complete system is time-consuming but still may be worth to consider as system-level approach often offers much better results. Therefore a system-level approach is performed here purposefully, e.g. for a structure and connections coupled optimization. It requires the right balance between the refinement of the structure model and the connection model. Focus on the bolt fastener, a complete model (rigorous geometry description with the head and the threads) is not necessary and should be avoided for a macroscopic assembly analysis used in a coupled optimization of both structure and connections, ditto for welding spots and other complex fasteners. Therefore, they should be simplified.

In [63], spot-welds and adhesive bonds are modeled by springs scaled by a penalization parameter. Two problems are considered. The first one aims to reduce cost by reducing the number of connections for a given performance of the structural system. A SIMP approach is then used to penalize spring rigidity which allows to limit the number of connections for 3d multi-components system. The second problem improves the compliance of the system for a given number of connections. A multi-point constraints (MPC) based method is applied in [134, 135] to define rivets or bolts connections in the design of multi-component systems. This method relies on nodal displacements analysis. Actually, an extremity of the connection on one part is identified as a node. The other extremity is its projection on the other part. The connection behavior is expressed through a stiffness matrix. Fatigue analysis is crucial for assembled structure design and for bolts characterization. In [61], bolts are modeled by bar elements connecting two circular surfaces embodying fastener holes. A control volume is defined around bolts to evaluate the stress state. The considered problem is to minimize the structure compliance under fatigue failure constraints with Sines criterion. An optimal layout of fasteners is determined in [87] with a fatigue design. The Von-Mises equivalent strain and shear loads in the joints are improved. In [136], connections are modeled by short beam elements but bolt-hole clearances are not represented. The stiffness distribution of joined structures is optimized to control fasteners shear loads. For more industrial implementations of connections optimization, one can refer to [34, 65, 75]. Recent advancements of topology optimization of multi-component structural design accentuate the interest in coupling structure and connections optimization (see e.g. [69, 125, 132]). Most of these works rely on gradient-based methods. Nevertheless, other methods are effective to optimize connections. For example, evolutionary and genetic algorithms are proposed in [68, 121, 120] to optimize structure and connections.

Assembly model with an idealized bolt connection

Contents

2.1 Bolt idealization	28
2.1.1 Generalities	28
2.1.2 Analytic constitutive behavior	28
2.1.3 Pre-stressed state and in-service state	30
2.2 Basis model : two elastic spheres linked by a pre-stressed spring .	32
2.2.1 Step 1 : pre-stressed state	32
2.2.2 Step 2 : in-service state	34
2.2.3 Existence and uniqueness	36
2.3 Variant model : two rigid spheres linked by a pre-stressed spring	37
2.3.1 Step 1 : pre-stressed state	38
2.3.2 Step 2 : in-service state	40
2.4 Mechanical constraints specific to the bolt	42
2.4.1 Torsor of inner efforts	42
2.4.2 Elasticity of the root	43
2.4.3 Fatigue of the root	44
2.4.4 Torsion locking of the root	45
2.4.5 Miscellaneous	45
2.5 Constraints integration in optimization problems	45
2.5.1 Setting of the problem	45
2.5.2 Adjoint state	46
2.5.3 Shape derivatives	48

This chapter establishes an idealized model of a standard long bolt in 3d. We consider here an assembly of two parts in contact linked by such an idealized bolt. This model embodies the head and the threads of the bolt by two spheres linked by a 6 degrees of freedom Euler-Bernoulli beam subjected to a prestressed state. The reference model deals with elastic spheres. A variant model, dealing with rigid spheres, is also studied. The tightening process provoking the prestress and the commissioning are described in two steps according to a mechanically and mathematically complete and rigorous formulation, which is commonly used in finite element models of assembled system. It is thus noticeable that the whole idealized model is equivalent to common finite element techniques for use at system-level interest. For the purpose of topology optimization, technological constraints, specific to bolt strength and resistance, are derived with regards to the idealized model.

2.1 Bolt idealization

2.1.1 Generalities

There exist different types of mechanical assembly, such as bolted, glued or welded joints. This thesis focuses on bolted assembly. The term "bolt" is often mixed up with the term "screw". Even if this work focuses on bolts, the present analysis is still accurate for screws. A complete description of bolts design and complex behavior is given in [23]. Bolts behavior has been analyzed by the finite element (FE) method in [76, 130, 129]. A larger bibliographical review of FE method applied for the analysis of bolted joints and other assemblies is given in [72]. This method provides a fine modelling with detailed local results but its computation is costly and useless for the purpose of system-level optimization. Then, it is worth to use simplified models of bolt connection in some contexts [21, 55] and even resort to analytical models [41, 57]. The framework of topology optimization does not require such detailed description of bolt connections.

2.1.2 Analytic constitutive behavior

We would rather consider an analytical formulation to establish an idealized model. Physical representativeness is kept at first order and analysis of results nearby the extremities of the bolt are not to be considered. This model aims to be easy to use for optimization process and topological derivative developments.

We propose a simple representation in which the bolt is embodied by two spheres symbolizing its head and its thread, respectively denoted by ω_A and ω_B (see Fig. 2.1). These spheres allow efforts transmission and displacements continuity between the bolt extremities and the jointed parts. They are separated by a distance ℓ , in the direction of a unit vector \mathbf{e} , and have a radius r_b . The length ℓ stands for the implantation length of the bolt in the assembly and the radius r_b corresponds to the effective radius of the bolt [57]. The idealized model is associated to the rigidity matrix, \mathbf{K}_b , obeying to the Euler-Bernoulli condition for long beam which is $\ell \geq 10r_b$.

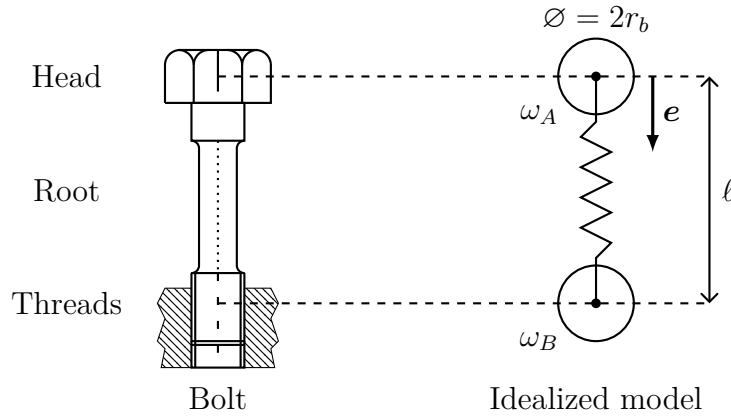


Figure 2.1: Standard bolt and the idealized model

Thus, the rigidity matrix depends on r_b and ℓ and reads at first order

$$\mathbf{K}_b = \frac{1}{1 + 1.6 \frac{r_b}{\ell}} \frac{E_b \pi r_b^2}{\ell} \begin{pmatrix} 1 & 0 & 0 & 0 & 0 & 0 \\ 0 & 3 \left(\frac{r_b}{\ell}\right)^2 & 0 & 0 & 0 & -\frac{3 r_b^2}{2 \ell} \\ 0 & 0 & 3 \left(\frac{r_b}{\ell}\right)^2 & 0 & \frac{3 r_b^2}{2 \ell} & 0 \\ \hline 0 & 0 & 0 & \frac{r_b^2}{4(1 + \nu)} & 0 & 0 \\ 0 & 0 & \frac{3 r_b^2}{2 \ell} & 0 & r_b^2 & 0 \\ 0 & -\frac{3 r_b^2}{2 \ell} & 0 & 0 & 0 & r_b^2 \end{pmatrix}, \quad (2.1)$$

where E_b is the Young modulus and ν is Poisson's ratio of the bolt root. The subscript "b" means that the matrix is written in the coordinate system of the bolt where the unit vector \mathbf{e} is oriented from ω_A to ω_B . The expression of the matrix \mathbf{K}_b (2.1) is obtained with an expansion at first order of mechanical considerations incorporating Euler-Bernoulli condition for long beam. For example, the numerical value $\left(1 + 1.6 \frac{r_b}{\ell}\right)$ comes from the calculation of the implementation length of the bolt (see technical documents [57, 58]). The degree of freedom (DOF) number 1 and 4 are in the axis \mathbf{e} . The DOFs number 2 and 3 as well as 5 and 6 are along orthogonal vectors to \mathbf{e} that constitute an orthonormal coordinate system. The spheres remotely interact with each other through the linear spring-like law

$$\mathbf{F}_b = \mathbf{K}_b \mathbf{L}_b, \quad (2.2)$$

with \mathbf{F}_b the generalized force and \mathbf{L}_b the generalized lengthening of the bolt in the coordinate system of the bolt. Vectors \mathbf{F}_b and \mathbf{L}_b have six components. The study is carried out in the framework of small deformations. Then, the first three ones of \mathbf{L}_b stand for translations and the last three components are infinitesimal rotations. Briefly stated, the idealized model corresponds to two spheres linked by a 6 DOFs linear-spring. Then the spheres are represented in the FE model while the root is only modeled by means of the analytical law (2.2).

The tightening of the bolt is modeled by a pre-stressed state computed over the whole assembly model. The pre-tension force is then the unique load which is remotely applied between the two spheres.

2.1.3 Pre-stressed state and in-service state

In practice, a bolted joint is carried out by applying a tightening torque to the head of the bolt. It creates a pre-stressed state, denoted "Step 1", characterized by an elongation of the root of the bolt and a local compression of the jointed parts. Thus, the pre-stress ensures the contact between parts and thus avoids detachment. In the following, the pre-stress is obtained by applying a given tension force inside the idealized bolt. This process is well developed in computational software, such as ABAQUS [106] and NASTRAN [1]. This section describes how our idealized model suits to this process too.

The rigidity matrix \mathbf{K}_b is decomposed into a traction/torsion matrix and a shear/flexion matrix, respectively denoted $\bar{\mathbf{K}}_b$ and $\tilde{\mathbf{K}}_b$. They read

$$\bar{\mathbf{K}}_b = \frac{1}{1 + 1.6 \frac{r_b}{\ell}} \frac{E_b \pi r_b^2}{\ell} \begin{pmatrix} 1 & 0 & 0 & 0 & 0 & 0 \\ 0 & 0 & 0 & 0 & 0 & 0 \\ 0 & 0 & 0 & 0 & 0 & 0 \\ \hline 0 & 0 & 0 & \frac{r_b^2}{4(1 + \nu)} & 0 & 0 \\ 0 & 0 & 0 & 0 & 0 & 0 \\ 0 & 0 & 0 & 0 & 0 & 0 \end{pmatrix}, \quad (2.3)$$

$$\tilde{\mathbf{K}}_b = \frac{1}{1 + 1.6 \frac{r_b}{\ell}} \frac{E_b \pi r_b^2}{\ell} \begin{pmatrix} 0 & 0 & 0 & 0 & 0 & 0 \\ 0 & 3 \left(\frac{r_b}{\ell}\right)^2 & 0 & 0 & 0 & -\frac{3 r_b^2}{2 \ell} \\ 0 & 0 & 3 \left(\frac{r_b}{\ell}\right)^2 & 0 & \frac{3 r_b^2}{2 \ell} & 0 \\ \hline 0 & 0 & 0 & 0 & 0 & 0 \\ 0 & 0 & \frac{3 r_b^2}{2 \ell} & 0 & r_b^2 & 0 \\ 0 & -\frac{3 r_b^2}{2 \ell} & 0 & 0 & 0 & r_b^2 \end{pmatrix}, \quad (2.4)$$

The matrix \mathbf{K}_b and its decomposed parts $\bar{\mathbf{K}}_b$ and $\tilde{\mathbf{K}}_b$, are symmetric. They are all rewritten in the Cartesian coordinates (remove the subscript "b"). They are then written as block matrices and notice that non-diagonal blocks are opposite

$$\mathbf{K} = \begin{pmatrix} \mathbf{K}_{11} & \mathbf{K}_{12} \\ -\mathbf{K}_{12} & \mathbf{K}_{22} \end{pmatrix}, \quad \bar{\mathbf{K}} = \begin{pmatrix} \bar{\mathbf{K}}_{11} & 0 \\ 0 & \bar{\mathbf{K}}_{22} \end{pmatrix} \quad \text{and} \quad \tilde{\mathbf{K}} = \begin{pmatrix} \tilde{\mathbf{K}}_{11} & \tilde{\mathbf{K}}_{12} \\ -\tilde{\mathbf{K}}_{12} & \tilde{\mathbf{K}}_{22} \end{pmatrix} \quad \text{such that} \quad \mathbf{K} = \bar{\mathbf{K}} + \tilde{\mathbf{K}}.$$

Diagonal blocks are symmetric matrices and non-diagonal blocks \mathbf{K}_{12} and $\tilde{\mathbf{K}}_{12}$ are skew-symmetric matrices, $\mathbf{K}_{12} = -\mathbf{K}_{12}^T$ and $\tilde{\mathbf{K}}_{12} = -\tilde{\mathbf{K}}_{12}^T$.

Let us consider two disjointed parts Ω_A and Ω_B to assemble with one idealized bolt. Then Ω_A and Ω_B are close to one another. Let Ω be the union of Ω_A and Ω_B . This union is assumed to be a smooth bounded domain of \mathbb{R}^3 . The boundary of this domain is made of two disjointed parts, $\partial\Omega = \Gamma_N \cup \Gamma_D$. Neumann and Dirichlet boundary conditions are respectively imposed on Γ_N and Γ_D . Let the domain Ω be filled by linear isotropic elastic materials. For a displacement field \mathbf{u} , the strain tensor is defined by $\varepsilon(\mathbf{u}) = \frac{1}{2}(\nabla \mathbf{u} + \nabla^T \mathbf{u})$. The stress tensor is then given by the Hooke's law

$$\mathbf{A}\varepsilon(\mathbf{u}) = \begin{cases} 2\mu_A \varepsilon(\mathbf{u}) + \lambda_A \text{tr}(\varepsilon(\mathbf{u})) \mathbf{I} & \text{in } \Omega_A \\ 2\mu_B \varepsilon(\mathbf{u}) + \lambda_B \text{tr}(\varepsilon(\mathbf{u})) \mathbf{I} & \text{in } \Omega_B \end{cases},$$

where μ_A and λ_A (resp. μ_B and λ_B) are the Lamé coefficients of the material Ω_A (resp. Ω_B). Fig. 2.2 pictures the pre-stressed state, or Step 1, resulting from tightening torque. It is executed in the absence of in-service external loads. Nevertheless, the assembly process may require some holding external forces \mathbf{f}_1 and \mathbf{g}_1 . This first step consists in identifying the extremities ω_A and ω_B in the domain Ω and having the root behave according to the rigidity matrix $\tilde{\mathbf{K}}$ (*i.e.* only in shear/flexion modes). A pre-stress external force of amplitude Φ is applied compressively and mutually between each domain ω_A and ω_B along the direction \mathbf{e} . This elasticity problem results in a displacement field \mathbf{u}_{S1} computed over the domain Ω . The subscript "S1" refers to Step 1. Besides for completion, the traction behavior of the root is considered only for internal forces and not for displacements. Euler-Bernoulli slenderness condition allows this approximation and it is noticeable that rigidity matrix $\bar{\mathbf{K}}$ does not interfere for Step 1 computation. Traction force induced by tightening in the root is equal to Φ for static equilibrium respect. Finally, complete realistic inner root forces are addition of both initial tightening force and the resulting force of the pre-displacement created by the pre-stressed state.

The second step consists in the evaluation of in-service equilibrium state for the previously stressed assembly. It is pictured in Fig. 2.3. The holding forces \mathbf{f}_1 and \mathbf{g}_1 are removed and in-service external loads \mathbf{f}_2 and \mathbf{g}_2 are applied in this step. The root behaves in all 6 degrees of freedom. The root is then associated to its rigidity matrix \mathbf{K} . The displacement field \mathbf{u}_{S1} involves a pre-stressed state in the assembly and is imposed as a pre-displacement field over the domain Ω . In the same manner, now in the second step, the pre-stress force of amplitude Φ is acting as an internal force. This second elasticity problem results in a displacement field \mathbf{u}_{S2} computed over the domain Ω . The subscript "S2" refers to Step 2.

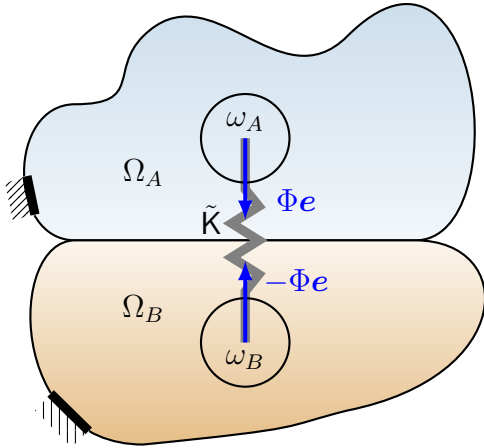


Figure 2.2: Step 1

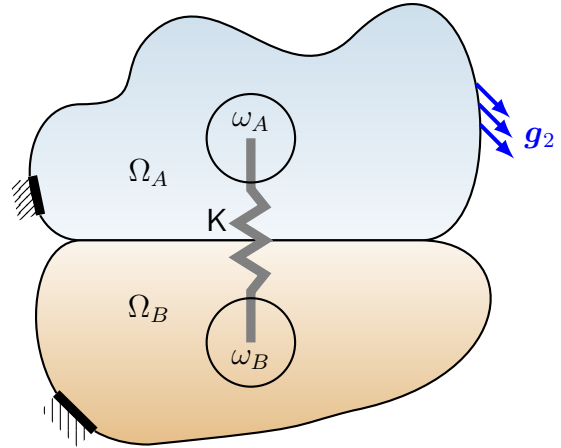


Figure 2.3: Step 2

In the following, we consider an average approach and a non-local interaction between ω_A and ω_B . Thus, the lengthening of the root is the difference between the average degrees of freedom in ω_A and ω_B . Let us introduce the notation \mathbf{W}^A , for the average degrees of freedom

on ω_A of an arbitrary displacement field \mathbf{w}

$$\mathbf{W}^A = \left(\begin{array}{c} \int_{\omega_A} \mathbf{w} dV \\ \frac{1}{2} \int_{\omega_A} \text{curl}(\mathbf{w}) dV \end{array} \right) = \left(\begin{array}{c} \frac{1}{|\omega_A|} \int_{\omega_A} \mathbf{w} dV \\ \frac{1}{2|\omega_A|} \int_{\omega_A} \text{curl}(\mathbf{w}) dV \end{array} \right).$$

Average degrees of freedom are denoted by the capital letter of the involved displacement field. The exponent A (resp. B) refers to ω_A (resp. ω_B), the domain on which the average is computed. Then it comes for Step 1 and Step 2

$$\mathbf{U}_{S1}^A = \left(\begin{array}{c} \int_{\omega_A} \mathbf{u}_{S1} dV \\ \frac{1}{2} \int_{\omega_A} \text{curl}(\mathbf{u}_{S1}) dV \end{array} \right) \text{ and } \mathbf{U}_{S2}^A = \left(\begin{array}{c} \int_{\omega_A} \mathbf{u}_{S2} dV \\ \frac{1}{2} \int_{\omega_A} \text{curl}(\mathbf{u}_{S2}) dV \end{array} \right),$$

and likewise for \mathbf{U}_{S1}^B and \mathbf{U}_{S2}^B .

The next two sections explicit the elasticity problem according to the current section. We consider first a basis model, then a variant model of the constitutive law for the two spheres ω_A and ω_B .

2.2 Basis model : two elastic spheres linked by a pre-stressed spring

This section gives the mathematical formulation of the two-steps elasticity problem for two parts in contact and joined by an idealized bolt. In this section, the head and the threads of the bolt, ω_A and ω_B , are elastic and are of the same material as the parts. The space of admissible displacements corresponds to zero displacement on Γ_D

$$\mathcal{W} = \{\mathbf{w} \in (H^1(\Omega))^3, \mathbf{w} = \mathbf{0} \text{ on } \Gamma_D\}. \quad (2.5)$$

2.2.1 Step 1 : pre-stressed state

Let E_{S1} be the energy functional

$$\begin{aligned} E_{S1}(\mathbf{w}) = & \frac{1}{2} \int_{\Omega} \mathbf{A} \varepsilon(\mathbf{w}) : \varepsilon(\mathbf{w}) dV - \int_{\Omega} \mathbf{f}_1 \cdot \mathbf{w} dV - \int_{\Gamma_N} \mathbf{g}_1 \cdot \mathbf{w} dS \\ & + \frac{1}{2} (\mathbf{W}^B - \mathbf{W}^A)^T \tilde{\mathbf{K}} (\mathbf{W}^B - \mathbf{W}^A) - \Phi \int_{\omega_A} \mathbf{w} \cdot \mathbf{e} dV - (-\Phi) \int_{\omega_B} \mathbf{w} \cdot \mathbf{e} dV. \end{aligned} \quad (2.6)$$

The first term is the elastic strain energy. Volumetric and surface holding forces \mathbf{f}_1 and \mathbf{g}_1 are applied to the assembly. The fourth term is the energy of the root working in shear and flexion solicitations. Finally, a pre-stress force of amplitude Φ is applied compressively along the axis \mathbf{e} from the head to the threads of the bolt. The minimum potential energy principle then states that the displacement field describing the system in the first step is the unique minimizer \mathbf{u}_{S1} of (2.6) in \mathcal{W} , *i.e.*,

$$E_{S1}(\mathbf{u}_{S1}) = \min_{\mathbf{w} \in \mathcal{W}} E_{S1}(\mathbf{w}). \quad (2.7)$$

It leads to the following variational problem :

$$\begin{aligned} \text{Find } \mathbf{u}_{S1} \in \mathcal{W} \text{ s.t. } \forall \mathbf{w} \in \mathcal{W}, & \int_{\Omega} \mathbf{A}\varepsilon(\mathbf{u}_{S1}) : \varepsilon(\mathbf{w}) dV - \int_{\Omega} \mathbf{f}_1 \cdot \mathbf{w} dV - \int_{\Gamma_N} \mathbf{g}_1 \cdot \mathbf{w} dS \\ & + (\mathbf{U}_{S1}^B - \mathbf{U}_{S1}^A)^T \tilde{\mathbf{K}}(\mathbf{W}^B - \mathbf{W}^A) + \Phi \left(\int_{\omega_B} \mathbf{w} \cdot \mathbf{e} dV - \int_{\omega_A} \mathbf{w} \cdot \mathbf{e} dV \right) = 0. \end{aligned} \quad (2.8)$$

Integrate (2.8) by parts and bring out the boundary terms on $\partial\omega_A$ and $\partial\omega_B$. The jump of displacement is denoted $[\mathbf{w}] = \mathbf{w}|_- - \mathbf{w}|_+$. The normal pointing inward (resp. outward) ω_A is denoted \mathbf{n}_- (resp. \mathbf{n}_+) and similarly for ω_B . The variational problem is then rewritten as

$$\begin{aligned} \text{Find } \mathbf{u}_{S1} \in \mathcal{W} \text{ s.t. } \forall \mathbf{w} \in \mathcal{W}, & - \int_{\Omega} \text{div} \mathbf{A}\varepsilon(\mathbf{u}_{S1}) \cdot \mathbf{w} dV - \int_{\Omega} \mathbf{f}_1 \cdot \mathbf{w} dV - \int_{\Gamma_N} \mathbf{g}_1 \cdot \mathbf{w} dS + \int_{\Gamma_N} \mathbf{A}\varepsilon(\mathbf{u}_{S1}) \mathbf{n} \cdot \mathbf{w} dS \\ & + \int_{\partial\omega_A \cup \partial\omega_B} \mathbf{A}\varepsilon([\mathbf{u}_{S1}]) \mathbf{n}_- \cdot \mathbf{w} dS + \Phi \left(\int_{\omega_B} \mathbf{w} \cdot \mathbf{e} dV - \int_{\omega_A} \mathbf{w} \cdot \mathbf{e} dV \right) \\ & + \left[\tilde{\mathbf{K}}_{11} \left(\int_{\omega_B} \mathbf{u}_{S1} dV - \int_{\omega_A} \mathbf{u}_{S1} dV \right) - \tilde{\mathbf{K}}_{12}^T \left(\frac{1}{2} \int_{\omega_B} \text{curl}(\mathbf{u}_{S1}) dV - \frac{1}{2} \int_{\omega_A} \text{curl}(\mathbf{u}_{S1}) dV \right) \right] \cdot \left(\int_{\omega_B} \mathbf{w} dV - \int_{\omega_A} \mathbf{w} dV \right) \\ & + \left[\tilde{\mathbf{K}}_{12}^T \left(\int_{\omega_B} \mathbf{u}_{S1} dV - \int_{\omega_A} \mathbf{u}_{S1} dV \right) \right. \\ & \left. + \tilde{\mathbf{K}}_{22} \left(\frac{1}{2} \int_{\omega_B} \text{curl}(\mathbf{u}_{S1}) dV - \frac{1}{2} \int_{\omega_A} \text{curl}(\mathbf{u}_{S1}) dV \right) \right] \cdot \left(\frac{1}{2} \int_{\omega_B} \text{curl}(\mathbf{w}) dV - \frac{1}{2} \int_{\omega_A} \text{curl}(\mathbf{w}) dV \right) = 0 \end{aligned}$$

Given the particular equality $\int_{\omega_A} \text{curl}(\mathbf{w}) dV = \frac{1}{|\omega_A|} \int_{\partial\omega_A} \mathbf{n}_+ \wedge \mathbf{w} dV = -\frac{1}{|\omega_A|} \int_{\partial\omega_A} \mathbf{n}_- \wedge \mathbf{w} dV$, the

strong form associated to the first step reads

$$\left\{ \begin{array}{l}
 -\operatorname{div} \mathbf{A} \varepsilon(\mathbf{u}_{S1}) = \mathbf{f}_1 \text{ in } \Omega \setminus (\omega_A \cup \omega_B) \\
 -\operatorname{div} \mathbf{A} \varepsilon(\mathbf{u}_{S1}) - \left[\frac{\tilde{\mathbf{K}}_{11}}{|\omega_A|} \left(\int_{\omega_B} \mathbf{u}_{S1} dV - \int_{\omega_A} \mathbf{u}_{S1} dV \right) - \frac{\tilde{\mathbf{K}}_{12}^T}{|\omega_A|} \left(\frac{1}{2} \int_{\omega_B} \operatorname{curl}(\mathbf{u}_{S1}) dV - \frac{1}{2} \int_{\omega_A} \operatorname{curl}(\mathbf{u}_{S1}) dV \right) \right] \\
 = \mathbf{f}_1 + \frac{\Phi}{|\omega_A|} \mathbf{e} \text{ in } \omega_A \\
 -\operatorname{div} \mathbf{A} \varepsilon(\mathbf{u}_{S1}) + \left[\frac{\tilde{\mathbf{K}}_{11}}{|\omega_B|} \left(\int_{\omega_B} \mathbf{u}_{S1} dV - \int_{\omega_A} \mathbf{u}_{S1} dV \right) - \frac{\tilde{\mathbf{K}}_{12}^T}{|\omega_B|} \left(\frac{1}{2} \int_{\omega_B} \operatorname{curl}(\mathbf{u}_{S1}) dV - \frac{1}{2} \int_{\omega_A} \operatorname{curl}(\mathbf{u}_{S1}) dV \right) \right] \\
 = \mathbf{f}_1 - \frac{\Phi}{|\omega_B|} \mathbf{e} \text{ in } \omega_B \\
 \mathbf{A} \varepsilon([\mathbf{u}_{S1}]) \mathbf{n}_- \\
 = - \left(\frac{\tilde{\mathbf{K}}_{12}^T}{2|\omega_A|} \left(\int_{\omega_B} \mathbf{u}_{S1} dV - \int_{\omega_A} \mathbf{u}_{S1} dV \right) + \frac{\tilde{\mathbf{K}}_{22}}{2|\omega_A|} \left(\frac{1}{2} \int_{\omega_B} \operatorname{curl}(\mathbf{u}_{S1}) dV - \frac{1}{2} \int_{\omega_A} \operatorname{curl}(\mathbf{u}_{S1}) dV \right) \right) \wedge \mathbf{n}_- \\
 \text{on } \partial\omega_A \\
 \mathbf{A} \varepsilon([\mathbf{u}_{S1}]) \mathbf{n}_- \\
 = \left(\frac{\tilde{\mathbf{K}}_{12}^T}{2|\omega_B|} \left(\int_{\omega_B} \mathbf{u}_{S1} dV - \int_{\omega_A} \mathbf{u}_{S1} dV \right) + \frac{\tilde{\mathbf{K}}_{22}}{2|\omega_B|} \left(\frac{1}{2} \int_{\omega_B} \operatorname{curl}(\mathbf{u}_{S1}) dV - \frac{1}{2} \int_{\omega_A} \operatorname{curl}(\mathbf{u}_{S1}) dV \right) \right) \wedge \mathbf{n}_- \\
 \text{on } \partial\omega_B \\
 \mathbf{A} \varepsilon(\mathbf{u}_{S1}) \mathbf{n} = \mathbf{g}_1 \text{ on } \Gamma_N \\
 \mathbf{u}_{S1} = \mathbf{0} \text{ on } \Gamma_D
 \end{array} \right. \quad (2.9)$$

2.2.2 Step 2 : in-service state

Consider the first step achieved and let E_{S2} be the energy functional

$$\begin{aligned}
 E_{S2}(\mathbf{w}) &= \frac{1}{2} \int_{\Omega} \mathbf{A} \varepsilon(\mathbf{w}) : \varepsilon(\mathbf{w}) dV - \int_{\Omega} \mathbf{f}_2 \cdot \mathbf{w} dV - \int_{\Gamma_N} \mathbf{g}_2 \cdot \mathbf{w} dS + \int_{\Omega} \mathbf{f}_1 \cdot \mathbf{w} dV + \int_{\Gamma_N} \mathbf{g}_1 \cdot \mathbf{w} dS \\
 &\quad + \frac{1}{2} (\mathbf{W}^B - \mathbf{W}^A)^T \mathbf{K} (\mathbf{W}^B - \mathbf{W}^A) \\
 &\quad - \int_{\Omega} \mathbf{A} \varepsilon(\mathbf{u}_{S1}) : \varepsilon(\mathbf{w}) dV - (\mathbf{U}_{S1}^B - \mathbf{U}_{S1}^A)^T \mathbf{K} (\mathbf{W}^B - \mathbf{W}^A).
 \end{aligned} \quad (2.10)$$

The first terms are the elastic strain energy. External in-service loads \mathbf{f}_2 and \mathbf{g}_2 are applied in the system. The holding force \mathbf{f}_1 and \mathbf{g}_1 are removed. This is why their opposite are present in the energy functional (2.10). The root now works according to all degrees of freedom according to the rigidity matrix \mathbf{K} . The first step induces a pre-displacement field \mathbf{u}_{S1} and an imposed pre-stress field in the assembly (both parts and bolt). They act as external forces and the corresponding energy is represented by the two last terms of E_{S2} . The minimum potential energy principle then states that the displacement field describing the system in the Step 2 is the unique minimizer \mathbf{u}_{S2} of (2.10) in \mathcal{W} , *i.e.*,

$$E_{S2}(\mathbf{u}_{S2}) = \min_{\mathbf{w} \in \mathcal{W}} E_{S2}(\mathbf{w}). \quad (2.11)$$

It leads to the following variational problem :

$$\begin{aligned} \text{Find } \mathbf{u}_{S2} \in \mathcal{W} \text{ s.t. } \forall \mathbf{w} \in \mathcal{W}, & \int_{\Omega} \mathbf{A}\varepsilon(\mathbf{u}_{S2}) : \varepsilon(\mathbf{w})dV - \int_{\Omega} (\mathbf{f}_2 - \mathbf{f}_1) \cdot \mathbf{w}dV - \int_{\Gamma_N} (\mathbf{g}_2 - \mathbf{g}_1) \cdot \mathbf{w}dS \\ & + (\mathbf{U}_{S2}^B - \mathbf{U}_{S2}^A)^T \mathbf{K}(\mathbf{W}^B - \mathbf{W}^A) - \int_{\Omega} \mathbf{A}\varepsilon(\mathbf{u}_{S1}) : \varepsilon(\mathbf{w})dV - (\mathbf{U}_{S1}^B - \mathbf{U}_{S1}^A)^T \mathbf{K}(\mathbf{W}^B - \mathbf{W}^A) = 0. \end{aligned} \quad (2.12)$$

Using the variational problem of Step 1 (2.8), the variational problem (2.12) is rewritten as

$$\begin{aligned} \text{Find } \mathbf{u}_{S2} \in \mathcal{W} \text{ s.t. } \forall \mathbf{w} \in \mathcal{W}, & \int_{\Omega} \mathbf{A}\varepsilon(\mathbf{u}_{S2}) : \varepsilon(\mathbf{w})dV - \int_{\Omega} \mathbf{f}_2 \cdot \mathbf{w}dV - \int_{\Gamma_N} \mathbf{g}_2 \cdot \mathbf{w}dS \\ & + (\mathbf{U}_{S2}^B - \mathbf{U}_{S2}^A)^T \mathbf{K}(\mathbf{W}^B - \mathbf{W}^A) - (\mathbf{U}_{S1}^B - \mathbf{U}_{S1}^A)^T \bar{\mathbf{K}}(\mathbf{W}^B - \mathbf{W}^A) + \Phi \left(\int_{\omega_B} \mathbf{w} \cdot \mathbf{e}dV - \int_{\omega_A} \mathbf{w} \cdot \mathbf{e}dV \right) = 0. \end{aligned} \quad (2.13)$$

The variational formulation (2.13) brings to light that the complete realistic inner root forces is

$$-(\mathbf{U}_{S1}^B - \mathbf{U}_{S1}^A)^T \bar{\mathbf{K}}(\mathbf{W}^B - \mathbf{W}^A) + \Phi \left(\int_{\omega_B} \mathbf{w} \cdot \mathbf{e}dV - \int_{\omega_A} \mathbf{w} \cdot \mathbf{e}dV \right).$$

Integrate (2.13) by part and, bring out the boundary terms on $\partial\omega_A$ and $\partial\omega_B$. The variational problem is written as

$$\begin{aligned} \text{Find } \mathbf{u}_{S2} \in \mathcal{W} \text{ s.t. } \forall \mathbf{w} \in \mathcal{W}, & - \int_{\Omega} \text{div} \mathbf{A}\varepsilon(\mathbf{u}_{S2}) \cdot \mathbf{w}dV - \int_{\Omega} \mathbf{f}_2 \cdot \mathbf{w}dV - \int_{\Gamma_N} \mathbf{g}_2 \cdot \mathbf{w}dS + \int_{\Gamma_N} \mathbf{A}\varepsilon(\mathbf{u}_{S2}) \mathbf{n} \cdot \mathbf{w}dS \\ & + \int_{\partial\omega_A \cup \partial\omega_B} \mathbf{A}\varepsilon([\mathbf{u}_{S2}]) \mathbf{n}_- \cdot \mathbf{w}dS + \Phi \left(\int_{\omega_B} \mathbf{w} \cdot \mathbf{e}dV - \int_{\omega_A} \mathbf{w} \cdot \mathbf{e}dV \right) + \left[\mathbf{K}_{11} \left(\int_{\omega_B} \mathbf{u}_{S2}dV - \int_{\omega_A} \mathbf{u}_{S2}dV \right) \right. \\ & - \mathbf{K}_{12}^T \left(\frac{1}{2} \int_{\omega_B} \text{curl}(\mathbf{u}_{S2})dV - \frac{1}{2} \int_{\omega_A} \text{curl}(\mathbf{u}_{S2})dV \right) - \bar{\mathbf{K}}_{11} \left(\int_{\omega_B} \mathbf{u}_{S1}dV - \int_{\omega_A} \mathbf{u}_{S1}dV \right) \left. \right] \cdot \left(\int_{\omega_B} \mathbf{w}dV - \int_{\omega_A} \mathbf{w}dV \right) \\ & + \left[\mathbf{K}_{12}^T \left(\int_{\omega_B} \mathbf{u}_{S2}dV - \int_{\omega_A} \mathbf{u}_{S2}dV \right) + \mathbf{K}_{22} \left(\frac{1}{2} \int_{\omega_B} \text{curl}(\mathbf{u}_{S2})dV - \frac{1}{2} \int_{\omega_A} \text{curl}(\mathbf{u}_{S2})dV \right) \right. \\ & \left. - \bar{\mathbf{K}}_{22} \left(\frac{1}{2} \int_{\omega_B} \text{curl}(\mathbf{u}_{S1})dV - \frac{1}{2} \int_{\omega_A} \text{curl}(\mathbf{u}_{S1})dV \right) \right] \cdot \left(\frac{1}{2} \int_{\omega_B} \text{curl}(\mathbf{w})dV - \frac{1}{2} \int_{\omega_A} \text{curl}(\mathbf{w})dV \right) = 0. \end{aligned}$$

The strong form associated to this problem reads

$$\left\{ \begin{array}{l}
 -\operatorname{div} \mathbf{A} \boldsymbol{\varepsilon}(\mathbf{u}_{S2}) = \mathbf{f}_2 \text{ in } \Omega \setminus (\omega_A \cup \omega_B) \\
 -\operatorname{div} \mathbf{A} \boldsymbol{\varepsilon}(\mathbf{u}_{S2}) - \left[\frac{\mathbf{K}_{11}}{|\omega_A|} \left(\int_{\omega_B} \mathbf{u}_{S2} dV - \int_{\omega_A} \mathbf{u}_{S2} dV \right) - \frac{\mathbf{K}_{12}^T}{|\omega_A|} \left(\frac{1}{2} \int_{\omega_B} \operatorname{curl}(\mathbf{u}_{S2}) dV - \frac{1}{2} \int_{\omega_A} \operatorname{curl}(\mathbf{u}_{S2}) dV \right) \right] \\
 = \mathbf{f}_2 - \frac{\bar{\mathbf{K}}_{11}}{|\omega_A|} \left(\int_{\omega_B} \mathbf{u}_{S1} dV - \int_{\omega_A} \mathbf{u}_{S1} dV \right) + \frac{\Phi}{|\omega_A|} \mathbf{e} \text{ in } \omega_A \\
 -\operatorname{div} \mathbf{A} \boldsymbol{\varepsilon}(\mathbf{u}_{S2}) + \left[\frac{\mathbf{K}_{11}}{|\omega_B|} \left(\int_{\omega_B} \mathbf{u}_{S2} dV - \int_{\omega_A} \mathbf{u}_{S2} dV \right) - \frac{\mathbf{K}_{12}^T}{|\omega_B|} \left(\frac{1}{2} \int_{\omega_B} \operatorname{curl}(\mathbf{u}_{S2}) dV - \frac{1}{2} \int_{\omega_A} \operatorname{curl}(\mathbf{u}_{S2}) dV \right) \right] \\
 = \mathbf{f}_2 + \frac{\bar{\mathbf{K}}_{11}}{|\omega_B|} \left(\int_{\omega_B} \mathbf{u}_{S1} dV - \int_{\omega_A} \mathbf{u}_{S1} dV \right) - \frac{\Phi}{|\omega_B|} \mathbf{e} \text{ in } \omega_B \\
 \mathbf{A} \boldsymbol{\varepsilon}([\mathbf{u}_{S2}]) \mathbf{n}_- = - \left[\frac{\mathbf{K}_{12}^T}{2|\omega_A|} \left(\int_{\omega_B} \mathbf{u}_{S2} dV - \int_{\omega_A} \mathbf{u}_{S2} dV \right) + \frac{\mathbf{K}_{22}}{2|\omega_A|} \left(\frac{1}{2} \int_{\omega_B} \operatorname{curl}(\mathbf{u}_{S2}) dV - \frac{1}{2} \int_{\omega_A} \operatorname{curl}(\mathbf{u}_{S2}) dV \right) \right] \\
 - \frac{\bar{\mathbf{K}}_{22}}{2|\omega_A|} \left(\frac{1}{2} \int_{\omega_B} \operatorname{curl}(\mathbf{u}_{S1}) dV - \frac{1}{2} \int_{\omega_A} \operatorname{curl}(\mathbf{u}_{S1}) dV \right) \wedge \mathbf{n}_- \text{ on } \partial\omega_A \\
 \mathbf{A} \boldsymbol{\varepsilon}([\mathbf{u}_{S2}]) \mathbf{n}_- = \left[\frac{\mathbf{K}_{12}^T}{2|\omega_B|} \left(\int_{\omega_B} \mathbf{u}_{S2} dV - \int_{\omega_A} \mathbf{u}_{S2} dV \right) + \frac{\mathbf{K}_{22}}{2|\omega_B|} \left(\frac{1}{2} \int_{\omega_B} \operatorname{curl}(\mathbf{u}_{S2}) dV - \frac{1}{2} \int_{\omega_A} \operatorname{curl}(\mathbf{u}_{S2}) dV \right) \right] \\
 - \frac{\bar{\mathbf{K}}_{22}}{2|\omega_B|} \left(\frac{1}{2} \int_{\omega_B} \operatorname{curl}(\mathbf{u}_{S1}) dV - \frac{1}{2} \int_{\omega_A} \operatorname{curl}(\mathbf{u}_{S1}) dV \right) \wedge \mathbf{n}_- \text{ on } \partial\omega_B \\
 \mathbf{A} \boldsymbol{\varepsilon}(\mathbf{u}_{S2}) \mathbf{n} = \mathbf{g}_2 \text{ on } \Gamma_N \\
 \mathbf{u}_{S2} = \mathbf{0} \text{ on } \Gamma_D
 \end{array} \right. \quad (2.14)$$

Remark 1. A sliding contact model, described in [74], is added to each step to avoid interpenetration of the jointed parts.

2.2.3 Existence and uniqueness

We recall that the root works only according to shear and flexion solicitations in Step 1, while all its degrees of freedom are involved in Step 2. The root is then described by the matrix $\tilde{\mathbf{K}}$ in Step 1 and by the matrix \mathbf{K} in Step 2. Let us define a_{S1} and a_{S2} such that $a_{S1} : \mathcal{W} \times \mathcal{W} \mapsto \mathbb{R}$, $a_{S2} : \mathcal{W} \times \mathcal{W} \mapsto \mathbb{R}$ and

$$\begin{aligned}
 a_{S1}(\mathbf{u}, \mathbf{w}) &= \int_{\Omega} \mathbf{A} \boldsymbol{\varepsilon}(\mathbf{u}) : \boldsymbol{\varepsilon}(\mathbf{w}) dV + (\mathbf{U}^B - \mathbf{U}^A)^T \tilde{\mathbf{K}} (\mathbf{W}^B - \mathbf{W}^A) \\
 a_{S2}(\mathbf{u}, \mathbf{w}) &= \int_{\Omega} \mathbf{A} \boldsymbol{\varepsilon}(\mathbf{u}) : \boldsymbol{\varepsilon}(\mathbf{w}) dV + (\mathbf{U}^B - \mathbf{U}^A)^T \mathbf{K} (\mathbf{W}^B - \mathbf{W}^A).
 \end{aligned}$$

We also define l_{S1} and l_{S2} such that $l_{S1} : \mathcal{W}^* \mapsto \mathbb{R}$, $l_{S2} : \mathcal{W}^* \mapsto \mathbb{R}$ and

$$l_{S1}(\mathbf{w}) = \int_{\Omega} \mathbf{f}_1 \cdot \mathbf{w} dV + \int_{\Gamma_N} \mathbf{g}_1 \cdot \mathbf{w} dS - \Phi \left(\int_{\omega_B} \mathbf{w} \cdot \mathbf{e} dV - \int_{\omega_A} \mathbf{w} \cdot \mathbf{e} dV \right)$$

$$l_{S2}(\mathbf{w}) = \int_{\Omega} \mathbf{f}_2 \cdot \mathbf{w} dV + \int_{\Gamma_N} \mathbf{g}_2 \cdot \mathbf{w} dS - \Phi \left(\int_{\omega_B} \mathbf{w} \cdot \mathbf{e} dV - \int_{\omega_A} \mathbf{w} \cdot \mathbf{e} dV \right) + (\mathbf{U}_{S1}^B - \mathbf{U}_{S1}^A)^T \bar{\mathbf{K}} (\mathbf{W}^B - \mathbf{W}^A).$$

Step 1 and Step 2 respectively correspond to the problems

$$\text{Find } \mathbf{u}_{S1} \in \mathcal{W} \text{ s.t. } \forall \mathbf{w} \in \mathcal{W}, a_{S1}(\mathbf{u}_{S1}, \mathbf{w}) = l_{S1}(\mathbf{w}), \quad (2.15)$$

$$\text{Find } \mathbf{u}_{S2} \in \mathcal{W} \text{ s.t. } \forall \mathbf{w} \in \mathcal{W}, a_{S2}(\mathbf{u}_{S2}, \mathbf{w}) = l_{S2}(\mathbf{w}). \quad (2.16)$$

Proposition 3. *The problem (2.15) (resp. (2.16)) admits an unique solution $\mathbf{u}_{S1} \in \mathcal{W}$ (resp. $\mathbf{u}_{S2} \in \mathcal{W}$).*

Proof. Assume that loads \mathbf{f}_1 and \mathbf{f}_2 (resp. \mathbf{g}_1 and \mathbf{g}_2) belong to $L^2(\Omega, \mathbb{R}^3)$ (resp. $L^2(\Gamma_N, \mathbb{R}^3)$). Functions a_{S1} and a_{S2} are obviously bilinear on $\mathcal{W} \times \mathcal{W}$. Likewise, functions l_{S1} and l_{S2} are clearly linear on \mathcal{W}^* .

The continuity of the term $\Phi \left(\int_{\omega_B} \mathbf{w} \cdot \mathbf{e} dV - \int_{\omega_A} \mathbf{w} \cdot \mathbf{e} dV \right)$ comes from Cauchy-Schwarz in-

equality. The term $(\mathbf{U}_{S1}^B - \mathbf{U}_{S1}^A)^T \bar{\mathbf{K}} (\mathbf{W}^B - \mathbf{W}^A)$ contains factors $\left(\int_{\omega_B} \mathbf{w} dV - \int_{\omega_A} \mathbf{w} dV \right)$ and

$\left(\frac{1}{2} \int_{\omega_B} \text{curl}(\mathbf{w}) dV - \frac{1}{2} \int_{\omega_A} \text{curl}(\mathbf{w}) dV \right)$. The first one is easily bounded by $\|\mathbf{w}\|_{\mathcal{W}}$ using Poincaré inequality. The second one is bounded using Cauchy-Schwarz inequality by noticing that $\text{curl}(\mathbf{w}) = \bar{\bar{\bar{\epsilon}}} : \nabla \mathbf{w}$ where the third-order tensor $\bar{\bar{\bar{\epsilon}}}$ is defined such that

- $\epsilon_{i,j,k} = 0$ when two or more indices are equal,
- $\epsilon_{i,j,k} = 1$ when (i, j, k) is an even permutation of $(1, 2, 3)$,
- $\epsilon_{i,j,k} = -1$ when (i, j, k) is an odd permutation of $(1, 2, 3)$.

Then, l_{S1} and l_{S2} are continuous on \mathcal{W}^* .

The elasticity term of a_{S1} and a_{S2} are classically proved to be continuous and coercive thanks to Korn-Poincaré inequality. Let us consider only the term $(\mathbf{U}^B - \mathbf{U}^A)^T \mathbf{K} (\mathbf{W}^B - \mathbf{W}^A)$ since matrices \mathbf{K} and $\tilde{\mathbf{K}}$ have the same structure. Its continuity is proved as above with Poincaré and Cauchy-Schwarz inequalities. The coercivity of bilinear forms is ensured by the coercivity of elastic terms and the fact that $(\mathbf{U}^B - \mathbf{U}^A)^T \mathbf{K} (\mathbf{U}^B - \mathbf{U}^A)$ is non-negative. Lax-Milgram theorem ensures the existence and uniqueness of the solution. \square

2.3 Variant model : two rigid spheres linked by a pre-stressed spring

This section establishes a variant model of the previous one. Rigid body motions, instead of elasticity constitutive behavior, are considered in the head and the threads of the bolt, *i.e.* the

spheres ω_A and ω_B .

The space of admissible displacements corresponds to zero displacement on Γ_D and rigid body motions in ω_A and ω_B

$$\mathcal{W}_{RB} = \left\{ \mathbf{w} \in (H^1(\Omega))^3, \mathbf{w} = \mathbf{0} \text{ on } \Gamma_D, \mathbf{w}(\mathbf{x}) = \mathbf{C}_a + \mathbf{R}_a \mathbf{x} \text{ in } \omega_A, \mathbf{w}(\mathbf{x}) = \mathbf{C}_b + \mathbf{R}_b \mathbf{x} \text{ in } \omega_B \right\}, \quad (2.17)$$

where $(\mathbf{C}_a, \mathbf{C}_b) \in \mathbb{R}^3 \times \mathbb{R}^3$ are translations and $\mathbf{R}_a = -\mathbf{R}_a^T$ and $\mathbf{R}_b = -\mathbf{R}_b^T$ are anti-symmetric 3x3 matrices modelling infinitesimal rotations.

The idealized model is described through Euler-Bernoulli theory which relies on the displacement of the neutral fibre of the bolt. It leads to rigidify the extremities of the bolt which is rigorously imposed here with rigid body motions in the head and the threads of the idealized bolt. The present section highlights a bit more complex model than the first one.

We remind here that the rest of the idealized bolt description and the two-steps process described in Section 2.1 are unchanged.

2.3.1 Step 1 : pre-stressed state

The only difference from the basis model stands in the space of admissible displacements \mathcal{W}_{RB} . Let E_{S1} be the energy functional

$$\begin{aligned} E_{S1}(\mathbf{w}) = & \frac{1}{2} \int_{\Omega \setminus (\omega_A \cup \omega_B)} \mathbf{A} \varepsilon(\mathbf{w}) : \varepsilon(\mathbf{w}) dV - \int_{\Omega} \mathbf{f}_1 \cdot \mathbf{w} dV - \int_{\Gamma_N} \mathbf{g}_1 \cdot \mathbf{w} dS \\ & + \frac{1}{2} (\mathbf{W}^B - \mathbf{W}^A)^T \tilde{\mathbf{K}} (\mathbf{W}^B - \mathbf{W}^A) - \Phi \int_{\omega_A} \mathbf{w} \cdot \mathbf{e} dV - (-\Phi) \int_{\omega_B} \mathbf{w} \cdot \mathbf{e} dV. \end{aligned} \quad (2.18)$$

The energy functional (2.18) differs from (2.8) by the elastic energy. The rigid body motions in each spheres implies that ω_A and ω_B have zero deformation. Thus, they are excluded from the elastic energy. The minimum potential energy principle then states that the displacement field describing the system in Step 1 is the unique minimizer \mathbf{u}_{S1} of (2.18) in \mathcal{W}_{RB} , *i.e.*,

$$E_{S1}(\mathbf{u}_{S1}) = \min_{\mathbf{w} \in \mathcal{W}_{RB}} E_{S1}(\mathbf{w}). \quad (2.19)$$

It leads to the following variational problem :

$$\begin{aligned} \text{Find } \mathbf{u}_{S1} \in \mathcal{W}_{RB} \text{ s.t. } \forall \mathbf{w} \in \mathcal{W}_{RB}, & \int_{\Omega \setminus (\omega_A \cup \omega_B)} \mathbf{A} \varepsilon(\mathbf{u}_{S1}) : \varepsilon(\mathbf{w}) dV - \int_{\Omega} \mathbf{f}_1 \cdot \mathbf{w} dV - \int_{\Gamma_N} \mathbf{g}_1 \cdot \mathbf{w} dS \\ & + (\mathbf{U}_{S1}^B - \mathbf{U}_{S1}^A)^T \tilde{\mathbf{K}} (\mathbf{W}^B - \mathbf{W}^A) + \Phi \left(\int_{\omega_B} \mathbf{w} \cdot \mathbf{e} dV - \int_{\omega_A} \mathbf{w} \cdot \mathbf{e} dV \right) = 0. \end{aligned} \quad (2.20)$$

Integrate (2.20) by parts and use the rigid body motions in ω_A and ω_B . The translations and rotations of both spheres are unknown. They are determined by forces and moments equilibrium on their boundary. The strong form associated to the first step then reads

$$\left\{ \begin{array}{l}
-\operatorname{div} \mathbf{A} \varepsilon(\mathbf{u}_{S1}) = \mathbf{f}_1 \text{ in } \Omega \setminus (\omega_A \cup \omega_B) \\
\mathbf{A} \varepsilon(\mathbf{u}_{S1}) \mathbf{n} = \mathbf{g}_1 \text{ on } \Gamma_N \\
\mathbf{u}_{S1} = \mathbf{0} \text{ on } \Gamma_D \\
\int_{\partial \omega_A} \mathbf{A} \varepsilon(\mathbf{u}_{S1}) \mathbf{n} dS = \left[\tilde{\mathbf{K}}_{11} \left(\int_{\omega_B} \mathbf{u}_{S1} dV - \int_{\omega_A} \mathbf{u}_{S1} dV \right) - \tilde{\mathbf{K}}_{12}^T \left(\frac{1}{2} \int_{\omega_B} \operatorname{curl}(\mathbf{u}_{S1}) dV - \frac{1}{2} \int_{\omega_A} \operatorname{curl}(\mathbf{u}_{S1}) dV \right) \right] \\
\quad + \int_{\omega_A} \mathbf{f}_1 dV + \Phi \mathbf{e} \\
\int_{\partial \omega_B} \mathbf{A} \varepsilon(\mathbf{u}_{S1}) \mathbf{n} dS = - \left[\tilde{\mathbf{K}}_{11} \left(\int_{\omega_B} \mathbf{u}_{S1} dV - \int_{\omega_A} \mathbf{u}_{S1} dV \right) - \tilde{\mathbf{K}}_{12}^T \left(\frac{1}{2} \int_{\omega_B} \operatorname{curl}(\mathbf{u}_{S1}) dV - \frac{1}{2} \int_{\omega_A} \operatorname{curl}(\mathbf{u}_{S1}) dV \right) \right] \\
\quad + \int_{\omega_B} \mathbf{f}_1 dV - \Phi \mathbf{e} \\
\int_{\partial \omega_A} \mathbf{A} \varepsilon(\mathbf{u}_{S1}) \mathbf{n} \wedge \mathbf{x} dS = - \left[\tilde{\mathbf{K}}_{12}^T \left(\int_{\omega_B} \mathbf{u}_{S1} dV + \int_{\omega_A} \mathbf{u}_{S1} dV \right) + \tilde{\mathbf{K}}_{22} \left(\frac{1}{2} \int_{\omega_B} \operatorname{curl}(\mathbf{u}_{S1}) dV - \frac{1}{2} \int_{\omega_A} \operatorname{curl}(\mathbf{u}_{S1}) dV \right) \right] \\
\quad + \left[\tilde{\mathbf{K}}_{11} \left(\int_{\omega_B} \mathbf{u}_{S1} dV - \int_{\omega_A} \mathbf{u}_{S1} dV \right) - \tilde{\mathbf{K}}_{12}^T \left(\frac{1}{2} \int_{\omega_B} \operatorname{curl}(\mathbf{u}_{S1}) dV - \frac{1}{2} \int_{\omega_A} \operatorname{curl}(\mathbf{u}_{S1}) dV \right) \right] \wedge \int_{\omega_A} \mathbf{x} dV \\
\quad + \int_{\omega_A} \mathbf{f}_1 \wedge \mathbf{x} dV + \Phi \int_{\omega_A} \mathbf{e} \wedge \mathbf{x} dV \\
\int_{\partial \omega_B} \mathbf{A} \varepsilon(\mathbf{u}_{S1}) \mathbf{n} \wedge \mathbf{x} dS = \left[\tilde{\mathbf{K}}_{12}^T \left(\int_{\omega_B} \mathbf{u}_{S1} dV + \int_{\omega_A} \mathbf{u}_{S1} dV \right) + \tilde{\mathbf{K}}_{22} \left(\frac{1}{2} \int_{\omega_B} \operatorname{curl}(\mathbf{u}_{S1}) dV - \frac{1}{2} \int_{\omega_A} \operatorname{curl}(\mathbf{u}_{S1}) dV \right) \right] \\
\quad - \left[\tilde{\mathbf{K}}_{11} \left(\int_{\omega_B} \mathbf{u}_{S1} dV - \int_{\omega_A} \mathbf{u}_{S1} dV \right) - \tilde{\mathbf{K}}_{12}^T \left(\frac{1}{2} \int_{\omega_B} \operatorname{curl}(\mathbf{u}_{S1}) dV - \frac{1}{2} \int_{\omega_A} \operatorname{curl}(\mathbf{u}_{S1}) dV \right) \right] \wedge \int_{\omega_B} \mathbf{x} dV \\
\quad + \int_{\omega_B} \mathbf{f}_1 \wedge \mathbf{x} dV - \Phi \int_{\omega_B} \mathbf{e} \wedge \mathbf{x} dV
\end{array} \right. \quad (2.21)$$

2.3.2 Step 2 : in-service state

Consider the first step achieved and let E_{S2} be the energy functional

$$\begin{aligned}
E_{S2}(\mathbf{w}) = & \frac{1}{2} \int_{\Omega \setminus (\omega_A \cup \omega_B)} \mathbf{A}\varepsilon(\mathbf{w}) : \varepsilon(\mathbf{w}) dV - \int_{\Omega} \mathbf{f}_2 \cdot \mathbf{w} dV - \int_{\Gamma_N} \mathbf{g}_2 \cdot \mathbf{w} dS + \int_{\Omega} \mathbf{f}_1 \cdot \mathbf{w} dV + \int_{\Gamma_N} \mathbf{g}_1 \cdot \mathbf{w} dS \\
& + \frac{1}{2} (\mathbf{W}^B - \mathbf{W}^A)^T \mathbf{K} (\mathbf{W}^B - \mathbf{W}^A) \\
& - \int_{\Omega \setminus (\omega_A \cup \omega_B)} \mathbf{A}\varepsilon(\mathbf{u}_{S1}) : \varepsilon(\mathbf{w}) dV - (\mathbf{U}_{S1}^B - \mathbf{U}_{S1}^A)^T \mathbf{K} (\mathbf{W}^B - \mathbf{W}^A).
\end{aligned} \tag{2.22}$$

The energy functional (2.22) differs from (2.10) by the elastic energy and the imposed stress field because of the rigid body motions in ω_A and ω_B . The minimum potential energy principle then states that the displacement field describing the system in Step 2 is the unique minimizer \mathbf{u}_{S2} of (2.22) in \mathcal{W}_{RB} , *i.e.*,

$$E_{S2}(\mathbf{u}_{S2}) = \min_{\mathbf{w} \in \mathcal{W}_{RB}} E_{S2}(\mathbf{w}). \tag{2.23}$$

It leads to the following variational problem :

$$\begin{aligned}
\text{Find } \mathbf{u}_{S2} \in \mathcal{W}_{RB} \text{ s.t. } \forall \mathbf{w} \in \mathcal{W}_{RB}, & \int_{\Omega \setminus (\omega_A \cup \omega_B)} \mathbf{A}\varepsilon(\mathbf{u}_{S2}) : \varepsilon(\mathbf{w}) dV - \int_{\Omega} \mathbf{f}_2 \cdot \mathbf{w} dV - \int_{\Gamma_N} \mathbf{g}_2 \cdot \mathbf{w} dS \\
& + (\mathbf{U}_{S2}^B - \mathbf{U}_{S2}^A)^T \mathbf{K} (\mathbf{W}^B - \mathbf{W}^A) - (\mathbf{U}_{S1}^B - \mathbf{U}_{S1}^A)^T \bar{\mathbf{K}} (\mathbf{W}^B - \mathbf{W}^A) + \Phi \left(\int_{\omega_B} \mathbf{w} \cdot \mathbf{e} dV - \int_{\omega_A} \mathbf{w} \cdot \mathbf{e} dV \right) = 0.
\end{aligned} \tag{2.24}$$

Integrate (2.24) by parts, use the expressions of the rigid body motions in ω_A and ω_B and finally use (2.20). The strong form associated to the second step then reads

$$\left\{ \begin{array}{l}
-\operatorname{div} \mathbf{A} \varepsilon(\mathbf{u}_{S2}) = \mathbf{f}_2 \text{ in } \Omega \setminus (\omega_A \cup \omega_B) \\
\mathbf{A} \varepsilon(\mathbf{u}_{S2}) \mathbf{n} = \mathbf{g}_2 \text{ on } \Gamma_N \\
\mathbf{u}_{S2} = \mathbf{0} \text{ on } \Gamma_D \\
\int_{\partial \omega_A} \mathbf{A} \varepsilon(\mathbf{u}_{S2}) \mathbf{n} dS = \left[\mathbf{K}_{11} \left(\int_{\omega_B} \mathbf{u}_{S2} dV - \int_{\omega_A} \mathbf{u}_{S2} dV \right) - \mathbf{K}_{12}^T \left(\frac{1}{2} \int_{\omega_B} \operatorname{curl}(\mathbf{u}_{S2}) dV - \frac{1}{2} \int_{\omega_A} \operatorname{curl}(\mathbf{u}_{S2}) dV \right) \right] \\
\quad + \int_{\omega_A} \mathbf{f}_2 dV + \Phi \mathbf{e} - \bar{\mathbf{K}}_{11} \left(\int_{\omega_B} \mathbf{u}_{S1} dV - \int_{\omega_A} \mathbf{u}_{S1} dV \right) \\
\int_{\partial \omega_B} \mathbf{A} \varepsilon(\mathbf{u}_{S2}) \mathbf{n} dS = - \left[\mathbf{K}_{11} \left(\int_{\omega_B} \mathbf{u}_{S2} dV - \int_{\omega_A} \mathbf{u}_{S2} dV \right) - \mathbf{K}_{12}^T \left(\frac{1}{2} \int_{\omega_B} \operatorname{curl}(\mathbf{u}_{S2}) dV - \frac{1}{2} \int_{\omega_A} \operatorname{curl}(\mathbf{u}_{S2}) dV \right) \right] \\
\quad + \int_{\omega_B} \mathbf{f}_2 dV - \Phi \mathbf{e} + \bar{\mathbf{K}}_{11} \left(\int_{\omega_B} \mathbf{u}_{S1} dV - \int_{\omega_A} \mathbf{u}_{S1} dV \right) \\
\int_{\partial \omega_A} \mathbf{A} \varepsilon(\mathbf{u}_{S2}) \mathbf{n} \wedge \mathbf{x} dS = - \left[\mathbf{K}_{12}^T \left(\int_{\omega_B} \mathbf{u}_{S2} dV + \int_{\omega_A} \mathbf{u}_{S2} dV \right) + \mathbf{K}_{22} \left(\frac{1}{2} \int_{\omega_B} \operatorname{curl}(\mathbf{u}_{S2}) dV - \frac{1}{2} \int_{\omega_A} \operatorname{curl}(\mathbf{u}_{S2}) dV \right) \right] \\
\quad + \left[\mathbf{K}_{11} \left(\int_{\omega_B} \mathbf{u}_{S2} dV - \int_{\omega_A} \mathbf{u}_{S2} dV \right) - \mathbf{K}_{12}^T \left(\frac{1}{2} \int_{\omega_B} \operatorname{curl}(\mathbf{u}_{S2}) dV - \frac{1}{2} \int_{\omega_A} \operatorname{curl}(\mathbf{u}_{S2}) dV \right) \right] \wedge \int_{\omega_A} \mathbf{x} dV \\
\quad + \int_{\omega_A} \mathbf{f}_2 \wedge \mathbf{x} dV + \Phi \int_{\omega_A} \mathbf{e} \wedge \mathbf{x} dV + \bar{\mathbf{K}}_{11} \left(\int_{\omega_B} \mathbf{u}_{S1} dV - \int_{\omega_A} \mathbf{u}_{S1} dV \right) \wedge \int_{\omega_A} \mathbf{x} dV \\
\quad - \bar{\mathbf{K}}_{22} \left(\frac{1}{2} \int_{\omega_B} \operatorname{curl}(\mathbf{u}_{S1}) dV - \frac{1}{2} \int_{\omega_A} \operatorname{curl}(\mathbf{u}_{S1}) dV \right) \\
\int_{\partial \omega_B} \mathbf{A} \varepsilon(\mathbf{u}_{S2}) \mathbf{n} \wedge \mathbf{x} dS = \left[\mathbf{K}_{12}^T \left(\int_{\omega_B} \mathbf{u}_{S2} dV + \int_{\omega_A} \mathbf{u}_{S2} dV \right) + \mathbf{K}_{22} \left(\frac{1}{2} \int_{\omega_B} \operatorname{curl}(\mathbf{u}_{S2}) dV - \frac{1}{2} \int_{\omega_A} \operatorname{curl}(\mathbf{u}_{S2}) dV \right) \right] \\
\quad - \left[\mathbf{K}_{11} \left(\int_{\omega_B} \mathbf{u}_{S2} dV - \int_{\omega_A} \mathbf{u}_{S2} dV \right) - \mathbf{K}_{12}^T \left(\frac{1}{2} \int_{\omega_B} \operatorname{curl}(\mathbf{u}_{S2}) dV - \frac{1}{2} \int_{\omega_A} \operatorname{curl}(\mathbf{u}_{S2}) dV \right) \right] \wedge \int_{\omega_B} \mathbf{x} dV \\
\quad + \int_{\omega_B} \mathbf{f}_2 \wedge \mathbf{x} dV - \Phi \int_{\omega_B} \mathbf{e} \wedge \mathbf{x} dV - \bar{\mathbf{K}}_{11} \left(\int_{\omega_B} \mathbf{u}_{S1} dV - \int_{\omega_A} \mathbf{u}_{S1} dV \right) \wedge \int_{\omega_B} \mathbf{x} dV \\
\quad + \bar{\mathbf{K}}_{22} \left(\frac{1}{2} \int_{\omega_B} \operatorname{curl}(\mathbf{u}_{S1}) dV - \frac{1}{2} \int_{\omega_A} \operatorname{curl}(\mathbf{u}_{S1}) dV \right)
\end{array} \right. \quad (2.25)$$

Remark 2. A sliding contact model is added to each step to avoid overlapping of the jointed parts.

Remark 3. *An other model would be to consider spheres with different material properties than the parts. The rest of the idealized bolt description and the two-steps elasticity problems described in Section 2.1 are unchanged. The Lamé tensor of elasticity on the spheres then reads*

$$\mathbf{A}^* = \alpha \mathbf{A},$$

with $\alpha > 0$. This model is a cross between the basis and the variant models. Actually, it matches with the basis model if $\alpha = 1$ and it gets close to the variant model if α becomes ever greater. Then α is a penalization coefficient of the material properties. In fact, the rigid body motion is implemented numerically by penalization of the material properties on the spheres (see numerical illustrations of Chapters 4, 6 and 9). This model, with a high coefficient α , provides an appropriate representation of the Euler-Bernoulli condition for long beam.

2.4 Mechanical constraints specific to the bolt

Avoiding malfunction or failure of bolted joints requires further mechanical considerations. This section provides main technological constraints to be controlled with a meaningful physical representation. Thus, expressions of these constraints are derived from technical documents [57, 58]. They require first the evaluation of the realistic efforts internal to the idealized bolt. Briefly stated, inner efforts torsor results from the root deformation and the tightening traction force Φ . The inner torsor is evaluated through the rigidity matrices and the continuous displacement fields \mathbf{u}_{S1} and \mathbf{u}_{S2} of the spheres ω_A and ω_B . Technological constraints formulations are thus suitable for chain rule derivation. They are then derived for the purpose of topology optimization in terms of constraints integration and for shape derivatives.

2.4.1 Torsor of inner efforts

We consider the torsor of the external efforts applied on the bolt by the part Ω_B at the center of ω_B as for the inner efforts torsor of the bolt. The torsor is evaluated in the orthonormal coordinate system $(\mathbf{e}, \mathbf{e}', \mathbf{e}'')$ where \mathbf{e} is the axis of the bolt. Denote by k_{ij} the components of the rigidity matrix \mathbf{K}_b with $1 \leq i, j \leq 6$. Denote F^n , with $1 \leq n \leq 3$, the resulting forces and M^n , with $1 \leq n \leq 3$, the resulting momentum. The torsor efforts at the end of the second step, in-service state, reads

$$\begin{aligned}
& \begin{pmatrix} F^1(\mathbf{u}_{S2}) \\ F^2(\mathbf{u}_{S2}) \\ F^3(\mathbf{u}_{S2}) \\ M^1(\mathbf{u}_{S2}) \\ M^2(\mathbf{u}_{S2}) \\ M^3(\mathbf{u}_{S2}) \end{pmatrix} = \mathbf{K}_b(\mathbf{U}_2^B - \mathbf{U}_2^A) - \bar{\mathbf{K}}_b(\mathbf{U}_1^B - \mathbf{U}_1^A) + \begin{pmatrix} \Phi \\ 0 \\ 0 \\ 0 \\ 0 \\ 0 \end{pmatrix} \\
& = \begin{pmatrix} k_{11} \left(\int_{\omega_B} \mathbf{u}_{S2} \cdot \mathbf{e} dV - \int_{\omega_A} \mathbf{u}_{S2} \cdot \mathbf{e} dV \right) - k_{11} \left(\int_{\omega_B} \mathbf{u}_{S1} \cdot \mathbf{e} dV - \int_{\omega_A} \mathbf{u}_{S1} \cdot \mathbf{e} dV \right) + \Phi \\ k_{22} \left(\int_{\omega_B} \mathbf{u}_{S2} \cdot \mathbf{e}' dV - \int_{\omega_A} \mathbf{u}_{S2} \cdot \mathbf{e}' dV \right) + k_{26} \left(\frac{1}{2} \int_{\omega_B} \text{curl}(\mathbf{u}_{S2}) \cdot \mathbf{e}'' dV - \frac{1}{2} \int_{\omega_A} \text{curl}(\mathbf{u}_{S2}) \cdot \mathbf{e}'' dV \right) \\ k_{33} \left(\int_{\omega_B} \mathbf{u}_{S2} \cdot \mathbf{e}'' dV - \int_{\omega_A} \mathbf{u}_{S2} \cdot \mathbf{e}'' dV \right) + k_{35} \left(\frac{1}{2} \int_{\omega_B} \text{curl}(\mathbf{u}_{S2}) \cdot \mathbf{e}' dV - \frac{1}{2} \int_{\omega_A} \text{curl}(\mathbf{u}_{S2}) \cdot \mathbf{e}' dV \right) \\ k_{44} \left(\frac{1}{2} \int_{\omega_B} \text{curl}(\mathbf{u}_{S2}) \cdot \mathbf{e} dV - \frac{1}{2} \int_{\omega_A} \text{curl}(\mathbf{u}_{S2}) \cdot \mathbf{e} dV \right) - k_{44} \left(\frac{1}{2} \int_{\omega_B} \text{curl}(\mathbf{u}_{S1}) \cdot \mathbf{e} dV - \frac{1}{2} \int_{\omega_A} \text{curl}(\mathbf{u}_{S1}) \cdot \mathbf{e} dV \right) \\ k_{53} \left(\int_{\omega_B} \mathbf{u}_{S2} \cdot \mathbf{e}'' dV - \int_{\omega_A} \mathbf{u}_{S2} \cdot \mathbf{e}'' dV \right) + k_{55} \left(\frac{1}{2} \int_{\omega_B} \text{curl}(\mathbf{u}_{S2}) \cdot \mathbf{e}' dV - \frac{1}{2} \int_{\omega_A} \text{curl}(\mathbf{u}_{S2}) \cdot \mathbf{e}' dV \right) \\ k_{62} \left(\int_{\omega_B} \mathbf{u}_{S2} \cdot \mathbf{e}' dV - \int_{\omega_A} \mathbf{u}_{S2} \cdot \mathbf{e}' dV \right) + k_{66} \left(\frac{1}{2} \int_{\omega_B} \text{curl}(\mathbf{u}_{S2}) \cdot \mathbf{e}'' dV - \frac{1}{2} \int_{\omega_A} \text{curl}(\mathbf{u}_{S2}) \cdot \mathbf{e}'' dV \right) \end{pmatrix}. \tag{2.26}
\end{aligned}$$

Remark 4. Efforts at the end of the first step, the pre-stressed state, can be evaluated by substituting \mathbf{u}_{S2} with \mathbf{u}_{S1} in (2.26) and thus reads

$$\begin{pmatrix} F^1(\mathbf{u}_{S1}) \\ F^2(\mathbf{u}_{S1}) \\ F^3(\mathbf{u}_{S1}) \\ M^1(\mathbf{u}_{S1}) \\ M^2(\mathbf{u}_{S1}) \\ M^3(\mathbf{u}_{S1}) \end{pmatrix} = \tilde{\mathbf{K}}_b(\mathbf{U}_1^B - \mathbf{U}_1^A) + \begin{pmatrix} \Phi \\ 0 \\ 0 \\ 0 \\ 0 \\ 0 \end{pmatrix}. \tag{2.27}$$

2.4.2 Elasticity of the root

Most of assembly designs require that the bolt roots stay in the elastic domain by controlling the Von Mises yield criterion as stated in [58]

$$\sqrt{(\sigma_t + \sigma_f)^2 + 3\tau^2} \leq 0.9Re_{min}, \tag{2.28}$$

where σ_t and σ_f are the tensile and flexural components of the normal stress, τ is the shear stress from transversal and torsional forces and Re_{min} is minimal yield stress of the root. The Von Mises criterion is evaluated from inner efforts torsor using theory of elasticity for long beam [66]. It is evaluated at its maximum possible local location: the rim (resp. the center) of the root, where the maximal flexural and torsional components of stress (resp. maximal transversal component stress), lie. Furthermore, total implantation length has to be considered to accurately evaluate worst lever-arm effect.

Remark 5. For long bolts, a healthy design implies that the Von Mises stress at the center is small than the Von Mises stress at the rim of the bolt root. Given the Euler-Bernoulli condition for long beam, it is very likely that the Von Mises criterion at the center is covered by the Von Mises criterion at the rim of the root during the optimization process. Then, the Von Mises criterion at the center of the root is optional and it is implemented whatever is necessary.

Denote $\ell_0 = \ell \left(1 + 1.6 \frac{r_b}{\ell}\right)$ the equivalent implementation length of the bolt [57]. For the sake of simplicity, the yield criterion is squared.

- At the rim of the root ($r = r_b$)

$$\left(\frac{\sqrt{(F^1)^2}}{\pi r_b^2} + \frac{\sqrt{(M^2 - \ell_0 F^3)^2 + (M^3 + \ell_0 F^2)^2}}{\frac{\pi}{4} r_b^3} \right)^2 + 3 \left(\frac{M^1}{\frac{\pi}{2} r_b^3} \right)^2 \leq (0.9 Re_{min})^2. \quad (2.29)$$

- At the center of the root ($r = 0$)

$$\left(\frac{F^1}{\pi r_b^2} \right)^2 + 3 \left(\frac{4 \sqrt{(F^2)^2 + (F^3)^2}}{3 \pi r_b^2} \right)^2 \leq (0.9 Re_{min})^2. \quad (2.30)$$

Criteria (2.29) and (2.30) must be verified for each state of the two-steps process.

2.4.3 Fatigue of the root

Fatigue is a decisive factor in structural design. And connections should be considered with fatigue condition while designing assemblies, especially when design process is automated as in optimization process using F.E.A. For an infinite lifetime in service, normalized standard bolts exhibit a maximal allowed stress amplitude given by [58]

$$\sigma_a = 0.855 \left(\frac{150}{d} + 45 \right), \quad (2.31)$$

Numerical values in (2.31) are given in MPa and mm. They must be converted according to the system unit of the user. Besides, root fatigue failure appears at engaged threads level, thus, total implantation length ℓ_0 has to be considered to accurately evaluate worst lever-arm effect. The fatigue constraint is then given by

$$\left(\frac{\sqrt{(\Delta F^1)^2}}{\pi r_b^2} + \frac{\sqrt{(\Delta M^2 - \ell_0 \Delta F^3)^2 + (\Delta M^3 + \ell_0 \Delta F^2)^2}}{\frac{\pi}{4} r_b^3} \right)^2 \leq (2\sigma_a)^2, \quad (2.32)$$

where Δ indicates the operating cycle between the two equilibrium states Step 1 and Step 2. For instance $\Delta F^1 = F^1(\mathbf{u}_{S2}) - F^1(\mathbf{u}_{S1})$ and likewise for the other components of the torsor efforts.

2.4.4 Torsion locking of the root

The bolt root should not be solicited in torsion during tightening process (Step 1) and during in-service operation (Step 2). This might result from action of holding or in-service external loads and boundaries conditions, combined with an ill-adapted design of the assembly. This condition supports and is consistent with the fatigue constraint expressed of Section 2.4.3. This condition is achieved by controlling the torsional relative rotation between the head and the threads of the bolt which reads as the kinematic constraint

$$\left(\left(\frac{1}{2} \int_{\omega_B} \text{curl}(\mathbf{u}_{S2}) dV - \frac{1}{2} \int_{\omega_A} \text{curl}(\mathbf{u}_{S2}) dV \right) \cdot \mathbf{e} - \left(\frac{1}{2} \int_{\omega_B} \text{curl}(\mathbf{u}_{S1}) dV - \frac{1}{2} \int_{\omega_A} \text{curl}(\mathbf{u}_{S1}) dV \right) \cdot \mathbf{e} \right)^2 = 0. \quad (2.33)$$

The torsion locking (2.33) is handled as an equality constraint with the Augmented Lagrangian method.

2.4.5 Miscellaneous

Other conditions deal with local behavior of the interface between the assembled parts and the bolt, as contact pressure under bolt head or threads stripping. It is not consistent with the scope of this thesis and thus they are not considered here, without restriction on the following.

2.5 Constraints integration in optimization problems

2.5.1 Setting of the problem

Consider an objective function $J(\Omega)$, a constraint $C(\omega_A, \omega_B, \mathbf{u}_{S2})$ and the optimization problem

$$\begin{aligned} \min_{\Omega} \quad & J(\Omega). \\ \text{s.t. } & C(\omega_A, \omega_B, \mathbf{u}_{S2}) \leq 0 \end{aligned} \quad (2.34)$$

The problem (2.34) is handled with the Augmented Lagrangian method as described in Section 1.1.5 and thus is written as

$$\min_{\Omega} \max_{\alpha \in \mathbb{R}} \left\{ \mathcal{L}(\Omega) = J(\Omega) + \alpha \widehat{C}(\omega_A, \omega_B, \mathbf{u}_{S2}) + \frac{\beta}{2} \widehat{C}(\omega_A, \omega_B, \mathbf{u}_{S2})^2 \right\}, \quad (2.35)$$

where $\widehat{C}(\omega_A, \omega_B, \mathbf{u}_{S2}) = \max \left(C(\omega_A, \omega_B, \mathbf{u}_{S2}), -\frac{\alpha}{\beta} \right)$, α is the Lagrange multiplier and $\beta > 0$ is the penalty parameter.

Bolts inner mechanical conditions are evaluated during in-service state (Step 2). The elasticity and the fatigue constraints given by (2.29), (2.30) and (2.32) are of the form

$$C(\omega_A, \omega_B, \mathbf{u}_{S2}) = \left(c_1(\omega_A, \omega_B, \mathbf{u}_{S2}) + c_2(\omega_A, \omega_B, \mathbf{u}_{S2}) \right)^2 + 3c_3(\omega_A, \omega_B, \mathbf{u}_{S2})^2 - c_0^2. \quad (2.36)$$

Functions c_1 , c_2 and c_3 , and so the torsor efforts, depend on $\omega_A, \omega_B, \mathbf{u}_{S1}$ and \mathbf{u}_{S2} but to simply matters, they are only expressed through \mathbf{u}_{S2} . They have the following expressions

- Elasticity constraint at the rim of the root ($r = r_b$)

$$c_1(\mathbf{u}_{S2}) = \frac{\sqrt{F^1(\mathbf{u}_{S2})^2}}{\pi r_b^2}, \quad c_2(\mathbf{u}_{S2}) = \frac{\sqrt{\left(M^2(\mathbf{u}_{S2}) - \ell_0 F^3(\mathbf{u}_{S2})\right)^2 + \left(M^3(\mathbf{u}_{S2}) + \ell_0 F^2(\mathbf{u}_{S2})\right)^2}}{\frac{\pi}{4} r_b^3},$$

$$c_3(\mathbf{u}_{S2}) = \frac{M^1(\mathbf{u}_{S2})}{\frac{\pi}{2} r_b^3},$$

- Elasticity constraint at the center of the root ($r = 0$)

$$c_1(\mathbf{u}_{S2}) = \frac{F^1(\mathbf{u}_{S2})}{\pi r_b^2}, \quad c_2(\mathbf{u}_{S2}) = 0, \quad c_3(\mathbf{u}_{S2}) = \frac{4}{3} \frac{\sqrt{F^2(\mathbf{u}_{S2})^2 + F^3(\mathbf{u}_{S2})^2}}{\pi r_b^2},$$

- Fatigue constraint

$$c_1(\mathbf{u}_{S2}) = \frac{\sqrt{(\Delta F^1)^2}}{\pi r_b^2}, \quad c_2(\mathbf{u}_{S2}) = \frac{\sqrt{\left(\Delta M^2 - \ell_0 \Delta F^3\right)^2 + \left(\Delta M^3 + \ell_0 \Delta F^2\right)^2}}{\frac{\pi}{4} r_b^3}, \quad c_3(\mathbf{u}_{S2}) = 0,$$

and c_0 takes the value

- Elasticity constraint at the rim and at the center of the root

$$c_0 = 0.9 Re_{min},$$

- Fatigue constraint

$$c_0 = 2\sigma_a.$$

2.5.2 Adjoint state

The adjoint state \mathbf{p}_{S2} at the end of Step 2, associated to the displacement field \mathbf{u}_{S2} under the constraint (2.29), (2.30) or (2.32), solves the following variational problem

$$\text{Find } \mathbf{p}_{S2} \in \mathcal{W} \text{ s.t. } \forall \mathbf{w} \in \mathcal{W}, \int_{\Omega} \mathbf{A} \varepsilon(\mathbf{p}_{S2}) : \varepsilon(\mathbf{w}) dV + (\mathbf{P}_{S2}^B - \mathbf{P}_{S2}^A)^T \mathbf{K} (\mathbf{W}^B - \mathbf{W}^A) + \left\langle \frac{\partial \hat{C}}{\partial \mathbf{v}}(\mathbf{u}_{S2}), \mathbf{w} \right\rangle = 0, \quad (2.37)$$

where

$$\left\langle \frac{\partial \hat{C}}{\partial \mathbf{v}}(\mathbf{u}_{S2}), \mathbf{w} \right\rangle = \begin{cases} 2(c_1(\mathbf{u}_{S2}) + c_2(\mathbf{u}_{S2})) \left(\left\langle \frac{\partial c_1}{\partial \mathbf{v}}(\mathbf{u}_{S2}), \mathbf{w} \right\rangle + \left\langle \frac{\partial c_2}{\partial \mathbf{v}}(\mathbf{u}_{S2}), \mathbf{w} \right\rangle \right) & \text{if } C(\mathbf{u}_{S2}) \geq -\frac{\alpha}{\beta} \\ + 6c_3(\mathbf{u}_{S2}) \left\langle \frac{\partial c_3}{\partial \mathbf{v}}(\mathbf{u}_{S2}), \mathbf{w} \right\rangle & \\ 0 & \text{if } C(\mathbf{u}_{S2}) \leq -\frac{\alpha}{\beta} \end{cases}$$

We recall that the derivative of a function c with respect to a displacement field \mathbf{v} in the direction \mathbf{w} is given by

$$\left\langle \frac{\partial c}{\partial \mathbf{v}}(\mathbf{v}), \mathbf{w} \right\rangle = \lim_{\delta \rightarrow 0} \frac{c(\mathbf{v} + \delta \mathbf{w}) - c(\mathbf{v})}{\delta}. \quad (2.38)$$

Then the constraints derivatives with respect to a displacement field \mathbf{v} in a direction \mathbf{w} are

- Elasticity constraint at the rim of the root ($r = r_b$)

$$\begin{aligned} \left\langle \frac{\partial c_1}{\partial \mathbf{v}}(\mathbf{v}), \mathbf{w} \right\rangle &= \frac{F^1(\mathbf{v})}{\pi r_b^2 \sqrt{F^1(\mathbf{v})}} \left\langle \frac{\partial F^1}{\partial \mathbf{v}}(\mathbf{v}), \mathbf{w} \right\rangle, \\ \left\langle \frac{\partial c_2}{\partial \mathbf{v}}(\mathbf{v}), \mathbf{w} \right\rangle &= \frac{M^2(\mathbf{v}) - \ell_0 F^3(\mathbf{v})}{\frac{\pi}{4} r_b^3 \sqrt{(M^2(\mathbf{v}) - \ell_0 F^3(\mathbf{v}))^2 + (M^3(\mathbf{v}) + \ell_0 F^2(\mathbf{v}))^2}} \left(\left\langle \frac{\partial M^2}{\partial \mathbf{v}}(\mathbf{v}), \mathbf{w} \right\rangle \right. \\ &\quad \left. - \ell_0 \left\langle \frac{\partial F^3}{\partial \mathbf{v}}(\mathbf{v}), \mathbf{w} \right\rangle \right) \\ &\quad + \frac{M^3(\mathbf{v}) + \ell_0 F^2(\mathbf{v})}{\frac{\pi}{4} r_b^3 \sqrt{(M^2(\mathbf{v}) - \ell_0 F^3(\mathbf{v}))^2 + (M^3(\mathbf{v}) + \ell_0 F^2(\mathbf{v}))^2}} \left(\left\langle \frac{\partial M^3}{\partial \mathbf{v}}(\mathbf{v}), \mathbf{w} \right\rangle \right. \\ &\quad \left. + \ell_0 \left\langle \frac{\partial F^2}{\partial \mathbf{v}}(\mathbf{v}), \mathbf{w} \right\rangle \right) \\ \left\langle \frac{\partial c_3}{\partial \mathbf{v}}(\mathbf{v}), \mathbf{w} \right\rangle &= \frac{1}{\frac{\pi}{2} r_b^3} \left\langle \frac{\partial M^1}{\partial \mathbf{v}}(\mathbf{v}), \mathbf{w} \right\rangle \end{aligned}$$

- Elasticity constraint at the center of the root ($r = 0$)

$$\begin{aligned} \left\langle \frac{\partial c_1}{\partial \mathbf{v}}(\mathbf{v}), \mathbf{w} \right\rangle &= \frac{1}{\pi r_b^2} \left\langle \frac{\partial F^1}{\partial \mathbf{v}}(\mathbf{v}), \mathbf{w} \right\rangle, \\ \left\langle \frac{\partial c_2}{\partial \mathbf{v}}(\mathbf{v}), \mathbf{w} \right\rangle &= 0, \\ \left\langle \frac{\partial c_3}{\partial \mathbf{v}}(\mathbf{v}), \mathbf{w} \right\rangle &= \frac{4(F^2(\mathbf{v}) + F^3(\mathbf{v}))}{3\pi r_b^2 \sqrt{F^2(\mathbf{v})^2 + F^3(\mathbf{v})^2}} \left(\left\langle \frac{\partial F^2}{\partial \mathbf{v}}(\mathbf{v}), \mathbf{w} \right\rangle + \left\langle \frac{\partial F^3}{\partial \mathbf{v}}(\mathbf{v}), \mathbf{w} \right\rangle \right) \end{aligned}$$

- Fatigue constraint

$$\begin{aligned} \left\langle \frac{\partial c_1}{\partial \mathbf{v}}(\mathbf{v}), \mathbf{w} \right\rangle &= \frac{\Delta F^1(\mathbf{v})}{\pi r_b^2 \sqrt{\Delta F^1(\mathbf{v})}} \left\langle \frac{\partial F^1}{\partial \mathbf{v}}(\mathbf{v}), \mathbf{w} \right\rangle, \\ \left\langle \frac{\partial c_2}{\partial \mathbf{v}}(\mathbf{v}), \mathbf{w} \right\rangle &= \frac{\Delta M^2(\mathbf{v}) - \ell_0 \Delta F^3(\mathbf{v})}{\frac{\pi}{4} r_b^3 \sqrt{(\Delta M^2(\mathbf{v}) - \ell_0 \Delta F^3(\mathbf{v}))^2 + (\Delta M^3(\mathbf{v}) + \ell_0 \Delta F^2(\mathbf{v}))^2}} \left(\left\langle \frac{\partial M^2}{\partial \mathbf{v}}(\mathbf{v}), \mathbf{w} \right\rangle \right. \\ &\quad \left. - \ell_0 \left\langle \frac{\partial F^3}{\partial \mathbf{v}}(\mathbf{v}), \mathbf{w} \right\rangle \right) \\ &\quad + \frac{\Delta M^3(\mathbf{v}) + \ell_0 \Delta F^2(\mathbf{v})}{\frac{\pi}{4} r_b^3 \sqrt{(\Delta M^2(\mathbf{v}) - \ell_0 \Delta F^3(\mathbf{v}))^2 + (\Delta M^3(\mathbf{v}) + \ell_0 \Delta F^2(\mathbf{v}))^2}} \left(\left\langle \frac{\partial M^3}{\partial \mathbf{v}}(\mathbf{v}), \mathbf{w} \right\rangle \right. \\ &\quad \left. + \ell_0 \left\langle \frac{\partial F^2}{\partial \mathbf{v}}(\mathbf{v}), \mathbf{w} \right\rangle \right) \\ \left\langle \frac{\partial c_3}{\partial \mathbf{v}}(\mathbf{v}), \mathbf{w} \right\rangle &= 0 \end{aligned}$$

Remark 6. The adjoint state (2.37) takes into account the product of $\text{curl}(\mathbf{u}_{S2})$ and $\text{curl}(\mathbf{w})$. This is unusual but consistent with the idealized bolt model and the optimization constraints. For instance, let us explicitly compute the term $c_3(\mathbf{u}_{S2}) \left\langle \frac{\partial c_3}{\partial \mathbf{v}}(\mathbf{u}_{S2}), \mathbf{w} \right\rangle$ for the elasticity constraint

at the rim of the root

$$\begin{aligned}
c_3(\mathbf{u}_{S2}) \left\langle \frac{\partial c_3}{\partial \mathbf{v}}(\mathbf{u}_{S2}), \mathbf{w} \right\rangle &= \frac{M^1(\mathbf{u}_{S2})}{\frac{\pi}{2} r_b^3} \frac{1}{\frac{\pi}{2} r_b^3} \left\langle \frac{\partial M^1}{\partial \mathbf{v}}(\mathbf{u}_{S2}), \mathbf{w} \right\rangle \\
&= \frac{k_{44}^2}{\frac{\pi^2}{4} r_b^6} \left(\frac{1}{2} \int_{\omega_B} \text{curl}(\mathbf{u}_{S2}) \cdot \mathbf{e} dV - \frac{1}{2} \int_{\omega_A} \text{curl}(\mathbf{u}_{S2}) \cdot \mathbf{e} dV \right. \\
&\quad \left. - \left(\frac{1}{2} \int_{\omega_B} \text{curl}(\mathbf{u}_{S1}) \cdot \mathbf{e} dV - \frac{1}{2} \int_{\omega_A} \text{curl}(\mathbf{u}_{S1}) \cdot \mathbf{e} dV \right) \right) \left(\frac{1}{2} \int_{\omega_B} \text{curl}(\mathbf{w}) \cdot \mathbf{e} dV - \frac{1}{2} \int_{\omega_A} \text{curl}(\mathbf{w}) \cdot \mathbf{e} dV \right)
\end{aligned}$$

2.5.3 Shape derivatives

We give now an important result for the computation of constraints shape derivatives.

Proposition 4. *Let ω be a smooth bounded, open set of \mathbb{R}^3 . Let $f \in W^{1,1}(\mathbb{R}^3, \mathbb{R}^3)$ and J a shape functional from \mathcal{W} to \mathbb{R} defined by*

$$J(\omega) = \int_{\omega} f dV = \frac{1}{|\omega|} \int_{\omega} f dV.$$

Then, J is shape differentiable and it holds

$$J'(\omega)(\boldsymbol{\theta}) = \frac{|\omega| \int_{\partial\omega} f \boldsymbol{\theta} \cdot \mathbf{n} dS - \left(\int_{\omega} f dV \right) \left(\int_{\partial\omega} \boldsymbol{\theta} \cdot \mathbf{n} dS \right)}{|\omega|^2}, \quad \forall \boldsymbol{\theta} \in W^{1,\infty}(\mathbb{R}^3, \mathbb{R}^3), \quad (2.39)$$

where \mathbf{n} is the outward normal to ω .

Proof. Given the fact that $|\omega| = \int_{\omega} dV$, the shape derivative (2.39) is easily obtained with quotient derivative and Proposition 1 (see Chapter 1). \square

Remark 7. *In the present thesis, the spheres representing the head and the threads of the idealized bolt have fixed shape. Therefore, the deformation vector $\boldsymbol{\theta}$ is constant on the given shape ω and the shape derivative is*

$$J'(\omega)(\boldsymbol{\theta}) = \frac{1}{|\omega|} \int_{\partial\omega} f \boldsymbol{\theta} \cdot \mathbf{n} dS, \quad \forall \boldsymbol{\theta} \in W^{1,\infty}(\mathbb{R}^3, \mathbb{R}^3). \quad (2.40)$$

This form of shape derivative is used to derive bolts constitutive behavior law and specific mechanical constraints. The resulting shape derivative will be used in a parametric gradient-based algorithm to optimize the location of springs or idealized bolts.

We recall that functions c_1 , c_2 , c_3 and the torsor efforts depend on $\omega_A, \omega_B, \mathbf{u}_{S1}$ and \mathbf{u}_{S2} . They are now only expressed through ω_A, ω_B to easy notations. The shape derivative of the constraint $C(\omega_A, \omega_B)$ is given by

$$C'(\omega_A, \omega_B)(\boldsymbol{\theta}) = 2 \left(c_1(\omega_A, \omega_B) + c_2(\omega_A, \omega_B) \right) \left(c_1'(\omega_A, \omega_B)(\boldsymbol{\theta}) + c_2'(\omega_A, \omega_B)(\boldsymbol{\theta}) \right) + 6c_3(\omega_A, \omega_B) c_3'(\omega_A, \omega_B)(\boldsymbol{\theta}) \quad (2.41)$$

where of the functions c_1 , c_2 and c_3 are given by

- Elasticity constraint at the rim of the root

$$c'_1(\omega_A, \omega_B)(\boldsymbol{\theta}) = \frac{F^1(\omega_A, \omega_B)}{\pi r_b^2 \sqrt{F^1(\omega_A, \omega_B)}} F^{1'}(\omega_A, \omega_B)(\boldsymbol{\theta}),$$

$$c'_2(\omega_A, \omega_B)(\boldsymbol{\theta}) = \frac{\left(M^2(\omega_A, \omega_B) - \ell_0 F^3(\omega_A, \omega_B)\right) \left(M^{2'}(\omega_A, \omega_B)(\boldsymbol{\theta}) - \ell_0 F^{3'}(\omega_A, \omega_B)(\boldsymbol{\theta})\right)}{\frac{\pi}{4} r_b^3 \sqrt{\left(M^2(\omega_A, \omega_B) - \ell_0 F^3(\omega_A, \omega_B)\right)^2 + \left(M^3(\omega_A, \omega_B) + \ell_0 F^2(\omega_A, \omega_B)\right)^2}} + \frac{\left(M^3(\omega_A, \omega_B) + \ell_0 F^2(\omega_A, \omega_B)\right) \left(M^{3'}(\omega_A, \omega_B)(\boldsymbol{\theta}) + \ell_0 F^{2'}(\omega_A, \omega_B)(\boldsymbol{\theta})\right)}{\frac{\pi}{4} r_b^3 \sqrt{\left(M^2(\omega_A, \omega_B) - \ell_0 F^3(\omega_A, \omega_B)\right)^2 + \left(M^3(\omega_A, \omega_B) + \ell_0 F^2(\omega_A, \omega_B)\right)^2}},$$

$$c'_3(\omega_A, \omega_B)(\boldsymbol{\theta}) = \frac{1}{\frac{\pi}{2} r_b^3} M^{1'}(\omega_A, \omega_B)(\boldsymbol{\theta})$$

- Elasticity constraint at the center of the root

$$c'_1(\omega_A, \omega_B)(\boldsymbol{\theta}) = \frac{1}{\pi r_b^2} F^{1'}(\omega_A, \omega_B)(\boldsymbol{\theta}),$$

$$c'_2(\omega_A, \omega_B)(\boldsymbol{\theta}) = 0,$$

$$c'_3(\omega_A, \omega_B)(\boldsymbol{\theta}) = \frac{4 \left(F^2(\omega_A, \omega_B) + F^3(\omega_A, \omega_B)\right)}{3\pi r_b^2 \sqrt{F^2(\omega_A, \omega_B)^2 + F^3(\omega_A, \omega_B)^2}} \left(F^{2'}(\omega_A, \omega_B)(\boldsymbol{\theta}) + F^{3'}(\omega_A, \omega_B)(\boldsymbol{\theta})\right),$$

- Fatigue constraint

$$c'_1(\omega_A, \omega_B)(\boldsymbol{\theta}) = \frac{\Delta F^1(\omega_A, \omega_B)}{\pi r_b^2 \sqrt{F^1(\omega_A, \omega_B)}} F^{1'}(\omega_A, \omega_B)(\boldsymbol{\theta}),$$

$$c'_2(\omega_A, \omega_B)(\boldsymbol{\theta}) = \frac{\left(\Delta M^2(\omega_A, \omega_B) - \ell_0 \Delta F^3(\omega_A, \omega_B)\right) \left(M^{2'}(\omega_A, \omega_B)(\boldsymbol{\theta}) - \ell_0 F^{3'}(\omega_A, \omega_B)(\boldsymbol{\theta})\right)}{\frac{\pi}{4} r_b^3 \sqrt{\left(\Delta M^2(\omega_A, \omega_B) - \ell_0 \Delta F^3(\omega_A, \omega_B)\right)^2 + \left(\Delta M^3(\omega_A, \omega_B) + \ell_0 \Delta F^2(\omega_A, \omega_B)\right)^2}} + \frac{\left(\Delta M^3(\omega_A, \omega_B) + \ell_0 \Delta F^2(\omega_A, \omega_B)\right) \left(M^{3'}(\omega_A, \omega_B)(\boldsymbol{\theta}) + \ell_0 F^{2'}(\omega_A, \omega_B)(\boldsymbol{\theta})\right)}{\frac{\pi}{4} r_b^3 \sqrt{\left(\Delta M^2(\omega_A, \omega_B) - \ell_0 \Delta F^3(\omega_A, \omega_B)\right)^2 + \left(\Delta M^3(\omega_A, \omega_B) + \ell_0 \Delta F^2(\omega_A, \omega_B)\right)^2}},$$

$$c'_3(\omega_A, \omega_B)(\boldsymbol{\theta}) = 0.$$

where the derivatives of the torsor effort components are computed with (2.40).

Part II

Topological sensitivity analysis

The toy model of Laplace equation

Contents

3.1	Setting of the problem	52
3.2	Topological sensitivity analysis with respect to a high conducting inclusion	53
3.2.1	Perturbation of the domain	53
3.2.2	Computation of the topological derivative	54
3.2.3	Numerical illustrations	63
3.3	Topological sensitivity analysis with respect to a thermal bridge	68
3.3.1	Perturbation of the domain	69
3.3.2	Computation of the topological derivative	73
3.3.3	Numerical illustrations	83

This chapter contains preliminary technical results for further topological sensitivity analysis for the purpose of elasticity problems. A simple physical model, ruled by Laplace equation for heat propagation, provides more pedagogical understanding of the analysis tricks and techniques, hence the term "toy model". This chapter does not explicitly concern structures optimization and mechanical connections. The topological derivative is first computed with regards to the creation of a small inclusion with a prescribed arbitrary temperature value. It corresponds to a high conducting inclusion. This perturbation shall correspond to a highly stiff or rigid inclusion for the elasticity problem. Then, the topological derivative is established with respect to a thermal bridge. This perturbation shall correspond to a linear spring for the elasticity problem. Two models of the thermal bridge are developed and the most convenient one is kept for the spring and then for the idealized bolt connection. All topological derivatives are given in 2d and 3d but proofs are carried out for the 3d problem. They are numerically illustrated with simple academic 2d and 3d test cases. The structure is not optimized.

3.1 Setting of the problem

Let us consider a smooth bounded domain $\Omega \subset \mathbb{R}^n$ with $n = 2$ or 3 . This domain is divided into two parts, namely Ω_1 and Ω_2 such that $\overline{\Omega} = \overline{\Omega_1} \cup \overline{\Omega_2}$ and $\Omega_1 \cap \Omega_2 = \emptyset$. The boundary of the domain is made of two disjoint parts, $\partial\Omega = \Gamma_N \cup \Gamma_D$, where Neumann and Dirichlet boundary conditions are respectively imposed on Γ_N and Γ_D . The unperturbed or background domain is ruled by Laplace equation. Then, the background solution u solves

$$\begin{cases} -\Delta u = 0 & \text{in } \Omega \\ \frac{\partial u}{\partial \mathbf{n}} = g & \text{on } \Gamma_N. \\ u = 0 & \text{on } \Gamma_D \end{cases} \quad (3.1)$$

Assume that the heat flux g belongs to $L^2(\Gamma_N)$. The existence and the uniqueness of the solution $u \in \mathcal{W}$ are easily verified with Lax-Milgram theorem, where

$$\mathcal{W} = \{w \in H^1(\Omega), w = 0 \text{ on } \Gamma_D\}. \quad (3.2)$$

Remark 8. *The following analysis can also be carried out for Poisson equation, i.e. with a non-zero right hand side in Ω for (3.1).*

The topological derivative can be computed with an objective function evaluated everywhere. For the sake of simplicity, the inclusion is nucleated in Ω_2 and the objective function is evaluated far from the influence area of the inclusion, that is, in Ω_1 . It avoids supplementary terms corresponding to the perturbation of the integration domain of the objective function. Consider the generic objective function

$$J_0(\Omega) = \int_{\Omega_1} F(u) dV + \int_{\Gamma_N} G(u) dS \quad (3.3)$$

which depends on the domain Ω through the function u solution of (3.1). The functions F and G are smooth, twice differentiable with respect to u and satisfy the following conditions

$$\exists \alpha > 0, \begin{cases} |F(u)| \leq \alpha(|u|^2 + 1), & |F'(u)| \leq \alpha(|u| + 1), & |F''(u)| \leq \alpha \\ |G(u)| \leq \alpha(|u|^2 + 1), & |G'(u)| \leq \alpha(|u| + 1), & |G''(u)| \leq \alpha \end{cases} \quad (3.4)$$

Remark 9. *Conditions (3.4) are simple and sufficient. They can be improved if necessary.*

Let us introduce the notation $\mathbf{1}_{\Omega_1}$ which stands for the characteristic function of the domain Ω_1 , i.e. the function equals to 1 inside Ω_1 and zero outside. The adjoint state p associated to (3.1) for a general objective function (3.3) satisfies

$$\begin{cases} -\Delta p = -F'(u)\mathbf{1}_{\Omega_1} & \text{in } \Omega \\ \frac{\partial p}{\partial \mathbf{n}} = -G'(u) & \text{on } \Gamma_N. \\ p = 0 & \text{on } \Gamma_D \end{cases} \quad (3.5)$$

The existence and uniqueness of the solution $p \in \mathcal{W}$ are classically given by Lax-Milgram theorem.

3.2 Topological sensitivity analysis with respect to a high conducting inclusion

The goal of this section is to compute the topological derivative with respect to a high conducting small inclusion inside the sub-domain Ω_2 . The conduction condition is described by an imposed homogeneous temperature value inside the inclusion.

3.2.1 Perturbation of the domain

The domain Ω is perturbed with a high conducting small inclusion inside the sub-domain Ω_2 (see Fig. 3.1). Denote Ω_ρ the perforated domain, *i.e.* the domain without the inclusion ω_ρ

$$\Omega_\rho = \Omega \setminus \omega_\rho. \quad (3.6)$$

The inclusion can be arbitrary shaped. For the sake of simplicity, the reference shape ω is the unit ball of \mathbb{R}^n , $n = 2$ or 3 , so that the coefficients of the topological derivative are explicitly computed. Let ω_ρ be a small inclusion of shape ω , rescaled by an adimensional factor $\rho > 0$ and centered at the point $\mathbf{x}_0 \in \Omega_2$,

$$\omega_\rho = \left\{ \mathbf{x} \in \mathbb{R}^n, \frac{\mathbf{x} - \mathbf{x}_0}{\rho} \in \omega \right\}. \quad (3.7)$$

In the following, the factor ρ refers abusively to the size of the inclusion.

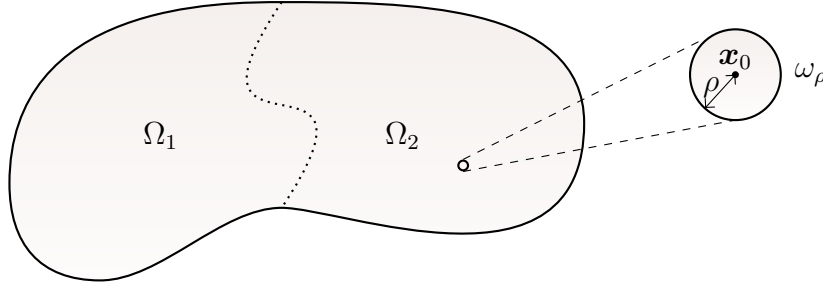


Figure 3.1: Perturbation of a domain Ω with a small inclusion ω_ρ

An arbitrary temperature value is imposed inside the inclusion ω_ρ . The space of admissible temperature fields corresponds to

$$\mathcal{W}_\rho = \{w \in H^1(\Omega), w = 0 \text{ on } \Gamma_D, w(\mathbf{x}) = \mathcal{C} \text{ in } \omega_\rho\}, \quad (3.8)$$

where $\mathcal{C} \in \mathbb{R}$ is an unknown temperature inside the ball ω_ρ . The variational problem is

$$\text{Find } u_\rho \in \mathcal{W}_\rho \text{ s.t. } \forall w \in \mathcal{W}_\rho, \int_{\Omega_\rho} \nabla u_\rho \cdot \nabla w dV - \int_{\Gamma_N} g w dS = 0. \quad (3.9)$$

The constant \mathcal{C} may depend on the inclusion size. The strong form associated to (3.9) reads

$$\left\{ \begin{array}{ll} -\Delta u_\rho = 0 & \text{in } \Omega_\rho \\ \frac{\partial u_\rho}{\partial \mathbf{n}} = g & \text{on } \Gamma_N \\ u_\rho = 0 & \text{on } \Gamma_D, \\ u_\rho(\mathbf{x}) = \mathcal{C}(\rho) & \text{in } \omega_\rho, \\ \int_{\partial \omega_\rho} \frac{\partial u_\rho}{\partial \mathbf{n}} dS = 0 & \end{array} \right. \quad (3.10)$$

where \mathbf{n} denotes the outward normal to Ω_ρ . The unknown homogeneous constant $\mathcal{C}(\rho)$ is completed by the equilibrium condition on the border of ω_ρ . It means that there is no heat source inside the inclusion.

In the sequel, we assume that u_ρ is as smooth as we want, which is always possible by assuming that the loads and the domain are smooth. The generic objective function (3.3) evaluated in the perturbed domain reads

$$J_\rho(\Omega) = \int_{\Omega_1} F(u_\rho) dV + \int_{\Gamma_N} G(u_\rho) dS. \quad (3.11)$$

Remark 10. *In the present case, the objective function in the perturbed domain should be denoted rigorously $J(\Omega_\rho)$ since the PDE describing the perturbation applies to Ω_ρ with a condition on ω_ρ . Throughout this thesis, the objective function in the perturbed domain is denoted J_ρ by abuse of notation. The objective function in the background domain (i.e. without perturbation) is denoted J_0 or J .*

Definition 3. *The objective function (3.11) is said to admit a topological derivative $DJ(\mathbf{x}_0)$ at the point \mathbf{x}_0 for a high conducting inclusion of shape ω , if the following asymptotic expansion holds for small $\rho > 0$*

$$J_\rho(\Omega) = J_0(\Omega) + \rho^n DJ(\mathbf{x}_0) + o(\rho^n), \quad n = 2 \text{ or } 3. \quad (3.12)$$

Theorem 1. *Take ω to be the unit ball of \mathbb{R}^n , $n = 2$ or 3 . The objective function (3.11) admits a topological derivative at \mathbf{x}_0 of the form*

$$J_\rho(\Omega) = J_0(\Omega) + n\rho^n |\omega| \nabla u(\mathbf{x}_0) \cdot \nabla p(\mathbf{x}_0) + O(\rho^{n+1}), \quad n = 2 \text{ or } 3, \quad (3.13)$$

where the temperature field u and the adjoint state p solve respectively (3.1) and (3.5).

3.2.2 Computation of the topological derivative

Approximation of the perturbed temperature field

The goal of this section is to study the influence of the small inclusion on the temperature field for the 3d problem. First, the behavior of the perturbed field is approximated with far field functions that zoom on the inclusion and ignore the boundary conditions on $\partial\Omega$. These functions can be explicitly computed thanks to the spherical shape of the inclusion. Then, the perturbation and its gradient are rigorously estimated with an asymptotic analysis using these far fields expression.

- **Far fields expression**

Since the inclusion is small, the perturbed temperature field u_ρ is expected to be approximately equal to the background field u in addition to the influence fields of the small inclusion ω_ρ , that is to formally assume the ansatz

$$u_\rho(\mathbf{x}) \approx u(\mathbf{x}) + v_0 \left(\frac{\mathbf{x} - \mathbf{x}_0}{\rho} \right) + \rho v_1 \left(\frac{\mathbf{x} - \mathbf{x}_0}{\rho} \right). \quad (3.14)$$

The perturbed field behavior is then estimated with these far field functions, v_0 and v_1 , centered on the inclusion and defined in \mathbb{R}^3 . They respectively express the zero and first-order influence

fields of the perturbation. Since the perturbations due to the inclusion are getting smaller far from the center \mathbf{x}_0 , the far field functions have to decay at infinity like $\lim_{\mathbf{y} \rightarrow \infty} v_0(\mathbf{y}) = 0$ and $\lim_{\mathbf{y} \rightarrow \infty} v_1(\mathbf{y}) = 0$. In other words, boundary conditions on $\partial\Omega$ are ignored and the far fields focus on the inclusion. It will be proved in the following that the zero-order function v_0 is null and the first-order zoom v_1 depends on the gradient of the background field u and the adjoint p at the point \mathbf{x}_0 .

The problem is rescaled with an inclusion of unit size $r_1 = 1$ by setting the rescaled variable $\mathbf{y} = \frac{\mathbf{x} - \mathbf{x}_0}{\rho}$. The background solution is expanded at first order

$$u(\mathbf{x}) = u(\mathbf{x}_0) + \nabla u(\mathbf{x}_0) \cdot (\mathbf{x} - \mathbf{x}_0) + O(\rho^2) \text{ in a neighbourhood of } \mathbf{x}_0. \quad (3.15)$$

The imposed constant temperature $\mathcal{C}(\rho)$ in ω_ρ is assumed to depend on ρ such that

$$\mathcal{C}(\rho) = \mathcal{C}_0 + \rho\mathcal{C}_1 + O(\rho^2). \quad (3.16)$$

Then, the function v_0 and v_1 respectively solve

$$\left\{ \begin{array}{ll} -\Delta v_0 = 0 & \text{in } \mathbb{R}^3 \setminus \omega \\ v_0(\mathbf{y}) = \mathcal{C}_0 - u(\mathbf{x}_0) & \text{in } \omega \\ \int_{\partial\omega} \frac{\partial v_0}{\partial \mathbf{n}} dS = 0 \\ \lim_{\mathbf{y} \rightarrow 0} v_0(\mathbf{y}) = 0 \end{array} \right. , \text{ and } \left\{ \begin{array}{ll} -\Delta v_1 = 0 & \text{in } \mathbb{R}^3 \setminus \omega \\ v_1(\mathbf{y}) = \mathcal{C}_1 - \nabla u(\mathbf{x}_0) \cdot \mathbf{y} & \text{in } \omega \\ \int_{\partial\omega} \frac{\partial v_1}{\partial \mathbf{n}} dS = 0 \\ \lim_{\mathbf{y} \rightarrow 0} v_1(\mathbf{y}) = 0 \end{array} \right. . \quad (3.17)$$

Lemma 1. *The function v_0 is zero in \mathbb{R}^3 .*

Proof. Since ω is the unit ball, v_0 is determined in radial coordinates. Its expression is of the form $v_0(r) = \frac{C_1}{r} + C_2$ with $r = \|\mathbf{y}\|$. Boundary conditions on $\partial\omega$ and at infinity lead to $v_0(r) = (C_0 - u(\mathbf{x}_0)) \frac{r_1}{r}$, where $r_1 = 1$ is the radius of the unit ball ω . The equilibrium condition gives $\int_{\partial\omega} \frac{\partial v_0}{\partial \mathbf{n}} dS = 4\pi(C_0 - u(\mathbf{x}_0)) = 0$. It means that $C_0 - u(\mathbf{x}_0) = 0$. Thus $v_0(r) = 0$. \square

Lemma 2. *The function v_1 is explicitly given by*

$$v_1(\mathbf{y}) = \begin{cases} -\nabla u(\mathbf{x}_0) \cdot \mathbf{y} \frac{r_1^3}{r^3} & \text{in } \mathbb{R}^3 \setminus \omega \\ -\nabla u(\mathbf{x}_0) \cdot \mathbf{y} & \text{in } \omega \end{cases}, \quad (3.18)$$

where $r = \|\mathbf{y}\|$ and $r_1 = 1$ is the radius of the unit ball.

Proof. Let us first determine v_1^a the solution of

$$\left\{ \begin{array}{ll} -\Delta v_1^a = 0 & \text{in } \mathbb{R}^3 \setminus \omega \\ v_1^a(\mathbf{y}) = -\nabla u(\mathbf{x}_0) \cdot \mathbf{y} & \text{in } \omega \\ \lim_{\mathbf{y} \rightarrow 0} v_1^a(\mathbf{y}) = 0 \end{array} \right. . \quad (3.19)$$

According to [113], v_1^a is explicitly given by

$$v_1^a = \begin{cases} -\nabla u(\mathbf{x}_0) \cdot \mathbf{y} f(r) + g(r) & \text{in } \mathbb{R}^3 \setminus \omega \\ -\nabla u(\mathbf{x}_0) \cdot \mathbf{y} & \text{in } \omega \end{cases},$$

where f and g are scalar functions satisfying

$$\begin{cases} f(r_1) = 1 \\ \lim_{r \rightarrow \infty} f(r) = 0 \end{cases} \text{ and } \begin{cases} g(r_1) = 0 \\ \lim_{r \rightarrow \infty} g(r) = 0 \end{cases} \quad (3.20)$$

Derivatives are rather computed in cartesian coordinates because of the structure of v_1^a . It follows that

$$-\Delta v_1^a(\mathbf{y}) = 0 \iff \begin{cases} f''(r) + \frac{4}{r}f'(r) = 0 \\ g''(r) + \frac{2}{r}g'(r) = 0 \end{cases}.$$

Using boundary conditions, one can find that $f(r) = \frac{r_1^3}{r^3}$ and $g(r) = 0$. Denote $v_1^b = v_1 - v_1^a$ the solution of

$$\begin{cases} -\Delta v_1^b = 0 & \text{in } \mathbb{R}^3 \setminus \omega \\ v_1^b(\mathbf{y}) = \mathcal{C}_1 & \text{in } \omega \\ \int_{\partial\omega} \frac{\partial v_1^b}{\partial \mathbf{n}} dS = 0 \\ \lim_{\mathbf{y} \rightarrow 0} v_1^b(\mathbf{y}) = 0 \end{cases} \quad (3.21)$$

Then, v_1^b exists as the linear combination of existing functions. Moreover, v_1^b has the same structure as v_0 . Thus, the same conclusion as Lemma 1 holds true and so $v_1^b(\mathbf{y}) = 0$ for all $\mathbf{y} \in \mathbb{R}^3$ and $\mathcal{C}_1 = 0$. All of that leads to $v_1 = v_1^a$. \square

• Asymptotic analysis of the perturbed temperature field

Let v_ρ be the difference between the perturbed and the background solutions

$$v_\rho = u_\rho - u. \quad (3.22)$$

This function represents the influence of the inclusion and solves

$$\begin{cases} -\Delta v_\rho = 0 & \text{in } \Omega_\rho \\ \frac{\partial v_\rho}{\partial \mathbf{n}} = 0 & \text{on } \Gamma_N \\ v_\rho = 0 & \text{on } \Gamma_D \\ v_\rho(\mathbf{x}) = \mathcal{C}(\rho) - u(\mathbf{x}) & \text{in } \omega_\rho \\ \int_{\partial\omega_\rho} \frac{\partial v_\rho}{\partial \mathbf{n}} dS = 0 \end{cases} \quad (3.23)$$

Set $\tilde{\mathbf{n}}$ the unit normal vector pointing outward ω_ρ . The equilibrium condition comes out from

$$\int_{\omega_\rho} \frac{\partial v_\rho}{\partial \mathbf{n}} dS = - \int_{\omega_\rho} \frac{\partial u}{\partial \mathbf{n}} dS = \int_{\omega_\rho} \frac{\partial u}{\partial \tilde{\mathbf{n}}} dS = \int_{\omega_\rho} \Delta u dV = 0.$$

Let us introduce the rescaled function $v_1^\rho(\mathbf{x}) = \rho v_1 \left(\frac{\mathbf{x} - \mathbf{x}_0}{\rho} \right)$. The following result proves that v_1^ρ is, in some sense, the limit of v_ρ as ρ goes to zero.

Proposition 5. *Let $\theta \in C_c^\infty(\Omega)$ be a cut-off function with compact support $\mathcal{U}_+ \subset \Omega$ such that $\theta \equiv 1$ in a neighborhood $\mathcal{U}_- \subset \mathcal{U}_+$ of \mathbf{x}_0 . There exists a constant $C > 0$ independent of ρ such that*

$$v_\rho = \theta v_1^\rho + \delta, \quad (3.24)$$

with

$$\|v_1^\rho\|_{L^2(\Omega_\rho)} \leq C\rho^{3/2+1}, \quad (3.25)$$

$$\|\varepsilon(v_1^\rho)\|_{L^2(\Omega_\rho)} \leq C\rho^{3/2}, \quad (3.26)$$

$$\|\delta\|_{H^1(\Omega_\rho)} \leq C\rho^{3/2+1}. \quad (3.27)$$

Remark 11. *The role of the cut-off function θ is to make sure that the product θv_1^ρ satisfies homogeneous boundary conditions on the boundary $\partial\Omega$, as does v_ρ . Since θ has a compact support, it implies that $\theta \equiv 0$ far from \mathbf{x}_0 . Consequently, θ vanishes far from the inclusion so that δ contains the far field influence of the inclusion. The function δ is an error term in the H^1 -norm. Indeed, its H^1 -norm is always asymptotically smaller than the one of θv_1^ρ . The L^2 -norm of δ is of the same order as its H^1 -norm. However, the L^2 -norm of v_1^ρ is always smaller by a factor ρ than its H^1 -norm.*

Proof. The explicit expression (3.18) of v_1 indicates that $v_1 = O(1/|\mathbf{y}|^2)$ and $\nabla v_1 = O(1/|\mathbf{y}|^3)$ at infinity. Thus, it follows by rescaling

$$\|v_1^\rho\|_{L^\infty(\Omega \setminus \mathcal{U}_-)} \leq C\rho^3 \text{ and } \|\nabla v_1^\rho\|_{L^\infty(\Omega \setminus \mathcal{U}_-)} \leq C\rho^3. \quad (3.28)$$

These L^∞ -norms are evaluated far from the neighborhood of \mathbf{x}_0 . Denote $\Omega_{\rho^{-1}}$ the translated and rescaled domain centered at the origin and of size $\frac{1}{\rho}|\Omega|$. The L^2 estimates of v_1^ρ and its gradient are simply obtained as follows

$$\int_{\Omega_\rho} |v_1^\rho|^2 dV \leq C\rho^2 \int_{\Omega_\rho} \left| v_1 \left(\frac{\mathbf{x} - \mathbf{x}_0}{\rho} \right) \right|^2 dV \leq C\rho^{3+2} \int_{\Omega_{\rho^{-1}}} |v_1(\mathbf{y})|^2 dV \leq C\rho^{3+2},$$

$$\int_{\Omega_\rho} |\nabla v_1^\rho|^2 dV \leq C \int_{\Omega_\rho} \left| \nabla v_1 \left(\frac{\mathbf{x} - \mathbf{x}_0}{\rho} \right) \right|^2 dV \leq C\rho^3 \int_{\Omega_{\rho^{-1}}} |\nabla v_1(\mathbf{y})|^2 dV \leq C\rho^3.$$

Let us now write the equations satisfied by δ

$$\left\{ \begin{array}{ll} -\Delta\delta = v_1^\rho \Delta\theta + 2\nabla\theta \cdot \nabla v_1^\rho & \text{in } \Omega_\rho \\ \frac{\partial\delta}{\partial\mathbf{n}} = 0 & \text{on } \Gamma_N \\ \delta = 0 & \text{on } \Gamma_D \\ \delta(\mathbf{x}) = \mathcal{C}(\rho) - u(\mathbf{x}) + \nabla u(\mathbf{x}_0) \cdot (\mathbf{x} - \mathbf{x}_0) & \text{in } \omega_\rho \\ \int_{\partial\omega_\rho} \frac{\partial\delta}{\partial\mathbf{n}} dS = 0 & \end{array} \right. \quad (3.29)$$

Multiply (3.29) by δ and integrate by parts, it follows that

$$\int_{\Omega_\rho} \nabla\delta \cdot \nabla\delta dV = \int_{\Omega_\rho} v_1^\rho \Delta\theta \delta dV + 2 \int_{\Omega_\rho} \nabla\theta \cdot \nabla v_1^\rho \delta dV + \int_{\partial\omega_\rho} \frac{\partial\delta}{\partial\mathbf{n}} \delta dS.$$

The derivatives of the cut-off function θ are zero in the direct influence area of the inclusion. The two first terms of the right-hand side are then easily estimated with the L^∞ -norms of v_1^ρ and its gradient in addition to Cauchy-Schwarz and Poincaré inequalities.

$$\begin{aligned} \left| \int_{\Omega_\rho} v_1^\rho \Delta \theta \delta dV \right| + 2 \left| \int_{\Omega_\rho} \nabla \theta \cdot \nabla v_1^\rho \delta dV \right| &\leq C \|v_1^\rho\|_{L^\infty(\Omega \setminus \mathcal{U}_-)} \|\Delta \theta\|_{L^\infty(\Omega \setminus \mathcal{U}_-)} \|\delta\|_{L^2(\Omega_\rho)} \\ &\quad + C \|\nabla \theta\|_{L^\infty(\Omega \setminus \mathcal{U}_-)} \|\nabla v_1^\rho\|_{L^\infty(\Omega \setminus \mathcal{U}_-)} \|\delta\|_{L^2(\Omega_\rho)} \\ &\leq C \rho^3 \|\nabla \delta\|_{L^2(\Omega_\rho)}. \end{aligned}$$

The last term of the right-hand side is more complex because of the expression of δ on $\partial\omega_\rho$. A Taylor expansion with integral remainder of the background solution u is

$$u(\mathbf{x}) = u(\mathbf{x}_0) + \nabla u(\mathbf{x}_0) \cdot (\mathbf{x} - \mathbf{x}_0) + \int_0^1 (1-t)(\mathbf{x} - \mathbf{x}_0)^T \mathbf{H}(u(\mathbf{x}_0 + t(\mathbf{x} - \mathbf{x}_0))) (\mathbf{x} - \mathbf{x}_0) dt, \quad (3.30)$$

with $\mathbf{H}(u)$ the Hessian matrix of u . The boundary term then reads

$$\int_{\partial\omega_\rho} \frac{\partial \delta}{\partial \mathbf{n}} \delta dS = - \int_{\partial\omega_\rho} \frac{\partial \delta}{\partial \mathbf{n}} \int_0^1 (1-t)(\mathbf{x} - \mathbf{x}_0)^T \mathbf{H}(u(\mathbf{x}_0 + t(\mathbf{x} - \mathbf{x}_0))) (\mathbf{x} - \mathbf{x}_0) dt dS.$$

The term $\int_0^1 (1-t)(\mathbf{x} - \mathbf{x}_0)^T \mathbf{H}(u(\mathbf{x}_0 + t(\mathbf{x} - \mathbf{x}_0))) (\mathbf{x} - \mathbf{x}_0) dt$ is extended in Ω_ρ .

Let $\varphi \in \mathcal{C}^\infty(\mathbb{R}^3)$ be a cut-off function such that $\varphi(\mathbf{y}) \equiv 1$ in ω , decreases to zero in a corona B_2 of size 2 and $\varphi(\mathbf{y}) \equiv 0$ far from the origin. Denote φ_ρ the rescaled cut-off function such that $\varphi_\rho(\mathbf{x}) = \varphi\left(\frac{\mathbf{x} - \mathbf{x}_0}{\rho}\right)$. Then, $\varphi_\rho(\mathbf{x}) \equiv 1$ in ω_ρ , decreases to zero in $B_{2\rho}$ a corona of size 2ρ and $\varphi_\rho(\mathbf{x}) \equiv 0$ far from \mathbf{x}_0 .

Setting $R_u(\mathbf{x}) = \varphi_\rho(\mathbf{x}) \int_0^1 (1-t)(\mathbf{x} - \mathbf{x}_0)^T \mathbf{H}(u(\mathbf{x}_0 + t(\mathbf{x} - \mathbf{x}_0))) (\mathbf{x} - \mathbf{x}_0) dt$, the boundary term is rewritten

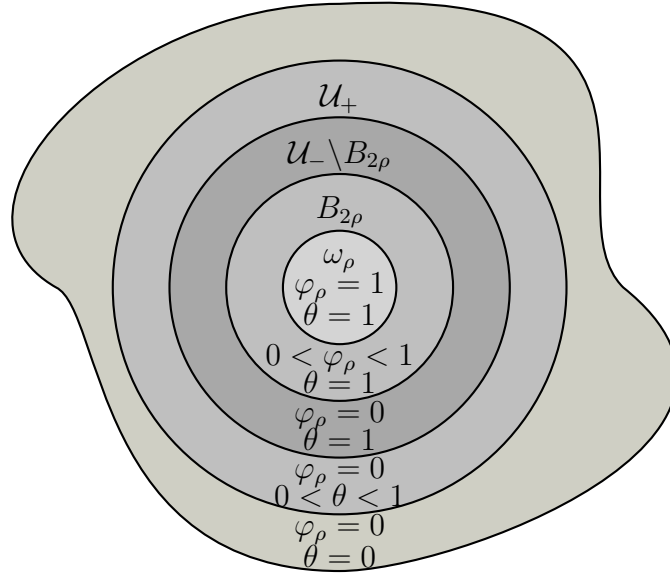
$$\int_{\partial\omega_\rho} \frac{\partial \delta}{\partial \mathbf{n}} \int_0^1 (1-t)(\mathbf{x} - \mathbf{x}_0)^T \mathbf{H}(u(\mathbf{x}_0 + t(\mathbf{x} - \mathbf{x}_0))) (\mathbf{x} - \mathbf{x}_0) dt dS = \int_{\partial\omega_\rho} \frac{\partial \delta}{\partial \mathbf{n}} R_u dS.$$

The function R_u is then defined in Ω_ρ . Integration by parts of the above term and use (3.29)

$$\begin{aligned} - \int_{\partial\omega_\rho} \frac{\partial \delta}{\partial \mathbf{n}} R_u dS &= - \int_{\Omega_\rho} \Delta \delta R_u dV - \int_{\Omega_\rho} \nabla \delta \cdot \nabla R_u dV \\ &\quad + \int_{\Omega_\rho} v_1^\rho \Delta \theta R_u dV + 2 \int_{\Omega_\rho} \nabla \theta \cdot \nabla v_1^\rho R_u dV - \int_{\Omega_\rho} \nabla \delta \cdot \nabla R_u dV = - \int_{\Omega_\rho} \nabla \delta \cdot \nabla R_u dV \end{aligned}$$

because $\text{supp}(R_u) \cap \text{supp}(\nabla \theta) = \emptyset$ (see Fig. 3.2). Decrease property of $\nabla \varphi_\rho$ implies that $\nabla \varphi_\rho$ behaves like $1/\rho$. Moreover, $\mathbf{x} - \mathbf{x}_0$ is of the order of ρ in $B_{2\rho}$. Hence,

$$\exists C > 0, |\nabla R_u| \leq C \rho \text{ in } B_{2\rho}. \quad (3.31)$$

Figure 3.2: Domains of definition of θ and φ_ρ

Remark 12. Since ∇R_u involves the third derivatives of the background solution, u shall at least belong to $\mathcal{C}^3(\Omega)$.

The last term is estimated with Cauchy-Schwarz inequality

$$\left| \int_{\partial\omega_\rho} \frac{\partial\delta}{\partial\mathbf{n}} R_u dS \right| \leq C \|\nabla\delta\|_{L^2(\Omega_\rho)} \sqrt{\int_{B_{2\rho}} |\nabla R_u|^2 dV} \leq C\rho \|\nabla\delta\|_{L^2(\Omega_\rho)} \sqrt{\int_{B_{2\rho}} dV} \leq C\rho^{3/2+1} \|\nabla\delta\|_{L^2(\Omega_\rho)}.$$

Regrouping all of that, the L^2 -norm of $\nabla\delta$ is bounded as follows

$$\|\nabla\delta\|_{L^2(\Omega_\rho)} \leq C(\rho^3 + \rho^{3/2+1}) \leq C\rho^{3/2+1}. \quad (3.32)$$

□

Approximation of the perturbed adjoint state

The adjoint state p_ρ associated to the problem (3.10) is approximated with the same methodology. It solves

$$\begin{cases} -\Delta p_\rho = -F'(u)\mathbf{1}_{\Omega_1} & \text{in } \Omega_\rho \\ \frac{\partial p_\rho}{\partial\mathbf{n}} = -G'(u) & \text{on } \Gamma_N \\ p_\rho = 0 & \text{on } \Gamma_D \\ p_\rho(\mathbf{x}) = \bar{\mathcal{C}}(\rho) & \text{in } \omega_\rho \\ \int_{\partial\omega_\rho} \frac{\partial p_\rho}{\partial\mathbf{n}} dS = 0 \end{cases} \quad (3.33)$$

The arbitrary constant $\bar{\mathcal{C}}(\rho)$ in ω_ρ is unknown so it is completed with the equilibrium condition on the border of ω_ρ .

Remark 13. *It has already been noticed in [8] that the adjoint problem (3.33) is not standard since the right hand side depends on u and not on u_ρ as expected in the perturbed domain. This adaptation is licit since the objective function is evaluated far from the influence area of the inclusion.*

The perturbation of the adjoint state is estimated by setting $q_\rho = p_\rho - p$, the difference between the perturbed and the background adjoint states. It solves

$$\left\{ \begin{array}{ll} -\Delta q_\rho = 0 & \text{in } \Omega_\rho \\ \frac{\partial q_\rho}{\partial \mathbf{n}} = 0 & \text{on } \Gamma_N \\ q_\rho = 0 & \text{on } \Gamma_D \\ q_\rho(\mathbf{x}) = \bar{\mathcal{C}}(\rho) - p(\mathbf{x}) & \text{in } \omega_\rho \\ \int_{\partial\omega_\rho} \frac{\partial q_\rho}{\partial \mathbf{n}} dS = 0 \end{array} \right. \quad (3.34)$$

The two first equations of (3.34) have zero right hand side because of the non-standard adjoint in the perturbed domain (3.33). Denote q_1^ρ the rescaled function such that

$$q_1^\rho(\mathbf{x}) = \rho q_1 \left(\frac{\mathbf{x} - \mathbf{x}_0}{\rho} \right), \quad (3.35)$$

where q_1 is the counterpart of v_1 and is explicitly given

$$q_1(\mathbf{y}) = \begin{cases} -\nabla p(\mathbf{x}_0) \cdot \mathbf{y} \frac{r_1^3}{r^3} & \text{in } \mathbb{R}^3 \setminus \omega \\ -\nabla p(\mathbf{x}_0) \cdot \mathbf{y} & \text{in } \omega \end{cases} \quad (3.36)$$

Proposition 6. *Let $\theta \in \mathcal{C}_c^\infty(\Omega)$ be a cut-off function with compact support $\mathcal{U}_+ \subset \Omega$ such that $\theta \equiv 1$ in a neighborhood $\mathcal{U}_- \subset \mathcal{U}_+$ of \mathbf{x}_0 . We have*

$$q_\rho = \theta q_1^\rho + \eta, \quad (3.37)$$

with

$$\|q_1^\rho\|_{L^2(\Omega_\rho)} \leq C\rho^{3/2+1}, \quad (3.38)$$

$$\|\nabla q_1^\rho\|_{L^2(\Omega_\rho)} \leq C\rho^{3/2}, \quad (3.39)$$

$$\|\eta\|_{H^1(\Omega_\rho)} \leq C\rho^{3/2+1}, \quad (3.40)$$

$$\|q_1^\rho\|_{L^\infty(\Omega \setminus \mathcal{U}_-)} \leq C\rho^3 \text{ and } \|\nabla q_1^\rho\|_{L^\infty(\Omega \setminus \mathcal{U}_-)} \leq C\rho^3. \quad (3.41)$$

Proof. The function η solves

$$\left\{ \begin{array}{ll} -\Delta \eta = q_1^\rho \Delta \theta + 2\nabla \theta \cdot \nabla q_1^\rho & \text{in } \Omega_\rho \\ \frac{\partial \eta}{\partial \mathbf{n}} = 0 & \text{on } \Gamma_N \\ \eta = 0 & \text{on } \Gamma_D \\ \eta(\mathbf{x}) = \bar{\mathcal{C}}(\rho) - p(\mathbf{x}) + \nabla p(\mathbf{x}_0) \cdot (\mathbf{x} - \mathbf{x}_0) & \text{in } \omega_\rho \\ \int_{\partial\omega_\rho} \frac{\partial \eta}{\partial \mathbf{n}} dS = 0 \end{array} \right. \quad (3.42)$$

Proposition 6 is proved by going back over the proof Proposition 5 and by substituting u with p and v_ρ with q_ρ . \square

Proof of the main result

The 3d result of Theorem 1 can now be proved using the far fields v_1^ρ and q_1^ρ and the estimates of u_ρ and p_ρ . Let us write a first-order Taylor expansion with exact remainder of the perturbed objective function

$$\begin{aligned} J_\rho(\Omega) &= \int_{\Omega_1} F(u_\rho) dV + \int_{\Gamma_N} G(u_\rho) dS = \int_{\Omega_1} F(u + v_\rho) dV + \int_{\Gamma_N} G(u + v_\rho) dS \\ &= J(\Omega) + \int_{\Omega_1} F'(u) v_\rho dV + \int_{\Gamma_N} G'(u) v_\rho dS + \frac{1}{2} \int_{\Omega_1} F''(\bar{u}) v_\rho v_\rho dV + \frac{1}{2} \int_{\Gamma_N} G''(\bar{u}) v_\rho v_\rho dS. \end{aligned}$$

The exact remainder is bounded thanks to assumptions (3.4) and Proposition 5

$$\begin{aligned} \left| \int_{\Omega_1} F''(\bar{u}) v_\rho v_\rho dV \right| &\leq C \|v_\rho\|_{L^2(\Omega_\rho)}^2 \leq C \rho^5, \\ \left| \int_{\Gamma_N} G''(\bar{u}) v_\rho v_\rho dS \right| &\leq C \|v_\rho\|_{L^2(\Gamma_N)}^2 \leq C \|\delta\|_{L^2(\Gamma_N)}^2 \text{ because } \theta = 0 \text{ on } \Gamma_N \\ &\leq C \|\delta\|_{H^1(\Omega_\rho)}^2 \text{ using the Trace theorem} \\ &\leq C \rho^5. \end{aligned}$$

The occurrence of v_ρ in the expansion of $J_\rho(\Omega)$ justifies the use of an adjoint state. Moreover, this expansion involves u instead of u_ρ . This is why (3.33) has been modified and is not standard. Multiplying (3.33) by v_ρ and integrating by parts twice, it follows

$$\begin{aligned} \int_{\Omega_1} F'(u) v_\rho dV + \int_{\Gamma_N} G'(u) v_\rho dS &= \int_{\partial\omega_\rho} \frac{\partial p_\rho}{\partial \mathbf{n}} v_\rho dS = \int_{\partial\omega_\rho} \frac{\partial p}{\partial \mathbf{n}} v_1^\rho dS + \int_{\partial\omega_\rho} \frac{\partial q_1^\rho}{\partial \mathbf{n}} v_1^\rho dS + \int_{\partial\omega_\rho} \frac{\partial \eta}{\partial \mathbf{n}} v_1^\rho dS \\ &\quad + \int_{\partial\omega_\rho} \frac{\partial p}{\partial \mathbf{n}} \delta dS + \int_{\partial\omega_\rho} \frac{\partial q_1^\rho}{\partial \mathbf{n}} \delta dS + \int_{\partial\omega_\rho} \frac{\partial \eta}{\partial \mathbf{n}} \delta dS. \end{aligned}$$

Propositions 5 and 6 imply that all terms involving δ and η are remainder terms. The topological derivative thus comes from the two first terms of the above equality. All these terms are estimated one by one.

★ 1st and 2nd terms

These two terms are handled together. They are explicitated first with $\tilde{\mathbf{n}}$, the unit normal vector pointing outward ω_ρ , and then with a rescaling

$$\begin{aligned} \int_{\partial\omega_\rho} \frac{\partial p}{\partial \mathbf{n}} v_1^\rho dS + \int_{\partial\omega_\rho} \frac{\partial q_1^\rho}{\partial \mathbf{n}} v_1^\rho dS &= -\rho^2 \int_{\partial\omega} \nabla p(\mathbf{x}_0 + \rho \mathbf{y}) \cdot \tilde{\mathbf{n}} v_1^\rho(\mathbf{x}_0 + \rho \mathbf{y}) dS - \rho^2 \int_{\partial\omega} \nabla q_1(\mathbf{y}) \cdot \tilde{\mathbf{n}} v_1^\rho(\mathbf{x}_0 + \rho \mathbf{y}) dS \\ &= \rho^3 \left(\int_{\partial\omega} \nabla p(\mathbf{x}_0) \cdot \tilde{\mathbf{n}} \nabla u(\mathbf{x}_0) \cdot \mathbf{y} dS + \int_{\partial\omega} \nabla q_1 \cdot \tilde{\mathbf{n}} \nabla u(\mathbf{x}_0) \cdot \mathbf{y} dS \right) + O(\rho^4) \end{aligned}$$

Recalling that $q_1(\mathbf{y}) = -\nabla p(\mathbf{x}_0) \cdot \mathbf{y} \frac{r_1^3}{r^3}$ in $\mathbb{R}^3 \setminus \omega$ and that $\tilde{\mathbf{n}} = \frac{\mathbf{y}}{r_1}$ on $\partial\omega$, where $r = \|\mathbf{y}\|$ and $r_1 = 1$ is the radius of the unit, it follows that

$$\nabla q_1 \cdot \tilde{\mathbf{n}} = 2 \frac{\nabla p(\mathbf{x}_0) \cdot \mathbf{y}}{r_1} \text{ on } \partial\omega.$$

Getting back to the ongoing equality,

$$\begin{aligned} \int_{\partial\omega_\rho} \frac{\partial p}{\partial \mathbf{n}} v_1^\rho dS + \int_{\partial\omega_\rho} \frac{\partial q_1^\rho}{\partial \mathbf{n}} v_1^\rho dS &= \frac{3\rho^3}{r_1} \int_{\partial\omega} \nabla u(\mathbf{x}_0) \cdot \mathbf{y} \nabla p(\mathbf{x}_0) \cdot \mathbf{y} dS + O(\rho^4) \\ &= \frac{3\rho^3}{r_1} \int_{\partial\omega} \mathbf{y} \mathbf{y}^T dS \nabla u(\mathbf{x}_0) \cdot \nabla p(\mathbf{x}_0) + O(\rho^4) \\ &= 3\rho^3 |\omega| \nabla u(\mathbf{x}_0) \cdot \nabla p(\mathbf{x}_0) + O(\rho^4). \end{aligned}$$

★ 3rd term

Multiply (3.42) by θv_1^ρ and integrate by parts

$$\int_{\partial\omega_\rho} \frac{\partial \eta}{\partial \mathbf{n}} v_1^\rho dS = \int_{\Omega_\rho} \theta \nabla \eta \cdot \nabla v_1^\rho dV + \int_{\Omega_\rho} v_1^\rho \nabla \eta \cdot \nabla \theta dV - \int_{\Omega_\rho} \theta q_1^\rho \Delta \theta v_1^\rho dV - 2 \int_{\Omega_\rho} \theta v_1^\rho \nabla q_1^\rho \cdot \nabla \theta dV.$$

As the derivatives of θ ignore the direct influence area of the inclusion, it comes that

$$\begin{aligned} \left| \int_{\partial\omega_\rho} \frac{\partial \eta}{\partial \mathbf{n}} v_1^\rho dS \right| &\leq C \|\theta\|_{L^\infty(\Omega \setminus \mathcal{U}_-)} \|\nabla \eta\|_{L^2(\Omega_\rho)} \|\nabla v_1^\rho\|_{L^2(\Omega_\rho)} + C \|v_1^\rho\|_{L^\infty(\Omega \setminus \mathcal{U}_-)} \|\nabla \eta\|_{L^2(\Omega_\rho)} \|\nabla \theta\|_{L^\infty(\Omega \setminus \mathcal{U}_-)} \\ &\quad + C \|\theta\|_{L^\infty(\Omega \setminus \mathcal{U}_-)} \|q_1^\rho\|_{L^\infty(\Omega \setminus \mathcal{U}_-)} \|\Delta \theta\|_{L^\infty(\Omega \setminus \mathcal{U}_-)} \|v_1^\rho\|_{L^\infty(\Omega \setminus \mathcal{U}_-)} \\ &\quad + C \|\theta\|_{L^\infty(\Omega \setminus \mathcal{U}_-)} \|v_1^\rho\|_{L^\infty(\Omega \setminus \mathcal{U}_-)} \|\nabla q_1^\rho\|_{L^\infty(\Omega \setminus \mathcal{U}_-)} \|\nabla \theta\|_{L^\infty(\Omega \setminus \mathcal{U}_-)} \\ &\leq C\rho^4 + C\rho^5 \leq C\rho^4. \end{aligned}$$

★ 4th term

Using the expansion of u on $\partial\omega_\rho$, it follows

$$\int_{\partial\omega_\rho} \frac{\partial p}{\partial \mathbf{n}} \delta dS = (\mathcal{C}(\rho) - u(\mathbf{x}_0)) \int_{\partial\omega_\rho} \frac{\partial p}{\partial \mathbf{n}} dS - \int_{\partial\omega_\rho} \frac{\partial p}{\partial \mathbf{n}} R_u dS = - \int_{\partial\omega_\rho} \frac{\partial p}{\partial \mathbf{n}} R_u dS.$$

Recalling the behavior of h implies that : $\exists C > 0, |R_u| \leq C\rho^2$ on $\partial\omega_\rho$. Cauchy-Schwarz inequality and a rescaling give

$$\left| \int_{\partial\omega_\rho} \frac{\partial p}{\partial \mathbf{n}} R_u dS \right| \leq \sqrt{\int_{\partial\omega_\rho} \left(\frac{\partial p}{\partial \mathbf{n}} \right)^2 dS} \sqrt{\int_{\partial\omega_\rho} R_u^2 dS} \leq C \sqrt{\rho^2 \int_{\partial\omega} \left(\frac{\partial p}{\partial \mathbf{n}}(\mathbf{x}_0) \right)^2 dS} \sqrt{\int_{\partial\omega_\rho} \rho^4 dS} \leq C\rho^4.$$

★ 5th term

This term is estimated as the previous one. Using the expansion of u on $\partial\omega_\rho$

$$\int_{\partial\omega_\rho} \frac{\partial q_1^\rho}{\partial \mathbf{n}} \delta dS = (\mathcal{C}(\rho) - u(\mathbf{x}_0)) \int_{\partial\omega_\rho} \frac{\partial q_1^\rho}{\partial \mathbf{n}} dS - \int_{\partial\omega_\rho} \frac{\partial q_1^\rho}{\partial \mathbf{n}} R_u dS = - \int_{\partial\omega_\rho} \frac{\partial q_1}{\partial \mathbf{n}} \left(\frac{\mathbf{x} - \mathbf{x}_0}{\rho} \right) R_u(\mathbf{x}) dS(\mathbf{x}).$$

Cauchy-Schwarz inequality and a rescaling give

$$\left| \int_{\partial\omega_\rho} \frac{\partial q_1}{\partial \mathbf{n}} \left(\frac{\mathbf{x} - \mathbf{x}_0}{\rho} \right) R_u(\mathbf{x}) dS(\mathbf{x}) \right| \leq \sqrt{\rho^2 \int_{\partial\omega} \left(\frac{\partial q_1}{\partial \mathbf{n}} \right)^2 dS} \sqrt{\int_{\partial\omega_\rho} R_u^2 dS} \leq C\rho^4.$$

★ 6th term

Multiply (3.42) by δ and integrate by parts

$$\int_{\partial\omega_\rho} \frac{\partial \eta}{\partial \mathbf{n}} \delta dS = \int_{\Omega_\rho} \nabla \eta \cdot \nabla \delta dV - \int_{\Omega_\rho} q_1^\rho \Delta \theta \delta dV - 2 \int_{\Omega_\rho} \delta \nabla q_1^\rho \nabla \theta dV.$$

The derivatives of θ are zero in the direct influence area of the inclusion. It comes with Cauchy-Schwarz and Poincaré inequalities and the L^∞ -norm of q_1^ρ and its gradient that

$$\begin{aligned} \left| \int_{\partial\omega_\rho} \frac{\partial \eta}{\partial \mathbf{n}} \delta dS \right| &\leq C \|\nabla \eta\|_{L^2(\Omega_\rho)} \|\nabla \delta\|_{L^2(\Omega_\rho)} + C \|q_1^\rho\|_{L^\infty(\Omega \setminus \mathcal{U}_-)} \|\Delta \theta\|_{L^\infty(\Omega \setminus \mathcal{U}_-)} \|\nabla \delta\|_{L^2(\Omega_\rho)} \\ &\quad + C \|\nabla \delta\|_{L^2(\Omega_\rho)} \|\nabla q_1^\rho\|_{L^\infty(\Omega \setminus \mathcal{U}_-)} \|\nabla \theta\|_{L^\infty(\Omega \setminus \mathcal{U}_-)} \\ &\leq C\rho^5. \end{aligned}$$

Remark 14. *The topological sensitivity with respect to an inclusion with a given conductivity κ for the Laplace equation has been derived in [11]. The inclusion becomes a high conducting one when its conductivity κ tends toward infinity. Then the topological derivative expressions in 2d and 3d described in [11] match with the expressions proposed in this section.*

3.2.3 Numerical illustrations

This section illustrates the topological sensitivity analysis in 2d and 3d with academical test cases with simple geometries and adimensional physical properties. For numerical purpose, the high conductivity of the inclusion is implemented with a large coefficient imposed inside ω_ρ . Thus, the conductivity of the background domain is simply $\kappa = 1$ while the one of the perturbed domain reads

$$\kappa = \begin{cases} 1 & \text{in } \Omega_\rho \\ 1 \times 10^6 & \text{in } \omega_\rho \end{cases}. \quad (3.43)$$

The problem is to use the topological derivative to put a small high conducting inclusion in order to decrease the thermal compliance $J(\Omega) = \int_{\Gamma_N} g u dS$, and consequently, increase the heat diffusion through the domain Ω . The new compliance, *i.e.* with the inclusion, is predicted with the estimator function

$$\mathcal{E}(\Omega_\rho) = J(\Omega) + \rho^n D J(\mathbf{x}_0). \quad (3.44)$$

It stands for the initial compliance perturbed with the topological derivative and its corresponding scaling of ρ . In other words, the estimator is the asymptotic expansion of the perturbed compliance at the first-order. Remainder terms are not taken into account.

2d test case

The geometry and the dimensions of the 2d test case are given in Fig. 3.3. The mesh is triangular with 31 778 elements and a minimal and maximal size of 4.5×10^{-3} and 1.0×10^{-2} . A Dirichlet condition $u = 0$ is imposed on the left border. The upper and the lower flux are respectively given by $g = 0.1x$ and $g = 0.1x - 1$. The oscillating flux on the right boundary is $g = 1.1 \left(1 + \cos \left(\frac{5\pi y}{0.5} \right) \right)$.

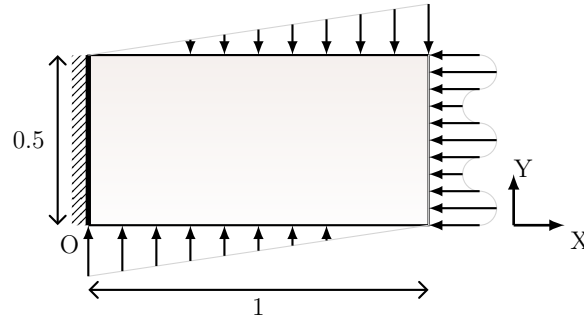


Figure 3.3: Dimensions and loading of the 2d test case

The initial compliance, *i.e.* without the inclusion, is $J_0(\Omega) = 0.309$. The size of the inclusion theoretically goes to zero. In practice, it depends on the mesh size. Let us take $\rho = 2.5 \times 10^{-2}$, which is consistent with the current mesh size. The topological derivative is computed strictly inside the domain. The design-space is explicitly defined in the mesh. It is delimited by the thin white line, visible in the following figures. The cartography of the topological derivative is displayed in Fig. 3.4a. The quantity $DJ(\mathbf{x}_0)$ is always negative and the best value is obviously the most negative one, that is $DJ(\mathbf{x}_0) = -11.81$. It puts the inclusion at the border of the design-space, close to the oscillating flux (see Fig. 3.4b). This new configuration leads to a thermal compliance of $J_\rho(\Omega) = 0.300$, which corresponds to a decrease of 3% of the initial value. The estimator is very satisfactory with a value of $\mathcal{E}(\Omega) = 0.302$.

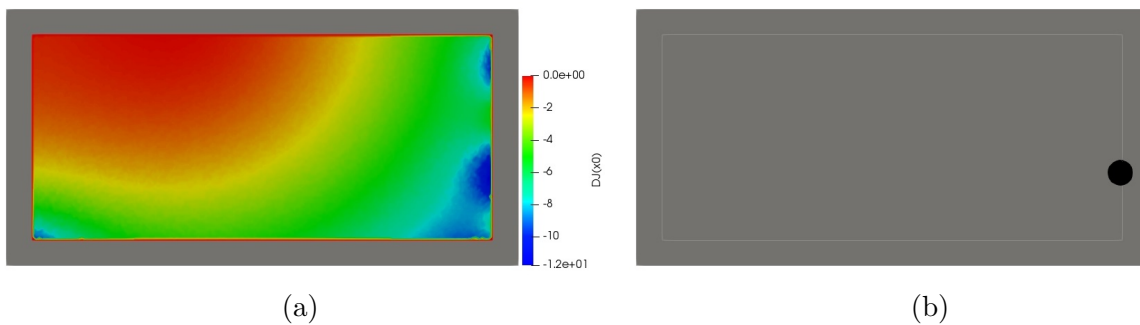


Figure 3.4: Cartography of $DJ(\mathbf{x}_0)$ (a) and the resulting high conducting inclusion (b)

The temperature fields u and the heat fluxes $-\kappa \nabla u$ in the background domain and in the perturbed domain are respectively displayed in Figs. 3.5 and 3.6. The influence of the inclusion is very local. The temperature decreases and the heat flux is much larger in the area of the inclusion. The punctual red flux in Fig. 3.6b shows that the heat diffuses more significantly in the inclusion and thus, contributes to decrease the thermal compliance.

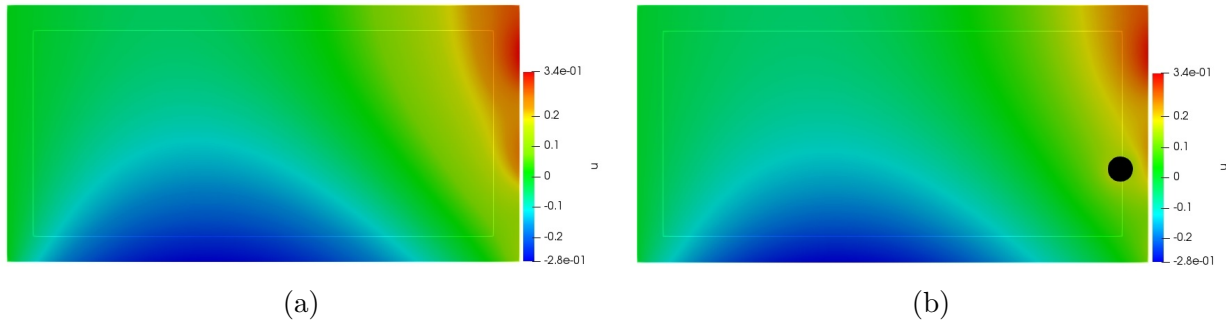


Figure 3.5: Temperature fields u in the background domain (a) and the perturbed domain (b)

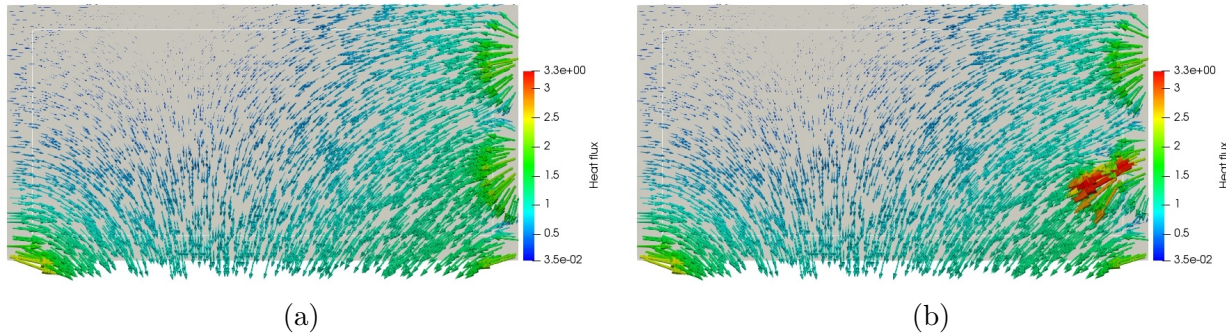


Figure 3.6: Heat fluxes $-\kappa \nabla u$ in the background domain (a) and the perturbed domain (b)

3d test case

The 3d test case is based on a hollow cylinder pictured in Fig. 3.7. This cylinder is meshed with 595 027 tetrahedron elements with a minimal and maximal size of 1.2×10^{-2} and 6.4×10^{-2} . A Dirichlet condition $u = 0$ is imposed on the external border of the cylinder. The internal cylinder is adiabatic. A constant flux $g = 1.5$ is imposed on the left hand-side of the cylinder, *i.e.* in the plan $Z = 0$, and an oscillating flux $g = 1 + \cos(5\pi y)$ is applied on the right-side, in the plan $Z = 2$.

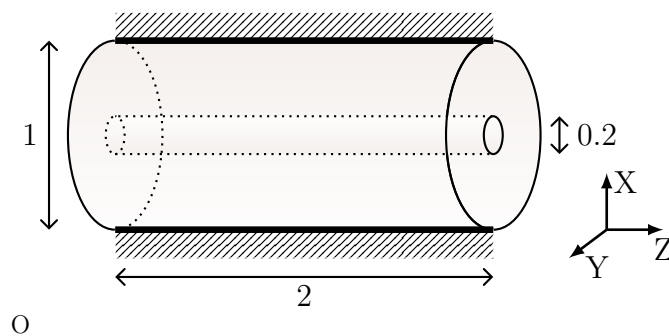


Figure 3.7: Dimensions of the 3d test case

The initial compliance is $J_0(\Omega) = 0.378$. Based on the mesh size, the radius of the inclusion is chosen to be $\rho = 5 \times 10^{-2}$. As for the 2d test case, the topological derivative is implemented strictly inside the domain. The inclusion is put at the most negative value of the topological derivative, that is $DJ(\mathbf{x}_0) = -15.20$. It corresponds to the point $\mathbf{x}_0 = (-0.23, 0.29, 0.10)$ (see Fig. 3.8). The new compliance with the inclusion is then $J_\rho(\Omega) = 0.373$. It corresponds to a decrease of 1.32% of the thermal compliance. The estimator gives $\mathcal{E}(\Omega) = 0.376$. Different

iso-values of $DJ(\mathbf{x}_0)$ are given in Fig. 3.9. The most interesting ones are naturally localized close to the constant flux that has the largest amplitude. The two fluxes do not interact because of the length of the cylinder. This is why there are two crowns of iso-values of the topological derivative (cf. Fig. 3.9a).

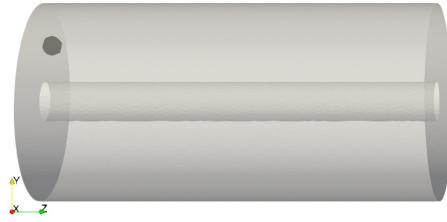


Figure 3.8: Location of the high conducting inclusion

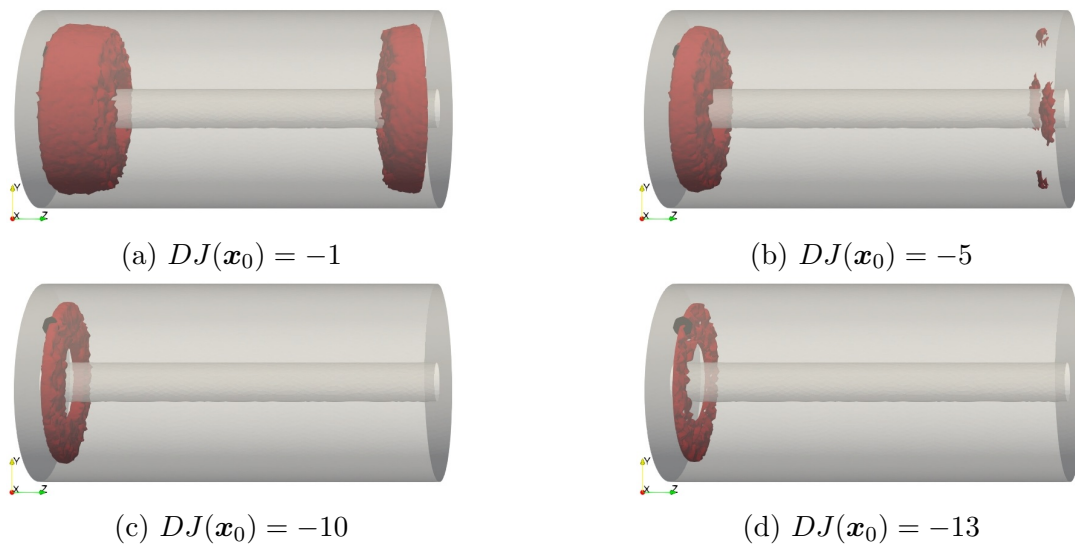


Figure 3.9: Iso-values of $DJ(\mathbf{x}_0)$

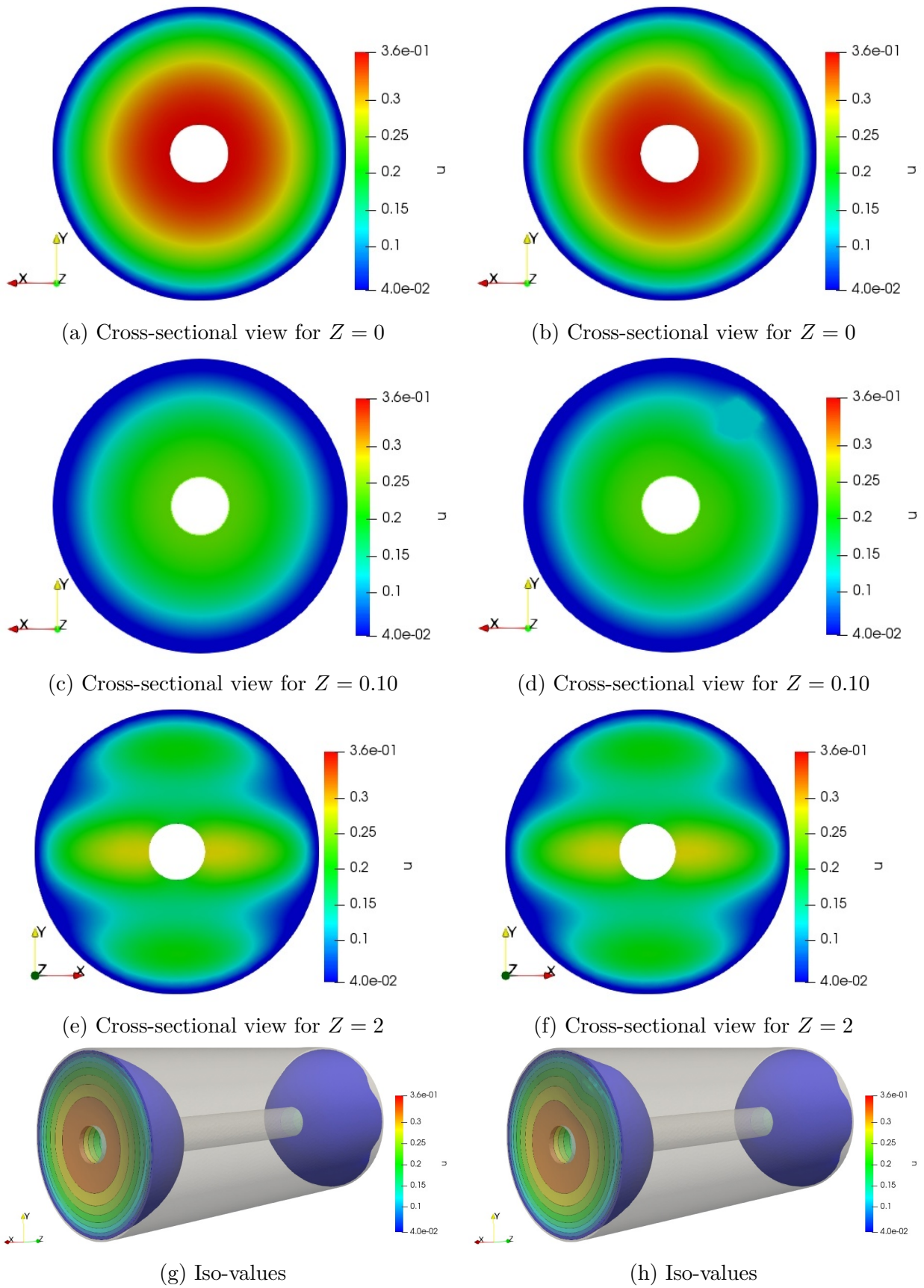


Figure 3.10: Temperature fields u and its iso-values in the background domain (a), (c), (e), (g) and in the domain with the inclusion (b), (d), (f), (h)

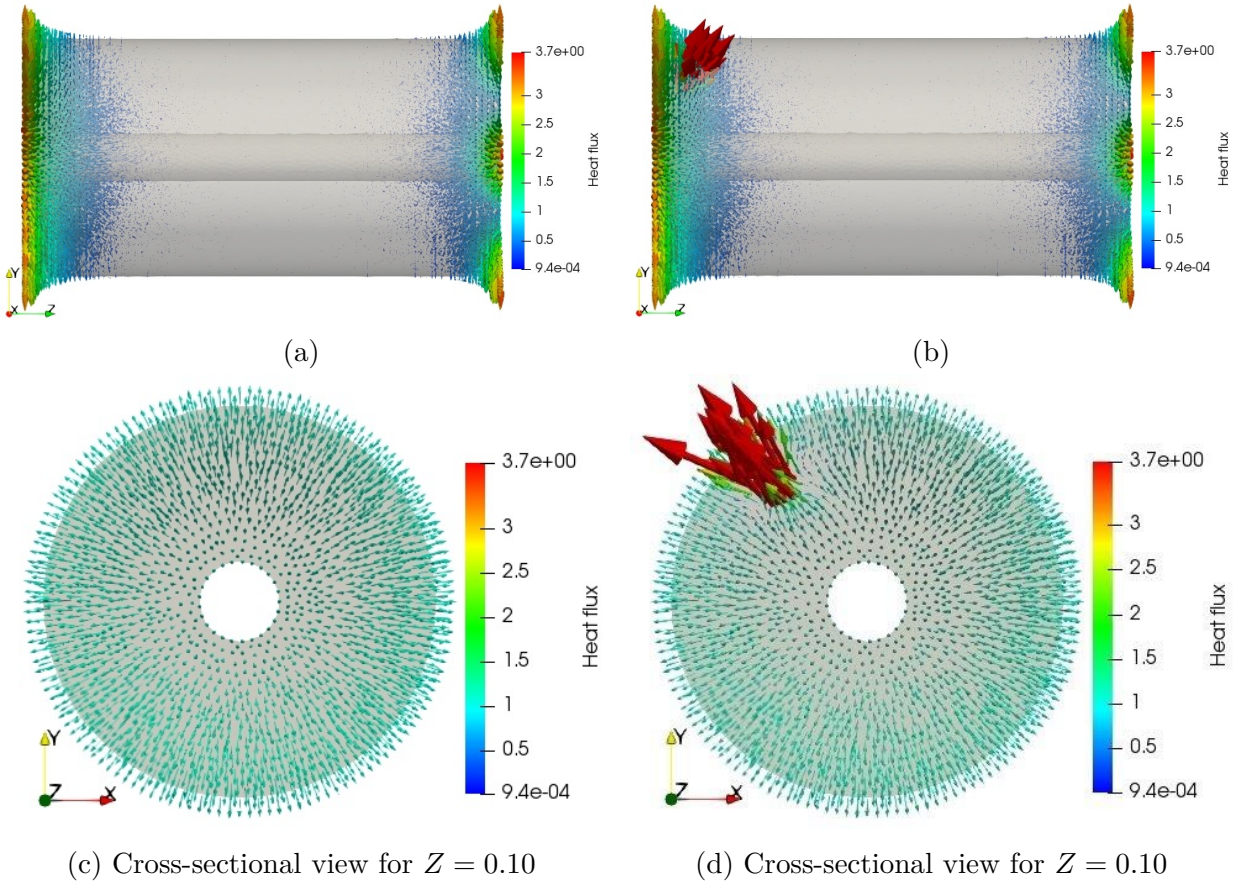


Figure 3.11: Heat fluxes $-\kappa\nabla u$ in the background domain (a), (c) and in the domain with the inclusion (b), (d)

The temperature fields u in the background and in the perturbed domains are displayed in Figs. 3.10. The high conducting inclusion influences locally the temperature field (see Figs. 3.10b and 3.10d). It does not impact the opposite side of the cylinder (see Figs. 3.10f and 3.10h). The local impact of the high conducting inclusion is much more visible on the heat flux of the perturbed domain (see Fig. 3.11). The inclusion diffuses locally an important quantity of heat. The heat diffusion is almost multiplied by a factor 4 in the inclusion area. However, the inclusion size is too small to induce more important decrease of the compliance. Then its impact is strictly local.

3.3 Topological sensitivity analysis with respect to a thermal bridge

This section deals with the asymptotic analysis with respect to a thermal bridge. It is modeled by two spherical inclusions of size $\rho > 0$, denoted ω_A and ω_B , linked by a bar or a bridge of thermal conductivity $\kappa(\rho)$. This bridge is equivalent to a spring in elasticity. It is modeled by two approaches : an average one and a point-to-point one. In other words, the bar links the average temperature of each sphere in the first case and it links each point of the two spheres in the other case. The goal of this section is to compute the topological derivative with respect to a small thermal bridge inside the sub-domain Ω_2 .

3.3.1 Perturbation of the domain

Let us perturb the background domain Ω with a small thermal bridge inside the sub-domain Ω_2 as illustrated in Fig. 3.12. Denote ω the unit ball of \mathbb{R}^n , $n = 2$ or 3 , as the reference shape of the inclusions. Denote also $r_1 = 1$ the radius of ω . This thermal bridge is modeled by two inclusions of shape ω resized by an adimensional factor $\rho > 0$, denoted ω_A and ω_B . In the following, the factor ρ refers abusively to the size of the inclusions. The first sphere, ω_A , is centered at the point $\mathbf{x}_0 \in \Omega_2$. The second one, ω_B , is the translation of ω_A at a distance $\ell > 0$ and in the direction \mathbf{e} , a unit vector, provided that ω_B is still inside Ω_2 . More specifically, it reads

$$\omega_A = \left\{ \mathbf{x} \in \mathbb{R}^n, \frac{\mathbf{x} - \mathbf{x}_0}{\rho} \in \omega \right\} \text{ and } \omega_B = \left\{ \mathbf{x} \in \mathbb{R}^n, \frac{\mathbf{x} - \mathbf{x}_0 - \ell \mathbf{e}}{\rho} \in \omega \right\}. \quad (3.45)$$

The inclusions are linked to each other by a bar of conductivity $\kappa(\rho)$. Let us assume the following scaling of the model

$$\kappa(\rho) = K \rho^k, \quad (3.46)$$

with $K > 0$ and $k \in \mathbb{R}$. It will be shown later that only those values $k > 0$ are covered by our asymptotic analysis. Denote Ω_ρ the perforated domain, in other words, the domain without the two spheres ω_A and ω_B

$$\Omega_\rho = \Omega \setminus (\omega_A \cup \omega_B). \quad (3.47)$$

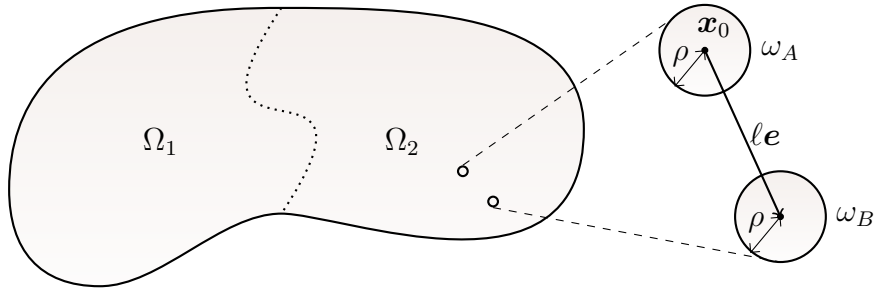


Figure 3.12: Perturbation of the domain Ω with a small thermal bridge in the subdomain Ω_2

Two models of thermal bridge are proposed here. The first one relies on an average approach. The bar links the average temperature of each sphere. Then, the bridge takes constant temperatures into account. The second model is a point-to-point approach. The bar links each point of a sphere to its translated in the other sphere. Both models are established with an energetic formulation.

- **Average approach**

Let us introduce the following notation for the average temperature on ω_A

$$\bar{f}_{\omega_A} = \frac{1}{|\omega_A|} \int_{\omega_A} f dV.$$

Let E_{av} be the energy functional

$$E_{av}(w) = \frac{1}{2} \int_{\Omega} |\nabla w|^2 dV - \int_{\Gamma_N} g w dS + \frac{1}{2} \kappa(\rho) \left(\bar{f}_{\omega_B} w dV - \bar{f}_{\omega_A} w dV \right)^2. \quad (3.48)$$

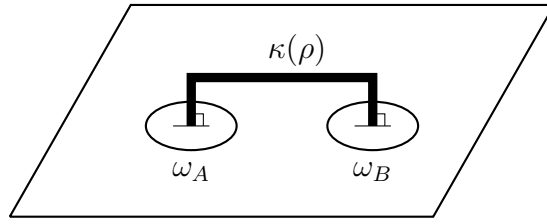


Figure 3.13: Graphical representation of the non-local conductivity $\kappa(\rho)$

The first term of (3.48) is the thermal energy. The last term is the energy of the thermal bridge of conductivity $\kappa(\rho)$. This is a non-local quantity that is depicted as an out-of-plane bar that links ω_A and ω_B (see Fig. 3.13).

The minimum potential energy principle states that the temperature field that describes the system with a thermal bridge is the unique minimizer u_ρ of (3.48) in \mathcal{W} defined by (3.2), *i.e.*,

$$E_{av}(u_\rho) = \min_{w \in \mathcal{W}} E_{av}(w). \quad (3.49)$$

It leads to the following variational problem :

$$\begin{aligned} \text{Find } u_\rho \in \mathcal{W} \text{ s.t. } \forall w \in \mathcal{W}, \int_{\Omega} \nabla u_\rho \cdot \nabla w dV - \int_{\Gamma_N} g w dS \\ + \kappa(\rho) \left(\int_{\omega_B} u_\rho dV - \int_{\omega_A} u_\rho dV \right) \left(\int_{\omega_B} w dV - \int_{\omega_A} w dV \right) = 0. \end{aligned} \quad (3.50)$$

Assuming that the heat flux g belongs to $L^2(\Gamma_N)$, Lax-Milgram theorem gives the existence and the uniqueness of the solution $u_\rho \in \mathcal{W}$. Then u_ρ solves

$$\left\{ \begin{array}{ll} -\Delta u_\rho = 0 & \text{in } \Omega_\rho \\ -\Delta u_\rho - \frac{\kappa(\rho)}{|\omega_A|} \left(\int_{\omega_B} u_\rho dV - \int_{\omega_A} u_\rho dV \right) = 0 & \text{in } \omega_A \\ -\Delta u_\rho + \frac{\kappa(\rho)}{|\omega_B|} \left(\int_{\omega_B} u_\rho dV - \int_{\omega_A} u_\rho dV \right) = 0 & \text{in } \omega_B \\ \frac{\partial u_\rho}{\partial \mathbf{n}} = g & \text{on } \Gamma_N \\ u_\rho = 0 & \text{on } \Gamma_D \end{array} \right. \quad (3.51)$$

- **Point-to-point approach**

Let E_{pt} be the energy functional

$$E_{pt}(w) = \frac{1}{2} \int_{\Omega} |\nabla w|^2 dV - \int_{\Gamma_N} g w dS + \frac{1}{2} \kappa(\rho) \int_{\omega_A} (w(\mathbf{x} + \ell \mathbf{e}) - w(\mathbf{x}))^2 dV. \quad (3.52)$$

The energy of the thermal bridge is divided by the volume of ω_A . Therefore, the energetic contribution of the bridge is a volumetric. Then, the point-to-point approach scaling of ρ is homogeneous to the average approach scaling. The two models are then comparable. The

minimum potential energy principle states that the temperature field that describes the system with a thermal bridge is the unique minimizer u_ρ of (3.52) in \mathcal{W} , i.e.,

$$E_{pt}(u_\rho) = \min_{w \in \mathcal{W}} E_{pt}(w). \quad (3.53)$$

It leads to the following variational problem :

$$\begin{aligned} \text{Find } u_\rho \in \mathcal{W} \text{ s.t. } \forall w \in \mathcal{W}, \int_{\Omega} \nabla u_\rho \cdot \nabla w dV - \int_{\Gamma_N} g w dS \\ + \kappa(\rho) \int_{\omega_A} (u_\rho(\mathbf{x} + \ell \mathbf{e}) - u_\rho(\mathbf{x})) (w(\mathbf{x} + \ell \mathbf{e}) - w(\mathbf{x})) dV = 0. \end{aligned} \quad (3.54)$$

Assuming that the heat flux g belongs to $L^2(\Gamma_N)$, Lax-Milgram theorem gives the existence and the uniqueness of the solution $u_\rho \in \mathcal{W}$. Then the strong form of the point-to-point approach is

$$\left\{ \begin{array}{ll} -\Delta u_\rho = 0 & \text{in } \Omega_\rho \\ -\Delta u_\rho - \frac{\kappa(\rho)}{|\omega_A|} (u_\rho(\mathbf{x} + \ell \mathbf{e}) - u_\rho(\mathbf{x})) = 0 & \text{in } \omega_A \\ -\Delta u_\rho + \frac{\kappa(\rho)}{|\omega_B|} (u_\rho(\mathbf{x}) - u_\rho(\mathbf{x} - \ell \mathbf{e})) = 0 & \text{in } \omega_B \\ \frac{\partial u_\rho}{\partial \mathbf{n}} = g & \text{on } \Gamma_N \\ u_\rho = 0 & \text{on } \Gamma_D \end{array} \right. \quad (3.55)$$

Remark 15. *The volume of ω_B appears is the volumetric loading in ω_B because the two spheres have the same volume.*

In the following, the perturbed domain is the domain with the thermal bridge either for the average approach or for the point-to-point one. For both models, the generic objective function (3.3) evaluated in the perturbed domain reads

$$J_\rho(\Omega) = \int_{\Omega_1} F(u_\rho) dV + \int_{\Gamma_N} G(u_\rho) dS. \quad (3.56)$$

Definition 4. *The objective function J_ρ is said to admit a topological derivative $DJ(\mathbf{x}_0, \mathbf{e})$ at the point \mathbf{x}_0 for a thermal bridge of direction \mathbf{e} and for a pair of inclusions of shape ω , if the following asymptotic expansion holds for small $\rho > 0$*

$$J_\rho(\Omega) = J_0(\Omega) + s(\rho) DJ(\mathbf{x}_0, \mathbf{e}) + o(s(\rho)), \quad (3.57)$$

where $s(\rho)$ is a positive scalar function of ρ which satisfies $\lim_{\rho \rightarrow 0} s(\rho) = 0$.

Remark 16. *The topological derivative given in this definition depends on two parameters, the location of the center of the first inclusion \mathbf{x}_0 and the direction of the bridge \mathbf{e} . In more classical definition [36, 86, 107], the topological derivative depends only on the center \mathbf{x}_0 of a single inclusion.*

Theorem 2. Take ω to be the unit ball of \mathbb{R}^n , $n = 2$ or 3 .

In 2d, the general objective function (3.56) admits a topological asymptotic expansion of the form (3.57), for all $k > 0$ with the average approach

$$J_\rho(\Omega) = J_0(\Omega) + K\rho^k(u(\mathbf{x}_0 + \ell\mathbf{e}) - u(\mathbf{x}_0)) \cdot \mathbf{e}(p(\mathbf{x}_0 + \ell\mathbf{e}) - p(\mathbf{x}_0)) \cdot \mathbf{e} + \begin{cases} O(\rho^{k+2}) & \text{if } k \geq 4 \\ O(\rho^{3k/2}) & \text{if } 0 < k < 4 \end{cases}, \quad (3.58)$$

where u and p are respectively the temperature and the adjoint state in the background domain that solve (3.1) and (3.5).

In 3d, the general objective function (3.56) admits a topological asymptotic expansion of the form (3.57), for all $k > 0$ with the average and point-to-point approaches, that is

$$J_\rho(\Omega) = J_0(\Omega) + s(\rho)DJ(\mathbf{x}_0, \mathbf{e}) + \mathcal{R}(s(\rho)), \quad (3.59)$$

with

$$DJ(\mathbf{x}_0, \mathbf{e}) = j(K, \omega)(u(\mathbf{x}_0 + \ell\mathbf{e}) - u(\mathbf{x}_0))(p(\mathbf{x}_0 + \ell\mathbf{e}) - p(\mathbf{x}_0)), \quad (3.60)$$

where u and p are respectively the temperature and the adjoint state in the background domain that solve (3.1) and (3.5). The scaling $s(\rho)$, the coefficient $j(K, \omega)$ and the remainder term $\mathcal{R}(s(\rho))$ are given, according to the value of the exponent k , by

		$j(K, \omega)$				
		$s(\rho)$	average	point-to-point	$\mathcal{R}(s(\rho))$	
$k > 1$	ρ^k	K	K	K	$k > 4$	$O(\rho^{k+2})$
					$2 \leq k \leq 4$	$O(\rho^{3k/2})$
					$k < 2$	$O(\rho^{2k-1})$
$k = 1$	ρ	$\left(\frac{1}{K} + \frac{4r_1^2}{5 \omega }\right)^{-1}$	$2\pi r_1 \left(1 - \frac{\tanh\left(r_1\sqrt{\frac{2K}{ \omega }}\right)}{r_1\sqrt{\frac{2K}{ \omega }}}\right)$	$2\pi r_1 \left(1 - \frac{\tanh\left(r_1\sqrt{\frac{2K}{ \omega }}\right)}{r_1\sqrt{\frac{2K}{ \omega }}}\right)$	$O(\rho^{3/2})$	
$0 < k < 1$	ρ	$\frac{5 \omega }{4r_1^2}$	$2\pi r_1 \left(1 - \frac{\tanh\left(r_1\sqrt{\frac{2K\rho^{k-1}}{ \omega }}\right)}{r_1\sqrt{\frac{2K\rho^{k-1}}{ \omega }}}\right)$	$2\pi r_1 \left(1 - \frac{\tanh\left(r_1\sqrt{\frac{2K\rho^{k-1}}{ \omega }}\right)}{r_1\sqrt{\frac{2K\rho^{k-1}}{ \omega }}}\right)$	$k \geq 2/3$	$O(\rho^{2-k})$
					$k < 2/3$	$O(\rho^{1+k/2})$

Remark 17. For all $k > 0$, topological derivatives depend on the temperature field u and the adjoint state p in the same way for both the average and the point-to-point approaches. They share the same behavior with regards to k but differ from their coefficients that stem from the far field expressions. For $k > 1$, both topological derivatives have the same expression. It shows up the predominance of the bar conductivity on the asymptotic analysis. The inclusions and the bar conductivities are on equal importance for $k = 1$. The case $0 < k < 1$ relies on the inclusion properties. The remainder term is the same whatever the bar is modeled by the average or the point-to-point approach.

3.3.2 Computation of the topological derivative

The computation of the topological derivative of both models follows the same methodology. For the sake of simplicity, it is fully developed for the average approach in 3d and main results are given for the point-to-point approach. This section aims to approximate the perturbation due to the two spherical inclusions linked by a thermal bridge of conductivity $\kappa(\rho)$. The behavior of the perturbed temperature field u_ρ is first approximated with explicit far field functions. They zoom on each spherical inclusion and ignore the boundary conditions on $\partial\Omega$. Then, rigorous estimates are established with an asymptotic analysis using these far field functions.

Approximation of the perturbed temperature field

- Far field expressions

Both inclusions ω_A and ω_B have a small size ρ . The perturbed temperature field u_ρ is then expected to be approximately equal to the background field u plus the influence fields of the inclusions ω_A and ω_B , respectively denoted v_a and v_b . In other words, we formally assume an ansatz that

$$u_\rho(\mathbf{x}) \approx u(\mathbf{x}) + v_a \left(\frac{\mathbf{x} - \mathbf{x}_0}{\rho} \right) + v_b \left(\frac{\mathbf{x} - \mathbf{x}_0 - \ell \mathbf{e}}{\rho} \right). \quad (3.61)$$

The functions v_a and v_b are defined in \mathbb{R}^3 . Perturbations due to the inclusions are getting smaller far from their center \mathbf{x}_0 and $\mathbf{x}_0 + \ell \mathbf{e}$. Then, they have to decay at infinity like $\lim_{\mathbf{y} \rightarrow \infty} v_a(\mathbf{y}) = 0$ and $\lim_{\mathbf{y} \rightarrow \infty} v_b(\mathbf{y}) = 0$. In other words, these functions allow a zoom on the inclusions and ignore boundary conditions on $\partial\Omega$. The goal of this subsection is to approximate the perturbed temperature field u_ρ using the behavior of the far fields v_a and v_b . For greater clarity, the far fields are differentiate with an exponent "av" for the average method and "pt" for the point-to-point formulation. In order to rescale the elasticity problem with inclusions of unit size ω , let us define rescaled variables $\mathbf{y}_a \in \mathbb{R}^3$ and $\mathbf{y}_b \in \mathbb{R}^3$ by

$$\mathbf{y}_a = \frac{\mathbf{x} - \mathbf{x}_0}{\rho} \text{ and } \mathbf{y}_b = \frac{\mathbf{x} - \mathbf{x}_0 - \ell \mathbf{e}}{\rho}. \quad (3.62)$$

Let us now set the following Taylor expansions of the background solution

$$u(\mathbf{x}) = u(\mathbf{x}_0) + O(\rho) \text{ in a neighbourhood of } \mathbf{x}_0, \quad (3.63)$$

$$u(\mathbf{x}) = u(\mathbf{x}_0 + \ell \mathbf{e}) + O(\rho) \text{ in a neighbourhood of } \mathbf{x}_0 + \ell \mathbf{e}. \quad (3.64)$$

Functions v_a and v_b are coupled in both models. For the average approach, they respectively solve

$$\begin{cases} -\Delta v_a^{av}(\mathbf{y}_a) = 0 & \text{in } \mathbb{R}^3 \setminus \omega \\ -\Delta v_a^{av}(\mathbf{y}_a) = \xi_u^{av}(\rho) & \text{in } \omega \\ \lim_{\mathbf{y}_a \rightarrow \mathbf{0}} v_a^{av}(\mathbf{y}_a) = 0 \end{cases} \text{ and } \begin{cases} -\Delta v_b^{av}(\mathbf{y}_b) = 0 & \text{in } \mathbb{R}^3 \setminus \omega \\ -\Delta v_b^{av}(\mathbf{y}_b) = -\xi_u^{av}(\rho) & \text{in } \omega \\ \lim_{\mathbf{y}_b \rightarrow \mathbf{0}} v_b^{av}(\mathbf{y}_b) = 0 \end{cases}, \quad (3.65)$$

with

$$\xi_u^{av}(\rho) = \frac{\kappa(\rho)}{\rho|\omega|} \left(\int_{\omega} (v_b^{av} - v_a^{av}) dV + u(\mathbf{x}_0 + \ell \mathbf{e}) - u(\mathbf{x}_0) \right). \quad (3.66)$$

Remark 18. *At first sight, the coefficient $\xi_u^{av}(\rho)$ does not depend on u as presumed by the subscript "u". The following lemmas prove that $\xi_u^{av}(\rho)$ actually depends on u thanks to explicit expressions of v_a^{av} and v_b^{av} .*

Lemma 3. *The functions v_a^{av} and v_b^{av} satisfying (3.65) verify*

$$\forall \mathbf{y} \in \mathbb{R}^3, v_a^{av}(\mathbf{y}) = -v_b^{av}(\mathbf{y}). \quad (3.67)$$

Proof. Setting $w = v_a^{av} + v_b^{av}$, it comes that w solves

$$\begin{cases} -\Delta w(\mathbf{y}) = 0 & \text{in } \mathbb{R}^3 \\ \lim_{\mathbf{y} \rightarrow \mathbf{0}} w(\mathbf{y}) = 0 \end{cases}. \quad (3.68)$$

One can easily see that $w = 0$, which implies that $v_a^{av} = -v_b^{av}$. \square

At first sight, the far fields v_a^{av} and v_b^{av} are coupled as expressed in (3.65). However, Lemma 3 means that these functions are actually decoupled. More precisely, they are opposite which states the equilibrium of the bridge. The same conclusion holds true for the far fields of the point-to-point approach, v_a^{pt} and v_b^{pt} .

Lemma 4. *The functions v_a^{av} and v_a^{pt} are explicitly given by*

$$v_a^{av}(r) = \begin{cases} \xi_u^{av}(\rho) \frac{r_1^3}{3r} & \text{in } \mathbb{R}^3 \setminus \omega \\ \xi_u^{av}(\rho) \left(\frac{r_1^2}{2} - \frac{r^2}{6} \right) & \text{in } \omega \end{cases}, \quad (3.69)$$

$$v_a^{pt}(r) = \begin{cases} \frac{1}{2r} \left(r_1 - \frac{\tanh(r_1 \sqrt{2\xi_u^{pt}(\rho)})}{\sqrt{2\xi_u^{pt}(\rho)}} \right) (u(\mathbf{x}_0 + \ell \mathbf{e}) - u(\mathbf{x}_0)) & \text{in } \mathbb{R}^3 \setminus \omega \\ \frac{1}{2} \left(1 - \frac{\sinh(r \sqrt{2\xi_u^{pt}(\rho)})}{r \sqrt{2\xi_u^{pt}(\rho)} \cosh(r_1 \sqrt{2\xi_u^{pt}(\rho)})} \right) (u(\mathbf{x}_0 + \ell \mathbf{e}) - u(\mathbf{x}_0)) & \text{in } \omega \end{cases}, \quad (3.70)$$

with

$$\xi_u^{av}(\rho) = \frac{\frac{\kappa(\rho)}{\rho|\omega|}}{1 + \frac{4\kappa(\rho)r_1^2}{5\rho|\omega|}} (u(\mathbf{x}_0 + \ell \mathbf{e}) - u(\mathbf{x}_0)) \text{ and } \xi_u^{pt}(\rho) = \frac{\kappa(\rho)}{\rho|\omega|}. \quad (3.71)$$

Remark 19. *The complexity of the expression of the far field for the point-to-point approach augurs harder calculus. There are not transcribed in the following. Nonetheless, the point-to-point approach provides theoretically the same estimates of the perturbed temperature field as the average approach.*

Proof. The proof is only performed for the average approach. The point-to-point can be solved with a similar methodology but it brings out more complex functions. There is no preferential direction in (3.65). Moreover, the inclusions are spheres. The far field function v_a^{av} is then determined in spherical coordinates, with $r = \|\mathbf{y}\|$. In $\mathbb{R}^3 \setminus \omega$, the solution is already known to be of the form $v_a^{av} = \frac{C_1}{r} + C_2$. In ω , the solution is determined by the variation of constants method, which gives $v_a^{av} = -\frac{\xi_u^{av}(\rho)}{6} r^2 + \frac{C_3}{r} + C_4$. The resolution is completed with continuity

conditions on $v_a^{av}(r)$ and $\nabla v_a^{av}(r)$ on $\partial\omega$, in other words, for $r = r_1$. Given the expression of v_a^{av} , its average on ω is

$$\int_{\omega} v_a^{av} dV = \frac{2}{5} r_1^2 \xi_u^{av}(\rho). \quad (3.72)$$

Then the explicit expression of $\xi_u^{av}(\rho)$, given by (3.71), results from the combination of (3.66) and (3.72) \square

- **Asymptotic analysis of the perturbed temperature field**

This part legitimates the previous approximation of the perturbed temperature field. Rigorous estimates are established using the behavior of the far field function v_a^{av} . Let v_ρ be the difference between the perturbed and the background temperature

$$v_\rho = u_\rho - u. \quad (3.73)$$

This function represents the influence of the bridge perturbation and it solves

$$\left\{ \begin{array}{ll} -\Delta v_\rho = 0 & \text{in } \Omega_\rho \\ -\Delta v_\rho - \frac{\kappa(\rho)}{|\omega_A|} \left(\int_{\omega_B} v_\rho dV - \int_{\omega_A} v_\rho dV \right) = \frac{\kappa(\rho)}{|\omega_A|} \left(\int_{\omega_B} u dV - \int_{\omega_A} u dV \right) & \text{in } \omega_A \\ -\Delta v_\rho + \frac{\kappa(\rho)}{|\omega_B|} \left(\int_{\omega_B} v_\rho dV - \int_{\omega_A} v_\rho dV \right) = -\frac{\kappa(\rho)}{|\omega_B|} \left(\int_{\omega_B} u dV - \int_{\omega_A} u dV \right) & \text{in } \omega_B \\ \frac{\partial v_\rho}{\partial \mathbf{n}} = 0 & \text{on } \Gamma_N \\ v_\rho = 0 & \text{on } \Gamma_D \end{array} \right. \quad (3.74)$$

The temperature field v_ρ is as smooth as u_ρ and u . Let us introduce the function

$$v(\mathbf{x}) = v_a^{av} \left(\frac{\mathbf{x} - \mathbf{x}_0}{\rho} \right) + v_b^{av} \left(\frac{\mathbf{x} - \mathbf{x}_0 - \ell \mathbf{e}}{\rho} \right), \quad (3.75)$$

where v_a^{av} and v_b^{av} verify Lemmas 3 and 4. As proved in the following result, v is in some sense, the limit of v_ρ as ρ goes to zero.

Proposition 7. *Let $\theta \in \mathcal{C}_c^\infty(\Omega)$ be a cut-off function with compact support $\mathcal{U}_+ \subset \Omega$ such that $\theta \equiv 1$ in a neighborhood $\mathcal{U}_- \subset \mathcal{U}_+$ of \mathbf{x}_0 and $\mathbf{x}_0 + \ell \mathbf{e}$. We have*

$$v_\rho = \theta v + \delta, \quad (3.76)$$

where δ is a remainder term as proved by the following estimates of the L^2 -norms of v and ∇v and H^1 -norm of δ . They are given, according to the value of the exponent k , by

	$\ v\ _{L^2(\Omega)}$	$\ \nabla v\ _{L^2(\Omega)}$	$\ \delta\ _{H^1(\Omega)}$
$k > 1$	$O(\rho^k)$	$O(\rho^{k-1/2})$	$O(\rho^k)$
$k = 1$	$O(\rho)$	$O(\sqrt{\rho})$	$O(\rho)$
$0 < k < 1$	$O(\rho)$	$O(\sqrt{\rho})$	$O(\rho)$

Proof. The explicit expressions of v_a^{av} and v_b^{av} indicate at infinity that $|v_a^{av}| = O\left(\frac{|\xi_u^{av}(\rho)|}{r}\right)$ and $|\nabla v_a^{av}| = O\left(\frac{|\xi_u^{av}(\rho)|}{r^2}\right)$. Thus, we deduce by rescaling

$$\|v\|_{L^\infty(\Omega \setminus \mathcal{U}_-)} \leq C\rho |\xi_u^{av}(\rho)| \text{ and } \|\varepsilon(v)\|_{L^\infty(\Omega \setminus \mathcal{U}_-)} \leq C\rho |\xi_u^{av}(\rho)|. \quad (3.77)$$

Let us define $\Omega_{\rho^{-1}}$ the rescaling of the domain Ω_ρ using $\mathbf{x} = \rho\mathbf{y} + \mathbf{x}_0$ for ρ small. We have

$$\begin{aligned} \|v\|_{L^2(\Omega)}^2 &\leq C\rho^3 \int_{\Omega_{\rho^{-1}}} |v_a|^2 dV + C\rho^3 \int_{\omega} |v_a|^2 dV \\ &\leq C\rho^3 |\xi_u(\rho)| \left(\frac{C \frac{\kappa(\rho)}{\rho}}{1 + C \frac{\kappa(\rho)}{\rho}} \right)^2 \int_{r_1}^{r_1/\rho} dr + C\rho^3 \left(\frac{C \frac{\kappa(\rho)}{\rho}}{1 + C \frac{\kappa(\rho)}{\rho}} \right)^2 \int_0^{r_1} r^6 dr \\ &\leq C\rho^2 \left(\frac{C \frac{\kappa(\rho)}{\rho}}{1 + C \frac{\kappa(\rho)}{\rho}} \right)^2. \end{aligned}$$

The denominator of the above upper bound is bounded if $k \geq 1$ and it goes to infinity otherwise. Therefore, for $k \geq 1$, one deduces

$$\|v\|_{L^2(\Omega)} \leq C\rho^k, \quad (3.78)$$

while, for $k < 1$,

$$\|v\|_{L^2(\Omega)} \leq C\rho. \quad (3.79)$$

Estimates of the L^2 -norm of ∇v are obtained with a similar argument

$$\begin{aligned} \|\nabla v\|_{L^2(\Omega)}^2 &\leq C\rho \int_{\Omega_{\rho^{-1}}} |\nabla v_a|^2 dV + C\rho \int_{\omega} |\nabla v_a|^2 dV \\ &\leq C\rho \left(\frac{C \frac{\kappa(\rho)}{\rho}}{1 + C \frac{\kappa(\rho)}{\rho}} \right)^2 \int_{r_1}^{r_1/\rho} \frac{1}{r^2} dr + C\rho \left(\frac{C \frac{\kappa(\rho)}{\rho}}{1 + C \frac{\kappa(\rho)}{\rho}} \right)^2 \int_0^{r_1} r^4 dr \\ &\leq C\rho \left(\frac{C \frac{\kappa(\rho)}{\rho}}{1 + C \frac{\kappa(\rho)}{\rho}} \right)^2. \end{aligned}$$

In particular, the upper bound for $\|\nabla v\|_{L^2(\Omega)}$ is larger, by a factor $1/\sqrt{\rho}$, than the upper bound for $\|v\|_{L^2(\Omega)}$.

Let us now write the equations satisfied by δ

$$\left\{ \begin{array}{ll} -\Delta\delta = v\Delta\theta + 2\nabla\theta \cdot \nabla v & \text{in } \Omega_\rho \\ -\Delta\delta - \frac{\kappa(\rho)}{|\omega_A|} \left(\int_{\omega_B} \delta dV - \int_{\omega_A} \delta dV \right) = \frac{\kappa(\rho)}{|\omega_A|} \left(\int_{\omega_B} u dV - \int_{\omega_A} u dV - (u(\mathbf{x}_0 + \ell\mathbf{e}) - u(\mathbf{x}_0)) \right) & \text{in } \omega_A \\ -\Delta\delta + \frac{\kappa(\rho)}{|\omega_B|} \left(\int_{\omega_B} \delta dV - \int_{\omega_A} \delta dV \right) = -\frac{\kappa(\rho)}{|\omega_A|} \left(\int_{\omega_B} u dV - \int_{\omega_A} u dV - (u(\mathbf{x}_0 + \ell\mathbf{e}) - u(\mathbf{x}_0)) \right) & \text{in } \omega_B \\ \frac{\partial\delta}{\partial\mathbf{n}} = 0 & \text{on } \Gamma_N \\ \delta = 0 & \text{on } \Gamma_D \end{array} \right. \quad (3.80)$$

A Taylor expansion with integral remainder at first order of the background solution in the neighborhood of \mathbf{x}_0 is

$$u(\mathbf{x}) = u(\mathbf{x}_0) + \nabla u(\mathbf{x}_0) \cdot (\mathbf{x} - \mathbf{x}_0) + \int_0^1 (1-t)(\mathbf{x} - \mathbf{x}_0)^T \mathbf{H}(u(\mathbf{x}_0 + t(\mathbf{x} - \mathbf{x}_0))) (\mathbf{x} - \mathbf{x}_0) dt, \quad (3.81)$$

with \mathbf{H} the Hessian matrix of u . Recalling that ω is the unit ball of \mathbb{R}^3 , it comes that $\int_{\omega_A} \nabla u(\mathbf{x}_0) \cdot (\mathbf{x} - \mathbf{x}_0) dV = \rho \int_{\omega} \nabla u(\mathbf{x}_0) \cdot \mathbf{y} dV = 0$. This particularity makes the first order term vanish in the sequel. Let us set the functions R_u^A and R_u^B that respectively stand for the integral remainder of the expansion of u in a neighborhood of \mathbf{x}_0 and $\mathbf{x}_0 + \ell\mathbf{e}$

$$\begin{aligned} R_u^A(\mathbf{x}) &= \int_0^1 (1-t)(\mathbf{x} - \mathbf{x}_0)^T \mathbf{H}(u(\mathbf{x}_0 + t(\mathbf{x} - \mathbf{x}_0))) (\mathbf{x} - \mathbf{x}_0) dt, \\ R_u^B(\mathbf{x}) &= \int_0^1 (1-t)(\mathbf{x} - \mathbf{x}_0 - \ell\mathbf{e})^T \mathbf{H}(u(\mathbf{x}_0 + \ell\mathbf{e} + t(\mathbf{x} - \mathbf{x}_0 - \ell\mathbf{e}))) (\mathbf{x} - \mathbf{x}_0 - \ell\mathbf{e}) dt. \end{aligned} \quad (3.82)$$

One can notice that $\mathbf{x} - \mathbf{x}_0$ is of the order of ρ in the neighborhood of \mathbf{x}_0 . Then, there exists $C > 0$ independent of ρ such that

$$|R_u^A| \leq C\rho^2 \text{ in the neighborhood of } \mathbf{x}_0. \quad (3.83)$$

Multiply (3.80) by δ , integrate by parts and apply the Taylor expansion (3.81). It follows that

$$\begin{aligned} \int_{\Omega} |\nabla\delta|^2 dV + \kappa(\rho) \left(\int_{\omega_B} \delta dV - \int_{\omega_A} \delta dV \right)^2 &= \int_{\Omega_\rho} v\Delta\theta\delta dV + 2 \int_{\Omega_\rho} \nabla\theta \cdot \nabla v \delta dV \\ &\quad - \kappa(\rho) \left(\int_{\omega_B} R_u^B dV - \int_{\omega_A} R_u^A dV \right) \left(\int_{\omega_B} \delta dV - \int_{\omega_A} \delta dV \right). \end{aligned}$$

Since the term $\kappa(\rho) \left(\int_{\omega_B} \delta dV - \int_{\omega_A} \delta dV \right)^2$ is positive, it is left apart for the rest of the analysis.

We recall that the derivatives of the cut-off function vanish in the direct influence area of the bridge. The two first right-hand terms are then estimated with Cauchy-Schwarz and Poincaré

inequalities and L^∞ -norms of v and ∇v

$$\begin{aligned} \left| \int_{\Omega_\rho} v \Delta \theta \delta dV \right| + 2 \left| \int_{\Omega_\rho} \nabla \theta \cdot \nabla v \delta dV \right| &\leq C \|v\|_{L^\infty(\Omega \setminus \mathcal{U}_-)} \|\Delta \theta\|_{L^\infty(\Omega \setminus \mathcal{U}_-)} \|\nabla \delta\|_{L^2(\Omega)} \\ &\quad + C \|\nabla \theta\|_{L^\infty(\Omega \setminus \mathcal{U}_-)} \|\nabla v\|_{L^\infty(\Omega \setminus \mathcal{U}_-)} \|\nabla \delta\|_{L^2(\Omega)} \\ &\leq C \rho |\xi_u^{av}(\rho)| \|\nabla \delta\|_{L^2(\Omega)}. \end{aligned}$$

The last right-hand term can also be bounded with Cauchy-Schwarz inequality but the resulting estimate is too restrictive in the framework of the current sensitivity analysis. Then, let us multiply (3.80) by v_ρ , integrate by parts and nd apply the Taylor expansion (3.81). It comes that

$$\begin{aligned} \kappa(\rho)(u(\mathbf{x}_0 + \ell \mathbf{e}) - u(\mathbf{x}_0)) \left(\int_{\omega_B} \delta dV - \int_{\omega_A} \delta dV \right) &= - \int_{\Omega_\rho} (\theta v^2 \Delta \theta + v \Delta \theta \delta + 2 \nabla \theta \cdot \nabla v \theta v + 2 \nabla \theta \cdot \nabla v \delta) dV \\ &\quad + \kappa(\rho) \left(\int_{\omega_B} R_u^B dV - \int_{\omega_A} R_u^A dV \right) \left(\int_{\omega_B} v dV - \int_{\omega_A} v dV \right). \end{aligned}$$

It follows the estimate

$$\begin{aligned} \kappa(\rho) \left| \int_{\omega_B} \delta dV - \int_{\omega_A} \delta dV \right| &\leq C \|v\|_{L^\infty(\Omega \setminus \mathcal{U}_-)}^2 + C \|v\|_{L^\infty(\Omega \setminus \mathcal{U}_-)} \|\delta\|_{L^2(\Omega)} + C \|\nabla v\|_{L^\infty(\Omega \setminus \mathcal{U}_-)} \|v\|_{L^\infty(\Omega \setminus \mathcal{U}_-)} \\ &\quad + C \|\nabla v\|_{L^\infty(\Omega \setminus \mathcal{U}_-)} \|\delta\|_{L^2(\Omega)} + C \rho^2 \kappa(\rho) |\xi_u^{av}(\rho)| \\ &\leq C \rho^2 |\xi_u^{av}(\rho)|^2 + C \rho^2 \kappa(\rho) |\xi_u^{av}(\rho)| + C \rho |\xi_u^{av}(\rho)| \|\nabla \delta\|_{L^2(\Omega)}. \end{aligned}$$

Regrouping all of that, we have

$$\|\nabla \delta\|_{L^2(\Omega)}^2 \leq C \rho |\xi_u^{av}(\rho)| \|\nabla \delta\|_{L^2(\Omega)} + C \rho^4 |\xi_u^{av}(\rho)| + C \rho^4 \kappa(\rho) |\xi_u^{av}(\rho)|.$$

Setting the following notations for a quick manipulation $X = \|\nabla \delta\|_{L^2(\Omega)}$, $a = C \rho |\xi_u^{av}(\rho)|$ and $b = C \rho^4 |\xi_u^{av}(\rho)|^2 + C \kappa(\rho) \rho^4 |\xi_u^{av}(\rho)|$, where X , a and b are non-negative, it comes that

$$\begin{aligned} \iff X^2 &\leq 2aX + b, \\ \iff |X - a| &\leq a^2 + b, \\ \iff X &\leq Ca + \sqrt{b}. \end{aligned}$$

As a result, there exists a constant $C > 0$ independent of ρ such that

$$\|\nabla \theta\|_{L^2(\Omega)} \leq C \rho |\xi_u(\rho)| + C \rho^2 |\xi_u(\rho)| + C \rho^2 \sqrt{\kappa(\rho) |\xi_u(\rho)|} \leq C \rho |\xi_u(\rho)| \text{ for } k > 0.$$

□

Approximation of the perturbed adjoint state

The adjoint state p_ρ associated to the perturbed problem (3.51) is approximated in the same manner. It solves

$$\left\{ \begin{array}{ll} -\Delta p_\rho = -F'(u) & \text{in } \Omega_\rho \\ -\Delta p_\rho - \frac{\kappa(\rho)}{|\omega_A|} \left(\int_{\omega_B} p_\rho dV - \int_{\omega_A} p_\rho dV \right) = 0 & \text{in } \omega_A \\ -\Delta p_\rho + \frac{\kappa(\rho)}{|\omega_B|} \left(\int_{\omega_B} p_\rho dV - \int_{\omega_A} p_\rho dV \right) = 0 & \text{in } \omega_B \\ \frac{\partial p_\rho}{\partial \mathbf{n}} = -G'(u) & \text{on } \Gamma_N \\ p_\rho = 0 & \text{on } \Gamma_D \end{array} \right. \quad (3.84)$$

Once again, the adjoint state is adapted to the sensitivity analysis. Therefore, the perturbed adjoint state depends on the background solution u and not on the perturbed solution u_ρ . The perturbation of the adjoint state is estimated with the $q_\rho = p_\rho - p$, the difference between the perturbed and the background adjoint states. It solves

$$\left\{ \begin{array}{ll} -\Delta q_\rho = 0 & \text{in } \Omega_\rho \\ -\Delta q_\rho - \frac{\kappa(\rho)}{|\omega_A|} \left(\int_{\omega_B} q_\rho dV - \int_{\omega_A} q_\rho dV \right) = \frac{\kappa(\rho)}{|\omega_A|} \left(\int_{\omega_B} p dV - \int_{\omega_A} p dV \right) & \text{in } \omega_A \\ -\Delta q_\rho + \frac{\kappa(\rho)}{|\omega_B|} \left(\int_{\omega_B} q_\rho dV - \int_{\omega_A} q_\rho dV \right) = -\frac{\kappa(\rho)}{|\omega_B|} \left(\int_{\omega_B} p dV - \int_{\omega_A} p dV \right) & \text{in } \omega_B \\ \frac{\partial q_\rho}{\partial \mathbf{n}} = 0 & \text{on } \Gamma_N \\ q_\rho = 0 & \text{on } \Gamma_D \end{array} \right. \quad (3.85)$$

We also introduce the functions q_a^{av} and q_b^{av} and the rescaled function

$$q(\mathbf{x}) = q_a^{av} \left(\frac{\mathbf{x} - \mathbf{x}_0}{\rho} \right) + q_b^{av} \left(\frac{\mathbf{x} - \mathbf{x}_0 - \ell \mathbf{e}}{\rho} \right), \quad (3.86)$$

such that q_a^{av} and q_b^{av} are respectively similar to v_a^{av} and v_b^{av} .

Proposition 8. *Let $\theta \in \mathcal{C}_c^\infty(\Omega)$ be a cut-off function with compact support $\mathcal{U}_+ \subset \Omega$ such that $\theta \equiv 1$ in a neighborhood $\mathcal{U}_- \subset \mathcal{U}_+$ of \mathbf{x}_0 and $\mathbf{x}_0 + \ell \mathbf{e}$. We have*

$$q_\rho = \theta q + \eta, \quad (3.87)$$

where η is a remainder term as can be checked by these estimates of the L^2 -norms of q and ∇q and the H^1 -norm of η . They are given, according to the value of the exponent k , by

Proof. The function η in the adjoint estimation is equivalent to the error term δ in the estimation

	$\ q\ _{L^2(\Omega)}$	$\ \nabla q\ _{L^2(\Omega)}$	$\ \eta\ _{H^1(\Omega)}$
$k > 1$	$O(\rho^k)$	$O(\rho^{k-1/2})$	$O(\rho^k)$
$k = 1$	$O(\rho)$	$O(\sqrt{\rho})$	$O(\rho)$
$k < 1$	$O(\rho)$	$O(\sqrt{\rho})$	$O(\rho)$

of the perturbed temperature field. Then, η solves

$$\left\{ \begin{array}{ll} -\Delta\eta = v\Delta\theta + 2\nabla\theta \cdot \nabla v & \text{in } \Omega_\rho \\ -\Delta\eta - \frac{\kappa(\rho)}{|\omega_A|} \left(\int_{\omega_B} \eta dV - \int_{\omega_A} \eta dV \right) = \frac{\kappa(\rho)}{|\omega_A|} \left(\int_{\omega_B} p dV - \int_{\omega_A} p dV - (p(\mathbf{x}_0 + \ell\mathbf{e}) - p(\mathbf{x}_0)) \right) & \text{in } \omega_A \\ -\Delta\eta + \frac{\kappa(\rho)}{|\omega_B|} \left(\int_{\omega_B} v dV - \int_{\omega_A} \eta dV \right) = -\frac{\kappa(\rho)}{|\omega_A|} \left(\int_{\omega_B} p dV - \int_{\omega_A} p dV - (p(\mathbf{x}_0 + \ell\mathbf{e}) - p(\mathbf{x}_0)) \right) & \text{in } \omega_B \\ \frac{\partial\eta}{\partial\mathbf{n}} = 0 & \text{on } \Gamma_N \\ \eta = 0 & \text{on } \Gamma_D \end{array} \right. \quad (3.88)$$

Proposition 8 is proved by going back over the proof of Proposition 7 and by substituting respectively u and v_ρ with p and q_ρ . \square

Proof of the main result

Theorem 2 is proved using the approximation of u_ρ and p_ρ . We recall the objective function in the background domain

$$J_0(\Omega) = \int_{\Omega_1} F(u) dV + \int_{\Gamma_N} G(u) dS.$$

Let us write a first-order Taylor expansion with exact remainder of the perturbed objective function

$$\begin{aligned} J_\rho(\Omega) &= \int_{\Omega_1} F(u_\rho) dV + \int_{\Gamma_N} G(u_\rho) dS = \int_{\Omega_1} F(u + v_\rho) dV + \int_{\Gamma_N} G(u + v_\rho) dS \\ &= J_0(\Omega) + \int_{\Omega_1} F'(u) v_\rho dV + \int_{\Gamma_N} G'(u) v_\rho dS + \frac{1}{2} \int_{\Omega_1} F''(\bar{u}) v_\rho v_\rho dV + \frac{1}{2} \int_{\Gamma_N} G''(\bar{u}) v_\rho v_\rho dS. \end{aligned}$$

The exact remainder is bounded thanks to assumptions (3.4) and Proposition 7

$$\left| \int_{\Omega_1} F''(\bar{u}) v_\rho v_\rho dV \right| \leq C \|v_\rho\|_{L^2(\Omega)}^2 \leq C \rho^2 |\xi_u^{av}(\rho)|^2 \leq C \frac{\kappa(\rho^2)}{\left(1 + C \frac{\kappa(\rho)}{\rho}\right)},$$

$$\begin{aligned}
\left| \int_{\Gamma_N} G''(\bar{u}) v_\rho v_\rho dS \right| &\leq C \|v_\rho\|_{L^2(\Gamma_N)}^2 \leq C \|\delta\|_{L^2(\Gamma_N)}^2 \text{ because } \theta = 0 \text{ on } \Gamma_N \\
&\leq C \|\delta\|_{H^1(\Omega)}^2 \text{ using the Trace theorem} \\
&\leq C \frac{\kappa(\rho^2)}{\left(1 + C \frac{\kappa(\rho)}{\rho}\right)}.
\end{aligned}$$

Multiply (3.84) by v_ρ and integrate by parts twice

$$\begin{aligned}
&\int_{\Omega_1} F'(u) v_\rho dV + \int_{\Gamma_N} G'(u) v_\rho dS = \kappa(\rho) \left(\int_{\omega_B} u dV - \int_{\omega_A} u dV \right) \left(\int_{\omega_B} p_\rho dV - \int_{\omega_A} p_\rho dV \right) \\
&= \kappa(\rho) \left(\int_{\omega_B} u dV - \int_{\omega_A} u dV \right) \left(\int_{\omega_B} p dV - \int_{\omega_A} p dV \right) + \kappa(\rho) \left(\int_{\omega_B} u dV - \int_{\omega_A} u dV \right) \left(\int_{\omega_B} q dV - \int_{\omega_A} q dV \right) \\
&\quad + \kappa(\rho) \left(\int_{\omega_B} u dV - \int_{\omega_A} u dV \right) \left(\int_{\omega_B} \eta dV - \int_{\omega_A} \eta dV \right).
\end{aligned}$$

These three terms are estimated one by one.

★ 1st term

We define R_p^A and R_p^B similarly to R_u^A and R_u^B . They are the integral remainder of the expansion of p around \mathbf{x}_0 and $\mathbf{x}_0 + \ell\mathbf{e}$. They are both of the order of ρ^2 in ω_A and ω_B . Both the background solution u and the adjoint p are expanded with integral remainder. The first term is then estimated as

$$\begin{aligned}
&\kappa(\rho) \left(\int_{\omega_B} u dV - \int_{\omega_A} u dV \right) \left(\int_{\omega_B} p dV - \int_{\omega_A} p dV \right) \\
&= \kappa(\rho) (u(\mathbf{x}_0 + \ell\mathbf{e}) - u(\mathbf{x}_0)) \cdot \mathbf{e} (p(\mathbf{x}_0 + \ell\mathbf{e}) - p(\mathbf{x}_0)) \cdot \mathbf{e} + O(\kappa(\rho)\rho^2) + O(\kappa(\rho)\rho^4).
\end{aligned}$$

The leading term will be an element of the topological derivative and will contribute to the scaling term $s(\rho)$. The bounded one will be part of the remainder term $\mathcal{R}(s(\rho))$.

★ 2nd term

Let us set the notation $\xi_p^{av}(\rho)$ in an equivalent manner as $\xi_u^{av}(\rho)$. It holds

$$\xi_p^{av}(\rho) = \frac{\frac{\kappa(\rho)}{\rho|\omega|}}{1 + \frac{4\kappa(\rho)}{5\rho|\omega|}r_1^2} (p(\mathbf{x}_0 + \ell\mathbf{e}) - p(\mathbf{x}_0)), \text{ and } \int_{\omega} q_a^{av} dV = \frac{2}{5} r_1^2 \xi_p^{av}(\rho). \quad (3.89)$$

The following term is evaluated by rescaling.

$$\begin{aligned}
&\kappa(\rho) \left(\int_{\omega_B} u dV - \int_{\omega_A} u dV \right) \left(\int_{\omega_B} q dV - \int_{\omega_A} q dV \right) \\
&= \kappa(\rho) \left((u(\mathbf{x}_0 + \ell\mathbf{e}) - u(\mathbf{x}_0)) + \int_{\omega_B} R_u^B dV - \int_{\omega_A} R_u^A dV \right) \left(-2 \int_{\omega} q_a^{av} dV \right) \\
&= -\frac{\frac{4\kappa(\rho)}{5\rho|\omega|}r_1^2}{1 + \frac{4\kappa(\rho)}{5\rho|\omega|}r_1^2} \kappa(\rho) (u(\mathbf{x}_0 + \ell\mathbf{e}) - u(\mathbf{x}_0)) (p(\mathbf{x}_0 + \ell\mathbf{e}) - p(\mathbf{x}_0)) + O\left(\frac{\kappa(\rho)^2 \rho}{1 + C \frac{\kappa(\rho)}{\rho}}\right).
\end{aligned}$$

★ 3rd term

The last term is expected to be a remainder term since it involves η . Let us begin with a rescaling.

$$\begin{aligned} \kappa(\rho) \left(\int_{\omega_B} u dV - \int_{\omega_A} u dV \right) \left(\int_{\omega_B} \eta dV - \int_{\omega_A} \eta dV \right) &= \kappa(\rho) (u(\mathbf{x}_0 + \ell \mathbf{e}) - u(\mathbf{x}_0)) \left(\int_{\omega_B} \eta dV - \int_{\omega_A} \eta dV \right) \\ &\quad + \kappa(\rho) \left(\int_{\omega_B} R_u^B dV - \int_{\omega_A} R_u^A dV \right) \left(\int_{\omega_B} \eta dV - \int_{\omega_A} \eta dV \right). \end{aligned}$$

To ease the notation, we set $X = \left| \int_{\omega_B} \eta dV - \int_{\omega_A} \eta dV \right|$. Multiplying (3.88) by η integrating by parts twice give us

$$\kappa(\rho) X^2 \leq C \rho |\xi_p^{av}(\rho)| \|\nabla \eta\|_{L^2(\Omega)} + C \kappa(\rho) \rho^2 X.$$

It leads to

$$X \leq C \sqrt{\frac{\rho |\xi_p^{av}(\rho)|}{\kappa(\rho)}} \sqrt{\|\nabla \eta\|_{L^2(\Omega)}} + C \rho^2.$$

The third term is then bounded as follows

$$\begin{aligned} \exists C > 0, \kappa(\rho) \left| \int_{\omega_B} u dV - \int_{\omega_A} u dV \right| \left| \int_{\omega_B} \eta dV - \int_{\omega_A} \eta dV \right| \\ \leq C \kappa(\rho)^{1/2} \rho |\xi_p^{av}(\rho)| + C \kappa(\rho)^{1/2} \rho^3 |\xi_p^{av}(\rho)| + C \kappa(\rho) \rho^2 + C \kappa(\rho) \rho^4 \leq C \frac{\kappa(\rho)^{3/2}}{1 + C \frac{\kappa(\rho)}{\rho}} + C \kappa(\rho) \rho^2. \end{aligned}$$

Regrouping all leading terms gives

$$\begin{aligned} &\frac{\kappa(\rho)}{1 + \frac{4\kappa(\rho)}{5\rho|\omega|} r_1^2} (u(\mathbf{x}_0 + \ell \mathbf{e}) - u(\mathbf{x}_0)) (p(\mathbf{x}_0 + \ell \mathbf{e}) - p(\mathbf{x}_0)) \\ &= \left(\frac{1}{\kappa(\rho)} + \frac{4r_1^2}{5\rho|\omega|} \right)^{-1} (u(\mathbf{x}_0 + \ell \mathbf{e}) - u(\mathbf{x}_0)) (p(\mathbf{x}_0 + \ell \mathbf{e}) - p(\mathbf{x}_0)). \end{aligned}$$

This term is then expanded with respect to ρ . The resulting leading term shall be the topological derivative and the inherent remainder term, denoted $\mathcal{R}(DJ(\mathbf{x}_0, \mathbf{e}))$, will be part of remainder term of the asymptotic expansion $\mathcal{R}(s(\rho))$, that reads

$$\mathcal{R}(s(\rho)) = O\left(\frac{\kappa(\rho)^2}{\left(1 + C \frac{\kappa(\rho)}{\rho}\right)^2}\right) + O(\kappa(\rho) \rho^2) + O\left(\frac{\kappa(\rho)^2 \rho}{1 + C \frac{\kappa(\rho)}{\rho}}\right) + O\left(\frac{\kappa(\rho)^{3/2}}{1 + C \frac{\kappa(\rho)}{\rho}}\right) + \mathcal{R}(DJ(\mathbf{x}_0, \mathbf{e})).$$

The quantity $\left(1 + \frac{4\kappa(\rho)}{5\rho|\omega|} r_1^2\right)$ is bounded if $k \geq 1$ and goes to infinity otherwise. Therefore, the results for $k \geq 1$ come easily. For $k < 1$, the topological derivative is as easy to compute. The only point of interest is for the remainder term that is $O(\rho^{1+k/2})$ for $k < 2/3$. Definition 4 actually states that $\lim_{\rho \rightarrow 0} \frac{\mathcal{R}(s(\rho))}{s(\rho)} = 0$. Since $s(\rho) = \rho$ when $k < 1$, this condition is fulfilled for k such that

$$\frac{k}{2} + 1 > 1 \iff k > 0. \quad (3.90)$$

Remark 20. For the point-to-point approach, the leading term is

$$3\kappa(\rho) \frac{r_1 \sqrt{2\xi_u^{pt}(\rho)} - \tanh(r_1 \sqrt{2\xi_u^{pt}(\rho)})}{r_1^3 (2\xi_u^{pt}(\rho))^{3/2}} (u(\mathbf{x}_0 + \ell \mathbf{e}) - u(\mathbf{x}_0)) (p(\mathbf{x}_0 + \ell \mathbf{e}) - p(\mathbf{x}_0)).$$

The point-to-point approach provides the same scaling of ρ and the same behavior with regards to the temperature and adjoint fields. Only the coefficient of the topological derivative differs from the average approach. However, the point-to-point approach is more complex to analyze and compute. Anyway, this thesis uses the average approach for an adaptation to the elasticity problem with a spring and with an idealized bolt. It is still interesting to know that an other modelling is available and usable for topological sensitivity analysis.

3.3.3 Numerical illustrations

The topological sensitivity analysis with respect to a small thermal bridge is illustrated with academic test cases in 2d and 3d. The problem is to put a small thermal bridge in order to decrease the thermal compliance $J(\Omega) = \int_{\Gamma_N} g u dS$. The new compliance, *i.e.* with the bridge, is predicted with estimator function

$$\mathcal{E}(\Omega) = J_0(\Omega) + s(\rho)DJ(\mathbf{x}_0, \mathbf{e}). \quad (3.91)$$

It stands for the expected value of the compliance given by the asymptotic expansion of the objective function in the perturbed domain.

Since the topological derivative depends on two parameters, namely \mathbf{x}_0 and \mathbf{e} , there are several possible test configurations. For graphical purposes, the direction \mathbf{e} is parameterized with an angle φ in 2d (resp. with angles φ and Ψ in 3d) such that $\mathbf{e} = (\cos(\varphi), \sin(\varphi))$ (resp. $\mathbf{e} = (\sin(\varphi) \cos(\Psi), \sin(\varphi) \sin(\Psi), \cos(\varphi))$). The first approach is to fix an orientation \mathbf{e} and then compute the topological derivative for all candidate point \mathbf{x}_0 . The bridge is put at the most negative value of $DJ(\mathbf{x}_0, \mathbf{e})$. The second approach is to fix a position \mathbf{x}_0 and then compute the topological derivative for a discrete number of directions \mathbf{e} . The best orientation corresponds to the minimum of $DJ(\mathbf{x}_0, \mathbf{e})$. The last approach is to search for both the position \mathbf{x}_0 , center of ω_A , and the orientation of the bridge \mathbf{e} .

The 2d test is performed on a plate with an opening gap. The bridge is expected to diffuse the heat over the gap. The 3d test case is based on a hollow cylinder under a sinusoidal heating.

2d test case

The plate is meshed with 30 137 triangular elements of minimal and maximal size of 4.7×10^{-3} and 1.0×10^{-2} . A Dirichlet condition $u = 0$ is imposed on the lower border. The upper flux is given by $g = x$. The initial thermal compliance is $J_0(\Omega) = 0.717349$. The structure has an adimensionned conductivity equal to 1. The bridge has a conductivity $K = 10$, a size $\rho = 2.5 \times 10^{-2}$ and a length $\ell = 0.15$. Let us search for the optimal thermal bridge with three configurations. The thermal conductivity depends on the size of the inclusion $\kappa(\rho) = K\rho^k$. The results behavior are the same for various values of k in 2d. Only the amplitude of temperature, the scaling of DJ and the bridge efficiency depend on k . In the following, bridge is implemented with the average formulation. Graphical results are given for $k = 0.5$. Nevertheless, various values of k are tested and results are gathered in Tables 3.1, 3.2 and 3.3.

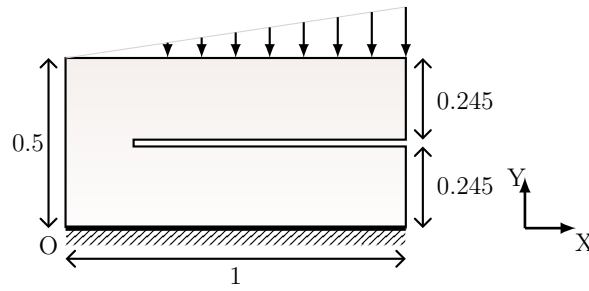


Figure 3.14: Dimensions and loading of the plate with an opening gap

- Fixed orientation $\mathbf{e} = \left(\frac{\sqrt{2}}{2}, \frac{\sqrt{2}}{2} \right)$ - search for the best location \mathbf{x}_0

The first test is to fix the orientation of the bridge. Let us chose $\varphi = \frac{\pi}{4}$, then the direction is $\mathbf{e} = \left(\frac{\sqrt{2}}{2}, \frac{\sqrt{2}}{2} \right)$. The topological derivative is computed strictly inside the plate (cf. Fig. 3.15a). The non design-space is then pictured in gray. Values of DJ for which ω_B would be totally or partially in the non design-space are truncated. They are displayed in white in Fig. 3.15a. Therefore, the optimal thermal bridge is given in Fig. 3.15b. The result is quite surprising because the bridge is expected to step over the gap. However, the dimensions of the non-design space and the length of the bridge do not allow the bridge to step over the gap for this particular orientation. This first test illustrates well the geometrical limits of this method. Despite this restriction, the topological derivative is still able to indicate a configuration that decreases the compliance (see Table 3.1). The bridge efficiency decreases as the bridge becomes smaller. The bridge is practically inactive for $k = 2$ and $k = 4$. In all cases, the estimator $\mathcal{E}(\Omega)$ provides satisfactory results.

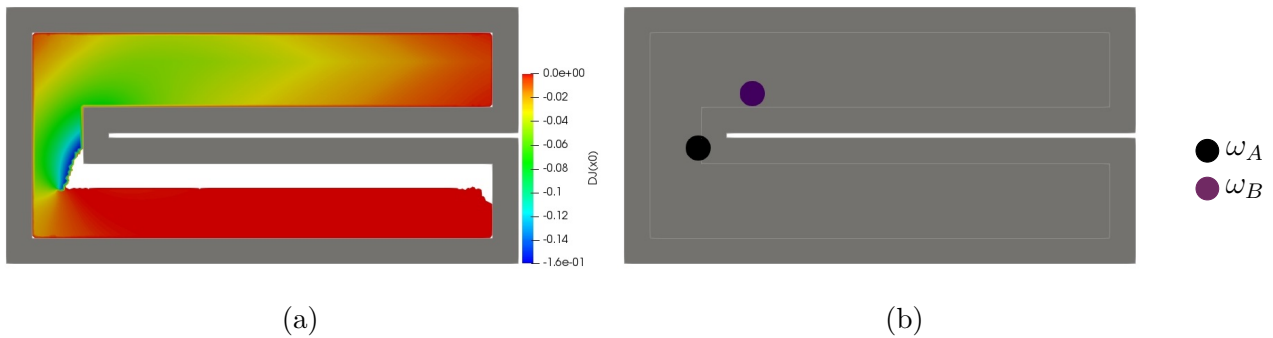
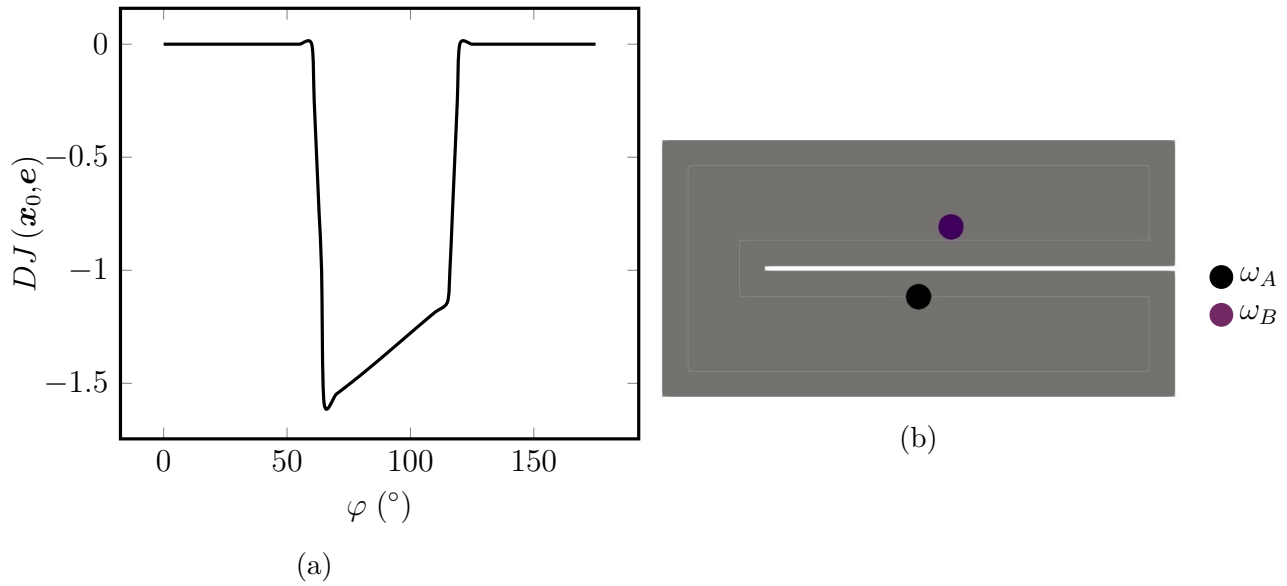


Figure 3.15: Cartography of $DJ(\mathbf{x}_0, \mathbf{e})$ inside the domain (a) and the corresponding thermal bridge (b)

- Fixed location $\mathbf{x}_0 = (0.50, 0.195)$ - search for the best orientation \mathbf{e}

Let us fix the location of the center of ω_A at the point $\mathbf{x}_0 = (0.50, 0.195)$ and search for the best orientation of the bridge for discrete values of φ from 0 to 180° every five degrees. The cartography of the topological derivative for $\mathbf{x}_0 = (0.50, 0.195)$ is plotted in Fig. 3.16a. A design-space is delimited in order to have the bridge strictly inside the plate. The topological derivative is computed such that those orientations that put ω_B outside the design-space are rejected and truncated to zero. The optimal thermal bridge is oriented at $\varphi = \frac{13\pi}{36}$ rad (or 65°) as displayed in Fig. 3.16b. Results are gathered in Table 3.2.

	$DJ(\mathbf{x}_0, \mathbf{e})$	\mathbf{x}_0	$J_\rho(\Omega)$	$\mathcal{E}(\Omega)$
$k = 0.5$	-0.159412	(0.14,0.23)	0.619864	0.674135
$k = 1$	-0.159412	(0.14,0.23)	0.685487	0.674135
$k = 2$	-1.59412	(0.14,0.23)	0.716359	0.716353
$k = 4$	-1.59412	(0.14,0.23)	0.717348	0.717348

Table 3.1: Summary of the topological derivative test for fixed \mathbf{e} (recall that $J_0(\Omega) = 0.717349$)Figure 3.16: Cartography of DJ for fixed $\mathbf{x}_0 = (0.50, 0.195)$ (a) and the corresponding thermal bridge (b)

	$DJ(\mathbf{x}_0, \mathbf{e})$	θ	$J_\rho(\Omega)$	$\mathcal{E}(\Omega)$
$k = 0.5$	-1.58708	$\frac{13\pi}{36}$	0.329797	0.287116
$k = 1$	-1.58708	$\frac{13\pi}{36}$	0.504679	0.287116
$k = 2$	-15.8708	$\frac{13\pi}{36}$	0.70764	0.70743
$k = 4$	-15.8708	$\frac{13\pi}{36}$	0.717343	0.717343

Table 3.2: Summary of the topological derivative test for fixed \mathbf{x}_0 (recall that $J_0(\Omega) = 0.717349$)

- Search for the best location \mathbf{x}_0 and orientation \mathbf{e}

This last test intends to search for both the optimal location \mathbf{x}_0 and orientation \mathbf{e} . The topological derivative is still computed inside the design-space defined previously. In this case,

there is no truncated value. The cartography and the corresponding optimal bridge are given in Fig. 3.17. The optimal bridge is plumb and put at the right end side of the structure. Results are summed up in Table 3.3. It reveals more than 60% of reduction for $k = 0.5$. This time, the estimator is not efficient anymore for $k = 0.5$ and $k = 1$. One more time, the very small bridges $k = 2$ and $k = 4$ are inactive and do not bring any improvement. For $k = 0.5$, we can notice the macroscopic impact of the bridge in Figs. 3.18 and 3.19. The temperature field has notably decreased due to the heat diffusion around the bridge.

The bridge has also been implemented with the point-to-point approach. It gives similar results as the average method. Then, the development of the sensitivity analysis and the numerical implementation are not getting any benefit from the point-to-point approach. On the contrary, this method is more difficult to compute analytically and numerically. It concludes that the average approach is much more user-friendly.

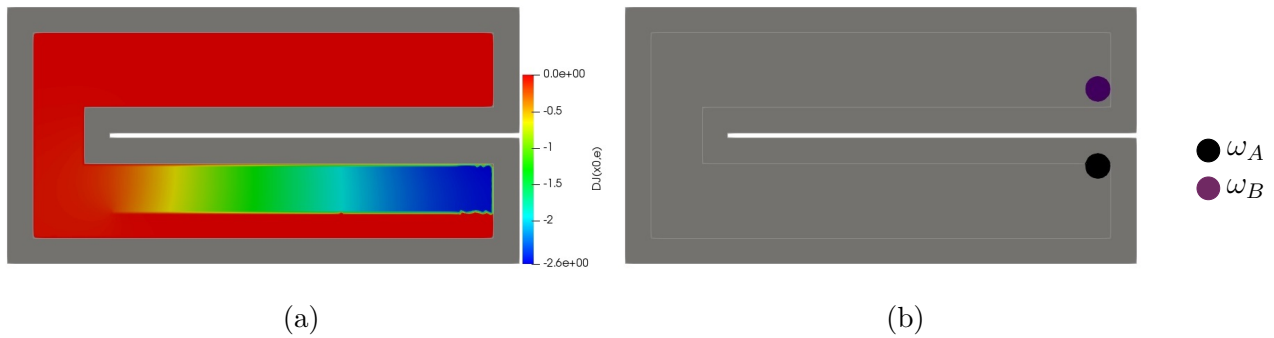


Figure 3.17: Cartography of $DJ(\mathbf{x}_0, \mathbf{e})$ inside the domain (a) and the corresponding thermal bridge (b)

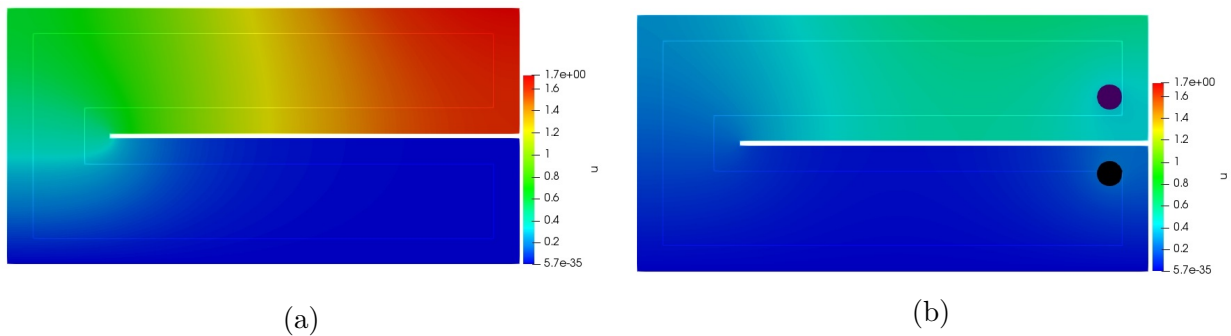
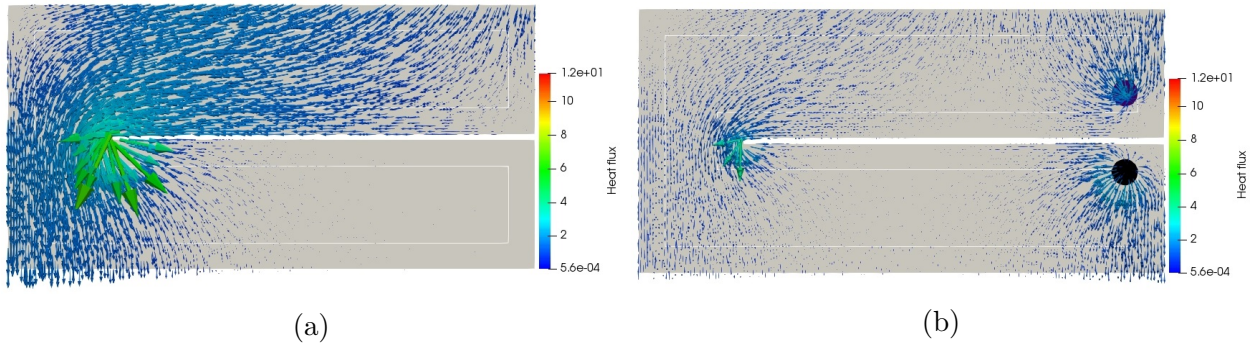


Figure 3.18: Temperature field u of the background domain (a) of the perturbed domain (b)

Figure 3.19: Heat fluxes $-\kappa\nabla u$ of the background domain (a) of the perturbed domain (b)

	$DJ(\mathbf{x}_0, \mathbf{e})$	\mathbf{x}_0	θ	$J_\rho(\Omega)$	$\mathcal{E}(\Omega)$
$k = 0.5$	-2.58198	(0.92,0.19)	$\frac{\pi}{2}$	0.279939	0.0174125
$k = 1$	-2.58198	(0.92,0.19)	$\frac{\pi}{2}$	0.438831	0.0174125
$k = 2$	-25.8198	(0.92,0.19)	$\frac{\pi}{2}$	0.701726	0.701212
$k = 4$	-25.8198	(0.92,0.19)	$\frac{\pi}{2}$	0.717339	0.717339

Table 3.3: Summary of the 2d use case results (recall that $J_0(\Omega) = 0.717349$)

3d test case

The 3d test case is based on a hollow cylinder pictured in Fig. 3.20. This cylinder is meshed with 595 027 tetrahedron elements with a minimal and maximal size of 1.2×10^{-2} and 6.4×10^{-2} . A Dirichlet condition $u = 0$ is imposed on the internal border of the cylinder. The extremities of the cylinder are adiabatic. A sinusoidal flux $g = z \cos\left(2\left(\arctan\left(\frac{y}{x}\right) + z\right)\right)$ is imposed on the external border. The bridge has a conductivity $K = 10$, a size $\rho = 5 \times 10^{-2}$ and a length $\ell = 0.5$.

The initial compliance is $J_0(\Omega) = 0.968213$. The topological derivative is computed to find both the best location \mathbf{x}_0 and orientation \mathbf{e} . The optimal thermal bridge is then given in Fig. 3.21. Iso-values of the topological derivative are given in Fig. 3.22. Results for various values of k are gathered in Table 3.4. The bridge is efficient for $k = 0.5$ and $k = 1$. It is inactive for $k = 2$ and $k = 4$. For active scaling of the bridge, it intends to link two areas of opposite temperature. Some comparisons of the temperature field with or without the bridge for $k = 0.5$ are displayed in Fig. 3.24. The heat fluxes with or without the bridge for $k = 0.5$ are also given in Fig. 3.23. These comparisons highlight well the impact of the bridge on heat diffusion. However, this influence is only local because of the dimensions of the structure and of the bridge, contrary to the 2d bridge case which has a global impact on the structure.

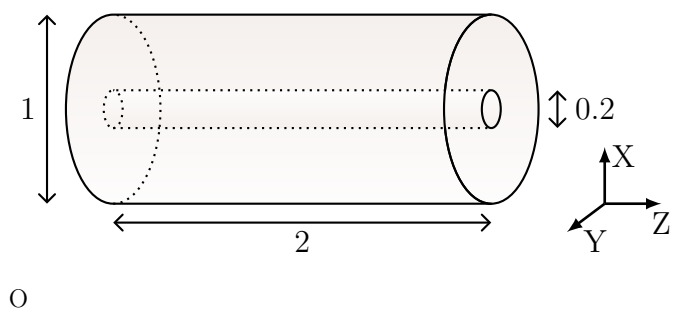


Figure 3.20: Dimensions of the 3d test case



Figure 3.21: Optimal thermal bridge

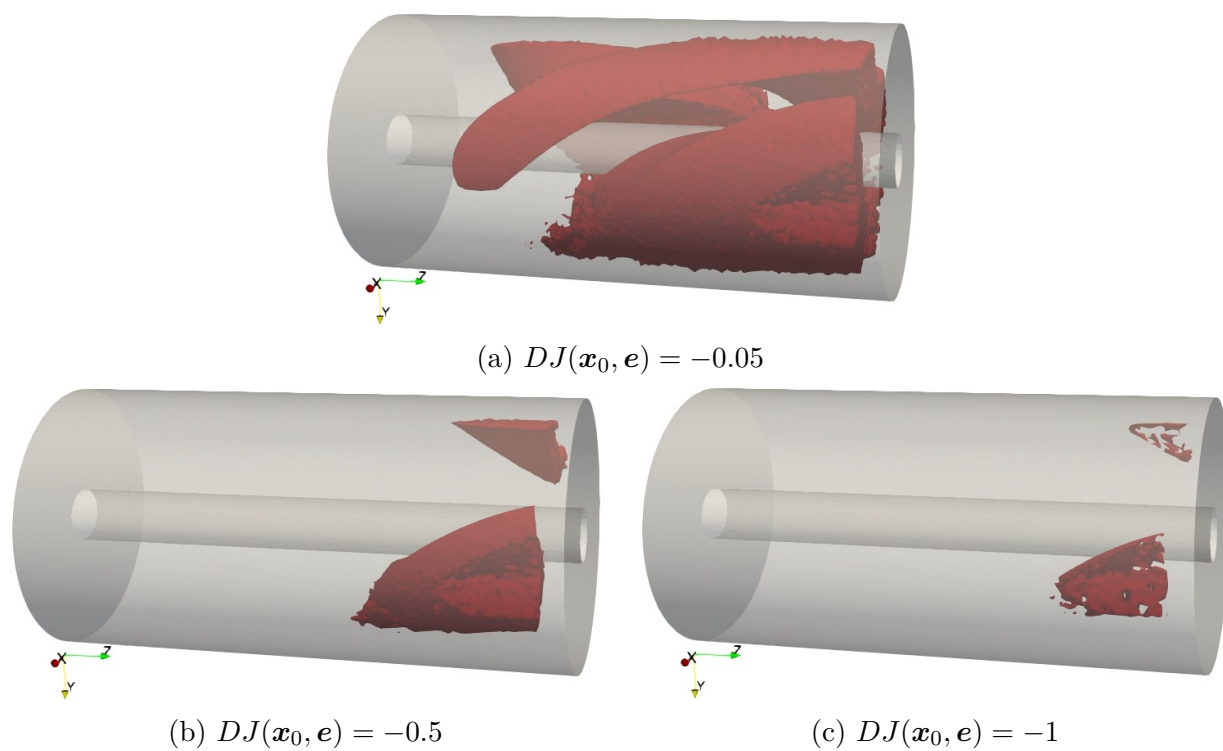


Figure 3.22: Iso-values of the topological derivatives

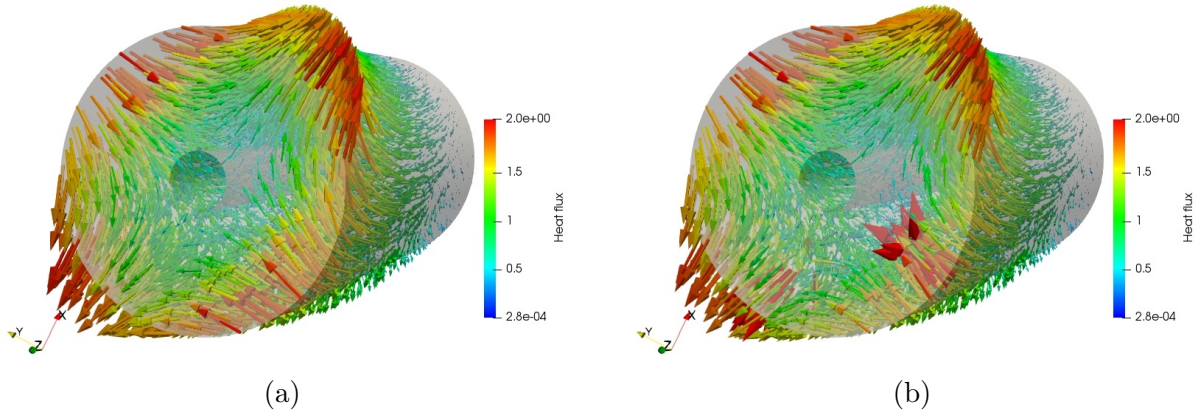
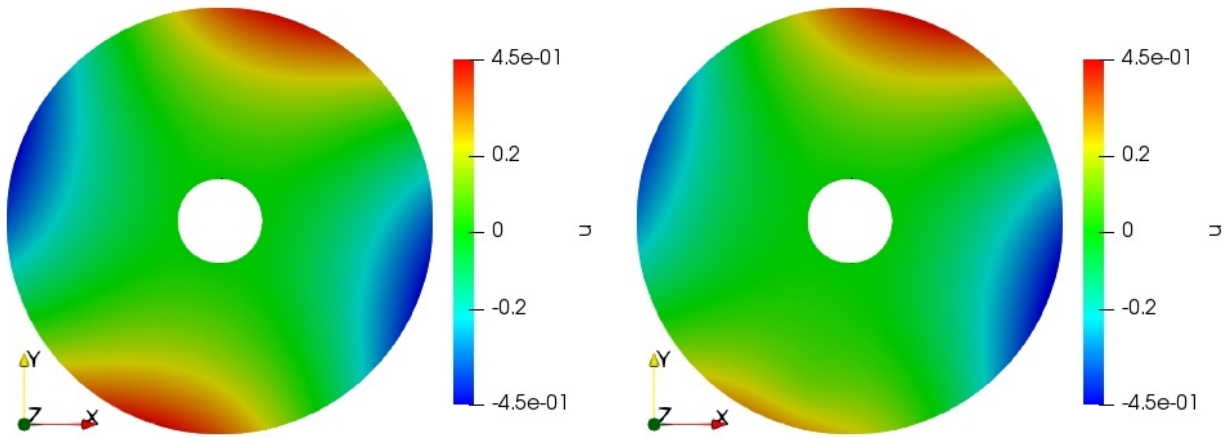


Figure 3.23: Heat fluxes $-\kappa\nabla u$ without the bridge (a) and with the bridge (b)

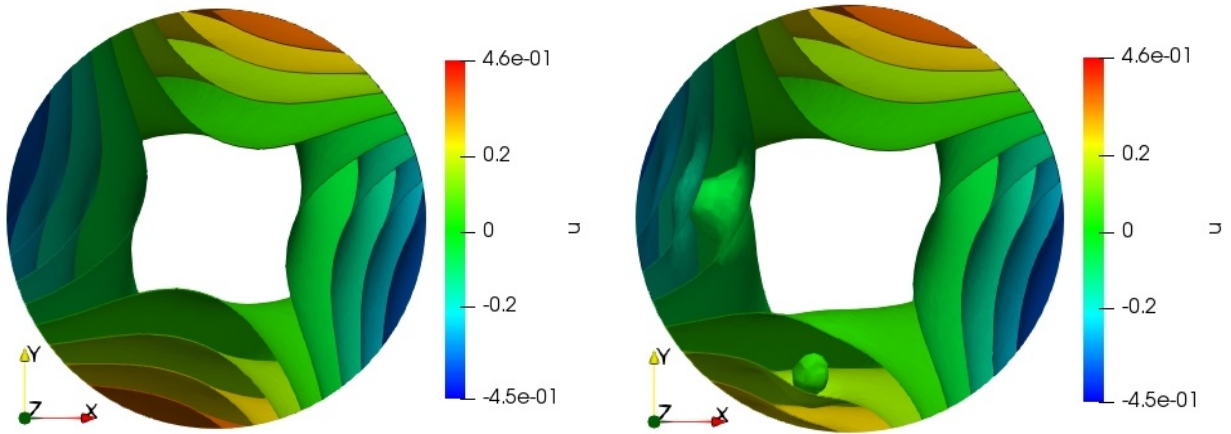
	$DJ(\mathbf{x}_0, \mathbf{e})$	\mathbf{x}_0	(θ, ψ)	$J_\rho(\Omega)$	$\mathcal{E}(\Omega)$
$k = 0.5$	-1.13771	(0.1,-0.39,1.89)	$\left(\frac{5\pi}{9}, \frac{2\pi}{3}\right)$	0.924645	0.911328
$k = 1$	-0.746726	(0.1,-0.39,1.89)	$\left(\frac{5\pi}{9}, \frac{2\pi}{3}\right)$	0.935001	0.930877
$k = 2$	-2.17287	(0.1,-0.39,1.89)	$\left(\frac{5\pi}{9}, \frac{2\pi}{3}\right)$	0.963341	0.962781
$k = 4$	-2.17287	(0.1,-0.39,1.89)	$\left(\frac{5\pi}{9}, \frac{2\pi}{3}\right)$	0.9682	0.9682

Table 3.4: Summary of the 3d use case results (recall that $J_0(\Omega) = 0.968213$)



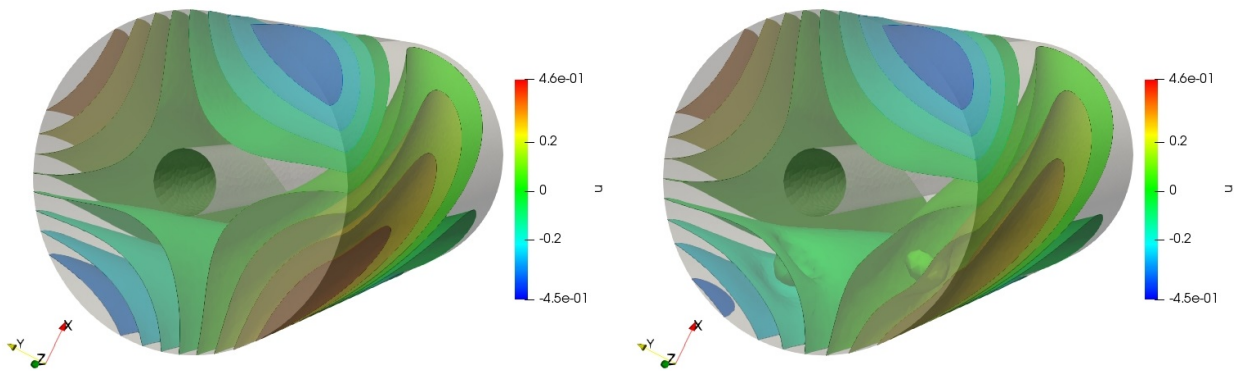
(a) Cross-sectional view for $Z = 2$

(b) Cross-sectional view for $Z = 2$



(c) Iso-values - Cross-sectional view for $Z = 2$

(d) Iso-values - Cross-sectional view for $Z = 2$



(e) Iso-values

(f) Iso-values

Figure 3.24: Temperature field u without the bridge (a), (c), (e) and with the bridge (b), (d), (f)

One rigid inclusion in elastic medium

Contents

4.1	Setting of the problem	92
4.1.1	Background domain	92
4.1.2	Perturbation of the domain with a small rigid inclusion	93
4.2	Computation of the topological derivative	95
4.2.1	Approximation of the perturbed displacement field	95
4.2.2	Approximation of the perturbed adjoint state	103
4.2.3	Proof of the main result	104
4.3	Numerical illustrations	110
4.3.1	2d test case : a L-beam	110
4.3.2	3d test case : the cantilever	117

The present chapter investigates the topological derivative for the linear elasticity problem with respect to the nucleation of one small rigid inclusion. According to the techniques developed in Chapter 3, the topological derivative is established with a variational approach. Main results are given in 2d and 3d but the proof is carried out for the 3d problem. They are numerically illustrated with simple academic 2d and 3d test cases. These examples intend to test the topological derivative efficiency. The structure is not optimized.

4.1 Setting of the problem

4.1.1 Background domain

Let Ω be an open bounded domain of \mathbb{R}^n , $n = 2$ or 3 , and Ω_1, Ω_2 a partition of it, namely $\bar{\Omega} = \bar{\Omega}_1 \cup \bar{\Omega}_2$ and $\Omega_1 \cap \Omega_2 = \emptyset$. The boundary of this domain is made of two disjoint parts, $\partial\Omega = \Gamma_N \cup \Gamma_D$. Neumann and Dirichlet boundary conditions are respectively imposed on Γ_N and Γ_D . This chapter aims to compute the topological derivative or the perturbation caused by a small rigid inclusion inside the subdomain Ω_2 . For the sake of simplicity, the objective function is evaluated in Ω_1 , far from the influence area of the inclusion. This avoids supplementary terms corresponding to the perturbation of the integration domain of the objective function. The topological derivative may be computed with an objective function evaluated everywhere but it requires more technical work and this is not the point here.

Let the domain Ω be filled with a linear isotropic elastic material. For a displacement field \mathbf{u} , the strain tensor is defined by

$$\varepsilon(\mathbf{u}) = \frac{1}{2}(\nabla\mathbf{u} + \nabla^T\mathbf{u}).$$

The stress tensor is given by the Hooke's law

$$\mathbf{A}\varepsilon(\mathbf{u}) = 2\mu\varepsilon(\mathbf{u}) + \lambda\text{tr}(\varepsilon(\mathbf{u}))\mathbf{1},$$

with μ and λ the Lamé coefficients of the material. The terms unperturbed, healthy or background domain refer to the system without any rigid inclusion. The background solution \mathbf{u} then satisfies the linear elasticity system

$$\begin{cases} -\text{div}(\mathbf{A}\varepsilon(\mathbf{u})) = \mathbf{0} & \text{in } \Omega \\ \mathbf{A}\varepsilon(\mathbf{u})\mathbf{n} = \mathbf{g} & \text{on } \Gamma_N. \\ \mathbf{u} = \mathbf{0} & \text{on } \Gamma_D \end{cases} \quad (4.1)$$

The domain Ω is assumed to be bounded and smooth. Assuming that surface load \mathbf{g} belong to $L^2(\Gamma_N)^n$, Lax-Milgram theorem, coupled with Korn's inequality, gives classically the existence and the uniqueness of the solution $\mathbf{u} \in \mathcal{W}$ where

$$\mathcal{W} = \{\mathbf{w} \in (H^1(\Omega))^n, \mathbf{w} = \mathbf{0} \text{ on } \Gamma_D\}. \quad (4.2)$$

In the following, we assume that \mathbf{u} is as smooth as we want, which is always possible by assuming that the load \mathbf{g} is smooth as well as the domain. The following analysis requires $\mathbf{u} \in \mathcal{C}^3(\Omega)^n$.

Remark 21. *This analysis can also be done with a non-zero right hand side in Ω_1 for (4.1).*

Consider the generic objective function

$$J_0(\Omega) = \int_{\Omega_1} F(\mathbf{u})dV + \int_{\Gamma_N} G(\mathbf{u})dS \quad (4.3)$$

which depends on the domain Ω through the function \mathbf{u} solution of (4.1). The functions F and G are smooth, twice differentiable with respect to \mathbf{u} and satisfy the following conditions

$$\exists\alpha > 0, \begin{cases} |F(\mathbf{u})| \leq \alpha(|\mathbf{u}|^2 + 1), & |\mathbf{F}'(\mathbf{u})| \leq \alpha(|\mathbf{u}| + 1), & |F''(\mathbf{u})| \leq \alpha \\ |G(\mathbf{u})| \leq \alpha(|\mathbf{u}|^2 + 1), & |\mathbf{G}'(\mathbf{u})| \leq \alpha(|\mathbf{u}| + 1), & |G''(\mathbf{u})| \leq \alpha \end{cases} \quad (4.4)$$

Remark 22. *Conditions (4.4) are simple and sufficient. They can be improved if necessary.*

Let us introduce the notation $\mathbf{1}_{\Omega_1}$ which stands for the characteristic function of the domain Ω_1 , *i.e.* the function equal to 1 inside Ω_1 and zero outside. The adjoint state \mathbf{p} associated to (4.1) for a general objective function (4.3) satisfies

$$\begin{cases} -\operatorname{div}(\mathbf{A}\varepsilon(\mathbf{p})) = -\mathbf{F}'(\mathbf{u})\mathbf{1}_{\Omega_1} & \text{in } \Omega \\ \mathbf{A}\varepsilon(\mathbf{p})\mathbf{n} = -\mathbf{G}'(\mathbf{u}) & \text{on } \Gamma_N, \\ \mathbf{p} = \mathbf{0} & \text{on } \Gamma_D \end{cases} \quad (4.5)$$

Lax-Milgram theorem, coupled with Korn's inequality, gives the existence and the uniqueness of the solution $\mathbf{p} \in \mathcal{W}$. In the sequel, we assume that \mathbf{p} is as smooth as required, similarly to the assumptions on \mathbf{u} , that is to say $\mathbf{p} \in \mathcal{C}^3(\Omega)^n$.

4.1.2 Perturbation of the domain with a small rigid inclusion

Let us focus on the 3d problem. The background domain is perturbed with a small rigid inclusion. The sensitivity analysis with regards to an inclusion with different material properties than the background domain has already been studied in [8, 86]. The rigid inclusion is the particular case of material properties tending to infinity. In this section, a rigid inclusion means that the displacement in the inclusion is exactly a rigid body motion. It will be shown at the end of the present analysis, in Remark 33, that the description with a rigid body motion provides the same topological derivative expression than the one with material properties tending to infinity.

Let us define the perforated domain Ω_ρ , *i.e.* the domain Ω without the inclusion ω_ρ

$$\Omega_\rho = \Omega \setminus \omega_\rho. \quad (4.6)$$

Generally, the shape ω of an inclusion can be arbitrary. In the sequel, ω is set to be the unit ball of \mathbb{R}^3 , which allows to explicitly compute the coefficients of the topological derivative (see *e.g.* [86] for diverse computations with a spherical inclusion). Let ω_ρ be a small rigid inclusion of shape ω , rescaled by an adimensional factor $\rho > 0$ and centered at the point $\mathbf{x}_0 \in \Omega_2$,

$$\omega_\rho = \left\{ \mathbf{x} \in \mathbb{R}^3, \frac{\mathbf{x} - \mathbf{x}_0}{\rho} \in \omega \right\}. \quad (4.7)$$

In the following, the factor ρ refers abusively to the size of the inclusion.

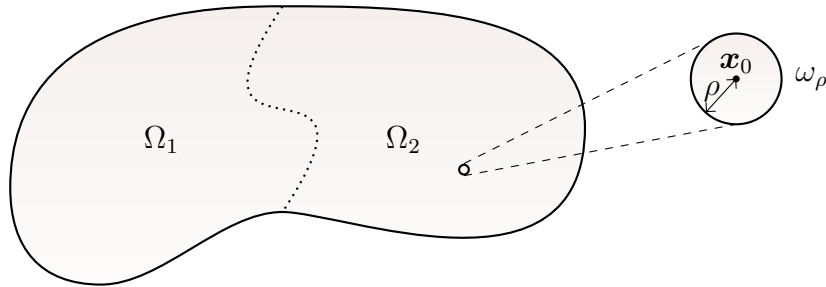


Figure 4.1: Perturbation of the domain Ω with a small inclusion ω_ρ in the subdomain Ω_2

A rigid body motion is imposed inside the inclusion ω_ρ . The suitable space of admissible displacements corresponds to zero displacement on Dirichlet boundary Γ_D and rigid body motion in ω_ρ

$$\mathcal{W}_{RB} = \{ \mathbf{w} \in (H^1(\Omega))^3, \mathbf{w} = \mathbf{0} \text{ on } \Gamma_D, \mathbf{w}(\mathbf{x}) = \mathbf{C} + \mathbf{R}\mathbf{x} \text{ in } \omega_\rho \}, \quad (4.8)$$

where $\mathbf{C} \in \mathbb{R}^3$ is a translation and $\mathbf{R} = -\mathbf{R}^T$ is a skew symmetric matrix 3x3 modelling infinitesimal rotations. The translation \mathbf{C} and rotation \mathbf{R} are unknown. The perturbed configuration solves the following variational problem :

$$\text{Find } \mathbf{u}_\rho \in \mathcal{W}_{RB} \text{ s.t. } \forall \mathbf{w} \in \mathcal{W}_{RB}, \int_{\Omega_\rho} \mathbf{A}\varepsilon(\mathbf{u}_\rho) : \varepsilon(\mathbf{w})dV - \int_{\Gamma_N} \mathbf{g} \cdot \mathbf{w}dS = \mathbf{0}. \quad (4.9)$$

The set \mathcal{W}_{RB} is a Hilbert space with respect to the H^1 -norm in Ω_ρ . The existence and uniqueness are given by Lax-Milgram theorem coupled with Korn-Poincaré inequality. The strong system associated to the variational formulation (4.9) reads

$$\left\{ \begin{array}{ll} -\text{div}(\mathbf{A}\varepsilon(\mathbf{u}_\rho)) = \mathbf{0} & \text{in } \Omega_\rho \\ \mathbf{A}\varepsilon(\mathbf{u}_\rho)\mathbf{n} = \mathbf{g} & \text{on } \Gamma_N \\ \mathbf{u}_\rho = \mathbf{0} & \text{on } \Gamma_D \\ \mathbf{u}_\rho(\mathbf{x}) = \mathbf{C}(\rho) + \mathbf{R}(\rho)\mathbf{x} & \text{in } \omega_\rho \\ \int_{\partial\omega_\rho} \mathbf{A}\varepsilon(\mathbf{u}_\rho)\mathbf{n}dS = \mathbf{0} & \\ \int_{\partial\omega_\rho} \mathbf{A}\varepsilon(\mathbf{u}_\rho)\mathbf{n} \wedge \mathbf{x}dS = \mathbf{0} & \end{array} \right. . \quad (4.10)$$

Translation $\mathbf{C}(\rho)$ and rotation $\mathbf{R}(\rho)$ may depend on the size ρ of the inclusion. The two last terms of (4.10) are forces and moments equilibrium on the boundary of ω_ρ . They are equal to zero which means that no external force, nor momentum, are exerted in the inclusion. The unit normal vector \mathbf{n} to $\partial\omega_\rho$ is pointing outward Ω_ρ . In the sequel, we assume that \mathbf{u}_ρ is as smooth as we want, which is always possible by assuming that the load and the domain are smooth. Denote J_ρ the generic objective function (4.3) evaluated in the perturbed domain

$$J_\rho(\Omega) = \int_{\Omega_2} F(\mathbf{u}_\rho)dV + \int_{\Gamma_N} G(\mathbf{u}_\rho)dS. \quad (4.11)$$

Remark 23. We recall that the objective function is abusively denoted J_ρ in the perturbed domain.

Definition 5. The objective function J_ρ is said to admit a topological derivative $DJ(\mathbf{x}_0)$ at the point \mathbf{x}_0 for a rigid inclusion of shape ω , if the following asymptotic expansion holds for small $\rho > 0$

$$J_\rho(\Omega) = J_0(\Omega) + \rho^n DJ(\mathbf{x}_0) + o(\rho^n), \quad n = 2 \text{ or } 3. \quad (4.12)$$

Theorem 3. Take ω to be the unit ball of \mathbb{R}^n , $n = 2$ or 3 . The objective function (4.11) admits a topological derivative at \mathbf{x}_0 of the form

$$J_\rho(\Omega) = J_0(\Omega) + \rho^2 \frac{(2\mu + \lambda)\pi r_1^2}{3\mu + \lambda} \left(4\mu\varepsilon(\mathbf{u})(\mathbf{x}_0) : \varepsilon(\mathbf{p})(\mathbf{x}_0) + (\mu + \lambda)\text{tr}(\varepsilon(\mathbf{u})(\mathbf{x}_0))\text{tr}(\varepsilon(\mathbf{p})(\mathbf{x}_0)) \right) + O(\rho^3) \text{ in } 2d, \quad (4.13)$$

$$J_\rho(\Omega) = J_0(\Omega) + \rho^3 \frac{4(2\mu + \lambda)\pi r_1^3}{8\mu + 3\lambda} \left(5\mu\varepsilon(\mathbf{u})(\mathbf{x}_0) : \varepsilon(\mathbf{p})(\mathbf{x}_0) + (\mu + \lambda)\text{tr}(\varepsilon(\mathbf{u})(\mathbf{x}_0))\text{tr}(\varepsilon(\mathbf{p})(\mathbf{x}_0)) \right) + O(\rho^4) \text{ in } 3d, \quad (4.14)$$

where the displacement field \mathbf{u} and the adjoint state \mathbf{p} solve respectively (4.1) and (4.5) and $r_1 = 1$ is the radius of the unit ball.

Remark 24. The topological derivative (4.14) reminds of the form of the topological sensitivity of a small hole with Neumann boundary condition [51]. Coefficients are different but both topological derivative involve the strain tensor $\varepsilon(\mathbf{u})$ instead of the displacement field \mathbf{u} . It may seem odd since a rigid body displacement field is here enforced on the inclusion. Thus, the current topological derivative should depend on displacement fields. However, this rigid body motion is unknown. Then, the problem turns out to be equivalent to a zero-average Neumann boundary condition.

Remark 25. It would be formally easier to use directly the numerical value $r_1 = 1$. However, the result will not have homogeneous dimensions.

4.2 Computation of the topological derivative

4.2.1 Approximation of the perturbed displacement field

Far fields expression

The behavior of the perturbed displacement field \mathbf{u}_ρ is estimated with far field functions in \mathbb{R}^3 . The perturbed field is expected to be approximately equal to the background solution \mathbf{u} plus the influence fields of the small inclusion ω_ρ , that is to formally assume the ansatz

$$\mathbf{u}_\rho(\mathbf{x}) \approx \mathbf{u}(\mathbf{x}) + \mathbf{v}_0 \left(\frac{\mathbf{x} - \mathbf{x}_0}{\rho} \right) + \rho \mathbf{v}_1 \left(\frac{\mathbf{x} - \mathbf{x}_0}{\rho} \right). \quad (4.15)$$

The functions \mathbf{v}_0 and \mathbf{v}_1 are defined in \mathbb{R}^3 . Since the perturbations due to the inclusion are getting smaller far from the center \mathbf{x}_0 , the far fields functions have to decay at infinity like $\lim_{\mathbf{y} \rightarrow \infty} \mathbf{v}_0(\mathbf{y}) = 0$ and $\lim_{\mathbf{y} \rightarrow \infty} \mathbf{v}_1(\mathbf{y}) = 0$. The functions \mathbf{v}_0 and \mathbf{v}_1 are respectively zero and first-order influence fields of the perturbation. They zoom on the inclusion and ignore boundary conditions on $\partial\Omega$. It will be proved in the following that the zero-order function \mathbf{v}_0 vanishes and the first-order zoom \mathbf{v}_1 depends on the strain strain tensor of the background solution \mathbf{u} at the point \mathbf{x}_0 .

Setting $\mathbf{y} = \frac{\mathbf{x} - \mathbf{x}_0}{\rho}$, the elasticity problem is rescaled with an inclusion of unit size ω . The ansatz (4.15) is put in (4.10). The systems solved by \mathbf{v}_0 and \mathbf{v}_1 are identified per power of ρ . The background solution is expanded at first-order

$$\mathbf{u}(\mathbf{x}) = \mathbf{u}(\mathbf{x}_0) + \nabla \mathbf{u}(\mathbf{x}_0)(\mathbf{x} - \mathbf{x}_0) + O(\rho^2) \text{ in a neighbourhood of } \mathbf{x}_0. \quad (4.16)$$

Assuming that the rigid body motion depends on ρ such that

$$\begin{cases} \mathbf{C}(\rho) = \mathbf{C}_0 + \rho \mathbf{C}_1 + O(\rho^2) \\ \mathbf{R}(\rho) = \mathbf{R}_0 + O(\rho) \end{cases}, \quad (4.17)$$

the function \mathbf{v}_0 satisfies

$$\left\{ \begin{array}{ll} -\operatorname{div}(\mathbf{A}\varepsilon(\mathbf{v}_0)) = \mathbf{0} & \text{in } \mathbb{R}^3 \setminus \omega \\ \mathbf{v}_0(\mathbf{y}) = \mathbf{C}_0 + \mathbf{R}_0 \mathbf{x}_0 - \mathbf{u}(\mathbf{x}_0) & \text{in } \omega \\ \int_{\partial\omega} \mathbf{A}\varepsilon(\mathbf{v}_0) \mathbf{n} dS = \mathbf{0} & \\ \lim_{\mathbf{y} \rightarrow \infty} \mathbf{v}_0(\mathbf{y}) = \mathbf{0} & \end{array} \right. , \quad (4.18)$$

and \mathbf{v}_1 is solution of

$$\left\{ \begin{array}{ll} -\operatorname{div}(\mathbf{A}\varepsilon(\mathbf{v}_1)) = \mathbf{0} & \text{in } \mathbb{R}^3 \setminus \omega \\ \mathbf{v}_1(\mathbf{y}) = \mathbf{C}_1 + \mathbf{R}_0 \mathbf{y} - \nabla \mathbf{u}(\mathbf{x}_0) \mathbf{y} & \text{in } \omega \\ \int_{\partial\omega} \mathbf{A}\varepsilon(\mathbf{v}_1) \mathbf{n} dS = \mathbf{0} & \\ \int_{\partial\omega} \mathbf{A}\varepsilon(\mathbf{v}_1) \mathbf{n} \wedge \mathbf{y} dS = \mathbf{0} & \\ \lim_{\mathbf{y} \rightarrow \infty} \mathbf{v}_1(\mathbf{y}) = \mathbf{0} & \end{array} \right. . \quad (4.19)$$

Lemma 5. *The function \mathbf{v}_0 is zero in \mathbb{R}^3 .*

Proof. According to [113], the solution of (4.18) has the explicit form

$$\mathbf{v}_0(\mathbf{y}) = \begin{cases} \boldsymbol{\xi}_{\mathbf{u},0} \cdot \mathbf{y} f_0(r) \mathbf{y} + \boldsymbol{\xi}_{\mathbf{u},0} g_0(r) & \text{in } \mathbb{R}^3 \setminus \omega \\ \boldsymbol{\xi}_{\mathbf{u},0} & \text{in } \omega \end{cases} , \quad (4.20)$$

where $\boldsymbol{\xi}_{\mathbf{u},0} = \mathbf{C}_0 + \mathbf{R}_0 \mathbf{x}_0 - \mathbf{u}(\mathbf{x}_0)$ and $r = \|\mathbf{y}\|$. Denoting $r_1 = 1$ the radius of the unit ball, the scalar functions f_0 and g_0 verify the conditions

$$\begin{cases} f_0(r_1) = 0, & g_0(r_1) = 1, \\ \lim_{r \rightarrow \infty} f_0(r) = 0, & \lim_{r \rightarrow \infty} g_0(r) = 0 \end{cases} . \quad (4.21)$$

Their expressions have been explicitly computed with Maple.

$$-\operatorname{div}(\mathbf{A}\varepsilon(\mathbf{v}_0)) = \mathbf{0} \iff \begin{cases} (2\mu + \lambda) f_0''(r) + (11\mu + 5\lambda) \frac{f_0'(r)}{r} = -(\mu + \lambda) \frac{g_0''(r)}{r^2} + (\mu + \lambda) \frac{g_0'(r)}{r^3} \\ (\mu + \lambda) r f_0'(r) + 2(3\mu + 2\lambda) f_0(r) = -(3\mu + \lambda) \frac{g_0'(r)}{r} - \mu g_0''(r) \end{cases} .$$

Adding boundary conditions, it follows

$$f_0(r) = \frac{3(\mu + \lambda)(r^2 - r_1^2)r_1}{2(2\mu + 5\lambda)r^5} \text{ and } g_0(r) = \frac{((9\mu + 3\lambda)r^2 + (\mu + \lambda)r_1^2)r_1}{2(2\mu + 5\lambda)r^3} . \quad (4.22)$$

One can verify that the momentum equilibrium $\int_{\partial\omega} \mathbf{A}\varepsilon(\mathbf{v}_0) \mathbf{n} \wedge \mathbf{y} dS = \mathbf{0}$ is satisfied for all constant vector $\boldsymbol{\xi}_{\mathbf{u},0}$. The equilibrium of forces has been computed with Maple and gives

$$\int_{\partial\omega} \mathbf{A}\varepsilon(\mathbf{v}_0) \mathbf{n} dS = \frac{12\mu(2\mu + \lambda)\pi r_1}{5\mu + 2\lambda} \boldsymbol{\xi}_{\mathbf{u},0} .$$

The condition $\int_{\partial\omega} \mathbf{A}\varepsilon(\mathbf{v}_0) \mathbf{n} dS = \mathbf{0}$ leads to $\boldsymbol{\xi}_{\mathbf{u},0} = \mathbf{0}$. Therefore, the function \mathbf{v}_0 is zero. \square

Remark 26. In the present case, Lemma 5 implies that $\mathbf{C}_0 + \mathbf{R}_0 \mathbf{x}_0 = \mathbf{u}(\mathbf{x}_0)$. In other words, the rigid body motion at zero-order of the inclusion is a translation that corresponds to the displacement of its center.

Lemma 6. The function \mathbf{v}_1 is explicitly given by

$$\mathbf{v}_1(\mathbf{y}) = \begin{cases} -\frac{15(\mu + \lambda)(r^2 - r_1^2)r_1^3}{2(8\mu + 3\lambda)r^7} \varepsilon(\mathbf{u})(\mathbf{x}_0) \mathbf{y} \cdot \mathbf{y} \mathbf{y} - \frac{(5\mu r^2 + 3(\mu + \lambda)r_1^2)r_1^3}{(8\mu + 3\lambda)r^5} \varepsilon(\mathbf{u})(\mathbf{x}_0) \mathbf{y} \\ + \frac{3(\mu + \lambda)(r^2 - r_1^2)r_1^3}{2(8\mu + 3\lambda)r^5} \text{tr}(\varepsilon(\mathbf{u})(\mathbf{x}_0)) \mathbf{y} \text{ in } \mathbb{R}^3 \setminus \omega \\ -\varepsilon(\mathbf{u})(\mathbf{x}_0) \mathbf{y} \text{ in } \omega \end{cases}, \quad (4.23)$$

where $r = \|\mathbf{y}\|$ and $r_1 = 1$ is the radius of the unit ball.

Proof. The solution of (4.19) is not obvious because of its boundary conditions on $\partial\omega$. The matrix $\nabla \mathbf{u}(\mathbf{x}_0)$ is divided into its antisymmetric and symmetric parts

$$\nabla \mathbf{u}(\mathbf{x}_0) = \frac{\nabla \mathbf{u}(\mathbf{x}_0) - \nabla^T \mathbf{u}(\mathbf{x}_0)}{2} + \varepsilon(\mathbf{u}(\mathbf{x}_0)).$$

The boundary condition then reads

$$\mathbf{v}_1(\mathbf{y}) = \mathbf{C}_1 + \left(\mathbf{R}_0 - \frac{\nabla \mathbf{u}(\mathbf{x}_0) - \nabla^T \mathbf{u}(\mathbf{x}_0)}{2} \right) \mathbf{y} - \varepsilon(\mathbf{u}(\mathbf{x}_0)) \mathbf{y} \text{ on } \partial\omega.$$

Let us first determine \mathbf{v}_1^a , the solution of

$$\left\{ \begin{array}{l} -\text{div}(\mathbf{A}\varepsilon(\mathbf{v}_1^a)) = \mathbf{0} \quad \text{in } \mathbb{R}^3 \setminus \omega \\ \mathbf{v}_1^a(\mathbf{y}) = \mathbf{C}_1 + \left(\mathbf{R}_0 - \frac{\nabla \mathbf{u}(\mathbf{x}_0) - \nabla^T \mathbf{u}(\mathbf{x}_0)}{2} \right) \mathbf{y} \quad \text{in } \omega \\ \int_{\partial\omega} \mathbf{A}\varepsilon(\mathbf{v}_1^a) \mathbf{n} dS = \mathbf{0} \\ \int_{\partial\omega} \mathbf{A}\varepsilon(\mathbf{v}_1^a) \mathbf{n} \wedge \mathbf{y} dS = \mathbf{0} \\ \lim_{\mathbf{y} \rightarrow \infty} \mathbf{v}_1^a(\mathbf{y}) = \mathbf{0} \end{array} \right., \quad (4.24)$$

which is explicitly given by

$$\mathbf{v}_1^a(\mathbf{y}) = \begin{cases} \mathbf{C}_1 \cdot \mathbf{y} f_a(r) \mathbf{y} + \mathbf{C}_1 g_a(r) + \mathbf{M} \mathbf{y} h_a(r) & \text{in } \mathbb{R}^3 \setminus \omega \\ \mathbf{C}_1 + \mathbf{M} \mathbf{y} & \text{in } \omega \end{cases}, \quad (4.25)$$

where $\mathbf{M} = \mathbf{R}_0 - \frac{\nabla \mathbf{u}(\mathbf{x}_0) - \nabla^T \mathbf{u}(\mathbf{x}_0)}{2}$ is a skew-matrix and f_a , g_a and h_a are scalar functions satisfying

$$\begin{cases} f_a(r_1) = 0, & g_a(r_1) = 1, & h_a(r_1) = 1, \\ \lim_{r \rightarrow \infty} f_a(r) = 0, & \lim_{r \rightarrow \infty} g_a(r) = 0, & \lim_{r \rightarrow \infty} h_a(r) = 0 \end{cases} \quad (4.26)$$

The system (4.24) has been computed with Maple. It follows that f_a , g_a and h_a verify

$$\begin{cases} (2\mu + \lambda)f_a''(r) + (11\mu + 5\lambda)\frac{f_a'(r)}{r} = -(\mu + \lambda)\frac{g_a''(r)}{r^2} + (\mu + \lambda)\frac{g_a'(r)}{r^3} \\ (\mu + \lambda)rf_a'(r) + 2(3\mu + 2\lambda)f_a(r) = -(3\mu + \lambda)\frac{g_a'(r)}{r} - \mu g_a''(r) \\ h_a''(r) + \frac{4}{r}h_a'(r) = 0 \end{cases}.$$

Adding conditions (4.26), it follows f_a and g_a are given by (4.22) and

$$h_a(r) = \frac{r_1^3}{r^3}. \quad (4.27)$$

Equilibrium of forces and momentum have been also computed with Maple.

The forces equilibrium condition $\int_{\partial\omega} \mathbf{A}\varepsilon(\mathbf{v}_1^a)\mathbf{n}dS = \mathbf{0}$ is satisfied for all matrix $\mathbf{M} = -\mathbf{M}^T$ and implies that $\mathbf{C}_1 = \mathbf{0}$.

The momentum equilibrium condition $\int_{\partial\omega} \mathbf{A}\varepsilon(\mathbf{v}_1^a)\mathbf{n} \wedge \mathbf{y}dS = \mathbf{0}$ implies that $\mathbf{M} = 0$. More precisely, it means that $\mathbf{R}_0 = \frac{\nabla\mathbf{u}(\mathbf{x}_0) - \nabla^T\mathbf{u}(\mathbf{x}_0)}{2}$. Therefore, \mathbf{v}_1^a is zero.

Now, let us determine \mathbf{v}_1^b , the solution of

$$\begin{cases} -\operatorname{div}(\mathbf{A}\varepsilon(\mathbf{v}_1^b)) = \mathbf{0} & \text{in } \mathbb{R}^3 \setminus \omega \\ \mathbf{v}_1^b(\mathbf{y}) = -\varepsilon(\mathbf{u})(\mathbf{x}_0)\mathbf{y} & \text{in } \omega \\ \lim_{\mathbf{y} \rightarrow \infty} \mathbf{v}_1^b(\mathbf{y}) = \mathbf{0} \end{cases}. \quad (4.28)$$

which is explicitly given by

$$\mathbf{v}_1^b(\mathbf{y}) = \begin{cases} -\varepsilon(\mathbf{u})(\mathbf{x}_0)\mathbf{y} \cdot \mathbf{y}f_b(r)\mathbf{y} - \varepsilon(\mathbf{u})(\mathbf{x}_0)\mathbf{y}g_b(r) - \operatorname{tr}(\varepsilon(\mathbf{u})(\mathbf{x}_0))\mathbf{y}h_b(r) & \text{on } \mathbb{R}^3 \setminus \omega \\ -\varepsilon(\mathbf{u})(\mathbf{x}_0)\mathbf{y} & \text{on } \omega \end{cases}. \quad (4.29)$$

The scalar functions f_b , g_b and h_b satisfy the following conditions

$$\begin{cases} f_b(r_1) = 0, & g_b(r_1) = 1, & h_b(r_1) = 0 \\ \lim_{r \rightarrow \infty} f_b(r) = 0, & \lim_{r \rightarrow \infty} g_b(r) = 0, & \lim_{r \rightarrow \infty} h_b(r) = 0 \end{cases}. \quad (4.30)$$

The system (4.28) has also been computed with Maple. It follows that f_b , g_b and h_b satisfy the following coupled equations system

$$\begin{cases} (2\mu + \lambda)f_b''(r) + (14\mu + 6\lambda)\frac{f_b'(r)}{r} = -(\mu + \lambda)\frac{g_b''(r)}{r^2} + (\mu + \lambda)\frac{g_b'(r)}{r^3} \\ 2(\mu + \lambda)rf_b'(r) + (14\mu + 10\lambda)f_b(r) = -\mu g_b''(r) - (6\mu + 2\lambda)\frac{g_b'(r)}{r} \\ 2\mu f_b(r) + (\mu + \lambda)\frac{g_b'(r)}{r} = -(2\mu + \lambda)h_b''(r) - 4(2\mu + \lambda)\frac{h_b'(r)}{r} \end{cases}.$$

Adding the conditions (4.30), the scalar functions are explicitly given by

$$\begin{cases} f_b(r) = \frac{15(\mu + \lambda)(r^2 - r_1^2)r_1^3}{2(3\mu + 8\lambda)r^7} \\ g_b(r) = \frac{(5\mu r^2 + 3(\mu + \lambda)r_1^2)r_1^3}{(3\mu + 8\lambda)r^5} \\ h_b(r) = -\frac{3(\mu + \lambda)(r^2 - r_1^2)r_1^3}{2(3\mu + 8\lambda)r^5} \end{cases}$$

It has been verified with Maple that both equilibrium on $\partial\omega$, forces and momentum, are satisfied by \mathbf{v}_1^b . This is why they are not enforced in the system (4.28). Actually, this problem has a Dirichlet boundary condition. As a conclusion, $\mathbf{v}_1 = \mathbf{v}_1^b$. \square

Remark 27. In 2d, the solution of the exterior problem is obtained with the same methodology and the solution reads

$$\mathbf{v}_1(\mathbf{y}) = \begin{cases} -\frac{2(\mu + \lambda)(r^2 - r_1^2)r_1^2}{(3\mu + \lambda)r^6} \varepsilon(\mathbf{u})(\mathbf{x}_0) \mathbf{y} \cdot \mathbf{y} \mathbf{y} - \frac{(2\mu r^2 + (\mu + \lambda)r_1^2)r_1^2}{(3\mu + \lambda)r^4} \varepsilon(\mathbf{u})(\mathbf{x}_0) \mathbf{y} \\ + \frac{1}{2} \frac{(\mu + \lambda)(r^2 - r_1^2)r_1^2}{(3\mu + \lambda)r^4} \text{tr}(\varepsilon(\mathbf{u})(\mathbf{x}_0)) \mathbf{y} \text{ in } \mathbb{R}^2 \setminus \omega \\ -\varepsilon(\mathbf{u})(\mathbf{x}_0) \mathbf{y} \text{ in } \omega. \end{cases} \quad (4.31)$$

Asymptotic analysis of the perturbed displacement

Let \mathbf{v}_ρ be the difference between the perturbed and the background displacement fields

$$\mathbf{v}_\rho = \mathbf{u}_\rho - \mathbf{u}. \quad (4.32)$$

This function represents the influence of the inclusion in terms of displacement and solves

$$\begin{cases} -\text{div}(\mathbf{A}\varepsilon(\mathbf{v}_\rho)) = \mathbf{0} & \text{in } \Omega_\rho \\ \mathbf{A}\varepsilon(\mathbf{v}_\rho)\mathbf{n} = \mathbf{0} & \text{on } \Gamma_N \\ \mathbf{v}_\rho = \mathbf{0} & \text{on } \Gamma_D \\ \mathbf{v}_\rho(\mathbf{x}) = \mathcal{C}(\rho) + \mathbf{R}(\rho)\mathbf{x} - \mathbf{u}(\mathbf{x}) & \text{in } \omega_\rho \\ \int_{\partial\omega_\rho} \mathbf{A}\varepsilon(\mathbf{v}_\rho)\mathbf{n} dS = \mathbf{0} \\ \int_{\partial\omega_\rho} \mathbf{A}\varepsilon(\mathbf{v}_\rho)\mathbf{n} \wedge \mathbf{x} dS = \mathbf{0} \end{cases} \quad (4.33)$$

Denote $\tilde{\mathbf{n}}$ the unit normal vector pointing outward ω_ρ , the equilibrium conditions come out from

$$\begin{aligned} \int_{\partial\omega_\rho} \mathbf{A}\varepsilon(\mathbf{v}_\rho)\mathbf{n} dS &= - \int_{\partial\omega_\rho} \mathbf{A}\varepsilon(\mathbf{u})\mathbf{n} dS = \int_{\partial\omega_\rho} \mathbf{A}\varepsilon(\mathbf{u})\tilde{\mathbf{n}} dS = \int_{\omega_\rho} \text{div}(\mathbf{A}\varepsilon(\mathbf{u})) dV = \mathbf{0}, \\ \int_{\partial\omega_\rho} \mathbf{A}\varepsilon(\mathbf{v}_\rho)\mathbf{n} \wedge \mathbf{x} dS &= - \int_{\omega_\rho} (\mathbf{x} \wedge \text{div}(\mathbf{A}\varepsilon(\mathbf{u})) + \overset{\equiv}{\bar{\bar{\bar{\epsilon}}}} : \mathbf{A}\varepsilon(\mathbf{u})) dV = - \int_{\omega_\rho} \overset{\equiv}{\bar{\bar{\bar{\epsilon}}}} : \mathbf{A}\varepsilon(\mathbf{u}) dV. \end{aligned}$$

The third-order tensor $\overset{\equiv}{\bar{\bar{\bar{\epsilon}}}}$ is defined such that

- $\epsilon_{i,j,k} = 0$ when two or more indices are equal,
- $\epsilon_{i,j,k} = 1$ when (i, j, k) is an even permutation of $(1, 2, 3)$,
- $\epsilon_{i,j,k} = -1$ when (i, j, k) is an odd permutation of $(1, 2, 3)$.

Thus, $\bar{\bar{\epsilon}} : \mathbf{A}\boldsymbol{\varepsilon}(\mathbf{u}) = \mathbf{0}$ since $\mathbf{A}\boldsymbol{\varepsilon}(\mathbf{u})$ is symmetric.

Let us introduce the rescaled function \mathbf{v}_1^ρ defined by

$$\mathbf{v}_1^\rho(\mathbf{x}) = \rho \mathbf{v}_1 \left(\frac{\mathbf{x} - \mathbf{x}_0}{\rho} \right). \quad (4.34)$$

The next result proves that \mathbf{v}_1^ρ is, in some sense, the limit of \mathbf{v}_ρ as ρ goes to zero.

Proposition 9. *Let $\theta \in \mathcal{C}_c^\infty(\Omega)$ be a cut-off function with compact support $\mathcal{U}_+ \subset \Omega$ such that $\theta \equiv 1$ in a neighborhood $\mathcal{U}_- \subset \mathcal{U}_+$ of \mathbf{x}_0 . There exists a constant $C > 0$ independent of ρ such that*

$$\mathbf{v}_\rho = \theta \mathbf{v}_1^\rho + \boldsymbol{\delta}, \quad (4.35)$$

with

$$\|\mathbf{v}_1^\rho\|_{L^2(\Omega_\rho)} \leq C\rho^{3/2+1}, \quad (4.36)$$

$$\|\boldsymbol{\varepsilon}(\mathbf{v}_1^\rho)\|_{L^2(\Omega_\rho)} \leq C\rho^{3/2}, \quad (4.37)$$

$$\|\boldsymbol{\delta}\|_{H^1(\Omega_\rho)} \leq C\rho^{3/2+1}. \quad (4.38)$$

Remark 28. *The role of the cut-off function θ is to make sure that the product $\theta \mathbf{v}_1^\rho$ satisfies homogeneous boundary conditions on the boundary $\partial\Omega$, as does \mathbf{v}_ρ . Since θ has a compact support, it implies that $\theta \equiv 0$ far from \mathbf{x}_0 . Consequently, θ vanishes far from the inclusion so that $\boldsymbol{\delta}$ contains the far field influence of the inclusion. The function $\boldsymbol{\delta}$ is an error term in the H^1 -norm. Indeed, its H^1 -norm is always asymptotically smaller than the one of $\theta \mathbf{v}_1^\rho$. The L^2 -norm of $\boldsymbol{\delta}$ is of the same order as its H^1 -norm. However, the L^2 -norm of \mathbf{v}_1^ρ is always smaller by a factor ρ than its H^1 -norm.*

Remark 29. *Considering the form of (4.23) and (4.31), we shall infer that norm estimations in 2d differs from (4.36), (4.37) and (4.38) by a factor of ρ .*

Proof. The explicit expression (4.23) of \mathbf{v}_1 indicates that $\mathbf{v}_1 = O(1/|\mathbf{y}|^2)$ and $\boldsymbol{\varepsilon}(\mathbf{v}_1) = O(1/|\mathbf{y}|^3)$ at infinity. Thus, it follows by rescaling

$$\|\mathbf{v}_1^\rho\|_{L^\infty(\Omega \setminus \mathcal{U}_-)} \leq C\rho^3 \text{ and } \|\boldsymbol{\varepsilon}(\mathbf{v}_1^\rho)\|_{L^\infty(\Omega \setminus \mathcal{U}_-)} \leq C\rho^3. \quad (4.39)$$

These L^∞ -norms are evaluated far from the neighborhood of \mathbf{x}_0 . Denote $\Omega_{\rho^{-1}}$ the translated and rescaled domain centered at the origin and of size $\frac{1}{\rho}|\Omega|$. The estimates (4.36) and (4.37) are simply obtained as follows

$$\int_{\Omega_\rho} |\mathbf{v}_1^\rho|^2 dV \leq C \int_{\Omega_\rho} \rho^2 \left| \mathbf{v}_1 \left(\frac{\mathbf{x} - \mathbf{x}_0}{\rho} \right) \right|^2 dV \leq C\rho^{3+2} \int_{\Omega_{\rho^{-1}}} |\mathbf{v}_1(\mathbf{y})|^2 dV \leq C\rho^{3+2} \int_{r_1}^{r_1/\rho} \frac{dr}{r^2} \leq C\rho^{3+2},$$

$$\int_{\Omega_\rho} |\varepsilon(\mathbf{v}_1^\rho)|^2 dV \leq C \int_{\Omega_\rho} \left| \varepsilon \left(\mathbf{v}_1 \left(\frac{\mathbf{x} - \mathbf{x}_0}{\rho} \right) \right) \right|^2 dV \leq C \rho^3 \int_{\Omega_{\rho^{-1}}} |\varepsilon(\mathbf{v}_1(y))|^2 dV \leq C \rho^3 \int_{r_1}^{r_1/\rho} \frac{dr}{r^4} \leq C \rho^3.$$

Let us now write the equations satisfied by $\boldsymbol{\delta}$

$$\left\{ \begin{array}{ll} -\operatorname{div}(\mathbf{A}\varepsilon(\boldsymbol{\delta})) = \operatorname{div}(\mathbf{A}(\mathbf{v}_1^\rho \otimes \nabla\theta)^s) + \mathbf{A}\varepsilon(\mathbf{v}_1^\rho)\nabla\theta & \text{in } \Omega_\rho \\ \mathbf{A}\varepsilon(\boldsymbol{\delta})\mathbf{n} = \mathbf{0} & \text{on } \Gamma_N \\ \boldsymbol{\delta} = \mathbf{0} & \text{on } \Gamma_D \\ \boldsymbol{\delta}(\mathbf{x}) = \mathbf{C}(\rho) + \mathbf{R}(\rho)\mathbf{x} - \mathbf{u}(\mathbf{x}) + \varepsilon(\mathbf{u})(\mathbf{x}_0)(\mathbf{x} - \mathbf{x}_0) & \text{in } \omega_\rho \\ \int_{\partial\omega_\rho} \mathbf{A}\varepsilon(\boldsymbol{\delta})\mathbf{n} dS = \mathbf{0} & \\ \int_{\partial\omega_\rho} \mathbf{A}\varepsilon(\boldsymbol{\delta})\mathbf{n} \wedge \mathbf{x} dS = \mathbf{0} & \end{array} \right. . \quad (4.40)$$

The exponent "s" stands for the symmetric part of the matrix $\mathbf{v}_1^\rho \otimes \nabla\theta$. Let us multiply (4.40) by $\boldsymbol{\delta}$ in Ω_ρ and integrate by parts

$$\int_{\Omega_\rho} \mathbf{A}\varepsilon(\boldsymbol{\delta}) : \varepsilon(\boldsymbol{\delta}) dV = - \int_{\Omega_\rho} \mathbf{A}(\mathbf{v}_1^\rho \otimes \nabla\theta)^s : \varepsilon(\boldsymbol{\delta}) dV + \int_{\Omega_\rho} \mathbf{A}\varepsilon(\mathbf{v}_1^\rho)\nabla\theta \cdot \boldsymbol{\delta} dV + \int_{\partial\omega_\rho} \mathbf{A}\varepsilon(\boldsymbol{\delta})\mathbf{n} \cdot \boldsymbol{\delta} dS.$$

The left hand side is bounded from below using the Poincaré-Korn inequality (since $\boldsymbol{\delta}$ vanishes on Γ_D)

$$\int_{\Omega_\rho} \mathbf{A}\varepsilon(\boldsymbol{\delta}) : \varepsilon(\boldsymbol{\delta}) dV = \int_{\Omega_\rho} (2\mu|\varepsilon(\boldsymbol{\delta})|^2 + \lambda \operatorname{tr}(\varepsilon(\boldsymbol{\delta}))^2) dV \geq C \|\varepsilon(\boldsymbol{\delta})\|_{L^2(\Omega_\rho)}^2 \geq C \|\boldsymbol{\delta}\|_{H^1(\Omega_\rho)}^2.$$

The two first terms of the right-hand side are bounded using Cauchy-Schwarz inequality and the L^∞ -norms of \mathbf{v}_1^ρ and $\varepsilon(\mathbf{v}_1^\rho)$ since $\nabla\theta$ is zero in the influence area of the inclusion. There exists $C > 0$ independent of ρ such that

$$\begin{aligned} & \left| \int_{\Omega_\rho} \mathbf{A}(\mathbf{v}_1^\rho \otimes \nabla\theta)^s : \varepsilon(\boldsymbol{\delta}) dV \right| + \left| \int_{\Omega_\rho} \mathbf{A}\varepsilon(\mathbf{v}_1^\rho)\nabla\theta \cdot \boldsymbol{\delta} dV \right| \\ & \leq C \|\mathbf{v}_1^\rho\|_{L^\infty(\Omega \setminus \mathcal{U}_-)} \|\nabla\theta\|_{L^\infty(\Omega \setminus \mathcal{U}_-)} \|\varepsilon(\boldsymbol{\delta})\|_{L^2(\Omega_\rho)} + C \|\varepsilon(\mathbf{v}_1^\rho)\|_{L^\infty(\Omega \setminus \mathcal{U}_-)} \|\nabla\theta\|_{L^\infty(\Omega \setminus \mathcal{U}_-)} \|\boldsymbol{\delta}\|_{L^2(\Omega_\rho)} \\ & \leq C \rho^3 \|\varepsilon(\boldsymbol{\delta})\|_{L^2(\Omega_\rho)}. \end{aligned}$$

The last term requires more attention. A Taylor expansion with integral remainder of each component u_i of the background solution \mathbf{u} in a neighborhood of \mathbf{x}_0 is

$$u_i(\mathbf{x}) = u_i(\mathbf{x}_0) + \nabla u_i(\mathbf{x}_0) \cdot (\mathbf{x} - \mathbf{x}_0) + \int_0^1 (1-t)(\mathbf{x} - \mathbf{x}_0)^T \mathbf{H}(u_i(\mathbf{x}_0 + t(\mathbf{x} - \mathbf{x}_0))) (\mathbf{x} - \mathbf{x}_0) dt, \quad (4.41)$$

with \mathbf{H} the Hessian matrix of u_i . The expansion of the background solution \mathbf{u} in a neighborhood of \mathbf{x}_0 is then

$$\mathbf{u}(\mathbf{x}) = \mathbf{u}(\mathbf{x}_0) + \nabla \mathbf{u}(\mathbf{x}_0)(\mathbf{x} - \mathbf{x}_0) + \int_0^1 (1-t)(\mathbf{x} - \mathbf{x}_0)^T \mathcal{D}^2(\mathbf{u}(\mathbf{x}_0 + t(\mathbf{x} - \mathbf{x}_0))) (\mathbf{x} - \mathbf{x}_0) dt, \quad (4.42)$$

where \mathcal{D}^2 is a third order tensor containing second derivatives of \mathbf{u} . Using (4.40), the above expansion of \mathbf{u} and the decomposition of $\nabla\mathbf{u}$ into its antisymmetric and symmetric parts, it follows that

$$\begin{aligned} \boldsymbol{\delta}(\mathbf{x}) = & \mathcal{C}(\rho) - \mathbf{u}(\mathbf{x}_0) + \frac{\nabla\mathbf{u}(\mathbf{x}_0) - \nabla^T\mathbf{u}(\mathbf{x}_0)}{2}\mathbf{x}_0 + \left(\mathbf{R}(\rho) - \frac{\nabla\mathbf{u}(\mathbf{x}_0) - \nabla^T\mathbf{u}(\mathbf{x}_0)}{2} \right) \mathbf{x} \\ & - \int_0^1 (1-t)(\mathbf{x} - \mathbf{x}_0)^T \mathcal{D}^2(\mathbf{u}(\mathbf{x}_0 + t(\mathbf{x} - \mathbf{x}_0))) (\mathbf{x} - \mathbf{x}_0) dt \text{ in } \omega_\rho. \end{aligned}$$

Then $\boldsymbol{\delta}$ is made up of a rigid body motion and the integral remainder of the expansion of \mathbf{u} . Considering the force and momentum equilibrium, the rigid body motion vanishes and the boundary term is then

$$\int_{\partial\omega_\rho} \mathbf{A}\varepsilon(\boldsymbol{\delta})\mathbf{n} \cdot \boldsymbol{\delta} dS = - \int_{\partial\omega_\rho} \mathbf{A}\varepsilon(\boldsymbol{\delta})\mathbf{n} \cdot \int_0^1 (1-t)(\mathbf{x} - \mathbf{x}_0)^T \mathcal{D}^2(\mathbf{u}(\mathbf{x}_0 + t(\mathbf{x} - \mathbf{x}_0))) (\mathbf{x} - \mathbf{x}_0) dt dS.$$

The term $\int_0^1 (1-t)(\mathbf{x} - \mathbf{x}_0)^T \mathcal{D}^2(\mathbf{u}(\mathbf{x}_0 + t(\mathbf{x} - \mathbf{x}_0))) (\mathbf{x} - \mathbf{x}_0) dt$ is extended in Ω_ρ .

Let $\varphi \in \mathcal{C}^\infty(\mathbb{R}^3)$ be a cut-off function such that $\varphi(\mathbf{y}) \equiv 1$ in ω , decreases to zero in a corona B_2 of size 2 and $\varphi(\mathbf{y}) \equiv 0$ far from the origin. Denote φ_ρ the rescaled cut-off function such that $\varphi_\rho(\mathbf{x}) = \varphi\left(\frac{\mathbf{x} - \mathbf{x}_0}{\rho}\right)$. Then, $\varphi_\rho(\mathbf{x}) \equiv 1$ in ω_ρ , decreases to zero in $B_{2\rho}$ a corona of size 2ρ and $\varphi_\rho(\mathbf{x}) \equiv 0$ far from x_0 .

Setting $\mathbf{R}_u(\mathbf{x}) = \varphi_\rho(\mathbf{x}) \int_0^1 (1-t)(\mathbf{x} - \mathbf{x}_0)^T \mathcal{D}^2(\mathbf{u}(\mathbf{x}_0 + t(\mathbf{x} - \mathbf{x}_0))) (\mathbf{x} - \mathbf{x}_0) dt$, the boundary term is rewritten

$$\int_{\partial\omega_\rho} \mathbf{A}\varepsilon(\boldsymbol{\delta}(\mathbf{x}))\mathbf{n} \cdot \int_0^1 (1-t)(\mathbf{x} - \mathbf{x}_0)^T \mathcal{D}^2(\mathbf{u}(\mathbf{x}_0 + t(\mathbf{x} - \mathbf{x}_0))) (\mathbf{x} - \mathbf{x}_0) dt dS = \int_{\partial\omega_\rho} \mathbf{A}\varepsilon(\boldsymbol{\delta})\mathbf{n} \cdot \mathbf{R}_u dS.$$

The function \mathbf{R}_u is defined in Ω_ρ . The above term is then integrated by parts

$$- \int_{\partial\omega_\rho} \mathbf{A}\varepsilon(\boldsymbol{\delta})\mathbf{n} \cdot \mathbf{R}_u dS = - \int_{\Omega_\rho} \operatorname{div}(\mathbf{A}\varepsilon(\boldsymbol{\delta})) \cdot \mathbf{R}_u dV - \int_{\Omega_\rho} \mathbf{A}\varepsilon(\boldsymbol{\delta}) : \varepsilon(\mathbf{R}_u) dV.$$

The first term of the right-hand side is evaluated using (4.40)

$$- \int_{\Omega_\rho} \operatorname{div}(\mathbf{A}\varepsilon(\boldsymbol{\delta})) \cdot \mathbf{R}_u dV = \int_{\Omega_\rho} \operatorname{div}(\mathbf{A}(\mathbf{v}_1^\rho \otimes \nabla\theta)^s) \cdot \mathbf{R}_u dV + \int_{\Omega_\rho} \mathbf{A}\varepsilon(\mathbf{v}_1^\rho) \nabla\theta \cdot \mathbf{R}_u dV = 0$$

because $\operatorname{supp}(\mathbf{R}_u) \cap \operatorname{supp}(\nabla\theta) = \emptyset$.

Decrease property of φ_ρ implies that $\nabla\varphi_\rho$ behaves like $1/\rho$. Moreover, $\mathbf{x} - \mathbf{x}_0$ is of the order of ρ in $B_{2\rho}$. Hence,

$$\exists C > 0, |\nabla\mathbf{R}_u| \leq C\rho \text{ in } B_{2\rho}. \quad (4.43)$$

Remark 30. Since $\nabla \mathbf{R}_u$ involves the third derivatives of the background solution, \mathbf{u} shall at least belong to $\mathcal{C}^3(\Omega)^3$.

The last term is estimated with Cauchy–Schwarz inequality

$$\left| \int_{\Omega_\rho} \mathbf{A}\varepsilon(\boldsymbol{\delta}) : \varepsilon(\mathbf{R}_u) dV \right| \leq C \|\varepsilon(\boldsymbol{\delta})\|_{L^2(\Omega_\rho)} \sqrt{\int_{B_{2\rho}} |\varepsilon(\mathbf{R}_u)|^2 dV} \leq C \rho^{3/2+1} \|\varepsilon(\boldsymbol{\delta})\|_{L^2(\Omega_\rho)}.$$

Regrouping all of that, the L^2 -norm of $\varepsilon(\boldsymbol{\delta})$ is bounded as follows

$$\|\varepsilon(\boldsymbol{\delta})\|_{L^2(\Omega_\rho)} \leq C(\rho^3 + \rho^{3/2+1}) \leq C\rho^{3/2+1}. \quad (4.44)$$

Finally, (4.38) is obtained with Korn inequality. \square

4.2.2 Approximation of the perturbed adjoint state

The perturbed adjoint state, \mathbf{p}_ρ , associated to the perturbed displacement \mathbf{u}_ρ , is estimated likewise. The adjoint problem is adapted for the purpose of the sensitivity analysis.

$$\left\{ \begin{array}{ll} -\operatorname{div}(\mathbf{A}\varepsilon(\mathbf{p}_\rho)) = -\mathbf{F}'(\mathbf{u})\mathbf{1}_{\Omega_1} & \text{in } \Omega_\rho \\ \mathbf{A}\varepsilon(\mathbf{p}_\rho)\mathbf{n} = -\mathbf{G}'(\mathbf{u}) & \text{on } \Gamma_N \\ \mathbf{p}_\rho = \mathbf{0} & \text{on } \Gamma_D \\ \mathbf{p}_\rho(\mathbf{x}) = \bar{\mathbf{C}}(\rho) + \bar{\mathbf{R}}(\rho)\mathbf{x} & \text{in } \omega_\rho \\ \int_{\partial\omega_\rho} \mathbf{A}\varepsilon(\mathbf{p}_\rho)\mathbf{n} dS = \mathbf{0} & \\ \int_{\partial\omega_\rho} \mathbf{A}\varepsilon(\mathbf{p}_\rho)\mathbf{n} \wedge \mathbf{x} dS = \mathbf{0} & \end{array} \right. . \quad (4.45)$$

The translation $\bar{\mathbf{C}}(\rho)$ is an unknown constant vector and the infinitesimal rotation $\bar{\mathbf{R}}(\rho)$ is an unknown constant anti-symmetric matrix. They both may depend on the inclusion size.

Remark 31. It has already been noticed in [8] that the adjoint problem (4.45) is not standard since the right hand side depends on \mathbf{u} and not on \mathbf{u}_ρ as expected in the perturbed domain. This adaptation is licit since the objective function is evaluated far from the influence area of the inclusion.

Let us define $\mathbf{q}_\rho = \mathbf{p}_\rho - \mathbf{p}$ the difference between the perturbed and the background adjoint states. It solves

$$\left\{ \begin{array}{ll} -\operatorname{div}(\mathbf{A}\varepsilon(\mathbf{q}_\rho)) = \mathbf{0} & \text{in } \Omega_\rho \\ \mathbf{A}\varepsilon(\mathbf{q}_\rho)\mathbf{n} = \mathbf{0} & \text{on } \Gamma_N \\ \mathbf{q}_\rho = \mathbf{0} & \text{on } \Gamma_D \\ \mathbf{q}_\rho(\mathbf{x}) = \bar{\mathbf{C}}(\rho) + \bar{\mathbf{R}}(\rho)\mathbf{x} - \mathbf{p}(\mathbf{x}) & \text{in } \omega_\rho \\ \int_{\partial\omega_\rho} \mathbf{A}\varepsilon(\mathbf{q}_\rho)\mathbf{n} dS = \mathbf{0} & \\ \int_{\partial\omega_\rho} \mathbf{A}\varepsilon(\mathbf{q}_\rho)\mathbf{n} \wedge \mathbf{x} dS = \mathbf{0} & \end{array} \right. . \quad (4.46)$$

The two first equations of (4.46) have zero right hand side because of the non-standard adjoint in the perturbed domain (4.45). The equilibrium conditions on $\partial\omega_\rho$ are obtained the same way as (4.33) equilibrium conditions are computed. Let us introduce the rescaled function \mathbf{q}_1^ρ such that

$$\mathbf{q}_1^\rho(\mathbf{x}) = \rho \mathbf{q}_1 \left(\frac{\mathbf{x} - \mathbf{x}_0}{\rho} \right), \quad (4.47)$$

where \mathbf{q}_1 is similar to \mathbf{v}_1 .

Proposition 10. *Let $\theta \in \mathbf{C}_c^\infty(\Omega)$ be a cut-off function with compact support $\mathcal{U}_+ \subset \Omega$ such that $\theta \equiv 1$ in a neighborhood $\mathcal{U}_- \subset \mathcal{U}_+$ of \mathbf{x}_0 . We have*

$$\mathbf{q}_\rho = \theta \mathbf{q}_1^\rho + \boldsymbol{\eta}, \quad (4.48)$$

with

$$\|\mathbf{q}_1^\rho\|_{L^2(\Omega_\rho)} \leq C\rho^{3/2+1}, \quad (4.49)$$

$$\|\varepsilon(\mathbf{q}_1^\rho)\|_{L^2(\Omega_\rho)} \leq C\rho^{3/2}, \quad (4.50)$$

$$\|\boldsymbol{\eta}\|_{H^1(\Omega_\rho)} \leq C\rho^{3/2+1}, \quad (4.51)$$

$$\|\mathbf{q}_1^\rho\|_{L^\infty(\Omega \setminus \mathcal{U}_-)} \leq C\rho^3 \text{ and } \|\varepsilon(\mathbf{q}_1^\rho)\|_{L^\infty(\Omega \setminus \mathcal{U}_-)} \leq C\rho^3. \quad (4.52)$$

Proof. The function $\boldsymbol{\eta}$ solves

$$\left\{ \begin{array}{ll} -\operatorname{div}(\mathbf{A}\varepsilon(\boldsymbol{\eta})) = \operatorname{div}(\mathbf{A}(\mathbf{q}_1^\rho \otimes \nabla\theta)^s) + \mathbf{A}\varepsilon(\mathbf{q}_1^\rho)\nabla\theta & \text{in } \Omega_\rho \\ \mathbf{A}\varepsilon(\boldsymbol{\eta})\mathbf{n} = \mathbf{0} & \text{on } \Gamma_N \\ \boldsymbol{\eta} = \mathbf{0} & \text{on } \Gamma_D \\ \boldsymbol{\eta}(\mathbf{x}) = \bar{\mathbf{C}}(\rho) + \bar{\mathbf{R}}(\rho)\mathbf{x} - \mathbf{p}(\mathbf{x}) + \varepsilon(\mathbf{p})(\mathbf{x}_0)(\mathbf{x} - \mathbf{x}_0) & \text{in } \omega_\rho \\ \int_{\partial\omega_\rho} \mathbf{A}\varepsilon(\boldsymbol{\eta})\mathbf{n}dS = \mathbf{0} \\ \int_{\partial\omega_\rho} \mathbf{A}\varepsilon(\boldsymbol{\eta})\mathbf{n} \wedge \mathbf{x}dS = \mathbf{0} \end{array} \right. . \quad (4.53)$$

Proposition 10 is proved by going back over the proof Proposition 9 and by substituting \mathbf{u} with \mathbf{p} and \mathbf{v}_ρ with \mathbf{q}_ρ . \square

4.2.3 Proof of the main result

The 3d result of Theorem 3 can now be proved using the estimates of perturbed displacement and adjoint fields, \mathbf{u}_ρ and \mathbf{p}_ρ . Let us write a first-order Taylor expansion with exact remainder of the perturbed objective function

$$\begin{aligned} J_\rho(\Omega) &= \int_{\Omega_1} F(\mathbf{u}_\rho)dV + \int_{\Gamma_N} G(\mathbf{u}_\rho)dS = \int_{\Omega_1} F(\mathbf{u} + \mathbf{v}_\rho)dV + \int_{\Gamma_N} G(\mathbf{u} + \mathbf{v}_\rho)dS \\ &= J_0(\Omega) + \int_{\Omega_1} \mathbf{F}'(\mathbf{u}) \cdot \mathbf{v}_\rho dV + \int_{\Gamma_N} \mathbf{G}'(\mathbf{u}) \cdot \mathbf{v}_\rho dS + \frac{1}{2} \int_{\Omega_1} \mathbf{v}_\rho^T F''(\bar{\mathbf{u}})\mathbf{v}_\rho dV + \frac{1}{2} \int_{\Gamma_N} \mathbf{v}_\rho^T G''(\bar{\mathbf{u}})\mathbf{v}_\rho dS. \end{aligned}$$

The exact remainder is bounded thanks to assumptions (4.4) and Proposition 9

$$\begin{aligned} \left| \int_{\Omega_1} \mathbf{v}_\rho^T F''(\bar{\mathbf{u}}) \mathbf{v}_\rho dV \right| &\leq C \|\mathbf{v}_\rho\|_{L^2(\Omega_\rho)}^2 \leq C\rho^5, \\ \left| \int_{\Gamma_N} \mathbf{v}_\rho^T G''(\bar{\mathbf{u}}) \mathbf{v}_\rho dS \right| &\leq C \|\mathbf{v}_\rho\|_{L^2(\Gamma_N)}^2 \leq C \|\boldsymbol{\delta}\|_{L^2(\Gamma_N)}^2 \text{ because } \theta = 0 \text{ on } \Gamma_N \\ &\leq C \|\boldsymbol{\delta}\|_{H^1(\Omega_\rho)}^2 \text{ using the Trace theorem} \\ &\leq C\rho^5. \end{aligned}$$

The occurrence of \mathbf{v}_ρ in the expansion of $J_\rho(\Omega)$ justifies the use of an adjoint state. Moreover, this expansion involves \mathbf{u} instead of \mathbf{u}_ρ . This is why (4.45) has been modified and is not the standard adjoint equation. Multiplying (4.45) by \mathbf{v}_ρ and integrating by parts twice, it follows

$$\begin{aligned} \int_{\Omega_1} \mathbf{F}'(\mathbf{u}) \cdot \mathbf{v}_\rho dV + \int_{\Gamma_N} \mathbf{G}'(\mathbf{u}) \cdot \mathbf{v}_\rho dS &= \int_{\partial\omega_\rho} \mathbf{A}\varepsilon(\mathbf{p}_\rho) \mathbf{n} \cdot \mathbf{v}_\rho dS = \int_{\partial\omega_\rho} \mathbf{A}\varepsilon(\mathbf{q}_\rho + \mathbf{p}) \mathbf{n} \cdot \mathbf{v}_\rho dS \\ &= \int_{\partial\omega_\rho} \mathbf{A}\varepsilon(\mathbf{q}_1^\rho) \mathbf{n} \cdot \mathbf{v}_1^\rho dS + \int_{\partial\omega_\rho} \mathbf{A}\varepsilon(\mathbf{p}) \mathbf{n} \cdot \mathbf{v}_1^\rho dS + \int_{\partial\omega_\rho} \mathbf{A}\varepsilon(\mathbf{q}_1^\rho) \mathbf{n} \cdot \boldsymbol{\delta} dS \\ &\quad + \int_{\partial\omega_\rho} \mathbf{A}\varepsilon(\mathbf{p}) \mathbf{n} \cdot \boldsymbol{\delta} dS + \int_{\partial\omega_\rho} \mathbf{A}\varepsilon(\boldsymbol{\eta}) \mathbf{n} \cdot \mathbf{v}_1^\rho dS + \int_{\partial\omega_\rho} \mathbf{A}\varepsilon(\boldsymbol{\eta}) \mathbf{n} \cdot \boldsymbol{\delta} dS. \end{aligned}$$

Propositions 9 and 10 imply that all terms involving $\boldsymbol{\delta}$ and $\boldsymbol{\eta}$ are remainder terms. The topological derivative thus comes from the two first terms of the above equality. All these terms are estimates one by one.

★ 1st and 2nd terms

These two terms are handled together. They are explicitated first with $\tilde{\mathbf{n}}$, the unit normal vector point outward ω_ρ , and then with a rescaling

$$\begin{aligned} \int_{\partial\omega_\rho} \mathbf{A}\varepsilon(\mathbf{q}_1^\rho) \mathbf{n} \cdot \mathbf{v}_1^\rho dS + \int_{\partial\omega_\rho} \mathbf{A}\varepsilon(\mathbf{p}) \mathbf{n} \cdot \mathbf{v}_1^\rho dS &= -\rho^3 \int_{\partial\omega} \mathbf{A}\varepsilon(\mathbf{q}_1) \tilde{\mathbf{n}} \cdot \mathbf{v}_1 dS - \rho^3 \int_{\partial\omega} \mathbf{A}\varepsilon(\mathbf{p}) (\rho\mathbf{y} + \mathbf{x}_0) \tilde{\mathbf{n}} \cdot \mathbf{v}_1(\mathbf{y}) dS \\ &= -\rho^3 \left(\int_{\partial\omega} \mathbf{A}\varepsilon(\mathbf{q}_1) \tilde{\mathbf{n}} \cdot \mathbf{v}_1 dS + \int_{\partial\omega} \mathbf{A}\varepsilon(\mathbf{p}) (\mathbf{x}_0) \tilde{\mathbf{n}} \cdot \mathbf{v}_1 dS \right) + O(\rho^4). \end{aligned}$$

The main point is to compute explicitly $\mathbf{A}\varepsilon(\mathbf{q}_1) \tilde{\mathbf{n}}$ on $\partial\omega$. First, let us give the expression of \mathbf{q}_1 in $\mathbb{R}^3 \setminus \omega$

$$\begin{aligned} \mathbf{q}_1(\mathbf{y}) &= -\frac{15(\mu + \lambda)(r^2 - r_1^2)r_1^3}{2(8\mu + 3\lambda)r^7} \varepsilon(\mathbf{p})(\mathbf{x}_0) \mathbf{y} \cdot \mathbf{y} \mathbf{y} - \frac{(5\mu r^2 + 3(\mu + \lambda)r_1^2)r_1^3}{(8\mu + 3\lambda)r^5} \varepsilon(\mathbf{p})(\mathbf{x}_0) \mathbf{y} \\ &\quad + \frac{3(\mu + \lambda)(r^2 - r_1^2)r_1^3}{2(8\mu + 3\lambda)r^5} \text{tr}(\varepsilon(\mathbf{p})(\mathbf{x}_0)) \mathbf{y}. \end{aligned}$$

Introduce the notations α , β , \mathbf{T} , \mathbf{U} , \mathbf{V} , \mathbf{W} and \mathbf{E} such that

$$\alpha = \frac{\mu + \lambda}{8\mu + 3\lambda}, \quad \beta = \frac{\mu}{8\mu + 3\lambda},$$

$$\mathbf{T}(\mathbf{y}) = \varepsilon(\mathbf{p})(\mathbf{x}_0)\mathbf{y} \cdot \mathbf{y} \frac{(r^2 - r_1^2)r_1^3}{r^7}\mathbf{y}, \quad \mathbf{U}(\mathbf{y}) = \varepsilon(\mathbf{p})(\mathbf{x}_0)\mathbf{y} \frac{r_1^3}{r^3}, \quad \mathbf{V}(\mathbf{y}) = \varepsilon(\mathbf{p})(\mathbf{x}_0)\mathbf{y} \frac{r_1^5}{r^5}, \quad \mathbf{W}(\mathbf{y}) = \frac{(r^2 - r_1^2)r_1^3}{r^5}\mathbf{y},$$

$$\mathbf{y} = \begin{pmatrix} y_1 \\ y_2 \\ y_3 \end{pmatrix}, \quad \mathbf{E}(\mathbf{y}) = \begin{pmatrix} y_1^2 & y_1y_2 & y_1y_3 \\ y_1y_2 & y_2^2 & y_2y_3 \\ y_1y_3 & y_2y_3 & y_3^2 \end{pmatrix}.$$

Then, the strain tensor of \mathbf{q}_1 on $\partial\omega$ is

$$\varepsilon(\mathbf{q}_1)(\mathbf{y}) = -\frac{15\alpha}{2}\varepsilon(\mathbf{T})(\mathbf{y}) - 5\beta\varepsilon(\mathbf{U})(\mathbf{y}) - 3\alpha\varepsilon(\mathbf{V})(\mathbf{y}) + \frac{3\alpha}{2}\text{tr}(\varepsilon(\mathbf{p})(\mathbf{x}_0))\varepsilon(\mathbf{W})(\mathbf{y}).$$

It has been established with Maple that

$$\left\{ \begin{array}{l} \varepsilon(\mathbf{T})(\mathbf{y}) = 2 \frac{\varepsilon(\mathbf{p})(\mathbf{x}_0)\mathbf{y} \cdot \mathbf{y}\mathbf{E}(\mathbf{y})}{r_1^4} \\ \varepsilon(\mathbf{U})(\mathbf{y}) = \varepsilon(\mathbf{p})(\mathbf{x}_0) - \frac{3}{2} \frac{\varepsilon(\mathbf{p})(\mathbf{x}_0)\mathbf{E}(\mathbf{y}) + \mathbf{E}(\mathbf{y})\varepsilon(\mathbf{p})(\mathbf{x}_0)}{r_1^2} \\ \varepsilon(\mathbf{V})(\mathbf{y}) = \varepsilon(\mathbf{p})(\mathbf{x}_0) - \frac{5}{2} \frac{\varepsilon(\mathbf{p})(\mathbf{x}_0)\mathbf{E}(\mathbf{y}) + \mathbf{E}(\mathbf{y})\varepsilon(\mathbf{p})(\mathbf{x}_0)}{r_1^2} \\ \varepsilon(\mathbf{W})(\mathbf{y}) = 2 \frac{\mathbf{E}(\mathbf{y})}{r_1^2} \end{array} \right.$$

Thus, the strain tensor of \mathbf{q}_1 on $\partial\omega$ is

$$\begin{aligned} \varepsilon(\mathbf{q}_1)(\mathbf{y}) &= -15\alpha \frac{\varepsilon(\mathbf{p})(\mathbf{x}_0)\mathbf{y} \cdot \mathbf{y}\mathbf{E}(\mathbf{y})}{r_1^4} + \frac{15}{2}(\alpha + \beta) \frac{\varepsilon(\mathbf{p})(\mathbf{x}_0)\mathbf{E}(\mathbf{y}) + \mathbf{E}(\mathbf{y})\varepsilon(\mathbf{p})(\mathbf{x}_0)}{r_1^2} \\ &\quad + 3\alpha \text{tr}(\varepsilon(\mathbf{p})(\mathbf{x}_0)) \frac{\mathbf{E}(\mathbf{y})}{r_1^2} - (5\beta + 3\alpha)\varepsilon(\mathbf{p})(\mathbf{x}_0). \end{aligned}$$

Now, the trace of $\varepsilon(\mathbf{q}_1)(\mathbf{y})$ is calculated using

$$\left\{ \begin{array}{l} \text{tr}(\mathbf{E}(\mathbf{y})) = r_1^2 \\ \text{tr}(\varepsilon(\mathbf{p})(\mathbf{x}_0)\mathbf{E}(\mathbf{y})) = \text{tr}(\mathbf{E}(\mathbf{y})\varepsilon(\mathbf{p})(\mathbf{x}_0)) = \varepsilon(\mathbf{p})(\mathbf{x}_0)\mathbf{y} \cdot \mathbf{y} \end{array} \right. \text{ on } \partial\omega,$$

so that

$$\text{tr}(\varepsilon(\mathbf{q}_1)(\mathbf{y})) = 5\beta \left(3 \frac{\varepsilon(\mathbf{p})(\mathbf{x}_0)\mathbf{y} \cdot \mathbf{y}}{r_1^2} - \text{tr}(\varepsilon(\mathbf{p})(\mathbf{x}_0)) \right).$$

Moreover, one can verify the following equalities on $\partial\omega$

$$\left\{ \begin{array}{l} \mathbf{E}(\mathbf{y})\mathbf{y} = r_1^2\mathbf{y} \\ \varepsilon(\mathbf{p})(\mathbf{x}_0)\mathbf{E}(\mathbf{y})\mathbf{y} = r_1^2\varepsilon(\mathbf{p})(\mathbf{x}_0)\mathbf{y} \\ \mathbf{E}(\mathbf{y})\varepsilon(\mathbf{p})(\mathbf{x}_0)\mathbf{y} = \varepsilon(\mathbf{p})(\mathbf{x}_0)\mathbf{y} \cdot \mathbf{y}\mathbf{y} \end{array} \right.$$

As ω is the unit ball, then $\tilde{\mathbf{n}} = \mathbf{y}/r_1$ on $\partial\omega$. Thus, the normal component of the stress tensor on $\partial\omega$ is given by

$$\begin{aligned} \mathbf{A}\varepsilon(\mathbf{q}_1)\tilde{\mathbf{n}} &= 2\mu\varepsilon(\mathbf{q}_1)\frac{\mathbf{y}}{r_1} + \lambda\text{tr}(\varepsilon(\mathbf{q}_1))\frac{\mathbf{y}}{r_1} \\ &= \mu \frac{14\mu + 9\lambda}{8\mu + 3\lambda} \frac{\varepsilon(\mathbf{p})(\mathbf{x}_0)\mathbf{y}}{r_1} + \mu \frac{6\mu + \lambda}{8\mu + 3\lambda} \frac{\text{tr}(\varepsilon(\mathbf{p})(\mathbf{x}_0))\mathbf{y}}{r_1}. \end{aligned}$$

Recalling that $\mathbf{v}_1(\mathbf{y}) = -\varepsilon(\mathbf{u})(\mathbf{x}_0)\mathbf{y}$ on $\partial\omega$, it finally follows

$$\begin{aligned} & \int_{\partial\omega} \mathbf{A}\varepsilon(\mathbf{q}_1)(\mathbf{y})\tilde{\mathbf{n}} \cdot \mathbf{v}_1(\mathbf{y})dS + \int_{\partial\omega} \mathbf{A}\varepsilon(\mathbf{p})(\mathbf{x}_0)\tilde{\mathbf{n}} \cdot \mathbf{v}_1(\mathbf{y})dS \\ &= -15\mu \frac{2\mu + \lambda}{(8\mu + 3\lambda)r_1} \int_{\partial\omega} \varepsilon(\mathbf{p})(\mathbf{x}_0)\mathbf{y} \cdot \varepsilon(\mathbf{u})(\mathbf{x}_0)\mathbf{y}dS - 3(\mu + \lambda) \frac{2\mu + \lambda}{(8\mu + 3\lambda)r_1} \int_{\partial\omega} \text{tr}(\varepsilon(\mathbf{p})(\mathbf{x}_0))\mathbf{y} \cdot \varepsilon(\mathbf{u})(\mathbf{x}_0)\mathbf{y}dS \\ &= -15\mu \frac{2\mu + \lambda}{(8\mu + 3\lambda)r_1} \int_{\partial\omega} \mathbf{y}\mathbf{y}^T dS \varepsilon(\mathbf{u})(\mathbf{x}_0) : \varepsilon(\mathbf{p})(\mathbf{x}_0) - 3(\mu + \lambda) \frac{2\mu + \lambda}{(8\mu + 3\lambda)r_1} \int_{\partial\omega} \mathbf{y}\mathbf{y}^T dS : \varepsilon(\mathbf{u})(\mathbf{x}_0) \text{tr}(\varepsilon(\mathbf{p})(\mathbf{x}_0)) \\ &= -\frac{4(2\mu + \lambda)\pi r_1^3}{8\mu + 3\lambda} (5\mu \varepsilon(\mathbf{u})(\mathbf{x}_0) : \varepsilon(\mathbf{p})(\mathbf{x}_0) + (\mu + \lambda) \text{tr}(\varepsilon(\mathbf{u})(\mathbf{x}_0)) \text{tr}(\varepsilon(\mathbf{p})(\mathbf{x}_0))). \end{aligned}$$

★ 3^{rd} term

Using the Taylor expansion of the background solution on $\partial\omega_\rho$ (4.42), the error term is

$$\delta(\mathbf{x}) = \mathbf{C}(\rho) - \mathbf{u}(\mathbf{x}_0) - \frac{\nabla \mathbf{u}(\mathbf{x}_0) - \nabla^T \mathbf{u}(\mathbf{x}_0)}{2} \mathbf{x}_0 + \left(\mathbf{R}(\rho) - \frac{\nabla \mathbf{u}(\mathbf{x}_0) - \nabla^T \mathbf{u}(\mathbf{x}_0)}{2} \right) \mathbf{x} - \mathbf{R}_u(\mathbf{x}) \text{ on } \partial\omega_\rho.$$

Since $\mathbf{R}(\rho) - \frac{\nabla \mathbf{u}(\mathbf{x}_0) - \nabla^T \mathbf{u}(\mathbf{x}_0)}{2}$ is an anti-symmetric matrix, there exists a constant vector $\mathbf{r}(\rho)$ such that

$$\left(\mathbf{R}(\rho) - \frac{\nabla \mathbf{u}(\mathbf{x}_0) - \nabla^T \mathbf{u}(\mathbf{x}_0)}{2} \right) \mathbf{x} = \mathbf{r}(\rho) \wedge \mathbf{x}.$$

Recalling that $\mathbf{R}_u(\mathbf{x}) = \varphi_\rho(\mathbf{x}) \int_0^1 (1-t)(\mathbf{x} - \mathbf{x}_0)^T \mathcal{D}^2(\mathbf{u}(\mathbf{x}_0 + t(\mathbf{x} - \mathbf{x}_0)))(\mathbf{x} - \mathbf{x}_0) dt$, where φ_ρ is equal to 1 on $\partial\omega_\rho$, one can notice that $\mathbf{x} - \mathbf{x}_0$ is of the order of ρ on $\partial\omega_\rho$. Hence,

$$\exists C > 0, |\mathbf{R}_u| \leq C\rho^2 \text{ on } \partial\omega_\rho. \quad (4.54)$$

Moreover, \mathbf{q}_1 satisfies the forces and momentum equilibrium $\int_{\partial\omega} \mathbf{A}\varepsilon(\mathbf{q}_1)\mathbf{n}dS = \mathbf{0}$ and

$$\int_{\partial\omega} \mathbf{A}\varepsilon(\mathbf{q}_1)\mathbf{n} \wedge \mathbf{y}dS = \mathbf{0} \text{ when } \omega \text{ is the unit ball.}$$

The third term is then calculated as follows

$$\begin{aligned} \int_{\partial\omega_\rho} \mathbf{A}\varepsilon(\mathbf{q}_1^\rho)\mathbf{n} \cdot \delta dS &= \rho^2 \left(\mathbf{C}(\rho) - \mathbf{u}(\mathbf{x}_0) - \frac{\nabla \mathbf{u}(\mathbf{x}_0) - \nabla^T \mathbf{u}(\mathbf{x}_0)}{2} \mathbf{x}_0 \right) \cdot \int_{\partial\omega} \mathbf{A}\varepsilon(\mathbf{q}_1)(\mathbf{y})\mathbf{n}dS \\ &\quad - \rho^2 \mathbf{r}(\rho) \cdot \int_{\partial\omega} \mathbf{A}\varepsilon(\mathbf{q}_1)(\mathbf{y})\mathbf{n} \wedge (\rho\mathbf{y} + \mathbf{x}_0)dS - \int_{\partial\omega_\rho} \mathbf{A}\varepsilon(\mathbf{q}_1^\rho)\mathbf{n} \cdot \mathbf{R}_u dS \\ &= - \int_{\partial\omega_\rho} \mathbf{A}\varepsilon(\mathbf{q}_1^\rho)\mathbf{n} \cdot \mathbf{R}_u dS. \end{aligned}$$

It follows the estimate

$$\begin{aligned} \left| \int_{\partial\omega_\rho} \mathbf{A}\varepsilon(\mathbf{q}_1^\rho)\mathbf{n} \cdot \delta dS \right| &\leq \sqrt{\int_{\partial\omega_\rho} \left| \mathbf{A}\varepsilon \left(\mathbf{q}_1 \left(\frac{\mathbf{x} - \mathbf{x}_0}{\rho} \right) \right) \mathbf{n} \right|^2 dS} \sqrt{\int_{\partial\omega_\rho} |\mathbf{R}_u(\mathbf{x})|^2 dS} \\ &\leq C\rho \sqrt{\int_{\partial\omega} |(\mathbf{A}\varepsilon(\mathbf{q}_1)\mathbf{n})|^2 dS} \sqrt{\rho^4 \int_{\partial\omega_\rho} dS} \leq C\rho^4. \end{aligned}$$

★ 4th term

The fourth term is first evaluated with the unit normal vector $\tilde{\mathbf{n}}$ and then it is computed like the third term.

$$\begin{aligned}
\int_{\partial\omega_\rho} \mathbf{A}\varepsilon(\mathbf{p})\mathbf{n} \cdot \boldsymbol{\delta} dS &= - \left(\mathbf{C}(\rho) - \mathbf{u}(\mathbf{x}_0) - \frac{\nabla\mathbf{u}(\mathbf{x}_0) - \nabla^T\mathbf{u}(\mathbf{x}_0)}{2}\mathbf{x}_0 \right) \cdot \int_{\omega_\rho} \operatorname{div}(\mathbf{A}\varepsilon(\mathbf{p})) dV \\
&\quad + \mathbf{r}(\rho) \cdot \int_{\partial\omega_\rho} \mathbf{A}\varepsilon(\mathbf{p})\tilde{\mathbf{n}} \wedge \mathbf{x} dS - \int_{\partial\omega_\rho} \mathbf{A}\varepsilon(\mathbf{p})\mathbf{n} \cdot \mathbf{R}_u dS \\
&= - \mathbf{r}(\rho) \cdot \int_{\omega_\rho} (\mathbf{x} \wedge \operatorname{div}(\mathbf{A}\varepsilon(\mathbf{p})) + \bar{\bar{\varepsilon}} : \mathbf{A}\varepsilon(\mathbf{p})) dV - \int_{\partial\omega_\rho} \mathbf{A}\varepsilon(\mathbf{p})\mathbf{n} \cdot \mathbf{R}_u dS \\
&= - \int_{\partial\omega_\rho} \mathbf{A}\varepsilon(\mathbf{p})\mathbf{n} \cdot \mathbf{R}_u dS.
\end{aligned}$$

The fourth term is then estimated as follows

$$\begin{aligned}
\left| \int_{\partial\omega_\rho} \mathbf{A}\varepsilon(\mathbf{p})\mathbf{n} \cdot \boldsymbol{\delta} dS \right| &\leq \sqrt{\int_{\partial\omega_\rho} |\mathbf{A}\varepsilon(\mathbf{p})\mathbf{n}|^2 dS} \sqrt{\int_{\partial\omega_\rho} |\mathbf{R}_u|^2 dS} \\
&\leq C\rho \sqrt{\int_{\partial\omega} |\mathbf{A}\varepsilon(\mathbf{p})(\rho\mathbf{y} + \mathbf{x}_0)\mathbf{n}|^2 dS} \sqrt{\rho^4 \int_{\partial\omega_\rho} dS} \leq C\rho^4.
\end{aligned}$$

Remark 32. Since $\mathbf{p} \in \mathcal{C}^3(\Omega)$, the integral $\int_{\partial\omega} |\mathbf{A}\varepsilon(\mathbf{p})(\rho\mathbf{y} + \mathbf{x}_0)\mathbf{n}|^2 dS$ is bounded by a constant C which depends on the \mathcal{C}^1 -norm of \mathbf{p} .

★ 5th term

Multiply (4.53) by $\theta\mathbf{v}_1^\rho$ and integrate by parts, it follows

$$\int_{\partial\omega_\rho} \mathbf{A}\varepsilon(\boldsymbol{\eta})\mathbf{n} \cdot \mathbf{v}_1^\rho dS = \int_{\Omega_\rho} \mathbf{A}\varepsilon(\boldsymbol{\eta}) : \varepsilon(\theta\mathbf{v}_1^\rho) dV - \int_{\Omega_\rho} \operatorname{div}(\mathbf{A}(\mathbf{q}_1^\rho \otimes \nabla\theta)^s) \cdot \theta\mathbf{v}_1^\rho dV - \int_{\Omega_\rho} \operatorname{div}(\theta\mathbf{A}\varepsilon(\mathbf{q}_1^\rho)) \cdot \theta\mathbf{v}_1^\rho dV.$$

Using the L^∞ -norms of \mathbf{v}_1^ρ and $\varepsilon(\mathbf{v}_1^\rho)$ (because $\nabla\theta$ vanishes in the neighborhood of the inclusion) and the L^2 -norm of $\varepsilon(\boldsymbol{\eta})$, the first term of the right-hand side of the above equality is estimated as

$$\begin{aligned}
\exists C > 0, \left| \int_{\Omega_\rho} \mathbf{A}\varepsilon(\boldsymbol{\eta}) : \varepsilon(\theta\mathbf{v}_1^\rho) dV \right| &\leq \left| \int_{\Omega_\rho} \mathbf{A}\varepsilon(\boldsymbol{\eta}) : (\mathbf{v}_1^\rho \otimes \nabla\theta)^s dV \right| + \left| \int_{\Omega_\rho} \theta\mathbf{A}\varepsilon(\boldsymbol{\eta}) : \varepsilon(\mathbf{v}_1^\rho) dV \right| \\
&\leq C\|\varepsilon(\boldsymbol{\eta})\|_{L^2(\Omega_\rho)}\|\mathbf{v}_1^\rho\|_{L^\infty(\Omega \setminus \mathcal{U}_-)} + C\|\varepsilon(\boldsymbol{\eta})\|_{L^2(\Omega_\rho)}\|\varepsilon(\mathbf{v}_1^\rho)\|_{L^2(\Omega_\rho)} \\
&\leq C\rho^{3/2+4} + C\rho^4 \leq C\rho^4.
\end{aligned}$$

The two last terms are first explicited and then estimated using the L^∞ -norms of \mathbf{q}_1^ρ and $\varepsilon(\mathbf{q}_1^\rho)$ and \mathbf{v}_1^ρ .

$$\begin{aligned}
& \int_{\Omega_\rho} \operatorname{div}(\mathbf{A}(\mathbf{q}_1^\rho \otimes \nabla\theta)^s) \cdot \theta \mathbf{v}_1^\rho dV + \int_{\Omega_\rho} \operatorname{div}(\theta \mathbf{A}\varepsilon(\mathbf{q}_1^\rho)) \cdot \theta \mathbf{v}_1^\rho dV \\
&= - \int_{\Omega_\rho} \mathbf{A}(\mathbf{q}_1^\rho \otimes \nabla\theta)^s : \varepsilon(\theta \mathbf{v}_1^\rho) dV + \int_{\Omega_\rho} \mathbf{A}\varepsilon(\mathbf{q}_1^\rho) \nabla\theta \cdot \theta \mathbf{v}_1^\rho dV \\
&= - \int_{\Omega_\rho} \mathbf{A}(\mathbf{q}_1^\rho \otimes \nabla\theta)^s : (\mathbf{v}_1^\rho \otimes \nabla\theta)^s dV - \int_{\Omega_\rho} \theta \mathbf{A}(\mathbf{q}_1^\rho \otimes \nabla\theta)^s : \varepsilon(\mathbf{v}_1^\rho) dV + \int_{\Omega_\rho} \mathbf{A}\varepsilon(\mathbf{q}_1^\rho) \nabla\theta \cdot \theta \mathbf{v}_1^\rho dV.
\end{aligned}$$

It follows the estimate

$$\begin{aligned}
& \left| \int_{\Omega_\rho} \operatorname{div}(\mathbf{A}(\mathbf{q}_1^\rho \otimes \nabla\theta)^s) \cdot \theta \mathbf{v}_1^\rho dV \right| + \left| \int_{\Omega_\rho} \operatorname{div}(\theta \mathbf{A}\varepsilon(\mathbf{q}_1^\rho)) \cdot \theta \mathbf{v}_1^\rho dV \right| \\
&\leq C \|\mathbf{q}_1^\rho\|_{L^\infty(\Omega \setminus \mathcal{U}_-)} \|\mathbf{v}_1^\rho\|_{L^\infty(\Omega \setminus \mathcal{U}_-)} + C \|\mathbf{q}_1^\rho\|_{L^\infty(\Omega \setminus \mathcal{U}_-)} \|\varepsilon(\mathbf{v}_1^\rho)\|_{L^2(\Omega_\rho)} + C \|\varepsilon(\mathbf{q}_1^\rho)\|_{L^\infty(\Omega \setminus \mathcal{U}_-)} \|\mathbf{v}_1^\rho\|_{L^2(\Omega_\rho)} \\
&\leq C\rho^6 + C\rho^{3/2+3} + C\rho^{3/2+4} \leq C\rho^{3/2+3}.
\end{aligned}$$

Regrouping these two estimates, the fifth term is smaller than $O(\rho^4)$.

★ 6th term

Multiply (4.53) by $\boldsymbol{\delta}$ and integrate by parts, it follows

$$\int_{\partial\omega_\rho} \mathbf{A}\varepsilon(\boldsymbol{\eta}) \mathbf{n} \cdot \boldsymbol{\delta} dS = \int_{\Omega_\rho} \mathbf{A}\varepsilon(\boldsymbol{\eta}) : \varepsilon(\boldsymbol{\delta}) dV + \int_{\Omega_\rho} \mathbf{A}(\mathbf{q}_1^\rho \otimes \nabla\theta)^s : \varepsilon(\boldsymbol{\delta}) dV - \int_{\Omega_\rho} \mathbf{A}\varepsilon(\mathbf{q}_1^\rho) \nabla\theta \cdot \boldsymbol{\delta} dV.$$

The sixth term is estimated using the L^∞ -norms of \mathbf{q}_1^ρ and $\varepsilon(\mathbf{q}_1^\rho)$ and the L^2 -norms of $\boldsymbol{\delta}$, $\varepsilon(\boldsymbol{\delta})$ and $\varepsilon(\boldsymbol{\eta})$

$$\begin{aligned}
\left| \int_{\partial\omega_\rho} \mathbf{A}\varepsilon(\boldsymbol{\eta}) \mathbf{n} \cdot \boldsymbol{\delta} dS \right| &\leq C \|\varepsilon(\boldsymbol{\eta})\|_{L^2(\Omega_\rho)} \|\varepsilon(\boldsymbol{\delta})\|_{L^2(\Omega_\rho)} + C \|\mathbf{q}_1^\rho\|_{L^\infty(\Omega \setminus \mathcal{U}_-)} \|\varepsilon(\boldsymbol{\delta})\|_{L^2(\Omega_\rho)} \\
&\quad + C \|\varepsilon(\mathbf{q}_1^\rho)\|_{L^\infty(\Omega \setminus \mathcal{U}_-)} \|\boldsymbol{\delta}\|_{L^2(\Omega_\rho)} \\
&\leq C\rho^5 + C\rho^{3/2+4} \leq C\rho^5.
\end{aligned}$$

Remark 33. For the objective function

$$J(\Omega) = \frac{1}{2} \int_{\Omega} \mathbf{A}\varepsilon(\mathbf{u}) : \varepsilon(\mathbf{u}) dV - \int_{\Gamma_N} \mathbf{g} \cdot \mathbf{u} dS, \tag{4.55}$$

the adjoint state verifies $\mathbf{p} = \frac{1}{2} \mathbf{u}$. Then J admits the following topological derivative

$$DJ(\mathbf{x}_0) = \frac{(2\mu + \lambda)\pi r_1^2}{3\mu + \lambda} \left(2\mu \varepsilon(\mathbf{u})(\mathbf{x}_0) : \varepsilon(\mathbf{u})(\mathbf{x}_0) + \frac{\mu + \lambda}{2} \text{tr}(\varepsilon(\mathbf{u})(\mathbf{x}_0)) \text{tr}(\varepsilon(\mathbf{u})(\mathbf{x}_0)) \right) \quad \text{in } 2d, \quad (4.56)$$

$$DJ(\mathbf{x}_0) = \frac{2(2\mu + \lambda)\pi r_1^3}{8\mu + 3\lambda} \left(5\mu \varepsilon(\mathbf{u})(\mathbf{x}_0) : \varepsilon(\mathbf{u})(\mathbf{x}_0) + (\mu + \lambda) \text{tr}(\varepsilon(\mathbf{u})(\mathbf{x}_0)) \text{tr}(\varepsilon(\mathbf{u})(\mathbf{x}_0)) \right) \quad \text{in } 3d. \quad (4.57)$$

These results have already been found in [8]. The authors evaluated the topological derivative of this objective function (4.55) with respect to the introduction of a damaged inclusion ω_ρ inside the healthy region. This damaged inclusion becomes rigid when its material properties are larger than the healthy domain properties. Therefore, when material properties of the inclusion tend toward infinity, the topological derivatives in 2d and 3d stated by [8] are respectively equal to (4.56) and (4.57).

4.3 Numerical illustrations

4.3.1 2d test case : a L-beam

The topological derivative efficiency, in 2d, is illustrated with the L-beam pictured in Fig. 4.2. Dimensions and material properties are given in adimensional units. The Young's modulus E is taken equal to 100 and the Poisson's coefficient is 0.3. The structure is solicited by \mathbf{g} , a vertical force of magnitude 1, applied at the middle of the tip of the L-beam. This test case is performed using a triangular mesh with 56 384 elements and a minimal and maximal mesh size of 0.38 and 0.92. Considering these mesh size, the radius of the inclusion is $\rho = 2.5$.

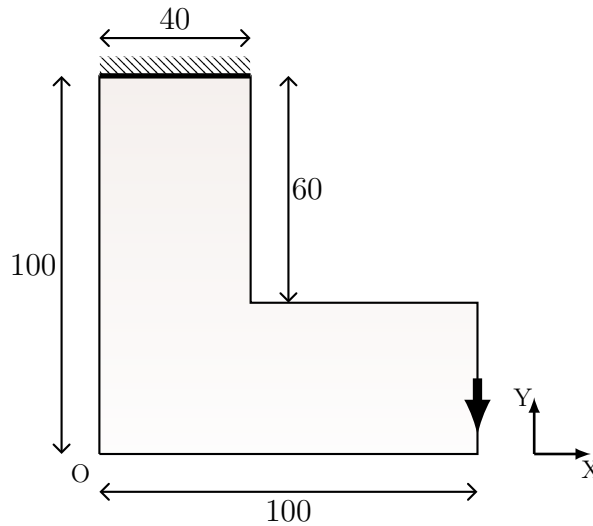


Figure 4.2: L-beam : its dimensions and load

The rigid body motion is numerically applied to the inclusion by penalization of its material properties. Therefore, the numerical problem considers the Lamé tensor of elasticity

$$\mathbf{A}^* = \begin{cases} \mathbf{A} & \text{in } \Omega_\rho \\ \frac{1}{\delta^2} \mathbf{A} & \text{in } \omega_\rho \end{cases},$$

where δ is a singular perturbation. Denote $\mathbf{x}_0 = (x_0, y_0)$ the center of ω_ρ . Since the inclusion is an homogeneous disc, its geometrical center \mathbf{x}_0 matches with its center of gravity. In 2d, the rigid body motion \mathbf{u}_ρ at a point $\mathbf{x} = (x, y)$ of the inclusion ω_ρ is given by

$$\mathbf{u}_\rho(\mathbf{x}) = \mathbf{u}_\rho(\mathbf{x}_0) + \varpi \begin{pmatrix} -y + y_0 \\ x - x_0 \end{pmatrix},$$

where the translation $\mathbf{u}_\rho(\mathbf{x}_0)$ is the displacement of the center of gravity of ω_ρ and ϖ is the rotation of ω_ρ . One can easily set that the translation $\mathbf{u}_\rho(\mathbf{x}_0)$ corresponds to the average displacement on ω_ρ , that is to say

$$\mathbf{u}_\rho(\mathbf{x}_0) = \frac{1}{|\omega_\rho|} \int_{\omega_\rho} \mathbf{u}_\rho dV.$$

Denote \mathbf{e}_x and \mathbf{e}_y the unit vector of the canonical basis of \mathbb{R}^2 and introduce the notations

$$u_{\rho,x} = \mathbf{u}_\rho \cdot \mathbf{e}_x, \quad u_{\rho,y} = \mathbf{u}_\rho \cdot \mathbf{e}_y.$$

The rotation satisfies

$$\varpi = \frac{1}{2}(\partial_x u_{\rho,y} - \partial_y u_{\rho,x}).$$

Since ϖ is constant, the following equality holds

$$\frac{1}{2}(\partial_x u_{\rho,y}(\mathbf{x}_0) - \partial_y u_{\rho,x}(\mathbf{x}_0)) = \frac{1}{2|\omega_\rho|} \int_{\omega_\rho} (\partial_x u_{\rho,y} - \partial_y u_{\rho,x}) dV.$$

A suitable value of δ is then numerically identified by comparing the displacement and the rotation at the point \mathbf{x}_0 to their average on ω_ρ , denoted as follows

$$\overline{u_{\rho,x}} = \frac{1}{|\omega_\rho|} \int_{\omega_\rho} \mathbf{u}_\rho \cdot \mathbf{e}_x dV, \quad \overline{u_{\rho,y}} = \frac{1}{|\omega_\rho|} \int_{\omega_\rho} \mathbf{u}_\rho \cdot \mathbf{e}_y dV, \quad \overline{R} = \frac{1}{2|\omega_\rho|} \int_{\omega_\rho} (\partial_x u_{\rho,y} - \partial_y u_{\rho,x}) dV.$$

Let us place an inclusion of radius $\rho = 2.5$ and centered at $\mathbf{x}_0 = (37.5, 37.5)$. The compliance, the displacement and the rotation are given in Fig. 4.3 for various values of the singular perturbation. The average quantities match with the displacement and the rotation at \mathbf{x}_0 and the compliance is constant for a perturbation larger than 10^3 . In the sequel, numerical tests are done with $\frac{1}{\delta^2} = 10^4$.

Remark 34. *An other method to validate the rigid body motion is to check the zero deformation of the inclusion according to the singular perturbation δ .*

Nucleation of a rigid inclusion using topological derivative informations

The topological derivative is tested to find the better location to create a rigid inclusion in order to decrease the compliance

$$J(\Omega) = \int_{\Gamma_N} \mathbf{g} \cdot \mathbf{u} dS. \quad (4.58)$$

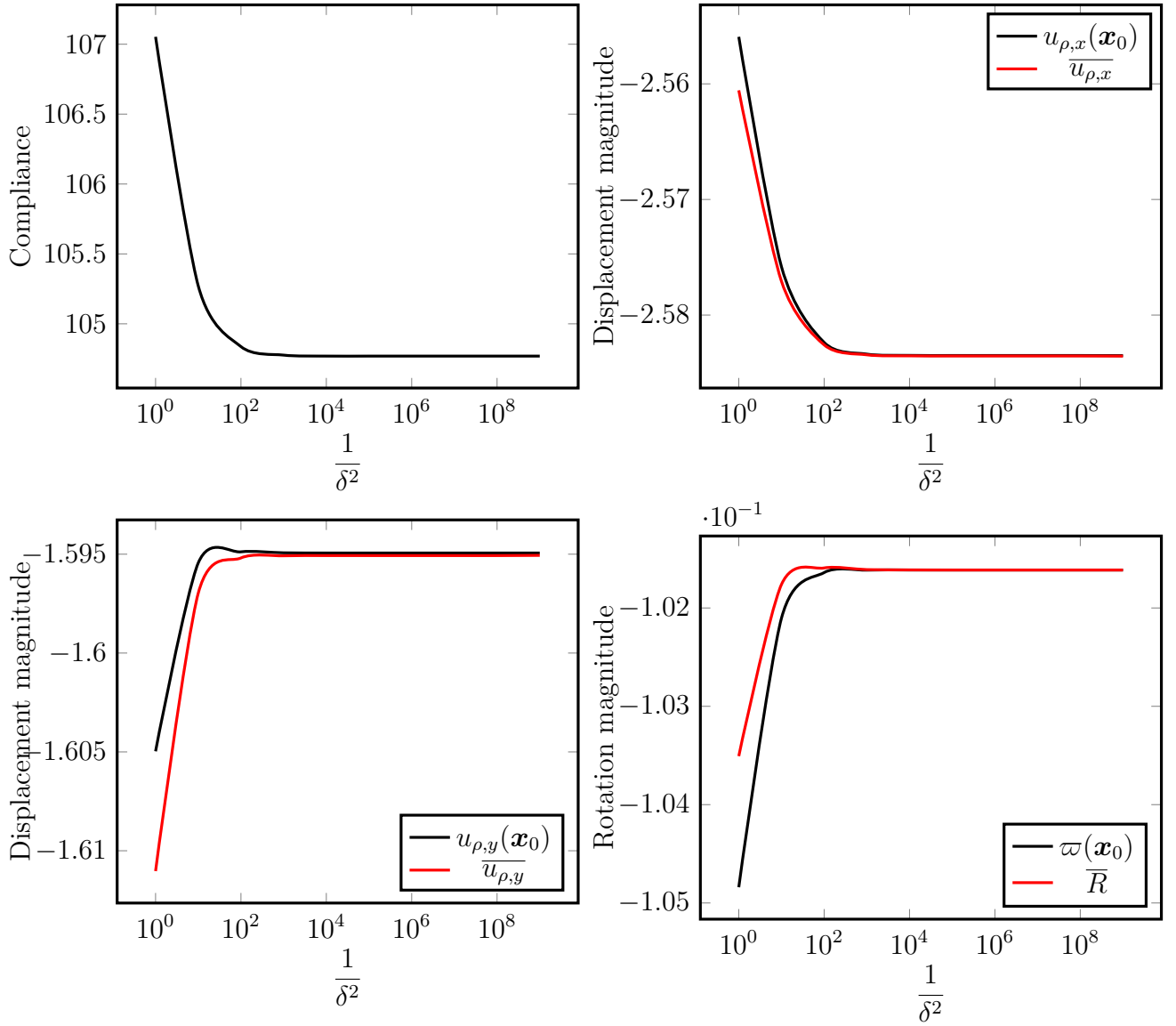


Figure 4.3: Comparison of displacements and rotation at the point \mathbf{x}_0 and their average

The system is consequently self-adjoint. In other words, the adjoint state satisfies $\mathbf{p} = -\mathbf{u}$. Thus, the topological derivative reads

$$DJ(\mathbf{x}_0) = -\frac{(2\mu + \lambda)\pi r_1^2}{3\mu + \lambda} \left(4\mu \varepsilon(\mathbf{u})(\mathbf{x}_0) : \varepsilon(\mathbf{u})(\mathbf{x}_0) + (\mu + \lambda) \text{tr}(\varepsilon(\mathbf{u})(\mathbf{x}_0)) \text{tr}(\varepsilon(\mathbf{u})(\mathbf{x}_0)) \right).$$

The topological derivative DJ is negative everywhere. It means that it is always favorable to add a rigid inclusion to stiffen the structure, which is expected. The rigid inclusion is nucleated at the most negative value of the topological derivative. The initial compliance, *i.e.* the one without the inclusion, is $J_0(\Omega) = 107.05$. Introduce an estimator function $\mathcal{E}(\Omega)$ as the topological asymptotic expansion without the remainder term

$$\mathcal{E}(\Omega) = J_0(\Omega) - \rho^2 \frac{(2\mu + \lambda)\pi r_1^2}{3\mu + \lambda} \left(4\mu \varepsilon(\mathbf{u})(\mathbf{x}_0) : \varepsilon(\mathbf{u})(\mathbf{x}_0) + (\mu + \lambda) \text{tr}(\varepsilon(\mathbf{u})(\mathbf{x}_0)) \text{tr}(\varepsilon(\mathbf{u})(\mathbf{x}_0)) \right).$$

It stands for the expected value of the compliance with the inclusion.

The topological derivative is implemented according to three configurations. It is first implemented everywhere in the L-beam domain. Then, it is truncated to keep the whole inclusion inside the L-beam domain. Finally, it is implemented according to a pre-defined design-space. Results of these three configurations are gathered in Table 4.1.

- First configuration : topological derivative computed everywhere

The topological derivative is computed everywhere in the L-beam domain. Its cartography is given in Fig. 4.4a. The minimum of the topological derivative, $DJ(\mathbf{x}_0) = -41.94$, is logically in the corner of the L-beam, where there is an area of stress concentration. It is exactly located at the point $\mathbf{x}_0 = (40, 40)$. Therefore, the inclusion is created in the corner of the L-beam as displayed in Fig. 4.4b. However, the inclusion is not entirely inside the domain. Nevertheless, its efficiency is proved by the decrease of the compliance that is $J_\rho(\Omega) = 100.50$. It represents a decrease of about 6% of the compliance. The estimator is unrealistically a negative value $\mathcal{E}(\Omega) = -155.07$. It comes from the size of the inclusion $\rho = 2.5$. It is actually a small value with regards to the characteristic dimension of the L-beam but it does not tends toward zero. Anyway, the mesh size does not allow an inclusion size that goes to zero.

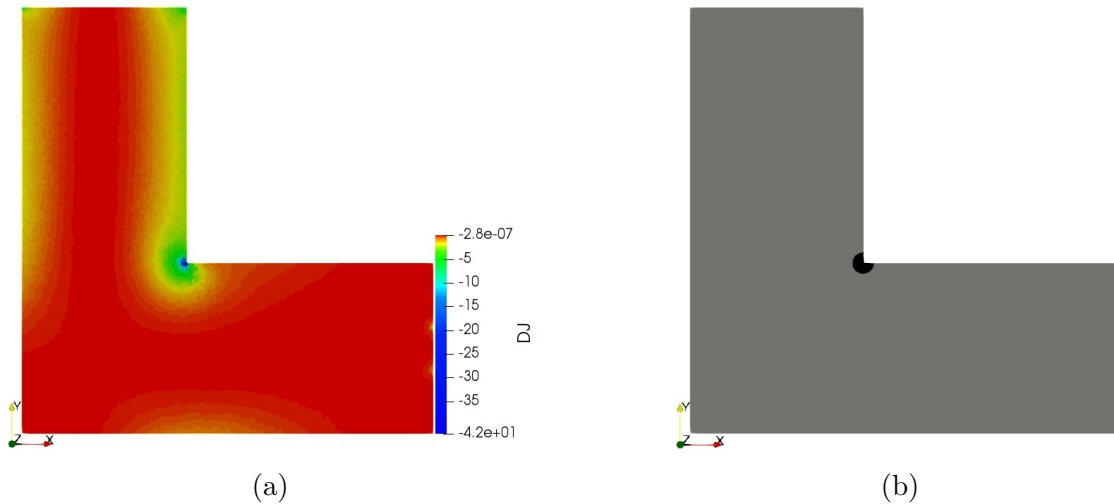


Figure 4.4: Cartography of $DJ(\mathbf{x}_0)$ computed everywhere in the domain (a) and the resulting rigid inclusion (b)

- Second configuration : truncated topological derivative

This second test aims to put entirely the inclusion inside the domain. The topological derivative is still implemented everywhere in the domain. The point \mathbf{x}_0 is still chosen as the minimum of the topological derivative. However, if this location implies that the inclusion is partially outside the domain, then $DJ(\mathbf{x}_0)$ is not retained and it is truncated to zero. This truncation is carried out until the inclusion is entirely inside the L-beam domain. The corresponding cartography of the truncated topological derivative is given in Fig. 4.5a. Those values around the L corner are put to zero. The minimum is now $DJ(\mathbf{x}_0) = -8.79$ for $\mathbf{x}_0 = (37.5, 40.5)$ (see Fig. 4.5b). The edge of the disc is against the corner of the L-beam. It makes sense to stiffness in the around the corner. This configuration provides a compliance of $J_\rho(\Omega) = 102.78$, which corresponds to a decrease of about 4% compared to the initial value. The estimator has now a positive value, $\mathcal{E}(\Omega) = 52.10$, but is still far from the compliance with the inclusion. This difference is still due to the size $\rho = 2.5$ of the inclusion that does not go to zero.

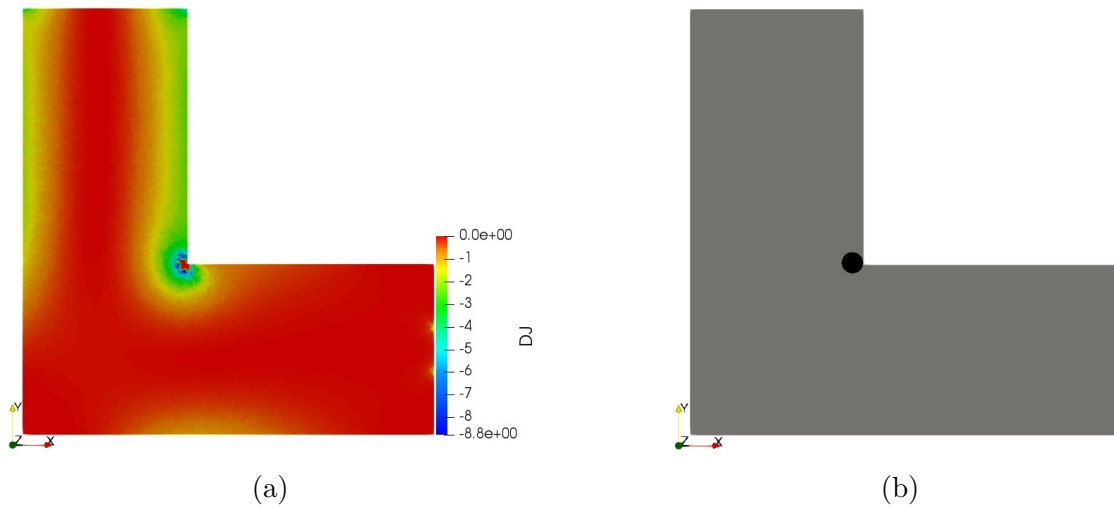


Figure 4.5: Cartography of $DJ(\mathbf{x}_0)$ with truncated values (a) and the resulting rigid inclusion (b)

- Third configuration : topological derivative computed inside a design space

The previous configurations predict an inclusion on the L-beam border or close to it. However, it does not respect the sensitivity analysis which assumes the inclusion is far from boundaries. This last test consists in implementing the topological strictly inside the L-beam domain. Its cartography is given in Fig. 4.6a. The most negative value, $DJ(\mathbf{x}_0) = -3.02$, is still around the corner of the L at the point $\mathbf{x}_0 = (34.5, 40.5)$. The corresponding rigid inclusion is completely enclosed inside the domain (see Fig. 4.6b). It gives a compliance of $J_\rho(\Omega) = 105.53$, which corresponds to a decrease of 1.4% of the initial value. The estimator, $\mathcal{E}(\Omega) = 88.16$, is relatively close to the compliance because the topological derivative amplitude is smaller than the one of the previous configurations.

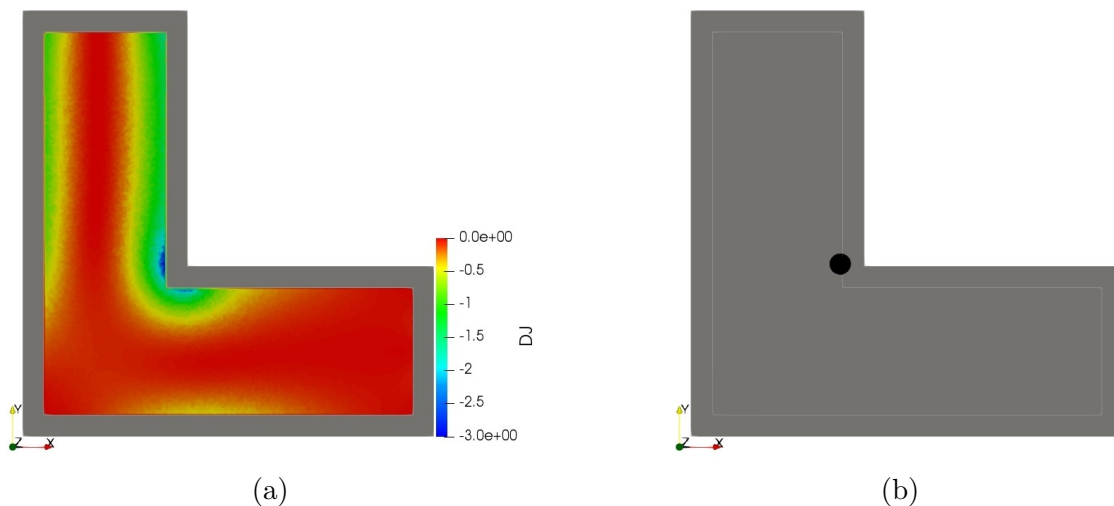


Figure 4.6: Cartography of $DJ(\mathbf{x}_0)$ computed strictly inside the domain (a) and the resulting rigid inclusion (b)

The best solution is well-known to be at the corner of the L-beam. The topological derivative is able to find this configuration when no restriction is applied. Moreover, the topological

	First configuration	Second configuration	Third configuration
$DJ(\mathbf{x}_0)$	-41.94	-8.79	-3.02
\mathbf{x}_0	(40,40)	(37.5,40.5)	(34.5,40.5)
$J_\rho(\Omega)$	100.50	102.78	105.53
Improvement	6%	4%	1.4%
$\mathcal{E}(\Omega)$	-155.07	52.10	88.16

Table 4.1: Summary of results (recall that $J_0(\Omega) = 107.05$)

derivative is still efficient with a restricted admissible domain when including some geometrical constraint. However, its estimator $\mathcal{E}(\Omega)$ depends highly on the mesh size.

Parametric optimization of the location of a rigid inclusion

The resolution of the elasticity problem is the most expansive operation for the computation process. The topological derivative requires only one resolution of the elasticity. The optimal location of a rigid inclusion is then obtained in one calculation. This paragraph compares the accuracy and efficiency of the topological derivative to a parametric optimization approach. Let us consider the same L-beam (see Fig. 4.2) with the same loading. The problem is to decrease the compliance. A rigid disc-shape inclusion of radius $\rho = 2.5$ is initially put in the domain. Fig. 4.7 displays three different initial locations.

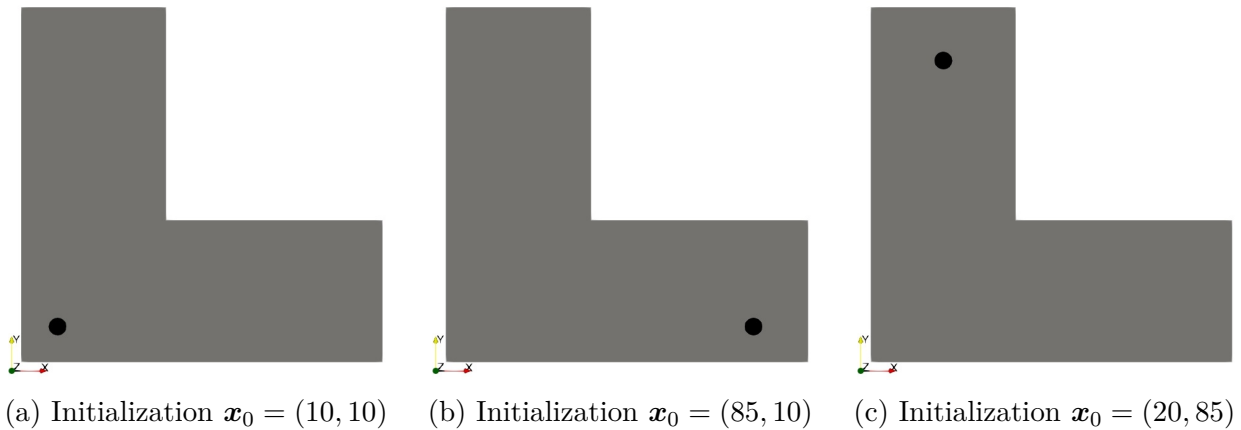


Figure 4.7: Different initial locations of the inclusion

Let us consider the bound delimiting the computation of the topological derivative in the third configuration (see Fig. 4.6). In the following, the inclusion is allowed to translate inside the domain delimited by these bounds. The coordinates of the center $\mathbf{x}_0 = (x_0, y_0)$ are optimized with a parametric gradient-based algorithm

$$x_0^{i+1} = x_0^i - \delta_x^i J'(x_0) \text{ and } y_0^{i+1} = y_0^i - \delta_y^i J'(y_0), \quad (4.59)$$

where (x_0^i, y_0^i) are the coordinates at iteration i and (δ_x^i, δ_y^i) are the descent steps. The derivatives $J'(x_0)$ and $J'(y_0)$ are computed with shape derivative techniques and read

$$J'(x_0) = - \int_{\partial\omega_\rho} \mathbf{A}^* \varepsilon(\mathbf{u}) : \varepsilon(\mathbf{u}) n_x dS \text{ and } J'(y_0) = - \int_{\partial\omega_\rho} \mathbf{A}^* \varepsilon(\mathbf{u}) : \varepsilon(\mathbf{u}) n_y dS,$$

where $\mathbf{n} = (n_x, n_y)$ is the normal unit vector of $\partial\omega_\rho$. In each case, the algorithm identifies an optimal location of $\mathbf{x}_0 = (35, 35)$ that corresponds to a compliance of $J(\Omega) = 106.04$. The optimum is reached after around ten iterations. The history of convergence for an inclusion initially placed at $\mathbf{x}_0 = (10, 10)$ is given in Fig. 4.8. There are few oscillations before convergence. They are due to the gradient-based algorithm that allows a slight increase of the compliance and to a too large descent step. The other initializations provide similar behavior. Results are summed up and compared to topological derivative ones in Table 4.2. It emphasizes the efficiency of the topological derivative. It actually requires only one resolution of the elasticity system. Moreover, the location suggested by the topological derivative provides better performance than the one given by a parametric optimization.

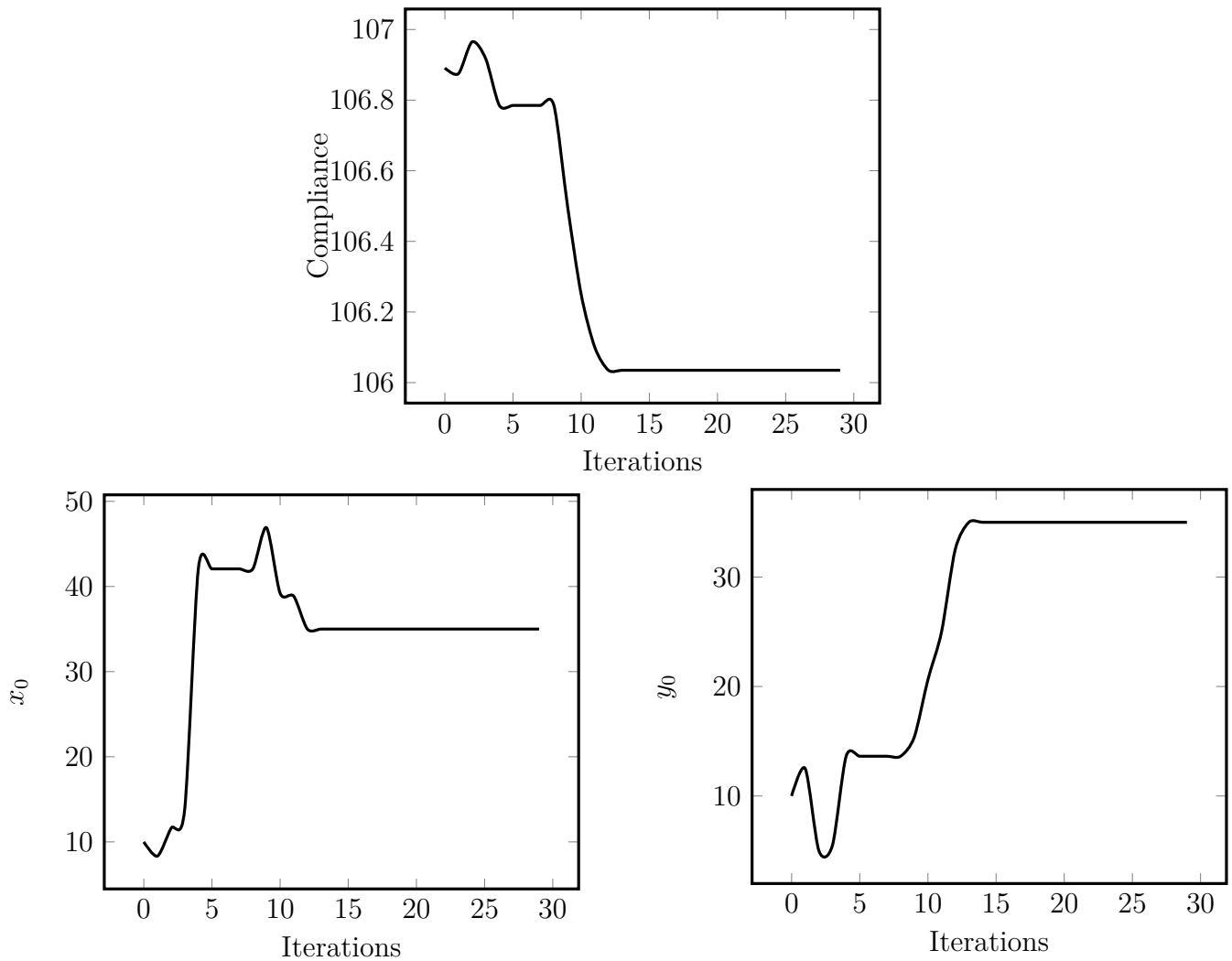


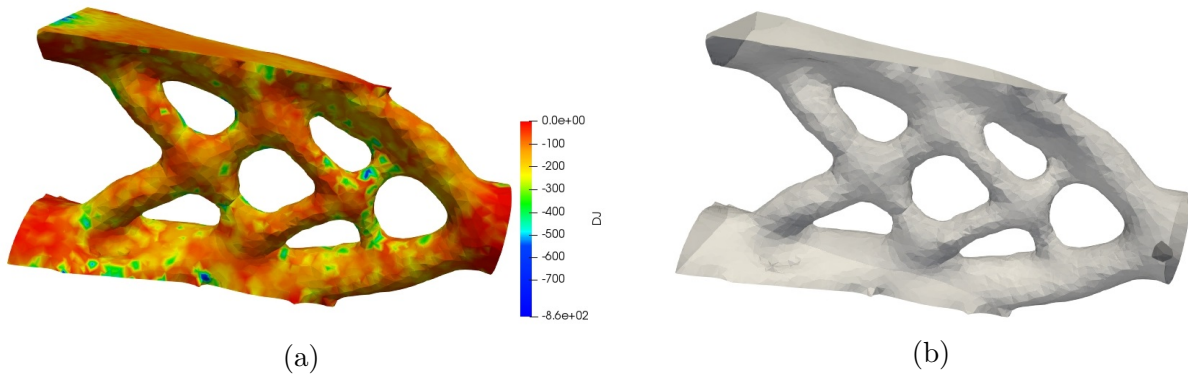
Figure 4.8: Results for an initial location at $\mathbf{x}_0 = (10, 10)$

	Parametric optimization			Topological derivative
	(10,10)	(85,10)	(20,85)	-
Initial \mathbf{x}_0	(10,10)	(85,10)	(20,85)	-
Initial compliance	106.89	106.93	107.00	107.05
Final \mathbf{x}_0	(35,35)	(35,35)	(35,35)	(34.5,40.5)
Final compliance	106.04	106.04	106.04	105.53
Nb of resolutions	12	10	7	1

Table 4.2: Comparison of parametric optimization and topological derivative

4.3.2 3d test case : the cantilever

The topological derivatives in 2d and in 3d have similar structure and differ from their coefficients. Therefore, they should have a similar efficiency level. Based on a classic optimized 3D-cantilever structure, the topological derivative is computed in order to decrease the compliance. Its initial value is $J_0(\Omega) = 0.42488$. The cartography of the topological derivative is given in Fig. 4.9a. It displays the values on the structure surface. The most negative value, *i.e.* the most interesting value, is inside the cantilever, close to the applied force. The small rigid inclusion (displayed in Fig. 4.9b) brings a compliance of $J_\rho(\Omega) = 0.413397$. It represents an improvement of 2.70%. The estimator function is quite good and indicates an expected compliance of $\mathcal{E}(\Omega) = 0.411392$.

Figure 4.9: Cartography of $DJ(\mathbf{x}_0)$ (a) and the resulting rigid inclusion (b)

Two elastic inclusions linked by a spring

Contents

5.1	Setting of the problem	119
5.1.1	Background domain	120
5.1.2	Perturbed domain	121
5.2	Computation of the topological derivative	124
5.2.1	Approximation of the perturbed displacement field	124
5.2.2	Adjoint state	131
5.2.3	Proof of the main result	133
5.3	Numerical illustrations in 2d	137
5.3.1	Analysis with one spring	137
5.3.2	Analysis with two springs	150
5.3.3	Summary of this 2d use case	162
5.4	Numerical illustrations in 3d	164
5.4.1	Tests of the topological derivative	164
5.4.2	Shape optimization	167
5.5	Conclusion of the chapter	168

The idealized bolt connection, described in Chapter 2, holds plenty of features. The sensitivity analysis of the idealized bolt model is established in Chapter 7. We would rather proceed step by step and per level of difficulty. In first instance, the idealized bolt connection is used without the pre-stressed state. This chapter is then devoted to the sensitivity analysis of the perturbation due to a fixed-length spring linking two small elastic spheres. The model is suited for the purpose of sensitivity analysis based on the techniques developed in Chapter 3. Then the spring works according to one degree of freedom. Main results are given in 2d and 3d but the proof is carried out for the 3d problem. The topological derivative is tested on 2d and 3d academic use cases. Thereafter, the resulting connection is involved in various structural optimization. In the

sequel, the term "spring" will abusively refer to the two small elastic inclusions linked by that spring.

5.1 Setting of the problem

Let Ω be the union of two disjointed parts Ω_A and Ω_B . This union is assumed to be a smooth bounded domain of \mathbb{R}^3 . Similar assumptions can be set in 2d. Here we focus on the 3d problem. The boundary of this domain is made of two disjointed parts, $\partial\Omega = \Gamma_N \cup \Gamma_D$. Neumann and Dirichlet boundary conditions are respectively imposed on Γ_N and Γ_D . Let the domain Ω be filled with a linear isotropic elastic material. For a displacement field \mathbf{u} , the strain tensor is defined by $\varepsilon(\mathbf{u}) = \frac{1}{2}(\nabla\mathbf{u} + \nabla^T\mathbf{u})$. The stress tensor is then given by the Hooke's law

$$\mathbf{A}\varepsilon(\mathbf{u}) = \begin{cases} 2\mu_A\varepsilon(\mathbf{u}) + \lambda_A\text{tr}(\varepsilon(\mathbf{u}))\mathbf{I} & \text{in } \Omega_A \\ 2\mu_B\varepsilon(\mathbf{u}) + \lambda_B\text{tr}(\varepsilon(\mathbf{u}))\mathbf{I} & \text{in } \Omega_B \end{cases},$$

where μ_A and λ_A (resp. μ_B and λ_B) are the Lamé coefficients of the material Ω_A (resp. Ω_B). We assume a perfect interface between Ω_A and Ω_B . Thus, there are usual transmission conditions between both parts that insure continuity of displacement and normal stress at the interface. The goal of this chapter is to compute the topological derivative with respect to two small elastic inclusions linked by a spring to join the parts Ω_A and Ω_B . The inclusions are of the same material as the parts. Let Ω_1 and Ω_2 be a partition of Ω , that is $\Omega = \Omega_1 \cup \Omega_2$ and $\Omega_1 \cap \Omega_2 = \emptyset$. For the sake of simplicity, the objective function is evaluated in Ω_1 , far from the influence area of the spring. The topological derivative is computed for a spring nucleated in Ω_2 . It avoids supplementary terms corresponding to the perturbation of the integration domain of the objective function. The topological derivative can be computed with an objective function evaluated everywhere but it requires more technical work, which is not the point here. Fig. 5.1 illustrates this decomposition of the domain Ω .

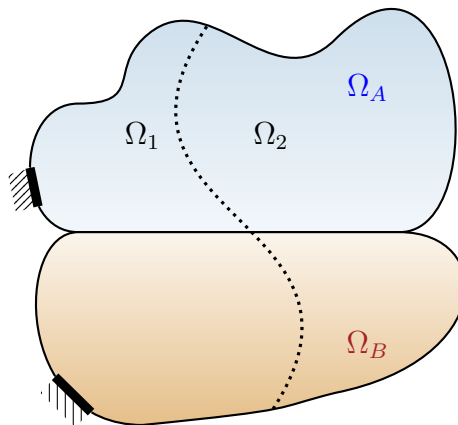


Figure 5.1: Decomposition of the domain Ω

The topological expansion takes only into account the leading term of the rigidity matrix of the spring with regards to the size of the inclusions. The other terms of the matrix would be remainder terms of the sensitivity analysis. This leading rigidity is the stiffness along the axis of the spring, that is to say its tension-compression behavior.

5.1.1 Background domain

The term unperturbed or background domain refers to the system in which one wants to nucleate a new spring. This domain may already contain n pre-existing springs. For the sake of simplicity, let us consider n 1 DOF springs modeled by a function \mathcal{S} that reads

$$\mathcal{S}(\mathbf{w}) = \sum_{i=1}^n \kappa_i \left(\int_{\omega_{B_i}} \mathbf{w} \cdot \mathbf{e}_i dV - \int_{\omega_{A_i}} \mathbf{w} \cdot \mathbf{e}_i dV \right) \left(\frac{\mathbb{1}_{\omega_{B_i}}}{|\omega_{B_i}|} - \frac{\mathbb{1}_{\omega_{A_i}}}{|\omega_{A_i}|} \right) \mathbf{e}_i, \quad (5.1)$$

where κ_i is the rigidity and \mathbf{e}_i the axis of the spring i . The notation $\mathbb{1}_{\omega_{A_i}}$ stands for the characteristic function equal to 1 inside the domain ω_{A_i} and 0 otherwise. The function \mathcal{S} is zero if there is no pre-existing spring in the unperturbed domain. The background solution \mathbf{u} then satisfies the linear elasticity system

$$\begin{cases} -\operatorname{div}(\mathbf{A}\varepsilon(\mathbf{u})) + \mathcal{S}(\mathbf{u}) = \mathbf{0} & \text{in } \Omega \\ \mathbf{A}\varepsilon(\mathbf{u})\mathbf{n} = \mathbf{g} & \text{on } \Gamma_N. \\ \mathbf{u} = \mathbf{0} & \text{on } \Gamma_D \end{cases} \quad (5.2)$$

Assuming that surface loads \mathbf{g} belong to $L^2(\Gamma_N)^3$, Lax-Milgram theorem, coupled with Korn's inequality, gives the existence and the uniqueness of the solution $\mathbf{u} \in \mathcal{W}$, where

$$\mathcal{W} = \left\{ \mathbf{w} \in (H^1(\Omega))^3, \mathbf{w} = \mathbf{0} \text{ in } \Gamma_D \right\}. \quad (5.3)$$

In the following, we assume that \mathbf{u} is as smooth as we want, which is always possible by assuming that the load \mathbf{g} is smooth as well as the domain. We recall that the transmission condition between Ω_A and Ω_B insures the continuity of displacement and normal stress.

Remark 35. *The following analysis can also be done with a non-zero right hand side in Ω for (5.2). An explicit traction-free condition on a boundary Γ can also be added. Since the perturbation occurs far from boundaries and loadings, these conditions are left apart.*

To avoid technicalities, the objective function is evaluated in Ω_1 , while the spring is included in Ω_2 . Consider the generic objective function

$$J_0(\Omega) = \int_{\Omega_1} F(\mathbf{u})dV + \int_{\Gamma_N} G(\mathbf{u})dS, \quad (5.4)$$

which depends on the domain Ω through the function \mathbf{u} solution of (5.2). The functions F and G are smooth, twice differentiable with respect to \mathbf{u} and satisfy the following conditions

$$\exists \alpha > 0, \begin{cases} |F(\mathbf{u})| \leq \alpha(|\mathbf{u}|^2 + 1), & |F'(\mathbf{u})| \leq \alpha(|\mathbf{u}| + 1), & |F''(\mathbf{u})| \leq \alpha \\ |G(\mathbf{u})| \leq \alpha(|\mathbf{u}|^2 + 1), & |G'(\mathbf{u})| \leq \alpha(|\mathbf{u}| + 1), & |G''(\mathbf{u})| \leq \alpha \end{cases} \quad (5.5)$$

Remark 36. *Conditions (5.5) are simple and sufficient. They can be improved if necessary.*

The adjoint state \mathbf{p} associated to (5.2) for a generic objective function (5.4) solves

$$\begin{cases} -\operatorname{div}(\mathbf{A}\varepsilon(\mathbf{p})) + \mathcal{S}(\mathbf{p}) = -\mathbf{F}'(\mathbf{u})\mathbb{1}_{\Omega_1} & \text{in } \Omega \\ \mathbf{A}\varepsilon(\mathbf{p})\mathbf{n} = -\mathbf{G}'(\mathbf{u}) & \text{on } \Gamma_N. \\ \mathbf{p} = \mathbf{0} & \text{on } \Gamma_D \end{cases} \quad (5.6)$$

Lax-Milgram theorem, coupled with Korn's inequality, gives the existence and the uniqueness of the solution $\mathbf{p} \in \mathcal{W}$. In the sequel, we assume that \mathbf{p} is as smooth as required, similarly to the assumptions on \mathbf{u} .

5.1.2 Perturbed domain

In the sequel, we choose the reference shape ω to be the unit ball of \mathbb{R}^3 , which allows us to compute explicitly the coefficients of the topological derivative. Let ω_A be a small inclusion of shape ω , rescaled by an adimensional factor $\rho > 0$ and centred at the point $\mathbf{x}_0 \in \Omega_2$. The second inclusion, denoted ω_B , is the translation of ω_A at a distance $\ell > 0$ and in the direction \mathbf{e} , a unit vector, oriented from ω_A to ω_B . More specifically, the inclusions read

$$\omega_A = \left\{ \mathbf{x} \in \mathbb{R}^3, \frac{\mathbf{x} - \mathbf{x}_0}{\rho} \in \omega \right\} \text{ and } \omega_B = \left\{ \mathbf{x} \in \mathbb{R}^3, \frac{\mathbf{x} - \mathbf{x}_0 - \ell \mathbf{e}}{\rho} \in \omega \right\}. \quad (5.7)$$

In the following, the factor ρ will abusively refer to the size of the inclusions.

We propose to perturb the background domain with a spring of rigidity $\kappa(\rho)$ linking small inclusions of size ρ as pictured in Fig. 5.2. This new configuration is named the perturbed domain. The inclusions, ω_A and ω_B , represent respectively the extremities of the spring. Let us assume the following scaling of the model

$$\kappa(\rho) = K\rho^k, \quad (5.8)$$

with $K > 0$ and $k \in \mathbb{R}$. It will be shown later that only those values $k > 0$ are covered by our asymptotic analysis.

Remark 37. *It makes sense that the rigidity of the spring goes to zero as the size of the inclusions goes to zero.*

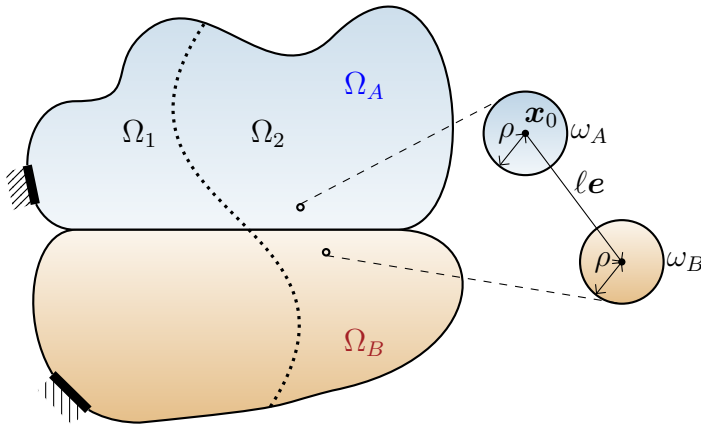


Figure 5.2: Perturbation of the domain Ω by a small spring

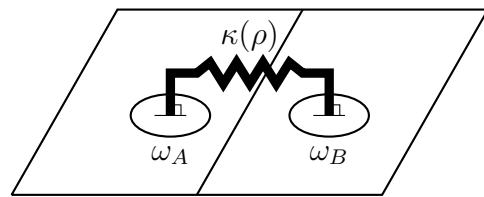


Figure 5.3: Graphical representation of the non-local rigidity $\kappa(\rho)$

Introduce the perforated domain Ω_ρ . It stands for the domain Ω without the extremities of the spring.

$$\Omega_\rho = \Omega \setminus (\omega_A \cup \omega_B). \quad (5.9)$$

Let us recall the notation for the average on ω_A of the projection of the displacement field \mathbf{u} along \mathbf{e} , the axis of the spring,

$$\overline{\mathbf{u} \cdot \mathbf{e}} = \frac{1}{|\omega_A|} \int_{\omega_A} \mathbf{u} \cdot \mathbf{e} dV.$$

The lengthening of the spring is the difference between the average displacements in ω_A and ω_B along the axis of the spring. We also recall that the model is based on an energy formulation. Let then E be the energy functional

$$E(\mathbf{w}) = \frac{1}{2} \int_{\Omega} \mathbf{A}\varepsilon(\mathbf{w}) : \varepsilon(\mathbf{w}) dV + \int_{\Omega_{\rho}} \mathbf{S}(\mathbf{w}) \cdot \mathbf{w} dV - \int_{\Gamma_N} \mathbf{g} \cdot \mathbf{w} dS + \frac{1}{2} \kappa(\rho) \left(\int_{\omega_B} \mathbf{w} \cdot \mathbf{e} dV - \int_{\omega_A} \mathbf{w} \cdot \mathbf{e} dV \right)^2. \quad (5.10)$$

The first term of (5.10) is the elastic energy. The last term is the energy of a spring of rigidity $\kappa(\rho)$. The so-called spring can be depicted as an out-of-plane non-local rigidity linking the cross-section of the two spheres (cf. Fig. 5.3). It is to be interpreted as a remote interaction law. The minimum potential energy principle then states that the displacement field describing the system with a spring linking two spheres is the unique minimizer \mathbf{u}_{ρ} of (5.10) in \mathcal{W} , i.e.,

$$E(\mathbf{u}_{\rho}) = \min_{\mathbf{w} \in \mathcal{W}} E(\mathbf{w}). \quad (5.11)$$

It leads to the following variational problem :

$$\begin{aligned} \text{Find } \mathbf{u}_{\rho} \in \mathcal{W} \text{ s.t. } \forall \mathbf{w} \in \mathcal{W}, \int_{\Omega} \mathbf{A}\varepsilon(\mathbf{u}_{\rho}) : \varepsilon(\mathbf{w}) dV + \int_{\Omega_{\rho}} \mathbf{S}(\mathbf{u}_{\rho}) \cdot \mathbf{w} dV - \int_{\Gamma_N} \mathbf{g} \cdot \mathbf{w} dV \\ + \kappa(\rho) \left(\int_{\omega_B} \mathbf{u}_{\rho} \cdot \mathbf{e} dV - \int_{\omega_A} \mathbf{u}_{\rho} \cdot \mathbf{e} dV \right) \left(\int_{\omega_B} \mathbf{w} \cdot \mathbf{e} dV - \int_{\omega_A} \mathbf{w} \cdot \mathbf{e} dV \right) = 0. \end{aligned} \quad (5.12)$$

Assuming that surface loads \mathbf{g} belong to $L^2(\Gamma_N)^3$, Lax-Milgram theorem, coupled with Korn's inequality, gives the existence and the uniqueness of the solution $\mathbf{u}_{\rho} \in \mathcal{W}$. Consequently, the displacement field in the perturbed domain \mathbf{u}_{ρ} solves

$$\left\{ \begin{array}{l} -\operatorname{div}(\mathbf{A}\varepsilon(\mathbf{u}_{\rho})) + \mathbf{S}(\mathbf{u}_{\rho}) = \mathbf{0} \quad \text{in } \Omega_{\rho} \\ -\operatorname{div}(\mathbf{A}\varepsilon(\mathbf{u}_{\rho})) - \frac{\kappa(\rho)}{|\omega_A|} \left(\int_{\omega_B} \mathbf{u}_{\rho} \cdot \mathbf{e} dV - \int_{\omega_A} \mathbf{u}_{\rho} \cdot \mathbf{e} dV \right) \mathbf{e} = \mathbf{0} \quad \text{in } \omega_A \\ -\operatorname{div}(\mathbf{A}\varepsilon(\mathbf{u}_{\rho})) + \frac{\kappa(\rho)}{|\omega_B|} \left(\int_{\omega_B} \mathbf{u}_{\rho} \cdot \mathbf{e} dV - \int_{\omega_A} \mathbf{u}_{\rho} \cdot \mathbf{e} dV \right) \mathbf{e} = \mathbf{0} \quad \text{in } \omega_B \\ \mathbf{A}\varepsilon(\mathbf{u}_{\rho}) \mathbf{n} = \mathbf{g} \quad \text{on } \Gamma_N \\ \mathbf{u}_{\rho} = \mathbf{0} \quad \text{on } \Gamma_D \end{array} \right., \quad (5.13)$$

In the sequel, the field \mathbf{u}_{ρ} is assumed to be as smooth as we want, which is always possible by assuming that the load and the domain are smooth. Denote by J_{ρ} the generic objective function (5.4) evaluated in the perturbed domain

$$J_{\rho}(\Omega) = \int_{\Omega_1} F(\mathbf{u}_{\rho}) dV + \int_{\Gamma_N} G(\mathbf{u}_{\rho}) dS. \quad (5.14)$$

Definition 6. *The objective function J_{ρ} is said to admit a topological derivative $DJ(\mathbf{x}_0, \mathbf{e})$ at the point \mathbf{x}_0 for a spring of direction \mathbf{e} and for a pair of inclusions of shape ω , if the following asymptotic expansion holds for small $\rho > 0$*

$$J_{\rho}(\Omega) = J_0(\Omega) + s(\rho) DJ(\mathbf{x}_0, \mathbf{e}) + o(s(\rho)), \quad (5.15)$$

where $s(\rho)$ is a positive scalar function of ρ which satisfies $\lim_{\rho \rightarrow 0} s(\rho) = 0$.

Theorem 4. Take ω to be the unit ball of \mathbb{R}^n , $n = 2$ or 3 .

In 2d, the general objective function (5.14) admits a topological asymptotic expansion of the form (5.15), for all $k > 0$

$$J_\rho(\Omega) = J_0(\Omega) + K \rho^k (\mathbf{u}(\mathbf{x}_0 + \ell \mathbf{e}) - \mathbf{u}(\mathbf{x}_0)) \cdot \mathbf{e} (\mathbf{p}(\mathbf{x}_0 + \ell \mathbf{e}) - \mathbf{p}(\mathbf{x}_0)) \cdot \mathbf{e} + \begin{cases} O(\rho^{k+2}) & \text{if } k \geq 4 \\ O(\rho^{3k/2}) & \text{if } 0 < k < 4 \end{cases}, \quad (5.16)$$

where \mathbf{u} and \mathbf{p} are respectively the displacement and the adjoint state in the background domain that solve (5.2) and (5.6).

In 3d, the general objective function (5.14) admits a topological asymptotic expansion of the form (5.15), for various values of k , that is

$$J_\rho(\Omega) = J_0(\Omega) + s(\rho) DJ(\mathbf{x}_0, \mathbf{e}) + \mathcal{R}(s(\rho)), \quad (5.17)$$

with

$$DJ(\mathbf{x}_0, \mathbf{e}) = j(K, \tau_A, \tau_B) (\mathbf{u}(\mathbf{x}_0 + \ell \mathbf{e}) - \mathbf{u}(\mathbf{x}_0)) \cdot \mathbf{e} (\mathbf{p}(\mathbf{x}_0 + \ell \mathbf{e}) - \mathbf{p}(\mathbf{x}_0)) \cdot \mathbf{e}, \quad (5.18)$$

where \mathbf{u} and \mathbf{p} are respectively the displacement and the adjoint state in the background domain that solve (5.2) and (5.6). The scaling $s(\rho)$, the coefficient $j(K, \tau_A, \tau_B)$ and the remainder term $\mathcal{R}(s(\rho))$ are given, according to the value of the exponent k , by

	$s(\rho)$	$j(K, \tau_A, \tau_B)$	$\mathcal{R}(s(\rho))$	
$k > 1$	ρ^k	K	$k > 4$	$O(\rho^{k+2})$
			$2 \leq k \leq 4$	$O(\rho^{3k/2})$
			$k < 2$	$O(\rho^{2k-1})$
$k = 1$	ρ	$\left(\frac{1}{K} + \frac{1}{ \omega } \left(\frac{1}{\tau_A} + \frac{1}{\tau_B} \right) \right)^{-1}$	$O(\rho^{3/2})$	
$0 < k < 1$	ρ	$\left(\frac{1}{ \omega } \left(\frac{1}{\tau_A} + \frac{1}{\tau_B} \right) \right)^{-1}$	$k \geq 2/3$	$O(\rho^{2-k})$
			$k < 2/3$	$O(\rho^{1+k/2})$

The coefficients τ_A and τ_B depend on material properties and read $\tau_A = \frac{15}{2} \frac{\mu_A(2\mu_A + \lambda_A)}{(5\mu_A + 2\lambda_A)r_1^2}$

and $\tau_B = \frac{15}{2} \frac{\mu_B(2\mu_B + \lambda_B)}{(5\mu_B + 2\lambda_B)r_1^2}$ with $r_1 = 1$ the radius of the unit ball.

Remark 38. In 2d and 3d, the topological derivative has the same dependence according to the displacement field \mathbf{u} and the adjoint state \mathbf{p} for all $k > 0$. In 3d, the coefficient of the topological derivative is of three different categories. They differ from each other by their coefficient and their scaling of ρ . The case $k > 1$ expresses fully the stiffness of the spring $\kappa(\rho) = K\rho^k$. For $k = 1$, the coefficient of the topological derivative corresponds to a harmonic mean of rigidities due to the interaction between the spheres and the spring that are on equal importance. The rigidity of the spheres predominates the asymptotic analysis for $0 < k < 1$.

5.2 Computation of the topological derivative

5.2.1 Approximation of the perturbed displacement field

This section aims to approximate the perturbed displacement field \mathbf{u}_ρ due to the small elastic spheres of size ρ linked by a spring of rigidity $\kappa(\rho)$.

Far fields expression

As the inclusions are small, the perturbed field \mathbf{u}_ρ is expected to be approximately equal to the background field \mathbf{u} plus the influence fields of the inclusions ω_A and ω_B , respectively denoted \mathbf{v}_a and \mathbf{v}_b . In other words, we formally assume an ansatz that

$$\mathbf{u}_\rho(\mathbf{x}) \approx \mathbf{u}(\mathbf{x}) + \mathbf{v}_a \left(\frac{\mathbf{x} - \mathbf{x}_0}{\rho} \right) + \mathbf{v}_b \left(\frac{\mathbf{x} - \mathbf{x}_0 - \ell \mathbf{e}}{\rho} \right). \quad (5.19)$$

The functions \mathbf{v}_a and \mathbf{v}_b are defined in \mathbb{R}^3 . Perturbations due to the inclusions are getting smaller far from their center \mathbf{x}_0 and $\mathbf{x}_0 + \ell \mathbf{e}$. Then, they have to decay at infinity like $\lim_{\mathbf{y} \rightarrow \infty} \mathbf{v}_a(\mathbf{y}) = 0$ and $\lim_{\mathbf{y} \rightarrow \infty} \mathbf{v}_b(\mathbf{y}) = 0$. In other words, these functions allow a zoom on the inclusions and ignore boundary conditions on $\partial\Omega$. The goal of this part is to approximate the perturbed displacement field \mathbf{u}_ρ using the behavior of the far fields \mathbf{v}_a and \mathbf{v}_b . In order to rescale the elasticity problem with inclusions of unit size ω , let us define rescaled variables $\mathbf{y}_a \in \mathbb{R}^3$ and $\mathbf{y}_b \in \mathbb{R}^3$ by

$$\mathbf{y}_a = \frac{\mathbf{x} - \mathbf{x}_0}{\rho} \quad \text{and} \quad \mathbf{y}_b = \frac{\mathbf{x} - \mathbf{x}_0 - \ell \mathbf{e}}{\rho}. \quad (5.20)$$

The background solution is expressed according to the following Taylor expansions

$$\mathbf{u}(\mathbf{x}) = \mathbf{u}(\mathbf{x}_0) + O(\rho) \quad \text{in a neighbourhood of } \mathbf{x}_0, \quad (5.21)$$

$$\mathbf{u}(\mathbf{x}) = \mathbf{u}(\mathbf{x}_0 + \ell \mathbf{e}) + O(\rho) \quad \text{in a neighbourhood of } \mathbf{x}_0 + \ell \mathbf{e}. \quad (5.22)$$

Functions \mathbf{v}_a and \mathbf{v}_b are coupled and they respectively solve

$$\left\{ \begin{array}{ll} -\operatorname{div}(\mathbf{A}\varepsilon(\mathbf{v}_a)(\mathbf{y}_a)) = \mathbf{0} & \text{in } \mathbb{R}^3 \setminus \omega \\ -\operatorname{div}(\mathbf{A}\varepsilon(\mathbf{v}_a)(\mathbf{y}_a)) = \xi_u(\rho) \mathbf{e} & \text{in } \omega \\ \lim_{\mathbf{y}_a \rightarrow \mathbf{0}} \mathbf{v}_a(\mathbf{y}_a) = \mathbf{0} & \end{array} \right. \quad \text{and} \quad \left\{ \begin{array}{ll} -\operatorname{div}(\mathbf{A}\varepsilon(\mathbf{v}_b)(\mathbf{y}_b)) = \mathbf{0} & \text{in } \mathbb{R}^3 \setminus \omega \\ -\operatorname{div}(\mathbf{A}\varepsilon(\mathbf{v}_b)(\mathbf{y}_b)) = -\xi_u(\rho) \mathbf{e} & \text{in } \omega \\ \lim_{\mathbf{y}_b \rightarrow \mathbf{0}} \mathbf{v}_b(\mathbf{y}_b) = \mathbf{0} & \end{array} \right., \quad (5.23)$$

with

$$\xi_u(\rho) = \frac{\kappa(\rho)}{\rho|\omega|} \left(\int_{\omega} (\mathbf{v}_b - \mathbf{v}_a) \cdot \mathbf{e} dV + (\mathbf{u}(\mathbf{x}_0 + \ell \mathbf{e}) - \mathbf{u}(\mathbf{x}_0)) \cdot \mathbf{e} \right). \quad (5.24)$$

Systems (5.23) respectively describe the zoom at zero-order on ω_A and ω_B . Since \mathbf{v}_a and \mathbf{v}_b are defined in \mathbb{R}^3 , they can be evaluated at any $\mathbf{y} \in \mathbb{R}^3$.

Remark 39. Existing springs modeled by the function \mathcal{S} are far from the inclusions. They are ignored by the zoom at zero-order on ω_A and ω_B .

Remark 40. At first sight, the coefficient $\xi_u(\rho)$ does not explicitly depend only on \mathbf{u} as presumed by the subscript "u". The following lemma proves that $\xi_u(\rho)$ actually depends only on \mathbf{u} thanks to the explicit expressions of \mathbf{v}_a and \mathbf{v}_b .

Remark 41. In 2d, \mathbf{v}_a and \mathbf{v}_b still solve the coupled equations (5.23) but the factor $\xi_u(\rho)$ changes because of the dimension. Actually, the rescaling gives

$$\xi_u(\rho) = \frac{\kappa(\rho)}{|\omega|} \left(\int_{\omega} (\mathbf{v}_b - \mathbf{v}_a) \cdot \mathbf{e} dV + (\mathbf{u}(\mathbf{x}_0 + \ell \mathbf{e}) - \mathbf{u}(\mathbf{x}_0)) \cdot \mathbf{e} \right). \quad (5.25)$$

Lemma 7. The function \mathbf{v}_a and \mathbf{v}_b are explicitly given by

$$\mathbf{v}_a(\mathbf{y}) = \begin{cases} \frac{r_1^3(5r^2 - 3r_1^2)(\mu_A + \lambda_A)}{30r^5\mu_A(2\mu_A + \lambda_A)} \xi_u(\rho) \mathbf{e} \cdot \mathbf{y} \mathbf{y} + \frac{r_1^3((15\mu_A + 5\lambda_A)r^2 + (\mu_A + \lambda_A)r_1^2)}{30r^3\mu_A(2\mu_A + \lambda_A)} \xi_u(\rho) \mathbf{e} & \text{in } \mathbb{R}^3 \setminus \omega \\ \frac{\mu_A + \lambda_A}{15\mu_A(2\mu_A + \lambda_A)} \xi_u(\rho) \mathbf{e} \cdot \mathbf{y} \mathbf{y} - \frac{(9\mu_A + 4\lambda_A)r^2 - (25\mu_A + 10\lambda_A)r_1^2}{30\mu_A(2\mu_A + \lambda_A)} \xi_u(\rho) \mathbf{e} & \text{in } \omega \end{cases}, \quad (5.26)$$

$$\mathbf{v}_b(\mathbf{y}) = \begin{cases} -\frac{r_1^3(5r^2 - 3r_1^2)(\mu_B + \lambda_B)}{30r^5\mu_B(2\mu_B + \lambda_B)} \xi_u(\rho) \mathbf{e} \cdot \mathbf{y} \mathbf{y} - \frac{r_1^3((15\mu_B + 5\lambda_B)r^2 + (\mu_B + \lambda_B)r_1^2)}{30r^3\mu_B(2\mu_B + \lambda_B)} \xi_u(\rho) \mathbf{e} & \text{in } \mathbb{R}^3 \setminus \omega \\ -\frac{\mu_B + \lambda_B}{15\mu_B(2\mu_B + \lambda_B)} \xi_u(\rho) \mathbf{e} \cdot \mathbf{y} \mathbf{y} + \frac{(9\mu_B + 4\lambda_B)r^2 - (25\mu_B + 10\lambda_B)r_1^2}{30\mu_B(2\mu_B + \lambda_B)} \xi_u(\rho) \mathbf{e} & \text{in } \omega \end{cases}, \quad (5.27)$$

where $r = \|\mathbf{y}\|$ and

$$\xi_u(\rho) = \frac{\frac{\kappa(\rho)}{\rho|\omega|}}{1 + \frac{\kappa(\rho)}{\rho|\omega|} \left(\frac{1}{\tau_A} + \frac{1}{\tau_B} \right)} (\mathbf{u}(\mathbf{x}_0 + \ell \mathbf{e}) - \mathbf{u}(\mathbf{x}_0)) \cdot \mathbf{e}. \quad (5.28)$$

Remark 42. If Ω_A and Ω_B are of the same material, then it follows that $\mathbf{v}_a = -\mathbf{v}_b$.

Proof. Considering the form of (5.23), it is enough to solve one system of equations. The other one is solved similarly. According to [113], the solution of (5.23) has the explicit form

$$\mathbf{v}_a(\mathbf{y}) = \begin{cases} \xi_u(\rho) \mathbf{e} \cdot \mathbf{y} f_R(r) \mathbf{y} + \xi_u(\rho) \mathbf{e} g_R(r) & \text{in } \mathbb{R}^3 \setminus \omega \\ \xi_u(\rho) \mathbf{e} \cdot \mathbf{y} f_\omega(r) \mathbf{y} + \xi_u(\rho) \mathbf{e} g_\omega(r) & \text{in } \omega \end{cases}, \quad (5.29)$$

where f_R, g_R, f_ω and g_ω are finite scalar functions satisfying the continuity of \mathbf{v}_a and $\varepsilon(\mathbf{v}_a)$ on $\partial\omega$ and that go to zero at infinity. Their expression have been explicitly computed with Maple. We give here main steps.

$$\begin{aligned} & -\operatorname{div}(\mathbf{A}\varepsilon(\mathbf{v}_a)) = \mathbf{0} \text{ in } \mathbb{R}^3 \setminus \omega \\ \Leftrightarrow & \begin{cases} (2\mu_A + \lambda_A) f_R''(r) + (11\mu_A + 5\lambda_A) \frac{f_R'(r)}{r} = (\mu_A + \lambda_A) \frac{g_R'(r)}{r^3} - (\mu_A + \lambda_A) \frac{g_R''(r)}{r^2}, \\ (\mu_A + \lambda_A) r f_R'(r) + (4\lambda_A + 6\mu_A) f_R(r) = -(3\mu_A + \lambda_A) \frac{g_R'(r)}{r} - \mu_A g_R''(r) \end{cases}, \end{aligned}$$

and

$$\begin{aligned} & -\operatorname{div}(\mathbf{A}\varepsilon(\mathbf{v}_a)) = \xi_u(\rho) \mathbf{e} \text{ in } \omega \\ \Leftrightarrow & \begin{cases} (2\mu_A + \lambda_A) f_\omega''(r) + (11\mu_A + 5\lambda_A) \frac{f_\omega'(r)}{r} = (\mu_A + \lambda_A) \frac{g_\omega'(r)}{r^3} - (\mu_A + \lambda_A) \frac{g_\omega''(r)}{r^2}, \\ (\mu_A + \lambda_A) r f_\omega'(r) + (4\lambda_A + 6\mu_A) f_\omega(r) = -(3\mu_A + \lambda_A) \frac{g_\omega'(r)}{r} - \mu_A g_\omega''(r) - 1 \end{cases}. \end{aligned}$$

These coupled equations systems are explicitly solved by adding boundary conditions. The far field \mathbf{v}_a goes to zero at infinity, which implies that

$$\lim_{r \rightarrow \infty} f_R(r) = 0 \text{ and } \lim_{r \rightarrow \infty} g_R(r) = 0.$$

Moreover \mathbf{v}_a is a finite quantity, so that

$$f_\omega(0) < \infty \text{ and } g_\omega(0) < \infty.$$

Recalling that $r_1 = 1$ is the radius of $\omega = \mathcal{B}(0, 1)$ the unit ball of \mathbb{R}^3 , the continuity of \mathbf{v}_a and $\varepsilon(\mathbf{v}_a)$ on $\partial\omega$ respectively lead to

$$f_R(r_1) = f_\omega(r_1) \text{ and } g_R(r_1) = g_\omega(r_1),$$

$$f'_R(r_1) = f'_\omega(r_1) \text{ and } g'_R(r_1) = g'_\omega(r_1).$$

It follows that

$$\begin{aligned} f_R(r) &= \frac{1}{30} \frac{r_1^3(5r^2 - 3r_1^2)(\mu_A + \lambda_A)}{r^5 \mu_A(2\mu_A + \lambda_A)}, & g_R(r) &= \frac{1}{30} \frac{r_1^3(15\mu_A r^2 + 5\lambda_A r^2 + \mu_A r_1^2 + \lambda_A r_1^2)}{r^3 \mu_A(2\mu_A + \lambda_A)}, \\ f_\omega(r) &= \frac{1}{15} \frac{\mu_A + \lambda_A}{\mu_A(2\mu_A + \lambda_A)}, & g_\omega(r) &= -\frac{1}{30} \frac{9\mu_A r^2 + 4\lambda_A r^2 - 25\mu_A r_1^2 - 10\lambda_A r_1^2}{\mu_A(2\mu_A + \lambda_A)}. \end{aligned} \quad (5.30)$$

The average of the far field on ω is then computed

$$\begin{aligned} \int_\omega \mathbf{v}_a \cdot \mathbf{e} dV &= \frac{1}{|\omega|} \int_\omega (\xi_u(\rho)(\mathbf{e} \cdot \mathbf{e}_r)^2 r^2 f_\omega(r) + \xi_u(\rho) \mathbf{e} \cdot \mathbf{e} g_\omega(r)) dV = \frac{\xi_u(\rho)}{r_1^3} \int_0^{r_1} (r^4 f_\omega(r) + 3r^2 g_\omega(r)) dr \\ &= \xi_u(\rho) \frac{2}{15} \frac{(5\mu_A + 2\lambda_A)r_1^2}{\mu_A(2\mu_A + \lambda_A)}, \end{aligned}$$

which is rewritten as follows

$$\int_\omega \mathbf{v}_a \cdot \mathbf{e} dV = \frac{\xi_u(\rho)}{\tau_A} \text{ with } \tau_A = \frac{15}{2} \frac{\mu_A(2\mu_A + \lambda_A)}{(5\mu_A + 2\lambda_A)r_1^2}. \quad (5.31)$$

A very similar resolution gives

$$\int_\omega \mathbf{v}_b \cdot \mathbf{e} dV = -\frac{\xi_u(\rho)}{\tau_B} \text{ with } \tau_B = \frac{15}{2} \frac{\mu_B(2\mu_B + \lambda_B)}{(5\mu_B + 2\lambda_B)r_1^2}. \quad (5.32)$$

The explicit expression of $\xi_u(\rho)$, given by (5.28), is a simple combination of (5.24), (5.31) and (5.32). \square

Remark 43. Lemma 7 shows that $|\mathbf{v}_a| = O\left(\frac{1}{r}\right)$ at infinity in 3d. A similar computation in 2d gives $|\mathbf{v}_a| = O(\log(r))$ at infinity. The solution has hence the same behavior at infinity as the solution of the Dirichlet problem.

Asymptotic analysis of the perturbed displacement

This part establishes rigorous estimates of the perturbation based on the behavior of the far fields functions \mathbf{v}_a and \mathbf{v}_b . Let \mathbf{v}_ρ be the difference between the perturbed and the background solution,

$$\mathbf{v}_\rho = \mathbf{u}_\rho - \mathbf{u}. \quad (5.33)$$

This function represents the influence of the inclusions in terms of displacement. The equation satisfied by \mathbf{v}_ρ is

$$\left\{ \begin{array}{l} -\operatorname{div}(\mathbf{A}\varepsilon(\mathbf{v}_\rho)) + \mathbf{S}(\mathbf{v}_\rho) = \mathbf{0} \quad \text{in } \Omega_\rho \\ -\operatorname{div}(\mathbf{A}\varepsilon(\mathbf{v}_\rho)) - \frac{\kappa(\rho)}{|\omega_A|} \left(\int_{\omega_B} \mathbf{f}(\mathbf{v}_\rho + \mathbf{u}) \cdot \mathbf{e} dV - \int_{\omega_A} \mathbf{f}(\mathbf{v}_\rho + \mathbf{u}) \cdot \mathbf{e} dV \right) \mathbf{e} = \mathbf{0} \quad \text{in } \omega_A \\ -\operatorname{div}(\mathbf{A}\varepsilon(\mathbf{v}_\rho)) + \frac{\kappa(\rho)}{|\omega_B|} \left(\int_{\omega_B} \mathbf{f}(\mathbf{v}_\rho + \mathbf{u}) \cdot \mathbf{e} dV - \int_{\omega_A} \mathbf{f}(\mathbf{v}_\rho + \mathbf{u}) \cdot \mathbf{e} dV \right) \mathbf{e} = \mathbf{0} \quad \text{in } \omega_B \\ \mathbf{A}\varepsilon(\mathbf{v}_\rho)\mathbf{n} = \mathbf{0} \quad \text{on } \Gamma_N \\ \mathbf{v}_\rho = \mathbf{0} \quad \text{on } \Gamma_D \end{array} \right. . \quad (5.34)$$

The field \mathbf{v}_ρ is as smooth as \mathbf{u}_ρ and \mathbf{u} . Let us introduce the function

$$\mathbf{v}(\mathbf{x}) = \mathbf{v}_a \left(\frac{\mathbf{x} - \mathbf{x}_0}{\rho} \right) + \mathbf{v}_b \left(\frac{\mathbf{x} - \mathbf{x}_0 - \ell \mathbf{e}}{\rho} \right), \quad (5.35)$$

where \mathbf{v}_a and \mathbf{v}_b are solutions of (5.23) and thus verify Lemma 7. As proved by the following result, \mathbf{v} is, in some sense, the limit of \mathbf{v}_ρ as ρ goes to zero.

Proposition 11. *Let $\theta \in \mathbf{C}_c^\infty(\Omega)$ be a cut-off function with compact support $\mathcal{U}_+ \subset \Omega$ such that $\theta \equiv 1$ in a neighborhood $\mathcal{U}_- \subset \mathcal{U}_+$ of \mathbf{x}_0 and $\mathbf{x}_0 + \ell \mathbf{e}$. We have*

$$\mathbf{v}_\rho = \theta \mathbf{v} + \boldsymbol{\delta}, \quad (5.36)$$

where $\boldsymbol{\delta}$ is a remainder term as can be checked by these estimates of the L^2 -norms of \mathbf{v} and $\varepsilon(\mathbf{v})$ and the H^1 -norm of $\boldsymbol{\delta}$. They are given, according to the value of the exponent k , by

	$\ \mathbf{v}\ _{L^2(\Omega)}$	$\ \varepsilon(\mathbf{v})\ _{L^2(\Omega)}$	$\ \boldsymbol{\delta}\ _{H^1(\Omega)}$
$k > 1$	$O(\rho^k)$	$O(\rho^{k-1/2})$	$O(\rho^k)$
$k = 1$	$O(\rho)$	$O(\sqrt{\rho})$	$O(\rho)$
$0 < k < 1$	$O(\rho)$	$O(\sqrt{\rho})$	$O(\rho)$

Remark 44. *The role of the cut-off function θ is to make sure that the product $\theta \mathbf{v}$ satisfies homogeneous boundary conditions on the boundary $\partial\Omega$, as does \mathbf{v}_ρ . Since θ has a compact support, it implies that $\theta \equiv 0$ far from \mathbf{x}_0 and $\mathbf{x}_0 + \ell \mathbf{e}$. Consequently, $\boldsymbol{\delta}$ also contains the far field influence of the inclusions. The function $\boldsymbol{\delta}$ is an error term in the H^1 -norm. Indeed, its H^1 -norm is always asymptotically smaller than the one of $\theta \mathbf{v}$. The L^2 -norm of $\boldsymbol{\delta}$ is of the same order as its H^1 -norm. However, the L^2 -norm of \mathbf{v} is always smaller by a factor $\sqrt{\rho}$ than its H^1 -norm.*

Proof. The explicit expressions of \mathbf{v}_a and \mathbf{v}_b indicate at infinity that $|\mathbf{v}_a| = O\left(\frac{|\xi_u(\rho)|}{r}\right)$ and $|\varepsilon(\mathbf{v}_a)| = O\left(\frac{|\xi_u(\rho)|}{r^2}\right)$ and so $|\mathbf{v}_b| = O\left(\frac{|\xi_u(\rho)|}{r}\right)$ and $|\varepsilon(\mathbf{v}_b)| = O\left(\frac{|\xi_u(\rho)|}{r^2}\right)$. Thus, we deduce by rescaling

$$\|\mathbf{v}\|_{L^\infty(\Omega \setminus \mathcal{U}_-)} \leq C\rho |\xi_u(\rho)| \quad \text{and} \quad \|\varepsilon(\mathbf{v})\|_{L^\infty(\Omega \setminus \mathcal{U}_-)} \leq C\rho |\xi_u(\rho)|. \quad (5.37)$$

These L^∞ -norms are evaluated far from the neighborhood of \mathbf{x}_0 and $\mathbf{x}_0 + \ell \mathbf{e}$. Denote $\Omega_{\rho^{-1}}$ the translated and rescaled domain centered at the origin and of size $\frac{1}{\rho}|\Omega|$. Using the behavior of \mathbf{v}_a and \mathbf{v}_b , it follows

$$\begin{aligned} \|\mathbf{v}\|_{L^2(\Omega)}^2 &\leq C\rho^3 \int_{\Omega_{\rho^{-1}}} |\mathbf{v}_a|^2 dV + C\rho^3 \int_{\omega} |\mathbf{v}_a|^2 dV \leq C\rho^3 |\xi_u(\rho)|^2 \int_{r_1}^{r_1/\rho} dr + C\rho^3 |\xi_u(\rho)|^2 \int_0^{r_1} r^6 dr \\ &\leq C\rho^2 |\xi_u(\rho)|^2 + C\rho^3 |\xi_u(\rho)|^2 \leq C\rho^2 |\xi_u(\rho)|^2. \end{aligned}$$

Using the expression (5.28) of $\xi_u(\rho)$, the L^2 -norm of \mathbf{v} is estimated as

$$\|\mathbf{v}\|_{L^2(\Omega)} \leq C\rho |\xi_u(\rho)| \leq C \frac{\kappa(\rho)}{1 + C \frac{\kappa(\rho)}{\rho}} \leq C \frac{\rho^k}{1 + C\rho^{k-1}}.$$

The denominator of the above upper bound is bounded if $k \geq 1$ and it goes to infinity otherwise. Therefore, for $k \geq 1$, one deduces

$$\|\mathbf{v}\|_{L^2(\Omega)} \leq C\rho^k, \quad (5.38)$$

while, for $k < 1$,

$$\|\mathbf{v}\|_{L^2(\Omega)} \leq C\rho. \quad (5.39)$$

Estimates of the L^2 -norm of $\varepsilon(\mathbf{v})$ are obtained by a similar argument

$$\begin{aligned} \|\varepsilon(\mathbf{v})\|_{L^2(\Omega)}^2 &\leq C\rho \int_{\Omega_{\rho^{-1}}} |\varepsilon(\mathbf{v}_a)|^2 dV + C\rho \int_{\omega} |\varepsilon(\mathbf{v}_a)|^2 dV \leq C\rho |\xi_u(\rho)|^2 \int_{r_1}^{r_1/\rho} \frac{1}{r^2} dr + C\rho |\xi_u(\rho)|^2 \int_0^{r_1} r^4 dr \\ &\leq C\rho |\xi_u(\rho)|^2. \end{aligned}$$

As a consequence, there exists $C > 0$ such that

$$\|\varepsilon(\mathbf{v})\|_{L^2(\Omega)} \leq C\sqrt{\rho} |\xi_u(\rho)| \leq C \frac{\frac{\kappa(\rho)}{\sqrt{\rho}}}{1 + C \frac{\kappa(\rho)}{\rho}} \leq C \frac{\rho^{k-1/2}}{1 + C\rho^{k-1}}.$$

In particular, the upper bound for $\|\varepsilon(\mathbf{v})\|_{L^2(\Omega)}$ is larger, by a factor $1/\sqrt{\rho}$, than the upper bound for $\|\mathbf{v}\|_{L^2(\Omega)}$.

Let us now write the equations satisfied by δ

$$\left\{ \begin{array}{l} -\operatorname{div}(\mathbf{A}\varepsilon(\delta)) + \mathbf{S}(\delta) = \operatorname{div}\mathbf{A}(\mathbf{v} \otimes \nabla\theta)^s + \mathbf{A}\varepsilon(\mathbf{v})\nabla\theta \quad \text{in } \Omega_\rho \\ -\operatorname{div}(\mathbf{A}\varepsilon(\delta)) - \frac{\kappa(\rho)}{|\omega_A|} \left(\int_{\omega_B} \delta \cdot \mathbf{e} dV - \int_{\omega_A} \delta \cdot \mathbf{e} dV \right) \mathbf{e} \\ \quad = \frac{\kappa(\rho)}{|\omega_A|} \left(\int_{\omega_B} \mathbf{u} \cdot \mathbf{e} dV - \int_{\omega_A} \mathbf{u} \cdot \mathbf{e} dV - (\mathbf{u}(\mathbf{x}_0 + \ell\mathbf{e}) - \mathbf{u}(\mathbf{x}_0)) \cdot \mathbf{e} \right) \mathbf{e} \quad \text{in } \omega_A \\ -\operatorname{div}(\mathbf{A}\varepsilon(\delta)) + \frac{\kappa(\rho)}{|\omega_B|} \left(\int_{\omega_B} \delta \cdot \mathbf{e} dV - \int_{\omega_A} \delta \cdot \mathbf{e} dV \right) \mathbf{e} \\ \quad = -\frac{\kappa(\rho)}{|\omega_B|} \left(\int_{\omega_B} \mathbf{u} \cdot \mathbf{e} dV - \int_{\omega_A} \mathbf{u} \cdot \mathbf{e} dV - (\mathbf{u}(\mathbf{x}_0 + \ell\mathbf{e}) - \mathbf{u}(\mathbf{x}_0)) \cdot \mathbf{e} \right) \mathbf{e} \quad \text{in } \omega_B \\ \mathbf{A}\varepsilon(\delta)\mathbf{n} = \mathbf{0} \quad \text{on } \Gamma_N \\ \delta = \mathbf{0} \quad \text{on } \Gamma_D \end{array} \right. \quad (5.40)$$

The exponent "s" stands for the symmetric part of the matrix $\mathbf{v} \otimes \nabla\theta$. A Taylor expansion with integral remainder at first order of each component u^i of the background solution \mathbf{u} in a neighbourhood of \mathbf{x}_0 is

$$u^i(\mathbf{x}) = u^i(\mathbf{x}_0) + \nabla u^i(\mathbf{x}_0) \cdot (\mathbf{x} - \mathbf{x}_0) + \int_0^1 (1-t)(\mathbf{x} - \mathbf{x}_0)^T \mathbf{H}(u^i(\mathbf{x}_0 + t(\mathbf{x} - \mathbf{x}_0))) (\mathbf{x} - \mathbf{x}_0) dt, \quad (5.41)$$

with \mathbf{H} the Hessian matrix of the component u^i . Then, one deduces the following expansion of the background solution \mathbf{u}

$$\mathbf{u}(\mathbf{x}) = \mathbf{u}(\mathbf{x}_0) + \nabla\mathbf{u}(\mathbf{x}_0)(\mathbf{x} - \mathbf{x}_0) + \int_0^1 (1-t)(\mathbf{x} - \mathbf{x}_0)^T \mathcal{D}^2(\mathbf{u}(\mathbf{x}_0 + t(\mathbf{x} - \mathbf{x}_0))) (\mathbf{x} - \mathbf{x}_0) dt, \quad (5.42)$$

where \mathcal{D}^2 is a third order tensor containing second derivatives of \mathbf{u} . Therefore, it implies that at least $\mathbf{u} \in (\mathcal{C}^2(\Omega))^3$.

Recalling that ω is the unit ball of \mathbb{R}^3 , it comes $\int_{\omega_A} \nabla\mathbf{u}(\mathbf{x}_0)(\mathbf{x} - \mathbf{x}_0) dV = \rho \int_{\omega} \nabla\mathbf{u}(\mathbf{x}_0)\mathbf{y} dV = \mathbf{0}$.

Let us set the functions \mathbf{R}_u^A and \mathbf{R}_u^B that respectively stand for the integral remainder of the expansion of \mathbf{u} in a neighborhood of \mathbf{x}_0 and $\mathbf{x}_0 + \ell\mathbf{e}$

$$\begin{aligned} \mathbf{R}_u^A(\mathbf{x}) &= \int_0^1 (1-t)(\mathbf{x} - \mathbf{x}_0)^T \mathcal{D}^2(\mathbf{u}(\mathbf{x}_0 + t(\mathbf{x} - \mathbf{x}_0))) (\mathbf{x} - \mathbf{x}_0) dt, \\ \mathbf{R}_u^B(\mathbf{x}) &= \int_0^1 (1-t)(\mathbf{x} - \mathbf{x}_0 - \ell\mathbf{e})^T \mathcal{D}^2(\mathbf{u}(\mathbf{x}_0 + \ell\mathbf{e} + t(\mathbf{x} - \mathbf{x}_0 - \ell\mathbf{e}))) (\mathbf{x} - \mathbf{x}_0 - \ell\mathbf{e}) dt. \end{aligned} \quad (5.43)$$

Write the variational formulation of (5.40) with δ as test function. Afterwards, apply the expansion (5.42) of \mathbf{u} . It follows that

$$\begin{aligned}
& \int_{\Omega} \mathbf{A}\varepsilon(\boldsymbol{\delta}) : \varepsilon(\boldsymbol{\delta})dV + \int_{\Omega_{\rho}} \boldsymbol{\mathcal{S}}(\boldsymbol{\delta}) \cdot \boldsymbol{\delta}dV + \kappa(\rho) \left(\int_{\omega_B} \boldsymbol{\delta} \cdot \mathbf{e}dV - \int_{\omega_A} \boldsymbol{\delta} \cdot \mathbf{e}dV \right)^2 \\
&= - \int_{\Omega_{\rho}} \mathbf{A}(\mathbf{v} \otimes \nabla\theta)^s : \varepsilon(\boldsymbol{\delta})dV + \int_{\Omega_{\rho}} \mathbf{A}\varepsilon(\mathbf{v})\nabla\theta \cdot \boldsymbol{\delta}dV \\
&\quad - \kappa(\rho) \left(\int_{\omega_B} \mathbf{R}_u^B \cdot \mathbf{e}dV - \int_{\omega_A} \mathbf{R}_u^A \cdot \mathbf{e}dV \right) \left(\int_{\omega_B} \boldsymbol{\delta} \cdot \mathbf{e}dV - \int_{\omega_A} \boldsymbol{\delta} \cdot \mathbf{e}dV \right).
\end{aligned}$$

The quadratic term containing pre-existing springs is positive

$$\int_{\Omega_{\rho}} \boldsymbol{\mathcal{S}}(\boldsymbol{\delta}) \cdot \boldsymbol{\delta}dV = \sum_{i=1}^n \kappa_i \left(\int_{\omega_{B_i}} \boldsymbol{\delta} \cdot \mathbf{e}dV - \int_{\omega_{A_i}} \boldsymbol{\delta} \cdot \mathbf{e}dV \right)^2 \geq 0.$$

The left hand side is then bounded from below using the Poincaré-Korn inequality (as $\boldsymbol{\delta}$ vanishes on Γ_D)

$$\exists C > 0, \left| \int_{\Omega} \mathbf{A}\varepsilon(\boldsymbol{\delta}) : \varepsilon(\boldsymbol{\delta})dV \right| \geq C \|\varepsilon(\boldsymbol{\delta})\|_{L^2(\Omega)}^2.$$

The right hand side is bounded using the L^{∞} -norms of \mathbf{v} and $\varepsilon(\mathbf{v})$ since $\nabla\theta = 0$ in the influence area of the inclusions

$$\begin{aligned}
\left| \int_{\Omega_{\rho}} \mathbf{A}(\mathbf{v} \otimes \nabla\theta)^s : \varepsilon(\boldsymbol{\delta})dV \right| + \left| \int_{\Omega_{\rho}} \mathbf{A}\varepsilon(\mathbf{v})\nabla\theta \cdot \boldsymbol{\delta}dV \right| &\leq C \|\mathbf{v}\|_{L^{\infty}(\Omega \setminus \mathcal{U}_-)} \|\varepsilon(\boldsymbol{\delta})\|_{L^2(\Omega)} \\
&\quad + C \|\varepsilon(\mathbf{v})\|_{L^{\infty}(\Omega \setminus \mathcal{U}_-)} \|\boldsymbol{\delta}\|_{L^2(\Omega)} \\
&\leq C \rho |\xi_u(\rho)| \|\varepsilon(\boldsymbol{\delta})\|_{L^2(\Omega)} \leq C \frac{\kappa(\rho)}{1 + C \frac{\kappa(\rho)}{\rho}} \|\varepsilon(\boldsymbol{\delta})\|_{L^2(\Omega)}.
\end{aligned}$$

Noticing that $\mathbf{x} - \mathbf{x}_0$ is of the order of ρ in a neighbourhood of \mathbf{x}_0 , one deduces for some constant $C > 0$ independent of ρ that

$$|\mathbf{R}_u^A| \leq C\rho^2 \text{ in } \omega_A. \tag{5.44}$$

A similar estimate can be established for \mathbf{R}_u^B and it results that

$$\exists C > 0, \left| \int_{\omega_B} \mathbf{R}_u^B \cdot \mathbf{e}dV - \int_{\omega_A} \mathbf{R}_u^A \cdot \mathbf{e}dV \right| \leq C\rho^2.$$

Let us multiply (5.40) by \mathbf{v}_{ρ} , integrate by parts, and then apply (5.42).

$$\begin{aligned}
& \kappa(\rho)(\mathbf{u}(\mathbf{x}_0 + \mathbf{le}) - \mathbf{u}(\mathbf{x}_0)) \cdot \mathbf{e} \left(\int_{\omega_B} \boldsymbol{\delta} \cdot \mathbf{e}dV - \int_{\omega_A} \boldsymbol{\delta} \cdot \mathbf{e}dV \right) = \int_{\Omega_{\rho}} \mathbf{A}(\mathbf{v} \otimes \nabla\theta)^s : (\mathbf{v} \otimes \nabla\theta)^s dV \\
&+ \int_{\Omega_{\rho}} \mathbf{A}(\mathbf{v} \otimes \nabla\theta)^s : \varepsilon(\mathbf{v})\theta dV + \int_{\Omega_{\rho}} \mathbf{A}(\mathbf{v} \otimes \nabla\theta)^s : \varepsilon(\boldsymbol{\delta})dV - \int_{\Omega_{\rho}} \mathbf{A}\varepsilon(\mathbf{v})\nabla\theta \cdot \mathbf{v}\theta dV - \int_{\Omega_{\rho}} \mathbf{A}\varepsilon(\mathbf{v})\nabla\theta \cdot \boldsymbol{\delta}dV \\
&+ \kappa(\rho) \left(\int_{\omega_B} \mathbf{R}_u^B \cdot \mathbf{e}dV - \int_{\omega_A} \mathbf{R}_u^A \cdot \mathbf{e}dV \right) \left(\int_{\omega_B} \mathbf{v} \cdot \mathbf{e}dV - \int_{\omega_A} \mathbf{v} \cdot \mathbf{e}dV \right).
\end{aligned}$$

It follows that

$$\begin{aligned} \kappa(\rho) \left| \int_{\omega_B} \boldsymbol{\delta} \cdot \mathbf{e} dV - \int_{\omega_A} \boldsymbol{\delta} \cdot \mathbf{e} dV \right| &\leq C \|\mathbf{v}\|_{L^\infty(\Omega \setminus \mathcal{U}_-)}^2 + C \|\mathbf{v}\|_{L^\infty(\Omega \setminus \mathcal{U}_-)} \|\varepsilon(\mathbf{v})\|_{L^\infty(\Omega \setminus \mathcal{U}_-)} \\ &\quad + C \|\mathbf{v}\|_{L^\infty(\Omega \setminus \mathcal{U}_-)} \|\varepsilon(\boldsymbol{\delta})\|_{L^2(\Omega)} + C \|\varepsilon(\mathbf{v})\|_{L^\infty(\Omega \setminus \mathcal{U}_-)} \|\mathbf{v}\|_{L^\infty(\Omega \setminus \mathcal{U}_-)} \\ &\quad + C \|\varepsilon(\mathbf{v})\|_{L^\infty(\Omega \setminus \mathcal{U}_-)} \|\boldsymbol{\delta}\|_{L^2(\Omega)} + C \kappa(\rho) \rho^2 |\xi_u(\rho)| \\ &\leq C \rho^2 |\xi_u(\rho)|^2 + C \kappa(\rho) \rho^2 |\xi_u(\rho)| + C \rho |\xi_u(\rho)| \|\varepsilon(\boldsymbol{\delta})\|_{L^2(\Omega)}. \end{aligned}$$

Remark 45. The term $\left| \int_{\omega_B} \boldsymbol{\delta} \cdot \mathbf{e} dV - \int_{\omega_A} \boldsymbol{\delta} \cdot \mathbf{e} dV \right|$ can be naively bounded using Cauchy-Schwarz inequality such that $\exists C > 0$, $\left| \int_{\omega_B} \boldsymbol{\delta} \cdot \mathbf{e} dV - \int_{\omega_A} \boldsymbol{\delta} \cdot \mathbf{e} dV \right| \leq C \rho^{-3/2} \|\boldsymbol{\delta}\|_{L^2(\Omega)}$. However, this estimate is too restrictive for the rest of the asymptotic analysis.

Regrouping all terms finally leads to

$$\|\varepsilon(\boldsymbol{\delta})\|_{L^2(\Omega)}^2 \leq C \rho |\xi_u(\rho)| \|\varepsilon(\boldsymbol{\delta})\|_{L^2(\Omega)} + C \rho^4 |\xi_u(\rho)|^2 + C \kappa(\rho) \rho^4 |\xi_u(\rho)|.$$

Setting the following notations for a quick manipulation $X = \|\varepsilon(\boldsymbol{\delta})\|_{L^2(\Omega)}$, $a = C \rho |\xi_u(\rho)|$ and $b = C \rho^4 |\xi_u(\rho)|^2 + C \kappa(\rho) \rho^4 |\xi_u(\rho)|$, where X , a and b are non-negative. It comes that

$$\begin{aligned} \iff X^2 &\leq 2aX + b, \\ \iff |X - a|^2 &\leq a^2 + b, \\ \iff X &\leq Ca + \sqrt{b}. \end{aligned}$$

As a result, there exists a constant $C > 0$ independent of ρ such that

$$\|\varepsilon(\boldsymbol{\delta})\|_{L^2(\Omega)} \leq C \rho |\xi_u(\rho)| + C \rho^2 |\xi_u(\rho)| + C \rho^2 \sqrt{\kappa(\rho) |\xi_u(\rho)|} \leq C \rho |\xi_u(\rho)| \text{ for } k > 0.$$

□

5.2.2 Adjoint state

A similar analysis can be carried out for the perturbed adjoint state \mathbf{p}_ρ associated to the perturbed displacement field \mathbf{u}_ρ . It solves

$$\left\{ \begin{array}{ll} -\operatorname{div}(\mathbf{A}\varepsilon(\mathbf{p}_\rho)) + \mathcal{S}(\mathbf{p}_\rho) = -\mathbf{F}'(\mathbf{u}) \mathbb{1}_{\Omega_1} & \text{in } \Omega_\rho \\ -\operatorname{div}(\mathbf{A}\varepsilon(\mathbf{p}_\rho)) - \frac{\kappa(\rho)}{|\omega_A|} \left(\int_{\omega_B} \mathbf{p}_\rho \cdot \mathbf{e} dV - \int_{\omega_A} \mathbf{p}_\rho \cdot \mathbf{e} dV \right) \mathbf{e} = \mathbf{0} & \text{in } \omega_A \\ -\operatorname{div}(\mathbf{A}\varepsilon(\mathbf{p}_\rho)) + \frac{\kappa(\rho)}{|\omega_B|} \left(\int_{\omega_B} \mathbf{p}_\rho \cdot \mathbf{e} dV - \int_{\omega_A} \mathbf{p}_\rho \cdot \mathbf{e} dV \right) \mathbf{e} = \mathbf{0} & \text{in } \omega_B \\ \mathbf{A}\varepsilon(\mathbf{p}_\rho) \mathbf{n} = -\mathbf{G}'(\mathbf{u}) & \text{on } \Gamma_N \\ \mathbf{p}_\rho = \mathbf{0} & \text{on } \Gamma_D \end{array} \right. \quad (5.45)$$

Remark 46. It has already been noticed in [8] that the adjoint problem (5.45) is not standard since the right hand side depends on \mathbf{u} and not on \mathbf{u}_ρ as expected in the perturbed domain.

Let us define \mathbf{q}_ρ the difference between the perturbed adjoint and the adjoint state of the background domain, $\mathbf{q}_\rho = \mathbf{p}_\rho - \mathbf{p}$, which satisfies

$$\left\{ \begin{array}{ll} -\operatorname{div}(\mathbf{A}\varepsilon(\mathbf{q}_\rho)) + \mathcal{S}(\mathbf{q}_\rho) = \mathbf{0} & \text{in } \Omega_\rho \\ -\operatorname{div}(\mathbf{A}\varepsilon(\mathbf{q}_\rho)) - \frac{\kappa(\rho)}{|\omega_A|} \left(\int_{\omega_B} \mathbf{f}(\mathbf{q}_\rho + \mathbf{p}) \cdot \mathbf{e} dV - \int_{\omega_A} \mathbf{f}(\mathbf{q}_\rho + \mathbf{p}) \cdot \mathbf{e} dV \right) \mathbf{e} = \mathbf{0} & \text{in } \omega_A \\ -\operatorname{div}(\mathbf{A}\varepsilon(\mathbf{q}_\rho)) + \frac{\kappa(\rho)}{|\omega_A|} \left(\int_{\omega_B} \mathbf{f}(\mathbf{q}_\rho + \mathbf{p}) \cdot \mathbf{e} dV - \int_{\omega_A} \mathbf{f}(\mathbf{q}_\rho + \mathbf{p}) \cdot \mathbf{e} dV \right) \mathbf{e} = \mathbf{0} & \text{in } \omega_B \\ \mathbf{A}\varepsilon(\mathbf{q}_\rho)\mathbf{n} = \mathbf{0} & \text{on } \Gamma_N \\ \mathbf{q}_\rho = \mathbf{0} & \text{on } \Gamma_D \end{array} \right. . \quad (5.46)$$

The two first equations of (5.46) have zero right hand side because of the non-standard adjoint in the perturbed domain (5.45). We also introduce the functions \mathbf{q}_a and \mathbf{q}_b and the rescaled function

$$\mathbf{q}(\mathbf{x}) = \mathbf{q}_a \left(\frac{\mathbf{x} - \mathbf{x}_0}{\rho} \right) + \mathbf{q}_b \left(\frac{\mathbf{x} - \mathbf{x}_0 - \ell \mathbf{e}}{\rho} \right), \quad (5.47)$$

such that \mathbf{q}_a and \mathbf{q}_b are respectively similar to \mathbf{v}_a and \mathbf{v}_b .

Proposition 12. *Let $\theta \in \mathcal{C}_c^\infty(\Omega)$ be a cut-off function with compact support $\mathcal{U}_+ \subset \Omega$ such that $\theta \equiv 1$ in a neighborhood $\mathcal{U}_- \subset \mathcal{U}_+$ of \mathbf{x}_0 and $\mathbf{x}_0 + \ell \mathbf{e}$. We have*

$$\mathbf{q}_\rho = \theta \mathbf{q} + \boldsymbol{\eta}, \quad (5.48)$$

where $\boldsymbol{\eta}$ is a remainder term as can be checked by these estimates of the L^2 -norms of \mathbf{q} and $\varepsilon(\mathbf{q})$ and the H^1 -norm of $\boldsymbol{\eta}$. They are given, according to the value of the exponent k , by

	$\ \mathbf{q}\ _{L^2(\Omega)}$	$\ \varepsilon(\mathbf{q})\ _{L^2(\Omega)}$	$\ \boldsymbol{\eta}\ _{H^1(\Omega)}$
$k > 1$	$O(\rho^k)$	$O(\rho^{k-1/2})$	$O(\rho^k)$
$k = 1$	$O(\rho)$	$O(\sqrt{\rho})$	$O(\rho)$
$k < 1$	$O(\rho)$	$O(\sqrt{\rho})$	$O(\rho)$

Proof. The function $\boldsymbol{\eta}$ solves

$$\left\{ \begin{array}{ll} -\operatorname{div}(\mathbf{A}\boldsymbol{\varepsilon}(\boldsymbol{\eta})) + \mathcal{S}(\boldsymbol{\eta}) = \operatorname{div}\mathbf{A}(\mathbf{q} \otimes \nabla\theta)^s + \mathbf{A}\boldsymbol{\varepsilon}(\mathbf{q})\nabla\theta & \text{in } \Omega_\rho \\ -\operatorname{div}(\mathbf{A}\boldsymbol{\varepsilon}(\boldsymbol{\eta})) - \frac{\kappa(\rho)}{|\omega_A|} \left(\int_{\omega_B} \boldsymbol{\eta} \cdot \mathbf{e} dV - \int_{\omega_A} \boldsymbol{\eta} \cdot \mathbf{e} dV \right) \mathbf{e} & \\ = \frac{\kappa(\rho)}{|\omega_A|} \left(\int_{\omega_B} \mathbf{p} \cdot \mathbf{e} dV - \int_{\omega_A} \mathbf{p} \cdot \mathbf{e} dV - (\mathbf{p}(\mathbf{x}_0 + \ell\mathbf{e}) - \mathbf{p}(\mathbf{x}_0)) \cdot \mathbf{e} \right) \mathbf{e} & \text{in } \omega_A \\ -\operatorname{div}(\mathbf{A}\boldsymbol{\varepsilon}(\boldsymbol{\eta})) + \frac{\kappa(\rho)}{|\omega_B|} \left(\int_{\omega_B} \boldsymbol{\eta} \cdot \mathbf{e} dV - \int_{\omega_A} \boldsymbol{\eta} \cdot \mathbf{e} dV \right) \mathbf{e} & \\ = -\frac{\kappa(\rho)}{|\omega_B|} \left(\int_{\omega_B} \mathbf{p} \cdot \mathbf{e} dV - \int_{\omega_A} \mathbf{p} \cdot \mathbf{e} dV - (\mathbf{p}(\mathbf{x}_0 + \ell\mathbf{e}) - \mathbf{p}(\mathbf{x}_0)) \cdot \mathbf{e} \right) \mathbf{e} & \text{in } \omega_B \\ \mathbf{A}\boldsymbol{\varepsilon}(\boldsymbol{\eta})\mathbf{n} = \mathbf{0} & \text{on } \Gamma_N \\ \boldsymbol{\eta} = \mathbf{0} & \text{on } \Gamma_D \end{array} \right. \quad (5.49)$$

Proposition 12 is proved by going back over the proof of Proposition 11 and by substituting respectively \mathbf{u} and \mathbf{v}_ρ with \mathbf{p} and \mathbf{q}_ρ . \square

5.2.3 Proof of the main result

Theorem 4 can now be proved using the approximations of \mathbf{u}_ρ and \mathbf{p}_ρ . Let us first recall the objective function (5.4) in the background domain.

$$J_0(\Omega) = \int_{\Omega_1} F(\mathbf{u})dV + \int_{\Gamma_N} G(\mathbf{u})dS.$$

A Taylor expansion at first-order with exact remainder of the objective function in the perturbed domain is

$$\begin{aligned} J_\rho(\Omega) &= \int_{\Omega_1} F(\mathbf{u}_\rho)dV + \int_{\Gamma_N} G(\mathbf{u}_\rho)dS = \int_{\Omega_1} F(\mathbf{u} + \mathbf{v}_\rho)dV + \int_{\Gamma_N} G(\mathbf{u} + \mathbf{v}_\rho)dS \\ &= J_0(\Omega) + \int_{\Omega_1} \mathbf{F}'(\mathbf{u}) \cdot \mathbf{v}_\rho dV + \int_{\Gamma_N} \mathbf{G}'(\mathbf{u}) \cdot \mathbf{v}_\rho dS + \frac{1}{2} \int_{\Omega_1} \mathbf{v}_\rho^T F''(\bar{\mathbf{u}}) \mathbf{v}_\rho dV + \frac{1}{2} \int_{\Gamma_N} \mathbf{v}_\rho^T G''(\bar{\mathbf{u}}) \mathbf{v}_\rho dS. \end{aligned}$$

The exact remainder is bounded using assumptions (5.5) and Proposition 11

$$\begin{aligned} \left| \int_{\Omega_1} \mathbf{v}_\rho^T F''(\bar{\mathbf{u}}) \mathbf{v}_\rho dV \right| &\leq C \|\mathbf{v}_\rho\|_{L^2(\Omega)}^2 \leq C \rho^2 |\xi_u(\rho)|^2 \leq C \frac{\kappa(\rho)^2}{(1 + C \frac{\kappa(\rho)}{\rho})^2}, \\ \left| \int_{\Gamma_N} \mathbf{v}_\rho^T G''(\bar{\mathbf{u}}) \mathbf{v}_\rho dS \right| &\leq C \|\mathbf{v}_\rho\|_{L^2(\Gamma_N)}^2 \leq C \|\boldsymbol{\delta}\|_{L^2(\Gamma_N)}^2 \text{ because } \theta = 0 \text{ on } \Gamma_N \\ &\leq C \|\boldsymbol{\delta}\|_{H^1(\Omega)}^2 \leq C \rho^2 |\xi_u(\rho)|^2 \leq C \frac{\kappa(\rho)^2}{(1 + C \frac{\kappa(\rho)}{\rho})^2}. \end{aligned}$$

The occurrence of \mathbf{v}_ρ in the expansion of $J_\rho(\Omega)$ justifies the use of an adjoint state. Moreover, this expansion involves \mathbf{u} instead of \mathbf{u}_ρ . That is why (5.45) has been modified and is not the standard adjoint equation. The variational formulation of (5.45) with \mathbf{v}_ρ as test function reads

$$\begin{aligned}
& \int_{\Omega_1} \mathbf{F}'(\mathbf{u}) \cdot \mathbf{v}_\rho dV + \int_{\Gamma_N} \mathbf{G}'(\mathbf{u}) \cdot \mathbf{v}_\rho dS \\
&= \kappa(\rho) \left(\int_{\omega_B} \mathbf{u} \cdot \mathbf{e} dV - \int_{\omega_A} \mathbf{u} \cdot \mathbf{e} dV \right) \left(\int_{\omega_B} \mathbf{p}_\rho \cdot \mathbf{e} dV - \int_{\omega_A} \mathbf{p}_\rho \cdot \mathbf{e} dV \right) \\
&= \kappa(\rho) \left(\int_{\omega_B} \mathbf{u} \cdot \mathbf{e} dV - \int_{\omega_A} \mathbf{u} \cdot \mathbf{e} dV \right) \left(\int_{\omega_B} \mathbf{p} \cdot \mathbf{e} dV - \int_{\omega_A} \mathbf{p} \cdot \mathbf{e} dV \right) \\
&\quad + \kappa(\rho) \left(\int_{\omega_B} \mathbf{u} \cdot \mathbf{e} dV - \int_{\omega_A} \mathbf{u} \cdot \mathbf{e} dV \right) \left(\int_{\omega_B} \mathbf{q} \cdot \mathbf{e} dV - \int_{\omega_A} \mathbf{q} \cdot \mathbf{e} dV \right) \\
&\quad + \kappa(\rho) \left(\int_{\omega_B} \mathbf{u} \cdot \mathbf{e} dV - \int_{\omega_A} \mathbf{u} \cdot \mathbf{e} dV \right) \left(\int_{\omega_B} \boldsymbol{\eta} \cdot \mathbf{e} dV - \int_{\omega_A} \boldsymbol{\eta} \cdot \mathbf{e} dV \right).
\end{aligned}$$

These three terms are estimated one by one.

★ 1st term

We define \mathbf{R}_p^A and \mathbf{R}_p^B similarly to \mathbf{R}_u^A and \mathbf{R}_u^B . They are the integral remainder of the expansion of \mathbf{p} around \mathbf{x}_0 and $\mathbf{x}_0 + \ell\mathbf{e}$. They are both of the order of ρ^2 in ω_A and ω_B . Both the background solution \mathbf{u} and the adjoint \mathbf{p} are expanded with integral remainder. The first term is then estimated as

$$\begin{aligned}
& \kappa(\rho) \left(\int_{\omega_B} \mathbf{u} \cdot \mathbf{e} dV - \int_{\omega_A} \mathbf{u} \cdot \mathbf{e} dV \right) \left(\int_{\omega_B} \mathbf{p} \cdot \mathbf{e} dV - \int_{\omega_A} \mathbf{p} \cdot \mathbf{e} dV \right) \\
&= \kappa(\rho) (\mathbf{u}(\mathbf{x}_0 + \ell\mathbf{e}) - \mathbf{u}(\mathbf{x}_0)) \cdot \mathbf{e} (\mathbf{p}(\mathbf{x}_0 + \ell\mathbf{e}) - \mathbf{p}(\mathbf{x}_0)) \cdot \mathbf{e} + O(\kappa(\rho)\rho^2) + O(\kappa(\rho)\rho^4).
\end{aligned}$$

The leading term will be an element of the topological derivative and will contribute to the scaling term $s(\rho)$. The bounded one will be part of the remainder term $\mathcal{R}(s(\rho))$.

★ 2nd term

Let us set the notation $\xi_p(\rho)$ in an equivalent manner as $\xi_u(\rho)$. It holds

$$\xi_p(\rho) = \frac{\frac{\kappa(\rho)}{\rho|\omega|}}{1 + \frac{\kappa(\rho)}{\rho|\omega|} \left(\frac{1}{\tau_A} + \frac{1}{\tau_B} \right)} (\mathbf{p}(\mathbf{x}_0 + \ell\mathbf{e}) - \mathbf{p}(\mathbf{x}_0)) \cdot \mathbf{e}, \quad \int_{\omega} \mathbf{q}_a \cdot \mathbf{e} dV = \frac{\xi_p(\rho)}{\tau_A} \quad \text{and} \quad \int_{\omega} \mathbf{q}_b \cdot \mathbf{e} dV = -\frac{\xi_p(\rho)}{\tau_B}. \tag{5.50}$$

Then, it comes

$$\begin{aligned}
& \kappa(\rho) \left(\int_{\omega_B} \mathbf{f} \mathbf{u} \cdot \mathbf{e} dV - \int_{\omega_A} \mathbf{f} \mathbf{u} \cdot \mathbf{e} dV \right) \left(\int_{\omega_B} \mathbf{f} \mathbf{q} \cdot \mathbf{e} dV - \int_{\omega_A} \mathbf{f} \mathbf{q} \cdot \mathbf{e} dV \right) \\
&= \kappa(\rho) \left((\mathbf{u}(\mathbf{x}_0 + \ell \mathbf{e}) - \mathbf{u}(\mathbf{x}_0)) \cdot \mathbf{e} + \int_{\omega_B} \mathbf{R}_u^B \cdot \mathbf{e} dV - \int_{\omega_A} \mathbf{R}_u^A \cdot \mathbf{e} dV \right) \int_{\omega} (\mathbf{q}_b - \mathbf{q}_a) \cdot \mathbf{e} dV \\
&= - \frac{\frac{\kappa(\rho)}{\rho|\omega|} \left(\frac{1}{\tau_A} + \frac{1}{\tau_B} \right)}{1 + \frac{\kappa(\rho)}{\rho|\omega|} \left(\frac{1}{\tau_A} + \frac{1}{\tau_B} \right)} \kappa(\rho) (\mathbf{u}(\mathbf{x}_0 + \ell \mathbf{e}) - \mathbf{u}(\mathbf{x}_0)) \cdot \mathbf{e} (\mathbf{p}(\mathbf{x}_0 + \ell \mathbf{e}) - \mathbf{p}(\mathbf{x}_0)) \cdot \mathbf{e} + O \left(\frac{\kappa(\rho)^2 \rho}{1 + C \frac{\kappa(\rho)}{\rho}} \right).
\end{aligned}$$

★ 3rd term

The last term is expected to be a remainder term since it involves $\boldsymbol{\eta}$. Let us begin with a rescaling.

$$\begin{aligned}
& \kappa(\rho) \left(\int_{\omega_B} \mathbf{f} \mathbf{u} \cdot \mathbf{e} dV - \int_{\omega_A} \mathbf{f} \mathbf{u} \cdot \mathbf{e} dV \right) \left(\int_{\omega_B} \mathbf{f} \boldsymbol{\eta} \cdot \mathbf{e} dV - \int_{\omega_A} \mathbf{f} \boldsymbol{\eta} \cdot \mathbf{e} dV \right) \\
&= \kappa(\rho) (\mathbf{u}(\mathbf{x}_0 + \ell \mathbf{e}) - \mathbf{u}(\mathbf{x}_0)) \cdot \mathbf{e} \left(\int_{\omega_B} \mathbf{f} \boldsymbol{\eta} \cdot \mathbf{e} dV - \int_{\omega_A} \mathbf{f} \boldsymbol{\eta} \cdot \mathbf{e} dV \right) \\
&+ \kappa(\rho) \left(\int_{\omega_B} \mathbf{R}_u^B \cdot \mathbf{e} dV - \int_{\omega_A} \mathbf{R}_u^A \cdot \mathbf{e} dV \right) \left(\int_{\omega_B} \mathbf{f} \boldsymbol{\eta} \cdot \mathbf{e} dV - \int_{\omega_A} \mathbf{f} \boldsymbol{\eta} \cdot \mathbf{e} dV \right).
\end{aligned}$$

To ease the notation, we set $X = \left| \int_{\omega_B} \mathbf{f} \boldsymbol{\eta} \cdot \mathbf{e} dV - \int_{\omega_A} \mathbf{f} \boldsymbol{\eta} \cdot \mathbf{e} dV \right|$. Multiplying (5.49) by $\boldsymbol{\eta}$ and integrating by parts twice give us

$$\kappa(\rho) X^2 \leq C \rho |\xi_p(\rho)| \|\varepsilon(\boldsymbol{\eta})\|_{L^2(\Omega)} + C \kappa(\rho) \rho^2 X.$$

It leads to

$$X \leq C \sqrt{\frac{\rho |\xi_p(\rho)|}{\kappa(\rho)}} \sqrt{\|\varepsilon(\boldsymbol{\eta})\|_{L^2(\Omega)}} + C \rho^2.$$

The third term is then bounded as follows

$$\begin{aligned}
& \exists C > 0, \kappa(\rho) \left| \int_{\omega_B} \mathbf{f} \mathbf{u} \cdot \mathbf{e} dV - \int_{\omega_A} \mathbf{f} \mathbf{u} \cdot \mathbf{e} dV \right| \left| \int_{\omega_B} \mathbf{f} \boldsymbol{\eta} \cdot \mathbf{e} dV - \int_{\omega_A} \mathbf{f} \boldsymbol{\eta} \cdot \mathbf{e} dV \right| \\
&\leq C \kappa(\rho)^{1/2} \rho |\xi_p(\rho)| + C \kappa(\rho)^{1/2} \rho^3 |\xi_p(\rho)| + C \kappa(\rho) \rho^2 + C \kappa(\rho) \rho^4 \leq C \frac{\kappa(\rho)^{3/2}}{1 + C \frac{\kappa(\rho)}{\rho}} + C \kappa(\rho) \rho^2.
\end{aligned}$$

Regrouping all leading terms gives

$$\begin{aligned}
& \frac{\kappa(\rho)}{1 + \frac{\kappa(\rho)}{\rho|\omega|} \left(\frac{1}{\tau_A} + \frac{1}{\tau_B} \right)} (\mathbf{u}(\mathbf{x}_0 + \ell \mathbf{e}) - \mathbf{u}(\mathbf{x}_0)) \cdot \mathbf{e} (\mathbf{p}(\mathbf{x}_0 + \ell \mathbf{e}) - \mathbf{p}(\mathbf{x}_0)) \cdot \mathbf{e} \\
&= \left(\frac{1}{\kappa(\rho)} + \frac{1}{\rho|\omega|} \left(\frac{1}{\tau_A} + \frac{1}{\tau_B} \right) \right)^{-1} (\mathbf{u}(\mathbf{x}_0 + \ell \mathbf{e}) - \mathbf{u}(\mathbf{x}_0)) \cdot \mathbf{e} (\mathbf{p}(\mathbf{x}_0 + \ell \mathbf{e}) - \mathbf{p}(\mathbf{x}_0)) \cdot \mathbf{e}.
\end{aligned}$$

This term is then expanded with respect to ρ . The resulting leading term shall be the topological derivative and the inherent remainder term, denoted $\mathcal{R}(DJ(\mathbf{x}_0, \mathbf{e}))$, will be part of remainder term of the asymptotic expansion $\mathcal{R}(s(\rho))$, that reads

$$\mathcal{R}(s(\rho)) = O\left(\frac{\kappa(\rho)^2}{\left(1 + C\frac{\kappa(\rho)}{\rho}\right)^2}\right) + O(\kappa(\rho)\rho^2) + O\left(\frac{\kappa(\rho)^2\rho}{1 + C\frac{\kappa(\rho)}{\rho}}\right) + O\left(\frac{\kappa(\rho)^{3/2}}{1 + C\frac{\kappa(\rho)}{\rho}}\right) + \mathcal{R}(DJ(\mathbf{x}_0, \mathbf{e})).$$

Remark 47. In 2d, the leading term is

$$\left(\frac{1}{\kappa(\rho)} + \frac{1}{|\omega|} \left(\frac{1}{\tau_A(\rho)} + \frac{1}{\tau_B(\rho)}\right)\right)^{-1} (\mathbf{u}(\mathbf{x}_0 + \ell\mathbf{e}) - \mathbf{u}(\mathbf{x}_0)) \cdot \mathbf{e} (\mathbf{p}(\mathbf{x}_0 + \ell\mathbf{e}) - \mathbf{p}(\mathbf{x}_0)) \cdot \mathbf{e}.$$

The coefficients are $\tau_A(\rho)$ and $\tau_B(\rho)$ depend on material properties and are of the order of $-\frac{1}{\ln(\rho)}$. Thus, for all $k > 0$, the largest term of the expansion with respect to ρ is

$$\kappa(\rho)(\mathbf{u}(\mathbf{x}_0 + \ell\mathbf{e}) - \mathbf{u}(\mathbf{x}_0)) \cdot \mathbf{e} (\mathbf{p}(\mathbf{x}_0 + \ell\mathbf{e}) - \mathbf{p}(\mathbf{x}_0)) \cdot \mathbf{e}.$$

Contrary to the 3d case, the topological derivative has a unique expression for all $k > 0$.

For $k > 1$

For these values of k , the topological derivative is given by

$$s(\rho) = \rho^k \text{ and } j(K, \tau_A, \tau_B) = K.$$

The remainder term is the largest term of ρ , so $\mathcal{R}(s(\rho)) = \begin{cases} O(\rho^{k+2}) & \text{if } k > 4 \\ O(\rho^{3k/2}) & \text{if } 2 \leq k \leq 4 \\ O(\rho^{2k-1}) & \text{if } k < 2 \end{cases}$.

For $k = 1$

It is easy to find $s(\rho) = \rho$, also $j(K, \tau_A, \tau_B) = \left(\frac{1}{K} + \frac{1}{|\omega|} \left(\frac{1}{\tau_A} + \frac{1}{\tau_B}\right)\right)^{-1}$ and

$$\mathcal{R}(s(\rho)) = O(\rho^{3/2}).$$

For $k < 1$

These values of k imply $\lim_{\rho \rightarrow 0} \rho^{k-1} = \infty$, which lead to

$$\left(1 + \frac{1}{|\omega|} \left(\frac{1}{\tau_A} + \frac{1}{\tau_B}\right) K \rho^{k-1}\right)^{-1} = \left(\frac{1}{|\omega|} \left(\frac{1}{\tau_A} + \frac{1}{\tau_B}\right) K \rho^{k-1}\right)^{-1} + O(\rho^{2-2k}).$$

It follows that $s(\rho) = \rho$, so that $j(K, \tau_A, \tau_B) = \left(\frac{1}{|\omega|} \left(\frac{1}{\tau_A} + \frac{1}{\tau_B}\right)\right)^{-1}$ and

$$\mathcal{R}(s(\rho)) = \begin{cases} O(\rho^{2-k}) & \text{if } k \geq 2/3 \\ O(\rho^{1+k/2}) & \text{if } k < 2/3 \end{cases}.$$

That last estimate gives a condition on k . Definition 6 actually states that $\lim_{\rho \rightarrow 0} \frac{\mathcal{R}(s(\rho))}{s(\rho)} = 0$.

Since $s(\rho)$ is equal to ρ when $k < 1$, this condition is fulfilled for k such that

$$\frac{k}{2} + 1 > 1 \iff k > 0. \quad (5.51)$$

5.3 Numerical illustrations in 2d

The small spring model is illustrated with several configurations on a simple but meaningful academic use case in 2d. The system is a plate of 2 units long and 1 unit wide with an opening gap through its center. The mesh contains 114 274 triangular elements with a minimal and maximal size of 3.3×10^{-3} and 1.2×10^{-2} . The plate is clamped on the bottom and is loaded on the upper border. The Young's modulus is taken equal to 10 and the Poisson's coefficient is 0.3. Let us take $\rho = 2.5 \times 10^{-2}$ and $\ell = 0.3$. The stiffness of the spring is $K = 5$. All these material properties are adimensional and can be changed as the user wants.

5.3.1 Analysis with one spring

Test of the topological derivative to put a first spring

The problem is to place a small spring in order to decrease the compliance $J(\Omega) = \int_{\Gamma_N} \mathbf{g} \cdot \mathbf{u} dS$.

The new compliance, *i.e.* with the spring, is predicted with the estimator function

$$\mathcal{E}(\Omega) = J_0(\Omega) + s(\rho)DJ(\mathbf{x}_0, \mathbf{e}). \quad (5.52)$$

It stands for the expected value of the compliance given by the asymptotic expansion of the objective function in the perturbed domain. Since the objective is the compliance, the system is self-adjoint. So the adjoint state \mathbf{p} satisfies $\mathbf{p} = -\mathbf{u}$. The topological derivative then reads

$$DJ(\mathbf{x}_0, \mathbf{e}) = -K(\mathbf{u}(\mathbf{x}_0 + \ell\mathbf{e}) - \mathbf{u}(\mathbf{x}_0)) \cdot \mathbf{e}. \quad (5.53)$$

One can notice that $DJ(\mathbf{x}_0, \mathbf{e})$ is the energy of the non-rescaled spring. Several load cases, depicted in Fig. 5.4, have been used to compute the topological derivative in order to search simultaneously the optimal location \mathbf{x}_0 and orientation \mathbf{e} .

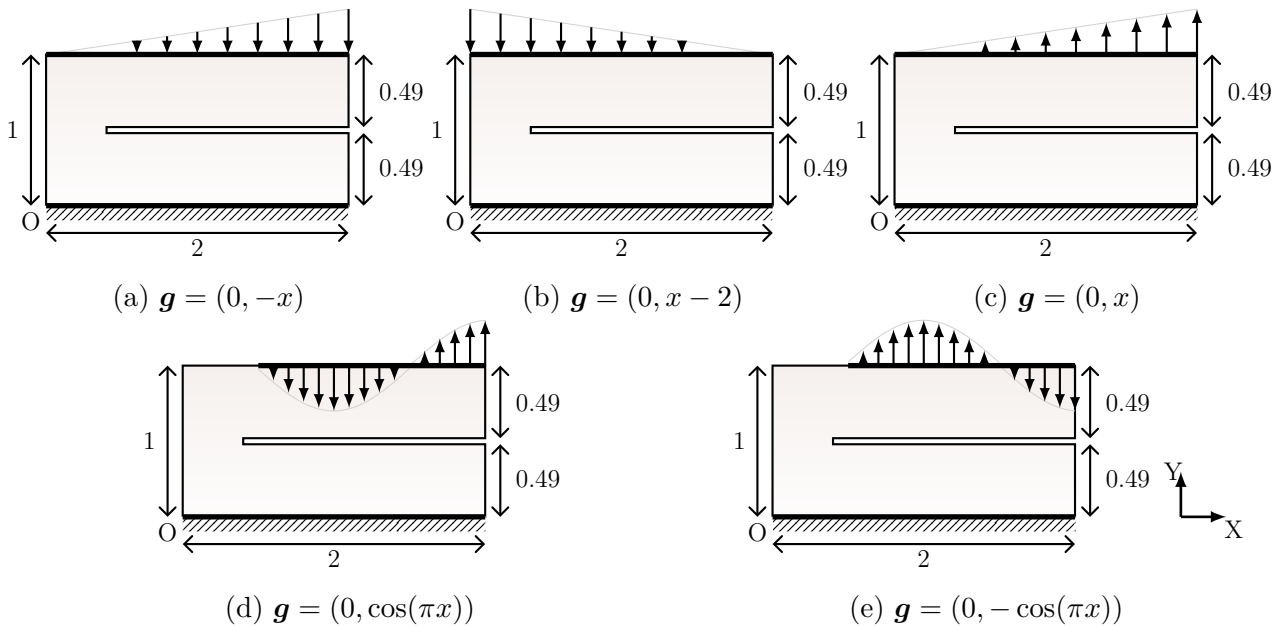


Figure 5.4: Potential load cases

All tests provide satisfactory results (see Fig. 5.5). The addition of a small spring decreases the compliance. Recalling that the topological derivative has the same expression for all $k > 0$ in 2d, the optimal location \mathbf{x}_0 and orientation \mathbf{e} are the same for any scaling $s(\rho) = \rho^k$. All optimal springs close the gap. Moreover, they are all localized at the right end of the plate with a quasi-vertical orientation.

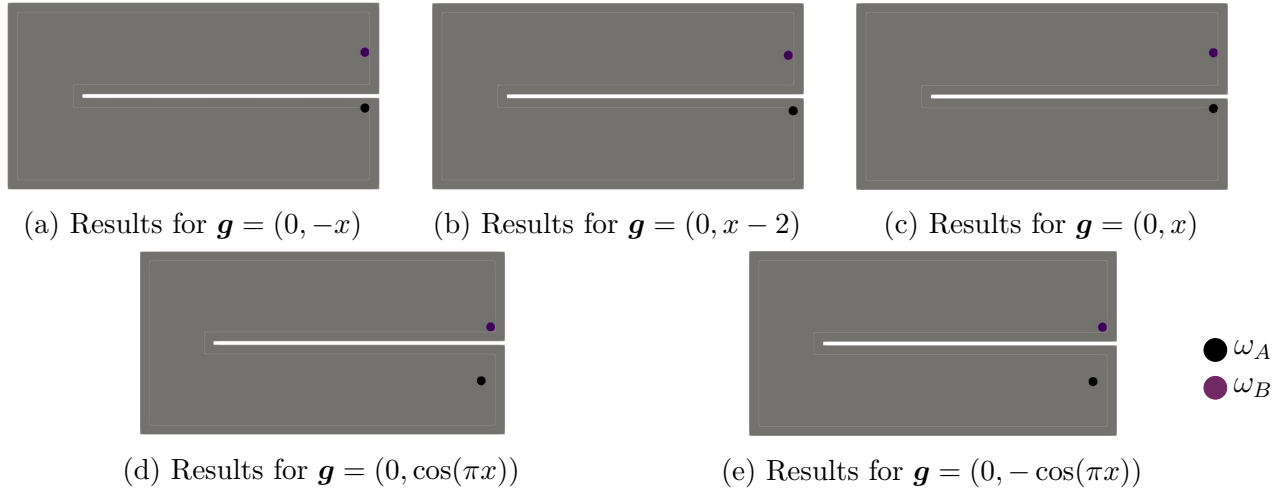


Figure 5.5: Optimal configurations to add one spring for potential load cases of Fig. 5.4

The sinusoidal loading of Fig. 5.6a presents a better potential for further studies such as a coupled optimization of both the structure and the spring location. This load case is kept in the sequel. The applied force is $\mathbf{g} = (0, g_y)$, where the vertical component g_y is given by

$$g_y = \begin{cases} -\cos(\pi x) & \text{for } 0.5 \leq x \leq 1.5 \\ -\frac{3}{4}\cos(\pi x) & \text{for } 1.5 \leq x \leq 2 \end{cases}.$$

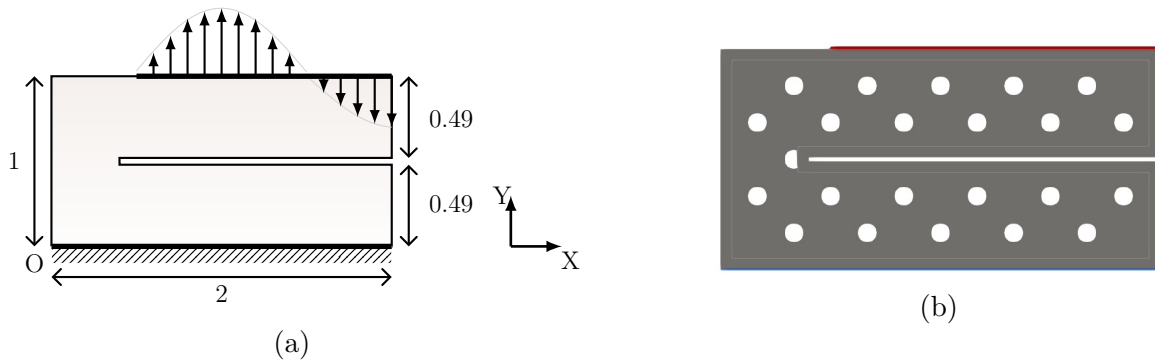


Figure 5.6: Current load case (a) and the initial topology of the structure (b)

The topology of the plate is initialized with holes (see Fig. 5.6b) for the purpose of further topology optimization. The initial compliance is then $J_0(\Omega) = 0.321001$. As stated in Section 3.3.3 about the thermal bridge, there are several configurations to compute the topological derivative with the couple $(\mathbf{x}_0, \mathbf{e})$. Nonetheless, let us recall these strategies. For graphical purposes, the direction \mathbf{e} is parameterized with an angle φ such that $\mathbf{e} = (\cos(\varphi), \sin(\varphi))$. The first test is to fix an orientation \mathbf{e} by choosing an angle φ . The topological derivative is then computed for all candidate point \mathbf{x}_0 . The spring is put at the most negative value of $DJ(\mathbf{x}_0, \mathbf{e})$.

The second approach consists in fixing a position \mathbf{x}_0 and computing DJ for a discrete number of orientations \mathbf{e} . The best direction matches with the minimum of $DJ(\mathbf{x}_0, \mathbf{e})$. Thus, these two tests allow some possible technical or industrial constraints. Actually, parts conception is ruled by standards that limit potential configurations of the couple $(\mathbf{x}_0, \mathbf{e})$. The last test is to search for both the position \mathbf{x}_0 and the orientation \mathbf{e} .

- Fix the orientation $\mathbf{e} = \left(\frac{\sqrt{2}}{2}, \frac{\sqrt{2}}{2}\right)$ and search for the best location \mathbf{x}_0

The topological derivative is computed inside a design-space for which both spheres, ω_A and ω_B , are entirely inside the structure. The non design-space is pictured in gray (see Fig. 5.7a). It is delimited by the thin white line in Fig. 5.7b. Moreover, negative values of DJ , for which ω_B would be partially or totally in the non-design-space, are truncated. They are excluded from the analysis and are displayed in white as well as the holes of the structure in Fig. 5.7a. The optimal small spring is given in Fig. 5.7b at the point $\mathbf{x}_0 = (1.07, 0.37)$.

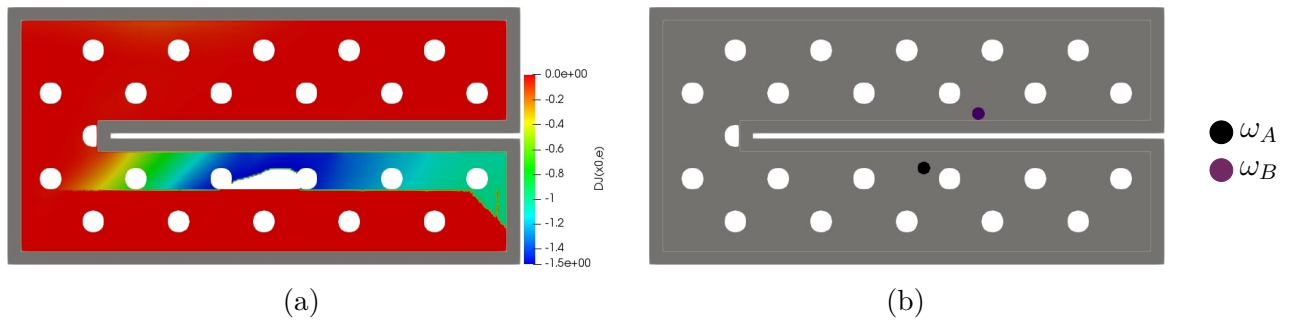


Figure 5.7: Cartography of DJ for fixed $\varphi = \frac{\pi}{4}$ rad (a) and the resulting optimal spring at $\mathbf{x}_0 = (1.07, 0.37)$ (b)

Table 5.1 gathers results for various values of the scaling factor k . The behavior of DJ does not depend on k . As a consequence, the optimal location \mathbf{x}_0 is the same for any value of k . However, the efficiency of the spring and the estimation of the asymptotic analysis are affected by the scaling k . The spring goes smaller as k increases, since ρ tends to zero. Therefore, its efficiency decreases as well. Then, the spring is almost inactive for $k = 2$ and $k = 4$. The biggest spring provides the best performance. This is here for $k = 0.5$, with a decrease of about 11% of the compliance. The more the spring is efficient, the more the estimator $\mathcal{E}(\Omega)$ is far from the real performance.

	$DJ(\mathbf{x}_0, \mathbf{e})$	\mathbf{x}_0	$J_\rho(\Omega)$	$\mathcal{E}(\Omega)$
$k = 0.5$	-1.52911	(1.07,0.37)	0.285309	0.0792276
$k = 1$	-1.52911	(1.07,0.37)	0.301023	0.282773
$k = 2$	-1.52911	(1.07,0.37)	0.320067	0.320045
$k = 4$	-1.52911	(1.07,0.37)	0.321	0.321

Table 5.1: Summary of the topological derivative test for fixed \mathbf{e} (recall that $J_0(\Omega) = 0.321001$)

- Fix the location $\mathbf{x}_0 = (1.75, 0.40)$ and search for the best orientation \mathbf{e}

Let us fix the location of the center of ω_A at the point $\mathbf{x}_0 = (1.75, 0.40)$ and search for the best orientation of the spring for discrete values of φ from 0 to 360° every five degrees. The cartography of the topological derivative for $\mathbf{x}_0 = (1.75, 0.40)$ is plotted in Fig. 5.8a. A design-space is delimited in order to have the spring strictly inside the plate. The topological derivative is computed such that those orientations that put ω_B outside the design-space are rejected and put to zero. The optimal spring is oriented at $\varphi = \frac{11\pi}{18}$ rad (or 110°) as displayed in Fig. 5.8b.

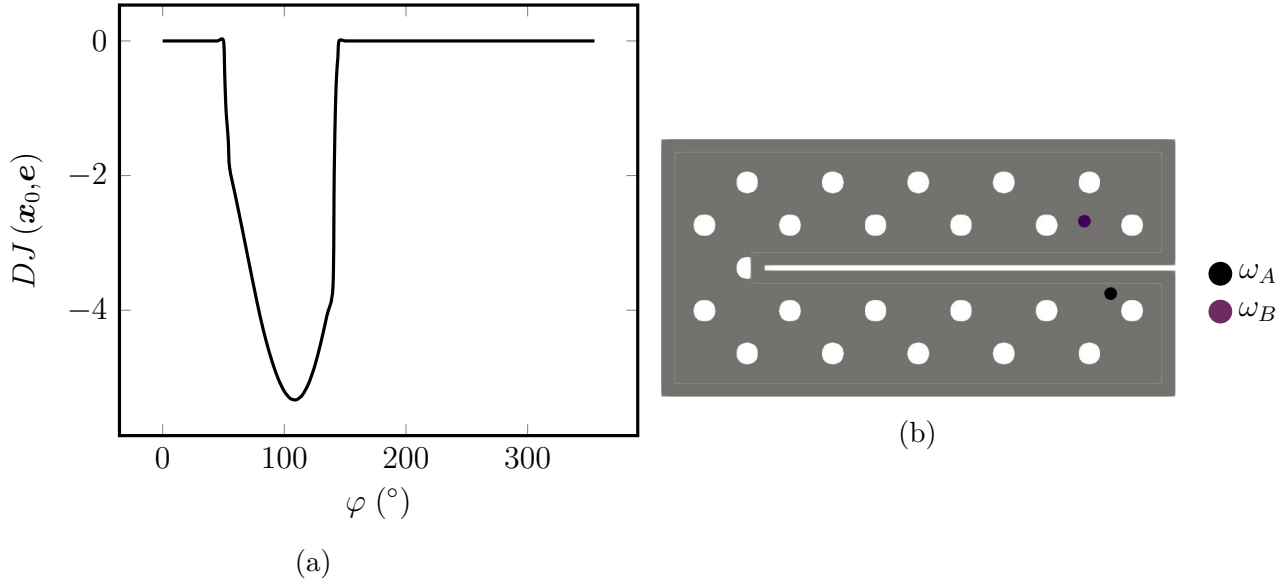


Figure 5.8: Cartography of DJ for fixed $\mathbf{x}_0 = (1.50, 0.40)$ in terms of the angle φ defining direction \mathbf{e} (a) and the resulting optimal spring (b)

Results are gathered in Table 5.2. As already noticed previously, the spring is more efficient for $k = 0.5$ among the set of values of k . The estimator gets a negative, and so non-representative, value. It means that the perturbation induces by this spring is too significant. Nevertheless, the spring for $k = 1$ is as much as efficient here as the case $k = 0.5$. The scale $k = 4$ gives once more a too small spring that does not affect the compliance.

	$DJ(\mathbf{x}_0, \mathbf{e})$	φ (rad)	$J_\rho(\Omega)$	$\mathcal{E}(\Omega)$
$k = 0.5$	-5.32963	$\frac{11\pi}{18}$	0.282258	-0.521688
$k = 1$	-5.32963	$\frac{11\pi}{18}$	0.289878	0.18776
$k = 2$	-5.32963	$\frac{11\pi}{18}$	0.317923	0.31767
$k = 4$	-5.32963	$\frac{11\pi}{18}$	0.320999	0.320999

Table 5.2: Summary of the topological derivative test for fixed \mathbf{x}_0 (recall that $J_0(\Omega) = 0.321001$)

- Search for the best location \mathbf{x}_0 and orientation \mathbf{e}

This test aims to search simultaneously for both the optimal location \mathbf{x}_0 and the best orientation \mathbf{e} to decrease the compliance. The topological derivative is computed inside the same design-space as previous tests. The minimum of DJ is obtained at the point $\mathbf{x}_0 = (1.53, 0.43)$ and for a direction oriented at $\varphi = \frac{7\pi}{12}$ rad (or 105°). Fig. 5.9a pictures the cartography of the topological derivative for the orientation $\varphi = \frac{7\pi}{12}$ rad. This particular direction \mathbf{e} does not require to truncate some value. The optimal spring is displayed in Fig. 5.9b.

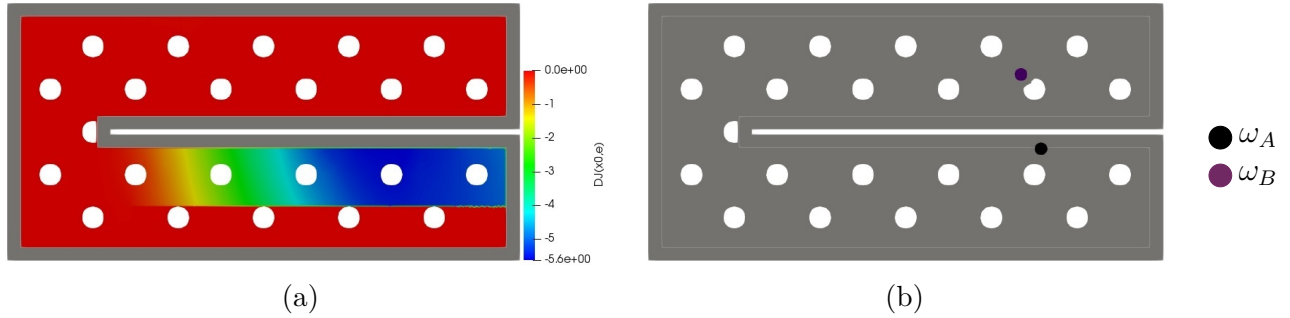


Figure 5.9: Cartography of DJ for $\varphi = \frac{7\pi}{12}$ rad (a) and the optimal spring at $\mathbf{x}_0 = (1.53, 0.43)$ oriented by the angle $\varphi = \frac{7\pi}{12}$ rad (b)

A surrounding of material is added around each inclusions. This non-design domain for the structure ensures the diffusion of efforts into the system. In the present study, this non-design domain is spherical-shaped and twice the size of the sphere. It is the slight extra material that modifies the hole next to ω_B (see Fig. 5.9b). This non-design domain is not taken into account by the asymptotic analysis. It is added in the structure after putting the spring indicated by the topological derivative. Nevertheless, the impact of this extra material is barely distinguishable. Let us take for instance $k = 0.5$. The compliance with the spring surrounded by the non-design domain is $J_\rho(\Omega) = 0.267431$ while it is $J_\rho(\Omega) = 0.267694$ when there is no extra material. The addition of a non-design domain around the spheres stiffens the system of about 0.1%, which is negligible.

Results are gathered in Table 5.3. One more time, the most efficient spring is for $k = 0.5$. It induces so much perturbation in the system that the estimator $\mathcal{E}(\Omega)$ is not representative at all. This spring brings an improvement of about 17% of the compliance. The estimator starts to be plausible from $k = 1$. Also, there is still a loss of the efficiency for $k = 2$ and $k = 4$. Nevertheless, the perturbation for $k = 4$ brings a slight improvement of 0.09%. This gain is not due to the spring but to the non-design domain added around each sphere. So this is a non-working spring. The extra material around each sphere barely stiffens the structure.

Deformations of the background domain and the domain with the optimal small spring for $k = 0.5$ are given in Fig. 5.10 with the same coefficient of deformation. The initial structure opens (see Fig. 5.10a) while the spring aims to close the opening (see Fig. 5.10b). The current structure is ruled by linear elasticity. So it does not use a contact model. This is why the branches extremities interpenetrate. Actually, the spring counteracts the traction. However, it does not impact well the pushing force that provokes the interpenetration. The contact model is added in Chapter 8. It will be added on further models and numerical illustrations.

	$DJ(\mathbf{x}_0, \mathbf{e})$	\mathbf{x}_0	φ (rad)	$J_\rho(\Omega)$	$\mathcal{E}(\Omega)$
$k = 0.5$	-5.64768	(1.53,0.43)	$\frac{7\pi}{12}$	0.267431	-0.571976
$k = 1$	-5.64768	(1.53,0.43)	$\frac{7\pi}{12}$	0.280287	0.179809
$k = 2$	-5.64768	(1.53,0.43)	$\frac{7\pi}{12}$	0.317391	0.317471
$k = 4$	-5.64768	(1.53,0.43)	$\frac{7\pi}{12}$	0.320708	0.320999

Table 5.3: Summary of the topological derivative test (recall that $J_0(\Omega) = 0.321001$)

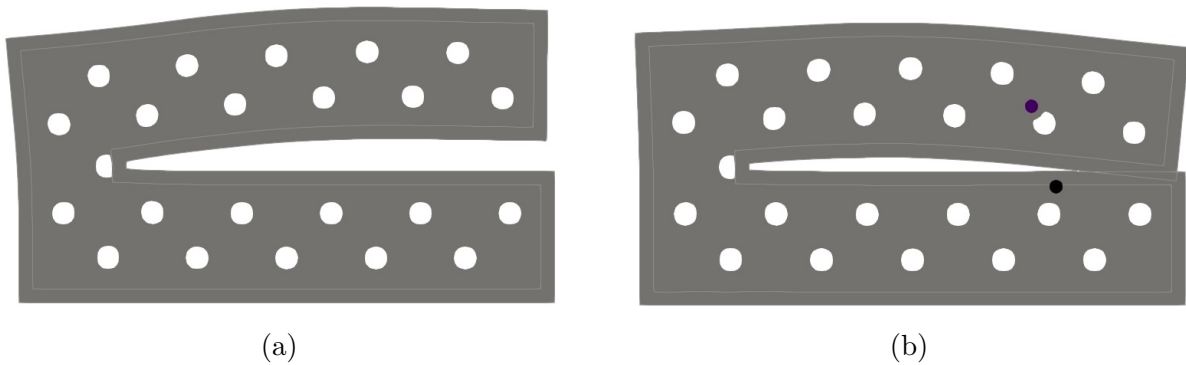


Figure 5.10: Deformations of the background domain (a) and the domain with the optimal small spring for $k = 0.5$ (b)

Fig. 5.11 shows the displacement fields in the background domain and in the domain with the optimal small spring for $k = 0.5$. Both vector fields have the same scale. It is obvious that the spring reduces the displacement amplitude and changes drastically the structure behavior in terms of displacement. Even if the spring is added locally, it impacts globally the structure.

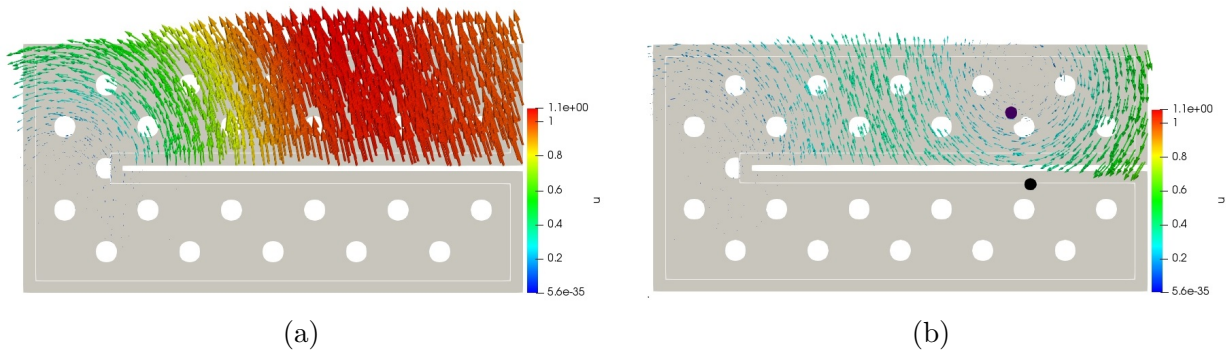


Figure 5.11: Displacement fields \mathbf{u} in the background domain (a) and in the domain with the optimal small spring for $k = 0.5$ (b)

Denote respectively σ_{xx} , σ_{yy} and σ_{xy} the stress fields in the direction X , Y and the shear stress. Von Mises stress, σ_{xx} , σ_{yy} and σ_{xy} of the background domain and of the domain with the spring for $k = 0.5$ are given in Fig. 5.12. The spring softens each stress fields. More particularly, the Von Mises stress (Fig. 5.12b), σ_{yy} (Fig. 5.12f) and the shear (Fig. 5.12h) concentrations in the corner of the opening diminish. The σ_{xx} field (Fig. 5.12d) is less affected by the spring.

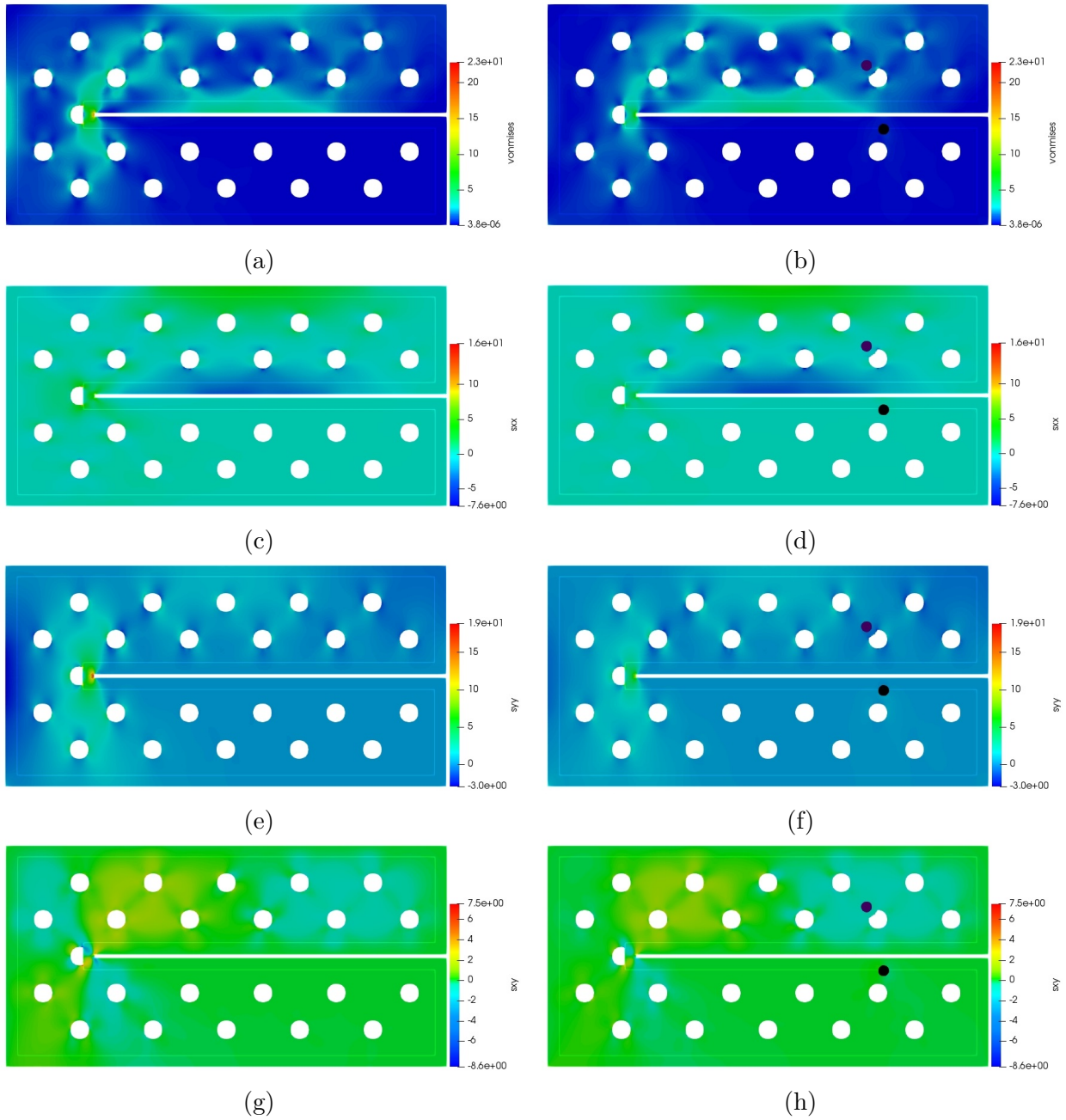


Figure 5.12: Von Mises stress, σ_{xx} , σ_{yy} and σ_{xy} of the background domain (a), (c), (e), (g) and of the domain with a spring scaled by $k = 0.5$ (b), (d), (f), (h)

Parametric optimization of the spring location \mathbf{x}_0

The spring connection has fixed shape and size ρ and its length ℓ is also unvarying. Its location is parameterized by the point \mathbf{x}_0 , the center of ω_A , and by its orientation \mathbf{e} . Based on the results of the topological derivative tests, this section intends to get better performance by optimizing the location of the point \mathbf{x}_0 . The orientation \mathbf{e} is fixed. The problem is to decrease the compliance. The location optimization is performed with a parametric gradient-based algorithm

$$\mathbf{x}_0^{i+1} = \mathbf{x}_0^i - \delta^i \frac{\partial J}{\partial \mathbf{x}_0}(\Omega, \mathbf{x}_0^i), \quad (5.54)$$

where \mathbf{x}_0^i is the center of ω_A at the iteration i , δ^i is the descent step and $\frac{\partial J}{\partial \mathbf{x}_0}(\Omega, \mathbf{x}_0^i)$ is the partial derivative of the compliance with regard to the point \mathbf{x}_0 computed with shape derivative techniques. Then the spheres are assumed to be transported like rigid bodies by a displacement field $\boldsymbol{\theta} = \vartheta \mathbf{d}$, where $\vartheta \in \mathbb{R}$ is small and $\mathbf{d} \in \mathbb{R}^2$ is the translation direction. The derivative reads

$$\begin{aligned} \frac{\partial J}{\partial \mathbf{x}_0}(\Omega, \mathbf{x}_0^i)(\vartheta) = & \int_{\partial\omega_A \cup \partial\omega_B} \vartheta \mathbf{d} \cdot \mathbf{n} \mathbf{A} \varepsilon(\mathbf{u}) : \varepsilon(\mathbf{p}) dS \\ & + \kappa(\rho) \left(\frac{\vartheta}{|\omega_B|} \int_{\partial\omega_B} (\mathbf{u} \cdot \mathbf{e})(\mathbf{d} \cdot \mathbf{n}) dS - \frac{\vartheta}{|\omega_A|} \int_{\partial\omega_A} (\mathbf{u} \cdot \mathbf{e})(\mathbf{d} \cdot \mathbf{n}) dS \right) \left(\int_{\omega_B} \mathbf{p} \cdot \mathbf{e} dV - \int_{\omega_A} \mathbf{p} \cdot \mathbf{e} dV \right) \\ & + \kappa(\rho) \left(\int_{\omega_B} \mathbf{u} \cdot \mathbf{e} dV - \int_{\omega_A} \mathbf{u} \cdot \mathbf{e} dV \right) \left(\frac{\vartheta}{|\omega_B|} \int_{\partial\omega_B} (\mathbf{p} \cdot \mathbf{e})(\mathbf{d} \cdot \mathbf{n}) dS - \frac{\vartheta}{|\omega_A|} \int_{\partial\omega_A} (\mathbf{p} \cdot \mathbf{e})(\mathbf{d} \cdot \mathbf{n}) dS \right), \end{aligned} \quad (5.55)$$

where \mathbf{u} and \mathbf{p} are respectively the displacement field and the associated adjoint state of the background domain and \mathbf{n} is the outward unit normal.

This algorithm is applied on the structure with holes and gives the results gathered in Table 5.4. There are significant changes of the location for $k = 0.5$ and $k = 1$. Previous section proved that the topological derivative proposition already improves the compliance for those values of k . Nevertheless, the addition of these springs impacts macroscopically the structure behavior. The location optimization then completes the topological derivative indication. It provides an extra improvement of about 20% for $k = 0.5$ and about 5% for $k = 1$. However, the spring barely moves for $k = 2$ and $k = 4$. As a consequence, these springs, more particularly for $k = 2$, are already at the optimal location as regards to the compliance. Actually, the spring scaled by $k = 4$ is inactive in the structure.

	Initial \mathbf{x}_0	Final \mathbf{x}_0	Initial $J(\Omega)$	Final $J(\Omega)$	Improvement
$k = 0.5$	(1.53,0.43)	(0.92,0.37)	0.267431	0.214311	19.86%
$k = 1$	(1.53,0.43)	(1.12,0.44)	0.280287	0.265019	5.45%
$k = 2$	(1.53,0.43)	(1.52,0.43)	0.317391	0.317436	-0.01%
$k = 4$	(1.53,0.43)	(1.53,0.43)	0.320708	0.320708	0.0%

Table 5.4: Summary of location optimization of the spring

Topology optimization of the structure

Let us now perform a topology optimization of the structure with a fixed spring. The problem is to minimize the volume of the structure under a constraint on the compliance. The volume $V(\Omega)$ and the compliance $C(\Omega)$ read

$$V(\Omega) = \int_{\Omega} dV \quad \text{and} \quad C(\Omega) = \int_{\Gamma_N} \mathbf{g} \cdot \mathbf{u} dS. \quad (5.56)$$

This optimization problem is formulated as follows

$$\begin{aligned} \min_{\Omega \in \mathcal{U}_{ad}} \quad & V(\Omega), \\ \text{s.t.} \quad & C(\Omega) \leq 0.35 \end{aligned} \quad (5.57)$$

where \mathcal{U}_{ad} is the set of admissible shapes of the structure. The constraint is taken into account with the Augmented Lagrangian functional $J(\Omega)$, so that the problem (5.57) is rewritten as

$$\min_{\Omega \in \mathcal{U}_{ad}} \max_{\alpha \geq 0} \left\{ J(\Omega) = V(\Omega) + \alpha(C(\Omega) - 0.35) + \frac{\beta}{2}(C(\Omega) - 0.35)^2 \right\}, \quad (5.58)$$

where α and β are respectively Lagrange multiplier and penalty parameter for the compliance constraint. The value of the constraint bound is chosen with respect to the behavior of the structure without any spring. Since the material properties are constant, the volume reduction is assimilated to weight reduction.

- Without any spring

The problem (5.58) is solved on the structure without any spring. It is performed in first instance as a base of comparison. The initial structure (see Fig. 5.6b) has a volume of $V(\Omega) = 1.83701$ with a compliance of $C(\Omega) = 0.320886$. Based on this initial value, the constraint bound of the compliance is defined at 0.35. It corresponds to an increase of about 9%. The optimal shape is displayed in Fig. 5.13. The final volume is $V(\Omega) = 0.874785$, which corresponds to an improvement of 52.40%. In further analysis, the addition of a spring or two is expected to provide supplementary weight reduction.

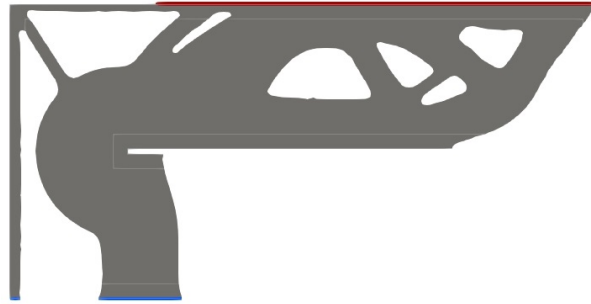


Figure 5.13: Optimal shape without any spring

- One spring put at the location given by the topological derivative

Let us consider the spring given by the topological derivative on the structure initialized with holes. The spring is put at the point $\mathbf{x}_0 = (1.53, 0.43)$ and oriented at $\varphi = \frac{7\pi}{12}$ rad. The optimal shapes for various values of k are given in Fig. 5.14. Results are gathered in Table 5.5. It highlights two sets of topologies. The first one concerns the springs scaled by $k = 0.5$ and $k = 1$. They respectively decrease the initial volume of about 65% and 63%. Both structures are then lighter than the optimal shape without any spring. The extra materials around each spheres connect to the structure through thin bars. Thus, the spring stiffens the structure that requires less material to satisfy the compliance constraint. Note that the thin bars may break on a coarser mesh. The second set of topologies concerns the springs scaled by $k = 2$ and $k = 4$. The topology is the same as the problem without spring. Actually, these springs are too small and they are ignored by the structure. They are still displayed because of the imposed extra material around each spheres. So very small springs do not affect the topology but their inherent non-design domains impact slightly the volume.

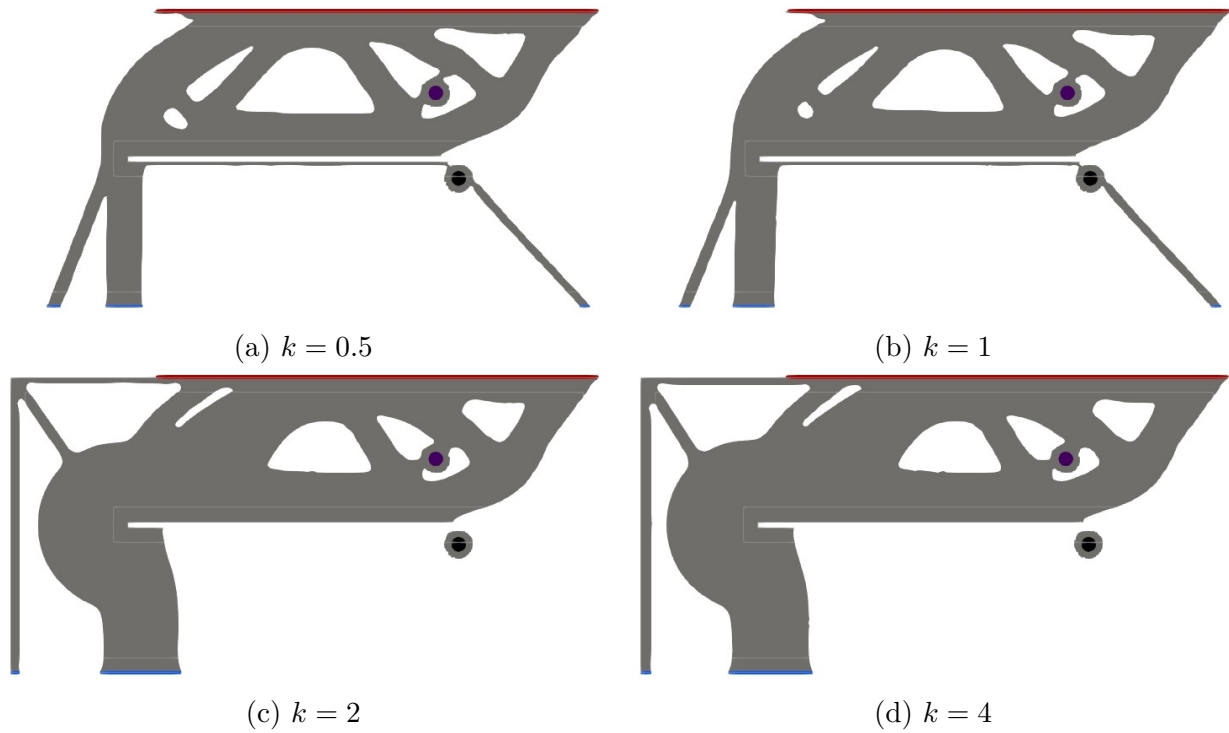


Figure 5.14: Optimal shapes for various values of k , for fixed $\mathbf{x}_0 = (1.53, 0.43)$ and $\varphi = \frac{7\pi}{12}$ rad

	Final Volume $V(\Omega)$	Improvement
$k = 0.5$	0.64361	64.98%
$k = 1$	0.679925	63.00%
$k = 2$	0.867537	52.79%
$k = 4$	0.882426	51.98%

Table 5.5: Summary of volumes for topology optimization with one fixed spring placed at $\mathbf{x}_0 = (1.53, 0.43)$ and oriented at $\varphi = \frac{7\pi}{12}$ rad for various values of k (recall the initial volume is $V(\Omega) = 1.83765$)

- One spring put at the location given by the parametric gradient

Let us now consider the springs resulting from the parametric optimization of their location \mathbf{x}_0 and solve the problem (5.58) on these various configurations. In other words, each springs are put at the final location \mathbf{x}_0 given in Table 5.4. They are all oriented at $\varphi = \frac{7\pi}{12}$ rad (or 105°). The optimal shapes are given in Fig. 5.15. Results are presented in Table 5.6. There is a slight variation between initial volumes for various k because the springs are placed at different locations and their inherent non-design domain exceeds differently of the initial structure. The optimization reveals three types of topologies.

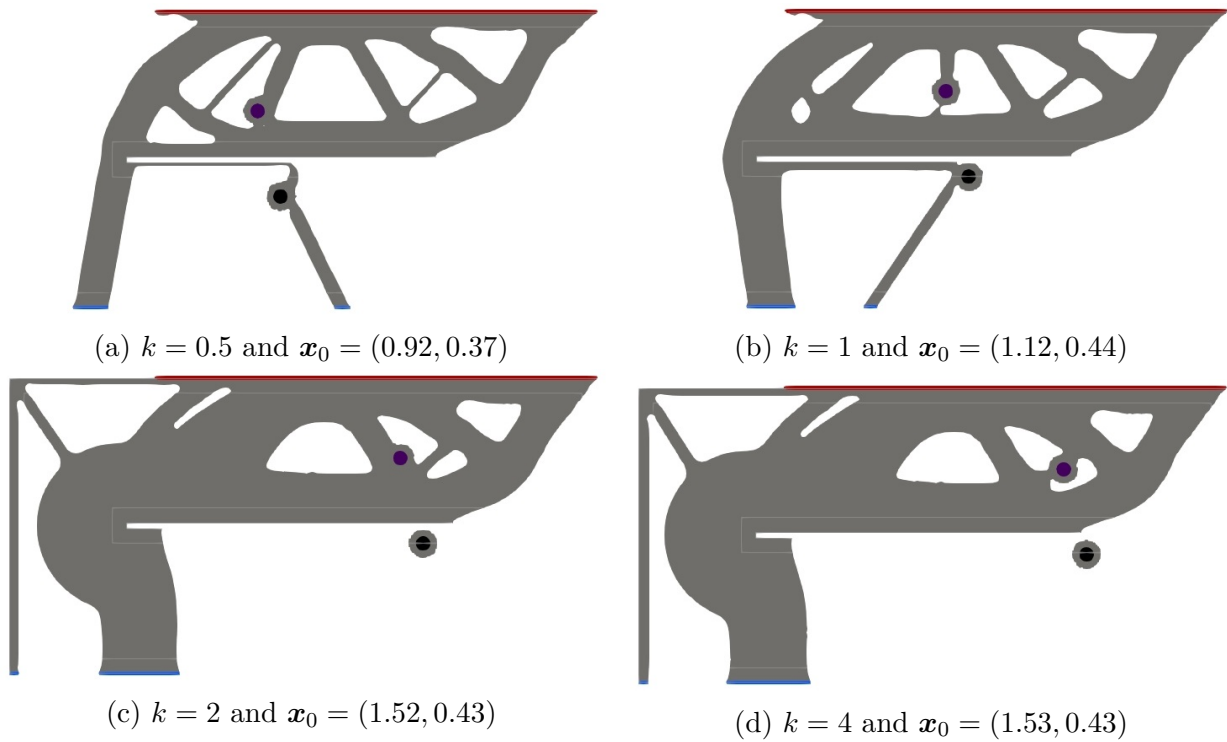


Figure 5.15: Optimal shapes for various values of k and for fixed $\varphi = \frac{7\pi}{12}$ rad

	Initial Volume	Final Volume	Improvement
$k = 0.5$	1.84246	0.518983	71.83%
$k = 1$	1.83701	0.64752	64.75%
$k = 2$	1.83701	0.867347	52.78%
$k = 4$	1.83758	0.882896	51.95%

Table 5.6: Summary of volumes for topology optimization with one fixed spring placed according to the parametric gradient and oriented at $\varphi = \frac{7\pi}{12}$ rad for various values of k

The first one occurs for $k = 0.5$. The volume has decreased more than 70% and the structure contains more thin bars. Topological changes between Fig. 5.14a (for $\mathbf{x}_0 = (1.53, 0.43)$) and Fig. 5.15a (for $\mathbf{x}_0 = (0.92, 0.37)$) are substantial. The optimization with the spring placed according to the parametric gradient provides a better weight reduction than the optimization with the spring put by the topological derivative.

The second type of topology concerns the case $k = 1$ for which the spring is put at the point $\mathbf{x}_0 = (1.12, 0.44)$ (see Fig. 5.15b). Compared to the previous optimization (see Fig. 5.14b), the tendency of the structure is quite similar. However, it should be noted that far left bar in Fig. 5.14b breaks in the present study. It is compensated by a thicker horizontal bar that links the head of the spring to the rest of the structure. A supplementary bar is created to link the other end of spring to the structure. This topology brings a weight reduction of 64.75%.

The last set of topologies includes the springs scaled by $k = 2$ and $k = 4$. As these springs are inactive, the topology is practically the same as the optimal structure without any spring (see Fig. 5.13). In other words, the structure reaches the compliance constraint without using the spring. The extra material around the spheres brings the only change in the final shape. This study proves that the optimization of an active spring location impacts highly the final topology and the weight of the structure.

Coupled optimization of both the structure and the location of the spring

This section focuses on a coupled optimization of both the structure of the plate and the location of the spring. The initial structure is the plate with holes (see Fig. 5.6b). The problem is still to solve (5.58), *i.e.* to minimize the volume under a compliance constraint. It will be shown that the initial location of the spring may influence the final topology. To avoid numerical instabilities, the structure and the location are not optimized in the same iteration. The algorithm alternates 4 iterations of structural optimization and 1 iteration of location optimization. The number of iterations between each type of optimization can obviously be modified.

- Initial location given by the topological derivative

Let us place the spring at the point $\mathbf{x}_0 = (1.53, 0.43)$ given by the topological derivative and oriented at $\varphi = \frac{7\pi}{12}$ rad. Optimal topologies and a summary of results for various of k are respectively given in Fig. 5.16 and Table 5.7.

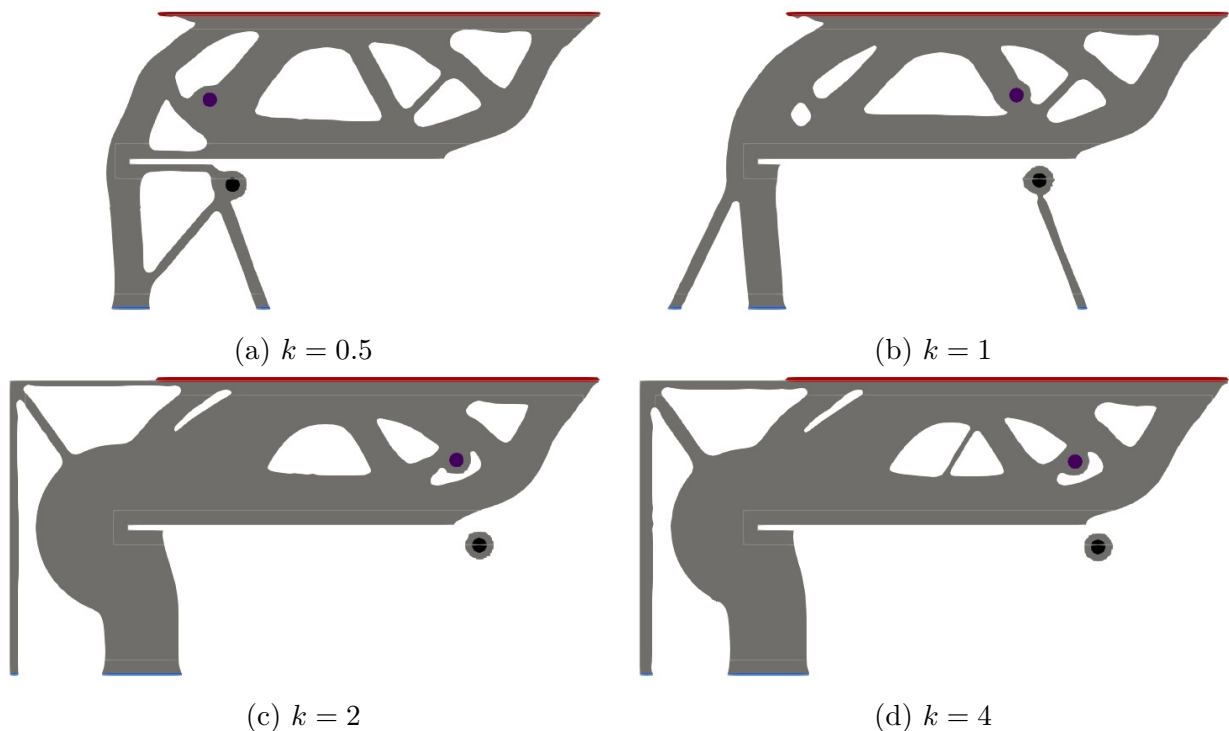


Figure 5.16: Optimal shapes and locations for various values of k and $\varphi = \frac{7\pi}{12}$ rad with initial spring placed by the topological derivative

The spring moves less and less as k increases. The springs scaled by $k = 2$ and $k = 4$ are once more inactive so the final structure is almost the one without spring. Nevertheless, there is a remaining thin bar in the middle of the structure for $k = 4$. The case $k = 1$ reminds of

the final topology with a spring placed by the topological derivative (cf. Fig. 5.14b). Since the location optimization aligns the spring to a thick bar of the structure (see Fig. 5.16b), the thin horizontal bar of Fig. 5.14b breaks. The weight reduction goes from 63% to almost 66%. So far, the best performance is for $k = 0.5$ that brings 70% of volume reduction. The main change is the bar structure that supports the head of the spring.

	Initial \mathbf{x}_0	Final \mathbf{x}_0	Initial $V(\Omega)$	Final $V(\Omega)$	Improvement
$k = 0.5$	(1.53,0.43)	(0.75,0.42)	1.83765	0.545951	70.29%
$k = 1$	(1.53,0.43)	(1.34,0.44)	1.83765	0.627541	65.85%
$k = 2$	(1.53,0.43)	(1.60,0.44)	1.83765	0.869887	52.66%
$k = 4$	(1.53,0.43)	(1.56,0.43)	1.83765	0.878118	52.22%

Table 5.7: Summary of results : coupled optimization of both structure and location with initial spring placed by the topological derivative

- Initial location given by the parametric gradient

The following analysis illustrates the potential impact of the initial location of the spring in a coupled optimization of both structure and location. Let us initially put the spring at the location given by the parametric gradient. Optimal topologies and a summary of results are respectively given in Fig. 5.17 and Table 5.8. The smallest spring with $k = 4$ is initially put at the point $\mathbf{x}_0 = (1.53, 0.43)$. So the corresponding optimal shape has already been found in the previous coupled optimization (cf. Fig. 5.16d). The cases $k = 1$ and $k = 2$ also provide the same results as the previous coupling. The major topological variation is for the spring scaled by $k = 0.5$. In the present coupling, the spring did not move as much as it did in Fig. 5.16a. The current topology is then more like the case $k = 1$. Nevertheless, the weight reduction is equivalent since the volume reduction is of 70%. As a conclusion, the initial location and the size of the spring may highly impact the final topology but not the final volume in this use case.

	Initial \mathbf{x}_0	Final \mathbf{x}_0	Initial $V(\Omega)$	Final $V(\Omega)$	Improvement
$k = 0.5$	(0.92,0.37)	(1.02,0.43)	1.84246	0.547063	70.31%
$k = 1$	(1.12,0.44)	(1.37,0.44)	1.83701	0.630422	65.68%
$k = 2$	(1.52,0.43)	(1.60,0.44)	1.83705	0.868192	52.74%

Table 5.8: Summary of results coupled optimization of both structure and location with initial spring placed by the parametric gradient

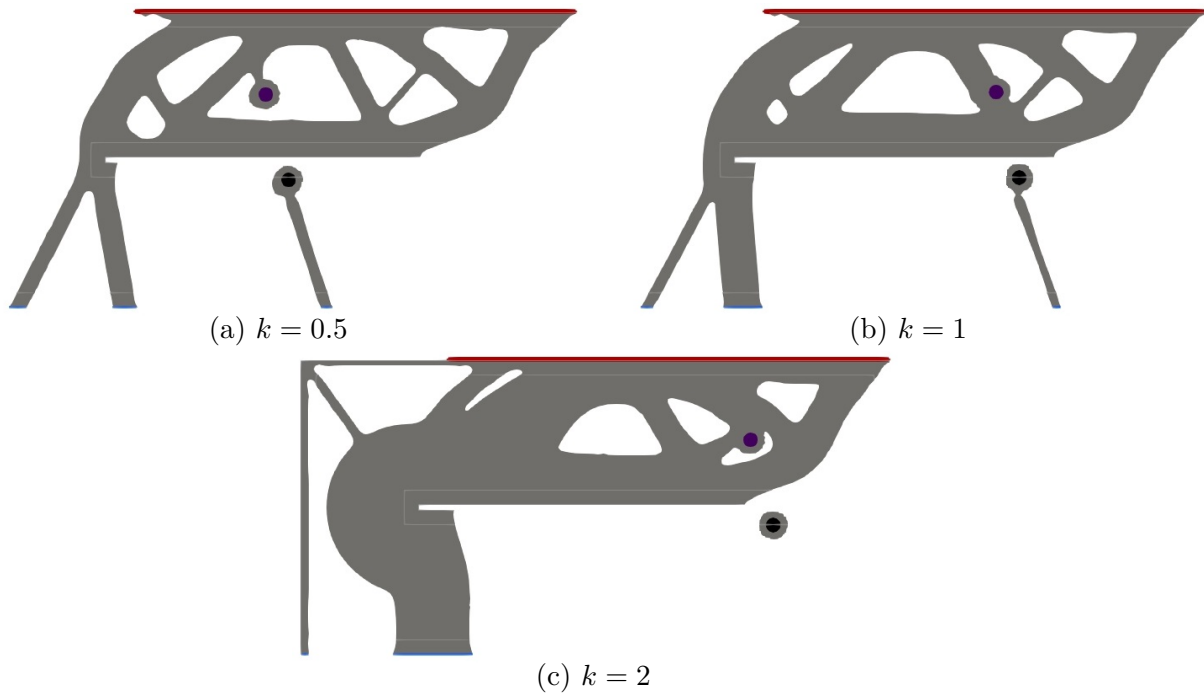


Figure 5.17: Optimal shapes and locations for various values of k and $\varphi = \frac{7\pi}{12}$ rad with initial spring placed by the parametric gradient

5.3.2 Analysis with two springs

This section reiterates the topological derivative test to put a second spring in order to decrease the compliance, followed by location and topology optimization. In the present study, both springs have the same scale size k . Note that it is possible to combine springs with different scales. However, these configurations are not tested here because there are too many combinations. In the sequel, the subscript "1" (resp. "2") refers to the first (resp. the second) spring.

Test of the topological derivative to put a second spring

- First spring put at the location given by the topological derivative

A new map of the topological derivative is computed for various values of k on the system that contains the spring placed by the previous topological derivative at the point $\mathbf{x}_{0,1} = (1.53, 0.43)$. Results are gathered in Table 5.9. The presence of a first spring of various scale size k influences largely the location $\mathbf{x}_{0,2}$ of the second spring and its orientation parameterized by the angle φ_2 . Compared to the compliance with one spring $J_1(\Omega)$, the compliance with two springs $J_2(\Omega)$ decreases for all values of k . The estimator $\mathcal{E}(\Omega)$ is plausible from $k = 1$. The maps of the topological derivative for various k and the corresponding optimal configurations are given in Fig. 5.18. The largest springs, for $k = 0.5$ still provide the best performance. The corresponding cartography (see Fig. 5.18a) contains truncated values in the right hand side. These values are excluded from the analysis because ω_{B_2} would be outside the design domain. The second spring is oriented at $\varphi_2 = \frac{13\pi}{36}$ rad (or 65°). It is put at the right end of the plate. By contrast, the second spring, for $k = 1$ or for and $k = 2$, is parallel to the first one. The cartography of DJ is exactly the same with or without one spring scaled by $k = 4$ (see Fig. 5.19). The second spring is then put at the same location $\mathbf{x}_{0,2} = \mathbf{x}_{0,1}$ with the same orientation $\mathbf{e}_2 = \mathbf{e}_1$. So, it has no interest to do further analysis with a spring scaled by $k = 4$.

	$DJ(\mathbf{x}_{0,2}, \mathbf{e}_2)$	$\mathbf{x}_{0,2}$	φ_2 (rad)	$J_1(\Omega)$	$J_2(\Omega)$	$\mathcal{E}(\Omega)$
$k = 0.5$	-1.42253	(1.80,0.31)	$\frac{13\pi}{36}$	0.267431	0.223093	0.0425098
$k = 1$	-1.19661	(1.09,0.43)	$\frac{7\pi}{12}$	0.280287	0.258277	0.250372
$k = 2$	-5.04662	(1.41,0.43)	$\frac{7\pi}{12}$	0.317391	0.31438	0.314237
$k = 4$	-5.64277	(1.53,0.43)	$\frac{7\pi}{12}$	0.320708	0.320706	0.320706

Table 5.9: Summary of the placement of a second spring (recall that $\mathbf{x}_{0,1} = (1.53, 0.43)$ and $\varphi_1 = \frac{7\pi}{12}$ rad for all k)

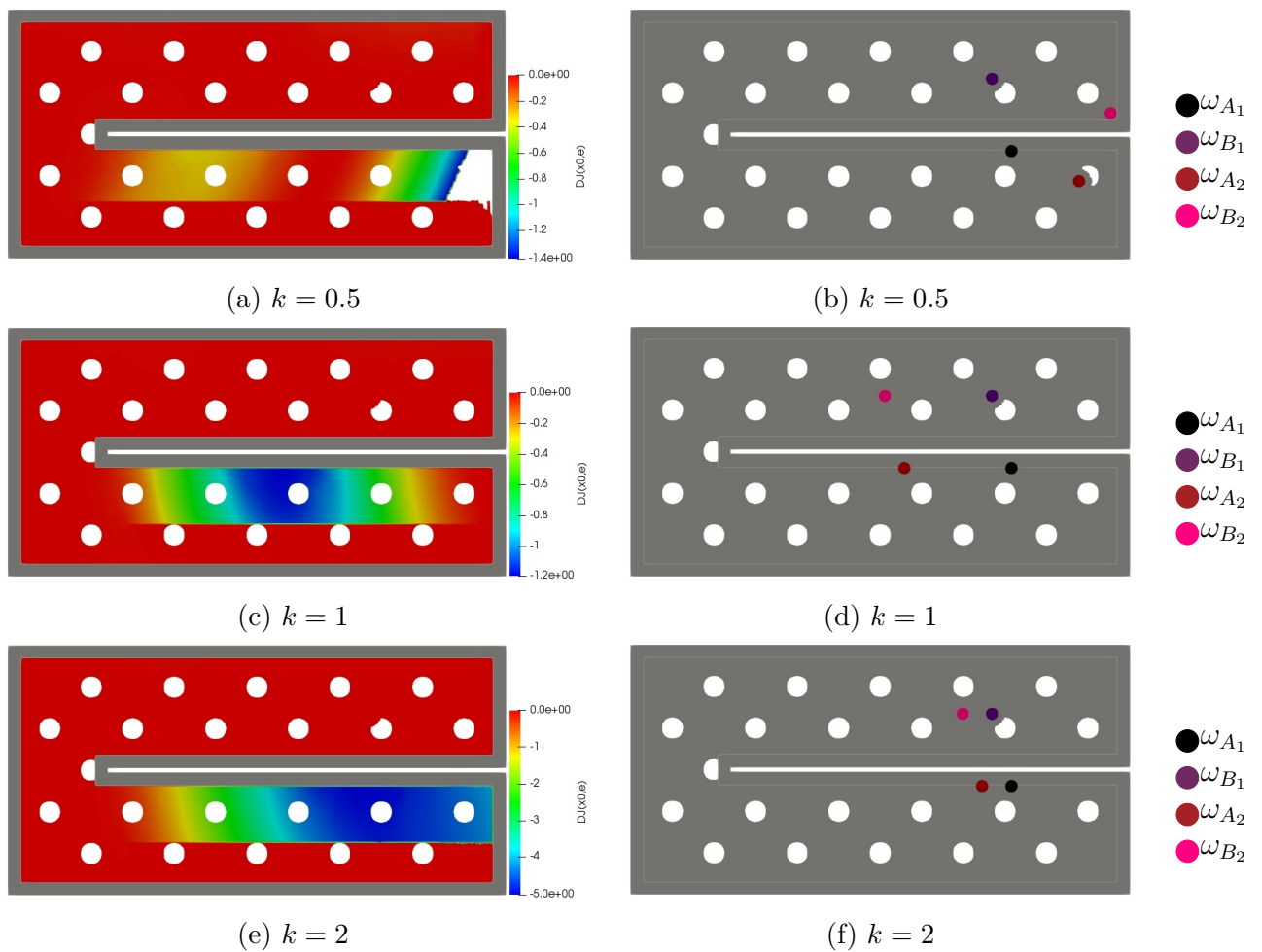


Figure 5.18: Cartography of DJ for various k to place a second spring (a), (c), (e) and the corresponding optimal configuration (b), (d), (f)

- First spring put at the location given by the parametric gradient

In this part, the topological derivative is computed for various k on a system containing a spring optimized according to the parametric gradient. Recall that these locations are gathered in Table 5.4. The objective is still to decrease the compliance. Cartographies of DJ for various

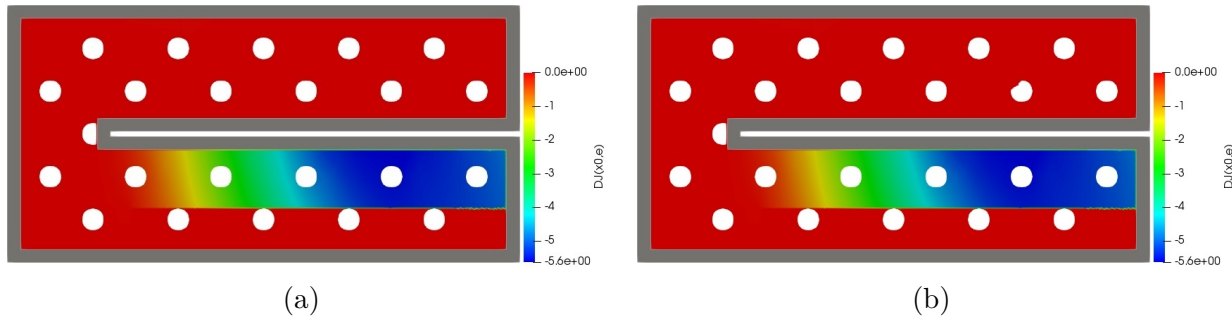


Figure 5.19: Cartography of DJ without spring (a) and with a spring scaled by $k = 4$ (b)

k and the corresponding configurations are displayed in Fig. 5.20. Results are summed up in Table 5.10.

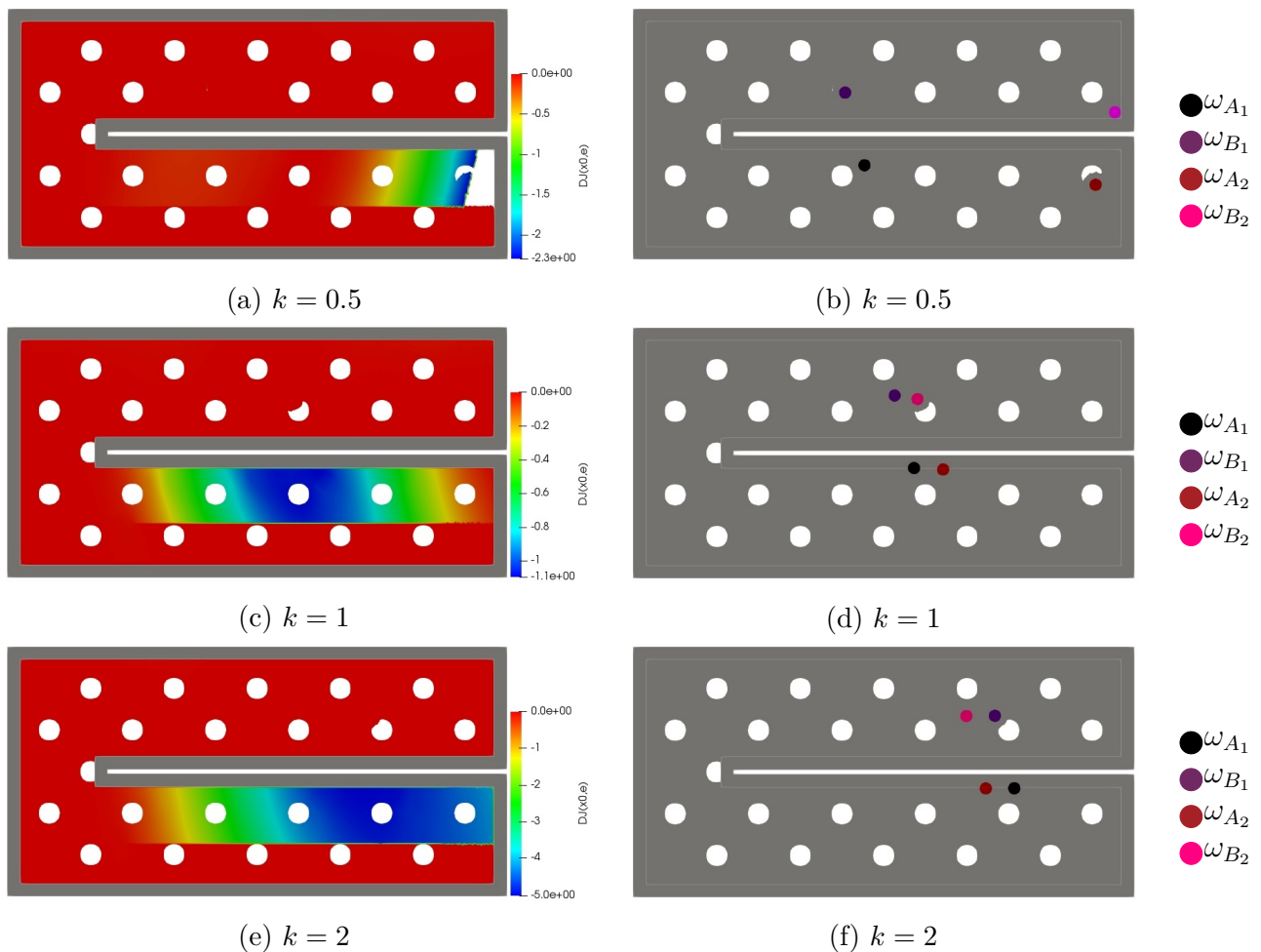


Figure 5.20: Cartography of DJ for various k (a), (c), (e) and the corresponding optimal configuration (b), (d), (f)

The largest springs, for $k = 0.5$ are very distant from each other. The second spring is oriented at $\varphi_2 = \frac{5\pi}{12}$ rad (or 75°). It counteracts the lever arm on the right end of the structure. As ω_{B_2} must be in the design space, there are truncated values of the topological derivative on the right side of the plate. In both cases $k = 1$ and $k = 2$, the second spring is much more close to the first spring. Then the two springs tend to work like a larger one. The springs scaled by

$k = 1$ are almost parallel since the second one is oriented at $\varphi_2 = \frac{11\pi}{18}$ rad (or 110°). On the other hand, the springs for $k = 2$ are perfectly parallel. Besides, this configuration is the same as the previous one (see Fig. 5.18f when the first spring is placed by the topological derivative). In all cases, the compliance with two springs is smaller than the one with a single spring.

	$DJ(\mathbf{x}_{0,2}, \mathbf{e}_2)$	$\mathbf{x}_{0,2}$	φ_2 (rad)	$J_1(\Omega)$	$J_2(\Omega)$	$\mathcal{E}(\Omega)$	$\mathbf{x}_{0,1}$
$k = 0.5$	-2.29932	(1.85,0.30)	$\frac{5\pi}{12}$	0.214316	0.189538	-0.149238	(0.92,0.37)
$k = 1$	-1.09927	(1.24,0.43)	$\frac{11\pi}{18}$	0.265019	0.247923	0.237537	(1.12,0.44)
$k = 2$	-5.04771	(1.41,0.43)	$\frac{7\pi}{12}$	0.317436	0.314461	0.314319	(1.52,0.43)

Table 5.10: Summary of the placement of a second spring (recall that $\varphi_1 = \frac{7\pi}{12}$ rad)

- Optimal shape with one first spring put at the location given by the topological derivative

Up to now, the topological derivative has been computed on the initial structure with holes (cf. Fig. 5.6b). Let us consider the optimal shapes resulting from a volume minimization on a system containing one spring located at the point $\mathbf{x}_{0,1} = (1.53, 0.43)$ and oriented at $\varphi_1 = \frac{7\pi}{12}$ rad. The topological derivative is computed on these systems and produces the results given in Fig. 5.21 and Table 5.11. It reveals two sets of configurations.

	$DJ(\mathbf{x}_{0,2}, \mathbf{e}_2)$	$\mathbf{x}_{0,2}$	φ_2 (rad)	$J_1(\Omega)$	$J_2(\Omega)$	$\mathcal{E}(\Omega)$
$k = 0.5$	-1.0044	(1.58,0.42)	$\frac{29\pi}{36}$	0.350154	0.319217	0.191345
$k = 1$	-1.87036	(1.59,0.42)	$\frac{29\pi}{36}$	0.351249	0.326451	0.30449
$k = 2$	-1.24877	(0.56,0.31)	$\frac{7\pi}{18}$	0.349743	0.348778	0.348963
$k = 4$	-1.26975	(0.56,0.31)	$\frac{7\pi}{18}$	0.349387	0.349237	0.349387

Table 5.11: Summary of results (recall that $\mathbf{x}_{0,1} = (1.53, 0.43)$ and $\varphi_1 = \frac{7\pi}{12}$ rad)

The theory of the asymptotic expansion states that the spring is added far from existing spring(s). Therefore, the extra material in the neighborhood of \mathbf{x}_0 is included in the non-design space of the second spring. As the structure is already optimized for one spring, there is no particular space left to put an other spring. Consequently, the results do not have a realistic physical meaning for the cases $k = 0.5$ and $k = 1$. The springs step over each other. These non-significant results occur because the objective is exclusively the compliance. Thus, the topological derivative depends on the square of displacements difference (see (5.53)). Its values are even larger as the lever arm is important, which should be around the right part of the structure. However, the lower part of the optimized structure contains only thin bars and the

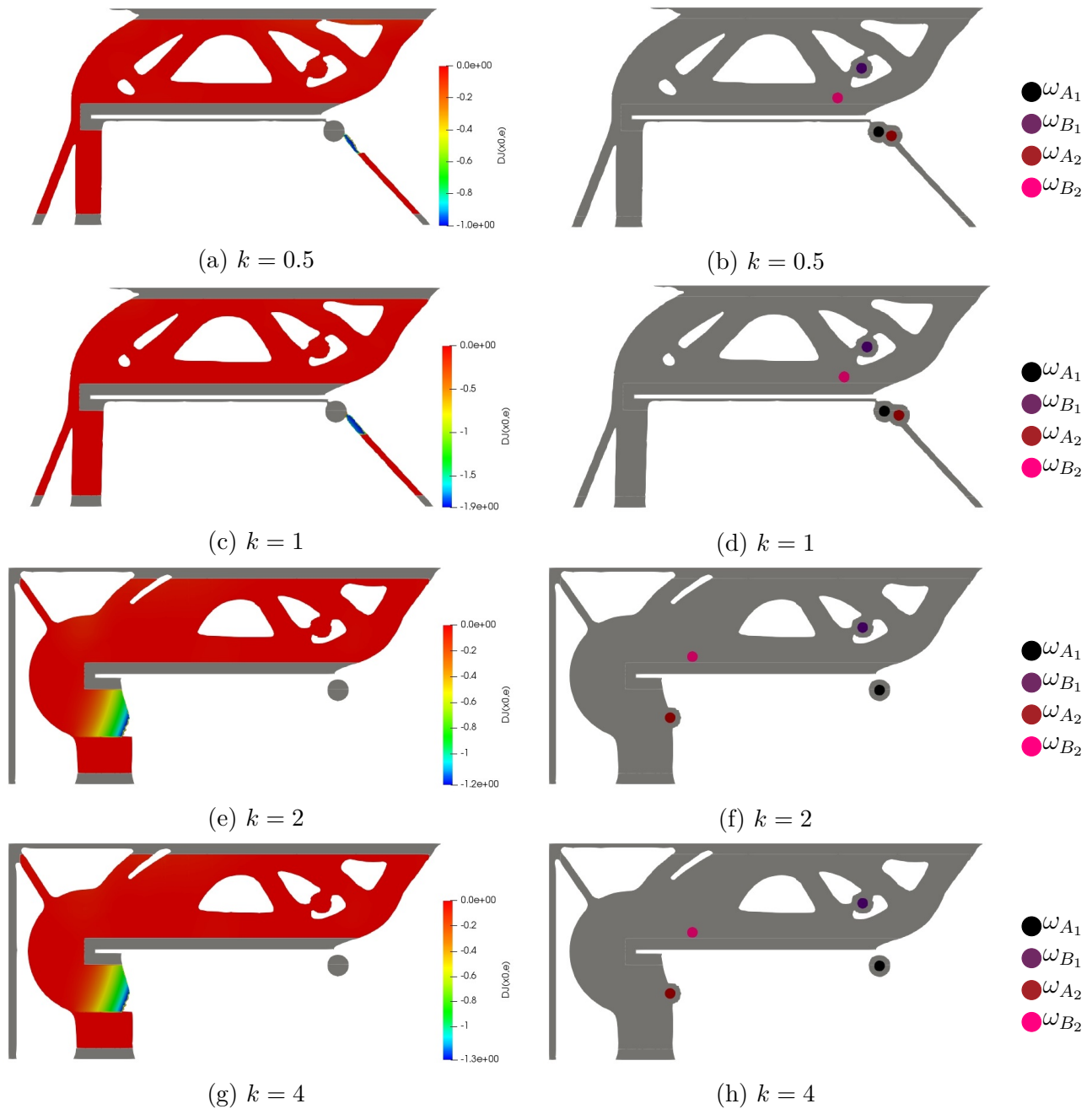


Figure 5.21: Cartography of DJ for various k (a), (c), (e) and the corresponding optimal configuration (b), (d), (f)

extra material of ω_{A_1} . So the potential location $\mathbf{x}_{0,2}$ has to be on the thin bars and should be very close to the head of the first spring. Moreover, the direction \mathbf{e} must be oriented inside the structure. Thus, the springs step over each other. Nevertheless, the second spring contributes to a noticeable reduction of the compliance. These crossing phenomenon could be avoided by defining a larger non-design space around the first spring.

The cases $k = 2$ and $k = 4$ provide almost the same result. Even if the first spring is inactive, the second one comes into play in the structure. Unfortunately, that spring is too small to bring important improvement. So it only implies a slight decrease of the compliance.

Optimization of both springs locations $\mathbf{x}_{0,1}$ and $\mathbf{x}_{0,2}$

In this section, let us consider the configurations of two springs successively placed by the topological derivative on the structure initialized with holes. It corresponds to the configurations given in Fig. 5.18. The problem is still to decrease the compliance. The locations are simultaneously optimized with the parametric gradient-based algorithm (5.54) with the corresponding derivative (5.55) for each springs. Summaries of locations and compliances evolution for various of k are given in Tables 5.12 and 5.13. In the case $k = 0.5$, the first spring moves largely while the second one practically stays stationary. It brings more than 20% of reduction of the compliance. For this spring size, the optimal location of the second spring is then at the right end of the structure. For $k = 1$, both springs have moved reasonably, which decreases the compliance of about 5%. However, the springs are superimposed for $k = 2$. It means this size scale rather use one spring at the point $\mathbf{x}_0 = (1.39, 0.44)$ than two distinct springs. This case is even more particular because the compliance increased slightly. So the result for $k = 2$ is not retained for further analysis.

	Initial $\mathbf{x}_{0,1}$	Final $\mathbf{x}_{0,1}$	Initial $\mathbf{x}_{0,2}$	Final $\mathbf{x}_{0,2}$
$k = 0.5$	(1.53,0.43)	(1.09,0.36)	(1.80,0.31)	(1.80,0.30)
$k = 1$	(1.53,0.43)	(1.06,0.40)	(1.09,0.43)	(0.99,0.44)
$k = 2$	(1.53,0.43)	(1.39,0.44)	(1.41,0.43)	(1.39,0.44)

Table 5.12: Summary of locations for parametric optimization of both springs location

	Initial $J(\Omega)$	Final $J(\Omega)$	Improvement
$k = 0.5$	0.223093	0.177062	20.63%
$k = 1$	0.258277	0.245551	4.93%
$k = 2$	0.31438	0.314611	-0.07%

Table 5.13: Summary of compliances for parametric optimization of both springs location

Topology optimization of the structure

Based on previous topological derivative tests with two springs, let us perform a topology optimization of the structure with fixed springs for various configurations. The problem is still to minimize the volume of the structure under a constraint on the compliance as formulated in (5.58). This section intends to show the importance of initial locations of the springs.

- Two springs put at the location given by the topological derivative

Let us begin with the structure initialized with holes and two springs placed by the topological derivative (cf. Fig. 5.18). The optimal shapes and the evolution of volumes for various k are

gathered in Fig. 5.22 and Table 5.14. For the case $k = 0.5$, the tendency of the structure is quite close to the one with one spring (cf. Fig. 5.14a) except around the springs. The two springs are involved in the structure and are connected through thin bars. More particularly, the bars joining the second spring are in the axis of that spring. In the case $k = 1$, the first spring does not contribute to the stiffness anymore. Then the topology has the tendency of the optimized structure with one spring placed according to the parametric gradient (cf. Fig. 5.15b). The last case, for $k = 2$, provides unsurprisingly the same optimal structure with or without springs. One can compare Tables 5.5 (with one spring) and 5.14 (with two springs). In any case, the weight reduction is comparable whatever the structure contains one or two springs.

	Initial Volume	Final Volume	Improvement
$k = 0.5$	1.84065	0.651709	64.59%
$k = 1$	1.83765	0.666643	63.72%
$k = 2$	1.83765	0.866165	52.87%

Table 5.14: Summary of volumes for topology optimization with two springs placed by the topological derivative for various values of k

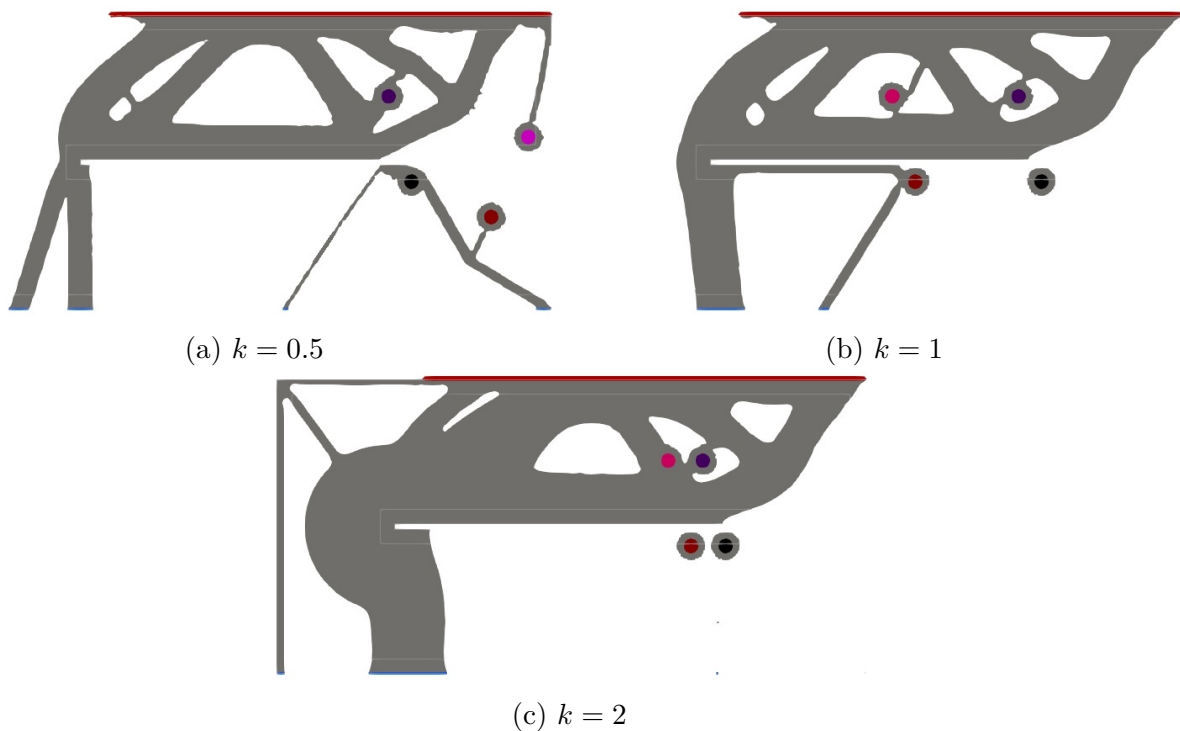


Figure 5.22: Optimal shapes for various values of k with two springs placed by the topological derivative

- First spring put at the location given by the parametric gradient and second spring put at the location given by the topological derivative

Let us consider the configuration for which the first spring is put at the location given by the parametric gradient and the second one is put at the location given by the topological derivative (cf Fig. 5.20 for the initialization). We focus only on the interesting cases $k = 0.5$ and $k = 1$. The optimal shapes and volumes evolution are given in Fig. 5.23 and Table 5.15. The structure for $k = 0.5$ tends to be a truss structure. This configuration supplies much more weight reduction than previous structures. Actually, the volume decreases by 78%. The topology tendency for $k = 1$ has already been found in previous tests. The interesting point is that the two springs are considered as one. Actually, they are close enough to merge their extra material and work as one bigger spring. It implies a better weight reduction of about 68%.

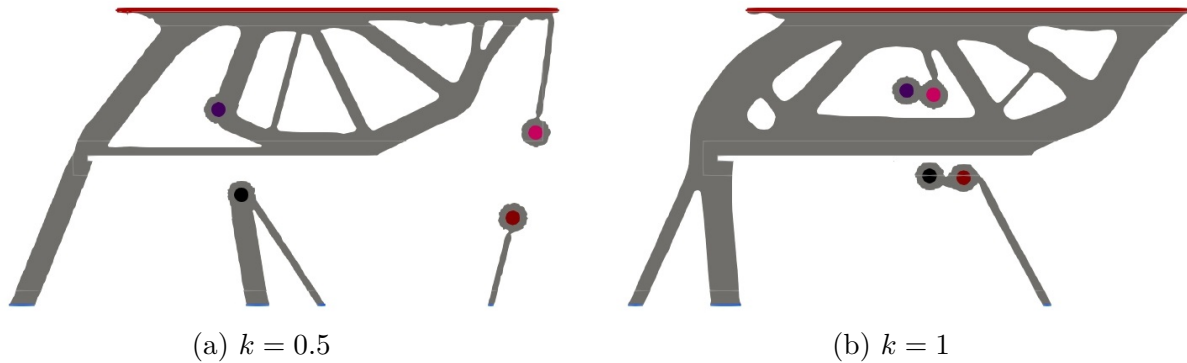


Figure 5.23: Optimal shapes for various values of k where the first spring is placed by the parametric gradient and the second one by the topological derivative

	Initial Volume	Final Volume	Improvement
$k = 0.5$	1.84583	0.404593	78.08%
$k = 1$	1.8388	0.595868	67.59%

Table 5.15: Summary of volumes for topology optimization with the first spring is placed by the parametric gradient and the second one by the topological derivative

- Both springs put at the location given by the parametric gradient

The following test is initialized with the springs resulting from the location optimization of $\mathbf{x}_{0,1}$ and $\mathbf{x}_{0,2}$. Their final values are given in Table 5.12. Results and the optimal shapes are given in Table 5.16 and Fig. 5.24. The case $k = 0.5$ provides one more time a bar structure but the current topology is quite different. The bars are thinner, which gives a weight reduction of more than 83%. This is the best performance so far for the scaling $k = 0.5$. The case $k = 1$ generates a more common topology for this use case. The main point is that the two springs work as one. It allows then a better weight reduction of more than 68%. This is also the best performance so far for the scaling $k = 1$.

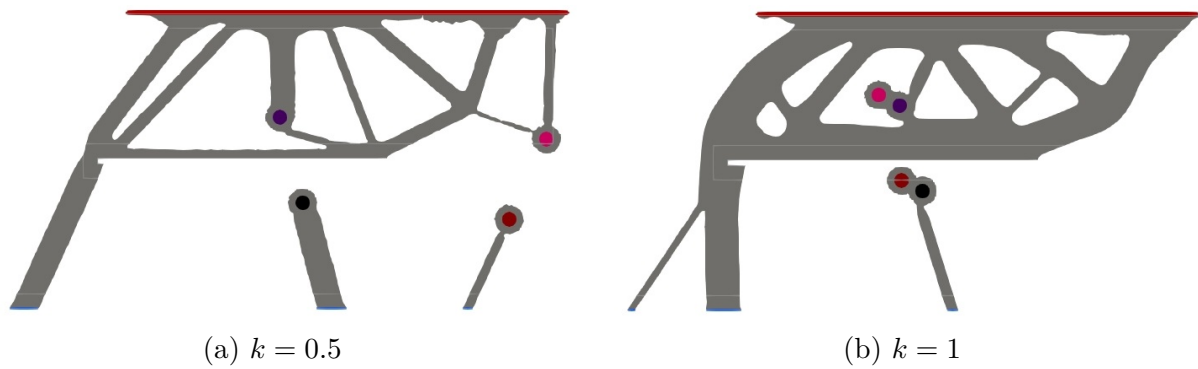


Figure 5.24: Optimal shapes for various values of k where both springs are placed according to the parametric gradient

	Initial Volume	Final Volume	Improvement
$k = 0.5$	1.84042	0.370452	83.45%
$k = 1$	1.83701	0.577531	68.56%

Table 5.16: Summary of volumes for topology optimization with both springs are placed according to the parametric gradient

- Second spring placed by the topological derivative on optimal shapes with one spring

Consider the configuration where a new spring is added on the optimal shape with one spring (cf. Fig. 5.20). New topologies and results are given in Fig. 5.25 and Table 5.17.

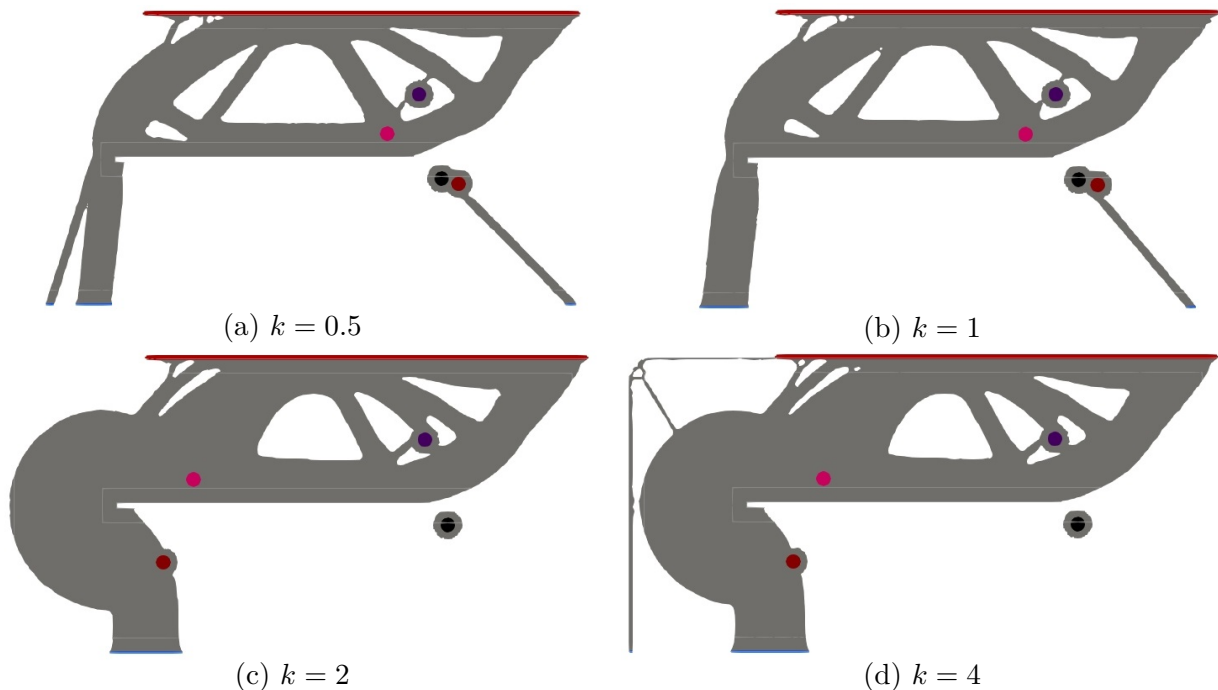


Figure 5.25: Optimal shapes for various values of k when the structure is initialized to the optimal shape with one spring

Even if the results were not always physically representative, it is still interesting to check potential topological changes. There were two types of topologies for the optimal shapes with one spring. The addition of a second spring implies four, look alike but different, topologies. For the cases $k = 0.5$ and $k = 1$, the thin bar linking the head of the spring to the structure breaks (cf. Figs. 5.14a and 5.14b) and some small bars appear in the top left corner. Moreover, the bar on the left side remains for $k = 0.5$ but disappears for $k = 1$. It is compensated but a thicker bar connecting Dirichlet boundary. The frame in the left corner disappears for $k = 2$ and becomes very thin for $k = 4$. It may breaks on a coarser mesh. In any case, the second spring brings an improvement in terms of volume.

	Initial Volume	Final Volume	Improvement
$k = 0.5$	0.646812	0.561626	13.17%
$k = 1$	0.678284	0.593736	12.47%
$k = 2$	0.871408	0.843039	3.26%
$k = 4$	0.88604	0.857378	3.23%

Table 5.17: Summary of volumes for structures initialized to the optimal shape with one spring

Coupled optimization of both structure and locations

This last section illustrates the coupled optimization of the structure and the location of both springs. The structure is initialized with holes. We propose here to test two initialization of the springs location. The problem is still to minimize the volume under a compliance constraint as stated in (5.58). The coupling strategy is still to perform 4 iterations of structural optimization and then 1 iteration of location optimization.

- Initial locations given by the topological derivative

The springs are initialized at the location given by the topological derivative (cf. Fig. 5.18). The final shapes and results are gathered in Fig. 5.26 and Tables 5.18 and 5.19.

	Initial $\mathbf{x}_{0,1}$	Final $\mathbf{x}_{0,1}$	Initial $\mathbf{x}_{0,2}$	Final $\mathbf{x}_{0,2}$
$k = 0.5$	(1.53,0.43)	(1.32,0.43)	(1.80,0.31)	(1.77,0.31)
$k = 1$	(1.53,0.43)	(1.41,0.42)	(1.09,0.43)	(1.07,0.40)
$k = 2$	(1.53,0.43)	(1.70,0.44)	(1.41,0.43)	(1.36,0.44)

Table 5.18: Summary of locations for coupled optimization of both structure and locations

All first springs change moderately their position. However, all second spring stay practically at the same location. The structure rather use only one spring for $k = 0.5$ and $k = 1$. The

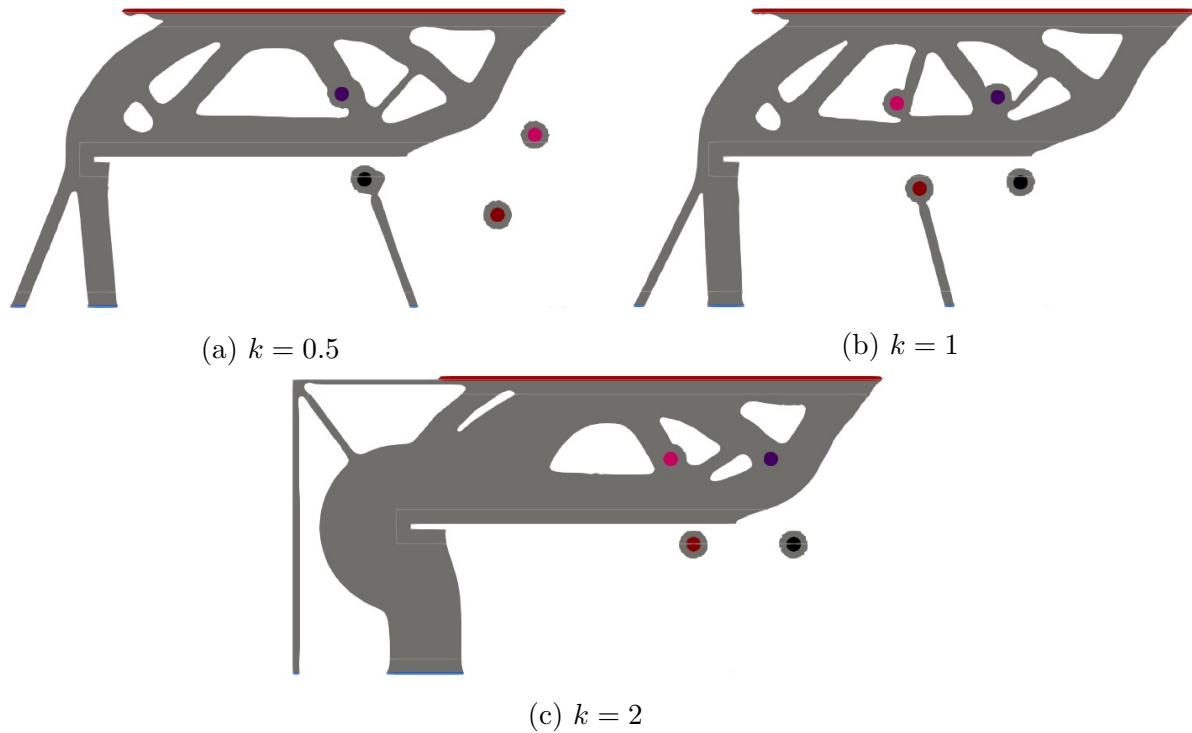


Figure 5.26: Optimal shapes for various values of k with two springs placed by the topological derivative

resulting topology is then similar to previous results with only one spring. For $k = 2$, the structure unsurprisingly disconnects both springs and gets the topology of the structure without any spring. In any case, volume improvements are of the same order of magnitude as the analysis with one spring.

	Initial Volume	Final Volume	Improvement
$k = 0.5$	1.84065	0.590111	67.94%
$k = 1$	1.83765	0.603912	67.14%
$k = 2$	1.83765	0.861603	53.11%

Table 5.19: Summary of volumes for coupled optimization of both structure and locations

Remark 48. *In every tests, each time a spring disconnects from the structure, the extra-material surrounding one extremity is, at least, included in the structure. Thus, this material contributes to stiffen the structure. However, the case $k = 0.5$ disconnects both extremities of the second spring which may seem awkward. Actually, this anomaly results from the coupling strategy that performs 4 iterations of structure optimization, followed by 1 iteration of location optimization, and so on. This process favors the structure and may oversight the springs behavior, which is the case here. Fig. 5.27 shows the optimal topology and location with a strategy of 1 iteration of structure optimization, followed by 1 iteration of location optimization, and so on. The second spring is indeed active in the system and the topology is relatively different. This strategy*

produces a final volume of $V(\Omega) = 0.55639$, which corresponds to an improvement of 69.77%. This strategy provides thus a better weight reduction than the previous one. The final spring locations are $\mathbf{x}_{0,1} = (1.18, 0.44)$ and $\mathbf{x}_{0,2} = (1.79, 0.31)$.

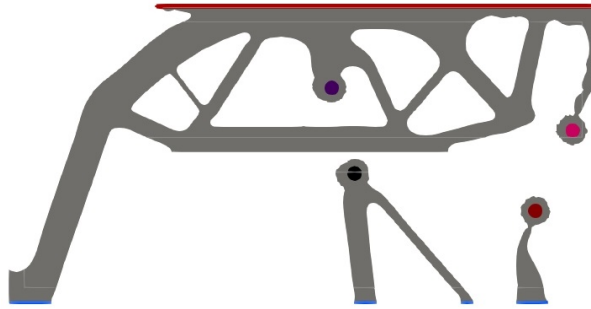


Figure 5.27: Alternate 1 structure and 1 location optimization for $k = 0.5$

- Initial locations given by the parametric gradient

The springs are now initialized at the location given by the parametric gradient (cf. Fig. 5.20). We keep here the alternate strategy of 4 iterations for the structure and 1 iteration for the locations. The final shapes and results are gathered in Fig. 5.28 and Tables 5.20 and 5.21. The springs almost remain at the same location. However, final topologies differ from the results with fixed springs given by the parametric gradient (cf. Fig. 5.24). The case $k = 0.5$ still tend to be a bar structure but the so-called bars are thicker and arranged differently. The case $k = 1$ still consider both springs as one bigger spring. The main difference comes from the small bars linking the extremity of the spring inside the structure. Volume reduction is comparable for $k = 1$ but it is way much better for $k = 0.5$ with fixed springs.

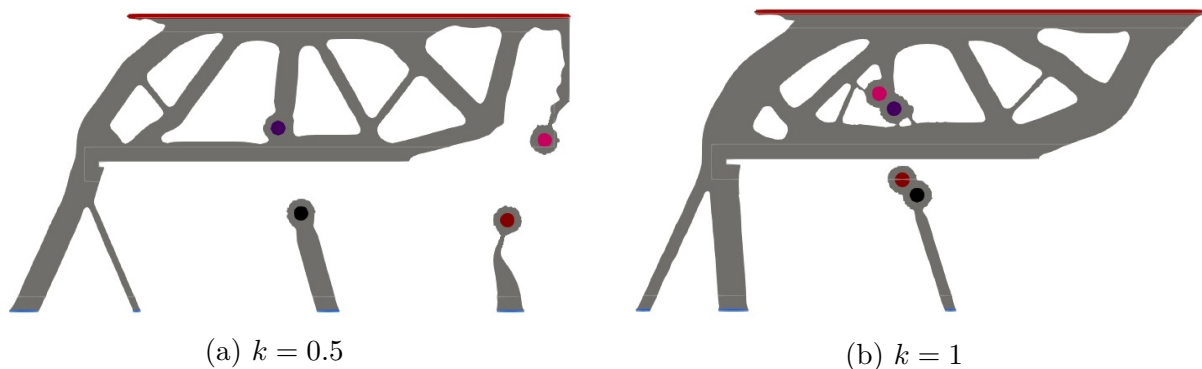


Figure 5.28: Optimal shapes for various values of k with two springs placed by the parametric gradient

	Initial $\mathbf{x}_{0,1}$	Final $\mathbf{x}_{0,1}$	Initial $\mathbf{x}_{0,2}$	Final $\mathbf{x}_{0,2}$
$k = 0.5$	(1.09,0.36)	(1.09,0.33)	(1.80,0.31)	(1.79,0.31)
$k = 1$	(1.06,0.40)	(0.99,0.44)	(1.04,0.39)	(0.99,0.44)

Table 5.20: Summary of locations for coupled optimization of both structure and locations

	Initial Volume	Final Volume	Improvement
$k = 0.5$	1.84042	0.485033	73.65%
$k = 1$	1.83701	0.567109	69.13%

Table 5.21: Summary of volumes for coupled optimization of both structure and locations

5.3.3 Summary of this 2d use case

The present study highlights four tools to deal with the topology optimization of both structure and spring(s) :

- Level-set method to optimize the structure
- Topological derivative to place and orient one new spring
- Parametric gradient to optimize the spring location
- Coupling level-set method and parametric gradient to optimize both the structure and the spring(s) location

These tools can be completed with a parametric gradient that optimize the orientation \mathbf{e} , the size ρ or the length ℓ of the spring. Fig. 5.29 sums up the ramifications of this 2d use case. We recall that the positioning with the topological derivative and the location optimization with the parametric gradient aim at minimizing the compliance. The structure and the coupled structure and location optimization goal is to minimize the volume under a constraint on the compliance.

A naive thought would be to expect the best performance from the coupled optimization of both structure and locations. However, as noticed in Remark 48, this strategy depends highly on the alternation between both design variables. In the case $k = 0.5$ for instance, the best strategy is so far to place and orient successively two springs with the topological derivative. The next step is to optimized locations with the parametric gradient. The final point is to optimize the structure. This use case illustrates well the non-convexity of the problem and the diversity of local minima. It also highlights the potential of the coupling for 3d use cases and industrial applications.

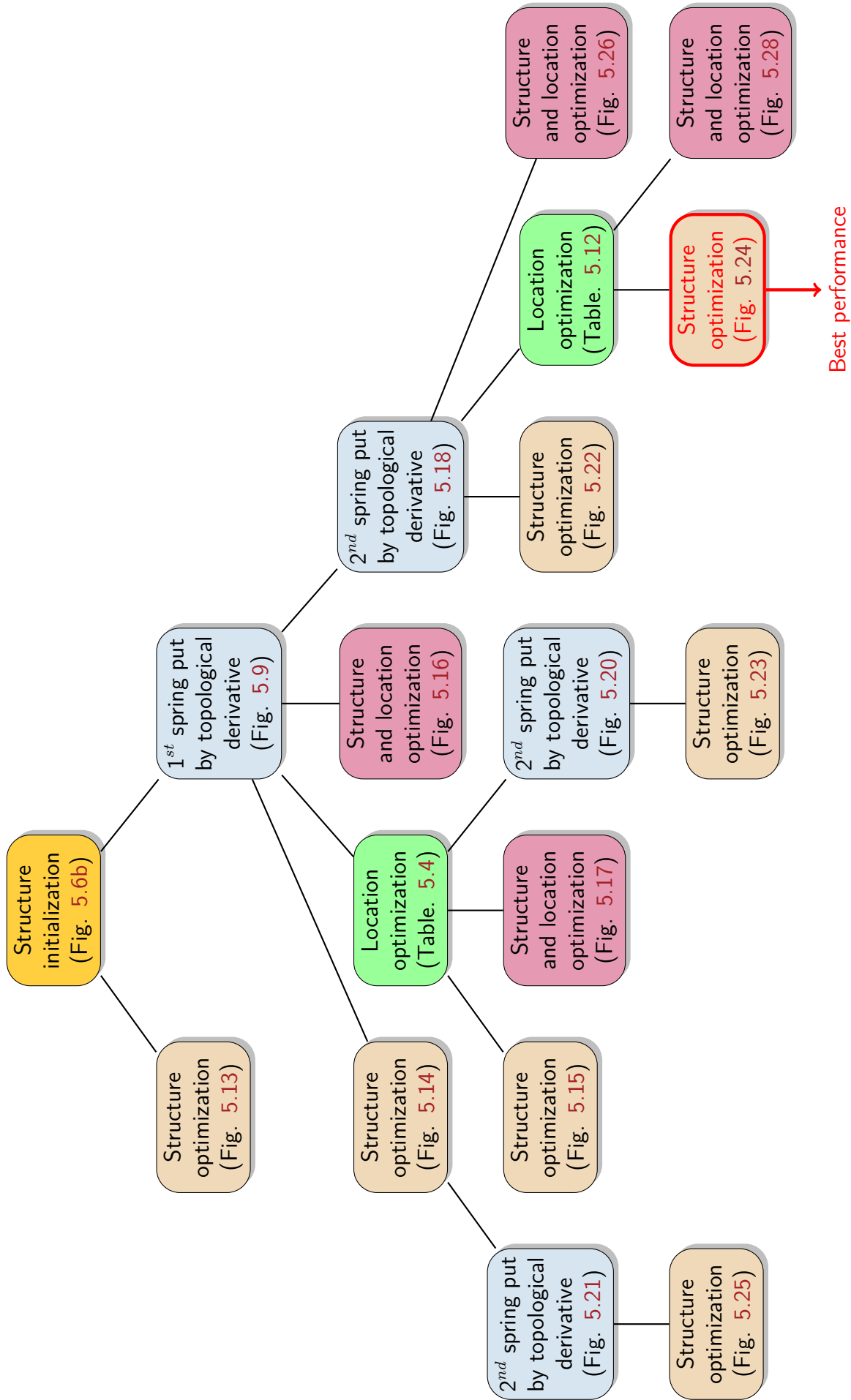


Figure 5.29: Summary of this 2d use case

5.4 Numerical illustrations in 3d

This section presents two main points with an illustrative use case in 3d. The first issue concerns the impact of the strategy in connections positioning with the topological derivative. The second issue is to perform a shape optimization with a spring placed by the topological derivative. The main idea is to compare the results with or without a fastener hole that is not taken into account in the topological derivative and brings an other perturbation on the assembly. The system contains two disjointed parts pictured in Fig. 5.30. They are not bounded to each other. All computations of the section are performed without a contact model. The mesh contains 435 604 tetrahedral elements with a minimal and maximal size of 8.9×10^{-2} and 6.3×10^{-1} . The assembly is clamped on the bottom and on the left. A force $\mathbf{g} = (0, 1, -3)$ is applied on the top. Both parts are of the same material. The Young's modulus is taken equal to 5 000 and the Poisson's coefficient is 0.3. All springs are characterized with a scale size of $\rho = 0.2$, a length of $\ell = 2$ and a stiffness of $K = 5000$. All these material properties are adimensional and can be changed as the user wants.

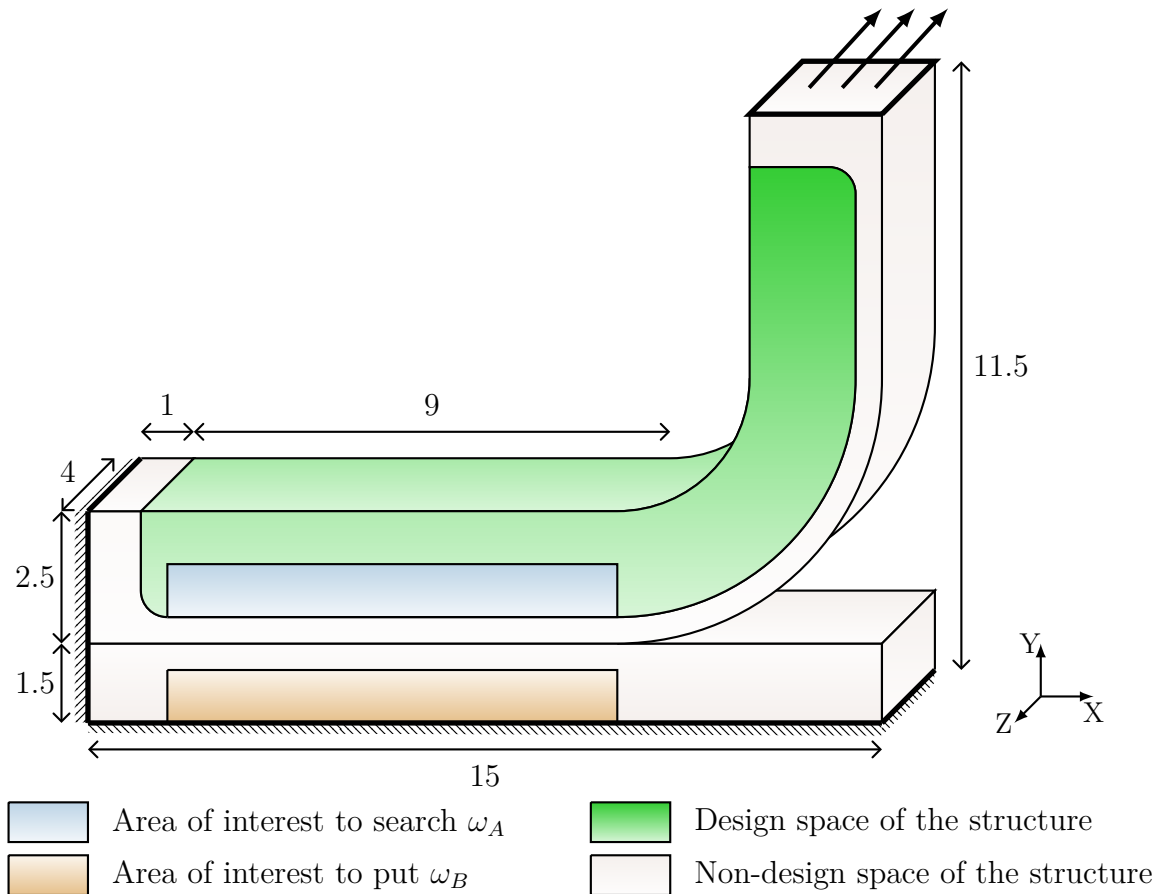


Figure 5.30: Setting of the 3d use case

5.4.1 Tests of the topological derivative

This section investigates two tests of the topological derivative involving two springs, named S_α and S_β , with the same physical properties. The first test starts with the assembly without any spring. It consists in choosing and fixing the location \mathbf{x}_{0,S_α} of the head of the spring S_α and then search for the best orientation with the topological derivative. Once, this first spring is

fully included in the system, the location \mathbf{x}_{0,S_β} of the head of the second spring S_β is chosen and fixed. Then, its optimal orientation is found with the topological derivative.

The second test starts with the assembly containing only the spring S_β provided by the first test. The location \mathbf{x}_{0,S_α} of the head of the spring S_α and its best orientation is found by the topological derivative.

For each tests, the problem is to place a small spring to decrease the compliance $J(\Omega) = \int_{\Gamma_N} \mathbf{g} \cdot \mathbf{u} dS$.

The initial compliance of the system without any spring is $J_0(\Omega) = 50.0209$. The system is self-adjoint and the topological derivative reads

$$DJ(\mathbf{x}_0, \mathbf{e}) = \begin{cases} -K(\mathbf{u}(\mathbf{x}_0 + \ell\mathbf{e}) - \mathbf{u}(\mathbf{x}_0)) \cdot \mathbf{e}^2 & \text{if } k > 1 \\ -\left(\frac{1}{K} + \frac{2}{|\omega|\tau}\right) (\mathbf{u}(\mathbf{x}_0 + \ell\mathbf{e}) - \mathbf{u}(\mathbf{x}_0)) \cdot \mathbf{e}^2 & \text{if } k = 1 \\ -\frac{|\omega|\tau}{2} (\mathbf{u}(\mathbf{x}_0 + \ell\mathbf{e}) - \mathbf{u}(\mathbf{x}_0)) \cdot \mathbf{e}^2 & \text{if } 0 < k < 1 \end{cases}, \quad (5.59)$$

where $\tau = \frac{15}{2} \frac{\mu(2\mu + \lambda)}{(5\mu + 2\lambda)r_1^2}$ with $r_1 = 1$ the radius of the unit ball. The behavior of DJ is independent of the scale size ρ of the inclusion. The optimal location \mathbf{x}_0 and orientation \mathbf{e} are the same whatever the value of k . However, the coefficient, in other words the amplitude, of the topological derivative depends on the scaling k . It has already been proved in the previous 2d use case that this scaling makes the efficiency of the spring vary. However, it does not impact the topological derivative indications. In the following, all springs are scaled by a factor $k = 2$. It means that the stiffness of the spring is proportional to the cross-section area of the spheres.

Test 1

Results are displayed in Fig. 5.31 and numerical results are given in Table 5.22. One after the other, both springs bring an improvement of the compliance. The final configuration, *i.e.* with both springs S_α and S_β , stiffens the assembly of about 10%.

	$DJ(\mathbf{x}_0, \mathbf{e})$	\mathbf{x}_0 (fixed)	(φ, Ψ)	$J_\rho(\Omega)$
Spring S_α	-118.224	(8,1,1)	$\left(\frac{\pi}{3}, \frac{55\pi}{36}\right)$	48.4245
Spring S_β	-127.425	(6,1,3.25)	$\left(\frac{4\pi}{9}, \frac{25\pi}{18}\right)$	45.2882

Table 5.22: Summary of the topological derivative test for the test 1

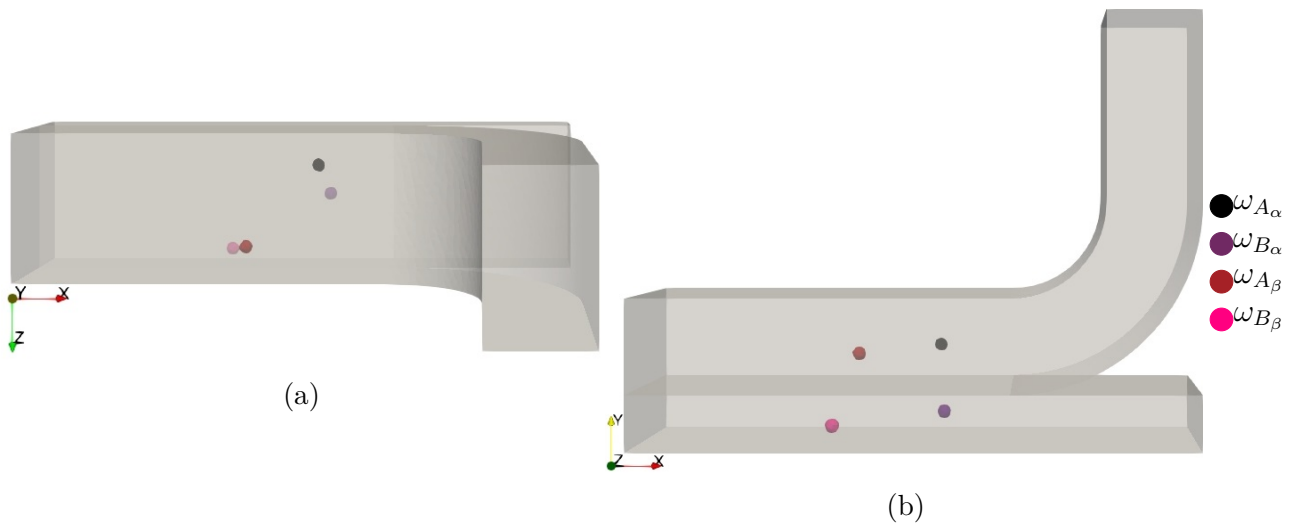


Figure 5.31: Results of the test 1

Test 2

Results are displayed in Fig. 5.32 and numerical results are given in Table 5.23. It is noteworthy that the compliance only with the spring S_β is quite close to the final compliance of test 1 with both springs S_α and S_β . It means that the spring S_α does practically not contribute to stiffen the system at the end of test 1. The optimal orientation of the spring S_α is investigated by the topological derivative on the system containing S_β . It gives an other configuration and a better performance than in test 1. This short example is enough to prove once more the importance of a shrewd strategy in connections positioning.

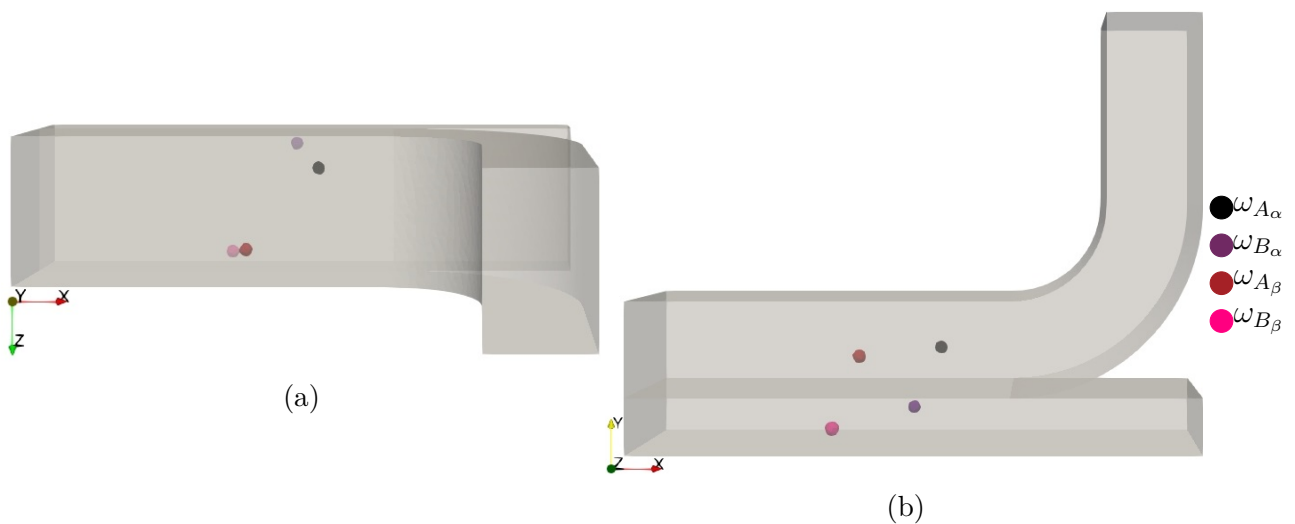


Figure 5.32: Results of the test 2

Remark 49. *This test case configures successively two springs. It provides different results, depending on the initialization. Since the locations of the springs are fixed, a proper strategy would be to orient successively the spring as the user wants and complete with a simultaneous parametric optimization of both springs orientation.*

	$DJ(\mathbf{x}_0, \mathbf{e})$	\mathbf{x}_0 (fixed)	(φ, Ψ)	$J_\rho(\Omega)$
Spring S_β (fixed)	-	(6,1,3.25)	$\left(\frac{4\pi}{9}, \frac{25\pi}{18}\right)$	45.4085
Spring S_α	-62.3433	(8,1,1)	$\left(\frac{7\pi}{12}, \frac{49\pi}{36}\right)$	44.3795

Table 5.23: Summary of the topological derivative test for the test 2

5.4.2 Shape optimization

Consider the filled structure to initialize shape optimization. Let us place one spring, vertically oriented, at the location indicated by the topological derivative to decrease the compliance. The spring is at the best position found at the point $\mathbf{x}_0 = (9.19, 0.74, 3.14)$. The problem is to minimize the volume of the design space of the structure (see the sub-domain in green in Fig. 5.30) under a constraint on the compliance of the system which is allowed to increase by 15%. It reads

$$\begin{aligned} \min_{\Omega \in \mathcal{U}_{ad}} \quad & V(\Omega_{DS}), \\ \text{s.t.} \quad & C(\Omega) \leq 1.15C_0 \end{aligned} \quad (5.60)$$

where $V(\Omega_{DS}) = \int_{\Omega_{DS}} dV$ with Ω_{DS} the design space of the structure, $C(\Omega) = \int_{\Gamma_N} \mathbf{g} \cdot \mathbf{u} dS$ and $C_0 = 44.4956$. The compliance constraint is handled with the Augmented Lagrangian method. The optimal structure is given in Fig. 5.33. The initial volume of the design space is $V_0 = 147.319$. Its final volume is $V(\Omega) = 113.83$, which correspond to a decrease of 22.73%.

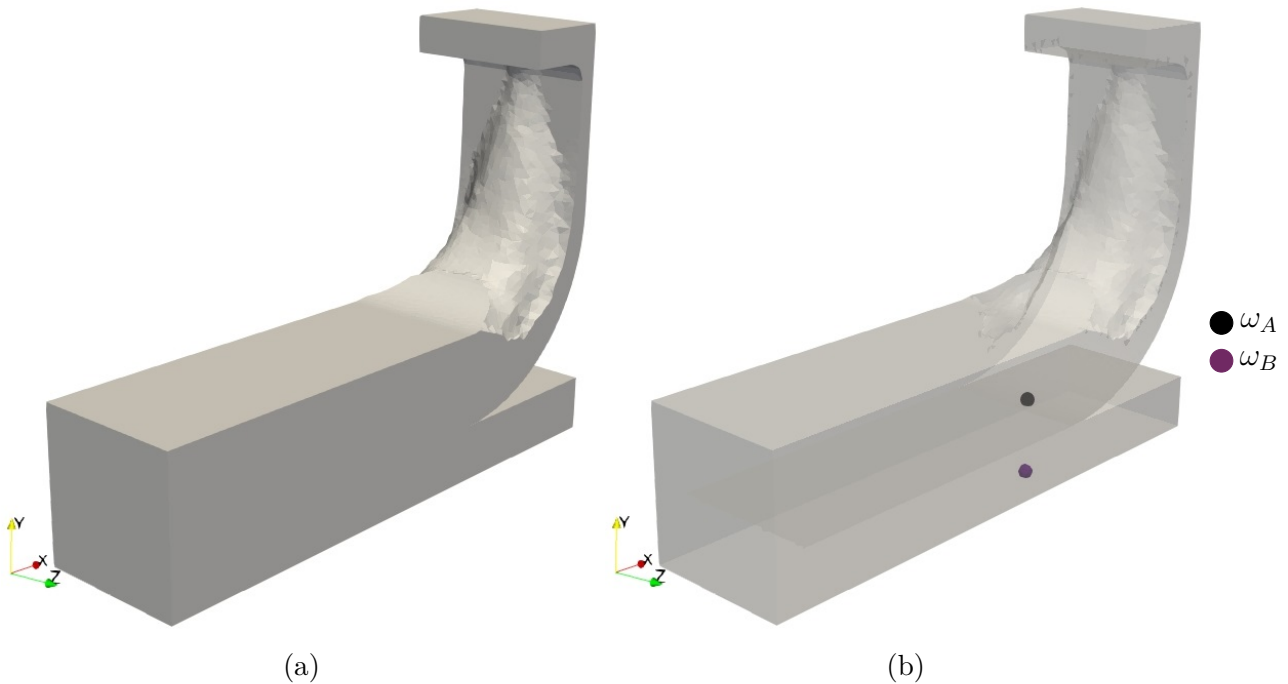


Figure 5.33: Optimal shape

Integration of a fastener hole

Consider the spring put at $\mathbf{x}_0 = (9.19, 0.74, 3.14)$ and vertically oriented on the filled structure. A fastener hole is added in the geometry of the system for more physical representativeness. This hole is vertically oriented and twice the width of the spheres. The optimization problem is still (5.60) with $C_0 = 44.9651$. This slight increase of the initial compliance is naturally due to the inclusion of the fastener hole. Also, the initial volume of the design space is $V_0 = 146.685$. The optimal structure is given in Fig. 5.34. The shape is very close to the optimal structure without the fastener hole. The final volume is $V(\Omega) = 114.535$, which correspond to a decrease of 21.92%. In the present test case, the performance of the assembly is very similar with or without a fastener hole.

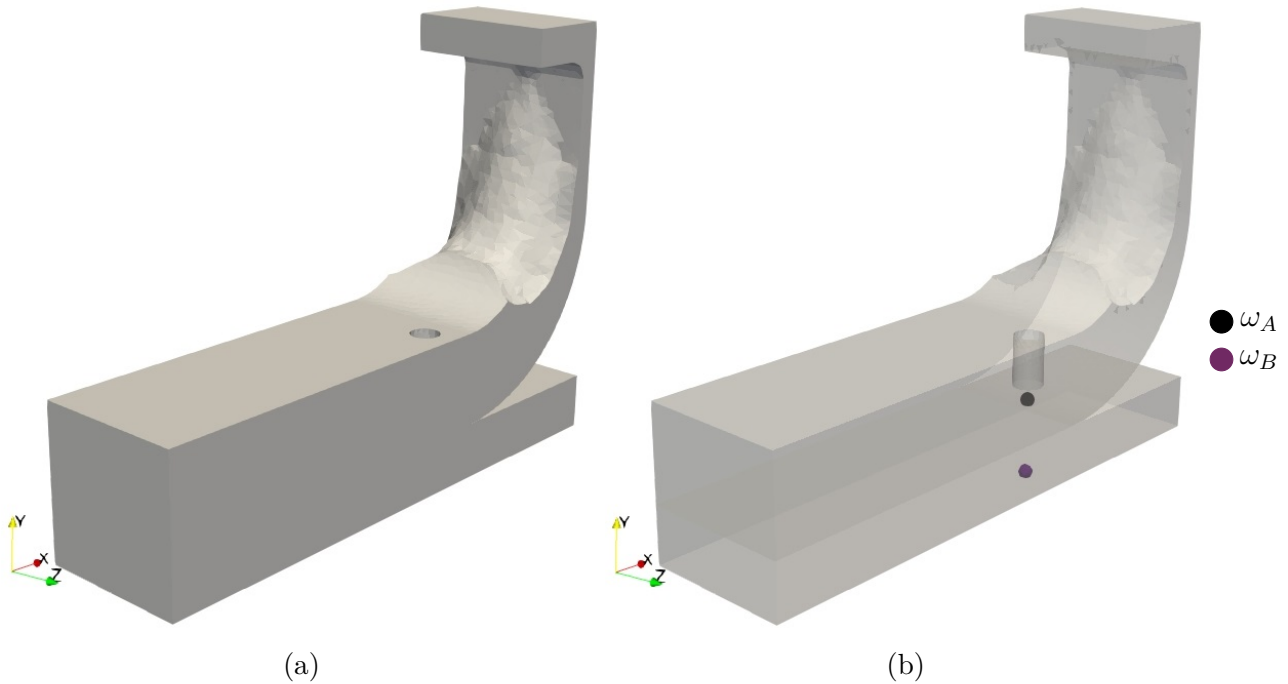


Figure 5.34: Optimal shape with a fastener hole

5.5 Conclusion of the chapter

This chapter investigates the topological derivative with respect to two small elastic inclusions linked by a small spring in 2d and 3d. It provides substantial key points for the topological derivative with respect to an idealized bolt developed in Chapter 7. The variety of numerical illustrations highlights the plenty of combinations for coupling the optimization of structure and springs. Four tools are involved in this coupling :

- Level-set method to optimize the structure
- Topological derivative to place and orient one new small spring
- Parametric gradient to optimize the spring(s) location
- Coupling level-set method and parametric gradient to optimize both the structure and the spring(s) location.

The coupling provides better results than a topology optimization with fixed connections. However, there is a lot of local minima and a shrewd strategy in the coupling is required for even better results. This strategy requires the choice of :

- the initial location of springs (placed by the topological derivative or optimized by the parametric gradient)
- running a structure advection with fixed but already optimized springs or couple the optimization of structure and location
- the alternating strategy between the structure advection and the parametric gradient for location optimization if structure and location optimizations are coupled.

Two rigid inclusions linked by a spring

Contents

6.1	Setting of the problem	171
6.1.1	Background domain	171
6.1.2	Perturbed domain	172
6.2	Computation of the topological derivative	175
6.2.1	Approximation of the perturbed displacement field	175
6.2.2	Adjoint state	184
6.2.3	Proof of the main result	185
6.3	Numerical illustrations in 2d	191
6.3.1	Analysis with one bolt-like connection	191
6.3.2	Analysis with two bolt-like connections	196
6.4	Numerical illustrations in 3d	196
6.5	Conclusion of the chapter	200

The idealized bolt connection is described in two manners in Chapter 2. The previous chapter focuses on the first model with elastic inclusions linked by a spring. We consider now the ingredient of rigid body motion on the inclusions to suit with the variant model of the idealized bolt connection. For the sake of simplicity, the pre-stressed state is still not taken into account. Then, the present chapter investigates the topological sensitivity analysis with regards to two small rigid inclusions linked by a spring. It mixes the tools of Chapters 4 and 5. This chapter aims at choosing the most suitable idealized bolt model for the purpose of topological sensitivity. Main results are given in 2d and 3d but the proof is carried out for the 3d problem. In the sequel, the term "bolt-like connection" will abusively refer to the two small rigid inclusions linked by a spring. The topological derivative is tested on the same 2d academic use case as the one of Chapter 5 and on an other 3d academic use case.

6.1 Setting of the problem

The following analysis is carried out within the framework of linear elasticity in 3d. Let Ω be the union of two disjointed parts Ω_A and Ω_B . This union is assumed to be a smooth bounded domain of \mathbb{R}^3 . The boundary of this domain is made of two disjointed parts, $\partial\Omega = \Gamma_N \cup \Gamma_D$. Neumann and Dirichlet boundary conditions are respectively imposed on Γ_N and Γ_D . Let the domain Ω be with a linear isotropic elastic material. For a displacement field \mathbf{u} , the strain tensor is defined by $\varepsilon(\mathbf{u}) = \frac{1}{2}(\nabla\mathbf{u} + \nabla^T\mathbf{u})$. The stress tensor is then given by the Hooke's law

$$\mathbf{A}\varepsilon(\mathbf{u}) = \begin{cases} 2\mu_A\varepsilon(\mathbf{u}) + \lambda_A\text{tr}(\varepsilon(\mathbf{u}))\mathbf{I} & \text{in } \Omega_A \\ 2\mu_B\varepsilon(\mathbf{u}) + \lambda_B\text{tr}(\varepsilon(\mathbf{u}))\mathbf{I} & \text{in } \Omega_B \end{cases},$$

where μ_A and λ_A (resp. μ_B and λ_B) are the Lamé coefficients of the material Ω_A (resp. Ω_B). We assume a perfect interface between Ω_A and Ω_B . Thus, there are usual transmission conditions between both parts that insure continuity of displacement and normal stress at the interface. The goal of this chapter is to compute the topological derivative with respect to two small rigid inclusions linked by a 1 DOF spring. The topological expansion takes only into account the leading term of the rigidity matrix of that spring with regards to the size of the inclusions. The other terms of the matrix would be remainder terms of the sensitivity analysis. This leading rigidity is the stiffness along the axis of the spring, that is to say its tension-compression behavior.

6.1.1 Background domain

The background domain refers to the system in which one wants to add a small bolt-like connection. It has been proved in Chapter 5 that pre-existing springs do not impact the topological sensitivity analysis. Then, we suppose here that the initial domain does not contain bolt-like connection yet. The background solution \mathbf{u} then satisfies the linear elasticity system

$$\begin{cases} -\text{div}(\mathbf{A}\varepsilon(\mathbf{u})) = \mathbf{0} & \text{in } \Omega \\ \mathbf{A}\varepsilon(\mathbf{u})\mathbf{n} = \mathbf{g} & \text{on } \Gamma_N. \\ \mathbf{u} = \mathbf{0} & \text{on } \Gamma_D \end{cases} \quad (6.1)$$

Assuming that surface loads \mathbf{g} belong to $L^2(\Gamma_N)^3$, Lax-Milgram theorem, coupled with Korn's inequality, gives the existence and the uniqueness of the solution $\mathbf{u} \in \mathcal{W}$, where

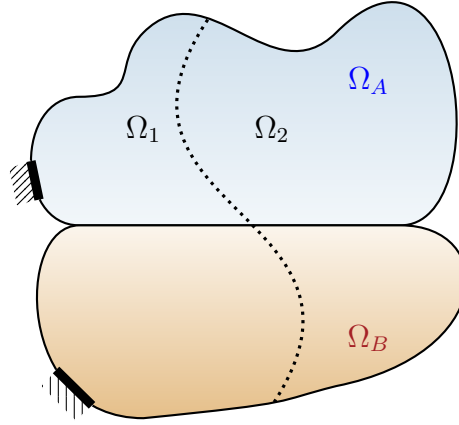
$$\mathcal{W} = \left\{ \mathbf{w} \in (H^1(\Omega))^3, \mathbf{w} = \mathbf{0} \text{ in } \Gamma_D \right\}. \quad (6.2)$$

In the following, we assume that \mathbf{u} is as smooth as we want, which is always possible by assuming that the load \mathbf{g} is smooth as well as the domain. We recall that the transmission condition between Ω_A and Ω_B insures the continuity of displacement and normal stress.

Let Ω_1 and Ω_2 be a partition of Ω , that is $\Omega = \Omega_1 \cup \Omega_2$ and $\Omega_1 \cap \Omega_2 = \emptyset$ as pictured in Fig. 6.1. To avoid technicalities, the objective function is evaluated in Ω_1 , while the bolt-like connection is included in Ω_2 .

Consider the generic objective function

$$J_0(\Omega) = \int_{\Omega_1} F(\mathbf{u})dV + \int_{\Gamma_N} G(\mathbf{u})dS, \quad (6.3)$$

Figure 6.1: Decomposition of the domain Ω

which depends on the domain Ω through the function \mathbf{u} solution of (6.1). The functions F and G are smooth, twice differentiable with respect to \mathbf{u} and satisfy the following conditions

$$\exists \alpha > 0, \begin{cases} |F(\mathbf{u})| \leq \alpha(|\mathbf{u}|^2 + 1), & |F'(\mathbf{u})| \leq \alpha(|\mathbf{u}| + 1), & |F''(\mathbf{u})| \leq \alpha \\ |G(\mathbf{u})| \leq \alpha(|\mathbf{u}|^2 + 1), & |G'(\mathbf{u})| \leq \alpha(|\mathbf{u}| + 1), & |G''(\mathbf{u})| \leq \alpha \end{cases}. \quad (6.4)$$

Remark 50. *Conditions (6.4) are simple and sufficient. They can be improved if necessary.*

The adjoint state \mathbf{p} associated to (6.1) for a generic objective function (6.3) solves

$$\begin{cases} -\operatorname{div}(\mathbf{A}\varepsilon(\mathbf{p})) = -\mathbf{F}'(\mathbf{u})\mathbf{1}_{\Omega_1} & \text{in } \Omega \\ \mathbf{A}\varepsilon(\mathbf{p})\mathbf{n} = -\mathbf{G}'(\mathbf{u}) & \text{on } \Gamma_N. \\ \mathbf{p} = \mathbf{0} & \text{on } \Gamma_D \end{cases} \quad (6.5)$$

Lax-Milgram theorem, coupled with Korn's inequality, gives the existence and the uniqueness of the solution $\mathbf{p} \in \mathcal{W}$. In the sequel, we assume that \mathbf{p} is as smooth as required, similarly to the assumptions on \mathbf{u} .

6.1.2 Perturbed domain

We choose the reference shape ω to be the unit ball of \mathbb{R}^3 , which allows us to compute explicitly the coefficients of the topological derivative. Let ω_A be a small inclusion of shape ω , rescaled by an adimensional factor $\rho > 0$ and centred at the point $\mathbf{x}_0 \in \Omega_2$. The second inclusion, denoted ω_B , is the translation of ω_A at a distance $\ell > 0$ and in the direction \mathbf{e} , a unit vector. More specifically, the inclusions read

$$\omega_A = \left\{ \mathbf{x} \in \mathbb{R}^3, \frac{\mathbf{x} - \mathbf{x}_0}{\rho} \in \omega \right\} \text{ and } \omega_B = \left\{ \mathbf{x} \in \mathbb{R}^3, \frac{\mathbf{x} - \mathbf{x}_0 - \ell\mathbf{e}}{\rho} \in \omega \right\}. \quad (6.6)$$

In the following, the factor ρ will abusively refer to the size of the inclusions.

We propose to perturb the background domain with two rigid inclusions linked by a spring of rigidity $\kappa(\rho)$ as pictured in Fig. 6.2. This new configuration is called the perturbed domain.

The inclusions, ω_A and ω_B , represent respectively the extremities of the spring. Let us assume the following scaling of the model

$$\kappa(\rho) = K\rho^k, \tag{6.7}$$

with $K > 0$ and $k \in \mathbb{R}$. It will be shown later that only those values $0 < k < 2$ are covered by our asymptotic analysis in 3d and $0 < k < 3/2$ in 2d.

Remark 51. *It makes sense that the rigidity of the spring goes to zero as the size of the inclusions goes to zero.*

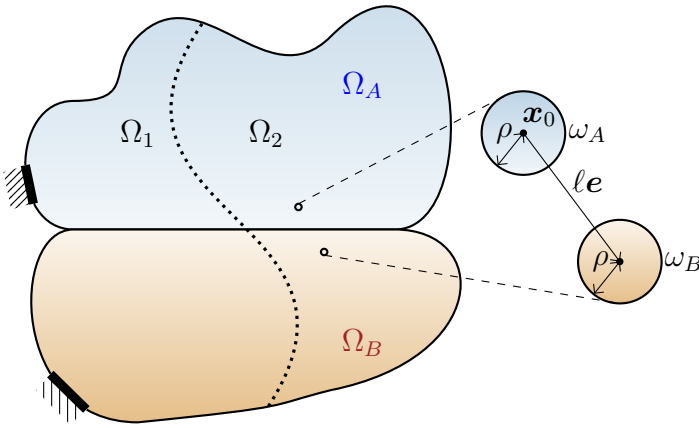


Figure 6.2: Perturbation of the domain Ω by a small spring

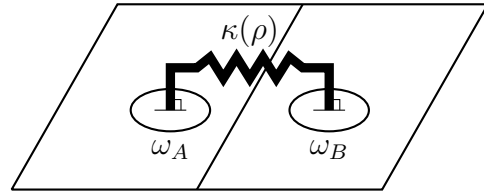


Figure 6.3: Graphical representation of the non-local rigidity $\kappa(\rho)$

Let us define the perforated domain Ω_ρ , *i.e.* the domain without the rigid inclusions

$$\Omega_\rho = \Omega \setminus (\omega_A \cup \omega_B). \tag{6.8}$$

The space of admissible displacements for this asymptotic analysis corresponds to zero displacement on Γ_D and rigid body motions in ω_A and ω_B ,

$$\mathcal{W}_{RB} = \left\{ \mathbf{w} \in (H^1(\Omega))^3, \mathbf{w} = \mathbf{0} \text{ on } \Gamma_D, \mathbf{w}(\mathbf{x}) = \mathbf{C}_a + \mathbf{R}_a \mathbf{x} \text{ in } \omega_A, \mathbf{w}(\mathbf{x}) = \mathbf{C}_b + \mathbf{R}_b \mathbf{x} \text{ in } \omega_B \right\}, \tag{6.9}$$

where $(\mathbf{C}_a, \mathbf{C}_b) \in \mathbb{R}^3 \times \mathbb{R}^3$ are translations and $\mathbf{R}_a = -\mathbf{R}_a^T$ and $\mathbf{R}_b = -\mathbf{R}_b^T$ are anti-symmetric 3x3 matrices modelling infinitesimal rotations. We recall the notation for the average on ω_A of the projection of the displacement along the axis of the spring \mathbf{e} , that is $\overline{\mathbf{w} \cdot \mathbf{e}} = \frac{1}{|\omega_A|} \int_{\omega_A} \mathbf{w} \cdot \mathbf{e} dV$.

For $\mathbf{w} \in \mathcal{W}_{RB}$, define the energy functional

$$E(\mathbf{w}) = \frac{1}{2} \int_{\Omega_\rho} \mathbf{A} \boldsymbol{\varepsilon}(\mathbf{w}) : \boldsymbol{\varepsilon}(\mathbf{w}) dV - \int_{\Gamma_N} \mathbf{g} \cdot \mathbf{w} dS + \frac{1}{2} \kappa(\rho) \left(\overline{\mathbf{w} \cdot \mathbf{e}}_{\omega_B} - \overline{\mathbf{w} \cdot \mathbf{e}}_{\omega_A} \right)^2. \tag{6.10}$$

As the idealized remote interaction model involves two rigid body motions in ω_A and ω_B , the space \mathcal{W}_{RB} is appropriate for the analysis. The first term of (6.10) is the elastic energy of the perforated domain Ω_ρ . The rigid body motions in each spheres implies that ω_A and ω_B

have zero deformation. Thus, they are excluded from the elastic energy. The last term is the energy of a spring of rigidity $\kappa(\rho)$. We recall in Fig. 6.3 the graphical representation of the out-of-plane non-local rigidity $\kappa(\rho)$. The minimum potential energy principle then states that the displacement field describing the system with a spring linking two rigid spheres is the unique minimizer \mathbf{u}_ρ of (6.10) in \mathcal{W}_{RB} , *i.e.*,

$$E(\mathbf{u}_\rho) = \min_{\mathbf{w} \in \mathcal{W}_{RB}} E(\mathbf{w}). \quad (6.11)$$

It leads to the following variational problem :

$$\begin{aligned} \text{Find } \mathbf{u}_\rho \in \mathcal{W}_{RB} \text{ s.t. } \forall \mathbf{w} \in \mathcal{W}_{RB}, \int_{\Omega_\rho} \mathbf{A}\varepsilon(\mathbf{u}_\rho) : \varepsilon(\mathbf{w})dV - \int_{\Gamma_N} \mathbf{g} \cdot \mathbf{w}dV \\ + \kappa(\rho) \left(\int_{\omega_B} \mathbf{u}_\rho \cdot \mathbf{e}dV - \int_{\omega_A} \mathbf{u}_\rho \cdot \mathbf{e}dV \right) \left(\int_{\omega_B} \mathbf{w} \cdot \mathbf{e}dV - \int_{\omega_A} \mathbf{w} \cdot \mathbf{e}dV \right) = 0. \end{aligned} \quad (6.12)$$

Assuming that surface loads \mathbf{g} belong to $L^2(\Gamma_N)^3$, Lax-Milgram theorem, coupled with Korn's inequality, gives the existence and the uniqueness of the solution $\mathbf{u}_\rho \in \mathcal{W}_{RB}$. In the sequel, we assume that \mathbf{u}_ρ is as smooth as we want, which is always possible by assuming that the loads and the domain are smooth. The rigid body motions in ω_A and ω_B may depend on the size of the inclusion. Translations and rotations are determined by forces and momentum equilibrium on the boundary of ω_A and ω_B . Denote the translations $(\mathbf{C}_a(\rho), \mathbf{C}_b(\rho)) \in \mathbb{R}^3 \times \mathbb{R}^3$ and the rotations $\mathbf{R}_a(\rho)$ and $\mathbf{R}_b(\rho)$ anti-symmetric matrices of size 3×3 . It follows then that the displacement field in the perturbed domain \mathbf{u}_ρ solves

$$\left\{ \begin{array}{ll} -\text{div}(\mathbf{A}\varepsilon(\mathbf{u}_\rho)) = \mathbf{0} & \text{in } \Omega_\rho \\ \mathbf{A}\varepsilon(\mathbf{u}_\rho)\mathbf{n} = \mathbf{g} & \text{on } \Gamma_N \\ \mathbf{u}_\rho = \mathbf{0} & \text{on } \Gamma_D \\ \mathbf{u}_\rho(\mathbf{x}) = \mathbf{C}_a(\rho) + \mathbf{R}_a(\rho)\mathbf{x} & \text{in } \omega_A \\ \mathbf{u}_\rho(\mathbf{x}) = \mathbf{C}_b(\rho) + \mathbf{R}_b(\rho)\mathbf{x} & \text{in } \omega_B \end{array} \right\}, \quad (6.13)$$

$$\left\{ \begin{array}{l} \int_{\partial\omega_A} \mathbf{A}\varepsilon(\mathbf{u}_\rho)\mathbf{n}dS = - \int_{\partial\omega_B} \mathbf{A}\varepsilon(\mathbf{u}_\rho)\mathbf{n}dS = \kappa(\rho) \left(\int_{\omega_B} \mathbf{u}_\rho \cdot \mathbf{e}dV - \int_{\omega_A} \mathbf{u}_\rho \cdot \mathbf{e}dV \right) \mathbf{e} \\ \int_{\partial\omega_A} \mathbf{A}\varepsilon(\mathbf{u}_\rho)\mathbf{n} \wedge \mathbf{x}dS = - \int_{\partial\omega_B} \mathbf{A}\varepsilon(\mathbf{u}_\rho)\mathbf{n} \wedge \mathbf{x}dS = \kappa(\rho) \left(\int_{\omega_B} \mathbf{u}_\rho \cdot \mathbf{e}dV - \int_{\omega_A} \mathbf{u}_\rho \cdot \mathbf{e}dV \right) \int_{\omega_A} \mathbf{e} \wedge \mathbf{x}dV \end{array} \right.$$

Remark 52. *The rigid body motion on ω_A and ω_B can be interpreted as very large material properties in ω_A and ω_B than the ones of the parts Ω_A and Ω_B . By the way, this is how the rigid spheres are implemented in numerical illustrations (see Sections 6.3 and 9.2).*

Denote by J_ρ the generic objective function (6.3) evaluated in the perturbed domain

$$J_\rho(\Omega) = \int_{\Omega_1} F(\mathbf{u}_\rho)dV + \int_{\Gamma_N} G(\mathbf{u}_\rho)dS. \quad (6.14)$$

Definition 7. The objective function J_ρ is said to admit a topological derivative $DJ(\mathbf{x}_0, \mathbf{e})$ at the point \mathbf{x}_0 for a bolt-like connection of direction \mathbf{e} and for a pair of inclusions of shape ω , if the following asymptotic expansion holds for small $\rho > 0$

$$J_\rho(\Omega) = J_0(\Omega) + s(\rho)DJ(\mathbf{x}_0, \mathbf{e}) + o(s(\rho)), \quad (6.15)$$

where $s(\rho)$ is a positive scalar function of ρ which satisfies $\lim_{\rho \rightarrow 0} s(\rho) = 0$.

Theorem 5. Take ω to be the unit ball of \mathbb{R}^n , $n = 2$ or 3 .

In 2d, the general objective function (6.14) admits a topological asymptotic expansion of the form (6.15),

$$J_\rho(\Omega) = J_0(\Omega) + K\rho^k(\mathbf{u}(\mathbf{x}_0 + \ell\mathbf{e}) - \mathbf{u}(\mathbf{x}_0)) \cdot \mathbf{e}(\mathbf{p}(\mathbf{x}_0 + \ell\mathbf{e}) - \mathbf{p}(\mathbf{x}_0)) \cdot \mathbf{e} + \begin{cases} O(\rho^{k/2+1}) & \text{if } 1 < k < 3/2 \\ O(\rho^{3k/2}) & \text{if } 0 < k < 1 \end{cases}, \quad (6.16)$$

where \mathbf{u} and \mathbf{p} are respectively the displacement and the adjoint state in the background domain that solve (6.1) and (6.5).

In 3d, the general objective function (6.14) admits a topological asymptotic expansion of the form (6.15), that is

$$J_\rho(\Omega) = J_0(\Omega) + s(\rho)DJ(\mathbf{x}_0, \mathbf{e}) + \mathcal{R}(s(\rho)), \quad (6.17)$$

with

$$DJ(\mathbf{x}_0, \mathbf{e}) = j(K, \tau_A, \tau_B)(\mathbf{u}(\mathbf{x}_0 + \ell\mathbf{e}) - \mathbf{u}(\mathbf{x}_0)) \cdot \mathbf{e}(\mathbf{p}(\mathbf{x}_0 + \ell\mathbf{e}) - \mathbf{p}(\mathbf{x}_0)) \cdot \mathbf{e}, \quad (6.18)$$

where \mathbf{u} and \mathbf{p} are respectively the displacement and the adjoint state in the background domain that solve (6.1) and (6.5). The scaling $s(\rho)$, the coefficient $j(K, \tau_A, \tau_B)$ and the remainder term $\mathcal{R}(s(\rho))$ are given, according to the value of the exponent k , by

	$s(\rho)$	$j(K, \tau_A, \tau_B)$	$\mathcal{R}(s(\rho))$	
$1 < k < 2$	ρ^k	K	$k \geq 5/3$	$O(\rho^{k/2+3/2})$
			$k < 5/3$	$O(\rho^{2k-1})$
$k = 1$	ρ	$\left(\frac{1}{K} + \frac{1}{ \omega } \left(\frac{1}{\tau_A} + \frac{1}{\tau_B}\right)\right)^{-1}$	$O(\rho^{3/2})$	
$0 < k < 1$	ρ	$\left(\frac{1}{ \omega } \left(\frac{1}{\tau_A} + \frac{1}{\tau_B}\right)\right)^{-1}$	$k \geq 2/3$	$O(\rho^{2-k})$
			$k < 2/3$	$O(\rho^{1+k/2})$

The coefficients τ_A and τ_B depend on material properties and read $\tau_A = \frac{9\mu_A(2\mu_A + \lambda_A)}{(5\mu_A + 2\lambda_A)r_1^2}$ and $\tau_B = \frac{9\mu_B(2\mu_B + \lambda_B)}{(5\mu_B + 2\lambda_B)r_1^2}$ with $r_1 = 1$ the radius of the unit ball.

6.2 Computation of the topological derivative

6.2.1 Approximation of the perturbed displacement field

This section aims to approximate the perturbed displacement field \mathbf{u}_ρ due to the small rigid inclusions of size ρ linked by a spring of rigidity $\kappa(\rho)$. The rigid inclusions are analyzed as in Chapter 4. The spring behavior is handled as in Chapter 5.

Far fields expression

As the inclusions are small, the perturbed field \mathbf{u}_ρ is expected to be approximately equal to the background field \mathbf{u} plus the influence fields of the inclusions ω_A and ω_B , respectively denoted \mathbf{v}_a and \mathbf{v}_b . In other words, we formally assume an ansatz that

$$\mathbf{u}_\rho(\mathbf{x}) \approx \mathbf{u}(\mathbf{x}) + \mathbf{v}_a \left(\frac{\mathbf{x} - \mathbf{x}_0}{\rho} \right) + \mathbf{v}_b \left(\frac{\mathbf{x} - \mathbf{x}_0 - \ell \mathbf{e}}{\rho} \right). \quad (6.19)$$

The functions \mathbf{v}_a and \mathbf{v}_b are defined in \mathbb{R}^3 . Perturbations due to the inclusions are getting smaller far from their center \mathbf{x}_0 and $\mathbf{x}_0 + \ell \mathbf{e}$. Thus, the far fields \mathbf{v}_a and \mathbf{v}_b have to decay at infinity like $\lim_{\mathbf{y} \rightarrow \infty} \mathbf{v}_a(\mathbf{y}) = 0$ and $\lim_{\mathbf{y} \rightarrow \infty} \mathbf{v}_b(\mathbf{y}) = 0$. In other words, these functions allow a zoom on the inclusions and ignore boundary conditions on $\partial\Omega$. The goal of this part is to approximate the perturbed displacement field \mathbf{u}_ρ using the behavior of the far fields \mathbf{v}_a and \mathbf{v}_b . In order to rescale the elasticity problem with inclusions of unit size ω , let us define rescaled variables $\mathbf{y}_a \in \mathbb{R}^3$ and $\mathbf{y}_b \in \mathbb{R}^3$ by

$$\mathbf{y}_a = \frac{\mathbf{x} - \mathbf{x}_0}{\rho} \quad \text{and} \quad \mathbf{y}_b = \frac{\mathbf{x} - \mathbf{x}_0 - \ell \mathbf{e}}{\rho}. \quad (6.20)$$

The background solution is expressed according to the following Taylor expansions

$$\mathbf{u}(\mathbf{x}) = \mathbf{u}(\mathbf{x}_0) + O(\rho) \quad \text{in a neighbourhood of } \mathbf{x}_0, \quad (6.21)$$

$$\mathbf{u}(\mathbf{x}) = \mathbf{u}(\mathbf{x}_0 + \ell \mathbf{e}) + O(\rho) \quad \text{in a neighbourhood of } \mathbf{x}_0 + \ell \mathbf{e}. \quad (6.22)$$

The constants of rigid body motion of (6.13) are assumed to admit the following formal expansions for small ρ

$$\mathbf{C}_a(\rho) = \frac{1}{\rho} \mathbf{C}_{a,-1} + \mathbf{C}_{a,0} + O(\rho) \quad \text{and} \quad \mathbf{C}_b(\rho) = \frac{1}{\rho} \mathbf{C}_{b,-1} + \mathbf{C}_{b,0} + O(\rho), \quad (6.23)$$

$$\mathcal{R}_a(\rho) = \frac{1}{\rho} \mathcal{R}_{a,-1} + \mathcal{R}_{a,0} + O(\rho) \quad \text{and} \quad \mathcal{R}_b(\rho) = \frac{1}{\rho} \mathcal{R}_{b,-1} + \mathcal{R}_{b,0} + O(\rho). \quad (6.24)$$

Remark 53. *It is noteworthy that $1/\rho$ terms compensate each other in the expansions (6.23) and (6.24). It means that $\mathbf{C}_{a,-1} + \mathcal{R}_{a,-1} \mathbf{x}_0 = \mathbf{0}$ and $\mathbf{C}_{b,-1} + \mathcal{R}_{b,-1}(\mathbf{x}_0 + \ell \mathbf{e}) = \mathbf{0}$.*

Functions \mathbf{v}_a and \mathbf{v}_b are coupled and respectively describe the zoom at zero-order on ω_A and ω_B . They respectively solve

$$\left\{ \begin{array}{l} -\operatorname{div}(\mathbf{A}\varepsilon(\mathbf{v}_a)(\mathbf{y}_a)) = \mathbf{0} \quad \text{in } \mathbb{R}^3 \setminus \omega \\ \mathbf{v}_a(\mathbf{y}_a) = \mathbf{C}_{a,0} + \mathcal{R}_{a,0} \mathbf{x}_0 - \mathbf{u}(\mathbf{x}_0) + \mathcal{R}_{a,-1} \mathbf{y}_a \quad \text{in } \omega \\ \int_{\partial\omega} \mathbf{A}\varepsilon(\mathbf{v}_a) \mathbf{n} dS = \frac{\kappa(\rho)}{\rho} \left(\int_{\omega} (\mathbf{v}_b - \mathbf{v}_a) \cdot \mathbf{e} dV + (\mathbf{u}(\mathbf{x}_0 + \ell \mathbf{e}) - \mathbf{u}(\mathbf{x}_0)) \cdot \mathbf{e} \right) \mathbf{e} \\ \int_{\partial\omega} \mathbf{A}\varepsilon(\mathbf{v}_a) \mathbf{n} \wedge \mathbf{y}_a dS = \mathbf{0} \\ \lim_{\mathbf{y}_a \rightarrow \infty} \mathbf{v}_a(\mathbf{y}_a) = \mathbf{0} \end{array} \right. , \quad (6.25)$$

$$\left\{ \begin{array}{ll} -\operatorname{div}(\mathbf{A}\varepsilon(\mathbf{v}_b)(\mathbf{y}_b)) = \mathbf{0} & \text{in } \mathbb{R}^3 \setminus \omega \\ \mathbf{v}_b(\mathbf{y}_b) = \mathbf{C}_{b,0} + \mathbf{R}_{b,0}(\mathbf{x}_0 + \ell \mathbf{e}) - \mathbf{u}(\mathbf{x}_0 + \ell \mathbf{e}) + \mathbf{R}_{b,-1}\mathbf{y}_b & \text{in } \omega \\ \int_{\partial\omega} \mathbf{A}\varepsilon(\mathbf{v}_b)\mathbf{n}dS = -\frac{\kappa(\rho)}{\rho} \left(\int_{\omega} (\mathbf{v}_b - \mathbf{v}_a) \cdot \mathbf{e}dV + (\mathbf{u}(\mathbf{x}_0 + \ell \mathbf{e}) - \mathbf{u}(\mathbf{x}_0)) \cdot \mathbf{e} \right) \mathbf{e} & \\ \int_{\partial\omega} \mathbf{A}\varepsilon(\mathbf{v}_b)\mathbf{n} \wedge \mathbf{y}_bdS = \mathbf{0} & \\ \lim_{\mathbf{y}_b \rightarrow \infty} \mathbf{v}_b(\mathbf{y}_b) = \mathbf{0} & \end{array} \right. \quad (6.26)$$

Remark 54. The moment equilibrium in (6.25) should be

$$\int_{\partial\omega} \mathbf{A}\varepsilon(\mathbf{v}_a)\mathbf{n} \wedge \mathbf{y}_adS = \frac{\kappa(\rho)}{\rho} \left(\int_{\omega} (\mathbf{v}_b - \mathbf{v}_a) \cdot \mathbf{e}dV + (\mathbf{u}(\mathbf{x}_0 + \ell \mathbf{e}) - \mathbf{u}(\mathbf{x}_0)) \cdot \mathbf{e} \right) \int_{\omega} \mathbf{e} \wedge \mathbf{y}_adS.$$

Since \mathbf{e} is a constant vector and as we choose ω to be the unit ball of \mathbb{R}^3 , the last integral is equal to zero. The moment equilibrium in (6.26) is obtained similarly.

Lemma 8. The far fields \mathbf{v}_a and \mathbf{v}_b are explicitly given by

$$\mathbf{v}_a(\mathbf{y}) = \begin{cases} \frac{3(\mu_A + \lambda_A)(r^2 - r_1^2)r_1^2}{2(5\mu_A + 2\lambda_A)r^5} \boldsymbol{\xi}_{u,a}(\rho) \cdot \mathbf{y}\mathbf{y} + \frac{((9\mu_A + 3\lambda_A)r^2 + (\mu_A + \lambda_A)r_1^2)r_1}{2(5\mu_A + 2\lambda_A)r^3} \boldsymbol{\xi}_{u,a}(\rho) & \text{in } \mathbb{R}^3 \setminus \omega, \\ \boldsymbol{\xi}_{u,a}(\rho) & \text{in } \omega \end{cases} \quad (6.27)$$

$$\mathbf{v}_b(\mathbf{y}) = \begin{cases} \frac{3(\mu_B + \lambda_B)(r^2 - r_1^2)r_1^2}{2(5\mu_B + 2\lambda_B)r^5} \boldsymbol{\xi}_{u,b}(\rho) \cdot \mathbf{y}\mathbf{y} + \frac{((9\mu_B + 3\lambda_B)r^2 + (\mu_B + \lambda_B)r_1^2)r_1}{2(5\mu_B + 2\lambda_B)r^3} \boldsymbol{\xi}_{u,b}(\rho) & \text{in } \mathbb{R}^3 \setminus \omega, \\ \boldsymbol{\xi}_{u,b}(\rho) & \text{in } \omega \end{cases} \quad (6.28)$$

where $r = \|\mathbf{y}\|$ and

$$\boldsymbol{\xi}_{u,a}(\rho) = \frac{\frac{\kappa(\rho)}{\rho|\omega|\tau_A}}{1 + \frac{\kappa(\rho)}{\rho|\omega|} \left(\frac{1}{\tau_A} + \frac{1}{\tau_B} \right)} \left((\mathbf{u}(\mathbf{x}_0 + \ell \mathbf{e}) - \mathbf{u}(\mathbf{x}_0)) \cdot \mathbf{e} \right) \mathbf{e}. \quad (6.29)$$

$$\boldsymbol{\xi}_{u,b}(\rho) = -\frac{\frac{\kappa(\rho)}{\rho|\omega|\tau_B}}{1 + \frac{\kappa(\rho)}{\rho|\omega|} \left(\frac{1}{\tau_B} + \frac{1}{\tau_A} \right)} \left((\mathbf{u}(\mathbf{x}_0 + \ell \mathbf{e}) - \mathbf{u}(\mathbf{x}_0)) \cdot \mathbf{e} \right) \mathbf{e}. \quad (6.30)$$

Remark 55. If Ω_A and Ω_B are of the same material, then the far fields verify $\mathbf{v}_a = -\mathbf{v}_b$.

Proof. Considering the form of (6.25) and (6.26), it is enough to solve only one system of equations. The other one is solved similarly. Let us determine \mathbf{v}_a . First, we set the notation

$$\boldsymbol{\xi}_{u,a}(\rho) = \mathbf{C}_{a,0} + \mathbf{R}_{a,0}\mathbf{x}_0 - \mathbf{u}(\mathbf{x}_0).$$

Similarly, we define for \mathbf{v}_b the notation $\boldsymbol{\xi}_{u,b}(\rho) = \mathbf{C}_{b,0} + \mathbf{R}_{b,0}(\mathbf{x}_0 + \ell \mathbf{e}) - \mathbf{u}(\mathbf{x}_0 + \ell \mathbf{e})$. Thanks to the expressions of \mathbf{v}_a and \mathbf{v}_b , the coefficients $\boldsymbol{\xi}_{u,a}(\rho)$ and $\boldsymbol{\xi}_{u,b}(\rho)$ will be explicitated according to \mathbf{u} at the end of this proof. According to [113], the solution of (6.25) has the explicit form

$$\mathbf{v}_a(\mathbf{y}) = \begin{cases} \boldsymbol{\xi}_{u,a}(\rho) \cdot \mathbf{y}f(r)\mathbf{y} + \boldsymbol{\xi}_{u,a}(\rho)g(r) + \mathbf{R}_{a,-1}\mathbf{y}h(r) & \text{in } \mathbb{R}^3 \setminus \omega \\ \boldsymbol{\xi}_{u,a}(\rho) + \mathbf{R}_{a,-1}\mathbf{y} & \text{in } \omega \end{cases}, \quad (6.31)$$

where f , g and h are finite scalar functions satisfying the continuity of \mathbf{v}_a on $\partial\omega$ and tending towards zero at infinity. Thus, they verify the conditions

$$\begin{cases} f(r_1) = 0, & g(r_1) = 1 & h(r_1) = 1 \\ \lim_{r \rightarrow \infty} f(r) = 0 & \lim_{r \rightarrow \infty} g(r) = 0 & \lim_{r \rightarrow \infty} h(r) = 0 \end{cases} \quad (6.32)$$

The solution of (6.25) has been computed on Maple and that leads to

$$\begin{cases} f(r) = \frac{3(\mu_A + \lambda_A)(r^2 - r_1^2)r_1^2}{2(5\mu_A + 2\lambda_A)r^5} \\ g(r) = \frac{((9\mu_A + 3\lambda_A)r^2 + (\mu_A + \lambda_A)r_1^2)r_1}{2(5\mu_A + 2\lambda_A)r^3} \\ h(r) = \frac{r_1^3}{r^3} \end{cases} \quad (6.33)$$

Using the explicit expression of \mathbf{v}_a in $\mathbb{R}^3 \setminus \omega$, forces and momentum equilibrium read

$$\int_{\partial\omega} \mathbf{A}\varepsilon(\mathbf{v}_a)\mathbf{n}dS = |\omega|\tau_A\boldsymbol{\xi}_{u,a}(\rho) \text{ with } \tau_A = \frac{9\mu_A(2\mu_A + \lambda_A)}{(5\mu_A + 2\lambda_A)r_1^2} \text{ and } \int_{\partial\omega} \mathbf{A}\varepsilon(\mathbf{v}_a)\mathbf{n} \wedge \mathbf{y}dS = 8\pi\mu \begin{pmatrix} \mathbf{R}_{a,-1(2,3)} \\ -\mathbf{R}_{a,-1(1,3)} \\ \mathbf{R}_{a,-1(1,2)} \end{pmatrix}.$$

The equilibrium of moments on $\partial\omega$ leads to

$$\mathbf{R}_{a,-1} = 0. \quad (6.34)$$

The rigid body motion in ω is then reduced to a translation which corresponds to the average displacement in ω . In other words, $\int_{\omega} \mathbf{v}_a \cdot \mathbf{e}dV = \boldsymbol{\xi}_{u,a}(\rho) \cdot \mathbf{e}$. The equilibrium of forces implies

$$|\omega|\tau_A\boldsymbol{\xi}_{u,a}(\rho) = \frac{\kappa(\rho)}{\rho} (\boldsymbol{\xi}_{u,b}(\rho) \cdot \mathbf{e} - \boldsymbol{\xi}_{u,a}(\rho) \cdot \mathbf{e} + (\mathbf{u}(\mathbf{x}_0 + \ell\mathbf{e}) - \mathbf{u}(\mathbf{x}_0)) \cdot \mathbf{e}) \mathbf{e}. \quad (6.35)$$

A similar resolution of (6.26) brings $\mathbf{R}_{b,-1} = 0$ and

$$|\omega|\tau_B\boldsymbol{\xi}_{u,b}(\rho) = -\frac{\kappa(\rho)}{\rho} (\boldsymbol{\xi}_{u,b}(\rho) \cdot \mathbf{e} - \boldsymbol{\xi}_{u,a}(\rho) \cdot \mathbf{e} + (\mathbf{u}(\mathbf{x}_0 + \ell\mathbf{e}) - \mathbf{u}(\mathbf{x}_0)) \cdot \mathbf{e}) \mathbf{e}. \quad (6.36)$$

A simple combination of (6.35) and (6.36) gives the explicit expressions (6.29) and (6.30) of $\boldsymbol{\xi}_{u,a}(\rho)$ and $\boldsymbol{\xi}_{u,b}(\rho)$. \square

Remark 56. Lemma 8 shows that $|\mathbf{v}_a| = O\left(\frac{1}{r}\right)$ at infinity in 3d. A similar computation in 2d gives $|\mathbf{v}_a| = O(\ln(r))$ at infinity. The solution has hence the same behavior at infinity as the solution of the Dirichlet problem. Chapters 4 and 5 highlight that the perturbation of a rigid body behaves like the solution of the Neumann problem while the perturbation of a spring is more like the solution of Dirichlet problem at infinity. The combination of these two kinds of perturbation adopts naturally the dominant behavior.

Asymptotic analysis of the perturbed displacement

This part establishes rigorous estimates of the perturbation based on the behavior of the far field functions \mathbf{v}_a and \mathbf{v}_b . Let \mathbf{v}_ρ be the difference between the perturbed and the background solution,

$$\mathbf{v}_\rho = \mathbf{u}_\rho - \mathbf{u}. \quad (6.37)$$

This function represents the influence of the inclusions in terms of displacement. The equation satisfied by \mathbf{v}_ρ is

$$\left\{ \begin{array}{ll} -\operatorname{div}(\mathbf{A}\varepsilon(\mathbf{v}_\rho)) = \mathbf{0} & \text{in } \Omega_\rho \\ \mathbf{A}\varepsilon(\mathbf{v}_\rho)\mathbf{n} = \mathbf{0} & \text{on } \Gamma_N \\ \mathbf{v}_\rho = \mathbf{0} & \text{on } \Gamma_D \\ \mathbf{v}_\rho(\mathbf{x}) = \mathbf{C}_a(\rho) + \mathbf{R}_a(\rho)\mathbf{x} - \mathbf{u}(\mathbf{x}) & \text{in } \omega_A \\ \mathbf{v}_\rho(\mathbf{x}) = \mathbf{C}_b(\rho) + \mathbf{R}_b(\rho)\mathbf{x} - \mathbf{u}(\mathbf{x}) & \text{in } \omega_B \\ \int_{\partial\omega_A} \mathbf{A}\varepsilon(\mathbf{v}_\rho)\mathbf{n}dS = - \int_{\partial\omega_B} \mathbf{A}\varepsilon(\mathbf{v}_\rho)\mathbf{n}dS = \kappa(\rho) \left(\int_{\omega_B} \mathbf{f}(\mathbf{v}_\rho + \mathbf{u}) \cdot \mathbf{e}dV - \int_{\omega_A} \mathbf{f}(\mathbf{v}_\rho + \mathbf{u}) \cdot \mathbf{e}dV \right) \mathbf{e} \\ \int_{\partial\omega_A} \mathbf{A}\varepsilon(\mathbf{v}_\rho)\mathbf{n} \wedge \mathbf{x}dS = - \int_{\partial\omega_B} \mathbf{A}\varepsilon(\mathbf{v}_\rho)\mathbf{n} \wedge \mathbf{x}dS = \kappa(\rho) \left(\int_{\omega_B} \mathbf{f}(\mathbf{v}_\rho + \mathbf{u}) \cdot \mathbf{e}dV - \int_{\omega_A} \mathbf{f}(\mathbf{v}_\rho + \mathbf{u}) \cdot \mathbf{e}dV \right) \int_{\omega_A} \mathbf{e} \wedge \mathbf{x}dV \end{array} \right. \quad (6.38)$$

The field \mathbf{v}_ρ is as smooth as \mathbf{u}_ρ and \mathbf{u} . Let us introduce the function

$$\mathbf{v}(\mathbf{x}) = \mathbf{v}_a \left(\frac{\mathbf{x} - \mathbf{x}_0}{\rho} \right) + \mathbf{v}_b \left(\frac{\mathbf{x} - \mathbf{x}_0 - \ell\mathbf{e}}{\rho} \right), \quad (6.39)$$

where \mathbf{v}_a and \mathbf{v}_b are solutions of (6.25) and (6.26) and thus verify Lemma 8. As proved by the following result, \mathbf{v} is, in some sense, the limit of \mathbf{v}_ρ as ρ goes to zero.

Proposition 13. *Let $\theta \in \mathbf{C}_c^\infty(\Omega)$ be a cut-off function with compact support $\mathcal{U}_+ \subset \Omega$ such that $\theta \equiv 1$ in a neighborhood $\mathcal{U}_- \subset \mathcal{U}_+$ of \mathbf{x}_0 . We have*

$$\mathbf{v}_\rho = \theta\mathbf{v} + \boldsymbol{\delta}, \quad (6.40)$$

where $\boldsymbol{\delta}$ is a remainder term as can be checked by these estimates of the L^2 -norms of \mathbf{v} and $\varepsilon(\mathbf{v})$ and the H^1 -norm of $\boldsymbol{\delta}$. They are given, according to the value of the exponent k , by

	$\ \mathbf{v}\ _{L^2(\Omega_\rho)}$	$\ \varepsilon(\mathbf{v})\ _{L^2(\Omega_\rho)}$	$\ \boldsymbol{\delta}\ _{H^1(\Omega_\rho)}$
$3/2 \leq k < 2$	$O(\rho^k)$	$O(\rho^{k-1/2})$	$O(\rho^{3/2})$
$1 < k \leq 3/2$	$O(\rho^k)$	$O(\rho^{k-1/2})$	$O(\rho^k)$
$k = 1$	$O(\rho)$	$O(\sqrt{\rho})$	$O(\rho)$
$0 < k < 1$	$O(\rho)$	$O(\sqrt{\rho})$	$O(\rho)$

Remark 57. *The role of the cut-off function θ is to make sure that the product $\theta\mathbf{v}$ satisfies homogeneous boundary conditions on the boundary $\partial\Omega$, as does \mathbf{v}_ρ . Since θ has a compact support, it implies that $\theta \equiv 0$ far from \mathbf{x}_0 and $\mathbf{x}_0 + \ell\mathbf{e}$. Consequently, θ vanishes far from the inclusions, and $\boldsymbol{\delta}$ contains the far field influence of the inclusions. The function $\boldsymbol{\delta}$ is an error term in the H^1 -norm. Indeed, its H^1 -norm is always asymptotically smaller than the one of*

$\theta \mathbf{v}$. The L^2 -norm of $\boldsymbol{\delta}$ is, a priori, of the same order as its H^1 -norm. However, the L^2 -norm of \mathbf{v} is always smaller than its H^1 -norm. Therefore, the L^2 -norm of \mathbf{v} can sometimes be smaller than the one of $\boldsymbol{\delta}$ (in which case $\boldsymbol{\delta}$ is not a small error term in the L^2 -norm). It happens for $3/2 \leq k < 2$ where the L^2 -norm of \mathbf{v} is smaller than the H^1 -norm of $\boldsymbol{\delta}$. For $k \leq 3/2$, the L^2 -norm of \mathbf{v} and the H^1 -norm of $\boldsymbol{\delta}$ are of the same order.

Remark 58. The sensitivity with regards to the rigid inclusions bounds the range of admissible scalings to $0 < k < 2$.

Proof. The explicit expressions of \mathbf{v}_a and \mathbf{v}_b indicate at infinity that $|\mathbf{v}_a| = O\left(\frac{|\boldsymbol{\xi}_{u,a}(\rho)|}{r}\right)$ and $|\varepsilon(\mathbf{v}_a)| = O\left(\frac{|\boldsymbol{\xi}_{u,a}(\rho)|}{r^2}\right)$ and so $|\mathbf{v}_b| = O\left(\frac{|\boldsymbol{\xi}_{u,b}(\rho)|}{r}\right)$ and $|\varepsilon(\mathbf{v}_b)| = O\left(\frac{|\boldsymbol{\xi}_{u,b}(\rho)|}{r^2}\right)$. Since the functions $\boldsymbol{\xi}_{u,a}(\rho)$ and $\boldsymbol{\xi}_{u,b}(\rho)$ have the same behavior with regards to ρ , the following estimates are expressed only with respect to $\boldsymbol{\xi}_{u,a}(\rho)$. Thus, we deduce by rescaling

$$\|\mathbf{v}\|_{L^\infty(\Omega \setminus \mathcal{U}_-)} \leq C\rho |\boldsymbol{\xi}_{u,a}(\rho)| \text{ and } \|\varepsilon(\mathbf{v})\|_{L^\infty(\Omega \setminus \mathcal{U}_-)} \leq C\rho |\boldsymbol{\xi}_{u,a}(\rho)|. \quad (6.41)$$

Let us define $\Omega_{\rho^{-1}}$ the rescaling of the domain Ω_ρ using $\mathbf{x} = \rho \mathbf{y} + \mathbf{x}_0$ for ρ small. We have

$$\|\mathbf{v}\|_{L^2(\Omega_\rho)}^2 \leq C\rho^3 \int_{\Omega_{\rho^{-1}}} |\mathbf{v}_a|^2 dV \leq C\rho^3 |\boldsymbol{\xi}_{u,a}(\rho)|^2 \int_{r_1}^{r_1/\rho} dr \leq C\rho^2 |\boldsymbol{\xi}_a(\rho)|^2 \leq C \left(\frac{\kappa(\rho)}{1 + C\frac{\kappa(\rho)}{\rho}} \right)^2.$$

The denominator of the above upper bound is bounded if $k \geq 1$ and it goes to infinity otherwise. Therefore, for $k \geq 1$, one deduces

$$\|\mathbf{v}\|_{L^2(\Omega)} \leq C\rho^k, \quad (6.42)$$

while, for $k < 1$,

$$\|\mathbf{v}\|_{L^2(\Omega)} \leq C\rho. \quad (6.43)$$

Estimates of the L^2 -norm of $\varepsilon(\mathbf{v})$ are obtained by a similar argument

$$\|\varepsilon(\mathbf{v})\|_{L^2(\Omega_\rho)}^2 \leq \rho \int_{\Omega_{\rho^{-1}}} |\varepsilon(\mathbf{v}_a)|^2 dV \leq C\rho |\boldsymbol{\xi}_u(\rho)|^2 \int_{r_1}^{r_1/\rho} \frac{1}{r^2} dr \leq C\rho |\boldsymbol{\xi}_u(\rho)|^2 \leq C \frac{1}{\rho} \left(\frac{\kappa(\rho)}{1 + C\frac{\kappa(\rho)}{\rho}} \right)^2.$$

The upper bound for $\|\varepsilon(\mathbf{v})\|_{L^2(\Omega_\rho)}$ is then larger, by a factor $1/\sqrt{\rho}$, than the upper bound for $\|\mathbf{v}\|_{L^2(\Omega_\rho)}$. Let us now write the equations satisfied by $\boldsymbol{\delta}$

$$\left\{ \begin{array}{ll} -\operatorname{div}(\mathbf{A}\varepsilon(\boldsymbol{\delta})) = \operatorname{div}(\mathbf{A}(\mathbf{v} \otimes \nabla\theta)^s) + \mathbf{A}\varepsilon(\mathbf{v})\nabla\theta & \text{in } \Omega_\rho \\ \mathbf{A}\varepsilon(\boldsymbol{\delta})\mathbf{n} = \mathbf{0} & \text{on } \Gamma_N \\ \boldsymbol{\delta} = \mathbf{0} & \text{on } \Gamma_D \\ \boldsymbol{\delta}(\mathbf{x}) = \mathbf{C}_a(\rho) + \mathbf{R}_a(\rho)\mathbf{x} - \mathbf{u}(\mathbf{x}) - \boldsymbol{\xi}_{u,a}(\rho) & \text{in } \omega_A \\ \boldsymbol{\delta}(\mathbf{x}) = \mathbf{C}_b(\rho) + \mathbf{R}_b(\rho)\mathbf{x} - \mathbf{u}(\mathbf{x}) + \boldsymbol{\xi}_{u,b}(\rho) & \text{in } \omega_B \end{array} \right. \quad (6.44)$$

$$\left\{ \begin{array}{l} \int_{\partial\omega_A} \mathbf{A}\varepsilon(\boldsymbol{\delta})\mathbf{n} dS = - \int_{\partial\omega_B} \mathbf{A}\varepsilon(\boldsymbol{\delta})\mathbf{n} dS = \kappa(\rho) \left(\int_{\omega_B} \boldsymbol{\delta} \cdot \mathbf{e} dV - \int_{\omega_A} \boldsymbol{\delta} \cdot \mathbf{e} dV \right) \mathbf{e} \\ \int_{\partial\omega_A} \mathbf{A}\varepsilon(\boldsymbol{\delta})\mathbf{n} \wedge \mathbf{x} dS = - \int_{\partial\omega_B} \mathbf{A}\varepsilon(\boldsymbol{\delta})\mathbf{n} \wedge \mathbf{x} dS = \kappa(\rho) \left(\int_{\omega_B} \boldsymbol{\delta} \cdot \mathbf{e} dV - \int_{\omega_A} \boldsymbol{\delta} \cdot \mathbf{e} dV \right) \int_{\omega_A} \mathbf{e} \wedge \mathbf{x} dV \end{array} \right.$$

The exponent "s" stands for the symmetric part of the matrix $\mathbf{v} \otimes \nabla\theta$. Multiplying (6.44) by $\boldsymbol{\delta}$ and integrate by parts, it follows

$$\int_{\Omega_\rho} \mathbf{A}\varepsilon(\boldsymbol{\delta}) : \varepsilon(\boldsymbol{\delta})dV = - \int_{\Omega_\rho} \mathbf{A}(\mathbf{v} \otimes \nabla\theta)^s : \varepsilon(\boldsymbol{\delta})dV + \int_{\Omega_\rho} \mathbf{A}\varepsilon(\mathbf{v})\nabla\theta \cdot \boldsymbol{\delta}dV + \int_{\partial\omega_A \cup \partial\omega_B} \mathbf{A}\varepsilon(\boldsymbol{\delta})\mathbf{n} \cdot \boldsymbol{\delta}dS. \quad (6.45)$$

The left hand side is bounded from below using the Poincaré-Korn inequality (since $\boldsymbol{\delta}$ vanishes on Γ_D)

$$\int_{\Omega_\rho} \mathbf{A}\varepsilon(\boldsymbol{\delta}) : \varepsilon(\boldsymbol{\delta})dV = \int_{\Omega_\rho} (2\mu|\varepsilon(\boldsymbol{\delta})|^2 + \lambda \text{tr}(\varepsilon(\boldsymbol{\delta}))^2)dV \geq C\|\varepsilon(\boldsymbol{\delta})\|_{L^2(\Omega_\rho)}^2 \geq C\|\boldsymbol{\delta}\|_{H^1(\Omega_\rho)}^2.$$

The two first terms of the right hand side are easily estimated using (6.41).

$$\begin{aligned} \left| \int_{\Omega_\rho} \mathbf{A}(\mathbf{v} \otimes \nabla\theta)^s : \varepsilon(\boldsymbol{\delta})dV \right| + \left| \int_{\Omega_\rho} \mathbf{A}\varepsilon(\mathbf{v})\nabla\theta \cdot \boldsymbol{\delta}dV \right| &\leq C\|\mathbf{v}\|_{L^\infty(\Omega \setminus \mathcal{U}_-)}\|\nabla\theta\|_{L^\infty(\Omega \setminus \mathcal{U}_-)}\|\varepsilon(\boldsymbol{\delta})\|_{L^2(\Omega_\rho)} \\ &\quad + C\|\varepsilon(\mathbf{v})\|_{L^\infty(\Omega \setminus \mathcal{U}_-)}\|\nabla\theta\|_{L^\infty(\Omega \setminus \mathcal{U}_-)}\|\boldsymbol{\delta}\|_{L^2(\Omega_\rho)} \\ &\leq C\rho|\boldsymbol{\xi}_{u,a}(\rho)|\|\varepsilon(\boldsymbol{\delta})\|_{L^2(\Omega_\rho)}, \end{aligned}$$

by Poincaré's inequality applied to $\boldsymbol{\delta}$.

The boundary term of (6.45) requires more attention. By continuity of $\boldsymbol{\delta}$, it satisfies

$$\begin{aligned} \boldsymbol{\delta}(\mathbf{x}) &= \mathbf{C}_a(\rho) + \mathbf{R}_a(\rho)\mathbf{x} - \mathbf{u}(\mathbf{x}) - \boldsymbol{\xi}_{u,a}(\rho) && \text{on } \partial\omega_A, \\ \boldsymbol{\delta}(\mathbf{x}) &= \mathbf{C}_b(\rho) + \mathbf{R}_b(\rho)\mathbf{x} - \mathbf{u}(\mathbf{x}) + \boldsymbol{\xi}_{u,b}(\rho) && \text{on } \partial\omega_B. \end{aligned}$$

Since $\mathbf{R}_a(\rho)$ and $\mathbf{R}_b(\rho)$ are anti-symmetric matrices, there exist $(\mathbf{r}_a(\rho), \mathbf{r}_b(\rho)) \in \mathbb{R}^3 \times \mathbb{R}^3$ such that $\mathbf{R}_a(\rho)\mathbf{x} = \mathbf{r}_a(\rho) \wedge \mathbf{x}$ and $\mathbf{R}_b(\rho)\mathbf{x} = \mathbf{r}_b(\rho) \wedge \mathbf{x}$. Then, we can notice that

$$\int_{\omega_A} (\boldsymbol{\delta} + \mathbf{u}) \cdot \mathbf{e}dV = (\mathbf{C}_a(\rho) - \boldsymbol{\xi}_{u,a}(\rho)) \cdot \mathbf{e} - \mathbf{r}_a(\rho) \cdot \int_{\omega_A} \mathbf{e} \wedge \mathbf{x}dV, \quad (6.46)$$

and reciprocally on ω_B . Coming back to the last term of (6.45) and using the boundary conditions in (6.44) and the equality (6.46)

$$\begin{aligned} &\int_{\partial\omega_A \cup \partial\omega_B} \mathbf{A}\varepsilon(\boldsymbol{\delta})\mathbf{n} \cdot \boldsymbol{\delta}dS = (\mathbf{C}_a(\rho) - \boldsymbol{\xi}_{u,a}(\rho)) \cdot \int_{\partial\omega_A} \mathbf{A}\varepsilon(\boldsymbol{\delta})\mathbf{n}dS - \mathbf{r}_a(\rho) \cdot \int_{\partial\omega_A} \mathbf{A}\varepsilon(\boldsymbol{\delta})\mathbf{n} \wedge \mathbf{x}dS - \int_{\partial\omega_A} \mathbf{A}\varepsilon(\boldsymbol{\delta})\mathbf{n} \cdot \mathbf{u}dS \\ &\quad - (\mathbf{C}_b(\rho) + \boldsymbol{\xi}_{u,b}(\rho)) \cdot \int_{\partial\omega_B} \mathbf{A}\varepsilon(\boldsymbol{\delta})\mathbf{n}dS + \mathbf{r}_b(\rho) \cdot \int_{\partial\omega_B} \mathbf{A}\varepsilon(\boldsymbol{\delta})\mathbf{n} \wedge \mathbf{x}dS - \int_{\partial\omega_B} \mathbf{A}\varepsilon(\boldsymbol{\delta})\mathbf{n} \cdot \mathbf{u}dS \\ &= \kappa(\rho) \left(\int_{\omega_B} \boldsymbol{\delta} \cdot \mathbf{e}dV - \int_{\omega_A} \boldsymbol{\delta} \cdot \mathbf{e}dV \right) \left(\int_{\omega_A} (\boldsymbol{\delta} + \mathbf{u}) \cdot \mathbf{e}dV - \int_{\omega_B} (\boldsymbol{\delta} + \mathbf{u}) \cdot \mathbf{e}dV \right) - \int_{\partial\omega_A \cup \partial\omega_B} \mathbf{A}\varepsilon(\boldsymbol{\delta})\mathbf{n} \cdot \mathbf{u}dS \\ &= -\kappa(\rho) \left(\int_{\omega_B} \boldsymbol{\delta} \cdot \mathbf{e}dV - \int_{\omega_A} \boldsymbol{\delta} \cdot \mathbf{e}dV \right)^2 + \kappa(\rho) \left(\int_{\omega_B} \boldsymbol{\delta} \cdot \mathbf{e}dV - \int_{\omega_A} \boldsymbol{\delta} \cdot \mathbf{e}dV \right) \mathbf{e} \cdot \int_{\omega_A} \mathbf{u}dV \\ &\quad - \kappa(\rho) \left(\int_{\omega_B} \boldsymbol{\delta} \cdot \mathbf{e}dV - \int_{\omega_A} \boldsymbol{\delta} \cdot \mathbf{e}dV \right) \mathbf{e} \cdot \int_{\omega_B} \mathbf{u}dV - \int_{\partial\omega_A \cup \partial\omega_B} \mathbf{A}\varepsilon(\boldsymbol{\delta})\mathbf{n} \cdot \mathbf{u}dS \\ &= -\kappa(\rho) \left(\int_{\omega_B} \boldsymbol{\delta} \cdot \mathbf{e}dV - \int_{\omega_A} \boldsymbol{\delta} \cdot \mathbf{e}dV \right)^2 + \int_{\partial\omega_A} \mathbf{A}\varepsilon(\boldsymbol{\delta})\mathbf{n} \cdot \left(\int_{\omega_A} \mathbf{u}dV - \mathbf{u} \right) dS + \int_{\partial\omega_B} \mathbf{A}\varepsilon(\boldsymbol{\delta})\mathbf{n} \cdot \left(\int_{\omega_B} \mathbf{u}dV - \mathbf{u} \right) dS. \end{aligned}$$

Therefore (6.45) is rewritten as follows

$$\begin{aligned} \kappa(\rho) \left(\int_{\omega_B} \boldsymbol{\delta} \cdot \mathbf{e} dV - \int_{\omega_A} \boldsymbol{\delta} \cdot \mathbf{e} dV \right)^2 + \int_{\Omega_\rho} \mathbf{A}\varepsilon(\boldsymbol{\delta}) : \varepsilon(\boldsymbol{\delta}) dV &= - \int_{\Omega_\rho} \mathbf{A}(\mathbf{v} \otimes \nabla\theta)^s : \varepsilon(\boldsymbol{\delta}) dV + \int_{\Omega_\rho} \mathbf{A}\varepsilon(\mathbf{v}) \nabla\theta \cdot \boldsymbol{\delta} dV \\ &+ \int_{\partial\omega_A} \mathbf{A}\varepsilon(\boldsymbol{\delta}) \mathbf{n} \cdot \left(\int_{\omega_A} \mathbf{u} dV - \mathbf{u} \right) dS + \int_{\partial\omega_B} \mathbf{A}\varepsilon(\boldsymbol{\delta}) \mathbf{n} \cdot \left(\int_{\omega_B} \mathbf{u} dV - \mathbf{u} \right) dS. \end{aligned} \quad (6.47)$$

The first term in the left hand-side of (6.47) is non-negative and the two first terms in the right hand-side have already been bounded. Therefore it is enough to bound the boundary term on $\partial\omega_A$ (a similar estimate will hold true for the other boundary term on $\partial\omega_B$).

A Taylor expansion with integral remainder of the background solution \mathbf{u} in a neighborhood of \mathbf{x}_0 is

$$\mathbf{u}(\mathbf{x}) = \mathbf{u}(\mathbf{x}_0) + \nabla\mathbf{u}(\mathbf{x}_0)(\mathbf{x} - \mathbf{x}_0) + \int_0^1 (1-t)(\mathbf{x} - \mathbf{x}_0)^T \mathcal{D}^2(\mathbf{u}(\mathbf{x}_0 + t(\mathbf{x} - \mathbf{x}_0)))(\mathbf{x} - \mathbf{x}_0) dt, \quad (6.48)$$

where $\mathcal{D}^2(\mathbf{u})$ is a third order tensor containing second derivatives of \mathbf{u} . Therefore, it implies that at least $\mathbf{u} \in (\mathcal{C}^2(\Omega))^3$. To lighten the notation, let us set

$$\mathbf{R}_u^A(\mathbf{x}) = \int_0^1 (1-t)(\mathbf{x} - \mathbf{x}_0)^T \mathcal{D}^2(\mathbf{u}(\mathbf{x}_0 + t(\mathbf{x} - \mathbf{x}_0)))(\mathbf{x} - \mathbf{x}_0) dt. \quad (6.49)$$

Recalling that ω is the unit ball of \mathbb{R}^3 , it comes $\int_{\omega_A} \nabla\mathbf{u}(\mathbf{x}_0)(\mathbf{x} - \mathbf{x}_0) dV = \rho \int_{\omega} \nabla\mathbf{u}(\mathbf{x}_0) \mathbf{y} dV = \mathbf{0}$.

Then the average displacement on ω_A is

$$\int_{\omega_A} \mathbf{u} dV = \mathbf{u}(\mathbf{x}_0) + \int_{\omega_A} \mathbf{R}_u^A dV.$$

The matrix $\nabla\mathbf{u}(\mathbf{x}_0)$ is decomposed into its symmetric and anti-symmetric part

$$\nabla\mathbf{u}(\mathbf{x}_0) = \varepsilon(\mathbf{u})(\mathbf{x}_0) + \varpi(\mathbf{u})(\mathbf{x}_0).$$

So there exists $\mathbf{r}_\varpi(\mathbf{x}_0) \in \mathbb{R}^3$ such that $\varpi(\mathbf{u})(\mathbf{x}_0)\mathbf{x} = \mathbf{r}_\varpi(\mathbf{x}_0) \wedge \mathbf{x}$. It follows

$$\begin{aligned} \int_{\partial\omega_A} \mathbf{A}\varepsilon(\boldsymbol{\delta}) \mathbf{n} \cdot \mathbf{u} dS &= \int_{\partial\omega_A} \mathbf{A}\varepsilon(\boldsymbol{\delta}) \mathbf{n} \cdot \mathbf{u}(\mathbf{x}_0) dS + \int_{\partial\omega_A} \mathbf{A}\varepsilon(\boldsymbol{\delta}) \mathbf{n} \cdot \varepsilon(\mathbf{u})(\mathbf{x}_0)(\mathbf{x} - \mathbf{x}_0) dS \\ &- \mathbf{r}_\varpi(\mathbf{x}_0) \cdot \int_{\partial\omega_A} \mathbf{A}\varepsilon(\boldsymbol{\delta}) \mathbf{n} \wedge (\mathbf{x} - \mathbf{x}_0) dS + \int_{\partial\omega_A} \mathbf{A}\varepsilon(\boldsymbol{\delta}) \mathbf{n} \cdot \mathbf{R}_u^A dS. \end{aligned}$$

The third term vanishes because of (6.44) and also because ω is the unit ball of \mathbb{R}^3

$$\begin{aligned} \mathbf{r}_\varpi(\mathbf{x}_0) \cdot \int_{\partial\omega_A} \mathbf{A}\varepsilon(\boldsymbol{\delta}) \mathbf{n} \wedge (\mathbf{x} - \mathbf{x}_0) dS &= \mathbf{r}_\varpi(\mathbf{x}_0) \cdot \kappa(\rho) \left(\int_{\omega_B} \boldsymbol{\delta} \cdot \mathbf{e} dV - \int_{\omega_A} \boldsymbol{\delta} \cdot \mathbf{e} dV \right) \int_{\omega_A} \mathbf{e} \wedge (\mathbf{x} - \mathbf{x}_0) dV \\ &= \mathbf{r}_\varpi(\mathbf{x}_0) \cdot \kappa(\rho) \left(\int_{\omega_B} \boldsymbol{\delta} \cdot \mathbf{e} dV - \int_{\omega_A} \boldsymbol{\delta} \cdot \mathbf{e} dV \right) \rho \int_{\omega} \mathbf{e} \wedge \mathbf{y} dV = 0. \end{aligned}$$

The boundary term on $\partial\omega_A$ is then estimated by

$$\int_{\partial\omega_A} \mathbf{A}\varepsilon(\boldsymbol{\delta})\mathbf{n} \cdot \left(\int_{\omega_A} \mathbf{u} dV - \mathbf{u} \right) dS = \int_{\partial\omega_A} \mathbf{A}\varepsilon(\boldsymbol{\delta})\mathbf{n} \cdot \left(\int_{\omega_A} \mathbf{R}_u^A dV - \varepsilon(\mathbf{u})(\mathbf{x}_0)(\mathbf{x} - \mathbf{x}_0) - \mathbf{R}_u^A \right) dS.$$

To bound the right hand side of the above equality, let us multiply the term containing the error \mathbf{R}_u^A by a cut-off function defined as follows. Let $\psi \in \mathbf{C}^\infty(\mathbb{R}^3)$ be a cut-off function with compact support in the ball \mathcal{B}_2 of radius 2, such that $\psi(\mathbf{y}) = 1$ in ω the unit ball of \mathbb{R}^3 . Denote ψ_{ω_A} and ψ_{ω_B} the rescaled cut-off functions such that

$$\psi_{\omega_A}(\mathbf{x}) = \psi\left(\frac{\mathbf{x} - \mathbf{x}_0}{\rho}\right) \text{ and } \psi_{\omega_B}(\mathbf{x}) = \psi\left(\frac{\mathbf{x} - \mathbf{x}_0 - \ell\mathbf{e}}{\rho}\right).$$

Therefore, $\psi_{\omega_A}(\mathbf{x}) = 1$ in ω_A and has compact support in $\mathcal{B}_{2\rho}^A$, the ball of radius 2ρ and center \mathbf{x}_0 (similarly for ψ_{ω_B}). Setting $\mathbf{h}_A(\mathbf{x}) = \psi_{\omega_A}(\mathbf{x}) \left(\int_{\omega_A} \mathbf{R}_u^A dV - \varepsilon(u(\mathbf{x}_0))(\mathbf{x} - \mathbf{x}_0) - \mathbf{R}_u^A \right)$, which has compact support in $\mathcal{B}_{2\rho}^A$, it follows

$$\begin{aligned} \int_{\partial\omega_A} \mathbf{A}\varepsilon(\boldsymbol{\delta})\mathbf{n} \cdot \left(\int_{\omega_A} \mathbf{u} dV - \mathbf{u} \right) dS &= \int_{\partial\omega_A} \mathbf{A}\varepsilon(\boldsymbol{\delta})\mathbf{n} \cdot \mathbf{h}_A dS = \int_{\mathcal{B}_{2\rho}^A} \operatorname{div} \mathbf{A}\varepsilon(\boldsymbol{\delta}) \cdot \mathbf{h}_A dV + \int_{\mathcal{B}_{2\rho}^A} \mathbf{A}\varepsilon(\boldsymbol{\delta}) : \varepsilon(\mathbf{h}_A) dV \\ &= - \int_{\mathcal{B}_{2\rho}^A} (\operatorname{div} \mathbf{A}(\mathbf{v} \otimes \nabla\theta)^s + \mathbf{A}\varepsilon(\mathbf{v})\nabla\theta) \cdot \mathbf{h}_A dV + \int_{\mathcal{B}_{2\rho}^A} \mathbf{A}\varepsilon(\boldsymbol{\delta}) : \varepsilon(\mathbf{h}_A) dV \\ &= \int_{\mathcal{B}_{2\rho}^A} \mathbf{A}\varepsilon(\boldsymbol{\delta}) : \varepsilon(\mathbf{h}_A) dV \end{aligned}$$

where we use equation (6.44) for $\boldsymbol{\delta}$ and the fact that θ is constant in $\mathcal{B}_{2\rho}^A$. Since $\mathbf{x} - \mathbf{x}_0$ is of the order of ρ in $\mathcal{B}_{2\rho}^A$ and $\nabla\psi_{\omega_A}$ behaves like $1/\rho$, it comes for some constant $C > 0$ independent of ρ

$$|\varepsilon(\mathbf{h}_A)| \leq C \text{ in } \mathcal{B}_{2\rho}^A.$$

Cauchy-Schwarz' inequality gives

$$\left| \int_{\mathcal{B}_{2\rho}^A} \mathbf{A}\varepsilon(\boldsymbol{\delta}) : \varepsilon(\mathbf{h}_A) dV \right| \leq C \|\varepsilon(\boldsymbol{\delta})\|_{L^2(\mathcal{B}_{2\rho}^A)} \|\varepsilon(\mathbf{h}_A)\|_{L^2(\mathcal{B}_{2\rho}^A)} \leq C\rho^{3/2} \|\varepsilon(\boldsymbol{\delta})\|_{L^2(\Omega_\rho)}.$$

Regrouping all terms finally leads to $\|\varepsilon(\boldsymbol{\delta})\|_{L^2(\Omega_\rho)} \leq C \frac{\kappa(\rho)}{1 + C\frac{\kappa(\rho)}{\rho}} + C\rho^{3/2}$.

The first term of the right-hand side is of the upper bound for $\|\mathbf{v}\|_{L^2(\Omega_\rho)}$ and it is smaller than $C\rho^{3/2}$ for $k \leq 3/2$. Recall that $\|\varepsilon(\mathbf{v}_a)\|_{L^2(\Omega_\rho)} \leq C\rho^{k-1/2}$ for $k > 1$. The function $\boldsymbol{\delta}$ should be a remainder term in the H^1 -norm, which requires that $k < 2$. \square

Remark 59. *The analysis in 2d leads to $\|\mathbf{v}\|_{H^1(\Omega_\rho)} \leq C\frac{\kappa(\rho)}{\sqrt{\rho}}$ and $\|\varepsilon(\boldsymbol{\delta})\|_{L^2(\Omega_\rho)} \leq C\kappa(\rho) + C\rho$. Then the error term is small in the H^1 -norm for $0 < k < 3/2$.*

6.2.2 Adjoint state

A similar analysis can be carried out for the perturbed adjoint state \mathbf{p}_ρ associated to the perturbed displacement field \mathbf{u}_ρ . It solves

$$\left\{ \begin{array}{ll} -\operatorname{div}(\mathbf{A}\varepsilon(\mathbf{p}_\rho)) = -\mathbf{F}'(\mathbf{u})\mathbf{1}_{\Omega_1} & \text{in } \Omega_\rho \\ \mathbf{A}\varepsilon(\mathbf{p}_\rho)\mathbf{n} = -\mathbf{G}'(\mathbf{u}) & \text{on } \Gamma_N \\ \mathbf{p}_\rho = \mathbf{0} & \text{on } \Gamma_D \\ \mathbf{p}_\rho(\mathbf{x}) = \bar{\mathbf{C}}_a(\rho) + \bar{\mathbf{R}}_a(\rho)\mathbf{x} & \text{in } \omega_A \\ \mathbf{p}_\rho(\mathbf{x}) = \bar{\mathbf{C}}_b(\rho) + \bar{\mathbf{R}}_b(\rho)\mathbf{x} & \text{in } \omega_B \end{array} \right. ,$$

$$\int_{\partial\omega_A} \mathbf{A}\varepsilon(\mathbf{p}_\rho)\mathbf{n}dS = - \int_{\partial\omega_B} \mathbf{A}\varepsilon(\mathbf{p}_\rho)\mathbf{n}dS = \kappa(\rho) \left(\int_{\omega_B} \mathbf{p}_\rho \cdot \mathbf{e}dV - \int_{\omega_A} \mathbf{p}_\rho \cdot \mathbf{e}dV \right) \mathbf{e}$$

$$\int_{\partial\omega_A} \mathbf{A}\varepsilon(\mathbf{p}_\rho)\mathbf{n} \wedge \mathbf{x}dS = - \int_{\partial\omega_B} \mathbf{A}\varepsilon(\mathbf{p}_\rho)\mathbf{n} \wedge \mathbf{x}dS = \kappa(\rho) \left(\int_{\omega_B} \mathbf{p}_\rho \cdot \mathbf{e}dV - \int_{\omega_A} \mathbf{p}_\rho \cdot \mathbf{e}dV \right) \int_{\omega_A} \mathbf{e} \wedge \mathbf{x}dV$$
(6.50)

where $(\bar{\mathbf{C}}_a(\rho), \bar{\mathbf{C}}_b(\rho)) \in (\mathbb{R}^3 \times \mathbb{R}^3)$ and $\bar{\mathbf{R}}_a(\rho)$ and $\bar{\mathbf{R}}_b(\rho)$ are 3x3 anti-symmetric matrices.

Remark 60. *It has already been noticed in [8] that the adjoint problem (6.50) is not standard since the right hand side depends on \mathbf{u} and not on \mathbf{u}_ρ as expected in the perturbed domain.*

Let us define \mathbf{q}_ρ the difference between the perturbed adjoint and the adjoint state of the background domain, $\mathbf{q}_\rho = \mathbf{p}_\rho - \mathbf{p}$, which satisfies

$$\left\{ \begin{array}{ll} -\operatorname{div}(\mathbf{A}\varepsilon(\mathbf{q}_\rho)) = \mathbf{0} & \text{in } \Omega_\rho \\ \mathbf{A}\varepsilon(\mathbf{q}_\rho)\mathbf{n} = \mathbf{0} & \text{on } \Gamma_N \\ \mathbf{q}_\rho = \mathbf{0} & \text{on } \Gamma_D \\ \mathbf{q}_\rho(\mathbf{x}) = \bar{\mathbf{C}}_a(\rho) + \bar{\mathbf{R}}_a(\rho)\mathbf{x} - \mathbf{p}(\mathbf{x}) & \text{in } \omega_A \\ \mathbf{q}_\rho(\mathbf{x}) = \bar{\mathbf{C}}_b(\rho) + \bar{\mathbf{R}}_b(\rho)\mathbf{x} - \mathbf{p}(\mathbf{x}) & \text{in } \omega_B \end{array} \right. .$$

$$\int_{\partial\omega_A} \mathbf{A}\varepsilon(\mathbf{q}_\rho)\mathbf{n}dS = - \int_{\partial\omega_B} \mathbf{A}\varepsilon(\mathbf{q}_\rho)\mathbf{n}dS = \kappa(\rho) \left(\int_{\omega_B} (\mathbf{p}_\rho + \mathbf{p}) \cdot \mathbf{e}dV - \int_{\omega_A} (\mathbf{p}_\rho + \mathbf{p}) \cdot \mathbf{e}dV \right) \mathbf{e}$$

$$\int_{\partial\omega_A} \mathbf{A}\varepsilon(\mathbf{q}_\rho)\mathbf{n} \wedge \mathbf{x}dS = - \int_{\partial\omega_B} \mathbf{A}\varepsilon(\mathbf{q}_\rho)\mathbf{n} \wedge \mathbf{x}dS = \kappa(\rho) \left(\int_{\omega_B} (\mathbf{p}_\rho + \mathbf{p}) \cdot \mathbf{e}dV - \int_{\omega_A} (\mathbf{p}_\rho + \mathbf{p}) \cdot \mathbf{e}dV \right) \int_{\omega_A} \mathbf{e} \wedge \mathbf{x}dV$$
(6.51)

The two first equations of (6.51) have zero right hand side because of the non-standard adjoint in the perturbed domain (6.50). We also introduce the functions \mathbf{q}_a and \mathbf{q}_b and the rescaled function

$$\mathbf{q}(\mathbf{x}) = \mathbf{q}_a \left(\frac{\mathbf{x} - \mathbf{x}_0}{\rho} \right) + \mathbf{q}_b \left(\frac{\mathbf{x} - \mathbf{x}_0 - \ell\mathbf{e}}{\rho} \right), \quad (6.52)$$

such that \mathbf{q}_a and \mathbf{q}_b are respectively similar to \mathbf{v}_a and \mathbf{v}_b .

Proposition 14. *Let $\theta \in \mathcal{C}_c^\infty(\Omega)$ be a cut-off function with compact support $\mathcal{U}_+ \subset \Omega$ such that $\theta \equiv 1$ in a neighborhood $\mathcal{U}_- \subset \mathcal{U}_+$ of \mathbf{x}_0 and $\mathbf{x}_0 + \ell\mathbf{e}$. We have*

$$\mathbf{q}_\rho = \theta\mathbf{q} + \boldsymbol{\eta}, \quad (6.53)$$

where $\boldsymbol{\eta}$ is a remainder term as can be checked by these estimates of the L^2 -norms of \mathbf{q} and $\varepsilon(\mathbf{q})$ and the H^1 -norm of $\boldsymbol{\eta}$. They are given, according to the value of the exponent k , by

	$\ \mathbf{q}\ _{L^2(\Omega_\rho)}$	$\ \varepsilon(\mathbf{q})\ _{L^2(\Omega_\rho)}$	$\ \boldsymbol{\eta}\ _{H^1(\Omega_\rho)}$
$3/2 \leq k < 2$	$O(\rho^k)$	$O(\rho^{k-1/2})$	$O(\rho^{3/2})$
$1 < k \leq 3/2$	$O(\rho^k)$	$O(\rho^{k-1/2})$	$O(\rho^k)$
$k = 1$	$O(\rho)$	$O(\sqrt{\rho})$	$O(\rho)$
$k < 1$	$O(\rho)$	$O(\sqrt{\rho})$	$O(\rho)$

Proof. The function $\boldsymbol{\eta}$ solves

$$\left\{ \begin{array}{ll} -\operatorname{div}(\mathbf{A}\varepsilon(\boldsymbol{\eta})) = \operatorname{div}(\mathbf{A}(\mathbf{q} \otimes \nabla \boldsymbol{\eta})^s) + \mathbf{A}\varepsilon(\mathbf{q})\nabla \boldsymbol{\eta} & \text{in } \Omega_\rho \\ \mathbf{A}\varepsilon(\boldsymbol{\eta})\mathbf{n} = \mathbf{0} & \text{on } \Gamma_N \\ \boldsymbol{\eta} = \mathbf{0} & \text{on } \Gamma_D \\ \boldsymbol{\eta}(\mathbf{x}) = \bar{\mathbf{C}}_a(\rho) + \bar{\mathcal{R}}_a(\rho)\mathbf{x} - \mathbf{p}(\mathbf{x}) - \bar{\mathbf{C}} & \text{in } \omega_A \\ \boldsymbol{\eta}(\mathbf{x}) = \bar{\mathbf{C}}_b(\rho) + \bar{\mathcal{R}}_b(\rho)\mathbf{x} - \mathbf{p}(\mathbf{x}) + \bar{\mathbf{C}} & \text{in } \omega_B \end{array} \right. \quad (6.54)$$

$$\int_{\partial\omega_A} \mathbf{A}\varepsilon(\boldsymbol{\eta})\mathbf{n}dS = - \int_{\partial\omega_B} \mathbf{A}\varepsilon(\boldsymbol{\eta})\mathbf{n}dS = \kappa(\rho) \left(\int_{\omega_B} \boldsymbol{\eta} \cdot \mathbf{e}dV - \int_{\omega_A} \boldsymbol{\eta} \cdot \mathbf{e}dV \right) \mathbf{e}$$

$$\int_{\partial\omega_A} \mathbf{A}\varepsilon(\boldsymbol{\eta})\mathbf{n} \wedge \mathbf{x}dS = - \int_{\partial\omega_B} \mathbf{A}\varepsilon(\boldsymbol{\eta})\mathbf{n} \wedge \mathbf{x}dS = \kappa(\rho) \left(\int_{\omega_B} \boldsymbol{\eta} \cdot \mathbf{e}dV - \int_{\omega_A} \boldsymbol{\eta} \cdot \mathbf{e}dV \right) \int_{\omega_A} \mathbf{e} \wedge \mathbf{x}dV$$

Proposition 14 is proved by going back over the proof of Proposition 13 and by substituting \mathbf{u} with \mathbf{p} and \mathbf{v}_ρ with \mathbf{q}_ρ . \square

6.2.3 Proof of the main result

Theorem 5 can now be proved using the approximations of \mathbf{u}_ρ and \mathbf{p}_ρ . Let us first recall the objective function (6.3) in the background domain.

$$J_0(\Omega) = \int_{\Omega_1} F(\mathbf{u})dV + \int_{\Gamma_N} G(\mathbf{u})dS.$$

A Taylor expansion at first-order with exact remainder of the objective function in the perturbed domain is

$$\begin{aligned} J_\rho(\Omega) &= \int_{\Omega_1} F(\mathbf{u}_\rho)dV + \int_{\Gamma_N} G(\mathbf{u}_\rho)dS = \int_{\Omega_1} F(\mathbf{u} + \mathbf{v}_\rho)dV + \int_{\Gamma_N} G(\mathbf{u} + \mathbf{v}_\rho)dS \\ &= J_0(\Omega) + \int_{\Omega_1} \mathbf{F}'(\mathbf{u}) \cdot \mathbf{v}_\rho dV + \int_{\Gamma_N} \mathbf{G}'(\mathbf{u}) \cdot \mathbf{v}_\rho dS + \frac{1}{2} \int_{\Omega_1} \mathbf{v}_\rho^T \mathbf{F}''(\bar{\mathbf{u}}) \mathbf{v}_\rho dV + \frac{1}{2} \int_{\Gamma_N} \mathbf{v}_\rho^T \mathbf{G}''(\bar{\mathbf{u}}) \mathbf{v}_\rho dS. \end{aligned}$$

The exact remainder is bounded using assumptions (6.4) and Proposition 13

$$\left| \int_{\Omega_1} \mathbf{v}_\rho^T \mathbf{F}''(\bar{\mathbf{u}}) \mathbf{v}_\rho dV \right| \leq C \|\mathbf{v}_\rho\|_{L^2(\Omega_\rho)}^2 \leq C \left(\frac{\kappa(\rho)}{1 + C \frac{\kappa(\rho)}{\rho}} \right)^2 + C \rho^3,$$

$$\begin{aligned} \left| \int_{\Gamma_N} \mathbf{v}_\rho^T G''(\bar{\mathbf{u}}) \mathbf{v}_\rho dS \right| &\leq C \|\mathbf{v}_\rho\|_{L^2(\Gamma_N)}^2 \leq C \|\boldsymbol{\delta}\|_{L^2(\Gamma_N)}^2 \text{ because } \theta = 0 \text{ on } \Gamma_N \\ &\leq C \|\boldsymbol{\delta}\|_{H^1(\Omega_\rho)}^2 \leq C \left(\frac{\kappa(\rho)}{1 + C \frac{\kappa(\rho)}{\rho}} \right)^2 + C \rho^3. \end{aligned}$$

The occurrence of \mathbf{v}_ρ in the expansion of $J_\rho(\Omega)$ justifies the use of an adjoint state. Moreover, this expansion involves \mathbf{u} instead of \mathbf{u}_ρ . That is why (6.50) has been modified and is not the standard adjoint equation. Multiply (6.50) by \mathbf{v}_ρ and integrate by parts twice,

$$\begin{aligned} &\int_{\Omega_1} \mathbf{F}'(\mathbf{u}) \cdot \mathbf{v}_\rho dV + \int_{\Gamma_N} \mathbf{G}'(\mathbf{u}) \cdot \mathbf{v}_\rho dS = \int_{\partial\omega_A \cup \partial\omega_B} \mathbf{A}\varepsilon(\mathbf{p}_\rho) \mathbf{n} \cdot \mathbf{v}_\rho dS - \int_{\partial\omega_A \cup \partial\omega_B} \mathbf{A}\varepsilon(\mathbf{v}_\rho) \mathbf{n} \cdot \mathbf{p}_\rho dS \\ &= \int_{\partial\omega_A \cup \partial\omega_B} \mathbf{A}\varepsilon(\mathbf{q}) \mathbf{n} \cdot \mathbf{v} dS + \int_{\partial\omega_A \cup \partial\omega_B} \mathbf{A}\varepsilon(\mathbf{p}) \mathbf{n} \cdot \mathbf{v} dS - \int_{\partial\omega_A \cup \partial\omega_B} \mathbf{A}\varepsilon(\mathbf{v}) \mathbf{n} \cdot \mathbf{q} dS - \int_{\partial\omega_A \cup \partial\omega_B} \mathbf{A}\varepsilon(\mathbf{v}) \mathbf{n} \cdot \mathbf{p} dS \\ &+ \int_{\partial\omega_A \cup \partial\omega_B} \mathbf{A}\varepsilon(\mathbf{q}) \mathbf{n} \cdot \boldsymbol{\delta} dS - \int_{\partial\omega_A \cup \partial\omega_B} \mathbf{A}\varepsilon(\boldsymbol{\delta}) \mathbf{n} \cdot \mathbf{q} dS + \int_{\partial\omega_A \cup \partial\omega_B} \mathbf{A}\varepsilon(\boldsymbol{\eta}) \mathbf{n} \cdot \mathbf{v} dS - \int_{\partial\omega_A \cup \partial\omega_B} \mathbf{A}\varepsilon(\mathbf{v}) \mathbf{n} \cdot \boldsymbol{\eta} dS \\ &+ \int_{\partial\omega_A \cup \partial\omega_B} \mathbf{A}\varepsilon(\mathbf{p}) \mathbf{n} \cdot \boldsymbol{\delta} dS - \int_{\partial\omega_A \cup \partial\omega_B} \mathbf{A}\varepsilon(\boldsymbol{\delta}) \mathbf{n} \cdot \mathbf{p} dS + \int_{\partial\omega_A \cup \partial\omega_B} \mathbf{A}\varepsilon(\boldsymbol{\eta}) \mathbf{n} \cdot \boldsymbol{\delta} dS - \int_{\partial\omega_A \cup \partial\omega_B} \mathbf{A}\varepsilon(\boldsymbol{\delta}) \mathbf{n} \cdot \boldsymbol{\eta} dS. \end{aligned}$$

All these terms are estimated one by one, mostly with a rescaling on the unit ball or with some integration by parts. Above all, let us set the notations $\boldsymbol{\xi}_{p,a}(\rho)$ and $\boldsymbol{\xi}_{p,b}(\rho)$ in an equivalent manner as $\boldsymbol{\xi}_{u,a}(\rho)$ and $\boldsymbol{\xi}_{u,b}(\rho)$ that read

$$\boldsymbol{\xi}_{p,a}(\rho) = \frac{\frac{\kappa(\rho)}{\rho|\omega|\tau_A}}{1 + \frac{\kappa(\rho)}{\rho|\omega|} \left(\frac{1}{\tau_A} + \frac{1}{\tau_B} \right)} \left((\mathbf{p}(\mathbf{x}_0 + \ell\mathbf{e}) - \mathbf{p}(\mathbf{x}_0)) \cdot \mathbf{e} \right) \mathbf{e}, \quad (6.55)$$

$$\boldsymbol{\xi}_{p,b}(\rho) = -\frac{\frac{\kappa(\rho)}{\rho|\omega|\tau_B}}{1 + \frac{\kappa(\rho)}{\rho|\omega|} \left(\frac{1}{\tau_B} + \frac{1}{\tau_B} \right)} \left((\mathbf{p}(\mathbf{x}_0 + \ell\mathbf{e}) - \mathbf{p}(\mathbf{x}_0)) \cdot \mathbf{e} \right) \mathbf{e}. \quad (6.56)$$

★ 1st term

The first term is evaluated by rescaling

$$\begin{aligned} &\int_{\partial\omega_A \cup \partial\omega_B} \mathbf{A}\varepsilon(\mathbf{q}) \mathbf{n} \cdot \mathbf{v} dS \\ &= \rho \int_{\partial\omega} \mathbf{A}\varepsilon(\mathbf{q}_a) \mathbf{n} \cdot \mathbf{v}_a dS + \rho \int_{\partial\omega} \mathbf{A}\varepsilon(\mathbf{q}_b) \mathbf{n} \cdot \mathbf{v}_b dS = \rho|\omega| \left(\tau_A \boldsymbol{\xi}_{u,a}(\rho) \cdot \boldsymbol{\xi}_{p,a}(\rho) + \tau_B \boldsymbol{\xi}_{u,b}(\rho) \cdot \boldsymbol{\xi}_{p,b}(\rho) \right) \\ &= \rho|\omega| \left(\tau_A \left(\frac{\frac{\kappa(\rho)}{\rho|\omega|\tau_A}}{1 + \frac{\kappa(\rho)}{\rho|\omega|} \left(\frac{1}{\tau_B} + \frac{1}{\tau_B} \right)} \right)^2 + \tau_B \left(\frac{\frac{\kappa(\rho)}{\rho|\omega|\tau_B}}{1 + \frac{\kappa(\rho)}{\rho|\omega|} \left(\frac{1}{\tau_B} + \frac{1}{\tau_B} \right)} \right)^2 \right) (\mathbf{u}(\mathbf{x}_0 + \ell\mathbf{e}) - \mathbf{u}(\mathbf{x}_0)) \cdot \mathbf{e} (\mathbf{p}(\mathbf{x}_0 + \ell\mathbf{e}) - \mathbf{p}(\mathbf{x}_0)) \cdot \mathbf{e}. \end{aligned}$$

★ 2nd term

The second term is also determined by rescaling

$$\int_{\partial\omega_A \cup \partial\omega_B} \mathbf{A}\varepsilon(\mathbf{p}) \mathbf{n} \cdot \mathbf{v} dS = \rho^2 \int_{\partial\omega} \mathbf{A}\varepsilon(\mathbf{p})(\rho\mathbf{y} + \mathbf{x}_0) \mathbf{n} \cdot \mathbf{v}_a(\mathbf{y}) dS + \rho^2 \int_{\partial\omega} \mathbf{A}\varepsilon(\mathbf{p})(\rho\mathbf{y} + \mathbf{x}_0 + \ell\mathbf{y}) \mathbf{n} \cdot \mathbf{v}_b(\mathbf{y}) dS.$$

It comes with Cauchy-Schwarz inequality

$$\begin{aligned} & \left| \int_{\partial\omega_A \cup \partial\omega_B} \mathbf{A}\varepsilon(\mathbf{p})\mathbf{n} \cdot \mathbf{v} dS \right| \\ & \leq C\rho^2 \left(|\xi_{u,a}(\rho)| \sqrt{\int_{\partial\omega} |\mathbf{A}\varepsilon(\mathbf{p})(\rho\mathbf{y} + \mathbf{x}_0)\mathbf{n}|^2 dS} + |\xi_{u,b}(\rho)| \sqrt{\int_{\partial\omega} |\mathbf{A}\varepsilon(\mathbf{p})(\rho\mathbf{y} + \mathbf{x}_0 + \ell\mathbf{e})\mathbf{n}|^2 dS} \right) \\ & \leq C\rho^2 \frac{\kappa(\rho)}{1 + C\frac{\kappa(\rho)}{\rho}}. \end{aligned}$$

Remark 61. Since $\mathbf{p} \in (\mathcal{C}^2(\Omega))^3$, the integrals $\int_{\partial\omega} |\mathbf{A}\varepsilon(\mathbf{p})(\rho\mathbf{y} + \mathbf{x}_0)\mathbf{n}|^2 dS$ and

$\int_{\partial\omega} |\mathbf{A}\varepsilon(\mathbf{p})(\rho\mathbf{y} + \mathbf{x}_0 + \ell\mathbf{e})\mathbf{n}|^2 dS$ are bounded by a constant C that depends on the $(\mathcal{C}^1)^3$ -norm of \mathbf{p} .

★ 3rd term

The term $\int_{\partial\omega_A \cup \partial\omega_B} \mathbf{A}\varepsilon(\mathbf{v})\mathbf{n} \cdot \mathbf{q} dS$ is computed by rescaling as the first term. It results that the third term annuls the first one.

★ 4th term

The fourth term requires more developments. Let us do the following expansion with integral remainder of the adjoint state

$$\mathbf{p}(\mathbf{x}) = \mathbf{p}(\mathbf{x}_0) + \int_0^1 (1-t)\nabla\mathbf{p}(\mathbf{x}_0 + t(\mathbf{x} - \mathbf{x}_0))(\mathbf{x} - \mathbf{x}_0) dt \text{ for } \mathbf{x} \in \omega_A, \quad (6.57)$$

and similarly in ω_B . The integral remainder is extended in Ω using the cut-off functions ψ_{ω_A} and ψ_{ω_B} such that

$$\mathbf{l}_p^A(\mathbf{x}) = \psi_{\omega_A}(\mathbf{x}) \int_0^1 (1-t)\nabla\mathbf{p}(\mathbf{x}_0 + t(\mathbf{x} - \mathbf{x}_0))(\mathbf{x} - \mathbf{x}_0) dt. \quad (6.58)$$

Noticing that $\mathbf{x} - \mathbf{x}_0$ is of the order of ρ around \mathbf{x}_0 , then for some constant $C > 0$ independent of ρ , we have $|\mathbf{l}_p^A| \leq C\rho$. Still by rescaling, it comes that

$$\begin{aligned} \int_{\partial\omega_A \cup \partial\omega_B} \mathbf{A}\varepsilon(\mathbf{v})\mathbf{n} \cdot \mathbf{p} dS &= \rho \left(\int_{\partial\omega} \mathbf{A}\varepsilon(\mathbf{v}_a)(\mathbf{y})\mathbf{n} \cdot \mathbf{p}(\rho\mathbf{y} + \mathbf{x}_0) dS + \int_{\partial\omega} \mathbf{A}\varepsilon(\mathbf{v}_b)(\mathbf{y})\mathbf{n} \cdot \mathbf{p}(\rho\mathbf{y} + \mathbf{x}_0 + \ell\mathbf{e}) dS \right) \\ &= \rho \left(\mathbf{p}(\mathbf{x}_0) \cdot \int_{\partial\omega} \mathbf{A}\varepsilon(\mathbf{v}_a)(\mathbf{y})\mathbf{n} dS + \mathbf{p}(\mathbf{x}_0 + \ell\mathbf{e}) \cdot \int_{\partial\omega} \mathbf{A}\varepsilon(\mathbf{v}_b)(\mathbf{y})\mathbf{n} dS \right) \\ &\quad + \rho \left(\int_{\partial\omega} \mathbf{A}\varepsilon(\mathbf{v}_a)(\mathbf{y})\mathbf{n} \cdot \mathbf{l}_p^A(\rho\mathbf{y} + \mathbf{x}_0) dS + \int_{\partial\omega} \mathbf{A}\varepsilon(\mathbf{v}_b)(\mathbf{y})\mathbf{n} \cdot \mathbf{l}_p^B(\rho\mathbf{y} + \mathbf{x}_0 + \ell\mathbf{e}) dS \right). \end{aligned}$$

The first terms are easily expressed as

$$\begin{aligned}
& \rho \left(\mathbf{p}(\mathbf{x}_0) \cdot \int_{\partial\omega} \mathbf{A}\varepsilon(\mathbf{v}_a)(\mathbf{y})\mathbf{n}dS + \mathbf{p}(\mathbf{x}_0 + \ell\mathbf{e}) \cdot \int_{\partial\omega} \mathbf{A}\varepsilon(\mathbf{v}_b)(\mathbf{y})\mathbf{n}dS \right) \\
&= \rho|\omega| (\mathbf{p}(\mathbf{x}_0) \cdot \mathbf{e}\tau_A \boldsymbol{\xi}_{u,a}(\rho) - \mathbf{p}(\mathbf{x}_0 + \ell\mathbf{e}) \cdot \mathbf{e}\tau_B \boldsymbol{\xi}_{u,b}(\rho)) \\
&= - \frac{\kappa(\rho)}{1 + \frac{\kappa(\rho)}{\rho|\omega|} \left(\frac{1}{\tau_A} + \frac{1}{\tau_B} \right)} (\mathbf{u}(\mathbf{x}_0 + \ell\mathbf{e}) - \mathbf{u}(\mathbf{x}_0)) \cdot \mathbf{e} (\mathbf{p}(\mathbf{x}_0 + \ell\mathbf{e}) - \mathbf{p}(\mathbf{x}_0)) \cdot \mathbf{e}.
\end{aligned}$$

The terms with the exact remainders are expected to be remainder terms. Using the explicit expression of \mathbf{v}_a and thus $\varepsilon(\mathbf{v}_a)$, it comes that

$$\begin{aligned}
\rho \left| \int_{\partial\omega} \mathbf{A}\varepsilon(\mathbf{v}_a)(\mathbf{y})\mathbf{n} \cdot \mathbf{l}_p^A(\rho\mathbf{y} + \mathbf{x}_0)dS \right| &\leq C\rho \sqrt{\int_{\partial\omega} |\varepsilon(\mathbf{v}_a)|^2 dS} \sqrt{\int_{\partial\omega} |\mathbf{l}_p^A(\rho\mathbf{y} + \mathbf{x}_0)|^2 dS} \\
&\leq C\rho^2 |\boldsymbol{\xi}_{u,a}(\rho)| \leq C\rho \frac{\kappa(\rho)}{1 + C\frac{\kappa(\rho)}{\rho}}.
\end{aligned}$$

The last term is estimated the same way.

★ 5th to 8th terms

Since \mathbf{v} and \mathbf{q} and also $\boldsymbol{\delta}$ and $\boldsymbol{\eta}$ have the same behavior, the integrals

$$\int_{\partial\omega_A \cup \partial\omega_B} \mathbf{A}\varepsilon(\mathbf{q})\mathbf{n} \cdot \boldsymbol{\delta}dS - \int_{\partial\omega_A \cup \partial\omega_B} \mathbf{A}\varepsilon(\boldsymbol{\delta})\mathbf{n} \cdot \mathbf{q}dS \quad \text{and} \quad \int_{\partial\omega_A \cup \partial\omega_B} \mathbf{A}\varepsilon(\boldsymbol{\eta})\mathbf{n} \cdot \mathbf{v}dS - \int_{\partial\omega_A \cup \partial\omega_B} \mathbf{A}\varepsilon(\mathbf{v})\mathbf{n} \cdot \boldsymbol{\eta}dS$$

have the same estimates. It is then enough to estimate one of them. Multiplying (6.44) by $\theta\mathbf{q}$ and integrating by parts twice gives us

$$\begin{aligned}
& \int_{\partial\omega_A \cup \partial\omega_B} \mathbf{A}\varepsilon(\mathbf{q})\mathbf{n} \cdot \boldsymbol{\delta}dS - \int_{\partial\omega_A \cup \partial\omega_B} \mathbf{A}\varepsilon(\boldsymbol{\delta})\mathbf{n} \cdot \mathbf{q}dS = - \int_{\Omega_\rho} \operatorname{div}\mathbf{A}\varepsilon(\boldsymbol{\delta}) \cdot \theta\mathbf{q}dV + \int_{\Omega_\rho} \operatorname{div}\mathbf{A}\varepsilon(\theta\mathbf{q}) \cdot \boldsymbol{\delta}dV \\
&= \int_{\Omega_\rho} (-\mathbf{A}(\mathbf{v} \otimes \nabla\theta)^s : (\mathbf{q} \otimes \nabla\theta)^s - \mathbf{A}(\mathbf{v} \otimes \nabla\theta)^s : \varepsilon(\mathbf{q})\theta + \mathbf{A}\varepsilon(\mathbf{v})\nabla\theta \cdot \theta\mathbf{q})dV \\
&\quad + \int_{\Omega_\rho} (-\mathbf{A}(\mathbf{q} \otimes \nabla\theta)^s : \varepsilon(\boldsymbol{\delta}) + \mathbf{A}\varepsilon(\mathbf{q})\nabla\theta \cdot \boldsymbol{\delta})dV.
\end{aligned}$$

Estimates on the L^∞ -norms of \mathbf{v} and $\varepsilon(\mathbf{v})$ and the estimate on the H^1 -norm of $\boldsymbol{\delta}$ imply

$$\begin{aligned}
& \left| \int_{\partial\omega_A \cup \partial\omega_B} \mathbf{A}\varepsilon(\mathbf{q})\mathbf{n} \cdot \boldsymbol{\delta}dS - \int_{\partial\omega_A \cup \partial\omega_B} \mathbf{A}\varepsilon(\boldsymbol{\delta})\mathbf{n} \cdot \mathbf{q}dS \right| \\
&\leq C\|\mathbf{v}\|_{L^\infty(\Omega \setminus \mathcal{U}_-)} \|\nabla\theta\|_{L^\infty(\Omega \setminus \mathcal{U}_-)} (\|\mathbf{q}\|_{L^\infty(\Omega \setminus \mathcal{U}_-)} + \|\varepsilon(\mathbf{q})\|_{L^\infty(\Omega \setminus \mathcal{U}_-)}) + C\|\varepsilon(\mathbf{v})\|_{L^\infty(\Omega \setminus \mathcal{U}_-)} \|\nabla\theta\|_{L^\infty(\Omega \setminus \mathcal{U}_-)} \|\mathbf{q}\|_{L^\infty(\Omega \setminus \mathcal{U}_-)} \\
&\quad + C\|\mathbf{q}\|_{L^\infty(\Omega \setminus \mathcal{U}_-)} \|\nabla\theta\|_{L^\infty(\Omega \setminus \mathcal{U}_-)} (\|\boldsymbol{\delta}\|_{L^2(\Omega_\rho)} + \|\varepsilon(\boldsymbol{\delta})\|_{L^2(\Omega_\rho)}) \\
&\leq C \left(\frac{\kappa(\rho)}{1 + C\frac{\kappa(\rho)}{\rho}} \right)^2 + C\rho^{3/2} \frac{\kappa(\rho)}{1 + C\frac{\kappa(\rho)}{\rho}}.
\end{aligned}$$

★ 9th term

The background displacement field is expanded as follows

$$\mathbf{u}(\mathbf{x}) = \mathbf{u}(\mathbf{x}_0) + \int_0^1 (1-t)\nabla\mathbf{u}(\mathbf{x}_0 + t(\mathbf{x} - \mathbf{x}_0))dt \quad \text{for } \mathbf{x} \in \omega_A. \quad (6.59)$$

The exact remainder is extended in Ω using the function ψ_{ω_A} such that

$$\mathbf{l}_u^A(\mathbf{x}) = \psi_{\omega_A}(\mathbf{x}) \int_0^1 (1-t) \nabla \mathbf{u}(\mathbf{x}_0 + t(\mathbf{x} - \mathbf{x}_0)) (\mathbf{x} - \mathbf{x}_0) dt. \quad (6.60)$$

Using the expression of $\boldsymbol{\delta}$ on $\partial\omega_A$, it follows

$$\begin{aligned} \int_{\partial\omega_A} \mathbf{A}\varepsilon(\mathbf{p})\mathbf{n} \cdot \boldsymbol{\delta} dS &= (\mathbf{C}_a(\rho) - \mathbf{u}(\mathbf{x}_0) - \boldsymbol{\xi}_{u,a}(\rho)) \cdot \int_{\partial\omega_A} \mathbf{A}\varepsilon(\mathbf{p})\mathbf{n} dS - r_a(\rho) \cdot \int_{\partial\omega_A} \mathbf{A}\varepsilon(\mathbf{p})\mathbf{n} \wedge \mathbf{x} dS \\ &\quad - \int_{\partial\omega_A} \mathbf{A}\varepsilon(\mathbf{p})\mathbf{n} \cdot h_u dS = - \int_{\partial\omega_A} \mathbf{A}\varepsilon(\mathbf{p})\mathbf{n} \cdot \mathbf{l}_u^A dS. \end{aligned}$$

It comes from Cauchy-Schwarz inequality

$$\begin{aligned} \left| \int_{\partial\omega_A} \mathbf{A}\varepsilon(\mathbf{p})\mathbf{n} \cdot h_u dS \right| &\leq \sqrt{\int_{\partial\omega_A} |\mathbf{A}\varepsilon(\mathbf{p})\mathbf{n}|^2 dS} \sqrt{\int_{\partial\omega_A} |\mathbf{l}_u^A|^2 dS} \\ &\leq C\rho \sqrt{\int_{\partial\omega} |\mathbf{A}\varepsilon(\mathbf{p})(\rho\mathbf{y} + \mathbf{x}_0)\mathbf{n}|^2 dS} \sqrt{\int_{\partial\omega_A} \rho^2 dS} \text{ because } |\mathbf{l}_u^A| \sim \rho \text{ on } \partial\omega_A \\ &\leq C\rho^3, \end{aligned}$$

and similarly on $\partial\omega_B$.

★ 10th term

Using again the expansion of the adjoint state (6.58) leads to

$$\begin{aligned} \int_{\partial\omega_A} \mathbf{A}\varepsilon(\boldsymbol{\delta})\mathbf{n} \cdot \mathbf{p} dS &= \mathbf{p}(\mathbf{x}_0) \cdot \int_{\partial\omega_A} \mathbf{A}\varepsilon(\boldsymbol{\delta})\mathbf{n} dS + \int_{\partial\omega_A} \mathbf{A}\varepsilon(\boldsymbol{\delta})\mathbf{n} \cdot h_p dS \\ &= \kappa(\rho) \left(\int_{\omega_B} \boldsymbol{\delta} \cdot \mathbf{e} dV - \int_{\omega_A} \boldsymbol{\delta} \cdot \mathbf{e} dV \right) \mathbf{p}(\mathbf{x}_0) \cdot \mathbf{e} + \int_{\mathcal{B}_{2\rho}^A} \mathbf{A}\varepsilon(\boldsymbol{\delta}) : \varepsilon(\mathbf{l}_p^A) dV. \end{aligned}$$

Estimates established in the proof of Proposition 13 give us

$$\kappa(\rho) \left(\int_{\omega_B} \boldsymbol{\delta} \cdot \mathbf{e} dV - \int_{\omega_A} \boldsymbol{\delta} \cdot \mathbf{e} dV \right)^2 \leq C(\rho|\boldsymbol{\xi}_{u,a}(\rho)| + \rho^{3/2}) \|\varepsilon(\boldsymbol{\delta})\|_{L^2(\Omega_\rho)} \leq C\|\varepsilon(\boldsymbol{\delta})\|_{L^2(\Omega_\rho)}^2.$$

That leads to

$$\kappa(\rho) \left| \int_{\omega_B} \boldsymbol{\delta} \cdot \mathbf{e} dV - \int_{\omega_A} \boldsymbol{\delta} \cdot \mathbf{e} dV \right| \leq C \left(\rho^{k/2} \frac{\kappa(\rho)}{1 + C\frac{\kappa(\rho)}{\rho}} + \rho^{k/2+3/2} \right).$$

We also recall that $|\varepsilon(\mathbf{l}_p^A)|$ is of the order of 1 in $\mathcal{B}_{2\rho}^A$. Then it follows that

$$\left| \int_{\mathcal{B}_{2\rho}^A} \mathbf{A}\varepsilon(\boldsymbol{\delta}) : \varepsilon(\mathbf{l}_p^A) dV \right| \leq C\rho^{3/2} \|\varepsilon(\boldsymbol{\delta})\|_{L^2(\Omega_\rho)} \leq C \left(\rho^{3/2} \frac{\kappa(\rho)}{1 + C\frac{\kappa(\rho)}{\rho}} + \rho^3 \right).$$

Finally, the tenth term is bounded as below

$$\int_{\partial\omega_A} \mathbf{A}\varepsilon(\boldsymbol{\delta})\mathbf{n} \cdot \mathbf{p}dS \leq C \left(\rho^{k/2} \frac{\kappa(\rho)}{1 + C\frac{\kappa(\rho)}{\rho}} + \rho^{k/2+3/2} + \rho^{3/2} \frac{\kappa(\rho)}{1 + C\frac{\kappa(\rho)}{\rho}} + \rho^3 \right).$$

★ 11th term and 12th term

Considering that $\boldsymbol{\delta}$ and $\boldsymbol{\eta}$ have the same behavior, the integrals $\int_{\partial\omega_A \cup \partial\omega_B} \mathbf{A}\varepsilon(\boldsymbol{\eta})\mathbf{n} \cdot \boldsymbol{\delta}dS$ and $\int_{\partial\omega_A \cup \partial\omega_B} \mathbf{A}\varepsilon(\boldsymbol{\delta})\mathbf{n} \cdot \boldsymbol{\eta}dS$ and also $\int_{\partial\omega_A \cup \partial\omega_B} \mathbf{A}\varepsilon(\boldsymbol{\delta})\mathbf{n} \cdot \boldsymbol{\delta}dS$ have the same estimate. We recall that

$$\int_{\partial\omega_A \cup \partial\omega_B} \mathbf{A}\varepsilon(\boldsymbol{\delta})\mathbf{n} \cdot \boldsymbol{\delta}dS = -\kappa(\rho) \left(\int_{\omega_B} \boldsymbol{\delta} \cdot \mathbf{e}dV - \int_{\omega_A} \boldsymbol{\delta} \cdot \mathbf{e}dV \right)^2 + \int_{\partial\omega_A} \mathbf{A}\varepsilon(\boldsymbol{\delta})\mathbf{n} \cdot \left(\int_{\omega_A} \mathbf{u}dV - \mathbf{u} \right) dS$$

$$+ \int_{\partial\omega_B} \mathbf{A}\varepsilon(\boldsymbol{\delta})\mathbf{n} \cdot \left(\int_{\omega_B} \mathbf{u}dV - \mathbf{u} \right) dS.$$

It follows that

$$\left| \int_{\partial\omega_A \cup \partial\omega_B} \mathbf{A}\varepsilon(\boldsymbol{\delta})\mathbf{n} \cdot \boldsymbol{\delta}dS \right| \leq \left| \int_{\partial\omega_A} \mathbf{A}\varepsilon(\boldsymbol{\delta})\mathbf{n} \cdot \left(\int_{\omega_A} \mathbf{u}dV - \mathbf{u} \right) dS \right| + \left| \int_{\partial\omega_B} \mathbf{A}\varepsilon(\boldsymbol{\delta})\mathbf{n} \cdot \left(\int_{\omega_B} \mathbf{u}dV - \mathbf{u} \right) dS \right|$$

$$\leq C\rho^{3/2} \|\varepsilon(\boldsymbol{\delta})\|_{L^2(\Omega_\rho)} \leq \left(\rho^{3/2} \frac{\kappa(\rho)}{1 + C\frac{\kappa(\rho)}{\rho}} + \rho^3 \right).$$

Finally, the leading term is

$$\frac{\kappa(\rho)}{1 + \frac{\kappa(\rho)}{\rho|\omega|} \left(\frac{1}{\tau_A} + \frac{1}{\tau_B} \right)} (\mathbf{u}(\mathbf{x}_0 + \ell\mathbf{e}) - \mathbf{u}(\mathbf{x}_0)) \cdot \mathbf{e} (\mathbf{p}(\mathbf{x}_0 + \ell\mathbf{e}) - \mathbf{p}(\mathbf{x}_0)) \cdot \mathbf{e}$$

$$= \left(\frac{1}{\kappa(\rho)} + \frac{1}{\rho|\omega|} \left(\frac{1}{\tau_A} + \frac{1}{\tau_B} \right) \right)^{-1} (\mathbf{u}(\mathbf{x}_0 + \ell\mathbf{e}) - \mathbf{u}(\mathbf{x}_0)) \cdot \mathbf{e} (\mathbf{p}(\mathbf{x}_0 + \ell\mathbf{e}) - \mathbf{p}(\mathbf{x}_0)) \cdot \mathbf{e}.$$

One can notice that this leading term has the same form as the one of the spring sensitivity analysis in Chapter 5. They differ from the coefficients τ_A and τ_B , which express the properties of the spheres. This leading term is then expanded with respect to ρ . The resulting leading term shall be the topological derivative and the inherent remainder term, denoted $\mathcal{R}(DJ(\mathbf{x}_0, \mathbf{e}))$, will be part of remainder term of the asymptotic expansion $\mathcal{R}(s(\rho))$, that reads

$$\mathcal{R}(s(\rho)) = O \left(\rho^2 \frac{\kappa(\rho)}{1 + C\frac{\kappa(\rho)}{\rho}} \right) + O \left(\rho \frac{\kappa(\rho)}{1 + C\frac{\kappa(\rho)}{\rho}} \right) + O \left(\left(\frac{\kappa(\rho)}{1 + C\frac{\kappa(\rho)}{\rho}} \right)^2 \right) + O \left(\rho^{3/2} \frac{\kappa(\rho)}{1 + C\frac{\kappa(\rho)}{\rho}} \right)$$

$$+ O(\rho^3) + O \left(\rho^{k/2} \frac{\kappa(\rho)}{1 + C\frac{\kappa(\rho)}{\rho}} \right) + O(\rho^{k/2+3/2}) + \mathcal{R}(DJ(\mathbf{x}_0, \mathbf{e})).$$

The remainder term is the largest term with regards to ρ . The only difference compared to the remainder term of spring sensitivity analysis (cf. Chapter 5) is for those values $1 < k < 2$. In this case, it infers that $\mathcal{R}(s(\rho)) = O(\rho^{k/2+3/2})$ if $5/3 \leq k < 2$ and $\mathcal{R}(s(\rho)) = O(\rho^{2k-1})$ if $1 < k < 5/3$. It would be consistent to expect the changing for $k = 3/2$ as the changing in the estimates of the error term $\boldsymbol{\delta}$ in Proposition 13. Actually, this difference results from the remainder term $\mathcal{R}(DJ(\mathbf{x}_0, \mathbf{e}))$ of the expansion of the leading term of the sensitivity analysis. Otherwise, the changing would have also been for $k = 3/2$.

6.3 Numerical illustrations in 2d

This part is based on the test case already deployed in Chapter 5, Section 5.3. We recall briefly the setting of the use case. The system is a plate of 2 units long and 1 unit wide with an opening gap through its center line. The mesh contains 114 274 triangular elements with a minimal and maximal size of 3.3×10^{-3} and 1.2×10^{-2} . The plate is clamped on the bottom and is loaded on the upper border. Material properties are adimensional. The Young's modulus is 10 and the Poisson's coefficient is 0.3. Let us take $\rho = 2.5 \times 10^{-2}$ and $\ell = 0.3$. The stiffness of the spring is $K = 5$. The applied force is $\mathbf{g} = (0, g_y)$, where the vertical component g_y is given by

$$g_y = \begin{cases} -\cos(\pi x) & \text{for } 0.5 \leq x \leq 1.5 \\ -\frac{3}{4}\cos(\pi x) & \text{for } 1.5 \leq x \leq 2 \end{cases}.$$

The topology of the plate is initialized with holes (see Fig. 6.4b) for the purpose of further topology optimization. The initial compliance is then $J_0(\Omega) = 0.321001$. In the same way as in Chapter 4, the rigid spheres are implemented by penalization of the material properties. Then the numerical problem considers the tensor of elasticity

$$\mathbf{A}^* = \begin{cases} \mathbf{A} & \text{in } \Omega \setminus (\omega_A \cup \omega_B) \\ \frac{1}{\delta^2} \mathbf{A} & \text{in } \omega_A \cup \omega_B \end{cases}.$$

The parameter δ is a singular perturbation. In the sequel, we consider $\delta = 10^{-3}$.

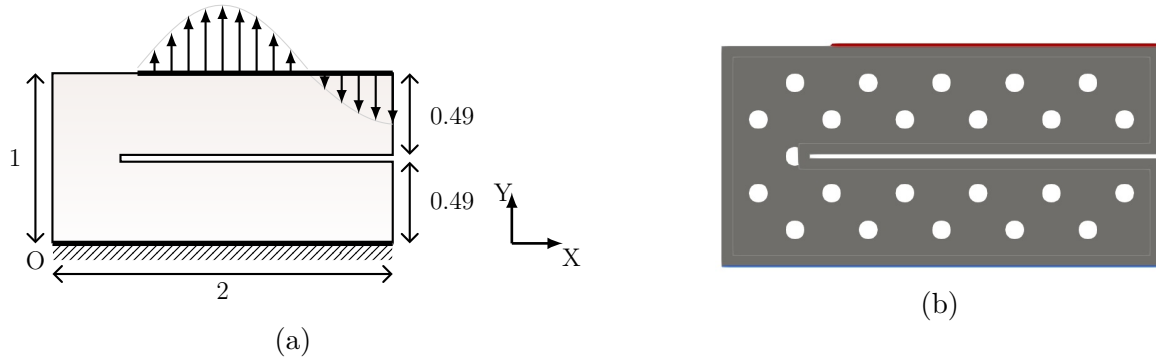


Figure 6.4: Current load case (a) and the initial topology of the structure (b)

6.3.1 Analysis with one bolt-like connection

Test of the topological derivative to put a first bolt-like connection

The problem is to place a small spring in order to decrease the compliance $J(\Omega) = \int_{\Gamma_N} \mathbf{g} \cdot \mathbf{u} dS$.

The topological derivative is applied to indicate both the location \mathbf{x}_0 and the orientation \mathbf{e} of a first spring. The background domain does not contain any bolt-like connection yet. Since the topological derivative expression is the same for the nucleation of two elastic inclusions linked by a spring and for two rigid inclusions linked by a spring, the value of the topological derivative, the best location \mathbf{x}_0 and the optimal orientation \mathbf{e} are the same in each case. The only difference lies on the efficiency of the connection (compare Tables 5.3 and 6.1). The difference between

both performances is of the order of 0.1%. The bolt-like connection always brings a slight improvement due to the rigid inclusions. Since the topological derivative with two rigid spheres linked by a spring is bounded such that $0 < k < 3/2$ in 2d, we only test the scalings $k = 0.5$ and $k = 1$.

	$DJ(\mathbf{x}_0, \mathbf{e})$	\mathbf{x}_0	φ (rad)	$J_\rho(\Omega)$	$\mathcal{E}(\Omega)$
$k = 0.5$	-5.64768	(1.53,0.43)	$\frac{7\pi}{12}$	0.266987	-0.571976
$k = 1$	-5.64768	(1.53,0.43)	$\frac{7\pi}{12}$	0.279894	0.179809

Table 6.1: Summary of the topological derivative test (recall that $J_0(\Omega) = 0.321001$)

Parametric optimization of the bolt-like connection location \mathbf{x}_0

Based on the previous results of the topological derivative, the location \mathbf{x}_0 is optimized with the parametric gradient-based algorithm described by

$$\mathbf{x}_0^{i+1} = \mathbf{x}_0^i - \delta^i \frac{\partial J}{\partial \mathbf{x}_0}(\Omega, \mathbf{x}_0^i), \quad (6.61)$$

$$\begin{aligned} \frac{\partial J}{\partial \mathbf{x}_0}(\Omega, \mathbf{x}_0^i)(\vartheta) &= \int_{\partial\omega_A \cup \partial\omega_B} \vartheta \mathbf{d} \cdot \mathbf{n} \frac{1}{\delta^2} \mathbf{A}\varepsilon(\mathbf{u}) : \varepsilon(\mathbf{p}) dS \\ &+ \kappa(\rho) \left(\frac{\vartheta}{|\omega_B|} \int_{\partial\omega_B} (\mathbf{u} \cdot \mathbf{e})(\mathbf{d} \cdot \mathbf{n}) dS - \frac{\vartheta}{|\omega_A|} \int_{\partial\omega_A} (\mathbf{u} \cdot \mathbf{e})(\mathbf{d} \cdot \mathbf{n}) dS \right) \left(\int_{\omega_B} \mathbf{p} \cdot \mathbf{e} dV - \int_{\omega_A} \mathbf{p} \cdot \mathbf{e} dV \right) \\ &+ \kappa(\rho) \left(\int_{\omega_B} \mathbf{u} \cdot \mathbf{e} dV - \int_{\omega_A} \mathbf{u} \cdot \mathbf{e} dV \right) \left(\frac{\vartheta}{|\omega_B|} \int_{\partial\omega_B} (\mathbf{p} \cdot \mathbf{e})(\mathbf{d} \cdot \mathbf{n}) dS - \frac{\vartheta}{|\omega_A|} \int_{\partial\omega_A} (\mathbf{p} \cdot \mathbf{e})(\mathbf{d} \cdot \mathbf{n}) dS \right). \end{aligned} \quad (6.62)$$

The goal is to decrease the compliance. It produces the results given in Table 6.2. The algorithm is implemented with the same descent steps as the location optimization of the spring (cf. Chapter 5). The final locations differ from the optimized location of the spring (compare with Table 5.4). Optimal locations are affected by the rigidity of the spheres. Nevertheless, the improvements are equivalent. Then the rigid bodies may provide other locations for equivalent performances.

	Initial \mathbf{x}_0	Final \mathbf{x}_0	Initial $J(\Omega)$	Final $J(\Omega)$	Improvement
$k = 0.5$	(1.53,0.43)	(0.95,0.32)	0.266987	0.215276	19.37%
$k = 1$	(1.53,0.43)	(1.11,0.35)	0.279894	0.264756	5.41%

Table 6.2: Summary of location optimization of the bolt-like connection

Topology optimization of the structure

The present section investigates various topology optimizations of the structure with fixed bolt-like connection. The problem is to minimize the volume under a constraint on the compliance. The constraint bound is defined at 0.35 to be comparable with results of Chapter 5. The volume $V(\Omega)$ and the compliance $C(\Omega)$ read

$$V(\Omega) = \int_{\Omega} dV \quad \text{and} \quad C(\Omega) = \int_{\Gamma_N} \mathbf{g} \cdot \mathbf{u} dS. \quad (6.63)$$

This optimization problem is formulated as follows

$$\begin{aligned} \min_{\Omega \in \mathcal{U}_{ad}} \quad & V(\Omega), \\ \text{s.t.} \quad & C(\Omega) \leq 0.35 \end{aligned} \quad (6.64)$$

where \mathcal{U}_{ad} is the set of admissible shapes of the structure. The constraint is taken into account with the Augmented Lagrangian functional $J(\Omega)$, so that the problem (6.64) is rewritten as

$$\min_{\Omega \in \mathcal{U}_{ad}} \max_{\alpha \geq 0} \left\{ J(\Omega) = V(\Omega) + \alpha(C(\Omega) - 0.35) + \frac{\beta}{2}(C(\Omega) - 0.35)^2 \right\}, \quad (6.65)$$

where α and β are Lagrange multiplier and penalty parameter for the compliance constraint.

- One bolt-like connection put at the location given by the topological derivative

Let us consider the bolt-like connection placed by the topological derivative at the point $\mathbf{x}_0 = (1.53, 0.43)$ and orientated at $\varphi = \frac{7\pi}{12}$ rad. The optimal structures and the final volumes are given in Fig. 6.5 and Table 6.3. The results are practically the same as the ones provided by the small spring model (compare with Fig. 5.14 and Table 5.5). Actually, the small bolt-like connection and the small spring are located and oriented the same way. Then for the same configuration of connection, the topology of the structure and the corresponding volume are the same whether the inclusions are rigid or elastic.

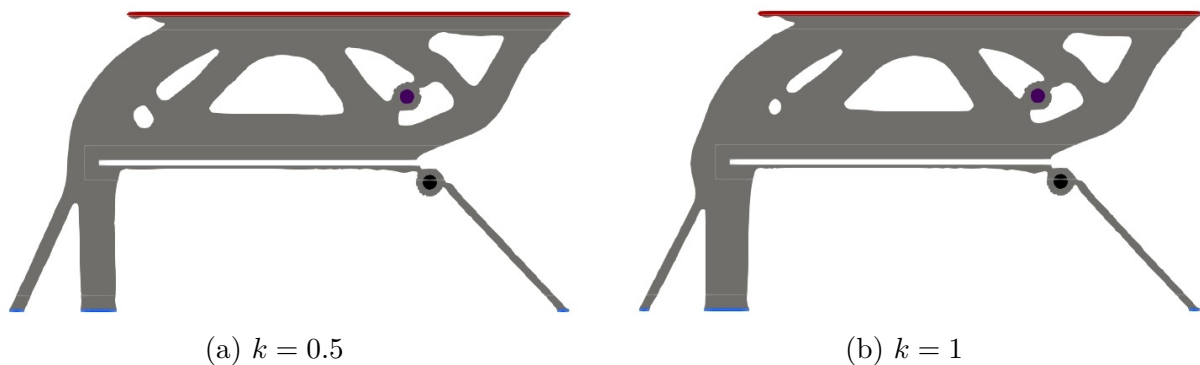


Figure 6.5: Optimal shapes for various values of k , for fixed $\mathbf{x}_0 = (1.53, 0.43)$ and $\varphi = \frac{7\pi}{12}$ rad

- One bolt-like connection put at the location given by the parametric gradient

	Final Volume $V(\Omega)$	Improvement
$k = 0.5$	0.656348	64.28%
$k = 1$	0.691963	62.35%

Table 6.3: Summary of volumes for topology optimization with one fixed bolt-like connection placed at $\mathbf{x}_0 = (1.53, 0.43)$ and oriented at $\varphi = \frac{7\pi}{12}$ rad (recall that the initial volume is $V(\Omega) = 1.83765$)

Consider now the bolt-like connection resulting from a location optimization with the parametric gradient-based algorithm. We recall that final locations \mathbf{x}_0 differ from final locations of the spring. It is then reasonable to expect different topologies. Actually the topology for $k = 0.5$ with a bolt-like connection (see Fig. 6.6a) differs substantially from the topology with a simple spring (see Fig. 5.15a). The structure with the spring is a single piece. By contrast, the head of the bolt-like connection is independently linked by thin bars to Dirichlet boundaries. In fact, the bolt-like connection is lower than the spring. It is more favorable to link up directly the head of the connection to Dirichlet boundaries than to attach this head to the structure. Their optimal volumes are equivalent as shown in Table 6.4. Even if the connections location are different, the topologies for $k = 1$ look alike with a bolt-like connection or with a simple spring. Moreover, the weight of the optimal structure are practically the same.

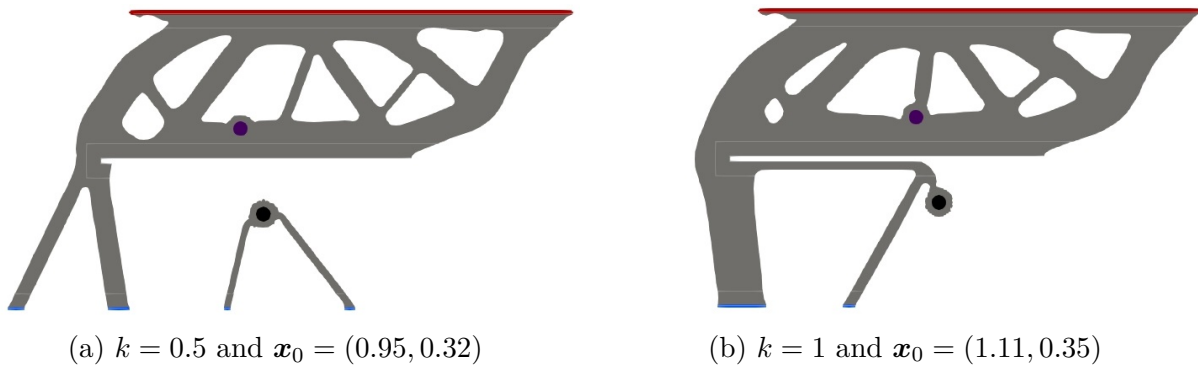


Figure 6.6: Optimal shapes for various values of k and for fixed $\varphi = \frac{7\pi}{12}$ rad

	Initial Volume $V(\Omega)$	Final Volume $V(\Omega)$	Improvement
$k = 0.5$	1.83791	0.526826	71.34%
$k = 1$	1.8387	0.647124	64.81%

Table 6.4: Summary of volumes for topology optimization with one fixed bolt-like connection placed according to the parametric gradient and oriented at $\varphi = \frac{7\pi}{12}$ rad

Coupled topology optimization of both the structure and location of the bolt-like connection

This section investigates a coupled optimization of both the structure of the plate and the location of the bolt-like connection. The problem is still to solve (6.65), *i.e.* to minimize the volume under a compliance constraint. To avoid numerical instabilities, the structure and the location are not optimized in the same iteration. The algorithm alternates 4 iterations of structural optimization and 1 iteration of location optimization.

The bolt-like connection is initially placed at the location given by the topological derivative. The coupled optimization of the structure and the location of the connection produces the topologies given in Fig. 6.7. Results are summarized in Table 6.5. Compare the case $k = 0.5$ with the optimal topologies with a simple spring (see Fig. 5.16). The final locations are about to be the same. The upper parts of the structure are similar. The only difference concerns the lower parts. The head of the bolt-like connection is only linked to a Dirichlet boundary while the head of the spring is attached to the structure through bars. The final volume are slightly different with a small benefit for the bolt-like connection case. The coupling with the size scale $k = 1$ provides different optimal location from the spring model (compare Tables 6.5 and 5.7). However, the topologies are comparable and the final volumes are almost the same.

The coupling has also been tested with a bolt-like connection initially placed at the location given by the parametric gradient. The final topologies differ a little bit from the results with the elastic inclusions. Nevertheless, their final volume are equivalent. As a conclusion, the volume improvement is the same whether the inclusions are rigid or elastic.

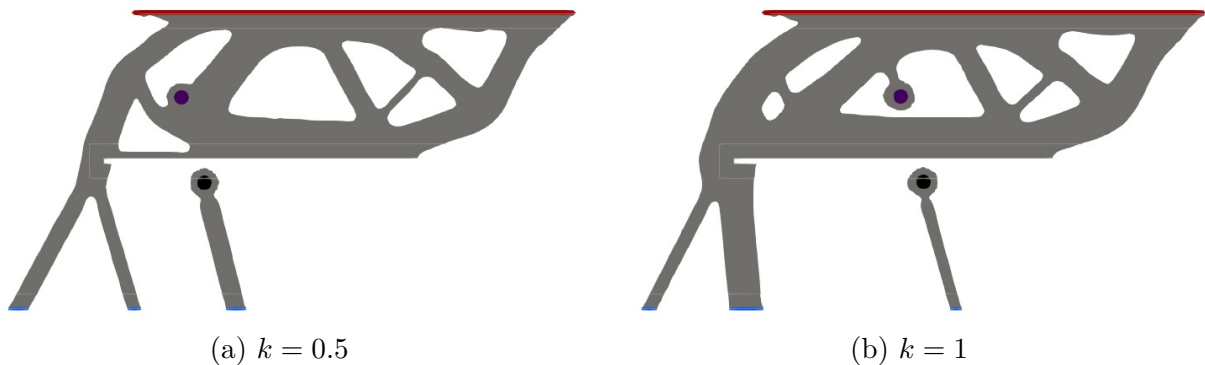


Figure 6.7: Optimal shapes and locations for various values of k and $\varphi = \frac{7\pi}{12}$ rad with initial spring placed by the topological derivative

	Initial \mathbf{x}_0	Final \mathbf{x}_0	Initial $V(\Omega)$	Final $V(\Omega)$	Improvement
$k = 0.5$	(1.53,0.43)	(0.74,0.43)	1.83765	0.529177	71.20%
$k = 1$	(1.53,0.43)	(1.05,0.43)	1.83765	0.626745	65.89%

Table 6.5: Summary of results : coupled optimization of both structure and location with initial spring placed by the topological derivative

6.3.2 Analysis with two bolt-like connections

Based on the results with one bolt-like connection, we intend to add a second bolt-like connection using the topological derivative. It provides practically the same results as the spring case. The location optimization still results to slight different locations from the spring case. However, the gain are still comparable. Moreover, the topology optimization with two bolt-like connections, no matter the initial location of the connections, still generates equivalent weight reduction to the spring case. Even if the bolt-like connection and the spring connection do not necessarily provide the same topology, both models are equally efficient in terms of volume minimization under a compliance constraint.

6.4 Numerical illustrations in 3d

The following test case comes from the numerical illustration of second part of the published article [96]:

L Rakotondrainibe, G Allaire, P Orval, Topology optimization of connections in mechanical systems. *Structural and Multidisciplinary Optimization*, 61:2253-2269, 2020.

The meaningfulness and accuracy of the topological derivative are checked on a very simple, academic, 3d test case. Fig. 6.8 presents a cube with a slit or opening, clamped at the bottom and on the left.

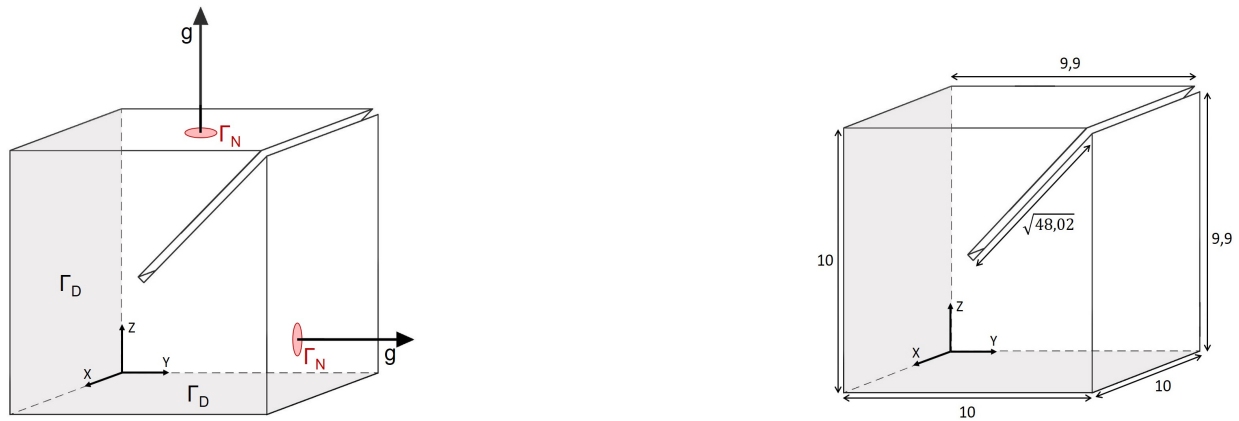


Figure 6.8: Cube with a slit, its loadings and dimensions

Dimensions of the cube are given in Fig. 6.8. The opening goes to the center of the face so that its length is $\sqrt{48.02}$. The Young's modulus E of the background domain is rescaled to 1 and its Poisson's coefficient is 0.3. Loads are Gaussian functions centered at points $\mathbf{x}_Y = (7.5, 10, 2.5)$ and $\mathbf{x}_Z = (5, 5, 10)$. They are deliberately non-symmetric so that horizontal and vertical configurations are different. They are explicitly given by $g = \exp(-((x - x_Y)^2 + (z - z_Y)^2))$ and $g = \exp(-((x - x_Z)^2 + (y - y_Z)^2))$ respectively on the face of normal \mathbf{Y} and \mathbf{Z} . Loads are applied simultaneously.

The length of the spring is $\ell = 1$. Setting the Young's modulus E_{spring} to 1, the rigidity of the spring is given by $K = \frac{E_{\text{spring}}\pi}{\ell}r_1$ where $r_1 = 1$ is the radius of the unit ball. The relative radius of the spheres is $\rho = 0.3$. Their rigid motion is implemented by setting rigid material properties on each sphere. In this test case, the Young modulus of the spheres is $100 * E$ and the Poisson's coefficient is unchanged. This test case was implemented on a tetrahedral mesh with 237 887

elements and a minimal mesh size of 0.1.

This test case is not an optimization problem. The topological derivative is used just to put an initial bolt-like connection in order to stiffen the cube. The problem here is to create a small pair of rigid inclusions linked by a spring to decrease the compliance, which reads

$$C(\Omega) = \int_{\Gamma_N} \mathbf{g} \cdot \mathbf{u} dS.$$

In other words, the topological derivative should indicate the most interesting location to add an idealized bolt-like connection, as well as the most favourable direction of the bolt axis. Since the objective is the compliance, the problem is self-adjoint so the topological derivative has the following form

$$DJ(\mathbf{x}_0, \mathbf{e}) = - \left(\frac{1}{K} + \frac{2}{\tau} \right)^{-1} ((\mathbf{u}(\mathbf{x}_0 + \ell\mathbf{e}) - \mathbf{u}(\mathbf{x}_0)) \cdot \mathbf{e})^2. \quad (6.66)$$

This topological derivative involves an harmonic mean of rigidities due to the interaction between the spring and the background material that are respectively depicted by K and τ . It is intuitive that the topological derivative corresponds to a certain energy of the spring. Formula (6.66) is still valid if one wants to add a new bolt-like connection in a domain already containing one bolt or more, provided that \mathbf{u} is computed in the domain featuring those previous bolt-like connection. For graphical purposes, it is more suitable to represent the vector \mathbf{e} in spherical coordinates $\mathbf{e} = (\sin(\varphi) \cos(\Psi), \sin(\varphi) \sin(\Psi), \cos(\varphi))$. The angles φ and Ψ are calculated every $\pi/18$ radian. The topological derivative is computed for any \mathbf{x}_0 in the domain which insures that both spheres are inside the cube and they do not stick to the point of application of forces. This is thus geometrically evaluated in a smaller cube and unsuitable values are truncated. Since it is always negative in this test case, one can choose \mathbf{x}_0 as the point of the most negative value of DJ .

It turns out that the compliance of the perturbed structure (with the inclusions linked by a spring) actually matches the initial compliance perturbed by the topological gradient. More precisely, denote by $C_\rho(\Omega)$ the compliance when the small bolt-like connection is added. For this test case, the initial compliance, *i.e.* the one without that small bolt, is $C_0(\Omega) = 7.01$. Define a so-called estimator \mathcal{E} , as the topological asymptotic expansion without the remainder term

$$\mathcal{E}(\Omega) = C_0(\Omega) - \rho \left(\frac{1}{K} + \frac{2}{\tau} \right)^{-1} ((\mathbf{u}(\mathbf{x}_0 + \ell\mathbf{e}) - \mathbf{u}(\mathbf{x}_0)) \cdot \mathbf{e})^2. \quad (6.67)$$

Fig. 6.9 and 6.10 represent iso-surfaces of the topological derivative field for two given orientations of the spring, namely horizontal and vertical. The small bolt-like connections are located in the area of the most negative value of the topological derivative. The topological derivative should be computed in the area of the gap. Nevertheless, it is computed everywhere to get all possible information for overall comprehension. There are some interesting iso-values around the application point of the horizontal load for the horizontal bolt-like connection (likewise for the vertical orientation) as displayed in Figs. 6.9a and 6.10a. It means that an horizontal connection could counter the horizontal force, likewise for the vertical orientation. In that case, this connection should not be considered as a bolt anymore. It should be seen as a tool to stiffen the structure. Concerning the bolt-like connection, it should be placed in the area of the gap. The topological derivative can be restricted to that zone. Yet, the better location aims to close the gap in both cases. Also, the estimator (6.67) is close to the value of the compliance of the perturbed domain $C_\rho(\Omega)$ (see Table 6.6). The difference corresponds to the remainder term.

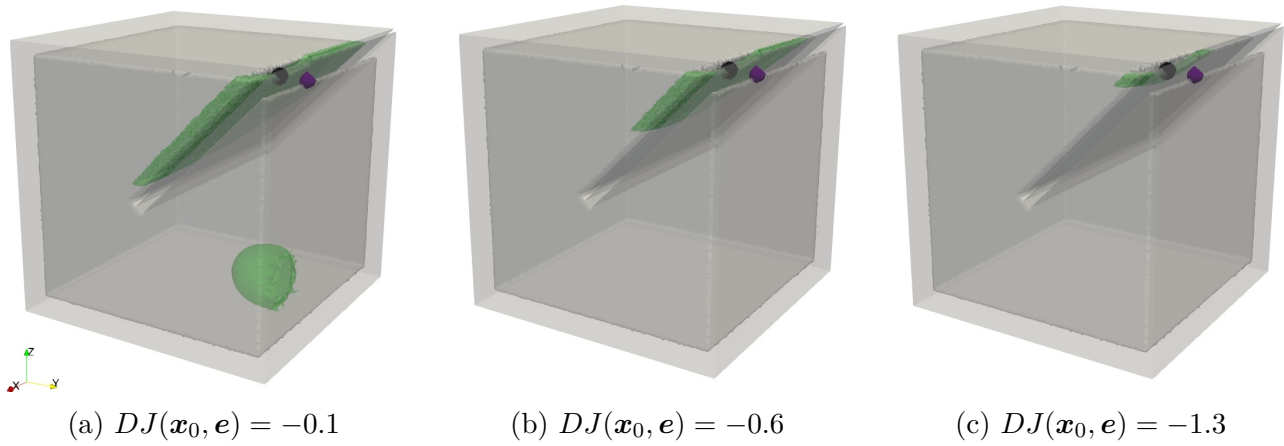


Figure 6.9: Optimal small bolt-like connection for a horizontal orientation ($\mathbf{e} = (0, 1, 0)$) and iso-values

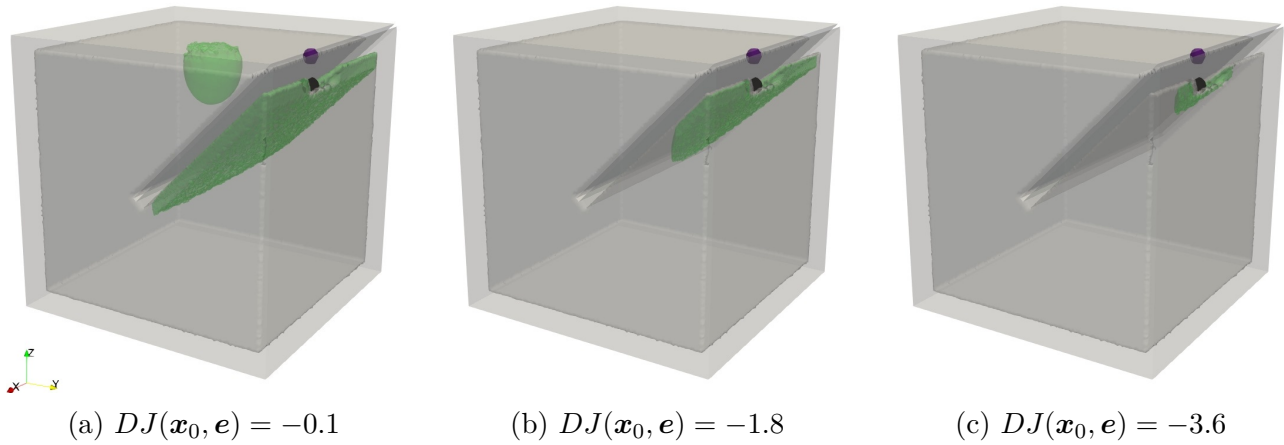


Figure 6.10: Optimal small bolt-like connection for a vertical orientation ($\mathbf{e} = (0, 0, 1)$) and iso-values

The compliance and the estimator should be closer if the size of the spheres is smaller. Actually, the asymptotic analysis of the topological derivative is more accurate for smaller values of ρ . However, the size of the spheres is numerically limited by the size of the mesh. Therefore, it has to be as fine as possible to get better accuracy of the topological derivative.

More generally, there are two strategies to seek for the best configuration of the couple $(\mathbf{x}_0, \mathbf{e})$. The first approach is to fix an orientation \mathbf{e} and then compute the topological derivative for all candidate point \mathbf{x}_0 . This evaluation is repeated for all directions \mathbf{e} . The best configuration then matches with the most negative value of the topological derivative among all tested orientations (see Fig. 6.11). It intuitively corresponds to a slanted orientation that closes the gap. The small bolt-like connection is in a path that connects the loads. The second strategy is to compute the topological derivative for a given point \mathbf{x}_0 and for all directions \mathbf{e} . It is applied for the optimal location given by the first approach and leads to the cartography given at Fig. 6.12. The best orientation for that location still matches with the most negative value of the topological derivative.

This test case proves the accuracy of the topological derivative approach in order to add one connection. Of course, after adding a new connection, a coupled optimization of both the structure and the connection position should be performed.

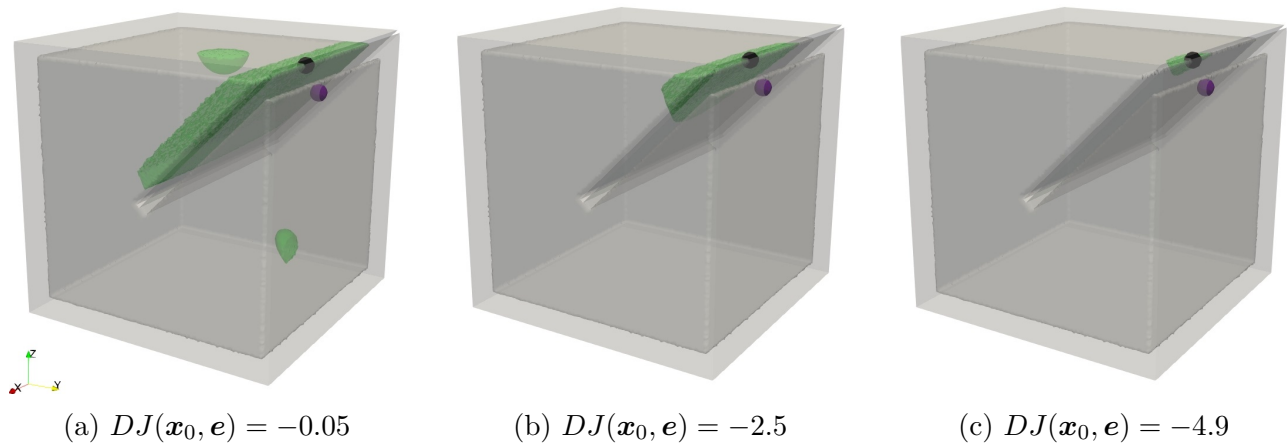


Figure 6.11: Optimal position and orientation ($\mathbf{e} = \left(0, \sin\left(\frac{5\pi}{6}\right), \cos\left(\frac{5\pi}{6}\right)\right)$) of the small bolt-like connection and iso-values

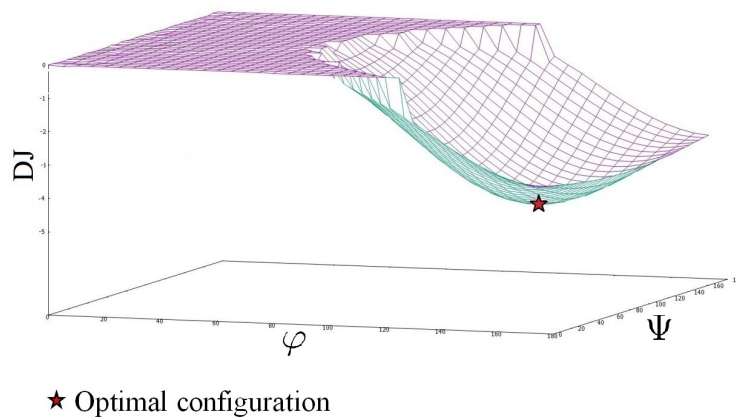


Figure 6.12: Cartography of DJ for fixed $\mathbf{x}_0 = (5.46, 9.25, 8.50)$ in terms of the angles (φ, Ψ) defining direction \mathbf{e}

Orientation	$C_\rho(\Omega)$	$\mathcal{E}(\Omega)$	\mathbf{x}_0	(φ, Ψ)	$DJ(\mathbf{x}_0, \mathbf{e})$
Horizontal	6.87	6.62	(7.76 , 8.44 , 9.03)	$\left(\frac{\pi}{2}, \frac{\pi}{2}\right)$	-1.31
Vertical	6.58	5.91	(5.63 , 9.00 , 8.42)	(0 , 0)	-3.67
Optimal	6.50	5.52	(5.46 , 9.25 , 8.50)	$\left(\frac{5\pi}{6}, \frac{\pi}{2}\right)$	-4.97

Table 6.6: Optimal values (recall that $C_0(\Omega) = 7.01$)

6.5 Conclusion of the chapter

This thesis considers two variant models of the idealized bolt. The basis model uses elastic spheres while the second one involves rigid spheres. Whatever these spheres are elastic or rigid, the topological derivative has the same form with regards to the displacement field \mathbf{u} and the adjoint state \mathbf{p} . However, topological derivatives differ from each other by their coefficients representing material properties. Besides, the rigidity of the spheres bounds the range of acceptable scaling k of the bolt-like connection. As a consequence, the asymptotic analysis covers only few values of scale ($0 < k < 3/2$ in 2d and $0 < k < 2$ in 3d) while it covers $k > 0$ in the elastic case. Moreover, numerical illustrations provide equivalent performance of the structure, in terms of volume minimization under a compliance constraint, whatever the spheres are elastic or rigid. Optimal shapes may differ but gains are similar. In other words, for the purpose of sensitivity analysis, the model with rigid spheres is more complex to compute and has restricted range of action compared to elastic spheres. Therefore, the model with elastic spheres is more suitable for further computations of sensitivity analysis with the idealized bolt model in Chapter 7. Nevertheless, the rigid spheres model is more representative in terms of mechanics as it stems from the Euler-Bernoulli condition for long beam.

As a conclusion, the model with elastic spheres is used for the purpose of topological sensitivity analysis in Chapter 7. The model with rigid spheres is used for realistic bolts in the industrial use case of Chapter 9.

Topological derivative of an idealized bolt

Contents

7.1	Setting of the problem	202
7.1.1	Step 1	205
7.1.2	Step 2	205
7.2	Computation of the topological derivative without contact	209
7.2.1	Step 1	209
7.2.2	Step 2	212
7.2.3	Proof of the main result	218
7.3	Computation of the topological derivative with sliding contact	224
7.3.1	Contact model	224
7.3.2	Step 1	225
7.3.3	Step 2	227
7.3.4	Proof of the main result	235

This chapter investigates the topological sensitivity analysis with respect to a small idealized bolt subjected to a pretension condition. The small bolt is made of two elastic spheres linked by a fixed-length one degree of freedom spring. The pretension condition is applied in a first step followed by a second step for application of in-service conditions. The sensitivity analysis is first carried out without contact condition and developed with regards to the two-steps linear elasticity problem. In a second part, the sensitivity analysis is complemented with a sliding contact condition. It will be shown that the topological derivative expression is the same with or without this contact condition. This chapter is fully about topological sensitivity analysis in 3d. Numerical illustrations with a contact model in 3d are given in Chapter 8.

7.1 Setting of the problem

Let Ω be the union of two disjointed parts Ω_A and Ω_B . This union is assumed to be a smooth bounded domain of \mathbb{R}^3 . The boundary of this domain is made of two disjointed parts, $\partial\Omega = \Gamma_N \cup \Gamma_D$. Neumann and Dirichlet boundary conditions are respectively imposed on Γ_N and Γ_D . Both parts Ω_A and Ω_B have a Dirichlet boundary to insure the problem is well-defined if necessary.

Remark 62. *A single Dirichlet boundary on $\partial\Omega_A$ or $\partial\Omega_B$ is required if Ω_A and Ω_B are assembled by a set of connections acting along 6 independent DOFs.*

Let the domain Ω be filled with a linear isotropic elastic material. For a displacement field \mathbf{u} , the strain tensor is defined by $\varepsilon(\mathbf{u}) = \frac{1}{2}(\nabla\mathbf{u} + \nabla^T\mathbf{u})$. The stress tensor is then given by the Hooke's law

$$\mathbf{A}\varepsilon(\mathbf{u}) = \begin{cases} 2\mu_A\varepsilon(\mathbf{u}) + \lambda_A\text{tr}(\varepsilon(\mathbf{u}))\mathbf{I} & \text{in } \Omega_A \\ 2\mu_B\varepsilon(\mathbf{u}) + \lambda_B\text{tr}(\varepsilon(\mathbf{u}))\mathbf{I} & \text{in } \Omega_B \end{cases},$$

where μ_A and λ_A (resp. μ_B and λ_B) are the Lamé coefficients of the material Ω_A (resp. Ω_B). We assume a perfect interface between Ω_A and Ω_B . Thus, there are usual transmission conditions between both parts that insure continuity of displacements and normal stress at the interface.

Remark 63. *In the sequel, this transmission condition is used only for the elasticity problem without contact condition in Section 7.2. It will be replaced by a sliding contact condition in Section 7.3.*

The goal of this chapter is to compute the topological derivative with respect to two small inclusions linked by a 1 DOF spring subjected to a prestressed state. The inclusions are elastic spheres of the same material as the parts. The topological expansion takes only into account the leading term of the rigidity matrix of the spring with regards to the size of the inclusions. The other terms of the matrix would be remainder terms of the sensitivity analysis. This leading rigidity is the stiffness along the axis of the spring, that is to say its tension-compression behavior.

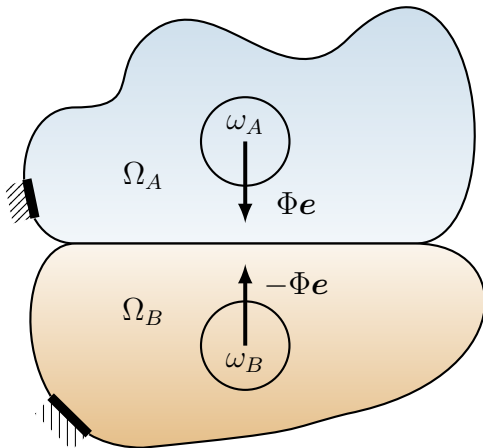


Figure 7.1: Step 1

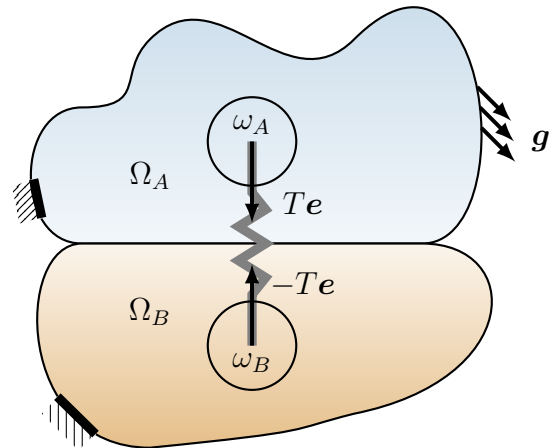


Figure 7.2: Step 2

The pre-stressed or pre-tensioned state comes from the tightening of the bolt. For simplicity, this is performed in the absence of external loads on the system. It consists in applying compressively a pre-tension force of amplitude $\Phi(\rho)$ on the pair of elastic spheres (see Fig. 7.1). This force corresponds to the compression of the tightened parts. The first step is described by a displacement field \mathbf{u}_{S1} . The second step consists in adding external in-service loads and the 1 DOF bolt root on this tightened system (see Fig. 7.2). We denote by $T(\rho)$ the amplitude of the resulting force acting compressively between both spheres ω_A and ω_B . That second step is described by a displacement field \mathbf{u}_{S2} that depends on the displacement field \mathbf{u}_{S1} of the first step. Notations of displacement fields and adjoint states of both steps are defined in Tables 7.1 and 7.2.

	Step 1	Step 2
Background solution	\mathbf{u}_1	\mathbf{u}_2
Perturbed solution	$\mathbf{u}_{\rho,1}$	$\mathbf{u}_{\rho,2}$
Perturbation field	$\mathbf{v}_{\rho,1}$	$\mathbf{v}_{\rho,2}$
Far field centered on ω_A	$\mathbf{v}_{a,1}$	$\mathbf{v}_{a,2}$
Far field centered on ω_B	$\mathbf{v}_{b,1}$	$\mathbf{v}_{b,2}$
Error term	$\boldsymbol{\delta}_1$	$\boldsymbol{\delta}_2$

Table 7.1: Displacement fields

	Step 1	Step 2
Background solution	-	\mathbf{p}_2
Perturbed solution	-	$\mathbf{p}_{\rho,2}$
Perturbation field	-	$\mathbf{q}_{\rho,2}$
Far field centered on ω_A	-	$\mathbf{q}_{a,2}$
Far field centered on ω_B	-	$\mathbf{q}_{b,2}$
Error term	-	$\boldsymbol{\eta}_2$

Table 7.2: Adjoint states

The background domain refers to the system in which one wants to add a small idealized bolt connection. This domain may already contain n pre-stressed idealized bolts of finite size as exposed in Chapter 2. For the sake of simplicity, these pre-existing bolts work according to 1 DOF, that is to say tension-compression behavior. Then, the constitutive behavior of the n pre-existing bolts are modeled by the function \mathcal{S} for a displacement field \mathbf{w} that reads

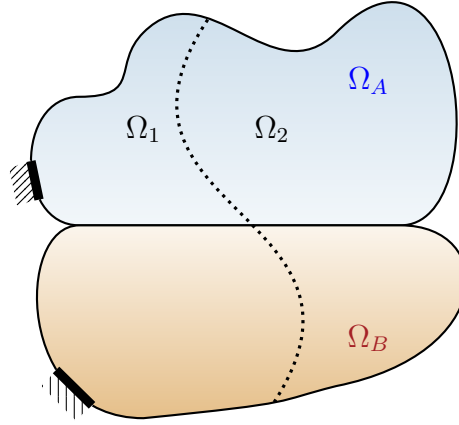
$$\mathcal{S}(\mathbf{w}) = \sum_{i=1}^n \kappa_i \left(\int_{\omega_{B_i}} \mathbf{w} \cdot \mathbf{e}_i dV - \int_{\omega_{A_i}} \mathbf{w} \cdot \mathbf{e}_i dV \right) \left(\frac{\mathbb{1}_{\omega_{B_i}}}{|\omega_{B_i}|} - \frac{\mathbb{1}_{\omega_{A_i}}}{|\omega_{A_i}|} \right) \mathbf{e}_i, \quad (7.1)$$

where κ_i and \mathbf{e}_i are respectively the tension-compression rigidity and the axis of the 1 DOF bolt i . Each pre-existing bolts are subjected to a prestressed state. The apparent force resulting for that prestress reads

$$\mathbf{t} = \sum_{i=1}^n \left(\kappa_i \left(\int_{\omega_{B_i}} \mathbf{u}_{S1,i} \cdot \mathbf{e}_i dV - \int_{\omega_{A_i}} \mathbf{u}_{S1,i} \cdot \mathbf{e}_i dV \right) - \Phi_i \right) \left(\frac{\mathbb{1}_{\omega_{B_i}}}{|\omega_{B_i}|} - \frac{\mathbb{1}_{\omega_{A_i}}}{|\omega_{A_i}|} \right) \mathbf{e}_i, \quad (7.2)$$

where Φ_i is the pre-tension force and $\mathbf{u}_{S1,i}$ the displacement field resulting from the tightening of the bolt i . The function \mathcal{S} and the apparent force \mathbf{t} are zero if there is no finite idealized bolt in the background domain.

Let Ω_1 and Ω_2 be a partition of Ω , that is $\Omega = \Omega_1 \cup \Omega_2$ and $\Omega_1 \cap \Omega_2 = \emptyset$. To avoid technicalities, loads are applied in Ω_1 and the small idealized bolt is included in Ω_2 (see Fig. 7.3). We propose to perturb the background domain with two small inclusions, ω_A and ω_B of size ρ , linked by a spring of rigidity $\kappa(\rho)$ subjected to a pre-tension force $\Phi(\rho)$. In the sequel,

Figure 7.3: Decomposition of the domain Ω

we choose the reference shape ω to be the unit ball of \mathbb{R}^3 , which allows us to compute explicitly the coefficients of the topological derivative. Let ω_A be a small inclusion of shape ω , rescaled by an adimensional factor $\rho > 0$ and centred at the point $\mathbf{x}_0 \in \Omega_2$. The second inclusion, denoted ω_B , is the translation of ω_A at a distance $\ell > 0$ and in the direction \mathbf{e} , a unit vector. More specifically, the inclusions read

$$\omega_A = \left\{ \mathbf{x} \in \mathbb{R}^3, \frac{\mathbf{x} - \mathbf{x}_0}{\rho} \in \omega \right\} \text{ and } \omega_B = \left\{ \mathbf{x} \in \mathbb{R}^3, \frac{\mathbf{x} - \mathbf{x}_0 - \ell \mathbf{e}}{\rho} \in \omega \right\}. \quad (7.3)$$

In the following, the factor ρ will abusively refer to the size of the inclusions. Let us assume the following scaling of the model

$$\kappa(\rho) = K\rho^k \text{ and } \Phi(\rho) = Q\rho^q, \quad (7.4)$$

with $K > 0, Q > 0, k \in \mathbb{R}$ and $q \in \mathbb{R}$. It will be shown later that only those values $k > 0$ and $q > 0$ are covered by our asymptotic analysis. The idealized bolt is defined by an average approach and a non-local interaction between ω_A and ω_B . Let us recall the notation for the average on ω_A of the projection of the displacement field \mathbf{u} along \mathbf{e} , the axis of the spring,

$$\overline{\mathbf{u} \cdot \mathbf{e}}_{\omega_A} = \frac{1}{|\omega_A|} \int_{\omega_A} \mathbf{u} \cdot \mathbf{e} dV.$$

The lengthening of the spring is the difference between the average displacements in ω_A and ω_B along the axis of the spring. The space of admissible displacements for this study corresponds to zero displacement on Γ_D

$$\mathcal{W} = \{\mathbf{w} \in (H^1(\Omega))^3, \mathbf{w} = \mathbf{0} \text{ on } \Gamma_D\}. \quad (7.5)$$

We define the perforated domain Ω_ρ , *i.e.* the domain Ω without the head and the tread of the idealized bolt

$$\Omega_\rho = \Omega \setminus (\omega_A \cup \omega_B). \quad (7.6)$$

7.1.1 Step 1

Background domain

For simplicity, the first step of pre-tension is done in the absence of external loads. The only solicitation comes from the pretension of existing bolts. The background solution \mathbf{u}_1 then satisfies the linear elasticity system

$$\begin{cases} -\operatorname{div}(\mathbf{A}\varepsilon(\mathbf{u}_1)) + \mathcal{S}(\mathbf{u}_1) = \mathbf{t} & \text{in } \Omega \\ \mathbf{A}\varepsilon(\mathbf{u}_1)\mathbf{n} = \mathbf{0} & \text{on } \Gamma_N. \\ \mathbf{u}_1 = \mathbf{0} & \text{on } \Gamma_D \end{cases} \quad (7.7)$$

We assume that \mathbf{u}_1 is smooth enough, which is always possible by assuming that the loads and the domain are smooth. In the absence of any tightened existing bolts, the displacement field \mathbf{u}_1 is zero. We recall that the transmission condition between Ω_A and Ω_B insures the continuity of displacements and normal stress.

Perturbed domain

The background domain (7.7) is perturbed by two small spheres solicited by a pre-tension force $\Phi(\rho)$. The displacement field in the perturbed domain $\mathbf{u}_{\rho,1}$ solves

$$\begin{cases} -\operatorname{div}(\mathbf{A}\varepsilon(\mathbf{u}_{\rho,1})) + \mathcal{S}(\mathbf{u}_{\rho,1}) = \mathbf{t} & \text{in } \Omega_\rho \\ -\operatorname{div}(\mathbf{A}\varepsilon(\mathbf{u}_{\rho,1})) = \frac{\Phi(\rho)}{|\omega_A|}\mathbf{e} & \text{in } \omega_A \\ -\operatorname{div}(\mathbf{A}\varepsilon(\mathbf{u}_{\rho,1})) = -\frac{\Phi(\rho)}{|\omega_B|}\mathbf{e} & \text{in } \omega_B \\ \mathbf{A}\varepsilon(\mathbf{u}_{\rho,1})\mathbf{n} = \mathbf{0} & \text{on } \Gamma_N \\ \mathbf{u}_{\rho,1} = \mathbf{0} & \text{on } \Gamma_D \end{cases} \quad (7.8)$$

We assume that $\mathbf{u}_{\rho,1}$ is as smooth as required, similarly to the assumptions on \mathbf{u}_1 .

7.1.2 Step 2

Background domain

External loads are applied in the second step. The background solution \mathbf{u}_2 solves

$$\begin{cases} -\operatorname{div}(\mathbf{A}\varepsilon(\mathbf{u}_2)) + \mathcal{S}(\mathbf{u}_2) = \mathbf{t} & \text{in } \Omega \\ \mathbf{A}\varepsilon(\mathbf{u}_2)\mathbf{n} = \mathbf{g} & \text{on } \Gamma_N. \\ \mathbf{u}_2 = \mathbf{0} & \text{on } \Gamma_D \end{cases} \quad (7.9)$$

Assuming that surface loads \mathbf{g} belong to $L^2(\Gamma_N)^3$, Lax-Milgram theorem, coupled with Korn's inequality, gives the existence and the uniqueness of the solution $\mathbf{u}_2 \in \mathcal{W}$. In the following, we assume that \mathbf{u}_2 is as smooth as we want, which is always possible by assuming that the loads \mathbf{g} and \mathbf{t} are smooth as well as the domain. We recall that the transmission condition between Ω_A and Ω_B insures the continuity of displacements and normal stress.

The objective function is evaluated away from the influence area of the perturbations and reads

$$J_0(\Omega) = \int_{\Omega_1} F(\mathbf{u}_2)dV + \int_{\Gamma_N} G(\mathbf{u}_2)dS. \quad (7.10)$$

The functions F and G are smooth, twice differentiable and satisfy conditions

$$\exists \alpha > 0, \begin{cases} |F(\mathbf{u})| \leq \alpha(|\mathbf{u}|^2 + 1), & |F'(\mathbf{u})| \leq \alpha(|\mathbf{u}| + 1), & |F''(\mathbf{u})| \leq \alpha \\ |G(\mathbf{u})| \leq \alpha(|\mathbf{u}|^2 + 1), & |G'(\mathbf{u})| \leq \alpha(|\mathbf{u}| + 1), & |G''(\mathbf{u})| \leq \alpha \end{cases}. \quad (7.11)$$

The adjoint state \mathbf{p}_2 associated to (7.9) for a generic objective function (7.10) solves

$$\begin{cases} -\operatorname{div}(\mathbf{A}\varepsilon(\mathbf{p}_2)) + \mathcal{S}(\mathbf{p}_2) = -\mathbf{F}'(\mathbf{u}_2)\mathbf{1}_{\Omega_1} & \text{in } \Omega \\ \mathbf{A}\varepsilon(\mathbf{p}_2)\mathbf{n} = -\mathbf{G}'(\mathbf{u}_2) & \text{on } \Gamma_N. \\ \mathbf{p}_2 = \mathbf{0} & \text{on } \Gamma_D \end{cases} \quad (7.12)$$

Lax-Milgram theorem, coupled with Korn's inequality, gives the existence and the uniqueness of the solution $\mathbf{p}_2 \in \mathcal{W}$. We assume that \mathbf{p}_2 is as smooth as required, similarly to the assumptions on \mathbf{u}_2 .

Remark 64. *The tightening \mathbf{t} of existing bolts is applied like an external load. Therefore, the adjoint state does not explicitly depend on the pre-stressed state of existing bolts. Nevertheless, it implicitly depends on this tightening through \mathbf{u}_2 .*

Perturbed domain

The background domain (7.9) is perturbed by two small elastic spheres linked by a fixed-length 1 DOF spring of rigidity $\kappa(\rho)$ subjected to an apparent force $T(\rho)$ that depends on $\kappa(\rho)$, $\Phi(\rho)$ and $\mathbf{u}_{\rho,1}$. We keep the previous form of the rigidity and the pre-tension force, respectively $\kappa(\rho) = K\rho^k$ and $\Phi(\rho) = Q\rho^q$ with $K > 0$ and $Q > 0$. The displacement field $\mathbf{u}_{\rho,2}$ verifies

$$\begin{cases} -\operatorname{div}(\mathbf{A}\varepsilon(\mathbf{u}_{\rho,2})) + \mathcal{S}(\mathbf{u}_{\rho,2}) = \mathbf{t} & \text{in } \Omega_\rho \\ -\operatorname{div}(\mathbf{A}\varepsilon(\mathbf{u}_{\rho,2})) - \frac{\kappa(\rho)}{|\omega_A|} \left(\int_{\omega_B} \mathbf{u}_{\rho,2} \cdot \mathbf{e} dV - \int_{\omega_A} \mathbf{u}_{\rho,2} \cdot \mathbf{e} dV \right) \mathbf{e} = \frac{T(\rho)}{|\omega_A|} \mathbf{e} & \text{in } \omega_A \\ -\operatorname{div}(\mathbf{A}\varepsilon(\mathbf{u}_{\rho,2})) + \frac{\kappa(\rho)}{|\omega_B|} \left(\int_{\omega_B} \mathbf{u}_{\rho,2} \cdot \mathbf{e} dV - \int_{\omega_A} \mathbf{u}_{\rho,2} \cdot \mathbf{e} dV \right) \mathbf{e} = -\frac{T(\rho)}{|\omega_B|} \mathbf{e} & \text{in } \omega_B \\ \mathbf{A}\varepsilon(\mathbf{u}_{\rho,2})\mathbf{n} = \mathbf{g} & \text{on } \Gamma_N \\ \mathbf{u}_{\rho,2} = \mathbf{0} & \text{on } \Gamma_D \end{cases}. \quad (7.13)$$

The force $T(\rho)$ depends on the rigidity of the spring $K(\rho)$, on $\mathbf{u}_{\rho,1}$, the perturbed displacement of Step 1 and also on the pre-tension $\Phi(\rho)$. It reads

$$T(\rho) = -\kappa(\rho) \left(\int_{\omega_B} \mathbf{u}_{\rho,1} \cdot \mathbf{e} dV - \int_{\omega_A} \mathbf{u}_{\rho,1} \cdot \mathbf{e} dV \right) + \Phi(\rho). \quad (7.14)$$

In the sequel, we assume that the loads and the domain are smooth, so that $\mathbf{u}_{\rho,2}$ is as smooth as we want. Denote J_ρ the generic objective function (7.10) evaluated in the perturbed domain

$$J_\rho(\Omega) = \int_{\Omega_1} F(\mathbf{u}_{\rho,2}) dV + \int_{\Gamma_N} G(\mathbf{u}_{\rho,2}) dS. \quad (7.15)$$

Definition 8. *The objective function J_ρ is said to admit a topological derivative $DJ(\mathbf{x}_0, \mathbf{e})$ at the point \mathbf{x}_0 for a bolt of direction \mathbf{e} and for a pair of inclusions of shape ω , if the following asymptotic expansion holds for small $\rho > 0$*

$$J_\rho(\Omega) = J_0(\Omega) + s(\rho)DJ(\mathbf{x}_0, \mathbf{e}) + o(s(\rho)), \quad (7.16)$$

where $s(\rho)$ is a positive scalar function of ρ which satisfies $\lim_{\rho \rightarrow 0} s(\rho) = 0$.

Theorem 6. *Take ω to be the unit ball of \mathbb{R}^3 . Let us set*

$$\begin{aligned} \mathbf{U}_1 &= \mathbf{u}_1(\mathbf{x}_0 + \ell \mathbf{e}) - \mathbf{u}_1(\mathbf{x}_0), \\ \mathbf{U}_2 &= \mathbf{u}_2(\mathbf{x}_0 + \ell \mathbf{e}) - \mathbf{u}_2(\mathbf{x}_0), \\ \mathbf{P}_2 &= \mathbf{p}_2(\mathbf{x}_0 + \ell \mathbf{e}) - \mathbf{p}_2(\mathbf{x}_0), \end{aligned} \quad (7.17)$$

where \mathbf{u}_1 , \mathbf{u}_2 and \mathbf{p}_2 are respectively solution of the background problems (7.7), (7.9) and the adjoint problem in the background domain (7.12). The general objective function (7.15) admits a topological asymptotic expansion of the form (7.16), for various values of k and q with

$$\tau_A = \frac{15 \mu_A (2\mu_A + \lambda_A)}{2 (5\mu_A + 2\lambda_A) r_1^2}, \quad \tau_B = \frac{15 \mu_B (2\mu_B + \lambda_B)}{2 (5\mu_B + 2\lambda_B) r_1^2} \quad \text{and } r_1 = 1 \text{ the radius of the unit ball, that is}$$

$$J_\rho(\Omega) = J_0(\Omega) + s(\rho)DJ(\mathbf{x}_0, \mathbf{e}) + \mathcal{R}(s(\rho)). \quad (7.18)$$

The expressions of $s(\rho)$, $DJ(\mathbf{x}_0, \mathbf{e})$ and $\mathcal{R}(s(\rho))$ are given as follows

- For $k > 1$ and $q > 1$

If $k > q$

$$s(\rho) = \rho^q, \quad (7.19)$$

$$DJ(\mathbf{x}_0, \mathbf{e}) = Q\mathbf{P}_2 \cdot \mathbf{e}, \quad (7.20)$$

$$\mathcal{R}(s(\rho)) = O(\rho^{q+2}) + O(\rho^{q+k/2}) + O(\rho^{2q}) + O(\rho^k), \quad (7.21)$$

If $k = q$

$$s(\rho) = \rho^k, \quad (7.22)$$

$$DJ(\mathbf{x}_0, \mathbf{e}) = K(\mathbf{U}_2 - \mathbf{U}_1) \cdot \mathbf{e}\mathbf{P}_2 \cdot \mathbf{e} + Q\mathbf{P}_2 \cdot \mathbf{e}, \quad (7.23)$$

$$\mathcal{R}(s(\rho)) = O(\rho^{k+2}) + O(\rho^{3k/2}) + O(\rho^{2k-1}), \quad (7.24)$$

If $k < q$

$$s(\rho) = \rho^k, \quad (7.25)$$

$$DJ(\mathbf{x}_0, \mathbf{e}) = K(\mathbf{U}_2 - \mathbf{U}_1) \cdot \mathbf{e}\mathbf{P}_2 \cdot \mathbf{e}, \quad (7.26)$$

$$\mathcal{R}(s(\rho)) = O(\rho^{k+2}) + O(\rho^{3k/2}) + O(\rho^{2k-1}) + O(\rho^q), \quad (7.27)$$

- For $k > 1$ and $q = 1$

$$s(\rho) = \rho, \quad (7.28)$$

$$DJ(\mathbf{x}_0, \mathbf{e}) = Q\mathbf{P}_2 \cdot \mathbf{e}, \quad (7.29)$$

$$\mathcal{R}(s(\rho)) = O(\rho^2) + O(\rho^k), \quad (7.30)$$

- For $k > 1$ and $0 < q < 1$

$$s(\rho) = \rho^q, \quad (7.31)$$

$$DJ(\mathbf{x}_0, \mathbf{e}) = Q\mathbf{P}_2 \cdot \mathbf{e}, \quad (7.32)$$

$$\mathcal{R}(s(\rho)) = O(\rho^{q+2}) + O(\rho^{q+k/2}) + O(\rho^k), \quad (7.33)$$

- For $k = 1$ and $q > 1$

$$s(\rho) = \rho, \quad (7.34)$$

$$DJ(\mathbf{x}_0, \mathbf{e}) = \left(\frac{1}{K} + \frac{1}{|\omega|} \left(\frac{1}{\tau_A} + \frac{1}{\tau_B} \right) \right)^{-1} (\mathbf{U}_2 - \mathbf{U}_1) \cdot \mathbf{e}\mathbf{P}_2 \cdot \mathbf{e}, \quad (7.35)$$

$$\mathcal{R}(s(\rho)) = O(\rho^{3/2}) + O(\rho^q), \quad (7.36)$$

- For $k = 1$ and $q = 1$

$$s(\rho) = \rho, \quad (7.37)$$

$$DJ(\mathbf{x}_0, \mathbf{e}) = \left(\frac{1}{K} + \frac{1}{|\omega|} \left(\frac{1}{\tau_A} + \frac{1}{\tau_B} \right) \right) (\mathbf{U}_2 - \mathbf{U}_1) \cdot \mathbf{e}\mathbf{P}_2 \cdot \mathbf{e}, \quad (7.38)$$

$$\mathcal{R}(s(\rho)) = O(\rho^{3/2}), \quad (7.39)$$

- For $k = 1$ and $0 < q < 1$

$$s(\rho) = \rho^q, \quad (7.40)$$

$$DJ(\mathbf{x}_0, \mathbf{e}) = Q\mathbf{P}_2 \cdot \mathbf{e}, \quad (7.41)$$

$$\mathcal{R}(s(\rho)) = O(\rho) + O(\rho^{2q}), \quad (7.42)$$

- For $0 < k < 1$ and $q > 1$

$$s(\rho) = \rho, \quad (7.43)$$

$$DJ(\mathbf{x}_0, \mathbf{e}) = \left(\frac{1}{|\omega|} \left(\frac{1}{\tau_A} + \frac{1}{\tau_B} \right) \right)^{-1} (\mathbf{U}_2 - \mathbf{U}_1) \cdot \mathbf{e}\mathbf{P}_2 \cdot \mathbf{e}, \quad (7.44)$$

$$\mathcal{R}(s(\rho)) = O(\rho^{2-k}) + O(\rho^q) + O(\rho^{1+k/2}), \quad (7.45)$$

- For $0 < k < 1$ and $q = 1$

$$s(\rho) = \rho, \quad (7.46)$$

$$DJ(\mathbf{x}_0, \mathbf{e}) = \left(\frac{1}{|\omega|} \left(\frac{1}{\tau_A} + \frac{1}{\tau_B} \right) \right) (\mathbf{U}_2 - \mathbf{U}_1) \cdot \mathbf{e}\mathbf{P}_2 \cdot \mathbf{e} + Q\mathbf{P}_2 \cdot \mathbf{e}, \quad (7.47)$$

$$\mathcal{R}(s(\rho)) = O(\rho^{1+k/2}), \quad (7.48)$$

- For $0 < k < 1$ and $0 < q < 1$

$$s(\rho) = \rho^q, \quad (7.49)$$

$$DJ(\mathbf{x}_0, \mathbf{e}) = Q\mathbf{P}_2 \cdot \mathbf{e}, \quad (7.50)$$

$$\mathcal{R}(s(\rho)) = O(\rho) + O(\rho^{q+k/2}) + O(\rho^{2q}). \quad (7.51)$$

Remark 65. The remainder term $\mathcal{R}(s(\rho))$ shall be simplified according to only one predominance of ρ . However, it implies plenty of cases between k and q . Thus, it is not done here to keep some lightness.

7.2 Computation of the topological derivative without contact

This section investigates the sensitivity analysis with regards to a pre-stressed small idealized bolt connection without a contact model. It will be shown in next section that the contact term is a remainder term for the topological expansion. The spring is mostly handled the same manner as in Chapter 5.

7.2.1 Step 1

Approximation of the perturbed displacement field

The topological derivative is computed at the end of the in-service state (Step 2). It depends on the displacement field of Step 1. Then, the perturbed field $\mathbf{u}_{\rho,1}$ is approximated for that purpose.

- **Far fields expression**

Similarly to the inclusions linked by a simple spring, the perturbed field $\mathbf{u}_{\rho,1}$ is expected to be approximately equal to the corresponding background field \mathbf{u}_1 plus the influence fields of each inclusions ω_A and ω_B , respectively denoted $\mathbf{v}_{a,1}$ and $\mathbf{v}_{b,1}$. That is to set

$$\mathbf{u}_{\rho,1}(\mathbf{x}) \approx \mathbf{u}_1(\mathbf{x}) + \mathbf{v}_{a,1}\left(\frac{\mathbf{x} - \mathbf{x}_0}{\rho}\right) + \mathbf{v}_{b,1}\left(\frac{\mathbf{x} - \mathbf{x}_0 - \ell\mathbf{e}}{\rho}\right). \quad (7.52)$$

The functions $\mathbf{v}_{a,1}$ and $\mathbf{v}_{b,1}$, defined in \mathbb{R}^3 , have to decay at infinity like $\lim_{\mathbf{y} \rightarrow \mathbf{0}} \mathbf{v}_{a,1}(\mathbf{y}) = \mathbf{0}$ and $\lim_{\mathbf{y} \rightarrow \mathbf{0}} \mathbf{v}_{b,1}(\mathbf{y}) = \mathbf{0}$ since perturbations are getting smaller far from the inclusions. The problem is rescaled with inclusions of unit size ω , so that $\mathbf{v}_{a,1}$ and $\mathbf{v}_{b,1}$ respectively solve

$$\begin{cases} -\operatorname{div}(\mathbf{A}\varepsilon(\mathbf{v}_{a,1})(\mathbf{y}_a)) = \mathbf{0} & \text{in } \mathbb{R}^3 \setminus \omega \\ -\operatorname{div}(\mathbf{A}\varepsilon(\mathbf{v}_{a,1})(\mathbf{y}_a)) = \xi_{u_1}(\rho)\mathbf{e} & \text{in } \omega \\ \lim_{\mathbf{y}_a \rightarrow \mathbf{0}} \mathbf{v}_{a,1}(\mathbf{y}_a) = \mathbf{0} \end{cases} \quad \text{and} \quad \begin{cases} -\operatorname{div}(\mathbf{A}\varepsilon(\mathbf{v}_{b,1})(\mathbf{y}_b)) = \mathbf{0} & \text{in } \mathbb{R}^3 \setminus \omega \\ -\operatorname{div}(\mathbf{A}\varepsilon(\mathbf{v}_{b,1})(\mathbf{y}_b)) = -\xi_{u_1}(\rho)\mathbf{e} & \text{in } \omega \\ \lim_{\mathbf{y}_b \rightarrow \mathbf{0}} \mathbf{v}_{b,1}(\mathbf{y}_b) = \mathbf{0} \end{cases}, \quad (7.53)$$

where $\mathbf{y}_a = \frac{\mathbf{x} - \mathbf{x}_0}{\rho}$, $\mathbf{y}_b = \frac{\mathbf{x} - \mathbf{x}_0 - \ell\mathbf{e}}{\rho}$ and $\xi_{u_1}(\rho) = \frac{\Phi(\rho)}{\rho|\omega|}$.

Remark 66. *Systems (7.53) respectively describe the zoom at zero-order on ω_A and ω_B . Existing pre-stressed bolts modeled by the functions \mathbf{S} and \mathbf{t} are far from the inclusions. They are ignored by the zoom at zero-order on ω_A and ω_B .*

Lemma 9. *The functions $\mathbf{v}_{a,1}$ and $\mathbf{v}_{b,1}$ are explicitly given by*

$$\mathbf{v}_{a,1}(\mathbf{y}) = \begin{cases} \frac{r_1^3(5r^2 - 3r_1^2)(\mu_A + \lambda_A)}{30r^5\mu_A(2\mu_A + \lambda_A)}\xi_{u_1}(\rho)\mathbf{e} \cdot \mathbf{y}\mathbf{y} + \frac{r_1^3((15\mu_A + 5\lambda_A)r^2 + (\mu_A + \lambda_A)r_1^2)}{30r^3\mu_A(2\mu_A + \lambda_A)}\xi_{u_1}(\rho)\mathbf{e} & \text{in } \mathbb{R}^3 \setminus \omega \\ \frac{\mu_A + \lambda_A}{15\mu_A(2\mu_A + \lambda_A)}\xi_{u_1}(\rho)\mathbf{e} \cdot \mathbf{y}\mathbf{y} - \frac{(9\mu_A + 4\lambda_A)r^2 - (25\mu_A + 10\lambda_A)r_1^2}{30\mu_A(2\mu_A + \lambda_A)}\xi_{u_1}(\rho)\mathbf{e} & \text{in } \omega \end{cases}, \quad (7.54)$$

$$\mathbf{v}_{b,1}(\mathbf{y}) = \begin{cases} -\frac{r_1^3(5r^2 - 3r_1^2)(\mu_B + \lambda_B)}{30r^5\mu_B(2\mu_B + \lambda_B)}\xi_{u_1}(\rho)\mathbf{e} \cdot \mathbf{y}\mathbf{y} - \frac{r_1^3((15\mu_B + 5\lambda_B)r^2 + (\mu_B + \lambda_B)r_1^2)}{30r^3\mu_B(2\mu_B + \lambda_B)}\xi_{u_1}(\rho)\mathbf{e} & \text{in } \mathbb{R}^3 \setminus \omega \\ -\frac{\mu_B + \lambda_B}{15\mu_B(2\mu_B + \lambda_B)}\xi_{u_1}(\rho)\mathbf{e} \cdot \mathbf{y}\mathbf{y} + \frac{(9\mu_B + 4\lambda_B)r^2 - (25\mu_B + 10\lambda_B)r_1^2}{30\mu_B(2\mu_B + \lambda_B)}\xi_{u_1}(\rho)\mathbf{e} & \text{in } \omega \end{cases}, \quad (7.55)$$

where $r = \|\mathbf{y}\|$ and

$$\xi_{u_1}(\rho) = \frac{\Phi(\rho)}{\rho|\omega|}. \quad (7.56)$$

Proof. The proof is the same as the one of Lemma 7 in Chapter 5. The average on ω of the far fields are likewise computed and it comes

$$\begin{aligned} \int_{\omega} \mathbf{v}_{a,1} \cdot \mathbf{e} dV &= \frac{\xi_{u_1}(\rho)}{\tau_A} \text{ with } \tau_A = \frac{15 \mu_A (2\mu_A + \lambda_A)}{2 (5\mu_A + 2\lambda_A) r_1^2}, \\ \int_{\omega} \mathbf{v}_{b,1} \cdot \mathbf{e} dV &= -\frac{\xi_{u_1}(\rho)}{\tau_B} \text{ with } \tau_B = \frac{15 \mu_B (2\mu_B + \lambda_B)}{2 (5\mu_B + 2\lambda_B) r_1^2}. \end{aligned}$$

□

- **Asymptotic analysis of the perturbed displacement**

Let $\mathbf{v}_{\rho,1} = \mathbf{u}_{\rho,1} - \mathbf{u}_1$ be the difference between the perturbed and the background displacement fields of Step 1. It solves

$$\left\{ \begin{array}{ll} -\operatorname{div}(\mathbf{A}\varepsilon(\mathbf{v}_{\rho,1})) + \mathcal{S}(\mathbf{v}_{\rho,1}) = \mathbf{0} & \text{in } \Omega_{\rho} \\ -\operatorname{div}(\mathbf{A}\varepsilon(\mathbf{v}_{\rho,1})) = \frac{\Phi(\rho)}{|\omega_A|} \mathbf{e} & \text{in } \omega_A \\ -\operatorname{div}(\mathbf{A}\varepsilon(\mathbf{v}_{\rho,1})) = -\frac{\Phi(\rho)}{|\omega_B|} \mathbf{e} & \text{in } \omega_B \\ \mathbf{A}\varepsilon(\mathbf{v}_{\rho,1})\mathbf{n} = \mathbf{0} & \text{on } \Gamma_N \\ \mathbf{v}_{\rho,1} = \mathbf{0} & \text{on } \Gamma_D \end{array} \right. \quad (7.57)$$

We introduce the function

$$\mathbf{v}_1(\mathbf{x}) = \mathbf{v}_{a,1} \left(\frac{\mathbf{x} - \mathbf{x}_0}{\rho} \right) + \mathbf{v}_{b,1} \left(\frac{\mathbf{x} - \mathbf{x}_0 - \ell \mathbf{e}}{\rho} \right), \quad (7.58)$$

where $\mathbf{v}_{a,1}$ and $\mathbf{v}_{b,1}$ solve (7.53) and thus verify Lemma 9. The proposition below proves that \mathbf{v}_1 is the limit, in some sense, of $\mathbf{v}_{\rho,1}$ as ρ goes to zero.

Proposition 15. *Let $\theta \in \mathcal{C}_c^\infty(\Omega)$ be a cut-off function with compact support $\mathcal{U}_+ \subset \Omega$ such that $\theta \equiv 1$ in a neighborhood $\mathcal{U}_- \subset \mathcal{U}_+$ of \mathbf{x}_0 and $\mathbf{x}_0 + \ell \mathbf{e}$. There exists a constant $C > 0$ independent of ρ such that*

$$\mathbf{v}_{\rho,1} = \theta \mathbf{v}_1 + \boldsymbol{\delta}_1, \quad (7.59)$$

with

$$\|\mathbf{v}_1\|_{L^2(\Omega)} \leq C\rho^q, \quad (7.60)$$

$$\|\varepsilon(\mathbf{v}_1)\|_{L^2(\Omega)} \leq C\rho^{q-1/2}, \quad (7.61)$$

$$\|\boldsymbol{\delta}\|_{H^1(\Omega)} \leq C\rho^q. \quad (7.62)$$

Proof. The explicit expression of $\mathbf{v}_{a,1}$ indicates at infinity that $|\mathbf{v}_{a,1}| = O\left(\frac{|\xi_{u_1}(\rho)|}{r}\right)$ and $|\varepsilon(\mathbf{v}_{a,1})| = O\left(\frac{|\xi_{u_1}(\rho)|}{r^2}\right)$. It leads by rescaling to $\|\mathbf{v}_1\|_{L^\infty(\Omega \setminus \mathcal{U}_-)} \leq C\rho|\xi_{u_1}(\rho)|$ and also $\|\varepsilon(\mathbf{v}_1)\|_{L^\infty(\Omega \setminus \mathcal{U}_-)} \leq C\rho|\xi_{u_1}(\rho)|$. Denote $\Omega_{\rho^{-1}}$ the translated and rescaled domain centered at the origin and of size $\frac{1}{\rho}|\Omega|$. We have

$$\begin{aligned} \|\mathbf{v}_1\|_{L^2(\Omega)}^2 &\leq C\rho^3 \int_{\Omega_{\rho^{-1}}} |\mathbf{v}_{a,1}|^2 dV + C\rho^3 \int_{\omega} |\mathbf{v}_{a,1}|^2 dV \leq C\rho^3 |\xi_{u_1}(\rho)|^2 \int_{r_1}^{r_1/\rho} dr + C\rho^3 |\xi_{u_1}(\rho)|^2 \int_0^{r_1} r^6 dr \\ &\leq C\rho^2 |\xi_{u_1}(\rho)|^2 + C\rho^3 |\xi_{u_1}(\rho)|^2 \leq C\rho^2 |\xi_{u_1}(\rho)|^2 \\ &\leq C\Phi(\rho)^2 \leq C\rho^{2q}. \end{aligned}$$

Estimates of the L^2 -norm of $\varepsilon(\mathbf{v}_1)$ are obtained by a similar argument

$$\begin{aligned} \|\varepsilon(\mathbf{v}_1)\|_{L^2(\Omega)}^2 &\leq C\rho \int_{\Omega_{\rho^{-1}}} |\varepsilon(\mathbf{v}_{a,1})|^2 dV + C\rho \int_{\omega} |\varepsilon(\mathbf{v}_{a,1})|^2 dV \leq C\rho |\xi_{u_1}(\rho)|^2 \int_{r_1}^{r_1/\rho} \frac{1}{r^2} dr + C\rho |\xi_{u_1}(\rho)|^2 \int_0^{r_1} r^4 dr \\ &\leq C\rho |\xi_{u_1}(\rho)|^2 \leq C \frac{\Phi(\rho)^2}{\rho} \leq C\rho^{2q-1}. \end{aligned}$$

Let us write the equations satisfied by δ_1

$$\begin{cases} -\operatorname{div}(\mathbf{A}\varepsilon(\delta_1)) + \mathcal{S}(\delta_1) = \operatorname{div}(\mathbf{A}(\mathbf{v}_1 \otimes \nabla\theta)^s) + \mathbf{A}\varepsilon(\mathbf{v}_1)\nabla\theta & \text{in } \Omega \\ \mathbf{A}\varepsilon(\delta_1)\mathbf{n} = \mathbf{0} & \text{on } \Gamma_N. \\ \delta_1 = \mathbf{0} & \text{on } \Gamma_D \end{cases} \quad (7.63)$$

Multiply (7.63) by δ_1 and integrate by parts

$$\int_{\Omega} \mathcal{S}(\delta_1) \cdot \delta_1 dV + \int_{\Omega} \mathbf{A}\varepsilon(\delta_1) : \varepsilon(\delta_1) dV = - \int_{\Omega} \mathbf{A}(\mathbf{v}_1 \otimes \nabla\theta)^s : \varepsilon(\delta_1) dV + \int_{\Omega} \mathbf{A}\varepsilon(\mathbf{v}_1)\nabla\theta \cdot \delta_1 dV.$$

The left hand side is bounded from below using the Poincaré-Korn inequality and the fact that the quadratic term $\mathcal{S}(\delta_1) \cdot \delta_1$ is positive

$$\exists C > 0, \left| \int_{\Omega} \mathbf{A}\varepsilon(\delta_1) : \varepsilon(\delta_1) dV \right| \geq C \|\varepsilon(\delta_1)\|_{L^2(\Omega)}^2.$$

The right hand side is bounded using L^∞ -norms of \mathbf{v}_1 and $\varepsilon(\mathbf{v}_1)$ since $\nabla\theta = 0$ in the influence area of the inclusions

$$\begin{aligned} \left| \int_{\Omega} \mathbf{A}(\mathbf{v}_1 \otimes \nabla\theta)^s : \varepsilon(\delta_1) dV \right| + \left| \int_{\Omega} \mathbf{A}\varepsilon(\mathbf{v}_1)\nabla\theta \cdot \delta_1 dV \right| &\leq C \|\mathbf{v}_1\|_{L^\infty(\Omega \setminus \mathcal{U}_-)} \|\varepsilon(\delta_1)\|_{L^2(\Omega)} \\ &\quad + C \|\varepsilon(\mathbf{v}_1)\|_{L^\infty(\Omega \setminus \mathcal{U}_-)} \|\delta_1\|_{L^2(\Omega)} \\ &\leq C\rho |\xi_{u_1}(\rho)| \|\varepsilon(\delta_1)\|_{L^2(\Omega)} \leq C\rho^q \|\varepsilon(\delta_1)\|_{L^2(\Omega)}. \end{aligned}$$

□

7.2.2 Step 2

This section analyses the perturbed displacement field $\mathbf{u}_{\rho,2}$ in presence of the small pre-stressed bolt. It relies on the techniques and tricks developed in Chapter 5 and also on the analysis of the perturbation of Step 1.

Approximation of the perturbed displacement field

- **Far fields expressions**

The displacement field $\mathbf{u}_{\rho,2}$ is approximated using the behavior of the far fields $\mathbf{v}_{a,2}$ and $\mathbf{v}_{b,2}$. It is now usual to set

$$\mathbf{u}_{\rho,2}(\mathbf{x}) \approx \mathbf{u}_2(\mathbf{x}) + \mathbf{v}_{a,2}\left(\frac{\mathbf{x} - \mathbf{x}_0}{\rho}\right) + \mathbf{v}_{b,2}\left(\frac{\mathbf{x} - \mathbf{x}_0 - \ell\mathbf{e}}{\rho}\right), \quad (7.64)$$

with $\lim_{\mathbf{y} \rightarrow \mathbf{0}} \mathbf{v}_{a,2}(\mathbf{y}) = \mathbf{0}$ and $\lim_{\mathbf{y} \rightarrow \mathbf{0}} \mathbf{v}_{b,2}(\mathbf{y}) = \mathbf{0}$. The problem is rescaled with inclusions of unit size ω . The functions $\mathbf{v}_{a,2}$ and $\mathbf{v}_{b,2}$ are then coupled and they respectively solve

$$\begin{cases} -\operatorname{div}(\mathbf{A}\varepsilon(\mathbf{v}_{a,2})(\mathbf{y}_a)) = \mathbf{0} & \text{in } \mathbb{R}^3 \setminus \omega \\ -\operatorname{div}(\mathbf{A}\varepsilon(\mathbf{v}_{a,2})(\mathbf{y}_a)) = \xi_{u_2}(\rho)\mathbf{e} & \text{in } \omega \\ \lim_{\mathbf{y}_a \rightarrow \mathbf{0}} \mathbf{v}_{a,2}(\mathbf{y}_a) = \mathbf{0} \end{cases} \quad \text{and} \quad \begin{cases} -\operatorname{div}(\mathbf{A}\varepsilon(\mathbf{v}_{b,2})(\mathbf{y}_b)) = \mathbf{0} & \text{in } \mathbb{R}^3 \setminus \omega \\ -\operatorname{div}(\mathbf{A}\varepsilon(\mathbf{v}_{b,2})(\mathbf{y}_b)) = -\xi_{u_2}(\rho)\mathbf{e} & \text{in } \omega \\ \lim_{\mathbf{y}_b \rightarrow \mathbf{0}} \mathbf{v}_{b,2}(\mathbf{y}_b) = \mathbf{0} \end{cases}, \quad (7.65)$$

where $\mathbf{y}_a = \frac{\mathbf{x} - \mathbf{x}_0}{\rho}$, $\mathbf{y}_b = \frac{\mathbf{x} - \mathbf{x}_0 - \ell\mathbf{e}}{\rho}$ and

$$\begin{aligned} \xi_{u_2}(\rho) = & \frac{\kappa(\rho)}{\rho|\omega|} \left(\int_{\omega} (\mathbf{v}_{b,2} - \mathbf{v}_{a,2}) \cdot \mathbf{e} dV + (\mathbf{u}_2(\mathbf{x}_0 + \ell\mathbf{e}) - \mathbf{u}_2(\mathbf{x}_0)) \cdot \mathbf{e} \right) \\ & - \frac{\kappa(\rho)}{\rho|\omega|} \left(\int_{\omega} (\mathbf{v}_{b,1} - \mathbf{v}_{a,1}) \cdot \mathbf{e} dV + (\mathbf{u}_1(\mathbf{x}_0 + \ell\mathbf{e}) - \mathbf{u}_1(\mathbf{x}_0)) \cdot \mathbf{e} \right) + \frac{\Phi(\rho)}{\rho|\omega|}. \end{aligned} \quad (7.66)$$

The two last terms of (7.66) come from a zero-order expansion of the force $T(\rho)$. They are simply obtained by using the ansatz (7.52) for $\mathbf{u}_{\rho,1}$ and the Taylor expansions of the background solution \mathbf{u}_1 in a neighborhood of \mathbf{x}_0 and $\mathbf{x}_0 + \ell\mathbf{e}$.

Remark 67. *At first sight, the coefficient $\xi_{u_2}(\rho)$ does not explicitly depend on \mathbf{u}_2 as presumed by the subscript "u₂". The following lemma proves that $\xi_{u_2}(\rho)$ actually depends on \mathbf{u}_2 thanks to the explicit expressions of $\mathbf{v}_{a,2}$ and $\mathbf{v}_{b,2}$.*

Lemma 10. *The functions $\mathbf{v}_{a,2}$ and $\mathbf{v}_{b,2}$ are explicitly given by*

$$\mathbf{v}_{a,2}(\mathbf{y}) = \begin{cases} \frac{r_1^3(5r^2 - 3r_1^2)(\mu_A + \lambda_A)}{30r^5\mu_A(2\mu_A + \lambda_A)} \xi_{u_2}(\rho)\mathbf{e} \cdot \mathbf{y}\mathbf{y} + \frac{r_1^3((15\mu_A + 5\lambda_A)r^2 + (\mu_A + \lambda_A)r_1^2)}{30r^3\mu_A(2\mu_A + \lambda_A)} \xi_{u_2}(\rho)\mathbf{e} & \text{in } \mathbb{R}^3 \setminus \omega \\ \frac{\mu_A + \lambda_A}{15\mu_A(2\mu_A + \lambda_A)} \xi_{u_2}(\rho)\mathbf{e} \cdot \mathbf{y}\mathbf{y} - \frac{(9\mu_A + 4\lambda_A)r^2 - (25\mu_A + 10\lambda_A)r_1^2}{30\mu_A(2\mu_A + \lambda_A)} \xi_{u_2}(\rho)\mathbf{e} & \text{in } \omega \end{cases}, \quad (7.67)$$

$$\mathbf{v}_{b,2}(\mathbf{y}) = \begin{cases} -\frac{r_1^3(5r^2 - 3r_1^2)(\mu_B + \lambda_B)}{30r^5\mu_B(2\mu_B + \lambda_B)} \xi_{u_2}(\rho)\mathbf{e} \cdot \mathbf{y}\mathbf{y} - \frac{r_1^3((15\mu_B + 5\lambda_B)r^2 + (\mu_B + \lambda_B)r_1^2)}{30r^3\mu_B(2\mu_B + \lambda_B)} \xi_{u_2}(\rho)\mathbf{e} & \text{in } \mathbb{R}^3 \setminus \omega \\ -\frac{\mu_B + \lambda_B}{15\mu_B(2\mu_B + \lambda_B)} \xi_{u_2}(\rho)\mathbf{e} \cdot \mathbf{y}\mathbf{y} + \frac{(9\mu_B + 4\lambda_B)r^2 - (25\mu_B + 10\lambda_B)r_1^2}{30\mu_B(2\mu_B + \lambda_B)} \xi_{u_2}(\rho)\mathbf{e} & \text{in } \omega \end{cases}, \quad (7.68)$$

where $r = \|\mathbf{y}\|$ and

$$\xi_{u_2}(\rho) = \frac{\frac{\kappa(\rho)}{\rho|\omega|}}{1 + \frac{\kappa(\rho)}{\rho|\omega|} \left(\frac{1}{\tau_A} + \frac{1}{\tau_B} \right)} \left((\mathbf{u}_2(\mathbf{x}_0 + \ell\mathbf{e}) - \mathbf{u}_2(\mathbf{x}_0)) \cdot \mathbf{e} - (\mathbf{u}_1(\mathbf{x}_0 + \ell\mathbf{e}) - \mathbf{u}_1(\mathbf{x}_0)) \cdot \mathbf{e} \right) + \frac{\Phi(\rho)}{\rho|\omega|}. \quad (7.69)$$

Proof. The proof is the same as the one of Lemma 7 in Chapter 5 by substituting $\xi_u(\rho)$ with $\xi_{u_2}(\rho)$. The average on ω of the far fields are likewise computed and it comes

$$\begin{aligned} \int_{\omega} \mathbf{v}_{a,2} \cdot \mathbf{e} dV &= \frac{\xi_{u_2}(\rho)}{\tau_A} \quad \text{with} \quad \tau_A = \frac{15}{2} \frac{\mu_A(2\mu_A + \lambda_A)}{(5\mu_A + 2\lambda_A)r_1^2}, \\ \int_{\omega} \mathbf{v}_{b,2} \cdot \mathbf{e} dV &= -\frac{\xi_{u_2}(\rho)}{\tau_B} \quad \text{with} \quad \tau_B = \frac{15}{2} \frac{\mu_B(2\mu_B + \lambda_B)}{(5\mu_B + 2\lambda_B)r_1^2}. \end{aligned} \quad (7.70)$$

The explicit expression of $\xi_{u_2}(\rho)$ is a combination of (7.66), (7.70) and results of Lemma 9. \square

• Asymptotic analysis of the perturbed displacement

Let $\mathbf{v}_{\rho,2} = \mathbf{u}_{\rho,2} - \mathbf{u}_2$ be the difference between the perturbed and the background displacement fields of Step 2. It solves

$$\left\{ \begin{array}{ll} -\operatorname{div}(\mathbf{A}\varepsilon(\mathbf{v}_{\rho,2})) + \mathcal{S}(\mathbf{v}_{\rho,2}) = \mathbf{0} & \text{in } \Omega_{\rho} \\ -\operatorname{div}(\mathbf{A}\varepsilon(\mathbf{v}_{\rho,2})) - \frac{\kappa(\rho)}{|\omega_A|} \left(\int_{\omega_B} (\mathbf{v}_{\rho,2} + \mathbf{u}_2) \cdot \mathbf{e} dV - \int_{\omega_A} (\mathbf{v}_{\rho,2} + \mathbf{u}_2) \cdot \mathbf{e} dV \right) \mathbf{e} = \frac{T(\rho)}{|\omega_A|} \mathbf{e} & \text{in } \omega_A \\ -\operatorname{div}(\mathbf{A}\varepsilon(\mathbf{v}_{\rho,2})) + \frac{\kappa(\rho)}{|\omega_A|} \left(\int_{\omega_B} (\mathbf{v}_{\rho,2} + \mathbf{u}_2) \cdot \mathbf{e} dV - \int_{\omega_A} (\mathbf{v}_{\rho,2} + \mathbf{u}_2) \cdot \mathbf{e} dV \right) \mathbf{e} = -\frac{T(\rho)}{|\omega_B|} \mathbf{e} & \text{in } \omega_B \\ \mathbf{A}\varepsilon(\mathbf{v}_{\rho,2})\mathbf{n} = \mathbf{0} & \text{on } \Gamma_N \\ \mathbf{v}_{\rho,2} = \mathbf{0} & \text{on } \Gamma_D \end{array} \right. \quad (7.71)$$

The field $\mathbf{v}_{\rho,2}$ is as smooth as $\mathbf{u}_{\rho,2}$ and \mathbf{u}_2 . We introduce the function

$$\mathbf{v}_2(\mathbf{x}) = \mathbf{v}_{a,2} \left(\frac{\mathbf{x} - \mathbf{x}_0}{\rho} \right) + \mathbf{v}_{b,2} \left(\frac{\mathbf{x} - \mathbf{x}_0 - \ell\mathbf{e}}{\rho} \right) \quad (7.72)$$

where $\mathbf{v}_{a,2}$ and $\mathbf{v}_{b,2}$ are solutions of (7.65) and thus verify Lemma 10. The proposition below proves that \mathbf{v}_2 is, in some sense, the limit of $\mathbf{v}_{\rho,2}$ as ρ goes to zero.

Proposition 16. *Let $\theta \in \mathcal{C}_c^\infty(\Omega)$ be a cut-off function with compact support $\mathcal{U}_+ \subset \Omega$ such that $\theta \equiv 1$ in a neighborhood $\mathcal{U}_- \subset \mathcal{U}_+$ of \mathbf{x}_0 and $\mathbf{x}_0 + \ell\mathbf{e}$. We have*

$$\mathbf{v}_{\rho,2} = \theta \mathbf{v}_2 + \boldsymbol{\delta}_2, \quad (7.73)$$

where $\boldsymbol{\delta}_2$ is a small remainder term as can be checked by these estimates of the L^2 -norms of \mathbf{v}_2 and $\varepsilon(\mathbf{v}_2)$ and the H^1 -norm of $\boldsymbol{\delta}_2$. They are given, according to the value of the exponents k and q , by

	$q > 1$		$q = 1$	$1 > q > 0$		$q > 1$		$q = 1$	$1 > q > 1/2$
$k > 1$	$k > q$	$O(\rho^q)$	$O(\rho)$	$O(\rho^q)$	$k > 1$	$k > q$	$O(\rho^{q-1/2})$	$O(\sqrt{\rho})$	$O(\rho^{q-1/2})$
	$k \leq q$	$O(\rho^k)$				$k \leq q$	$O(\rho^{k-1/2})$		
$k = 1$	$O(\rho)$		$O(\rho)$	$O(\rho^q)$	$k = 1$	$O(\sqrt{\rho})$		$O(\sqrt{\rho})$	$O(\rho^{q-1/2})$
$k < 1$	$O(\rho)$		$O(\rho)$	$O(\rho^q)$	$k < 1$	$O(\sqrt{\rho})$		$O(\sqrt{\rho})$	$O(\rho^{q-1/2})$

Estimates of $\|\mathbf{v}_2\|_{L^2(\Omega)}$ and $\|\boldsymbol{\delta}_2\|_{H^1(\Omega)}$ Estimates of $\|\varepsilon(\mathbf{v}_2)\|_{L^2(\Omega)}$

Proof. The explicit expression of $\mathbf{v}_{a,2}$ indicates at infinity that $|\mathbf{v}_{a,2}| = O\left(\frac{|\xi_{u_2}(\rho)|}{r}\right)$ and $|\varepsilon(\mathbf{v}_{a,2})| = O\left(\frac{|\xi_{u_2}(\rho)|}{r^2}\right)$. It leads by rescaling to $\|\mathbf{v}_2\|_{L^\infty(\Omega \setminus \mathcal{U}_-)} \leq C\rho|\xi_{u_2}(\rho)|$ and also to $\|\varepsilon(\mathbf{v}_2)\|_{L^\infty(\Omega \setminus \mathcal{U}_-)} \leq C\rho|\xi_{u_2}(\rho)|$. Quick manipulations, as in the proof of Proposition 15 give

$$\|\mathbf{v}_2\|_{L^2(\Omega)} \leq C\rho|\xi_{u_2}(\rho)| \leq C\frac{\kappa(\rho)}{1 + C\frac{\kappa(\rho)}{\rho}} + C\Phi(\rho) \leq C\frac{\rho^k}{1 + C\rho^{k-1}} + C\rho^q,$$

$$\|\varepsilon(\mathbf{v}_2)\|_{L^2(\Omega)} \leq C\sqrt{\rho}|\xi_{u_2}(\rho)| \leq C\frac{\frac{\kappa(\rho)}{\sqrt{\rho}}}{1 + C\frac{\kappa(\rho)}{\rho}} + C\frac{\Phi(\rho)}{\sqrt{\rho}} \leq C\frac{\rho^{k-1/2}}{1 + C\rho^{k-1}} + C\rho^{q-1/2}.$$

Let us now write the equations satisfied by δ_2

$$\left\{ \begin{array}{l} -\operatorname{div}(\mathbf{A}\varepsilon(\boldsymbol{\delta}_2)) + \mathbf{S}(\boldsymbol{\delta}_2) = \operatorname{div}\mathbf{A}(\mathbf{v}_2 \otimes \nabla\theta)^s + \mathbf{A}\varepsilon(\mathbf{v}_2)\nabla\theta \quad \text{in } \Omega_\rho \\ -\operatorname{div}(\mathbf{A}\varepsilon(\boldsymbol{\delta}_2)) - \frac{\kappa(\rho)}{|\omega_A|} \left(\int_{\omega_B} (\boldsymbol{\delta}_2 - \boldsymbol{\delta}_1) \cdot \mathbf{e} dV - \int_{\omega_A} (\boldsymbol{\delta}_2 - \boldsymbol{\delta}_1) \cdot \mathbf{e} dV \right) \mathbf{e} \\ = \frac{\kappa(\rho)}{|\omega_A|} \left(\int_{\omega_B} \mathbf{u}_2 \cdot \mathbf{e} dV - \int_{\omega_A} \mathbf{u}_2 \cdot \mathbf{e} dV - (\mathbf{u}_2(\mathbf{x}_0 + \ell\mathbf{e}) - \mathbf{u}_2(\mathbf{x}_0)) \cdot \mathbf{e} \right) \mathbf{e} \\ - \frac{\kappa(\rho)}{|\omega_A|} \left(\int_{\omega_B} \mathbf{u}_1 \cdot \mathbf{e} dV - \int_{\omega_A} \mathbf{u}_1 \cdot \mathbf{e} dV - (\mathbf{u}_1(\mathbf{x}_0 + \ell\mathbf{e}) - \mathbf{u}_1(\mathbf{x}_0)) \cdot \mathbf{e} \right) \mathbf{e} \quad \text{in } \omega_A \\ -\operatorname{div}(\mathbf{A}\varepsilon(\boldsymbol{\delta}_2)) + \frac{\kappa(\rho)}{|\omega_B|} \left(\int_{\omega_B} (\boldsymbol{\delta}_2 - \boldsymbol{\delta}_1) \cdot \mathbf{e} dV - \int_{\omega_A} (\boldsymbol{\delta}_2 - \boldsymbol{\delta}_1) \cdot \mathbf{e} dV \right) \mathbf{e} \\ = -\frac{\kappa(\rho)}{|\omega_B|} \left(\int_{\omega_B} \mathbf{u}_2 \cdot \mathbf{e} dV - \int_{\omega_A} \mathbf{u}_2 \cdot \mathbf{e} dV - (\mathbf{u}_2(\mathbf{x}_0 + \ell\mathbf{e}) - \mathbf{u}_2(\mathbf{x}_0)) \cdot \mathbf{e} \right) \mathbf{e} \\ + \frac{\kappa(\rho)}{|\omega_B|} \left(\int_{\omega_B} \mathbf{u}_1 \cdot \mathbf{e} dV - \int_{\omega_A} \mathbf{u}_1 \cdot \mathbf{e} dV - (\mathbf{u}_1(\mathbf{x}_0 + \ell\mathbf{e}) - \mathbf{u}_1(\mathbf{x}_0)) \cdot \mathbf{e} \right) \mathbf{e} \quad \text{in } \omega_B \\ \mathbf{A}\varepsilon(\boldsymbol{\delta}_2)\mathbf{n} = \mathbf{0} \quad \text{on } \Gamma_N \\ \boldsymbol{\delta}_2 = \mathbf{0} \quad \text{on } \Gamma_D \end{array} \right. \quad (7.74)$$

Denote respectively $\mathbf{R}_{u_1}^A$ and $\mathbf{R}_{u_2}^A$ the integral remainder of the Taylor expansions with integral remainder at first order of \mathbf{u}_1 and \mathbf{u}_2 in a neighbourhood of \mathbf{x}_0 . Similar functions, $\mathbf{R}_{u_1}^B$ and

$\mathbf{R}_{u_2}^B$, are set in a neighbourhood of $\mathbf{x}_0 + \ell \mathbf{e}$. All these functions are respectively of the order of ρ^2 in ω_A and ω_B . The equations satisfied by δ_2 are then rewritten

$$\left\{ \begin{array}{ll} -\operatorname{div}(\mathbf{A}\varepsilon(\boldsymbol{\delta}_2)) + \mathcal{S}(\boldsymbol{\delta}_2) = \operatorname{div}\mathbf{A}(\mathbf{v}_2 \otimes \nabla\theta)^s + \mathbf{A}\varepsilon(\mathbf{v}_2)\nabla\theta & \text{in } \Omega_\rho \\ -\operatorname{div}(\mathbf{A}\varepsilon(\boldsymbol{\delta}_2)) - \frac{\kappa(\rho)}{|\omega_A|} \left(\int_{\omega_B} (\boldsymbol{\delta}_2 - \boldsymbol{\delta}_1) \cdot \mathbf{e} dV - \int_{\omega_A} (\boldsymbol{\delta}_2 - \boldsymbol{\delta}_1) \cdot \mathbf{e} dV \right) \mathbf{e} \\ = \frac{\kappa(\rho)}{|\omega_A|} \left(\int_{\omega_B} (\mathbf{R}_{u_2}^B - \mathbf{R}_{u_1}^B) \cdot \mathbf{e} dV - \int_{\omega_A} (\mathbf{R}_{u_2}^A - \mathbf{R}_{u_1}^A) \cdot \mathbf{e} dV \right) \mathbf{e} & \text{in } \omega_A \\ -\operatorname{div}(\mathbf{A}\varepsilon(\boldsymbol{\delta}_2)) + \frac{\kappa(\rho)}{|\omega_B|} \left(\int_{\omega_B} (\boldsymbol{\delta}_2 - \boldsymbol{\delta}_1) \cdot \mathbf{e} dV - \int_{\omega_A} (\boldsymbol{\delta}_2 - \boldsymbol{\delta}_1) \cdot \mathbf{e} dV \right) \mathbf{e} \\ = -\frac{\kappa(\rho)}{|\omega_B|} \left(\int_{\omega_B} (\mathbf{R}_{u_2}^B - \mathbf{R}_{u_1}^B) \cdot \mathbf{e} dV - \int_{\omega_A} (\mathbf{R}_{u_2}^A - \mathbf{R}_{u_1}^A) \cdot \mathbf{e} dV \right) \mathbf{e} & \text{in } \omega_B \\ \mathbf{A}\varepsilon(\boldsymbol{\delta}_2)\mathbf{n} = \mathbf{0} & \text{on } \Gamma_N \\ \boldsymbol{\delta}_2 = \mathbf{0} & \text{on } \Gamma_D \end{array} \right. \quad (7.75)$$

Multiply (7.75) by δ_2 , then integrate by parts and finally add the term $\frac{\kappa(\rho)}{4} \left(\int_{\omega_B} \boldsymbol{\delta}_1 \cdot \mathbf{e} dV - \int_{\omega_A} \boldsymbol{\delta}_1 \cdot \mathbf{e} dV \right)^2$

on the left and right hand sides. It leads to

$$\begin{aligned} & \int_{\Omega} \mathbf{A}\varepsilon(\boldsymbol{\delta}_2) : \varepsilon(\boldsymbol{\delta}_2) dV + \int_{\Omega_\rho} \mathcal{S}(\boldsymbol{\delta}_2) \cdot \boldsymbol{\delta}_2 dV \\ & + \kappa(\rho) \left(\int_{\omega_B} \boldsymbol{\delta}_2 \cdot \mathbf{e} dV - \int_{\omega_A} \boldsymbol{\delta}_2 \cdot \mathbf{e} dV - \frac{1}{2} \left(\int_{\omega_B} \boldsymbol{\delta}_1 \cdot \mathbf{e} dV - \int_{\omega_A} \boldsymbol{\delta}_1 \cdot \mathbf{e} dV \right) \right)^2 \\ & = - \int_{\Omega_\rho} \mathbf{A}(\mathbf{v}_2 \otimes \nabla\theta)^s : \varepsilon(\boldsymbol{\delta}_2) dV + \int_{\Omega_\rho} \mathbf{A}\varepsilon(\mathbf{v}_2)\nabla\theta \cdot \boldsymbol{\delta}_2 dV + \frac{\kappa(\rho)}{4} \left(\int_{\omega_B} \boldsymbol{\delta}_1 \cdot \mathbf{e} dV - \int_{\omega_A} \boldsymbol{\delta}_1 \cdot \mathbf{e} dV \right)^2 \\ & - \kappa(\rho) \left(\int_{\omega_B} (\mathbf{R}_{u_2}^B - \mathbf{R}_{u_1}^B) \cdot \mathbf{e} dV - \int_{\omega_A} (\mathbf{R}_{u_2}^A - \mathbf{R}_{u_1}^A) \cdot \mathbf{e} dV \right) \left(\int_{\omega_B} \boldsymbol{\delta}_2 \cdot \mathbf{e} dV - \int_{\omega_A} \boldsymbol{\delta}_2 \cdot \mathbf{e} dV \right). \end{aligned}$$

The left-hand side is as usual bounded from below with the Poincaré-Korn inequality

$$\exists C > 0, \left| \int_{\Omega} \mathbf{A}\varepsilon(\boldsymbol{\delta}_2) : \varepsilon(\boldsymbol{\delta}_2) dV \right| \geq C \|\varepsilon(\boldsymbol{\delta}_2)\|_{L^2(\Omega)}^2.$$

The first two right-hand terms are estimated as previously

$$\exists C > 0, \left| \int_{\Omega_\rho} \mathbf{A}(\mathbf{v}_2 \otimes \nabla\theta)^s : \varepsilon(\boldsymbol{\delta}_2) dV \right| + \left| \int_{\Omega_\rho} \mathbf{A}\varepsilon(\mathbf{v}_2)\nabla\theta \cdot \boldsymbol{\delta}_2 dV \right| \leq C\rho|\xi_{u_2}(\rho)| \|\varepsilon(\boldsymbol{\delta}_2)\|_{L^2(\Omega)}.$$

The third right-hand term is estimated by multiplying (7.57) by $\boldsymbol{\delta}_1$ and integrating by parts twice,

$$-\Phi(\rho) \left(\int_{\omega_B} \boldsymbol{\delta}_1 \cdot \mathbf{e} dV - \int_{\omega_A} \boldsymbol{\delta}_1 \cdot \mathbf{e} dV \right) = \int_{\Omega_\rho} \operatorname{div} \mathbf{A}(\mathbf{v}_1 \otimes \nabla \theta)^s \cdot \mathbf{v}_{\rho,1} dV + \int_{\Omega_\rho} \mathbf{A} \varepsilon(\mathbf{v}_1) \nabla \theta \cdot \mathbf{v}_{\rho,1} dV.$$

Since $\nabla \theta = 0$ vanishes in \mathcal{U}_- , it comes that

$$\begin{aligned} \Phi(\rho) \left| \int_{\omega_B} \boldsymbol{\delta}_1 \cdot \mathbf{e} dV - \int_{\omega_A} \boldsymbol{\delta}_1 \cdot \mathbf{e} dV \right| &\leq \left| \int_{\Omega_\rho} \operatorname{div} \mathbf{A}(\mathbf{v}_1 \otimes \nabla \theta)^s \cdot \mathbf{v}_{\rho,1} dV \right| + \left| \int_{\Omega_\rho} \mathbf{A} \varepsilon(\mathbf{v}_1) \nabla \theta \cdot \mathbf{v}_{\rho,1} dV \right| \\ &\leq C \|\nabla \mathbf{v}_1\|_{L^\infty(\Omega \setminus \mathcal{U}_-)} \|\mathbf{v}_{\rho,1}\|_{L^2(\Omega)} + C \|\varepsilon(\mathbf{v}_1)\|_{L^\infty(\Omega \setminus \mathcal{U}_-)} \|\mathbf{v}_{\rho,1}\|_{L^2(\Omega)} \\ &\leq C \rho^2 |\xi_{u_1}|^2 \leq C \Phi(\rho)^2. \end{aligned}$$

More particularly, it means that

$$\exists C > 0, \left| \int_{\omega_B} \boldsymbol{\delta}_1 \cdot \mathbf{e} dV - \int_{\omega_A} \boldsymbol{\delta}_1 \cdot \mathbf{e} dV \right| \leq C \Phi(\rho) \leq C \rho^q. \quad (7.76)$$

As noticed with Remark 45, a naive estimate using Poincaré inequality of average terms is too restrictive. We'd rather multiply (7.57) by $\boldsymbol{\delta}_2$ and integrate by parts once

$$\begin{aligned} \Phi(\rho) \left(\int_{\omega_B} \boldsymbol{\delta}_2 \cdot \mathbf{e} dV - \int_{\omega_A} \boldsymbol{\delta}_2 \cdot \mathbf{e} dV \right) &= - \int_{\Omega_\rho} \boldsymbol{\mathcal{S}}(\mathbf{v}_{\rho,1}) \cdot \boldsymbol{\delta}_2 dV - \int_{\Omega} \mathbf{A} \varepsilon(\mathbf{v}_{\rho,1}) : \varepsilon(\boldsymbol{\delta}_2) dV \\ &= - \sum_{i=1}^n \kappa_i \left(\int_{\omega_{B_i}} \boldsymbol{\delta}_1 \cdot \mathbf{e} dV - \int_{\omega_{A_i}} \boldsymbol{\delta}_1 \cdot \mathbf{e} dV \right) \left(\int_{\omega_{B_i}} \boldsymbol{\delta}_2 \cdot \mathbf{e} dV - \int_{\omega_{A_i}} \boldsymbol{\delta}_2 \cdot \mathbf{e} dV \right) \\ &\quad - \int_{\Omega} \theta \mathbf{A} \varepsilon(\mathbf{v}_1) : \varepsilon(\boldsymbol{\delta}_2) dV - \int_{\Omega} \mathbf{A}(\mathbf{v}_1 \otimes \nabla \theta)^s : \varepsilon(\boldsymbol{\delta}_2) dV - \int_{\Omega} \mathbf{A} \varepsilon(\boldsymbol{\delta}_1) : \varepsilon(\boldsymbol{\delta}_2) dV. \end{aligned}$$

It follows that for some $C > 0$ independent of ρ

$$\begin{aligned} \Phi(\rho) \left| \int_{\omega_B} \boldsymbol{\delta}_2 \cdot \mathbf{e} dV - \int_{\omega_A} \boldsymbol{\delta}_2 \cdot \mathbf{e} dV \right| &\leq C \|\boldsymbol{\delta}_1\|_{L^2(\Omega)} \|\boldsymbol{\delta}_2\|_{L^2(\Omega)} + C \|\varepsilon(\mathbf{v}_1)\|_{L^2(\Omega)} \|\varepsilon(\boldsymbol{\delta}_2)\|_{L^2(\Omega)} \\ &\quad + C \|\mathbf{v}_1\|_{L^\infty(\Omega \setminus \mathcal{U}_-)} \|\varepsilon(\boldsymbol{\delta}_2)\|_{L^2(\Omega)} + C \|\varepsilon(\boldsymbol{\delta}_1)\|_{L^2(\Omega)} \|\varepsilon(\boldsymbol{\delta}_2)\|_{L^2(\Omega)} \\ &\leq C \Phi(\rho) \|\varepsilon(\boldsymbol{\delta}_2)\|_{L^2(\Omega)} + C \frac{\Phi(\rho)}{\sqrt{\rho}} \|\varepsilon(\boldsymbol{\delta}_2)\|_{L^2(\Omega)} \\ &\leq C \frac{\Phi(\rho)}{\sqrt{\rho}} \|\varepsilon(\boldsymbol{\delta}_2)\|_{L^2(\Omega)}. \end{aligned}$$

It results that $\exists C > 0, \left| \int_{\omega_B} \boldsymbol{\delta}_2 \cdot \mathbf{e} dV - \int_{\omega_A} \boldsymbol{\delta}_2 \cdot \mathbf{e} dV \right| \leq C \rho^{-1/2} \|\varepsilon(\boldsymbol{\delta}_2)\|_{L^2(\Omega)}$.

Finally, the definition of the exact remainder terms implies the estimate

$$\exists C > 0, \left| \int_{\omega_B} (\mathbf{R}_{u_2}^B - \mathbf{R}_{u_1}^B) \cdot \mathbf{e} dV - \int_{\omega_A} (\mathbf{R}_{u_2}^A - \mathbf{R}_{u_1}^A) \cdot \mathbf{e} dV \right| \leq C \rho^2.$$

Regrouping all terms finally leads to

$$\|\varepsilon(\boldsymbol{\delta}_2)\|_{L^2(\Omega)}^2 \leq (C\rho|\xi_{u_2}(\rho)| + C\rho^{k+3/2})\|\varepsilon(\boldsymbol{\delta}_2)\|_{L^2(\Omega)} + C\rho^{k+2q}.$$

Setting the notations $X = \|\varepsilon(\boldsymbol{\delta}_2)\|_{L^2(\Omega)}$, $a = C\rho|\xi_{u_2}(\rho)| + C\rho^{k+3/2}$, $b = C\rho^{k+2q}$, it comes that $X \leq Ca + \sqrt{b}$. Finally, we have

$$\|\varepsilon(\boldsymbol{\delta}_2)\|_{L^2(\Omega)} \leq C\rho|\xi_{u_2}(\rho)| + C\rho^{k+3/2} + C\rho^{k/2+q} \leq C\rho|\xi_{u_2}(\rho)| \text{ for } k > 0.$$

□

Adjoint state

We recall that the transmission condition between Ω_A and Ω_B insures the continuity of displacement and normal stress. The adjoint state $\mathbf{p}_{\rho,2}$ associated to the perturbed displacement field $\mathbf{u}_{\rho,2}$ solves

$$\left\{ \begin{array}{ll} -\operatorname{div}(\mathbf{A}\varepsilon(\mathbf{p}_{\rho,2})) + \mathcal{S}(\mathbf{p}_{\rho,2}) = -\mathbf{F}'(\mathbf{u}_2)\mathbb{1}_{\Omega_2} & \text{in } \Omega_\rho \\ -\operatorname{div}(\mathbf{A}\varepsilon(\mathbf{p}_{\rho,2})) - \frac{\kappa(\rho)}{|\omega_A|} \left(\int_{\omega_B} \mathbf{p}_{\rho,2} \cdot \mathbf{e} dV - \int_{\omega_A} \mathbf{p}_{\rho,2} \cdot \mathbf{e} dV \right) \mathbf{e} = \mathbf{0} & \text{in } \omega_A \\ -\operatorname{div}(\mathbf{A}\varepsilon(\mathbf{p}_{\rho,2})) + \frac{\kappa(\rho)}{|\omega_B|} \left(\int_{\omega_B} \mathbf{p}_{\rho,2} \cdot \mathbf{e} dV - \int_{\omega_A} \mathbf{p}_{\rho,2} \cdot \mathbf{e} dV \right) \mathbf{e} = \mathbf{0} & \text{in } \omega_B \\ \mathbf{A}\varepsilon(\mathbf{p}_{\rho,2})\mathbf{n} = -\mathbf{G}'(\mathbf{u}_2) & \text{on } \Gamma_N \\ \mathbf{p}_{\rho,2} = \mathbf{0} & \text{on } \Gamma_D \end{array} \right. \quad (7.77)$$

The adjoint state $\mathbf{p}_{\rho,2}$ is assumed to be as smooth as the perturbed displacement field $\mathbf{u}_{\rho,2}$.

Remark 68. *Once more, the adjoint problem is adapted to the sensitivity analysis. The right hand side of depends on \mathbf{u}_2 and not on $\mathbf{u}_{\rho,2}$ as expected in the perturbed domain. Tightening is an external solicitation. As a consequence, the adjoint state is not affected by the pretension force. Therefore, the perturbed adjoint problem of Step 2 has the same form as the perturbed adjoint problem of the simple spring (5.45).*

Denote \mathbf{q}_2 the function such that $\mathbf{q}_2(\mathbf{x}) = \mathbf{q}_{a,2} \left(\frac{\mathbf{x} - \mathbf{x}_0}{\rho} \right) + \mathbf{q}_{b,2} \left(\frac{\mathbf{x} - \mathbf{x}_0 - \ell\mathbf{e}}{\rho} \right)$, where $\mathbf{q}_{a,2}$ and $\mathbf{q}_{b,2}$ are the same as \mathbf{q}_a and \mathbf{q}_b the far fields of the simple spring problem (cf. Chapter 5).

Proposition 17. *Let $\theta \in \mathcal{C}_c^\infty(\Omega)$ be a cut-off function with compact support $\mathcal{U}_+ \subset \Omega$ such that $\theta \equiv 1$ in a neighbourhood $\mathcal{U}_- \subset \mathcal{U}_+$ of \mathbf{x}_0 and $\mathbf{x}_0 + \ell\mathbf{e}$. We have*

$$\mathbf{q}_{\rho,2} = \theta\mathbf{q}_2 + \boldsymbol{\eta}_2, \quad (7.78)$$

where $\boldsymbol{\eta}_2$ is an error term as shown by the following estimates of the L^2 -norm of \mathbf{q}_2 and $\varepsilon(\mathbf{q}_2)$ and H^1 -norm of $\boldsymbol{\eta}_2$ for various values of k . They are given, according to the value of the exponent k , by

	$\ \mathbf{q}_2\ _{L^2(\Omega)}$	$\ \varepsilon(\mathbf{q}_2)\ _{L^2(\Omega)}$	$\ \boldsymbol{\eta}_2\ _{H^1(\Omega)}$
$k > 1$	$O(\rho^k)$	$O(\rho^{k-1/2})$	$O(\rho^k)$
$k = 1$	$O(\rho)$	$O(\sqrt{\rho})$	$O(\rho)$
$0 < k < 1$	$O(\rho)$	$O(\sqrt{\rho})$	$O(\rho)$

Proof. The error term $\boldsymbol{\eta}_2$ solves

$$\left\{ \begin{array}{l} -\operatorname{div}(\mathbf{A}\varepsilon(\boldsymbol{\eta}_2)) + \mathbf{S}(\boldsymbol{\eta}_2) = \operatorname{div}\mathbf{A}(\mathbf{q}_2 \otimes \nabla\theta)^s + \mathbf{A}\varepsilon(\mathbf{q}_2)\nabla\theta \quad \text{in } \Omega_\rho \\ -\operatorname{div}(\mathbf{A}\varepsilon(\boldsymbol{\eta}_2)) - \frac{\kappa(\rho)}{|\omega_A|} \left(\int_{\omega_B} \boldsymbol{\eta}_2 \cdot \mathbf{e} dV - \int_{\omega_A} \boldsymbol{\eta}_2 \cdot \mathbf{e} dV \right) \mathbf{e} \\ \quad = \frac{\kappa(\rho)}{|\omega_A|} \left(\int_{\omega_B} \mathbf{p}_2 \cdot \mathbf{e} dV - \int_{\omega_A} \mathbf{p}_2 \cdot \mathbf{e} dV - (\mathbf{p}_2(\mathbf{x}_0 + \ell\mathbf{e}) - \mathbf{p}_2(\mathbf{x}_0)) \cdot \mathbf{e} \right) \mathbf{e} \quad \text{in } \omega_A \\ -\operatorname{div}(\mathbf{A}\varepsilon(\boldsymbol{\eta}_2)) + \frac{\kappa(\rho)}{|\omega_B|} \left(\int_{\omega_B} \boldsymbol{\eta}_2 \cdot \mathbf{e} dV - \int_{\omega_A} \boldsymbol{\eta}_2 \cdot \mathbf{e} dV \right) \mathbf{e} \\ \quad = -\frac{\kappa(\rho)}{|\omega_B|} \left(\int_{\omega_B} \mathbf{p}_2 \cdot \mathbf{e} dV - \int_{\omega_A} \mathbf{p}_2 \cdot \mathbf{e} dV - (\mathbf{p}_2(\mathbf{x}_0 + \ell\mathbf{e}) - \mathbf{p}_2(\mathbf{x}_0)) \cdot \mathbf{e} \right) \mathbf{e} \quad \text{in } \omega_B \\ \mathbf{A}\varepsilon(\boldsymbol{\eta}_2)\mathbf{n} = \mathbf{0} \quad \text{on } \Gamma_N \\ \boldsymbol{\eta}_2 = \mathbf{0} \quad \text{on } \Gamma_D \end{array} \right. \quad (7.79)$$

The proof of Proposition 17 is the same as the proof of Proposition 12. \square

7.2.3 Proof of the main result

Let us recall the objective function (7.10) in the background domain.

$$J_0(\Omega) = \int_{\Omega_1} F(\mathbf{u}_2) dV + \int_{\Gamma_N} G(\mathbf{u}_2) dS.$$

The Taylor expansion with exact remainder of (7.10) is

$$J_\rho(\Omega) = J_0(\Omega) + \int_{\Omega_1} \mathbf{F}'(\mathbf{u}_2) \cdot \mathbf{v}_{\rho,2} dV + \int_{\Gamma_N} \mathbf{G}'(\mathbf{u}_2) \cdot \mathbf{v}_{\rho,2} dS + \frac{1}{2} \int_{\Omega_1} \mathbf{v}_{\rho,2}^T F''(\bar{\mathbf{u}}_2) \mathbf{v}_{\rho,2} dV + \frac{1}{2} \int_{\Gamma_N} \mathbf{v}_{\rho,2}^T G''(\bar{\mathbf{u}}_2) \mathbf{v}_{\rho,2} dS.$$

The exact remainder terms are bounded as below

$$\left| \int_{\Omega_1} \mathbf{v}_{\rho,2}^T F''(\bar{\mathbf{u}}_2) \mathbf{v}_{\rho,2} dV \right| \leq C\rho^2 |\xi_{u_2}(\rho)|^2 \leq C \frac{\kappa(\rho)^2}{\left(1 + C \frac{\kappa(\rho)}{\rho}\right)^2} + C \frac{\kappa(\rho)\Phi(\rho)}{1 + C \frac{\kappa(\rho)}{\rho}} + C\Phi(\rho)^2,$$

$$\left| \int_{\Gamma_N} \mathbf{v}_{\rho,2}^T G''(\bar{\mathbf{u}}_2) \mathbf{v}_{\rho,2} dS \right| \leq C\rho^2 |\xi_{u_2}(\rho)|^2 \leq C \frac{\kappa(\rho)^2}{\left(1 + C \frac{\kappa(\rho)}{\rho}\right)^2} + C \frac{\kappa(\rho)\Phi(\rho)}{1 + C \frac{\kappa(\rho)}{\rho}} + C\Phi(\rho)^2.$$

Multiplying (7.77) by $\mathbf{v}_{\rho,2}$ and integrating by parts twice, one gets

$$\begin{aligned} & \int_{\Omega_1} \mathbf{F}'(\mathbf{u}_2) \cdot \mathbf{v}_{\rho,2} dV + \int_{\Gamma_N} \mathbf{G}'(\mathbf{u}_2) \cdot \mathbf{v}_{\rho,2} dS \\ &= \left(\kappa(\rho) \left(\int_{\omega_B} \mathbf{u}_2 \cdot \mathbf{e} dV - \int_{\omega_A} \mathbf{u}_2 \cdot \mathbf{e} dV \right) + T(\rho) \right) \left(\int_{\omega_B} \mathbf{p}_{\rho,2} \cdot \mathbf{e} dV - \int_{\omega_A} \mathbf{p}_{\rho,2} \cdot \mathbf{e} dV \right) \\ & \text{with } T(\rho) = -\kappa(\rho) \left(\int_{\omega_B} \mathbf{u}_{\rho,1} \cdot \mathbf{e} dV - \int_{\omega_A} \mathbf{u}_{\rho,1} \cdot \mathbf{e} dV \right) + \Phi(\rho). \end{aligned}$$

We recall that $\mathbf{u}_{\rho,1} = \mathbf{u}_1 + \theta \mathbf{v}_1 + \boldsymbol{\delta}_1$ and $\mathbf{p}_{\rho,2} = \mathbf{p}_2 + \theta \mathbf{q}_2 + \boldsymbol{\eta}_2$. The topological derivative and the remainder term are then evaluated by the estimation of the following terms.

$$\begin{aligned} & \int_{\Omega_1} \mathbf{F}'(\mathbf{u}_2) \cdot \mathbf{v}_{\rho,2} dV + \int_{\Gamma_N} \mathbf{G}'(\mathbf{u}_2) \cdot \mathbf{v}_{\rho,2} dS \\ &= \left(\kappa(\rho) \left(\int_{\omega_B} (\mathbf{u}_2 - \mathbf{u}_{\rho,1}) \cdot \mathbf{e} dV - \int_{\omega_A} (\mathbf{u}_2 - \mathbf{u}_{\rho,1}) \cdot \mathbf{e} dV \right) + \Phi(\rho) \right) \left(\int_{\omega_B} \mathbf{p}_{\rho,2} \cdot \mathbf{e} dV - \int_{\omega_A} \mathbf{p}_{\rho,2} \cdot \mathbf{e} dV \right) \\ &= \left(\kappa(\rho) \left(\int_{\omega_B} (\mathbf{u}_2 - \mathbf{u}_1) \cdot \mathbf{e} dV - \int_{\omega_A} (\mathbf{u}_2 - \mathbf{u}_1) \cdot \mathbf{e} dV \right) + \Phi(\rho) \right) \left(\int_{\omega_B} \mathbf{p}_2 \cdot \mathbf{e} dV - \int_{\omega_A} \mathbf{p}_2 \cdot \mathbf{e} dV \right) \\ &+ \left(\kappa(\rho) \left(\int_{\omega_B} (\mathbf{u}_2 - \mathbf{u}_1) \cdot \mathbf{e} dV - \int_{\omega_A} (\mathbf{u}_2 - \mathbf{u}_1) \cdot \mathbf{e} dV \right) + \Phi(\rho) \right) \left(\int_{\omega_B} \mathbf{q}_2 \cdot \mathbf{e} dV - \int_{\omega_A} \mathbf{q}_2 \cdot \mathbf{e} dV \right) \\ &+ \left(\kappa(\rho) \left(\int_{\omega_B} (\mathbf{u}_2 - \mathbf{u}_1) \cdot \mathbf{e} dV - \int_{\omega_A} (\mathbf{u}_2 - \mathbf{u}_1) \cdot \mathbf{e} dV \right) + \Phi(\rho) \right) \left(\int_{\omega_B} \boldsymbol{\eta}_2 \cdot \mathbf{e} dV - \int_{\omega_A} \boldsymbol{\eta}_2 \cdot \mathbf{e} dV \right) \\ &- \kappa(\rho) \left(\int_{\omega_B} \mathbf{v}_1 \cdot \mathbf{e} dV - \int_{\omega_A} \mathbf{v}_1 \cdot \mathbf{e} dV \right) \left(\int_{\omega_B} \mathbf{p}_2 \cdot \mathbf{e} dV - \int_{\omega_A} \mathbf{p}_2 \cdot \mathbf{e} dV \right) \\ &- \kappa(\rho) \left(\int_{\omega_B} \mathbf{v}_1 \cdot \mathbf{e} dV - \int_{\omega_A} \mathbf{v}_1 \cdot \mathbf{e} dV \right) \left(\int_{\omega_B} \mathbf{q}_2 \cdot \mathbf{e} dV - \int_{\omega_A} \mathbf{q}_2 \cdot \mathbf{e} dV \right) \\ &- \kappa(\rho) \left(\int_{\omega_B} \mathbf{v}_1 \cdot \mathbf{e} dV - \int_{\omega_A} \mathbf{v}_1 \cdot \mathbf{e} dV \right) \left(\int_{\omega_B} \boldsymbol{\eta}_2 \cdot \mathbf{e} dV - \int_{\omega_A} \boldsymbol{\eta}_2 \cdot \mathbf{e} dV \right) \\ &- \kappa(\rho) \left(\int_{\omega_B} \boldsymbol{\delta}_1 \cdot \mathbf{e} dV - \int_{\omega_A} \boldsymbol{\delta}_1 \cdot \mathbf{e} dV \right) \left(\int_{\omega_B} \mathbf{p}_2 \cdot \mathbf{e} dV - \int_{\omega_A} \mathbf{p}_2 \cdot \mathbf{e} dV \right) \\ &- \kappa(\rho) \left(\int_{\omega_B} \boldsymbol{\delta}_1 \cdot \mathbf{e} dV - \int_{\omega_A} \boldsymbol{\delta}_1 \cdot \mathbf{e} dV \right) \left(\int_{\omega_B} \mathbf{q}_2 \cdot \mathbf{e} dV - \int_{\omega_A} \mathbf{q}_2 \cdot \mathbf{e} dV \right) \\ &- \kappa(\rho) \left(\int_{\omega_B} \boldsymbol{\delta}_1 \cdot \mathbf{e} dV - \int_{\omega_A} \boldsymbol{\delta}_1 \cdot \mathbf{e} dV \right) \left(\int_{\omega_B} \boldsymbol{\eta}_2 \cdot \mathbf{e} dV - \int_{\omega_A} \boldsymbol{\eta}_2 \cdot \mathbf{e} dV \right) \end{aligned}$$

These terms are estimated one by one. Most of them are evaluated by rescaling. Each

leading term will be part of the topological derivative and contribute to the scaling term $s(\rho)$. All bounded terms are elements of $\mathcal{R}(s(\rho))$. To lighten calculations, let us set the notations

$$\begin{aligned} \mathbf{U}_1 &= \mathbf{u}_1(\mathbf{x}_0 + \ell \mathbf{e}) - \mathbf{u}_1(\mathbf{x}_0), \\ \mathbf{U}_2 &= \mathbf{u}_2(\mathbf{x}_0 + \ell \mathbf{e}) - \mathbf{u}_2(\mathbf{x}_0), \\ \mathbf{P}_2 &= \mathbf{p}_2(\mathbf{x}_0 + \ell \mathbf{e}) - \mathbf{p}_2(\mathbf{x}_0). \end{aligned}$$

★ 1st term

This term is fully evaluated by rescaling. We introduce the functions $\mathbf{R}_{p_2}^A$ and $\mathbf{R}_{p_2}^B$ that stand for the integral remainder of the expansion at first order of \mathbf{p}_2 around \mathbf{x}_0 and $\mathbf{x}_0 + \ell \mathbf{e}$. These functions are respectively of the order of ρ^2 in ω_A and ω_B .

$$\begin{aligned} & \left(\kappa(\rho) \left(\int_{\omega_B} (\mathbf{u}_2 - \mathbf{u}_1) \cdot \mathbf{e} dV - \int_{\omega_A} (\mathbf{u}_2 - \mathbf{u}_1) \cdot \mathbf{e} dV \right) + \Phi(\rho) \right) \left(\int_{\omega_B} \mathbf{p}_2 \cdot \mathbf{e} dV - \int_{\omega_A} \mathbf{p}_2 \cdot \mathbf{e} dV \right) \\ &= \left(\kappa(\rho) (\mathbf{U}_2 - \mathbf{U}_1) \cdot \mathbf{e} + \Phi(\rho) \right) \mathbf{P}_2 \cdot \mathbf{e} + \kappa(\rho) \left(\int_{\omega_B} (\mathbf{R}_{u_2}^B - \mathbf{R}_{u_1}^B) \cdot \mathbf{e} dV - \int_{\omega_A} (\mathbf{R}_{u_2}^A - \mathbf{R}_{u_1}^A) \cdot \mathbf{e} dV \right) \mathbf{P}_2 \cdot \mathbf{e} \\ &+ \left(\kappa(\rho) (\mathbf{U}_2 - \mathbf{U}_1) \cdot \mathbf{e} + \Phi(\rho) \right) \left(\int_{\omega_B} \mathbf{R}_{p_2}^B \cdot \mathbf{e} dV - \int_{\omega_A} \mathbf{R}_{p_2}^A \cdot \mathbf{e} dV \right) \\ &+ \kappa(\rho) \left(\int_{\omega_B} (\mathbf{R}_{u_2}^B - \mathbf{R}_{u_1}^B) \cdot \mathbf{e} dV - \int_{\omega_A} (\mathbf{R}_{u_2}^A - \mathbf{R}_{u_1}^A) \cdot \mathbf{e} dV \right) \left(\int_{\omega_B} \mathbf{R}_{p_2}^B \cdot \mathbf{e} dV - \int_{\omega_A} \mathbf{R}_{p_2}^A \cdot \mathbf{e} dV \right) \\ &= \left(\kappa(\rho) (\mathbf{U}_2 - \mathbf{U}_1) \cdot \mathbf{e} + \Phi(\rho) \right) \mathbf{P}_2 \cdot \mathbf{e} + O(\kappa(\rho)\rho^2) + O(\Phi(\rho)\rho^2). \end{aligned}$$

★ 2nd term

First of all, we define the quantity $\xi_{p_2}(\rho)$ as in Chapter 5.

$$\xi_{p_2}(\rho) = \frac{\frac{\kappa(\rho)}{\rho|\omega|}}{1 + \frac{\kappa(\rho)}{\rho|\omega|} \left(\frac{1}{\tau_A} + \frac{1}{\tau_B} \right)} \mathbf{P}_2 \cdot \mathbf{e}, \quad \int_{\omega} \mathbf{q}_{a,2} \cdot \mathbf{e} dV = \frac{\xi_{p_2}(\rho)}{\tau_A} \quad \text{and} \quad \int_{\omega} \mathbf{q}_{b,2} \cdot \mathbf{e} dV = -\frac{\xi_{p_2}(\rho)}{\tau_B}. \quad (7.80)$$

The second term is fully evaluated by rescaling.

$$\begin{aligned} & \left(\kappa(\rho) \left(\int_{\omega_B} (\mathbf{u}_2 - \mathbf{u}_1) \cdot \mathbf{e} dV - \int_{\omega_A} (\mathbf{u}_2 - \mathbf{u}_1) \cdot \mathbf{e} dV \right) + \Phi(\rho) \right) \left(\int_{\omega_B} \mathbf{q}_2 \cdot \mathbf{e} dV - \int_{\omega_A} \mathbf{q}_2 \cdot \mathbf{e} dV \right) \\ &= \left(\kappa(\rho) \left(\mathbf{U}_2 - \mathbf{U}_1 + \int_{\omega_B} (\mathbf{R}_{u_2}^B - \mathbf{R}_{u_1}^B) dV - \int_{\omega_A} (\mathbf{R}_{u_2}^A - \mathbf{R}_{u_1}^A) dV \right) \cdot \mathbf{e} + \Phi(\rho) \right) \int_{\omega} (\mathbf{q}_{b,2} - \mathbf{q}_{a,2}) \cdot \mathbf{e} dV \\ &= -\frac{\frac{\kappa(\rho)}{\rho|\omega|} \left(\frac{1}{\tau_A} + \frac{1}{\tau_B} \right)}{1 + \frac{\kappa(\rho)}{\rho|\omega|} \left(\frac{1}{\tau_A} + \frac{1}{\tau_B} \right)} \left(\kappa(\rho) (\mathbf{U}_2 - \mathbf{U}_1) \cdot \mathbf{e} + \Phi(\rho) \right) \mathbf{P}_2 \cdot \mathbf{e} + O\left(\frac{\kappa(\rho)^2 \rho}{1 + C \frac{\kappa(\rho)}{\rho}} \right). \end{aligned}$$

★ 3rd term

The occurrence of $\boldsymbol{\eta}_2$ indicates that the third term should be a remainder term. Let us begin with a rescaling to handle the terms with \mathbf{u}_1 and \mathbf{u}_2 .

$$\begin{aligned} & \left(\kappa(\rho) \left(\int_{\omega_B} \mathbf{f}(\mathbf{u}_2 - \mathbf{u}_1) \cdot \mathbf{e} dV - \int_{\omega_A} \mathbf{f}(\mathbf{u}_2 - \mathbf{u}_1) \cdot \mathbf{e} dV \right) + \Phi(\rho) \right) \left(\int_{\omega_B} \mathbf{f} \boldsymbol{\eta}_2 \cdot \mathbf{e} dV - \int_{\omega_A} \mathbf{f} \boldsymbol{\eta}_2 \cdot \mathbf{e} dV \right) \\ &= \left(\kappa(\rho) (\mathbf{U}_2 - \mathbf{U}_1) \cdot \mathbf{e} + \Phi(\rho) \right) \left(\int_{\omega_B} \mathbf{f} \boldsymbol{\eta}_2 \cdot \mathbf{e} dV - \int_{\omega_A} \mathbf{f} \boldsymbol{\eta}_2 \cdot \mathbf{e} dV \right) \\ &+ \kappa(\rho) \left(\int_{\omega_B} \mathbf{f}(\mathbf{R}_{u_2}^B - \mathbf{R}_{u_1}^B) \cdot \mathbf{e} dV - \int_{\omega_A} \mathbf{f}(\mathbf{R}_{u_2}^A - \mathbf{R}_{u_1}^A) \cdot \mathbf{e} dV \right) \left(\int_{\omega_B} \mathbf{f} \boldsymbol{\eta}_2 \cdot \mathbf{e} dV - \int_{\omega_A} \mathbf{f} \boldsymbol{\eta}_2 \cdot \mathbf{e} dV \right). \end{aligned}$$

Let us set a better estimation of the term $\left| \int_{\omega_B} \mathbf{f} \boldsymbol{\eta}_2 \cdot \mathbf{e} dV - \int_{\omega_A} \mathbf{f} \boldsymbol{\eta}_2 \cdot \mathbf{e} dV \right|$ using the variational formulation of (7.79) with $\boldsymbol{\eta}_2$ as test function

$$\exists C > 0, \kappa(\rho) \left| \int_{\omega_B} \mathbf{f} \boldsymbol{\eta}_2 \cdot \mathbf{e} dV - \int_{\omega_A} \mathbf{f} \boldsymbol{\eta}_2 \cdot \mathbf{e} dV \right|^2 \leq C \rho |\xi_{p_2}(\rho)| \|\varepsilon(\boldsymbol{\eta}_2)\|_{L^2(\Omega)} \leq C \rho^2 |\xi_{p_2}(\rho)|^2.$$

In other words

$$\exists C > 0, \left| \int_{\omega_B} \mathbf{f} \boldsymbol{\eta}_2 \cdot \mathbf{e} dV - \int_{\omega_A} \mathbf{f} \boldsymbol{\eta}_2 \cdot \mathbf{e} dV \right| \leq C \kappa(\rho)^{-1/2} \rho |\xi_{p_2}(\rho)|. \quad (7.81)$$

It follows the estimation

$$\begin{aligned} \exists C > 0, & \left| \left(\kappa(\rho) \int_{\omega_B} \mathbf{f}(\mathbf{u}_2 - \mathbf{u}_1) \cdot \mathbf{e} dV - \int_{\omega_A} \mathbf{f}(\mathbf{u}_2 - \mathbf{u}_1) \cdot \mathbf{e} dV \right) + \Phi(\rho) \right| \left| \int_{\omega_B} \mathbf{f} \boldsymbol{\eta}_2 \cdot \mathbf{e} dV - \int_{\omega_A} \mathbf{f} \boldsymbol{\eta}_2 \cdot \mathbf{e} dV \right| \\ & \leq C \kappa(\rho)^{1/2} \rho |\xi_{p_2}(\rho)| + C \Phi(\rho) \kappa(\rho)^{-1/2} \rho |\xi_{p_2}(\rho)| + C \kappa(\rho)^{1/2} \rho^3 |\xi_{p_2}(\rho)| \\ & \leq C \frac{\kappa(\rho)^{3/2}}{1 + C \frac{\kappa(\rho)}{\rho}} + C \frac{\Phi(\rho) \kappa(\rho)^{1/2}}{1 + C \frac{\kappa(\rho)}{\rho}}. \end{aligned}$$

★ 4th term

This term is fully evaluated by rescaling.

$$\begin{aligned} & - \kappa(\rho) \left(\int_{\omega_B} \mathbf{f} \mathbf{v}_1 \cdot \mathbf{e} dV - \int_{\omega_A} \mathbf{f} \mathbf{v}_1 \cdot \mathbf{e} dV \right) \left(\int_{\omega_B} \mathbf{f} \mathbf{p}_2 \cdot \mathbf{e} dV - \int_{\omega_A} \mathbf{f} \mathbf{p}_2 \cdot \mathbf{e} dV \right) \\ &= - \kappa(\rho) \int_{\omega} \mathbf{f}(\mathbf{v}_{b,1} - \mathbf{v}_{a,1}) \cdot \mathbf{e} dV \left(\mathbf{P}_2 \cdot \mathbf{e} + \int_{\omega_B} \mathbf{R}_{p_2}^B \cdot \mathbf{e} dV - \int_{\omega_A} \mathbf{R}_{p_2}^A \cdot \mathbf{e} dV \right) \\ &= \frac{\kappa(\rho) \Phi(\rho)}{\rho |\omega|} \left(\frac{1}{\tau_A} + \frac{1}{\tau_B} \right) \mathbf{P}_2 \cdot \mathbf{e} + O(\kappa(\rho) \Phi(\rho) \rho). \end{aligned}$$

★ 5th term

This term is also fully evaluated by rescaling.

$$\begin{aligned}
& -\kappa(\rho) \left(\int_{\omega_B} \mathbf{v}_1 \cdot \mathbf{e} dV - \int_{\omega_A} \mathbf{v}_1 \cdot \mathbf{e} dV \right) \left(\int_{\omega_B} \mathbf{q}_2 \cdot \mathbf{e} dV - \int_{\omega_A} \mathbf{q}_2 \cdot \mathbf{e} dV \right) \\
&= -\kappa(\rho) \int_{\omega} (\mathbf{v}_{b,1} - \mathbf{v}_{a,1}) \cdot \mathbf{e} dV \int_{\omega} (\mathbf{q}_{b,2} - \mathbf{q}_{a,2}) \cdot \mathbf{e} dV \\
&= -\kappa(\rho) \frac{\Phi(\rho)}{\rho|\omega|} \left(\frac{1}{\tau_A} + \frac{1}{\tau_B} \right) \frac{\frac{\kappa(\rho)}{\rho|\omega|} \left(\frac{1}{\tau_A} + \frac{1}{\tau_B} \right)}{1 + \frac{\kappa(\rho)}{\rho|\omega|} \left(\frac{1}{\tau_A} + \frac{1}{\tau_B} \right)} \mathbf{P}_2 \cdot \mathbf{e}.
\end{aligned}$$

★ 6th term

This term is expected to be a remainder term since it involves $\boldsymbol{\eta}_2$. First by rescaling

$$\begin{aligned}
& -\kappa(\rho) \left(\int_{\omega_B} \mathbf{v}_1 \cdot \mathbf{e} dV - \int_{\omega_A} \mathbf{v}_1 \cdot \mathbf{e} dV \right) \left(\int_{\omega_B} \boldsymbol{\eta}_2 \cdot \mathbf{e} dV - \int_{\omega_A} \boldsymbol{\eta}_2 \cdot \mathbf{e} dV \right) \\
&= \frac{\kappa(\rho)\Phi(\rho)}{\rho|\omega|} \left(\frac{1}{\tau_A} + \frac{1}{\tau_B} \right) \left(\int_{\omega_B} \boldsymbol{\eta}_2 \cdot \mathbf{e} dV - \int_{\omega_A} \boldsymbol{\eta}_2 \cdot \mathbf{e} dV \right).
\end{aligned}$$

Using the estimate (7.81), it follows

$$\begin{aligned}
& \exists C > 0, \kappa(\rho) \left| \int_{\omega_B} \mathbf{v}_1 \cdot \mathbf{e} dV - \int_{\omega_A} \mathbf{v}_1 \cdot \mathbf{e} dV \right| \left| \int_{\omega_B} \boldsymbol{\eta}_2 \cdot \mathbf{e} dV - \int_{\omega_A} \boldsymbol{\eta}_2 \cdot \mathbf{e} dV \right| \\
& \leq C \frac{\kappa(\rho)^{1/2} \Phi(\rho)}{\rho} \frac{\kappa(\rho)}{1 + C \frac{\kappa(\rho)}{\rho}} \leq C \frac{\kappa(\rho)^{3/2} \Phi(\rho)}{\rho} \frac{1}{1 + C \frac{\kappa(\rho)}{\rho}}.
\end{aligned}$$

★ 7th term

First by rescaling and then using (7.76), one obtains

$$\begin{aligned}
& -\kappa(\rho) \left(\int_{\omega_B} \boldsymbol{\delta}_1 \cdot \mathbf{e} dV - \int_{\omega_A} \boldsymbol{\delta}_1 \cdot \mathbf{e} dV \right) \left(\int_{\omega_B} \mathbf{p}_2 \cdot \mathbf{e} dV - \int_{\omega_A} \mathbf{p}_2 \cdot \mathbf{e} dV \right) \\
&= -\kappa(\rho) \left(\int_{\omega_B} \boldsymbol{\delta}_1 \cdot \mathbf{e} dV - \int_{\omega_A} \boldsymbol{\delta}_1 \cdot \mathbf{e} dV \right) \left(\mathbf{P}_2 \cdot \mathbf{e} + \int_{\omega_B} \mathbf{R}_{p_2}^B \cdot \mathbf{e} dV - \int_{\omega_A} \mathbf{R}_{p_2}^A \cdot \mathbf{e} dV \right),
\end{aligned}$$

There exists $C > 0$ such that

$$\begin{aligned}
& \kappa(\rho) \left| \int_{\omega_B} \boldsymbol{\delta}_1 \cdot \mathbf{e} dV - \int_{\omega_A} \boldsymbol{\delta}_1 \cdot \mathbf{e} dV \right| \left| \int_{\omega_B} \mathbf{p}_2 \cdot \mathbf{e} dV - \int_{\omega_A} \mathbf{p}_2 \cdot \mathbf{e} dV \right| \\
& \leq C\kappa(\rho)\Phi(\rho) + C\kappa(\rho)\Phi(\rho)\rho^2 \leq C\kappa(\rho)\Phi(\rho).
\end{aligned}$$

★ 8th term

Also by rescaling and using (7.76), it follows

$$\begin{aligned} & -\kappa(\rho) \left(\int_{\omega_B} \boldsymbol{\delta}_1 \cdot \mathbf{e} dV - \int_{\omega_A} \boldsymbol{\delta}_1 \cdot \mathbf{e} dV \right) \left(\int_{\omega_B} \mathbf{q}_2 \cdot \mathbf{e} dV - \int_{\omega_A} \mathbf{q}_2 \cdot \mathbf{e} dV \right) \\ &= -\kappa(\rho) \left(\int_{\omega_B} \boldsymbol{\delta}_1 \cdot \mathbf{e} dV - \int_{\omega_A} \boldsymbol{\delta}_1 \cdot \mathbf{e} dV \right) \int_{\omega} (\mathbf{q}_{b,2} - \mathbf{q}_{a,2}) \cdot \mathbf{e} dV \\ &= \kappa(\rho) \left(\int_{\omega_B} \boldsymbol{\delta}_1 \cdot \mathbf{e} dV - \int_{\omega_A} \boldsymbol{\delta}_1 \cdot \mathbf{e} dV \right) \frac{\frac{\kappa(\rho)}{\rho|\omega|} \left(\frac{1}{\tau_A} + \frac{1}{\tau_B} \right)}{1 + \frac{\kappa(\rho)}{\rho|\omega|} \left(\frac{1}{\tau_A} + \frac{1}{\tau_B} \right)} \mathbf{P}_2 \cdot \mathbf{e}. \end{aligned}$$

As a consequence, there exists $C > 0$ such that

$$\kappa(\rho) \left| \int_{\omega_B} \boldsymbol{\delta}_1 \cdot \mathbf{e} dV - \int_{\omega_A} \boldsymbol{\delta}_1 \cdot \mathbf{e} dV \right| \left| \int_{\omega_B} \mathbf{q}_2 \cdot \mathbf{e} dV - \int_{\omega_A} \mathbf{q}_2 \cdot \mathbf{e} dV \right| \leq C \frac{1}{\rho} \frac{\kappa(\rho)^2 \Phi(\rho)}{1 + C \frac{\kappa(\rho)}{\rho}}.$$

★ 9th term

That last term is fully estimated by using (7.76) and (7.81)

$$\begin{aligned} \exists C > 0, \kappa(\rho) \left| \int_{\omega_B} \boldsymbol{\delta}_1 \cdot \mathbf{e} dV - \int_{\omega_A} \boldsymbol{\delta}_1 \cdot \mathbf{e} dV \right| \left| \int_{\omega_B} \boldsymbol{\eta}_2 \cdot \mathbf{e} dV - \int_{\omega_A} \boldsymbol{\eta}_2 \cdot \mathbf{e} dV \right| \\ \leq C \kappa(\rho) \Phi(\rho) \kappa(\rho)^{-1/2} \rho |\xi_{u_2}(\rho)| \leq C \kappa(\rho)^{1/2} \Phi(\rho) \frac{\kappa(\rho)}{1 + \frac{\kappa(\rho)}{\rho}} \leq C \frac{\kappa(\rho)^{3/2} \Phi(\rho)}{1 + \frac{\kappa(\rho)}{\rho}}. \end{aligned}$$

All leading terms are gathered and finally give

$$\left(\frac{1}{\kappa(\rho)} + \frac{1}{\rho|\omega| \left(\frac{1}{\tau_A} + \frac{1}{\tau_B} \right)} \right)^{-1} (\mathbf{U}_2 - \mathbf{U}_1) \cdot \mathbf{e} \mathbf{P}_2 \cdot \mathbf{e} + \Phi(\rho) \mathbf{P}_2 \cdot \mathbf{e}.$$

This expression is then expanded with respect to ρ . The resulting leading term shall be the topological derivative and the remainder term, denoted $\mathcal{R}(DJ(\mathbf{x}_0, \mathbf{e}))$, will be part of remainder term of the asymptotic expansion $\mathcal{R}(s(\rho))$, that reads

$$\begin{aligned} \mathcal{R}(s(\rho)) &= O(\kappa(\rho)\rho^2) + O(\Phi(\rho)\rho^2) + O\left(\frac{\kappa(\rho)^2\rho}{1 + C\frac{\kappa(\rho)}{\rho}}\right) + O\left(\frac{\kappa(\rho)^{3/2}}{1 + C\frac{\kappa(\rho)}{\rho}}\right) + O\left(\frac{\Phi(\rho)\kappa(\rho)^{1/2}}{1 + C\frac{\kappa(\rho)}{\rho}}\right) \\ &+ O(\kappa(\rho)\Phi(\rho)\rho) + O\left(\frac{1}{\rho} \frac{\kappa(\rho)^{3/2}\Phi(\rho)}{1 + C\frac{\kappa(\rho)}{\rho}}\right) + O(\kappa(\rho)\Phi(\rho)) + O\left(\frac{1}{\rho} \frac{\kappa(\rho)^2\Phi(\rho)}{1 + C\frac{\kappa(\rho)}{\rho}}\right) \\ &+ O\left(\frac{\kappa(\rho)^{3/2}\Phi(\rho)}{1 + C\frac{\kappa(\rho)}{\rho}}\right) + O\left(\frac{\kappa(\rho)^2}{\left(1 + C\frac{\kappa(\rho)}{\rho}\right)^2}\right) + O\left(\frac{\kappa(\rho)\Phi(\rho)}{1 + C\frac{\kappa(\rho)}{\rho}}\right) + O(\Phi(\rho)^2) + \mathcal{R}(DJ(\mathbf{x}_0, \mathbf{e})). \end{aligned}$$

Based on the work done at the end of Section 5.2.3 in Chapter 5, the topological derivative $DJ(\mathbf{x}_0, \mathbf{e})$ and its associated scaling coefficient $s(\rho)$ are easily computed. The factor

$\left(\frac{1}{\kappa(\rho)} + \frac{1}{\rho|\omega| \left(\frac{1}{\tau_A} + \frac{1}{\tau_B} \right)} \right)^{-1}$ is evaluated in the same manner. The resulting coefficient is then

compared to $\Phi(\rho)$. Given the fact that the denominator $1 + C\frac{\kappa(\rho)}{\rho}$ is bounded if $k \geq 1$ and goes to infinity otherwise, the remainder term is the larger quantity in terms of ρ .

7.3 Computation of the topological derivative with sliding contact

A penalized and regularized model of sliding contact is added to the model, replacing the interface transmission conditions between Ω_A and Ω_B . We keep the framework of the above two-step pre-tensioning problem. This section proves that the contact term does not affect the topological sensitivity. Actually, the small inclusions perturb the interior of the domain, not its boundaries. Even if the geometric model of the spring crosses the contact boundary, it does not perturb, the interface behavior. The topological sensitivity with regards to a hole with traction-free boundary (the Neumann problem) has been studied in [53] for contact problem in elasticity. The authors consider a sliding contact problem. They prove that the contact influence is part of the remainder term. As a consequence, the topological derivative expression is the same as the one of the contact-less problem. Nevertheless, the contact is implicitly expressed in the displacement field and the adjoint state of the background domain.

7.3.1 Contact model

The bolt connection model is complemented with a contact model to avoid interpenetration of parts. We use the penalized and regularized formulation of sliding contact studied in [74]. Denote \mathbf{S} the interface between Ω_A and Ω_B and \mathbf{S}_- and \mathbf{S}_+ the two sides of \mathbf{S} . The normal to \mathbf{S}_- pointing toward \mathbf{S}_+ is denoted \mathbf{n}_- . The jump of a displacement field \mathbf{w} through \mathbf{S} is

$$[\mathbf{w}] = \mathbf{w}|_{\mathbf{S}_-} - \mathbf{w}|_{\mathbf{S}_+}. \quad (7.82)$$

The contact condition is enforced by adding the penalized function $j_{N,\epsilon}$ in energy formulations

$$j_{N,\epsilon}(\mathbf{u}) = \int_{\mathbf{S}} \int_0^{[\mathbf{u}] \cdot \mathbf{n}_-} \phi_r(t) dt dS, \quad (7.83)$$

where the function ϕ_r is a smooth regularization of the function $\mathbf{x} \mapsto \frac{1}{\epsilon} \mathbf{x} \mathcal{H}(\mathbf{x})$ with \mathcal{H} the Heaviside function and $\epsilon > 0$ the penalization parameter. The regularized function is twice differentiable and satisfies the conditions

$$\exists C > 0, |\phi_r(\mathbf{x})| \leq C(|\mathbf{x}|^2 + 1), |\phi_r'(\mathbf{x})| \leq C(|\mathbf{x}| + 1), |\phi_r''(\mathbf{x})| \leq C. \quad (7.84)$$

The contact model is taken into in the variational formulation by adding the term

$$j'_{N,\epsilon}(\mathbf{u}, \mathbf{w}) = \int_{\mathbf{S}} \phi_r([\mathbf{u}] \cdot \mathbf{n}_-) \mathbf{n}_- \cdot [\mathbf{w}] dS. \quad (7.85)$$

The solution of the penalized problem tends to the solution of the real one when the parameter ϵ goes to zero. This convergence is proved in [39] and [46].

7.3.2 Step 1

The transmission condition at the interface used in Section 7.1.1 is replaced by a sliding contact model. The background solution \mathbf{u}_1 and the perturbed solution $\mathbf{u}_{\rho,1}$ respectively solves

$$\left\{ \begin{array}{ll} -\operatorname{div}(\mathbf{A}\varepsilon(\mathbf{u}_1)) + \mathcal{S}(\mathbf{u}_1) = \mathbf{t} & \text{in } \Omega \\ \mathbf{A}\varepsilon(\mathbf{u}_1)\mathbf{n} = \mathbf{0} & \text{on } \Gamma_N \\ \mathbf{u}_1 = \mathbf{0} & \text{on } \Gamma_D \\ \mathbf{A}\varepsilon(\mathbf{u}_1|_{\mathcal{S}_-})\mathbf{n}_- = \mathbf{A}\varepsilon(\mathbf{u}_1|_{\mathcal{S}_+})\mathbf{n}_- = -\phi_r([\mathbf{u}_1] \cdot \mathbf{n}_-)\mathbf{n}_- & \text{on } \mathcal{S} \end{array} \right. \quad (7.86)$$

$$\left\{ \begin{array}{ll} -\operatorname{div}(\mathbf{A}\varepsilon(\mathbf{u}_{\rho,1})) + \mathcal{S}(\mathbf{u}_{\rho,1}) = \mathbf{t} & \text{in } \Omega_\rho \\ -\operatorname{div}(\mathbf{A}\varepsilon(\mathbf{u}_{\rho,1})) = \frac{\Phi(\rho)}{|\omega_A|}\mathbf{e} & \text{in } \omega_A \\ -\operatorname{div}(\mathbf{A}\varepsilon(\mathbf{u}_{\rho,1})) = -\frac{\Phi(\rho)}{|\omega_B|}\mathbf{e} & \text{in } \omega_B \\ \mathbf{A}\varepsilon(\mathbf{u}_{\rho,1})\mathbf{n} = \mathbf{0} & \text{on } \Gamma_N \\ \mathbf{u}_{\rho,1} = \mathbf{0} & \text{on } \Gamma_D \\ \mathbf{A}\varepsilon(\mathbf{u}_{\rho,1}|_{\mathcal{S}_-})\mathbf{n}_- = \mathbf{A}\varepsilon(\mathbf{u}_{\rho,1}|_{\mathcal{S}_+})\mathbf{n}_- = -\phi_r([\mathbf{u}_{\rho,1}] \cdot \mathbf{n}_-)\mathbf{n}_- & \text{on } \mathcal{S} \end{array} \right. \quad (7.87)$$

Smoothness of each solution is guaranteed by the regularity of the penalized function ϕ_r that satisfies conditions (7.84) and the smoothness of the loads and the domain. The perturbed solution is approximated as before.

Approximation of the perturbed displacement field

- Far fields

As usual, let us set far fields $\mathbf{v}_{a,1}$ and $\mathbf{v}_{b,1}$ such that $\lim_{\mathbf{y} \rightarrow \mathbf{0}} \mathbf{v}_{a,1}(\mathbf{y}) = \mathbf{0}$ and $\lim_{\mathbf{y} \rightarrow \mathbf{0}} \mathbf{v}_{b,1}(\mathbf{y}) = \mathbf{0}$ and

$$\mathbf{u}_{\rho,1}(\mathbf{x}) \approx \mathbf{u}_1(\mathbf{x}) + \mathbf{v}_{a,1}\left(\frac{\mathbf{x} - \mathbf{x}_0}{\rho}\right) + \mathbf{v}_{b,1}\left(\frac{\mathbf{x} - \mathbf{x}_0 - \ell\mathbf{e}}{\rho}\right).$$

The far fields $\mathbf{v}_{a,1}$ and $\mathbf{v}_{b,1}$ respectively solve

$$\left\{ \begin{array}{ll} -\operatorname{div}(\mathbf{A}\varepsilon(\mathbf{v}_{a,1})(\mathbf{y}_a)) = \mathbf{0} & \text{in } \mathbb{R}^3 \setminus \omega \\ -\operatorname{div}(\mathbf{A}\varepsilon(\mathbf{v}_{a,1})(\mathbf{y}_a)) = \xi_{u_1}(\rho)\mathbf{e} & \text{in } \omega \\ \lim_{\mathbf{y}_a \rightarrow \mathbf{0}} \mathbf{v}_{a,1}(\mathbf{y}_a) = \mathbf{0} & \end{array} \right. \quad \text{and} \quad \left\{ \begin{array}{ll} -\operatorname{div}(\mathbf{A}\varepsilon(\mathbf{v}_{b,1})(\mathbf{y}_b)) = \mathbf{0} & \text{in } \mathbb{R}^3 \setminus \omega \\ -\operatorname{div}(\mathbf{A}\varepsilon(\mathbf{v}_{b,1})(\mathbf{y}_b)) = -\xi_{u_1}(\rho)\mathbf{e} & \text{in } \omega \\ \lim_{\mathbf{y}_b \rightarrow \mathbf{0}} \mathbf{v}_{b,1}(\mathbf{y}_b) = \mathbf{0} & \end{array} \right. , \quad (7.88)$$

where $\mathbf{y}_a = \frac{\mathbf{x} - \mathbf{x}_0}{\rho}$, $\mathbf{y}_b = \frac{\mathbf{x} - \mathbf{x}_0 - \ell\mathbf{e}}{\rho}$ and $\xi_{u_1}(\rho) = \frac{\Phi(\rho)}{\rho|\omega|}$. The far fields problem is the same, with or without contact. Therefore, $\mathbf{v}_{a,1}$ and $\mathbf{v}_{b,1}$ satisfy Lemma 9.

- Asymptotic analysis of the perturbed displacement

Let $\mathbf{v}_{\rho,1} = \mathbf{u}_{\rho,1} - \mathbf{u}_1$ be the difference between the perturbed and the background displacement

fields of Step 1. It solves

$$\left\{ \begin{array}{ll} -\operatorname{div}(\mathbf{A}\varepsilon(\mathbf{v}_{\rho,1})) + \mathcal{S}(\mathbf{v}_{\rho,1}) = \mathbf{0} & \text{in } \Omega_\rho \\ -\operatorname{div}(\mathbf{A}\varepsilon(\mathbf{v}_{\rho,1})) = \frac{\Phi(\rho)}{|\omega_A|} \mathbf{e} & \text{in } \omega_A \\ -\operatorname{div}(\mathbf{A}\varepsilon(\mathbf{v}_{\rho,1})) = -\frac{\Phi(\rho)}{|\omega_B|} \mathbf{e} & \text{in } \omega_B . \\ \mathbf{A}\varepsilon(\mathbf{v}_{\rho,1})\mathbf{n} = \mathbf{0} & \text{on } \Gamma_N \\ \mathbf{v}_{\rho,1} = \mathbf{0} & \text{on } \Gamma_D \\ \mathbf{A}\varepsilon(\mathbf{v}_{\rho,1}|_{\mathbf{S}_-})\mathbf{n}_- = \mathbf{A}\varepsilon(\mathbf{v}_{\rho,1}|_{\mathbf{S}_+})\mathbf{n}_- = -\phi_r([\mathbf{u}_{\rho,1}] \cdot \mathbf{n}_-)\mathbf{n}_- + \phi_r([\mathbf{u}_1] \cdot \mathbf{n}_-)\mathbf{n}_- & \text{on } \mathbf{S} \end{array} \right. \quad (7.89)$$

The field $\mathbf{v}_{\rho,1}$ is as smooth as $\mathbf{u}_{\rho,1}$ and \mathbf{u}_1 .

Remark 69. In (7.89), the contact term is expected to depend on $\mathbf{v}_{\rho,1}$ on \mathbf{S} . However, the function ϕ_r is not linear. Therefore, to obtain explicitly $\mathbf{v}_{\rho,1}$ in the contact condition, one has to perform a Taylor expansion of $\phi_r([\mathbf{u}_{\rho,1}] \cdot \mathbf{n}_-)$. Nevertheless, the occurrence of $\mathbf{u}_{\rho,1}$ and \mathbf{u}_1 is kept for further use.

As usual, the rescaled function \mathbf{v}_1 is defined by

$$\mathbf{v}_1(\mathbf{x}) = \mathbf{v}_{a,1} \left(\frac{\mathbf{x} - \mathbf{x}_0}{\rho} \right) + \mathbf{v}_{b,1} \left(\frac{\mathbf{x} - \mathbf{x}_0 - \ell \mathbf{e}}{\rho} \right).$$

As proved by the following result, in some sense, \mathbf{v}_1 is the limit of $\mathbf{v}_{\rho,1}$ as ρ goes to zero.

Proposition 18. Let $\theta \in \mathcal{C}_c^\infty(\Omega)$ be a cut-off function with compact support $\mathcal{U}_+ \subset \Omega$ such that $\theta \equiv 1$ in a neighborhood $\mathcal{U}_A \subset \mathcal{U}_+$ of \mathbf{x}_0 and $\theta \equiv 1$ in a neighborhood $\mathcal{U}_B \subset \mathcal{U}_+$ of $\mathbf{x}_0 + \ell \mathbf{e}$. There exists a constant $C > 0$ independent of ρ such that

$$\mathbf{v}_{\rho,1} = \theta \mathbf{v}_1 + \boldsymbol{\delta}_1, \quad (7.90)$$

with

$$\|\mathbf{v}_1\|_{L^2(\Omega)} \leq C\rho^q, \quad (7.91)$$

$$\|\varepsilon(\mathbf{v}_1)\|_{L^2(\Omega)} \leq C\rho^{q-1/2}, \quad (7.92)$$

$$\|\boldsymbol{\delta}\|_{H^1(\Omega)} \leq C\rho^q. \quad (7.93)$$

Remark 70. Denote $\mathcal{U}_- = \mathcal{U}_A \cup \mathcal{U}_B$. Based on the systems (7.88), the far fields $\mathbf{v}_{a,1}$ and $\mathbf{v}_{b,1}$ do not consider the contact interface (no more than other boundaries). Then, the cut-off function vanishes on \mathbf{S} to make sure that the product $\theta \mathbf{v}_1$ satisfy homogeneous boundary condition on $\partial\Omega$.

Proof. The behavior at infinity of the far fields has been studied in the proof of Proposition 15 and we have $\|\mathbf{v}_1\|_{L^\infty(\Omega \setminus \mathcal{U}_-)} \leq C\rho^q$ and $\|\varepsilon(\mathbf{v}_1)\|_{L^\infty(\Omega \setminus \mathcal{U}_-)} \leq C\rho^q$. The L^2 -norms of \mathbf{v} and $\varepsilon(\mathbf{v})$ have also been estimated in the proof of Proposition 15 so that $\|\mathbf{v}_1\|_{L^2(\Omega)} \leq C\rho^q$ and $\|\varepsilon(\mathbf{v}_1)\|_{L^2(\Omega)} \leq C\rho^{q-1/2}$. The key point here is to handle the influence of the contact term in the error term $\boldsymbol{\delta}_1$. We write the system of equations satisfied by $\boldsymbol{\delta}_1$

$$\left\{ \begin{array}{ll} -\operatorname{div}(\mathbf{A}\varepsilon(\boldsymbol{\delta}_1)) + \mathcal{S}(\boldsymbol{\delta}_1) = \operatorname{div}\mathbf{A}(\mathbf{v}_1 \otimes \nabla\theta)^s + \mathbf{A}\varepsilon(\mathbf{v}_1)\nabla\theta & \text{in } \Omega \\ \mathbf{A}\varepsilon(\boldsymbol{\delta}_1)\mathbf{n} = \mathbf{0} & \text{on } \Gamma_N \\ \boldsymbol{\delta}_1 = \mathbf{0} & \text{on } \Gamma_D \\ \mathbf{A}\varepsilon(\boldsymbol{\delta}_1|_{\mathbf{S}_-})\mathbf{n}_- = \mathbf{A}\varepsilon(\boldsymbol{\delta}_1|_{\mathbf{S}_+})\mathbf{n}_- = -\phi_r([\mathbf{u}_{\rho,1}] \cdot \mathbf{n}_-)\mathbf{n}_- + \phi_r([\mathbf{u}_1] \cdot \mathbf{n}_-)\mathbf{n}_- & \text{on } \mathbf{S} \end{array} \right. \quad (7.94)$$

The variational formulation of (7.94) with $\boldsymbol{\delta}_1$ as test function gives

$$\begin{aligned} \int_{\Omega} \boldsymbol{S}(\boldsymbol{\delta}_1) \cdot \boldsymbol{\delta}_1 dV + \int_{\Omega} \mathbf{A}\varepsilon(\boldsymbol{\delta}_1) : \varepsilon(\boldsymbol{\delta}_1) dV &= - \int_{\Omega} \mathbf{A}(\mathbf{v}_1 \otimes \nabla\theta)^s : \varepsilon(\boldsymbol{\delta}_1) dV + \int_{\Omega} \mathbf{A}\varepsilon(\mathbf{v}_1) \nabla\theta \cdot \boldsymbol{\delta}_1 dV \\ &+ \int_{\mathbf{S}} \mathbf{A}\varepsilon(\boldsymbol{\delta}_1|_{\mathbf{s}_-}) \mathbf{n}_- \cdot [\boldsymbol{\delta}_1] dS. \end{aligned}$$

Only the last term of the right hand side is estimated. The others have already been estimated in the proof of Proposition 15. Using the explicit expression of boundary terms on \mathbf{S} , it follows

$$\int_{\mathbf{S}} \mathbf{A}(\mathbf{v}_1|_{\mathbf{s}_-} \otimes \nabla\theta)^s \mathbf{n}_- \cdot \boldsymbol{\delta}_1|_{\mathbf{s}_-} dS = - \int_{\mathbf{S}} (\phi_r([\mathbf{u}_{\rho,1}] \cdot \mathbf{n}_-) - \phi_r([\mathbf{u}_1] \cdot \mathbf{n}_-)) \mathbf{n}_- \cdot [\boldsymbol{\delta}_1] dS.$$

The right hand side is expressed using the fact that $\boldsymbol{\delta}_1 = \mathbf{u}_{\rho,1} - \mathbf{u}_1 - \theta \mathbf{v}_1$ and that θ is zero on \mathbf{S} .

$$\int_{\mathbf{S}} \mathbf{A}\varepsilon(\boldsymbol{\delta}_1|_{\mathbf{s}_-}) \mathbf{n}_- \cdot [\boldsymbol{\delta}_1] dS = - \int_{\mathbf{S}} (\phi_r([\mathbf{u}_{\rho,1}] \cdot \mathbf{n}_-) - \phi_r([\mathbf{u}_1] \cdot \mathbf{n}_-)) ([\mathbf{u}_{\rho,1}] \cdot \mathbf{n}_- - [\mathbf{u}_1] \cdot \mathbf{n}_-) dS.$$

By definition, ϕ_r is a non-decreasing function, so that

$$(\phi_r([\mathbf{u}_{\rho,1}] \cdot \mathbf{n}_-) - \phi_r([\mathbf{u}_1] \cdot \mathbf{n}_-)) ([\mathbf{u}_{\rho,1}] \cdot \mathbf{n}_- - [\mathbf{u}_1] \cdot \mathbf{n}_-) \geq 0.$$

This non-negative term is then passed to the left-hand side and can be ignored in the analysis. In other words, the estimate of the L^2 -norm of $\boldsymbol{\delta}_1$ is the same with or without the contact model. Then,

$$\exists C > 0, \|\varepsilon(\boldsymbol{\delta}_1)\|_{L^2(\Omega)} \leq C\rho^q.$$

□

7.3.3 Step 2

The transmission condition at the interface of Section 7.1.2 is replaced by a sliding contact model. The background displacement fields solves

$$\left\{ \begin{array}{ll} -\operatorname{div}(\mathbf{A}\varepsilon(\mathbf{u}_2)) + \boldsymbol{S}(\mathbf{u}_2) = \mathbf{t} & \text{in } \Omega \\ \mathbf{A}\varepsilon(\mathbf{u}_2)\mathbf{n} = \mathbf{g} & \text{on } \Gamma_N \\ \mathbf{u}_2 = \mathbf{0} & \text{on } \Gamma_D \\ \mathbf{A}\varepsilon(\mathbf{u}_2|_{\mathbf{s}_-})\mathbf{n}_- = \mathbf{A}\varepsilon(\mathbf{u}_2|_{\mathbf{s}_+})\mathbf{n}_- = -\phi_r([\mathbf{u}_2] \cdot \mathbf{n}_-)\mathbf{n}_- & \text{on } \mathbf{S} \end{array} \right. \quad (7.95)$$

The background displacement field \mathbf{u}_2 is assumed to be smooth enough, which is true if the loads \mathbf{t} and \mathbf{g} are smooth, so are the domain and the regularized function ϕ_r . The objective function is still given in the generic form

$$J_0(\Omega) = \int_{\Omega_1} F(\mathbf{u}_2) dV + \int_{\Gamma_N} G(\mathbf{u}_2) dS. \quad (7.96)$$

Then the adjoint state \mathbf{p}_2 associated to (7.95) for a generic objective function (7.96) verifies

$$\left\{ \begin{array}{ll} -\operatorname{div}(\mathbf{A}\varepsilon(\mathbf{p}_2)) + \boldsymbol{S}(\mathbf{p}_2) = -\mathbf{F}'(\mathbf{u}_2)\mathbb{1}_{\Omega_1} & \text{in } \Omega \\ \mathbf{A}\varepsilon(\mathbf{p}_2)\mathbf{n} = -\mathbf{G}'(\mathbf{u}_2) & \text{on } \Gamma_N \\ \mathbf{p}_2 = \mathbf{0} & \text{on } \Gamma_D \\ \mathbf{A}\varepsilon(\mathbf{p}_2|_{\mathbf{s}_-})\mathbf{n}_- = \mathbf{A}\varepsilon(\mathbf{p}_2|_{\mathbf{s}_+})\mathbf{n}_- = -[\mathbf{p}_2] \cdot \mathbf{n}_- \phi_r'([\mathbf{u}_2] \cdot \mathbf{n}_-)\mathbf{n}_- & \text{on } \mathbf{S} \end{array} \right. \quad (7.97)$$

The adjoint state \mathbf{p}_2 is assumed to be as smooth as required, similarly to the assumptions on \mathbf{u}_2 . The perturbed displacement field solves

$$\left\{ \begin{array}{ll} -\operatorname{div}(\mathbf{A}\varepsilon(\mathbf{u}_{\rho,2})) + \mathcal{S}(\mathbf{u}_{\rho,2}) = \mathbf{t} & \text{in } \Omega_\rho \\ -\operatorname{div}(\mathbf{A}\varepsilon(\mathbf{u}_{\rho,2})) - \frac{\kappa(\rho)}{|\omega_A|} \left(\int_{\omega_B} \mathbf{u}_{\rho,2} \cdot \mathbf{e} dV - \int_{\omega_A} \mathbf{u}_{\rho,2} \cdot \mathbf{e} dV \right) \mathbf{e} = \frac{T(\rho)}{|\omega_A|} \mathbf{e} & \text{in } \omega_A \\ -\operatorname{div}(\mathbf{A}\varepsilon(\mathbf{u}_{\rho,2})) + \frac{\kappa(\rho)}{|\omega_B|} \left(\int_{\omega_B} \mathbf{u}_{\rho,2} \cdot \mathbf{e} dV - \int_{\omega_A} \mathbf{u}_{\rho,2} \cdot \mathbf{e} dV \right) \mathbf{e} = -\frac{T(\rho)}{|\omega_B|} \mathbf{e} & \text{in } \omega_B, \\ \mathbf{A}\varepsilon(\mathbf{u}_{\rho,2})\mathbf{n} = \mathbf{g} & \text{on } \Gamma_N \\ \mathbf{u}_{\rho,2} = \mathbf{0} & \text{on } \Gamma_D \\ \mathbf{A}\varepsilon(\mathbf{u}_{\rho,2}|_{\mathbf{s}_-})\mathbf{n}_- = \mathbf{A}\varepsilon(\mathbf{u}_{\rho,2}|_{\mathbf{s}_+})\mathbf{n}_- = -\phi_r([\mathbf{u}_{\rho,2}] \cdot \mathbf{n}_-)\mathbf{n}_- & \text{on } \mathbf{S} \end{array} \right. \quad (7.98)$$

where the apparent tension force is

$$T(\rho) = -\kappa(\rho) \left(\int_{\omega_B} \mathbf{u}_{\rho,1} \cdot \mathbf{e} dV - \int_{\omega_A} \mathbf{u}_{\rho,1} \cdot \mathbf{e} dV \right) + \Phi(\rho).$$

The smoothness of $\mathbf{u}_{\rho,2}$ is given by the regularity of ϕ_r and the smoothness of the loads and of the domain. The objective function in the perturbed domain reads

$$J_\rho(\Omega) = \int_{\Omega_1} F(\mathbf{u}_{\rho,2}) dV + \int_{\Gamma_N} G(\mathbf{u}_{\rho,2}) dS. \quad (7.99)$$

Theorem 7. Take ω to be the unit ball of \mathbb{R}^3 . Let us set

$$\begin{aligned} \mathbf{U}_1 &= \mathbf{u}_1(\mathbf{x}_0 + \ell\mathbf{e}) - \mathbf{u}_1(\mathbf{x}_0), \\ \mathbf{U}_2 &= \mathbf{u}_2(\mathbf{x}_0 + \ell\mathbf{e}) - \mathbf{u}_2(\mathbf{x}_0), \\ \mathbf{P}_2 &= \mathbf{p}_2(\mathbf{x}_0 + \ell\mathbf{e}) - \mathbf{p}_2(\mathbf{x}_0), \end{aligned} \quad (7.100)$$

where \mathbf{u}_1 , \mathbf{u}_2 and \mathbf{p}_2 are respectively solution of the background problems (7.7), (7.9) and the adjoint problem in the background domain (7.12). The general objective function (7.15) admits a topological asymptotic expansion of the form (7.16), for various values of k and q with

$$\tau_A = \frac{15}{2} \frac{\mu_A(2\mu_A + \lambda_A)}{(5\mu_A + 2\lambda_A)r_1^2}, \quad \tau_B = \frac{15}{2} \frac{\mu_B(2\mu_B + \lambda_B)}{(5\mu_B + 2\lambda_B)r_1^2} \quad \text{and } r_1 = 1 \text{ the radius of the unit ball, that is}$$

$$J_\rho(\Omega) = J_0(\Omega) + s(\rho)DJ(\mathbf{x}_0, \mathbf{e}) + \mathcal{R}(s(\rho)). \quad (7.101)$$

The expressions of $s(\rho)$, $DJ(\mathbf{x}_0, \mathbf{e})$ and $\mathcal{R}(s(\rho))$ are the same as in Theorem 6.

Approximation of the perturbed displacement field

• Far fields expressions

As usual, the behavior of the perturbed displacement field is first approximated with far fields $\mathbf{v}_{a,2}$ and $\mathbf{v}_{b,2}$ such that

$$\mathbf{u}_{\rho,2}(\mathbf{x}) \approx \mathbf{u}_2(\mathbf{x}) + \mathbf{v}_{a,2} \left(\frac{\mathbf{x} - \mathbf{x}_0}{\rho} \right) + \mathbf{v}_{b,2} \left(\frac{\mathbf{x} - \mathbf{x}_0 - \ell\mathbf{e}}{\rho} \right), \quad (7.102)$$

with $\lim_{\mathbf{y} \rightarrow \mathbf{0}} \mathbf{v}_{a,2}(\mathbf{y}) = \mathbf{0}$ and $\lim_{\mathbf{y} \rightarrow \mathbf{0}} \mathbf{v}_{b,2}(\mathbf{y}) = \mathbf{0}$. Since these far fields ignore the contact interface, the rescaled problem is identical to the one described in Section 7.2.2. Thus, the functions $\mathbf{v}_{a,2}$ and $\mathbf{v}_{b,2}$ satisfy Lemma 10.

• **Asymptotic analysis of the perturbed displacement**

Let $\mathbf{v}_{\rho,2} = \mathbf{u}_{\rho,2} - \mathbf{u}_2$ be the difference between the perturbed and the background displacement fields of the second step. The field $\mathbf{v}_{\rho,2}$ is as smooth as $\mathbf{u}_{\rho,2}$ and \mathbf{u}_2 . It solves

$$\left\{ \begin{array}{ll} -\operatorname{div}(\mathbf{A}\varepsilon(\mathbf{v}_{\rho,2})) + \mathcal{S}(\mathbf{v}_{\rho,2}) = \mathbf{0} & \text{in } \Omega_\rho \\ -\operatorname{div}(\mathbf{A}\varepsilon(\mathbf{v}_{\rho,2})) - \frac{\kappa(\rho)}{|\omega_A|} \left(\int_{\omega_B} (\mathbf{v}_{\rho,2} + \mathbf{u}_2) \cdot \mathbf{e} dV - \int_{\omega_A} (\mathbf{v}_{\rho,2} + \mathbf{u}_2) \cdot \mathbf{e} dV \right) \mathbf{e} = \frac{T(\rho)}{|\omega_A|} \mathbf{e} & \text{in } \omega_A \\ -\operatorname{div}(\mathbf{A}\varepsilon(\mathbf{v}_{\rho,2})) + \frac{\kappa(\rho)}{|\omega_A|} \left(\int_{\omega_B} (\mathbf{v}_{\rho,2} + \mathbf{u}_2) \cdot \mathbf{e} dV - \int_{\omega_A} (\mathbf{v}_{\rho,2} + \mathbf{u}_2) \cdot \mathbf{e} dV \right) \mathbf{e} = -\frac{T(\rho)}{|\omega_B|} \mathbf{e} & \text{in } \omega_B \\ \mathbf{A}\varepsilon(\mathbf{v}_{\rho,2})\mathbf{n} = \mathbf{0} & \text{on } \Gamma_N \\ \mathbf{v}_{\rho,2} = \mathbf{0} & \text{on } \Gamma_D \\ \mathbf{A}\varepsilon(\mathbf{v}_{\rho,2}|_{\mathbf{s}_-})\mathbf{n}_- = \mathbf{A}\varepsilon(\mathbf{v}_{\rho,2}|_{\mathbf{s}_+})\mathbf{n}_- = -\phi_r([\mathbf{u}_{\rho,2}] \cdot \mathbf{n}_-)\mathbf{n}_- + \phi_r([\mathbf{u}_2] \cdot \mathbf{n}_-)\mathbf{n}_- & \text{on } \mathbf{S} \end{array} \right. \quad (7.103)$$

Remark 71. As already noticed in the analysis of Step 1, in Remark 69, the contact term involves $\mathbf{u}_{\rho,2}$ and \mathbf{u}_2 instead of $\mathbf{v}_{\rho,2}$.

As usual, we define the rescaled function \mathbf{v}_2 such that

$$\mathbf{v}_2(\mathbf{x}) = \mathbf{v}_{a,2} \left(\frac{\mathbf{x} - \mathbf{x}_0}{\rho} \right) + \mathbf{v}_{b,2} \left(\frac{\mathbf{x} - \mathbf{x}_0 - \ell \mathbf{e}}{\rho} \right). \quad (7.104)$$

The proposition below proves that \mathbf{v}_2 is, in some sense, the limit of $\mathbf{v}_{\rho,2}$ as ρ goes to zero.

Proposition 19. Let $\theta \in \mathcal{C}_c^\infty(\Omega)$ be a cut-off function with compact support $\mathcal{U}_+ \subset \Omega$ such that $\theta \equiv 1$ in a neighborhood $\mathcal{U}_A \subset \mathcal{U}_+$ of \mathbf{x}_0 and $\theta \equiv 1$ in a neighborhood $\mathcal{U}_B \subset \mathcal{U}_+$ of $\mathbf{x}_0 + \ell \mathbf{e}$. We have

$$\mathbf{v}_{\rho,2} = \theta \mathbf{v}_2 + \boldsymbol{\delta}_2, \quad (7.105)$$

where $\boldsymbol{\delta}_2$ is a small remainder term as can be checked by these estimates of the L^2 -norms of \mathbf{v}_2 and $\varepsilon(\mathbf{v}_2)$ and the H^1 -norm of $\boldsymbol{\delta}_2$. They are given, according to the value of the exponents k and q , by

	$q > 1$			$q = 1$	$1 > q > 0$	$q > 1$			$q = 1$	$1 > q > 1/2$
$k > 1$	$k > q$	$O(\rho^q)$		$O(\rho)$	$O(\rho^q)$	$k > 1$	$k > q$	$O(\rho^{q-1/2})$	$O(\sqrt{\rho})$	$O(\rho^{q-1/2})$
	$k \leq q$	$O(\rho^k)$					$k \leq q$	$O(\rho^{k-1/2})$		
$k = 1$	$O(\rho)$			$O(\rho)$	$O(\rho^q)$	$k = 1$	$O(\sqrt{\rho})$			$O(\rho^{q-1/2})$
$k < 1$	$O(\rho)$			$O(\rho)$	$O(\rho^q)$	$k < 1$	$O(\sqrt{\rho})$			$O(\rho^{q-1/2})$
Estimates of $\ \mathbf{v}_2\ _{L^2(\Omega)}$ and $\ \boldsymbol{\delta}_2\ _{H^1(\Omega)}$						Estimates of $\ \varepsilon(\mathbf{v}_2)\ _{L^2(\Omega)}$				

Remark 72. Denote $\mathcal{U}_- = \mathcal{U}_A \cup \mathcal{U}_B$. Since the far fields $\mathbf{v}_{a,1}$ and $\mathbf{v}_{b,1}$ do not ignore the contact interface, the cut-off function vanishes on \mathbf{S} to make sure that the product $\theta \mathbf{v}_1$ satisfy homogeneous boundary condition on $\partial\Omega$.

Proof. Propositions 16 and 19 give the same estimates of $\|\mathbf{v}_2\|_{L^2(\Omega)}$, $\|\varepsilon(\mathbf{v}_2)\|_{L^2(\Omega)}$ and $\|\delta_2\|_{H^1(\Omega)}$. The goal of this proof is to show that the contact term does not affect the asymptotic analysis. Since the far fields are independent of the contact behavior, estimates of $\|\mathbf{v}_2\|_{L^2(\Omega)}$ and $\|\varepsilon(\mathbf{v}_2)\|_{L^2(\Omega)}$ are established in the proof of Proposition 16. Only the error term δ_2 is affected by the contact. Let us write the system of equations satisfied by δ_2

$$\left\{ \begin{array}{l} -\operatorname{div}(\mathbf{A}\varepsilon(\delta_2)) + \mathbf{S}(\delta_2) = \operatorname{div}\mathbf{A}(\mathbf{v}_2 \otimes \nabla\theta)^s + \mathbf{A}\varepsilon(\mathbf{v}_2)\nabla\theta \quad \text{in } \Omega_\rho \\ -\operatorname{div}(\mathbf{A}\varepsilon(\delta_2)) - \frac{\kappa(\rho)}{|\omega_A|} \left(\int_{\omega_B} (\delta_2 - \delta_1) \cdot \mathbf{e} dV - \int_{\omega_A} (\delta_2 - \delta_1) \cdot \mathbf{e} dV \right) \mathbf{e} \\ = \frac{\kappa(\rho)}{|\omega_A|} \left(\int_{\omega_B} \mathbf{u}_2 \cdot \mathbf{e} dV - \int_{\omega_A} \mathbf{u}_2 \cdot \mathbf{e} dV - (\mathbf{u}_2(\mathbf{x}_0 + \ell\mathbf{e}) - \mathbf{u}_2(\mathbf{x}_0)) \cdot \mathbf{e} \right) \mathbf{e} \\ - \frac{\kappa(\rho)}{|\omega_A|} \left(\int_{\omega_B} \mathbf{u}_1 \cdot \mathbf{e} dV - \int_{\omega_A} \mathbf{u}_1 \cdot \mathbf{e} dV - (\mathbf{u}_1(\mathbf{x}_0 + \ell\mathbf{e}) - \mathbf{u}_1(\mathbf{x}_0)) \cdot \mathbf{e} \right) \mathbf{e} \quad \text{in } \omega_A \\ -\operatorname{div}(\mathbf{A}\varepsilon(\delta_2)) + \frac{\kappa(\rho)}{|\omega_B|} \left(\int_{\omega_B} (\delta_2 - \delta_1) \cdot \mathbf{e} dV - \int_{\omega_A} (\delta_2 - \delta_1) \cdot \mathbf{e} dV \right) \mathbf{e} \\ = -\frac{\kappa(\rho)}{|\omega_B|} \left(\int_{\omega_B} \mathbf{u}_2 \cdot \mathbf{e} dV - \int_{\omega_A} \mathbf{u}_2 \cdot \mathbf{e} dV - (\mathbf{u}_2(\mathbf{x}_0 + \ell\mathbf{e}) - \mathbf{u}_2(\mathbf{x}_0)) \cdot \mathbf{e} \right) \mathbf{e} \\ + \frac{\kappa(\rho)}{|\omega_B|} \left(\int_{\omega_B} \mathbf{u}_1 \cdot \mathbf{e} dV - \int_{\omega_A} \mathbf{u}_1 \cdot \mathbf{e} dV - (\mathbf{u}_1(\mathbf{x}_0 + \ell\mathbf{e}) - \mathbf{u}_1(\mathbf{x}_0)) \cdot \mathbf{e} \right) \mathbf{e} \quad \text{in } \omega_B \\ \mathbf{A}\varepsilon(\delta_2)\mathbf{n} = \mathbf{0} \quad \text{on } \Gamma_N \\ \delta_2 = \mathbf{0} \quad \text{on } \Gamma_D \\ \mathbf{A}\varepsilon(\delta_2|_{\mathbf{S}_-})\mathbf{n}_- = \mathbf{A}\varepsilon(\delta_2|_{\mathbf{S}_+})\mathbf{n}_- = -\phi_r([\mathbf{u}_{\rho,2}] \cdot \mathbf{n}_-)\mathbf{n}_- + \phi_r([\mathbf{u}_2] \cdot \mathbf{n}_-)\mathbf{n}_- \quad \text{on } \mathbf{S} \end{array} \right. \quad (7.106)$$

Denote respectively $\mathbf{R}_{u_1}^A$ and $\mathbf{R}_{u_2}^A$ the integral remainder of the Taylor expansions with integral remainder at first order of \mathbf{u}_1 and \mathbf{u}_2 in a neighborhood of \mathbf{x}_0 . Similar functions, $\mathbf{R}_{u_1}^B$ and $\mathbf{R}_{u_2}^B$, are set in a neighborhood of $\mathbf{x}_0 + \ell\mathbf{e}$. These functions are respectively of the order of ρ^2 in ω_A and ω_B . Then, let us multiply (7.106) by δ_2 , integrate by parts and apply the Taylor expansion of \mathbf{u}_1 and

\mathbf{u}_2 . The term $\frac{\kappa(\rho)}{4} \left(\int_{\omega_B} \delta_1 \cdot \mathbf{e} dV - \int_{\omega_A} \delta_1 \cdot \mathbf{e} dV \right)^2$ is added on the left and right hand sides so that

$$\begin{aligned}
& \int_{\Omega} \mathbf{A}\varepsilon(\boldsymbol{\delta}_2) : \varepsilon(\boldsymbol{\delta}_2) dV + \int_{\Omega_\rho} \mathcal{S}(\boldsymbol{\delta}_2) \cdot \boldsymbol{\delta}_2 dV \\
& + \kappa(\rho) \left(\int_{\omega_B} \boldsymbol{\delta}_2 \cdot \mathbf{e} dV - \int_{\omega_A} \boldsymbol{\delta}_2 \cdot \mathbf{e} dV - \frac{1}{2} \left(\int_{\omega_B} \boldsymbol{\delta}_1 \cdot \mathbf{e} dV - \int_{\omega_A} \boldsymbol{\delta}_1 \cdot \mathbf{e} dV \right) \right)^2 \\
& = - \int_{\Omega_\rho} \mathbf{A}(\mathbf{v}_2 \otimes \nabla\theta)^s : \varepsilon(\boldsymbol{\delta}_2) dV + \int_{\Omega_\rho} \mathbf{A}\varepsilon(\mathbf{v}_2) \nabla\theta \cdot \boldsymbol{\delta}_2 dV + \frac{\kappa(\rho)}{4} \left(\int_{\omega_B} \boldsymbol{\delta}_1 \cdot \mathbf{e} dV - \int_{\omega_A} \boldsymbol{\delta}_1 \cdot \mathbf{e} dV \right)^2 \\
& - \kappa(\rho) \left(\int_{\omega_B} (\mathbf{R}_{u_2}^B - \mathbf{R}_{u_1}^B) \cdot \mathbf{e} dV - \int_{\omega_A} (\mathbf{R}_{u_2}^A - \mathbf{R}_{u_1}^A) \cdot \mathbf{e} dV \right) \left(\int_{\omega_B} \boldsymbol{\delta}_2 \cdot \mathbf{e} dV - \int_{\omega_A} \boldsymbol{\delta}_2 \cdot \mathbf{e} dV \right) \\
& + \int_{\mathbb{S}} \mathbf{A}\varepsilon(\boldsymbol{\delta}_2|_{\mathbb{S}_-}) \mathbf{n}_- \cdot [\boldsymbol{\delta}_2] dS.
\end{aligned}$$

The left-hand side is as usual bounded from below with the Poincaré-Korn's inequality and using the fact that the quadratic term $\mathcal{S}(\boldsymbol{\delta}_2) \cdot \boldsymbol{\delta}_2$ is positive

$$\exists C > 0, \left| \int_{\Omega} \mathbf{A}\varepsilon(\boldsymbol{\delta}_2) : \varepsilon(\boldsymbol{\delta}_2) dV \right| \geq C \|\varepsilon(\boldsymbol{\delta}_2)\|_{L^2(\Omega)}^2.$$

The first two right-hand terms are estimated as previously

$$\exists C > 0, \left| \int_{\Omega_\rho} \mathbf{A}(\mathbf{v}_2 \otimes \nabla\theta)^s : \varepsilon(\boldsymbol{\delta}_2) dV \right| + \left| \int_{\Omega_\rho} \mathbf{A}\varepsilon(\mathbf{v}_2) \nabla\theta \cdot \boldsymbol{\delta}_2 dV \right| \leq C\rho |\xi_{u_2}(\rho)| \|\varepsilon(\boldsymbol{\delta}_2)\|_{L^2(\Omega)}.$$

Using the fact that $\theta = 0$ on \mathbb{S} , the variational formulation of (7.89) with $\boldsymbol{\delta}_1$ as test function gives

$$-\Phi(\rho) \left(\int_{\omega_B} \boldsymbol{\delta}_1 \cdot \mathbf{e} dV - \int_{\omega_A} \boldsymbol{\delta}_1 \cdot \mathbf{e} dV \right) = \int_{\Omega_\rho} \operatorname{div} \mathbf{A}(\mathbf{v}_1 \otimes \nabla\theta)^s \cdot \mathbf{v}_{\rho,1} dV + \int_{\Omega_\rho} \mathbf{A}\varepsilon(\mathbf{v}_1) \nabla\theta \cdot \mathbf{v}_{\rho,1} dV$$

This is the same estimate as the one of the contact-less model. Then, it holds

$$\exists C > 0, \left| \int_{\omega_B} \boldsymbol{\delta}_1 \cdot \mathbf{e} dV - \int_{\omega_A} \boldsymbol{\delta}_1 \cdot \mathbf{e} dV \right| \leq C\rho^q.$$

The difference of the averages of $\boldsymbol{\delta}_2$ is estimated likewise. We write the variational formulation of (7.89) with $\boldsymbol{\delta}_2$ as test function

$$\begin{aligned}
\Phi(\rho) \left(\int_{\omega_B} \boldsymbol{\delta}_2 \cdot \mathbf{e} dV - \int_{\omega_A} \boldsymbol{\delta}_2 \cdot \mathbf{e} dV \right) & = - \int_{\Omega_\rho} \mathcal{S}(\mathbf{v}_{\rho,1}) \cdot \boldsymbol{\delta}_2 dV - \int_{\Omega} \mathbf{A}\varepsilon(\mathbf{v}_{\rho,1}) : \varepsilon(\boldsymbol{\delta}_2) dV + \int_{\mathbb{S}} \mathbf{A}\varepsilon(\mathbf{v}_{\rho,1}|_{\mathbb{S}_-}) \mathbf{n}_- \cdot [\boldsymbol{\delta}_2] dS \\
& = - \sum_{i=1}^n \kappa_i \left(\int_{\omega_{B_i}} \boldsymbol{\delta}_1 \cdot \mathbf{e} dV - \int_{\omega_{A_i}} \boldsymbol{\delta}_1 \cdot \mathbf{e} dV \right) \left(\int_{\omega_{B_i}} \boldsymbol{\delta}_2 \cdot \mathbf{e} dV - \int_{\omega_{A_i}} \boldsymbol{\delta}_2 \cdot \mathbf{e} dV \right) - \int_{\Omega} \theta \mathbf{A}\varepsilon(\mathbf{v}_1) : \varepsilon(\boldsymbol{\delta}_2) dV \\
& - \int_{\Omega} \mathbf{A}(\mathbf{v}_1 \otimes \nabla\theta)^s : \varepsilon(\boldsymbol{\delta}_2) dV - \int_{\Omega} \mathbf{A}\varepsilon(\boldsymbol{\delta}_1) : \varepsilon(\boldsymbol{\delta}_2) dV - \int_{\mathbb{S}} (\phi_r([\mathbf{u}_{\rho,1}] \cdot \mathbf{n}_-) - \phi_r([\mathbf{u}_1] \cdot \mathbf{n}_-)) [\boldsymbol{\delta}_2] \cdot \mathbf{n}_- dS
\end{aligned}$$

The function ϕ_r is expanded at first order with exact remainder. Then we have

$$\begin{aligned}
\Phi(\rho) & \left(\int_{\omega_B} \boldsymbol{\delta}_2 \cdot \mathbf{e} dV - \int_{\omega_A} \boldsymbol{\delta}_2 \cdot \mathbf{e} dV \right) = - \sum_{i=1}^n \kappa_i \left(\int_{\omega_{B_i}} \boldsymbol{\delta}_1 \cdot \mathbf{e} dV - \int_{\omega_{A_i}} \boldsymbol{\delta}_1 \cdot \mathbf{e} dV \right) \left(\int_{\omega_{B_i}} \boldsymbol{\delta}_2 \cdot \mathbf{e} dV - \int_{\omega_{A_i}} \boldsymbol{\delta}_2 \cdot \mathbf{e} dV \right) \\
& - \int_{\Omega} \theta \mathbf{A} \boldsymbol{\varepsilon}(\mathbf{v}_1) : \boldsymbol{\varepsilon}(\boldsymbol{\delta}_2) dV - \int_{\Omega} \mathbf{A}(\mathbf{v}_1 \otimes \nabla \theta)^s : \boldsymbol{\varepsilon}(\boldsymbol{\delta}_2) dV - \int_{\Omega} \mathbf{A} \boldsymbol{\varepsilon}(\boldsymbol{\delta}_1) : \boldsymbol{\varepsilon}(\boldsymbol{\delta}_2) dV \\
& - \int_{\mathbb{S}} \phi'_r([\mathbf{u}_1] \cdot \mathbf{n}_-) [\mathbf{v}_{\rho,1}] \cdot \mathbf{n}_- [\boldsymbol{\delta}_2] \cdot \mathbf{n}_- dS.
\end{aligned}$$

It follows the estimate

$$\begin{aligned}
\Phi(\rho) \left| \int_{\omega_B} \boldsymbol{\delta}_2 \cdot \mathbf{e} dV - \int_{\omega_A} \boldsymbol{\delta}_2 \cdot \mathbf{e} dV \right| & \leq C \|\boldsymbol{\delta}_1\|_{L^2(\Omega)} \|\boldsymbol{\delta}_2\|_{L^2(\Omega)} + C \|\boldsymbol{\varepsilon}(\mathbf{v}_1)\|_{L^2(\Omega)} \|\boldsymbol{\varepsilon}(\boldsymbol{\delta}_2)\|_{L^2(\Omega)} \\
& + C \|\mathbf{v}_1\|_{L^\infty(\Omega \setminus \mathcal{U}_-)} \|\boldsymbol{\varepsilon}(\boldsymbol{\delta}_2)\|_{L^2(\Omega)} + C \|\boldsymbol{\varepsilon}(\boldsymbol{\delta}_1)\|_{L^2(\Omega)} \|\boldsymbol{\varepsilon}(\boldsymbol{\delta}_2)\|_{L^2(\Omega)} \\
& + C \|\mathbf{v}_{\rho,1}\|_{H^1(\Omega)} \|\boldsymbol{\delta}_2\|_{H^1(\Omega)} + C \|\mathbf{v}_{\rho,1}\|_{H^1(\Omega)}^2 \|\boldsymbol{\delta}_2\|_{H^1(\Omega)} \\
& \leq C \rho^{q-1/2} \|\boldsymbol{\varepsilon}(\boldsymbol{\delta}_2)\|_{L^2(\Omega)}.
\end{aligned}$$

Finally, the difference of averages is estimated as

$$\exists C > 0, \left| \int_{\omega_B} \boldsymbol{\delta}_2 \cdot \mathbf{e} dV - \int_{\omega_A} \boldsymbol{\delta}_2 \cdot \mathbf{e} dV \right| \leq C \rho^{-1/2} \|\boldsymbol{\varepsilon}(\boldsymbol{\delta}_2)\|_{L^2(\Omega)}.$$

Regrouping all terms finally leads to

$$\|\boldsymbol{\varepsilon}(\boldsymbol{\delta}_2)\|_{L^2(\Omega)}^2 \leq (C \rho |\xi_{u_2}(\rho)| + C \rho^{k+3/2}) \|\boldsymbol{\varepsilon}(\boldsymbol{\delta}_2)\|_{L^2(\Omega)} + C \rho^{k+2q} + C \rho^2 |\xi_{u_2}(\rho)|^2.$$

Setting the notations $X = \|\boldsymbol{\varepsilon}(\boldsymbol{\delta}_2)\|_{L^2(\Omega)}$, $a = C \rho |\xi_{u_2}(\rho)| + C \rho^{k+3/2}$, $b = C \rho^{k+2q} + C \rho^2 |\xi_{u_2}(\rho)|^2$, it follows that $X \leq Ca + \sqrt{b}$. Finally,

$$\exists C > 0, \|\boldsymbol{\varepsilon}(\boldsymbol{\delta}_2)\|_{L^2(\Omega)} \leq C \rho |\xi_{u_2}(\rho)| + C \rho^{k+3/2} + C \rho^{k/2+q} \leq C \rho |\xi_{u_2}(\rho)| \text{ for } k > 0.$$

□

Adjoint state

The adjoint state $\mathbf{p}_{\rho,2}$ associated to the perturbed displacement field $\mathbf{u}_{\rho,2}$ solves

$$\left\{ \begin{array}{ll}
-\operatorname{div}(\mathbf{A} \boldsymbol{\varepsilon}(\mathbf{p}_{\rho,2})) + \mathcal{S}(\mathbf{p}_{\rho,2}) = -\mathbf{F}'(\mathbf{u}_2) \mathbf{1}_{\Omega_1} & \text{in } \Omega_\rho \\
-\operatorname{div}(\mathbf{A} \boldsymbol{\varepsilon}(\mathbf{p}_{\rho,2})) - \frac{\kappa(\rho)}{|\omega_A|} \left(\int_{\omega_B} \mathbf{p}_{\rho,2} \cdot \mathbf{e} dV - \int_{\omega_A} \mathbf{p}_{\rho,2} \cdot \mathbf{e} dV \right) \mathbf{e} = \mathbf{0} & \text{in } \omega_A \\
-\operatorname{div}(\mathbf{A} \boldsymbol{\varepsilon}(\mathbf{p}_{\rho,2})) + \frac{\kappa(\rho)}{|\omega_B|} \left(\int_{\omega_B} \mathbf{p}_{\rho,2} \cdot \mathbf{e} dV - \int_{\omega_A} \mathbf{p}_{\rho,2} \cdot \mathbf{e} dV \right) \mathbf{e} = \mathbf{0} & \text{in } \omega_B \cdot \\
\mathbf{A} \boldsymbol{\varepsilon}(\mathbf{p}_{\rho,2}) \mathbf{n} = -\mathbf{G}'(\mathbf{u}_2) & \text{on } \Gamma_N \\
\mathbf{p}_{\rho,2} = \mathbf{0} & \text{on } \Gamma_D \\
\mathbf{A} \boldsymbol{\varepsilon}(\mathbf{p}_{\rho,2}|_{\mathbb{S}_-}) \mathbf{n}_- = \mathbf{A} \boldsymbol{\varepsilon}(\mathbf{p}_{\rho,2}|_{\mathbb{S}_+}) \mathbf{n}_- = -[\mathbf{p}_{\rho,2}] \cdot \mathbf{n}_- \phi'_r([\mathbf{u}_2] \cdot \mathbf{n}_-) \mathbf{n}_- & \text{on } \mathbb{S}
\end{array} \right. \quad (7.107)$$

The adjoint state $\mathbf{p}_{\rho,2}$ is as smooth as required, similarly to assumptions on $\mathbf{u}_{\rho,2}$.

Remark 73. *Once more the perturbed adjoint state $\mathbf{p}_{\rho,2}$ is independent of the pre-stressed state.*

Let us introduce the function \mathbf{q}_2 defined by

$$\mathbf{q}_2(\mathbf{x}) = \mathbf{q}_{a,2} \left(\frac{\mathbf{x} - \mathbf{x}_0}{\rho} \right) + \mathbf{q}_{b,2} \left(\frac{\mathbf{x} - \mathbf{x}_0 - \ell \mathbf{e}}{\rho} \right), \quad (7.108)$$

where $\mathbf{q}_{a,2}$ and $\mathbf{q}_{b,2}$ are far fields respectively centered on ω_A and ω_B . Similarly to $\mathbf{v}_{a,2}$ and $\mathbf{v}_{b,2}$, their behavior is independent of the contact term. Therefore, their explicit expression is unchanged, with or without contact.

Proposition 20. *Let $\theta \in \mathcal{C}_c^\infty(\Omega)$ be a cut-off function with compact support $\mathcal{U}_+ \subset \Omega$ such that $\theta \equiv 1$ in a neighborhood $\mathcal{U}_A \subset \mathcal{U}_+$ of \mathbf{x}_0 and $\theta \equiv 1$ in a neighborhood $\mathcal{U}_B \subset \mathcal{U}_+$ of $\mathbf{x}_0 + \ell \mathbf{e}$. We have*

$$\mathbf{q}_{\rho,2} = \theta \mathbf{q}_2 + \boldsymbol{\eta}_2, \quad (7.109)$$

where $\boldsymbol{\eta}_2$ is a small remainder term as can be checked by these estimates of the L^2 -norms of \mathbf{q}_2 and $\varepsilon(\mathbf{q}_2)$ and the H^1 -norm of $\boldsymbol{\eta}_2$. They are given, according to the value of the exponent k , by

	$\ \mathbf{q}_2\ _{L^2(\Omega)}$	$\ \varepsilon(\mathbf{q}_2)\ _{L^2(\Omega)}$	$\ \boldsymbol{\eta}_2\ _{H^1(\Omega)}$
$k > 1$	$O(\rho^k)$	$O(\rho^{k-1/2})$	$O(\rho^k)$
$k = 1$	$O(\rho)$	$O(\sqrt{\rho})$	$O(\rho)$
$k < 1$	$O(\rho)$	$O(\sqrt{\rho})$	$O(\rho)$

Proof. First, let us write the equations solved by $\boldsymbol{\eta}_2$

$$\left\{ \begin{array}{ll} -\operatorname{div}(\mathbf{A}\varepsilon(\boldsymbol{\eta}_2)) + \boldsymbol{\mathcal{S}}(\boldsymbol{\eta}_2) = \operatorname{div}\mathbf{A}(\mathbf{q}_2 \otimes \nabla\theta)^s + \mathbf{A}\varepsilon(\mathbf{q}_2)\nabla\theta & \text{in } \Omega_\rho \\ -\operatorname{div}(\mathbf{A}\varepsilon(\boldsymbol{\eta}_2)) - \frac{\kappa(\rho)}{|\omega_A|} \left(\int_{\omega_B} \boldsymbol{\eta}_2 \cdot \mathbf{e} dV - \int_{\omega_A} \boldsymbol{\eta}_2 \cdot \mathbf{e} dV \right) \mathbf{e} & \\ = \frac{\kappa(\rho)}{|\omega_A|} \left(\int_{\omega_B} \mathbf{p}_2 \cdot \mathbf{e} dV - \int_{\omega_A} \mathbf{p}_2 \cdot \mathbf{e} dV - (\mathbf{p}_2(\mathbf{x}_0 + \ell \mathbf{e}) - \mathbf{p}_2(\mathbf{x}_0)) \cdot \mathbf{e} \right) \mathbf{e} & \text{in } \omega_A \\ -\operatorname{div}(\mathbf{A}\varepsilon(\boldsymbol{\eta}_2)) + \frac{\kappa(\rho)}{|\omega_B|} \left(\int_{\omega_B} \boldsymbol{\eta}_2 \cdot \mathbf{e} dV - \int_{\omega_A} \boldsymbol{\eta}_2 \cdot \mathbf{e} dV \right) \mathbf{e} & \\ = -\frac{\kappa(\rho)}{|\omega_B|} \left(\int_{\omega_B} \mathbf{p}_2 \cdot \mathbf{e} dV - \int_{\omega_A} \mathbf{p}_2 \cdot \mathbf{e} dV - (\mathbf{p}_2(\mathbf{x}_0 + \ell \mathbf{e}) - \mathbf{p}_2(\mathbf{x}_0)) \cdot \mathbf{e} \right) \mathbf{e} & \text{in } \omega_B \\ \mathbf{A}\varepsilon(\boldsymbol{\eta}_2)\mathbf{n} = \mathbf{0} & \text{on } \Gamma_N \\ \boldsymbol{\eta}_2 = \mathbf{0} & \text{on } \Gamma_D \\ \mathbf{A}\varepsilon(\boldsymbol{\eta}_2|_{\mathcal{S}_-})\mathbf{n}_- = \mathbf{A}\varepsilon(\boldsymbol{\eta}_2|_{\mathcal{S}_+})\mathbf{n}_- = -[\boldsymbol{\eta}_2] \cdot \mathbf{n}_- \phi'_r([\mathbf{u}_2] \cdot \mathbf{n}_-)\mathbf{n}_- & \text{on } \mathcal{S} \end{array} \right. \quad (7.110)$$

This proof aims to evaluate the influence of the contact term in the error estimation $\|\boldsymbol{\eta}_2\|_{H^1(\Omega)}$. We define the functions $\mathbf{R}_{p_2}^A$ and $\mathbf{R}_{p_2}^B$ as the integral remainder of the Taylor expansion at first

order of \mathbf{p}_2 in a neighborhood of \mathbf{x}_0 and $\mathbf{x}_0 + \ell \mathbf{e}$ and respectively of the order of ρ^2 in ω_A and ω_B . Multiplying (7.110) by $\boldsymbol{\eta}_2$ and integrating by parts lead to

$$\begin{aligned} & \int_{\Omega} \mathbf{A}\varepsilon(\boldsymbol{\eta}_2) : \varepsilon(\boldsymbol{\eta}_2) dV + \int_{\Omega_\rho} \mathbf{S}(\boldsymbol{\eta}_2) \cdot \boldsymbol{\eta}_2 dV + \kappa(\rho) \left(\int_{\omega_B} \boldsymbol{\eta}_2 \cdot \mathbf{e} dV - \int_{\omega_A} \boldsymbol{\eta}_2 \cdot \mathbf{e} dV \right)^2 \\ & - \int_{\mathbb{S}} \mathbf{A}\varepsilon(\boldsymbol{\eta}_2|_{\mathbb{S}_-}) \mathbf{n}_- \cdot [\boldsymbol{\eta}_2] dS \\ = & - \int_{\Omega_\rho} \mathbf{A}(\mathbf{q}_2 \otimes \nabla \theta)^s : \varepsilon(\boldsymbol{\eta}_2) dV + \int_{\Omega_\rho} \mathbf{A}\varepsilon(\mathbf{q}_2) \nabla \theta \cdot \boldsymbol{\eta}_2 dV \\ & - \kappa(\rho) \left(\int_{\omega_B} \mathbf{R}_{p_2}^B \cdot \mathbf{e} dV - \int_{\omega_A} \mathbf{R}_{p_2}^A \cdot \mathbf{e} dV \right) \left(\int_{\omega_B} \boldsymbol{\eta}_2 \cdot \mathbf{e} dV - \int_{\omega_A} \boldsymbol{\eta}_2 \cdot \mathbf{e} dV \right). \end{aligned}$$

Focus on the contact term,

$$- \int_{\mathbb{S}} \mathbf{A}\varepsilon(\boldsymbol{\eta}_2|_{\mathbb{S}_-}) \mathbf{n}_- \cdot [\boldsymbol{\eta}_2] dS = \int_{\mathbb{S}} \phi'_r([\mathbf{u}_2] \cdot \mathbf{n}_-) ([\boldsymbol{\eta}_2] \cdot \mathbf{n}_-)^2 dS,$$

it is non-negative because ϕ_r is a non-decreasing function, so that $\phi'_r > 0$. Then, the left-hand side is bounded from below with the Poincaré-Korn inequality

$$\exists C > 0, \left| \int_{\Omega} \mathbf{A}\varepsilon(\boldsymbol{\eta}_2) : \varepsilon(\boldsymbol{\eta}_2) dV \right| \geq C \|\varepsilon(\boldsymbol{\eta}_2)\|_{L^2(\Omega)}^2.$$

The first two right-hand terms are estimated as previously. There exists $C > 0$ such that

$$\begin{aligned} \left| \int_{\Omega_\rho} \mathbf{A}(\mathbf{q}_2 \otimes \nabla \theta)^s : \varepsilon(\boldsymbol{\eta}_2) dV \right| + \left| \int_{\Omega_\rho} \mathbf{A}\varepsilon(\mathbf{q}_2) \nabla \theta \cdot \boldsymbol{\eta}_2 dV \right| & \leq C \|\mathbf{q}_2\|_{L^\infty(\Omega \setminus \mathcal{U}_-)} \|\varepsilon(\boldsymbol{\eta}_2)\|_{L^2(\Omega)} \\ & + C \|\varepsilon(\mathbf{q}_2)\|_{L^\infty(\Omega \setminus \mathcal{U}_-)} \|\boldsymbol{\eta}_2\|_{L^2(\Omega)} \\ & \leq C \rho |\xi_{p_2}(\rho)| \|\varepsilon(\boldsymbol{\eta}_2)\|_{L^2(\Omega)}. \end{aligned}$$

Write the variational formulation of (7.89) with $\boldsymbol{\eta}_2$ as test function and then expand the function ϕ_r at first order with exact remainder

$$\begin{aligned} & \Phi(\rho) \left(\int_{\omega_B} \boldsymbol{\eta}_2 \cdot \mathbf{e} dV - \int_{\omega_A} \boldsymbol{\eta}_2 \cdot \mathbf{e} dV \right) \\ = & - \int_{\Omega_\rho} \mathbf{S}(\mathbf{v}_{\rho,1}) \cdot \boldsymbol{\eta}_2 dV - \int_{\Omega} \mathbf{A}\varepsilon(\mathbf{v}_{\rho,1}) : \varepsilon(\boldsymbol{\eta}_2) dV + \int_{\mathbb{S}} \mathbf{A}\varepsilon([\mathbf{v}_{\rho,1}]) \mathbf{n}_- \cdot [\boldsymbol{\eta}_2] dS \\ = & - \sum_{i=1}^n \kappa_i \left(\int_{\omega_{B_i}} \boldsymbol{\delta}_1 \cdot \mathbf{e} dV - \int_{\omega_{A_i}} \boldsymbol{\delta}_1 \cdot \mathbf{e} dV \right) \left(\int_{\omega_{B_i}} \boldsymbol{\eta}_2 \cdot \mathbf{e} dV - \int_{\omega_{A_i}} \boldsymbol{\eta}_2 \cdot \mathbf{e} dV \right) - \int_{\Omega} \theta \mathbf{A}\varepsilon(\mathbf{v}_1) : \varepsilon(\boldsymbol{\eta}_2) dV \\ & - \int_{\Omega} \mathbf{A}(\mathbf{v}_1 \otimes \nabla \theta)^s : \varepsilon(\boldsymbol{\eta}_2) dV - \int_{\Omega} \mathbf{A}\varepsilon(\boldsymbol{\delta}_1) : \varepsilon(\boldsymbol{\eta}_2) dV - \int_{\mathbb{S}} \phi'_r([\mathbf{u}_1] \cdot \mathbf{n}_-) [\mathbf{v}_{\rho,1}] \cdot \mathbf{n}_- [\boldsymbol{\eta}_2] \cdot \mathbf{n}_- dS \\ & - \frac{1}{2} \int_{\mathbb{S}} \phi''_r([\bar{\mathbf{u}}_1] \cdot \mathbf{n}_-) ([\mathbf{v}_{\rho,1}] \cdot \mathbf{n}_-)^2 [\boldsymbol{\eta}_2] \cdot \mathbf{n}_- dS. \end{aligned}$$

It follows that

$$\begin{aligned} \exists C > 0, \Phi(\rho) \left| \int_{\omega_B} \boldsymbol{\eta}_2 \cdot \mathbf{e} dV - \int_{\omega_A} \boldsymbol{\eta}_2 \cdot \mathbf{e} dV \right| &\leq C \|\boldsymbol{\delta}_1\|_{L^2(\Omega)} \|\boldsymbol{\eta}_2\|_{L^2(\Omega)} + C \|\varepsilon(\mathbf{v}_1)\|_{L^2(\Omega)} \|\varepsilon(\boldsymbol{\eta}_2)\|_{L^2(\Omega)} \\ &+ C \|\mathbf{v}_1\|_{L^\infty(\Omega \setminus \mathcal{U}_-)} \|\varepsilon(\boldsymbol{\eta}_2)\|_{L^2(\Omega)} + C \|\varepsilon(\boldsymbol{\delta}_1)\|_{L^2(\Omega)} \|\varepsilon(\boldsymbol{\eta}_2)\|_{L^2(\Omega)} \\ &+ C \|\mathbf{v}_{\rho,1}\|_{H^1(\Omega)} \|\boldsymbol{\eta}_2\|_{H^1(\Omega)} + C \|\mathbf{v}_{\rho,1}\|_{H^1(\Omega)}^2 \|\boldsymbol{\eta}_2\|_{H^1(\Omega)} \\ &\leq C \rho^{q-1/2} \|\varepsilon(\boldsymbol{\eta}_2)\|_{L^2(\Omega)}. \end{aligned}$$

Thus we have

$$\exists C > 0, \left| \int_{\omega_B} \boldsymbol{\eta}_2 \cdot \mathbf{e} dV - \int_{\omega_A} \boldsymbol{\eta}_2 \cdot \mathbf{e} dV \right| \leq C \rho^{-1/2} \|\varepsilon(\boldsymbol{\eta}_2)\|_{L^2(\Omega)}.$$

Regrouping all terms, it results that

$$\|\varepsilon(\boldsymbol{\eta}_2)\|_{L^2(\Omega)} \leq C \rho |\xi_{p_2}(\rho)| + C \rho^{k+3/2} \leq C \rho |\xi_{p_2}(\rho)| \text{ for } k > 0.$$

□

7.3.4 Proof of the main result

Let us recall the objective function (7.99) in the background domain.

$$J_\rho(\Omega) = \int_{\Omega_1} F(\mathbf{u}_{\rho,2}) dV + \int_{\Gamma_N} G(\mathbf{u}_{\rho,2}) dS.$$

The Taylor expansion at first-order with exact remainder of (7.99) is

$$J_\rho(\Omega) = J_0(\Omega) + \int_{\Omega_1} \mathbf{F}'(\mathbf{u}_2) \cdot \mathbf{v}_{\rho,2} dV + \int_{\Gamma_N} \mathbf{G}'(\mathbf{u}_2) \cdot \mathbf{v}_{\rho,2} dS + \frac{1}{2} \int_{\Omega_1} \mathbf{v}_{\rho,2}^T F''(\bar{\mathbf{u}}_2) \mathbf{v}_{\rho,2} dV + \frac{1}{2} \int_{\Gamma_N} \mathbf{v}_{\rho,2}^T G''(\bar{\mathbf{u}}_2) \mathbf{v}_{\rho,2} dS.$$

The exact remainder terms are bounded as below

$$\begin{aligned} \left| \int_{\Omega_1} \mathbf{v}_{\rho,2}^T F''(\bar{\mathbf{u}}_2) \mathbf{v}_{\rho,2} dV \right| &\leq C \rho^2 |\xi_{u_2}(\rho)|^2 \leq C \frac{\kappa(\rho)^2}{\left(1 + C \frac{\kappa(\rho)}{\rho}\right)^2} + C \frac{\kappa(\rho) \Phi(\rho)}{1 + C \frac{\kappa(\rho)}{\rho}} + C \Phi(\rho)^2, \\ \left| \int_{\Gamma_N} \mathbf{v}_{\rho,2}^T G''(\bar{\mathbf{u}}_2) \mathbf{v}_{\rho,2} dS \right| &\leq C \rho^2 |\xi_{u_2}(\rho)|^2 \leq C \frac{\kappa(\rho)^2}{\left(1 + C \frac{\kappa(\rho)}{\rho}\right)^2} + C \frac{\kappa(\rho) \Phi(\rho)}{1 + C \frac{\kappa(\rho)}{\rho}} + C \Phi(\rho)^2. \end{aligned}$$

Multiplying (7.107) by $\mathbf{v}_{\rho,2}$ and integrating by parts twice, it follows

$$\begin{aligned} &\int_{\Omega_1} \mathbf{F}'(\mathbf{u}_2) \cdot \mathbf{v}_{\rho,2} dV + \int_{\Gamma_N} \mathbf{G}'(\mathbf{u}_2) \cdot \mathbf{v}_{\rho,2} dS \\ &= \left(\kappa(\rho) \left(\int_{\omega_B} \mathbf{u}_2 \cdot \mathbf{e} dV - \int_{\omega_A} \mathbf{u}_2 \cdot \mathbf{e} dV \right) + T(\rho) \right) \left(\int_{\omega_B} \mathbf{p}_{\rho,2} \cdot \mathbf{e} dV - \int_{\omega_A} \mathbf{p}_{\rho,2} \cdot \mathbf{e} dV \right) \\ &\quad - \int_{\mathbb{S}} [\mathbf{p}_{\rho,2}] \cdot \mathbf{n}_- \phi'_r([\mathbf{u}_2] \cdot \mathbf{n}_-) [\mathbf{v}_{\rho,2}] \cdot \mathbf{n}_- dS + \int_{\mathbb{S}} (\phi_r([\mathbf{u}_{\rho,2}] \cdot \mathbf{n}_-) - \phi_r([\mathbf{u}_2] \cdot \mathbf{n}_-)) [\mathbf{p}_{\rho,2}] \cdot \mathbf{n}_- dS. \end{aligned}$$

The function ϕ_r is expanded at first order with exact remainder. It follows

$$\begin{aligned} & \int_{\Omega_1} \mathbf{F}'(\mathbf{u}_2) \cdot \mathbf{v}_{\rho,2} dV + \int_{\Gamma_N} \mathbf{G}'(\mathbf{u}_2) \cdot \mathbf{v}_{\rho,2} dS \\ &= \left(\kappa(\rho) \left(\int_{\omega_B} \mathbf{u}_2 \cdot \mathbf{e} dV - \int_{\omega_A} \mathbf{u}_2 \cdot \mathbf{e} dV \right) + T(\rho) \right) \left(\int_{\omega_B} \mathbf{p}_{\rho,2} \cdot \mathbf{e} dV - \int_{\omega_A} \mathbf{p}_{\rho,2} \cdot \mathbf{e} dV \right) \\ & \quad + \frac{1}{2} \int_{\mathbf{S}} \phi_r''([\bar{\mathbf{u}}_2] \cdot \mathbf{n}_-) ([\mathbf{v}_{\rho,2}] \cdot \mathbf{n}_-)^2 [\mathbf{p}_{\rho,2}] \cdot \mathbf{n}_- dS \end{aligned}$$

The first member of the right-hand side has already been evaluated in Section 7.2.2. The contact term is expected to be a remainder term. Given the fact that $\theta = 0$ on \mathbf{S} , it is expanded as follows

$$\begin{aligned} & \frac{1}{2} \int_{\mathbf{S}} \phi_r''([\bar{\mathbf{u}}_2] \cdot \mathbf{n}_-) ([\mathbf{v}_{\rho,2}] \cdot \mathbf{n}_-)^2 [\mathbf{p}_{\rho,2}] \cdot \mathbf{n}_- dS \\ &= \frac{1}{2} \int_{\mathbf{S}} \phi_r''([\bar{\mathbf{u}}_2] \cdot \mathbf{n}_-) ([\boldsymbol{\delta}_2] \cdot \mathbf{n}_-)^2 [\mathbf{p}_2] \cdot \mathbf{n}_- dS + \frac{1}{2} \int_{\mathbf{S}} \phi_r''([\bar{\mathbf{u}}_2] \cdot \mathbf{n}_-) ([\boldsymbol{\delta}_2] \cdot \mathbf{n}_-)^2 [\boldsymbol{\eta}_2] \cdot \mathbf{n}_- dS. \end{aligned}$$

Estimates are established with Cauchy-Schwarz inequality and the Trace inequality as follows

$$\begin{aligned} \frac{1}{2} \left| \int_{\mathbf{S}} \phi_r''([\bar{\mathbf{u}}_2] \cdot \mathbf{n}_-) ([\boldsymbol{\delta}_2] \cdot \mathbf{n}_-)^2 [\mathbf{p}_2] \cdot \mathbf{n}_- dS \right| &\leq C \|\boldsymbol{\delta}_2\|_{H^1(\Omega)}^2 \|\mathbf{p}_2\|_{H^1(\Omega)} \leq C \|\boldsymbol{\delta}_2\|_{H^1(\Omega)}^2 \\ &\leq C \frac{\kappa(\rho)^2}{\left(1 + C \frac{\kappa(\rho)}{\rho}\right)^2} + C \frac{\kappa(\rho)\Phi(\rho)}{1 + C \frac{\kappa(\rho)}{\rho}} + C\Phi(\rho)^2. \\ \frac{1}{2} \left| \int_{\mathbf{S}} \phi_r''([\bar{\mathbf{u}}_2] \cdot \mathbf{n}_-) ([\boldsymbol{\delta}_2] \cdot \mathbf{n}_-)^2 [\boldsymbol{\eta}_2] \cdot \mathbf{n}_- dS \right| &\leq C \|\boldsymbol{\delta}_2\|_{H^1(\Omega)}^2 \|\boldsymbol{\eta}_2\|_{H^1(\Omega)} \\ &\leq C \frac{\kappa(\rho)^3}{\left(1 + C \frac{\kappa(\rho)}{\rho}\right)^3} + C \frac{\kappa(\rho)^2\Phi(\rho)}{\left(1 + C \frac{\kappa(\rho)}{\rho}\right)^2} + C \frac{\Phi(\rho)}{1 + C \frac{\kappa(\rho)}{\rho}}. \end{aligned}$$

Let us define the function $\mathcal{R}_{contact}$ that contains all remainder terms resulting from the current contact model.

$$\begin{aligned} \mathcal{R}_{contact}(\rho) &= O\left(\frac{\kappa(\rho)^2}{\left(1 + C \frac{\kappa(\rho)}{\rho}\right)^2}\right) + O\left(\frac{\kappa(\rho)\Phi(\rho)}{1 + C \frac{\kappa(\rho)}{\rho}}\right) + O(\Phi(\rho)^2) + O\left(\frac{\kappa(\rho)^3}{\left(1 + C \frac{\kappa(\rho)}{\rho}\right)^3}\right) \\ & \quad + O\left(\frac{\kappa(\rho)^2\Phi(\rho)}{\left(1 + C \frac{\kappa(\rho)}{\rho}\right)^2}\right) + O\left(\frac{\Phi(\rho)}{1 + C \frac{\kappa(\rho)}{\rho}}\right). \end{aligned}$$

It is evaluated for various values of $k > 0$ and $q > 0$ and results are gathered in Table 7.3.

	$q > 1$		$q = 1$	$0 < q < 1$
$k > 1$	$k > q$	$O(\rho^{k+2q})$	$O(\rho^{k+2})$	$O(\rho^{k+2q})$
	$k \leq q$	$O(\rho^{3k})$		
$k = 1$	$O(\rho^3)$		$O(\rho^3)$	$O(\rho^{1+2q})$
$0 < k < 1$	$O(\rho^3)$		$O(\rho^3)$	$O(\rho^{1+2q})$

Table 7.3: Expressions of $\mathcal{R}_{contact}(\rho)$ for various k and q

Each values of $\mathcal{R}_{contact}(\rho)$ are smaller than the one of $\mathcal{R}(s(\rho))$ (see Theorem 6) so that the contact model does not affect the topological sensitivity analysis with respect to a small idealized bolt.

Part III

Application to bolted assemblies with
pre-tension and contact condition

Academic use cases with sliding contact condition

Contents

8.1	The small spring in 2d	240
8.1.1	Applications with one spring	240
8.1.2	Applications with two springs	245
8.2	The small 1 DOF idealized bolt	248
8.3	The 6 DOFs idealized bolt	250
8.3.1	Test of the topological derivative	251
8.3.2	Parametric optimization of the bolt location	252
8.3.3	Shape optimization	253
8.3.4	Coupled optimization of structure and bolt location	257
8.3.5	Summary	266

This chapter exhibits a set of test cases in 2d and 3d using the sliding contact code of Jeet DESAI [44] in the framework of project TOP (Topology Optimization Platform) within IRT System'X. The optimization problems of Chapter 5 are reproduced to compare results with and without a contact interface. Then, a quick use of the topological derivative for a small idealized bolt with one degree of freedom in 3d, computed in Chapter 7, depicts a particular case where non-overlapping condition between bolts is required. Finally, the 6 degrees of freedom idealized bolt model with the technological constraints set in Chapter 2 is implemented.

8.1 The small spring in 2d

8.1.1 Applications with one spring

Let us go back over the 2d test case of the small spring model developed in Section 5.3. The geometry is modified in the area of the opening gap in order to suit the contact model of [44]. Introduce a small parameter $gap = 2.5 \times 10^{-3}$, the current geometry is given in Fig. 8.1a. The mesh contains 69420 triangular elements with a minimal and maximal size of 5.7×10^{-3} and 2×10^{-2} . Material properties are unchanged, that is to set Young's modulus to 10 and Poisson's coefficient to 0.3. The spring properties are also the same, with a size of $\rho = 2.5 \times 10^{-2}$, a length of $\ell = 0.3$ and a stiffness of $K = 5$. We recall that these material properties are adimensional. The plate is still clamped on the bottom and solicited on the upper border by a sinusoidal load $\mathbf{g} = (0, g_y)$, with

$$g_y = \begin{cases} -\cos(\pi x) & \text{for } 0.5 \leq x \leq 1.5 \\ -\frac{3}{4}\cos(\pi x) & \text{for } 1.5 \leq x \leq 2 \end{cases}.$$

The structure is initialized with the same distribution of holes (see Fig. 8.1b) as in the contact-less case (see Fig. 5.6b) for the purpose of further topology optimization. One of the main objective of the following results is to highlight the impact of a contact model on the structure behavior with a small spring.

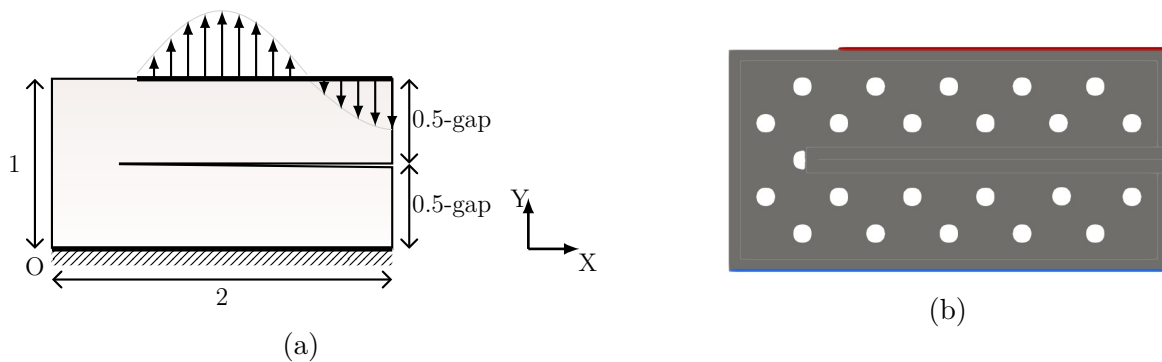


Figure 8.1: Current load case (a) and the initial topology of the structure (b)

Topological derivative test

The problem is to place a small spring in order to decrease the compliance $J(\Omega) = \int_{\Gamma_N} \mathbf{g} \cdot \mathbf{u} dS$.

The initial compliance, without spring, is $J_0(\Omega) = 0.298831$ while it is $J_0(\Omega) = 0.321001$ in the contact-less study. This difference comes from the geometry modification in the gap area because the branches extremities are not in contact in the initial configuration. The objective is to search for both the optimal location \mathbf{x}_0 and the orientation \mathbf{e} . The results are gathered in Table 8.1. The cartography of DJ and the optimal spring are displayed in Fig. 8.2. The current loading opens the structure without spring (cf. Fig. 8.3a). The optimal location and orientation are then expected to be the same as the contact-less case. Indeed, both best orientations are $\varphi = \frac{7\pi}{12}$ rad (or 105°). The optimal location are though slightly different. We get $\mathbf{x}_0 = (1.53, 0.43)$ in the contact-less case. In the contact case, the best location is $\mathbf{x}_0 = (1.54, 0.39)$. This slight

difference results from the different mesh sizes and probably from the geometry modification too. While the spring-less deformations are the same with or without the contact model (see Figs. 5.10a and 8.3a), the deformation with the small spring is substantially modified by the contact condition (see Fig. 8.3b). In fact, the interpenetration in the contact-less case (cf. Fig. 5.10b) turns into a contact zone in the present study (see Fig. 8.3b). The spring brings notable improvement of the compliance for the scales $k = 0.5$ and $k = 1$. However, this addition is no incentive for $k = 2$ and $k = 4$. Thus, these scalings will not be taken into account anymore in further studies.

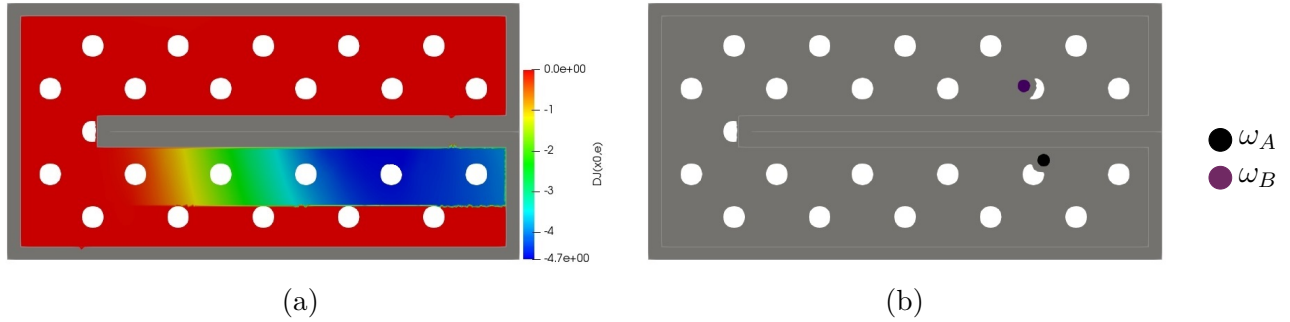


Figure 8.2: Cartography of DJ for $\varphi = \frac{7\pi}{12}$ rad (a) and the optimal spring at $\mathbf{x}_0 = (1.54, 0.39)$ oriented by the angle $\varphi = \frac{7\pi}{12}$ rad (b)

	$DJ(\mathbf{x}_0, \mathbf{e})$	\mathbf{x}_0	φ (rad)	$J_\rho(\Omega)$	$\mathcal{E}(\Omega)$
$k = 0.5$	-4.68716	(1.54,0.39)	$\frac{7\pi}{12}$	0.213352	-0.442274
$k = 1$	-4.68716	(1.54,0.39)	$\frac{7\pi}{12}$	0.261684	0.181652
$k = 2$	-4.68716	(1.54,0.39)	$\frac{7\pi}{12}$	0.295285	0.295902
$k = 4$	-4.68716	(1.54,0.39)	$\frac{7\pi}{12}$	0.298029	0.298829

Table 8.1: Summary of the topological derivative test (recall that $J_0(\Omega) = 0.298831$)

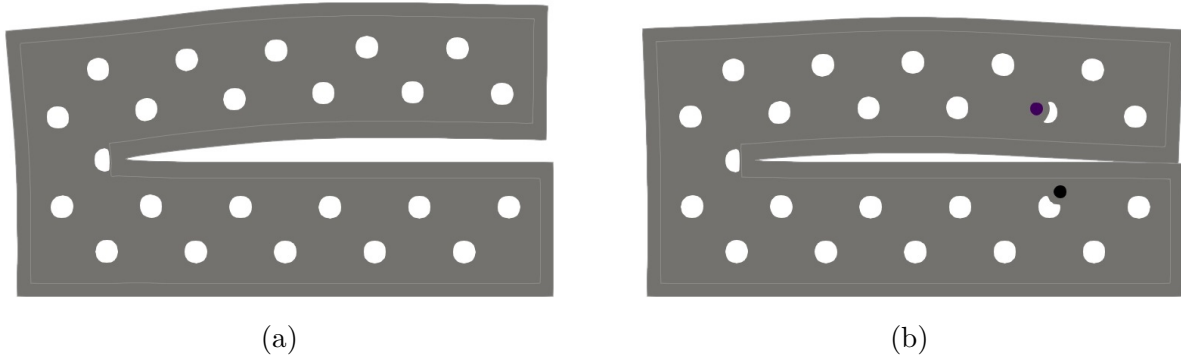


Figure 8.3: Deformations of the background domain (a) and the domain with the optimal small spring for $k = 0.5$ (b)

Parametric optimization of the spring location \mathbf{x}_0

Consider the small spring generated by the topological derivative on the structure with holes. Its location is further optimized with the parametric gradient-based algorithm described by (5.54) and (5.55). The goal is to decrease the compliance. It produces the results summed up in Table 8.2. It provides equivalent improvements as the contact-less case.

	Initial \mathbf{x}_0	Final \mathbf{x}_0	Initial $J(\Omega)$	Final $J(\Omega)$	Improvement
$k = 0.5$	(1.54,0.39)	(1.11,0.41)	0.213352	0.168923	20.82%
$k = 1$	(1.54,0.39)	(1.15,0.44)	0.261684	0.2465419	5.78%

Table 8.2: Summary of parametric optimization of the spring location

Topology optimization of the structure

Based on the initial structure with holes and the sets of initial locations suggested by the topological derivative and the parametric gradient, let us now perform a topology optimization of the structure with fixed spring. The problem is to minimize the volume under a constraint on the compliance. The constraint bound is taken to 0.325, that is an increase of about 9% of the initial compliance without spring. The volume $V(\Omega)$ and the compliance $C(\Omega)$ read

$$V(\Omega) = \int_{\Omega} dV \quad \text{and} \quad C(\Omega) = \int_{\Gamma_N} \mathbf{g} \cdot \mathbf{u} dS. \quad (8.1)$$

This optimization problem is formulated as follows

$$\begin{aligned} \min_{\Omega \in \mathcal{U}_{ad}} \quad & V(\Omega), \\ \text{s.t.} \quad & C(\Omega) \leq 0.325 \end{aligned} \quad (8.2)$$

where \mathcal{U}_{ad} is the set of admissible shapes of the structure. The constraint is taken into account with the augmented Lagrangian functional $J(\Omega)$, so that the problem (8.2) is rewritten as

$$\min_{\Omega \in \mathcal{U}_{ad}} \max_{\alpha \geq 0} \left\{ J(\Omega) = V(\Omega) + \alpha(C(\Omega) - 0.325) + \frac{\beta}{2}(C(\Omega) - 0.325)^2 \right\}, \quad (8.3)$$

where α and β are respectively Lagrange multiplier and penalty parameter for the constraint.

- One spring put at the location given by the topological derivative

Consider first the spring placed by the topological derivative at $\mathbf{x}_0 = (1.54, 0.39)$ and oriented at $\varphi = \frac{7\pi}{12}$ rad. The optimal shapes and volumes are given in Fig. 8.4 and Table 8.3.

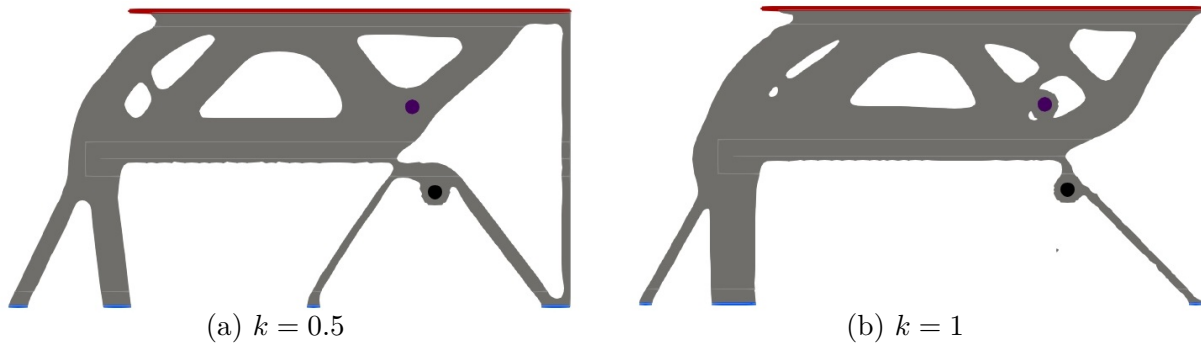


Figure 8.4: Optimal shapes for various values of k , for fixed $\mathbf{x}_0 = (1.54, 0.39)$ and $\varphi = \frac{7\pi}{12}$ rad

In the case $k = 0.5$, the left portion of structure is similar to the contact-less case (compare with Fig. 5.14a). The right portion mainly differs by the addition of a slanted bar to support the head of the spring and two vertical bars in contact at the extremity of the structure. We recall that this spring scaling induces important interpenetration in the contact-less case. Thus these vertical bars in contact counteract the compression caused by the spring. The weight is equivalent to the contact-less result. The topology is practically similar with or without the contact condition in the case $k = 1$. The structure is a little bit heavier here because the compliance bound is lower than the one of the contact-less case.

	Final Volume $V(\Omega)$	Improvement
$k = 0.5$	0.652062	65.20%
$k = 1$	0.727252	61.19%

Table 8.3: Summary of volumes for topology optimization with one fixed spring placed at $\mathbf{x}_0 = (1.54, 0.39)$ and oriented at $\varphi = \frac{7\pi}{12}$ rad for various values of k (recall the initial volume is $V(\Omega) = 1.87392$)

- One spring put at the location given by the parametric gradient

Consider now the springs placed by the parametric gradient for the scales $k = 0.5$ and $k = 1$. The optimal shapes and volumes are given in Fig. 8.5 and Table 8.4. Again, the case $k = 0.5$ creates two bars in contact at the right extremity of the structure in order to counteract the compression due to the spring. Moreover, the topology is completely different from the contact-less case (compare Fig. 5.15a). The current topology tends to be more like a bar structure. In contrast, the case $k = 1$ provides practically the same topology as the contact-less case. In terms of weight, the size scale $k = 0.5$ offers a better volume reduction than the contact-less case while the case $k = 1$ brings a heavier structure.

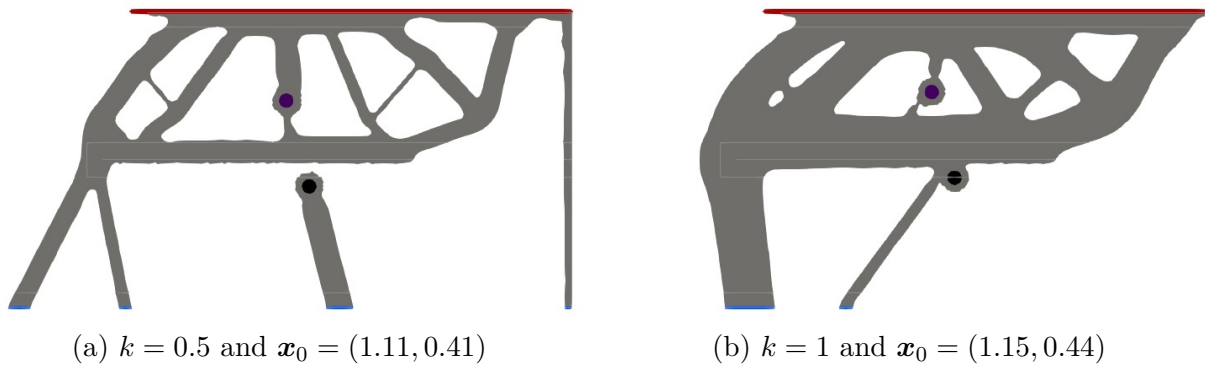


Figure 8.5: Optimal shapes for various values of k and for fixed $\varphi = \frac{7\pi}{12}$ rad

	Initial Volume	Final Volume	Improvement
$k = 0.5$	1.86956	0.458903	74.45%
$k = 1$	1.86956	0.693413	62.91%

Table 8.4: Summary of volumes for topology optimization with one fixed spring placed by parametric gradient and oriented at $\varphi = \frac{7\pi}{12}$ rad for various values of k

Coupled optimization of both structure and spring location

This last section illustrates the coupled optimization of the structure shape and the spring location. The structure is initialized with holes. We propose here to test two initializations of the spring location. The problem is still to minimize the volume under a compliance constraint as stated in (8.3). The coupling strategy is to perform 4 iterations of structural optimization and then 1 iteration of location parametric optimization and so on until convergence.

- Initial location given by the topological derivative

Consider first the spring placed by the topological derivative. The final shapes and results are gathered in Fig. 8.6 and Table 8.5. Once more, the optimal structure for $k = 0.5$ uses a kind of cane at the right end to counteract the pushing force. The resulting topology and location are substantially different from the contact-less case. The structure is also lighter. The optimal structures for $k = 1$ are of the same type with or without the contact model. Nevertheless, the locations are different and the structure with contact is heavier.

	Initial \mathbf{x}_0	Final \mathbf{x}_0	Initial $V(\Omega)$	Final $V(\Omega)$	Improvement
$k = 0.5$	(1.54,0.39)	(1.18,0.39)	1.87392	0.484364	74.15%
$k = 1$	(1.54,0.39)	(1.61,0.42)	1.87392	0.722326	61.45%

Table 8.5: Summary of results : coupled optimization of both structure and location with initial spring placed by the topological derivative

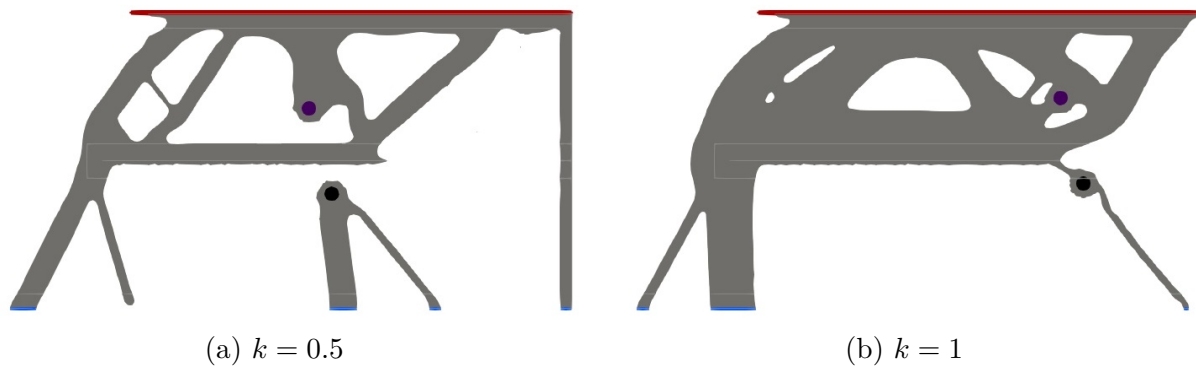


Figure 8.6: Optimal shapes and locations for fixed $\varphi = \frac{7\pi}{12}$ rad with initial spring placed by the topological derivative

- Initial location given by the parametric gradient

Consider now the spring placed according to the parametric gradient-based algorithm. The final shapes and results are gathered in Fig. 8.7 and Table 8.6. Again the optimal structure for $k = 0.5$ contains a cane at the right end and the case $k = 1$ is of the same type as the contact-less result.

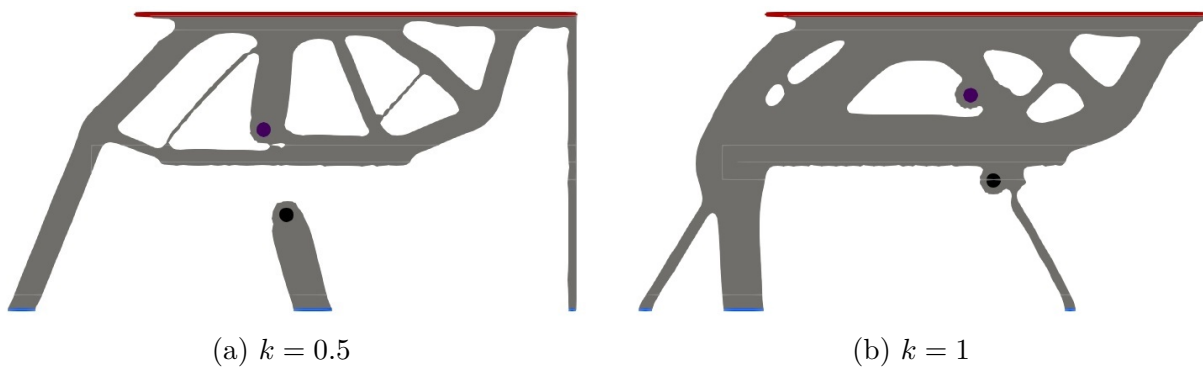


Figure 8.7: Optimal shapes and locations for fixed $\varphi = \frac{7\pi}{12}$ rad with initial spring placed by the parametric gradient

	Initial \mathbf{x}_0	Final \mathbf{x}_0	Initial $V(\Omega)$	Final $V(\Omega)$	Improvement
$k = 0.5$	(1.11,0.41)	(1.01,0.32)	1.86956	0.460668	75.36%
$k = 1$	(1.15,0.44)	(1.27,0.44)	1.86956	0.694767	62.84%

Table 8.6: Summary of results : coupled optimization of both structure and location with initial spring placed by the parametric gradient

8.1.2 Applications with two springs

This section reiterates the topological derivative test to put a second spring in order to decrease the compliance, followed by location and topology optimization. In the present study, both

springs have the same scale size k . In the sequel, the subscript "1" (resp. "2") refers to the first (resp. the second) spring.

Topological derivative test

The objective is to decrease the compliance. A new map of the topological derivative is computed for various values of k on the system that contains the spring placed by the previous topological derivative at the point $\mathbf{x}_{0,1} = (1.54, 0.39)$. It places and orients the second spring as displayed in Fig. 8.8. Compared to the contact-less case (see Fig. 5.18), the topological derivative depends on the contact state and thus it indicates different configurations. It comes as no surprise, the second spring improves the compliance (see Table 8.7).

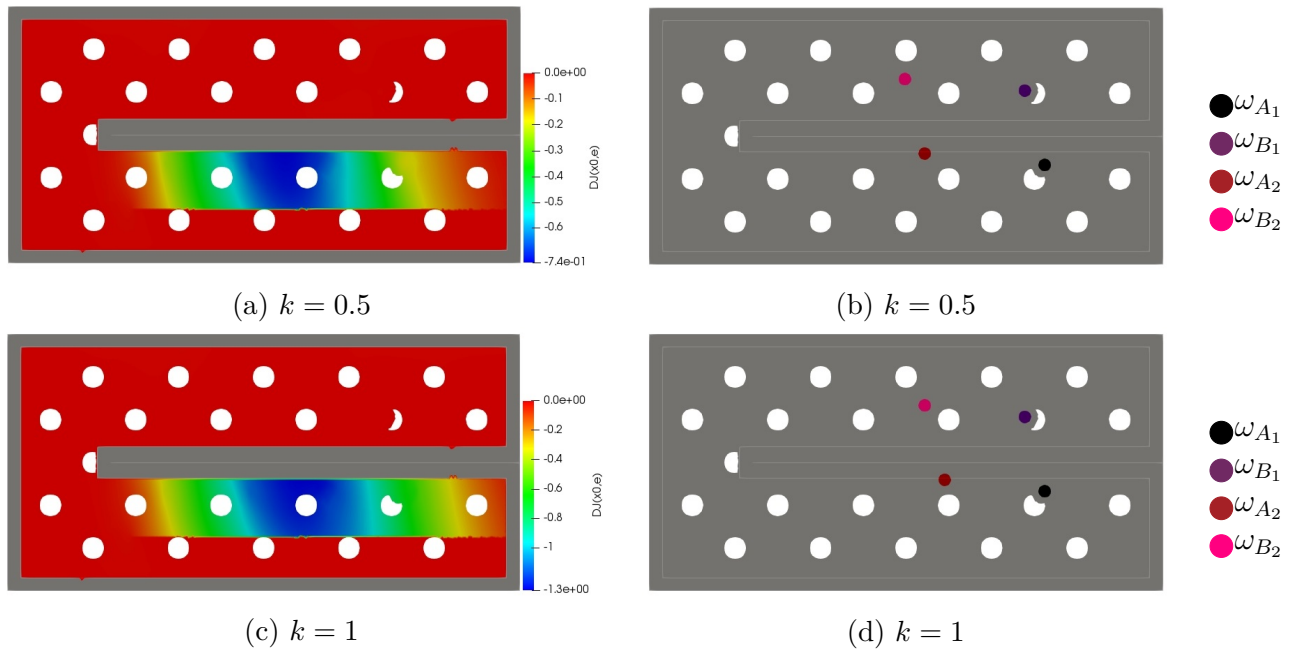


Figure 8.8: Cartography of DJ for various k to place a second spring (a), (c), (e) and the corresponding optimal configuration (b), (d), (f)

	$DJ(\mathbf{x}_{0,2}, \mathbf{e}_2)$	$\mathbf{x}_{0,2}$	φ_2 (rad)	$J_1(\Omega)$	$J_2(\Omega)$	$\mathcal{E}(\Omega)$
$k = 0.5$	-0.735957	(1.07,0.43)	$\frac{7\pi}{12}$	0.213352	0.149983	0.0969872
$k = 1$	-1.29283	(1.15,0.43)	$\frac{7\pi}{12}$	0.261684	0.23447	0.229363

Table 8.7: Summary of the placement of a second spring (recall that $\mathbf{x}_{0,1} = (1.54, 0.39)$ and $\varphi_1 = \frac{7\pi}{12}$ rad for all k)

Topology optimization of the structure

The analysis of two small springs with a contact model in 2d concludes with a topology optimization of the structure. Both springs are placed as indicated by the topological derivative.

Final topologies are displayed in Fig. 8.9 and results are gathered in Table 8.8. The case $k = 0.5$ is once more as a bar structure and uses a cane at the right end extremity to counteract the pushing force. The case $k = 1$ provides a topology of the same type as previous results for this size scaling.

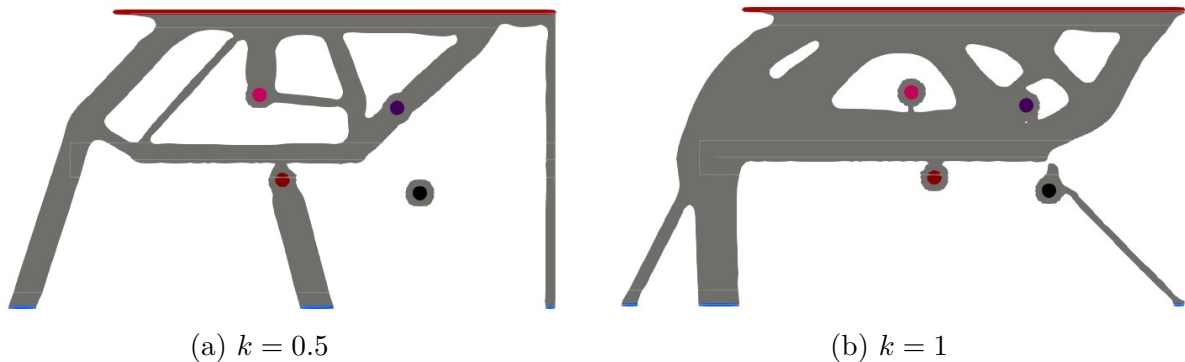


Figure 8.9: Optimal shapes for various values of k with two springs placed by the topological derivative

	Initial Volume	Final Volume	Improvement
$k = 0.5$	1.87392	0.45363	75.79%
$k = 1$	1.87392	0.726294	60.48%

Table 8.8: Summary of volumes for topology optimization with two springs placed by the topological derivative for various values of k

So far the best performance for the contactless problem was obtained with scaling $k = 0.5$ by placing and orienting successively two springs with the topological derivative. Then, their locations were optimized with the parametric gradient. The final step was to optimize the structure. The same strategy is reproduced with the contact model and provides the optimal structure given in Fig. 8.10. The final volume is $V(\Omega) = 0.520252$, which corresponds to an improvement of 72.18%. Although it represents great improvement, this is not the best performance for the contact model. As a conclusion, the optimal path is not unique and the strategy of finding the best possible result depends on the model of the test case.

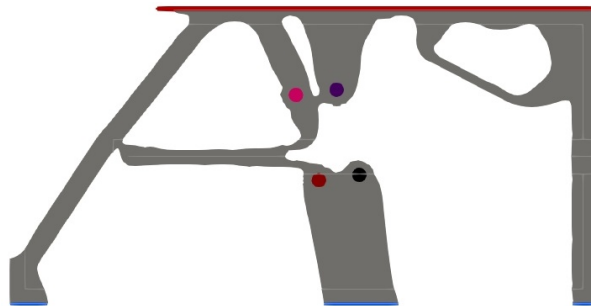


Figure 8.10: Optimal shape for $k = 0.5$ with two springs placed by the parametric gradient

8.2 The small 1 DOF idealized bolt

This section employs the topological derivative with respect to a small bolt with pre-stressed state that has been computed in Chapter 7. Let us consider two disjointed cube shaped parts pictured in Fig. 8.11. They are not bounded to each other but are in contact. The mesh contains 36 733 tetrahedral elements with a minimal and maximal size of 2.9×10^{-2} and 7.2×10^{-2} . The assembly is clamped on the bottom and on the left. A force $\mathbf{g} = \left(0, -5 \cos\left(\frac{x}{2}\right), 0\right)$ is applied on the top. Both parts are of the same material with an adimensioned Young's modulus $E = 1$. The Poisson's coefficient is 0.3. Bolts are all characterized with a size of $\rho = 5 \times 10^{-2}$, a length $\ell = 5 \times 10^{-1}$, a rigidity $K = 1$ and a pre-tension force $Q = 1$. Plenty of previous numerical test cases illustrate the role of the scaling factor k on the optimal shape and on the efficiency of the connection. Same conclusions can be ensured for the scaling factor q of the pre-tension force. Then, the rigidity and the pre-tension force are scaled by $k = 2$ and $q = 2$. It has the physical meaning that the spring rigidity and the pre-stress force are proportional to the cross-section of the spheres and the root, which leads to finite inner stresses in the small idealized bolt root.

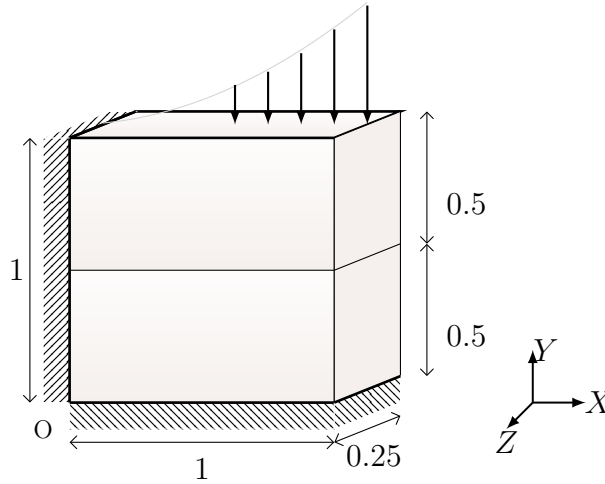


Figure 8.11: Setting of the 3d use case

The problem is to decrease the compliance $J(\Omega) = \int_{\Gamma_N} \mathbf{g} \cdot \mathbf{u} dS$ of the system by introducing a first then a second small bolt with the topological derivative. Since the external force presses down the assembly, the small bolt aims to relax the system. The initial compliance of the system without bolt is $J_0(\Omega) = 4.756$. The topological derivative reads

$$DJ(\mathbf{x}_0, \mathbf{e}) = K \left((\mathbf{u}_2(\mathbf{x}_0 + \ell \mathbf{e}) - \mathbf{u}_2(\mathbf{x}_0)) - (\mathbf{u}_1(\mathbf{x}_0 + \ell \mathbf{e}) - \mathbf{u}_1(\mathbf{x}_0)) \right) \cdot \mathbf{e} \left(\mathbf{p}_2(\mathbf{x}_0 + \ell \mathbf{e}) - \mathbf{p}_2(\mathbf{x}_0) \right) \cdot \mathbf{e} + Q \left(\mathbf{p}_2(\mathbf{x}_0 + \ell \mathbf{e}) - \mathbf{p}_2(\mathbf{x}_0) \right) \cdot \mathbf{e}, \quad (8.4)$$

where \mathbf{u}_1 , \mathbf{u}_2 and \mathbf{p}_2 are respectively solution of the background domain of Step 1 (7.7), of Step 2 (7.9) and the adjoint problem in the background domain (7.12). Let us fix the orientation of bolts to the vertical axis. The cartography of the topological derivative to place the first bolt and resulting small bolt are displayed in Fig. 8.12. The optimal small bolt is placed at the point $\mathbf{x}_{0,1} = (0.90, 0.86, 0.15)$. The new compliance is $J_\rho(\Omega) = 3.008$, which is quite efficient.

Let us place the second spring with the topological derivative. The cartography of the topological derivative to place the second bolt and the resulting small bolt are displayed in

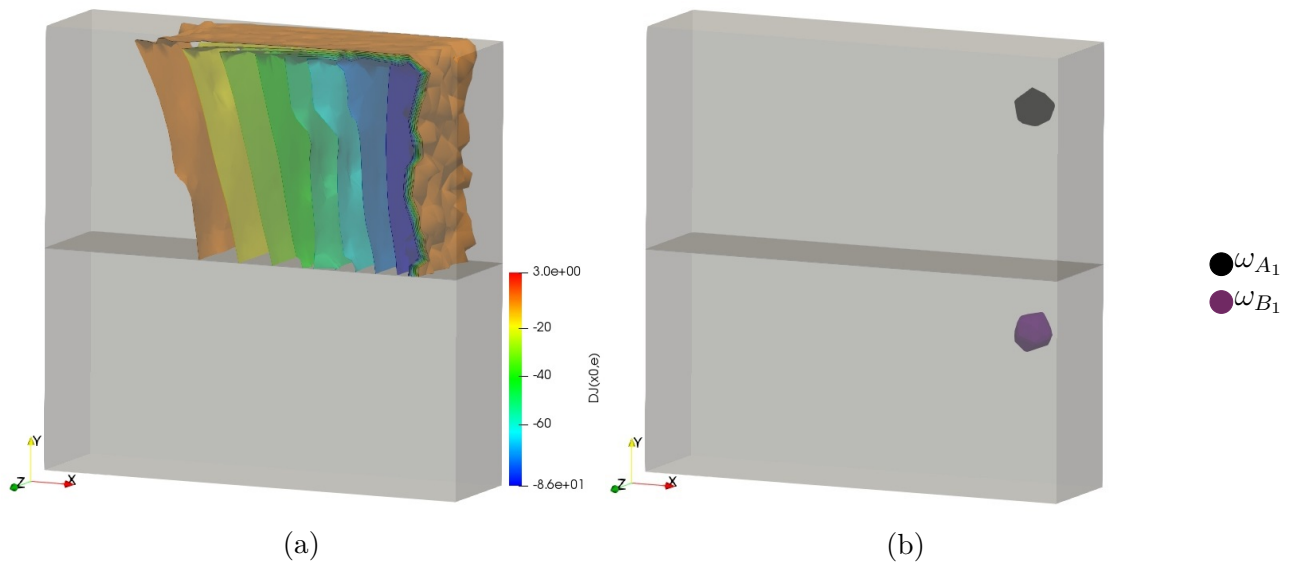


Figure 8.12: Cartography of the topological derivative (a) and the resulting optimal small bolt (b)

Fig. 8.13. This cartography pictures well the behavior change without bolt (see Fig. 8.12) and with one pre-existing small bolt. The second bolt it put at $x_{0,2} = (0.84, 0.89, 0.13)$, which overlaps the first one. There are two manners to interpret this result. The first point of view is to conclude that the maximum number of required bolts is reached. In this case, it means that one bolt is enough. The second interpretation is the need of a bigger bolt. The compliance with both bolts is still $J_\rho(\Omega) = 3.008$. Theoretically, the second small bolt should improve the assembly but it does not bring anything more numerically. Let us add a geometric non-overlapping condition between bolts to separate them.

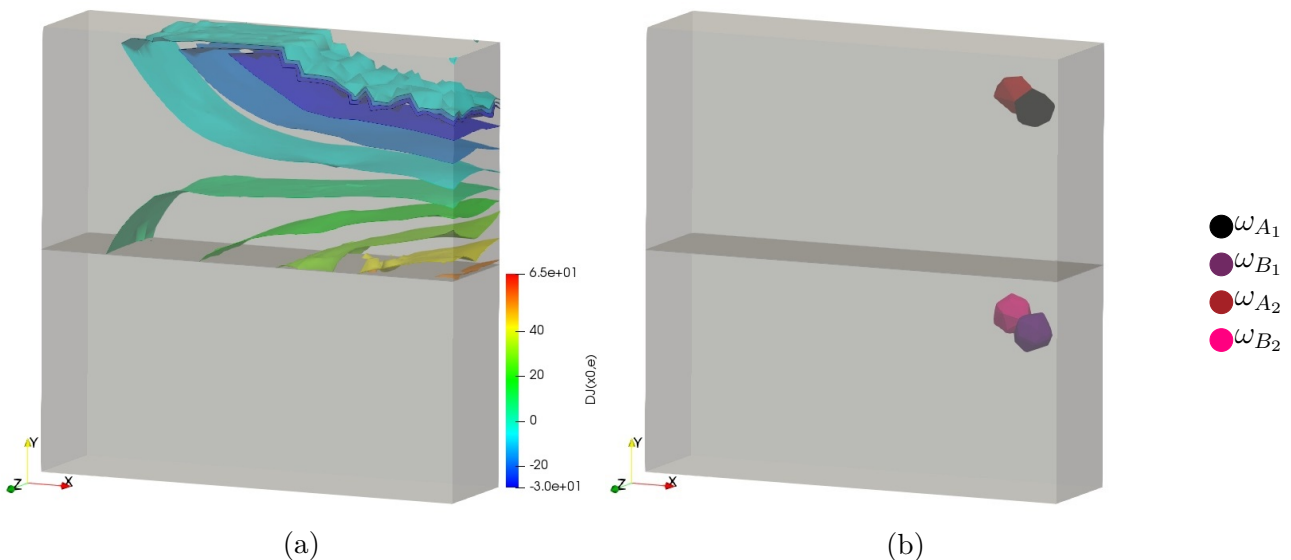


Figure 8.13: Cartography of the topological derivative (a) and the resulting second optimal small bolt (b)

In the present case, the non-overlapping condition is a prescribed distance between bolts locations. It states that bolts must be at least at fourth times the radius of the spheres away from each other. Values of the topological derivative that do not respect this condition are truncated.

The new cartography and the second optimal small bolt placed at $\mathbf{x}_{0,2} = (0.65, 0.89, 0.12)$ are displayed in Fig. 8.14. The new compliance is $J_\rho(\Omega) = 3.004$. It represents a very slight improvement compared to just one small bolt.

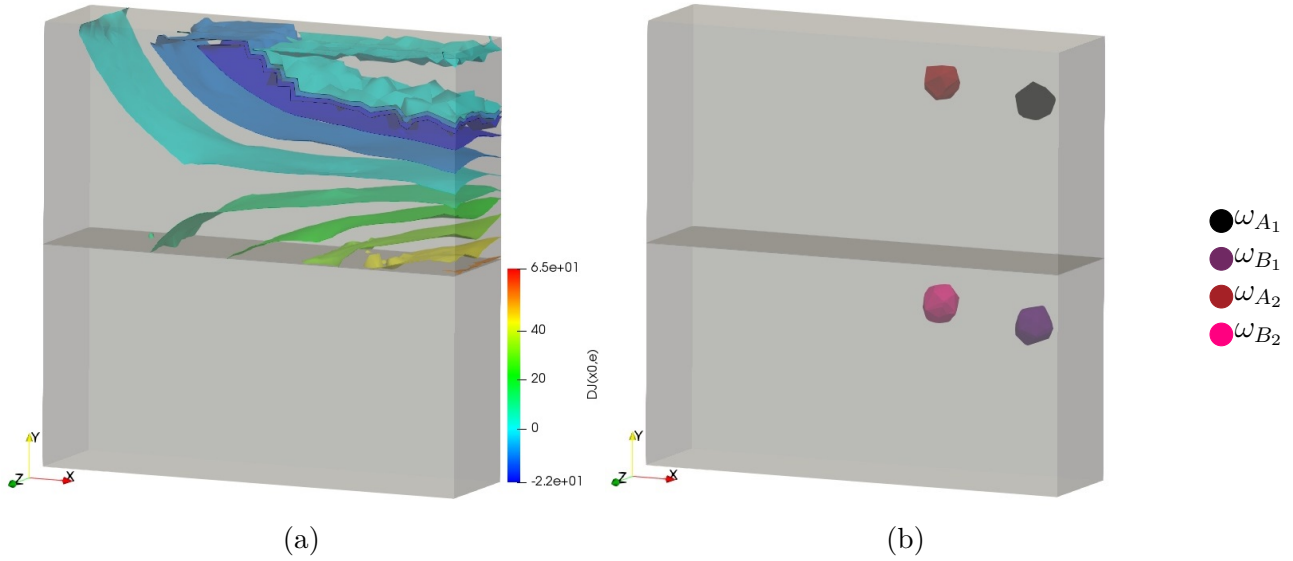


Figure 8.14: Cartography of the topological derivative with a non-overlapping condition (a) and the resulting second optimal small bolt (b)

We recall that the problem is to decrease the compliance. A naive thought would be to state that the more there are bolts in the system, the more it is stiffened so better the compliance is. In this test case, the topological derivative concludes that a single bolt is enough to enhance the system, which is justified by numerical results. It proves the efficiency of the topological derivative.

8.3 The 6 DOFs idealized bolt

This academic 3d use case prepares the more significant and complete simplified industrial use case developed in Chapter 9. Here, mechanical constraints specific to the bolt, are implemented one by one. Let us consider the cube of side $L = 100$ mm with a crack on the middle, as pictured in Fig. 8.15. The cube is clamped on the left and a sinusoidal force $\mathbf{g} = \left(\sin\left(\frac{\pi z}{2}\right) \times 10^5, 0, 0 \right)$ is applied on a small portion of the right. Young's modulus and Poisson's coefficient of the cube are $E_{cube} = 210$ GPa and $\nu_{cube} = 0.3$. A sliding contact condition [44] is applied on the crack. The mesh contains initially 31 569 tetrahedral elements. For an accurate computation of the displacement field in the spheres, the mesh is refined around them with `mmg3d` [45] whenever is necessary.

Let us consider an idealized bolt with elastic spheres as described in Chapter 2. The bolt has the following properties :

- radius $r_b = 5$ mm
- length $\ell = 50$ mm
- Young's modulus $E = 200$ GPa
- Poisson's coefficient $\nu = 0.3$

- Pre-tension force $\Phi = 30\,000$ N
- Minimal yield stress of the root $Re_{min} = 900$ MPa

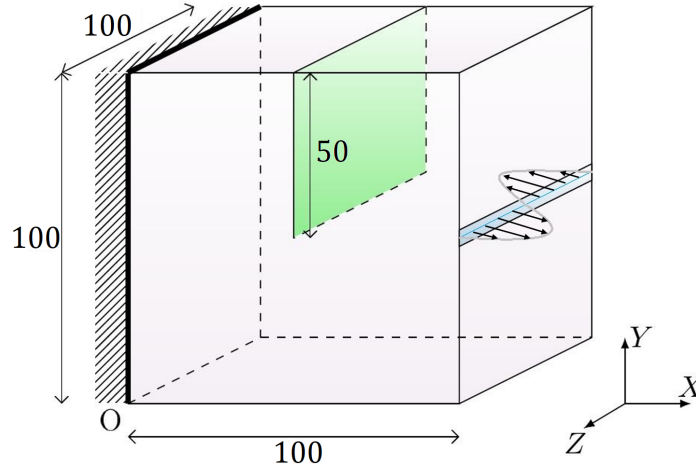


Figure 8.15: Cube with a crack

8.3.1 Test of the topological derivative

In view of the cube size ($L = 100$ mm) and the spheres radius ($r_b = 5$ mm), the size of the bolt is directly effective of a topological derivative use. Let us fix the orientation of the bolt. The topological derivative is used to place one idealized bolt. Actually, it indicates the best location to put a 1 DOF bolt. The goal is to decrease the compliance $J(\Omega) = \int_{\Gamma_N} \mathbf{g} \cdot \mathbf{u} dS$. In the present case, we put a 6 DOFs bolt at the location given by the topological derivative for a 1 DOF bolt, that is $\mathbf{x}_0 = (-26.8, 32.5, 32.4)$ (see Fig. 8.16). The initial and the final compliance, resp. without and with the bolt, are $J_0(\Omega) = 102$ J and $J_\rho(\Omega) = 95$ J. Then the location given by the topological derivative still provides improvements with a 6 DOFs bolt.

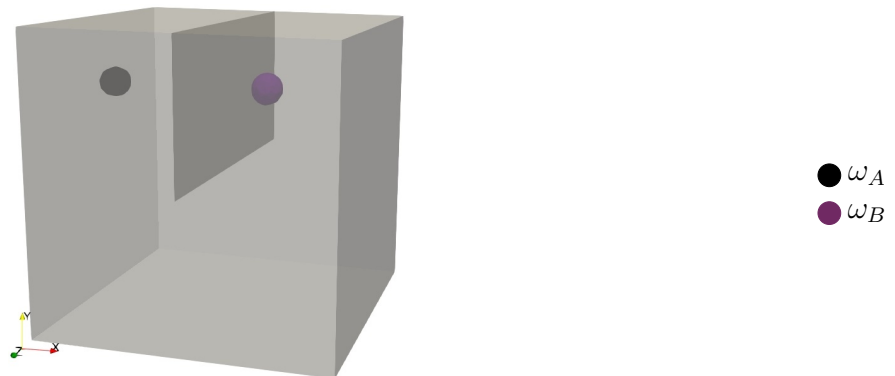


Figure 8.16: Optimal location of the bolt to decrease the compliance

8.3.2 Parametric optimization of the bolt location

This section performs a parametric optimization of the previous bolt location with regards to each mechanical constraints specific to the bolt given in Section 2.4. The problems are then to minimize separately the Von Mises stress at the rim, at the center and the fatigue of the bolt root that are respectively defined by (2.29), (2.30) and (2.32). The history of convergence of locations are given in Fig. 8.17 and improvements are given in Table 8.9. Each constraint has its specificity and thus leads to different optimal locations.

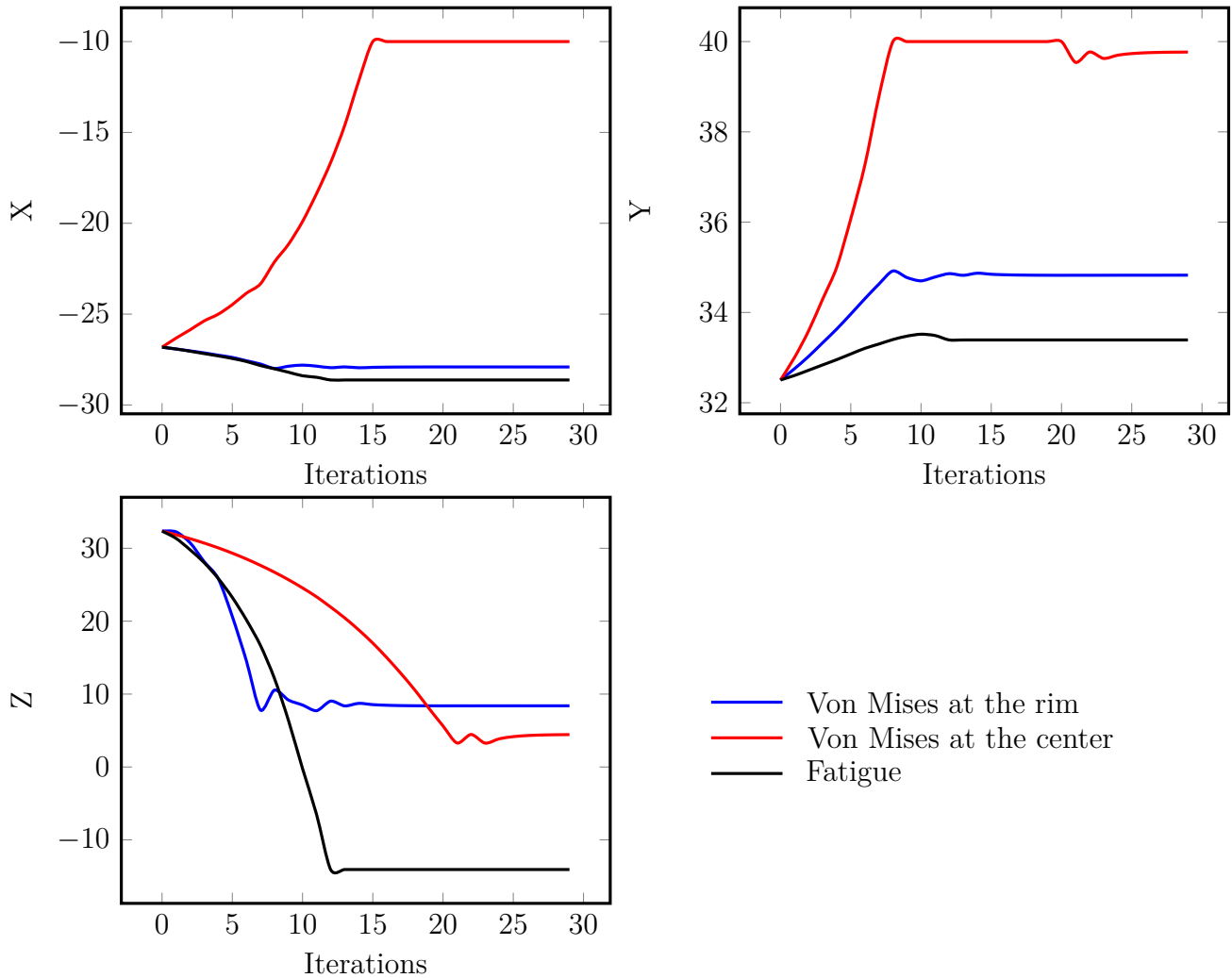


Figure 8.17: History of convergence of locations parametric optimization with regards to mechanical constraints on the bolt

	Von Mises at the rim	Von Mises at the center	Fatigue
Initial	364	320	55
Final	231	185	1.01

Table 8.9: Summary of constraints improvement (in MPa) with parametric optimization of bolt location

8.3.3 Shape optimization

The structure is initialized with holes (see Fig. 8.18). This section contains five shape optimization problems with one fixed bolt placed by the topological derivative. They are all volume minimization problems under a compliance constraint and none or one mechanical constraint on the bolt. Given the initial value of compliance (*i.e.* without the bolt), the bound is set to $C_{comp,0} = 110$ J.

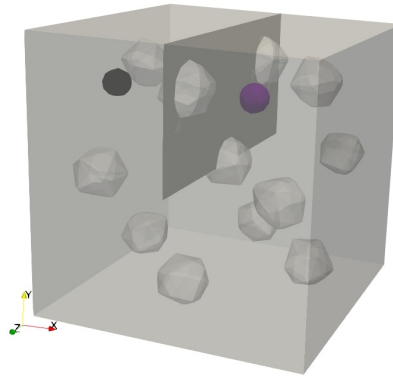


Figure 8.18: Initialization of the structure topology and the bolt location

Compliance constraint

Fig 8.19 gives different views of the optimal shape for the problem of volume minimization under a compliance constraint. The final volume is $V(\Omega) = 390\,295 \text{ mm}^3$. The reserve of material around each sphere aims to insure appropriate diffusion of efforts into the structure.

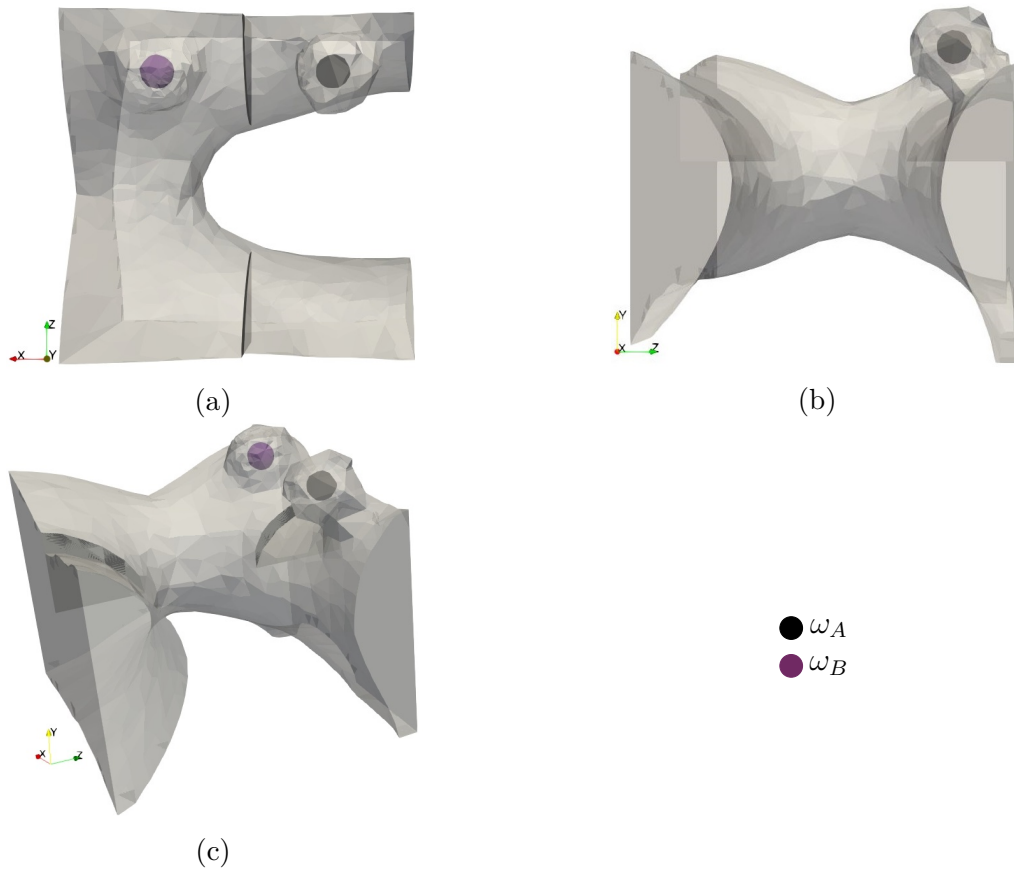


Figure 8.19: Optimal structure for the problem of volume minimization under a compliance constraint

Elasticity constraint at the center on the root

The Von Mises criterion at the center of the root has always been satisfied in the problem of volume minimization under a compliance constraint (see Fig. 8.19). Then, the stress threshold has been decreased by a coefficient 0.86 to activate the constraint.

Remark 74. *An other reduction coefficient would be fine. We choose 0.86 because it activates quickly the constraint.*

The optimal shape is given in Fig. 8.20. The final volume is $V(\Omega) = 424\,730 \text{ mm}^3$. There is no change in the topology of the structure. The only modification lies in the reserve of material around each spheres. They are a little more bulky with the active Von Mises criterion. It explains the slight increase of the final volume.

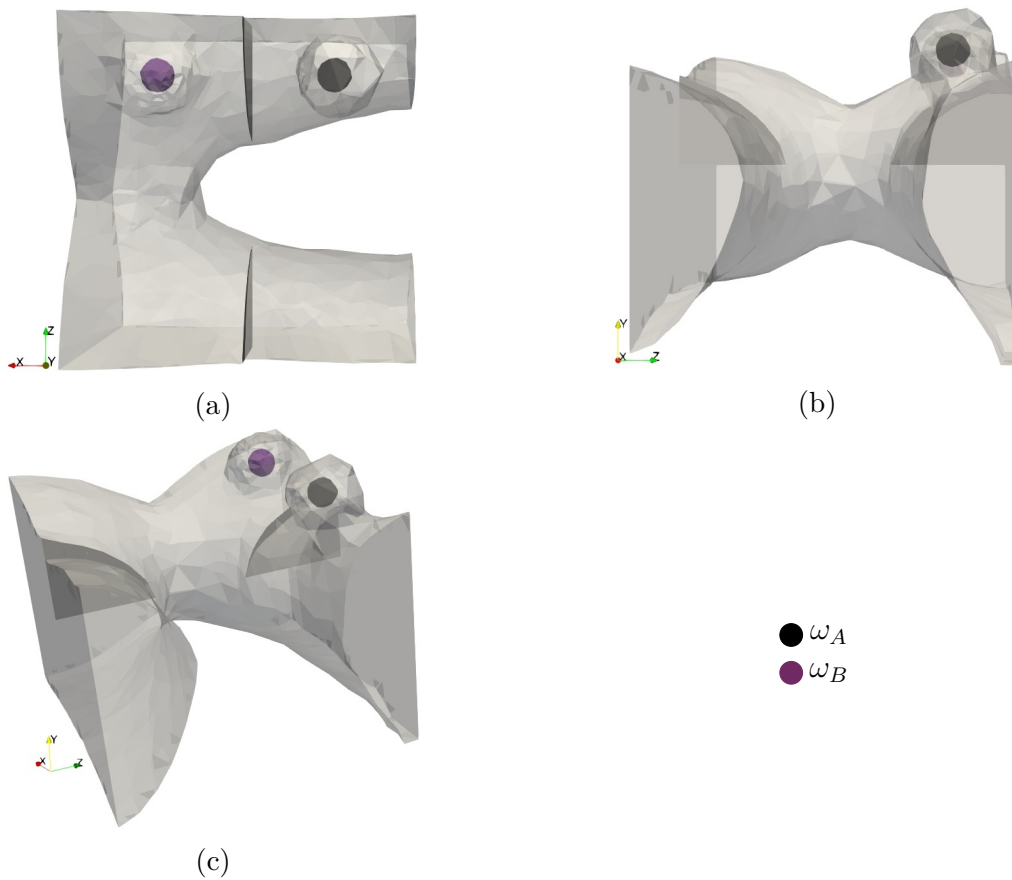


Figure 8.20: Optimal structure for the problem of volume minimization under a compliance constraint and Von Mises criterion at the center of the bolt root

Elasticity constraint at the rim on the root

Let us focus on the problem of volume minimization under a compliance constraint and the Von Mises criterion at the rim of the bolt root. This criterion is harder to achieve than the Von Mises criterion at the center of the root. Then, the amplitude of the pre-tension force has been decreased to $\Phi = 25\,000$ N to relax the criterion. Actually, the value $\Phi = 30\,000$ N is too high to achieve the criterion. The optimal shape is given in Fig. 8.21. The final volume is $V(\Omega) = 539\,829$ mm³.

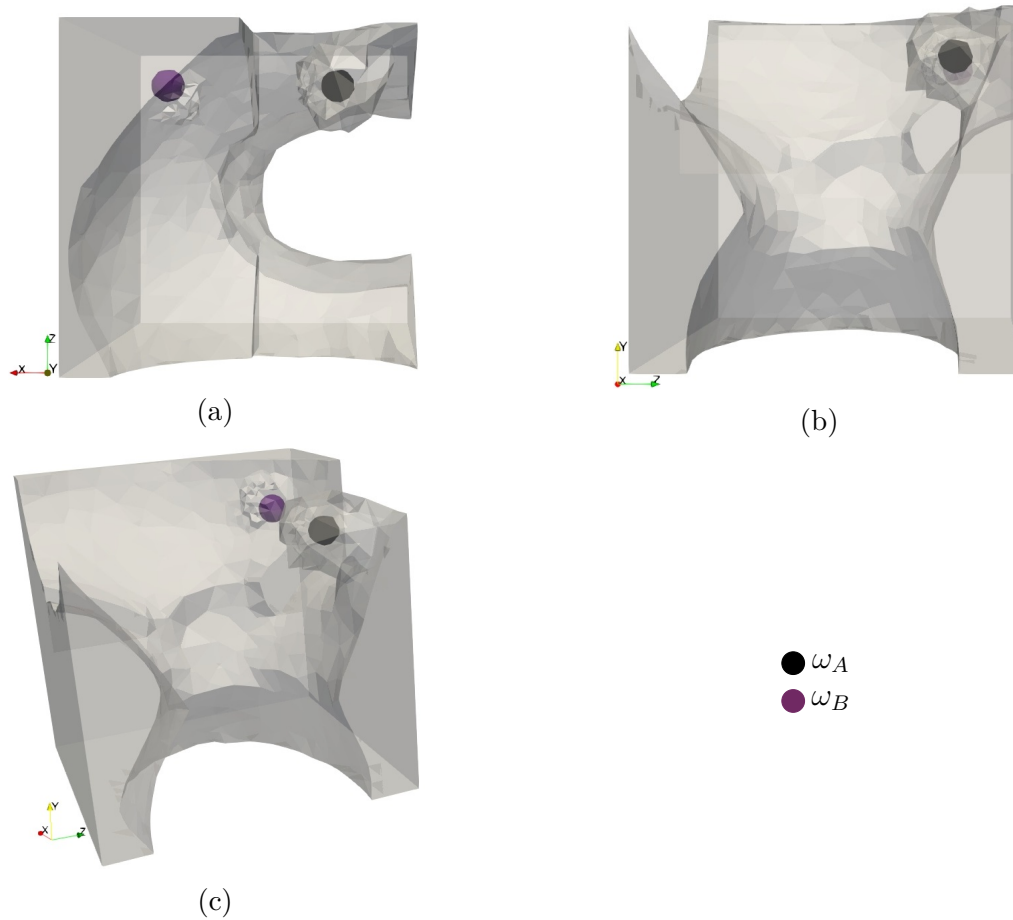


Figure 8.21: Optimal structure for the problem of volume minimization under a compliance constraint and Von Mises criterion at the rim of the bolt root

Fatigue constraint on the root

The fatigue constraint on the bolt root is almost as difficult to achieve as the Von Mises criterion at the rim of the bolt root. Then, it is activated on the pre-optimized structure of Fig. 8.19. The optimal shape is given in Fig. 8.22. The final volume is $V(\Omega) = 674\,574\text{ mm}^3$. The topology is unchanged but the volume increases a lot to fulfill the fatigue constraint on the bolt root. In other words, the fatigue constraint requires much more material to be achieved.

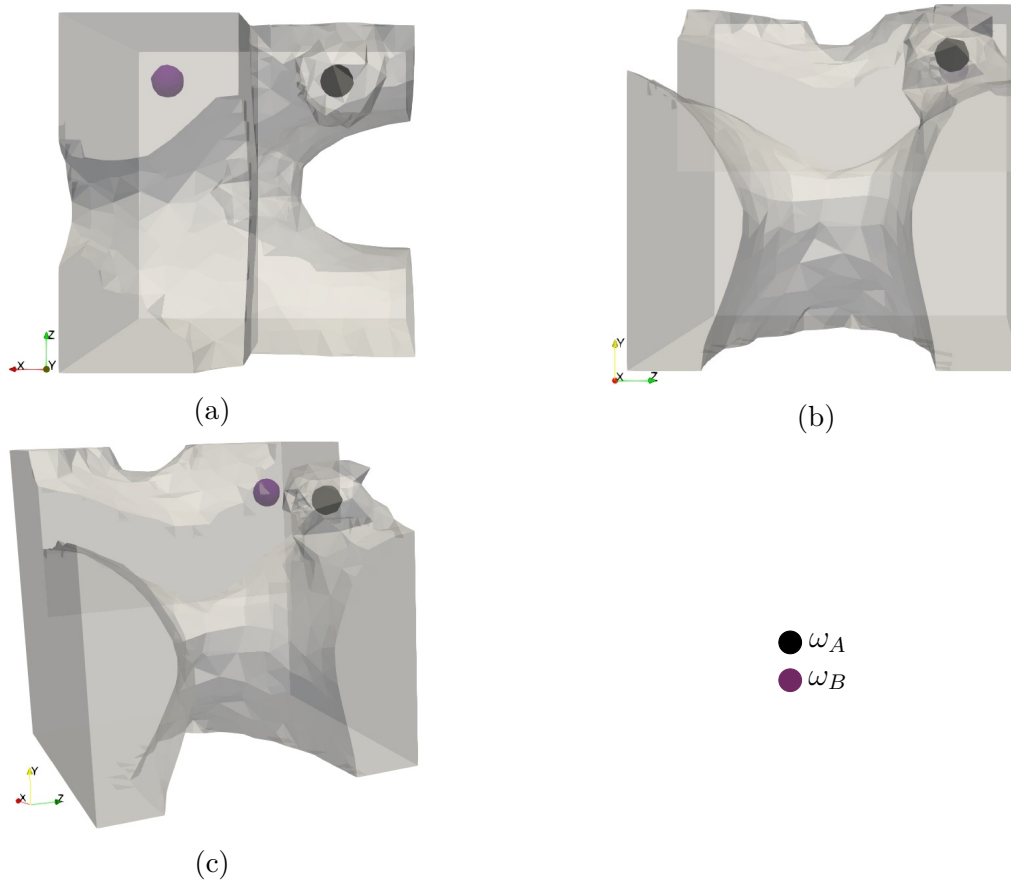


Figure 8.22: Optimal structure for the problem of volume minimization under a compliance constraint and fatigue constraint on the bolt root

Torsion locking of the bolt root

Let us focus on the problem of volume minimization under a compliance constraint and the torsion locking of the bolt root, defined at Section 2.4.4. The external force \mathbf{g} does not induce torsion solicitation of the bolt. Thus, the torsional relative rotation is always of the order of 10^{-13} , which is considered to be zero. Consequently, we skip this optimization problem for this use case.

8.3.4 Coupled optimization of structure and bolt location

This section performs a coupled optimization of both the structure and the bolt location. The chosen strategy here is to make 3 iterations of structure advection and 1 iteration of parametric gradient for the location, and so on until convergence. The problem is still to minimize the volume under a compliance constraint and none or one mechanical constraint on the bolt. We

consider successively and independently the Von Mises at the center, the Von Mises at the rim and the fatigue of the bolt root. As noticed in the previous section, the torsion locking of the bolt root is not required in this load case. For all problems, the structure is still initialized with holes (see Fig. 8.18). The bolt is initially placed at the point $\mathbf{x}_0 = (-26.8, 32.5, 32.4)$ given by the topological derivative.

Remark 75. *The bolt is movable in the following optimization problems. Since the initial mesh is rather coarse (with 31569 tetrahedral elements), we need to remesh around the spheres each time their location changes. It insures a correct computation of the displacement field of the bolt. This remeshing process would not be required on an adequately refined mesh. We chose here a coarse mesh to save computation time. Consequently, numerical results may present some fluctuations because of the remeshing.*

Compliance constraint

Fig. 8.23 gives different views of the optimal structure and bolt location for the problem of volume minimization under a compliance constraint. The optimal bolt is at the point $\mathbf{x}_0 = (-40, 35.3, 40)$. The final volume is $V(\Omega) = 382\,237\text{ mm}^3$. The volume has slightly decreased compared to the optimal result with fixed bolt.

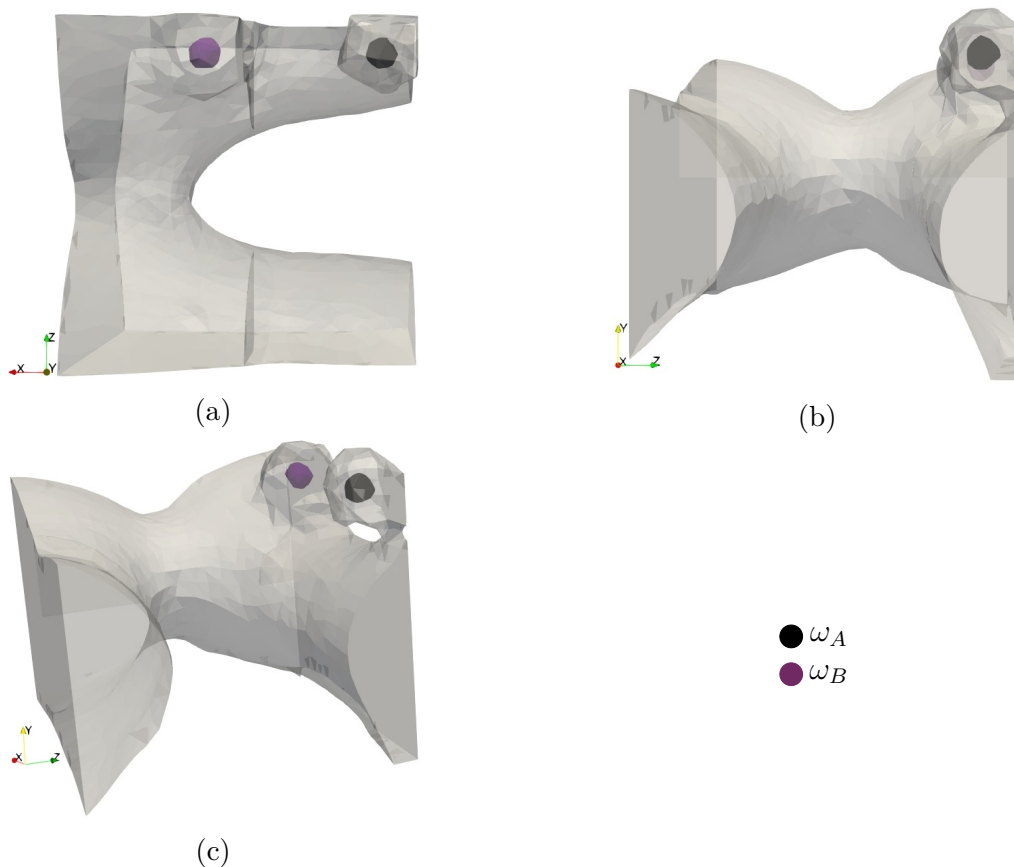


Figure 8.23: Optimal structure and bolt location for the problem of volume minimization under a compliance constraint with an alternating strategy of 3 iterations of structure advection and 1 iteration of parametric gradient for bolt location

Elasticity constraint at the center of the root

The optimal structure and bolt location are given in Fig. 8.24. The final volume is $V(\Omega) = 382\,330 \text{ mm}^3$. The optimal bolt is at the point $\mathbf{x}_0 = (-10.5, 35.6, 36)$. This is quite an improvement compared to the structure optimization with the fixed bolt for which the final volume was $V(\Omega) = 424\,730 \text{ mm}^3$.

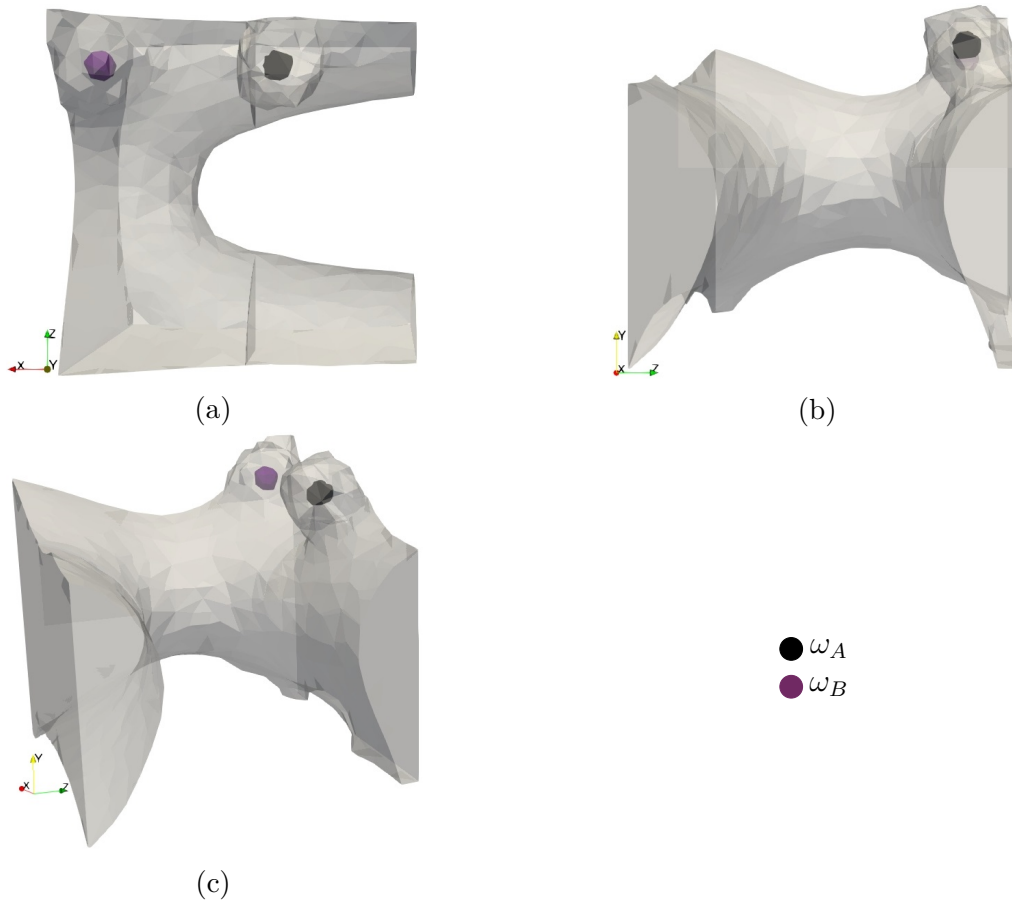


Figure 8.24: Optimal structure and bolt location for the problem of volume minimization under a compliance constraint and Von Mises criterion at the center of the bolt root with an alternating strategy of 3 iterations of structure advection and 1 iteration of parametric gradient for bolt location

Results may highly depend on the alternating strategy between structure and location optimization. We remake, for instance, the same minimization problem with a strategy of 1 iteration for structure advection and 1 iteration for parametric gradient. The optimal structure and bolt location are given in Fig. 8.25. The final volume is $V(\Omega) = 376\,452\text{ mm}^3$. The optimal bolt is at the point $\mathbf{x}_0 = (-16.3, 27.9, 40)$. The change of the alternating strategy brings additional gain on weight reduction. Actually, the bolt location is different, which allows this additional gain while respecting optimization constraints.

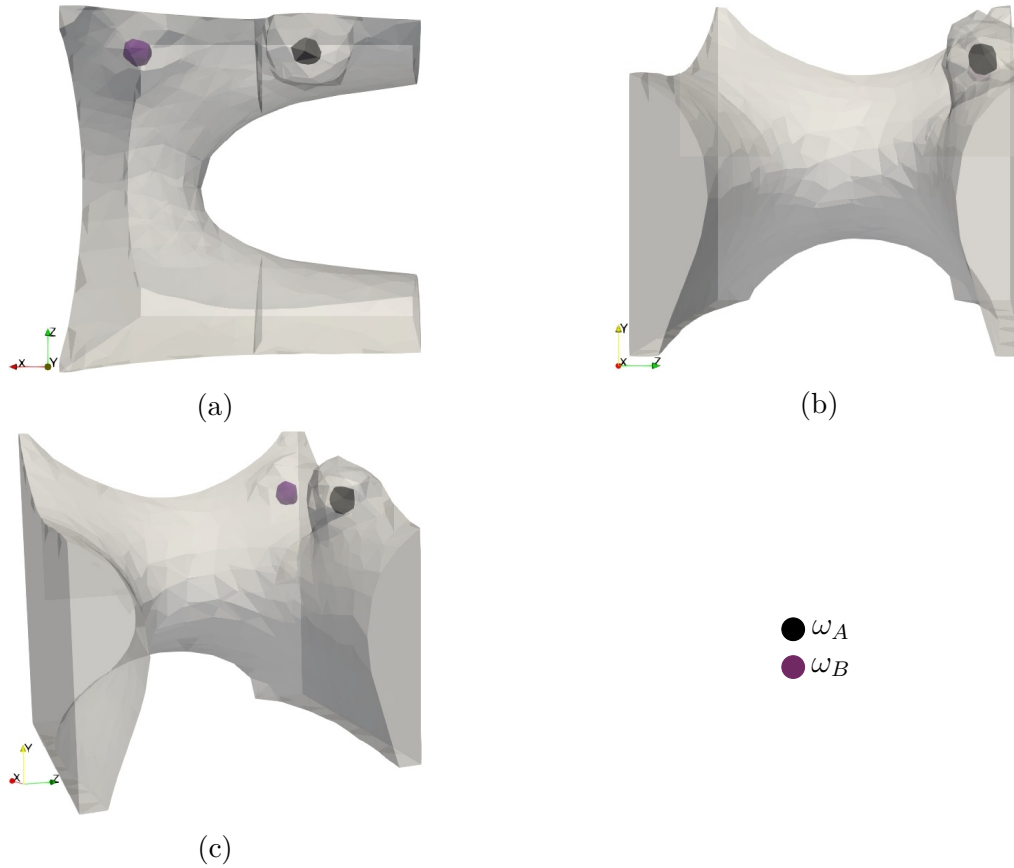


Figure 8.25: Optimal structure and bolt location for the problem of volume minimization under a compliance constraint and Von Mises criterion at the center of the bolt root with an alternating strategy of 1 iteration of structure advection and 1 iteration of parametric gradient for bolt location

Elasticity constraint at the rim of the root

The amplitude of the pre-tension force is still $\Phi = 25\,000$ N when considering the Von Mises criterion at the rim of the bolt root. The optimal structure and bolt location are given in Fig. 8.26. The final volume is $V(\Omega) = 439\,943$ mm³. The optimal bolt is at the point $\mathbf{x}_0 = (-10.6, 32.7, 33.1)$. This is quite an improvement compared to the structure optimization with fixed bolt for which the final volume was $V(\Omega) = 539\,829$ mm³.

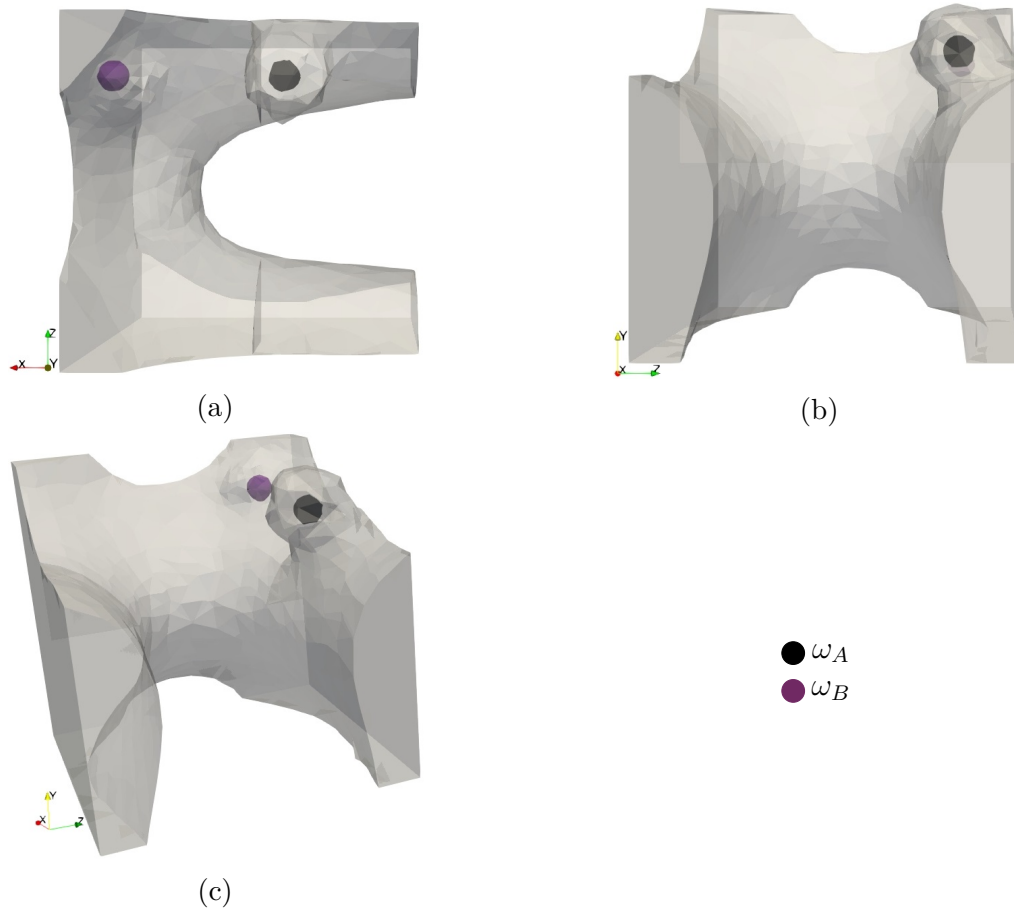


Figure 8.26: Optimal structure and bolt location for the problem of volume minimization under a compliance constraint and Von Mises criterion at the rim of the bolt root with an alternating strategy of 3 iterations of structure advection and 1 iteration of parametric gradient for bolt location

The history of convergence is given in Fig. 8.27. We display deliberately all iterations, even those which have been rejected. It is quite noticeable how the brutal violation of the Von Mises constraint leads to an important response of the bolt location, and not of the structure. The parametric optimization of the bolt location brings the constraint back in the admissible domain and proves its usefulness for the integration of specific mechanical constraint on the bolt. Actually, the change of location does not affect the oscillations of the compliance constraint around the bound. Note that these oscillations are customary for the Augmented Lagrangian method.

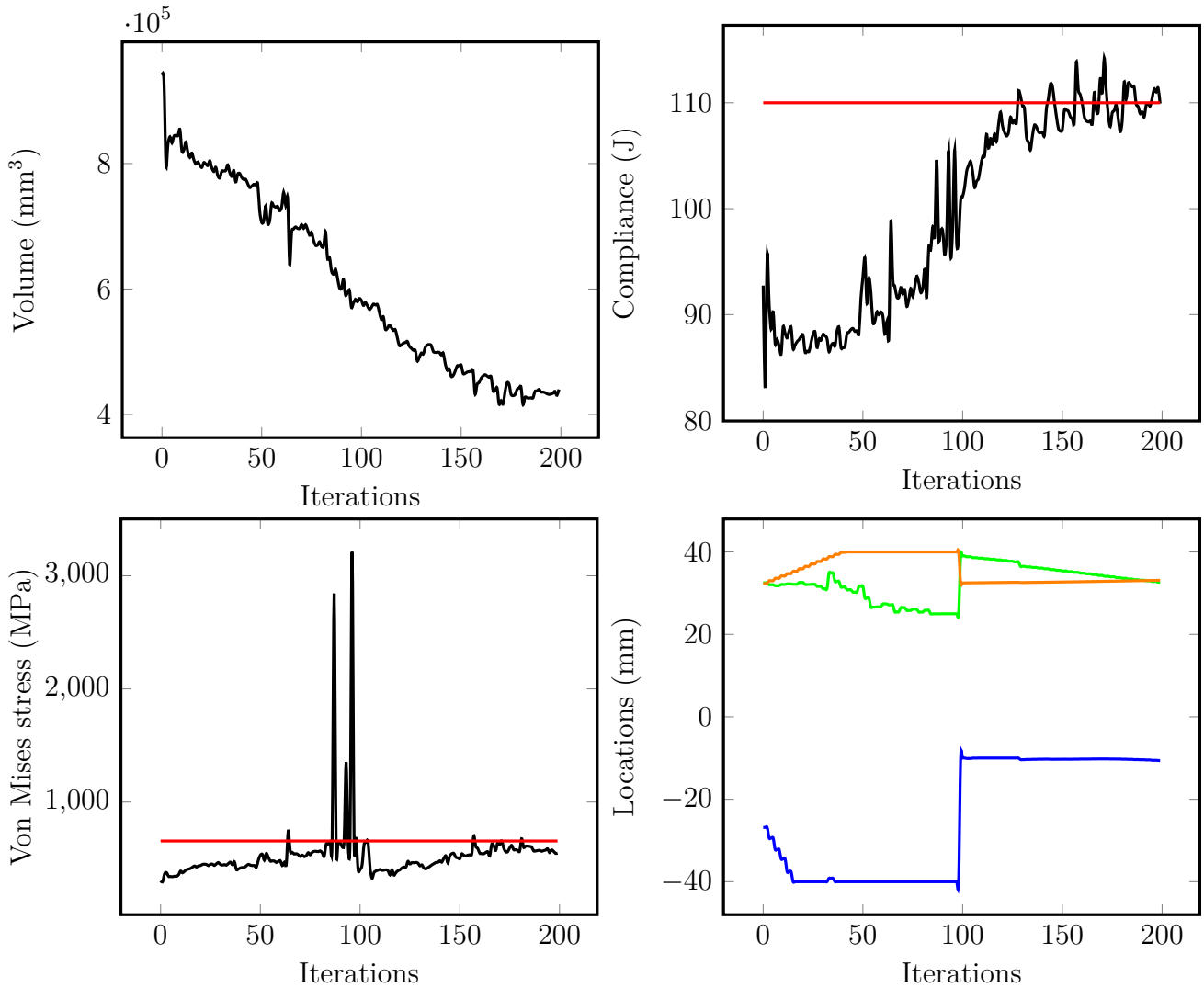


Figure 8.27: History of convergence of the problem of volume minimization under a compliance constraint and Von Mises criterion at the rim of the bolt root with an alternating strategy of 3 iterations of structure advection and 1 iteration of parametric gradient for bolt location (X in blue, Y in green and Z in orange)

We also remake the same optimization problem with a strategy of 1 iteration of structure advection and 1 iteration of parametric gradient. The optimal structure and bolt location are given in Fig. 8.28. The final volume of $V(\Omega) = 424\,601\text{ mm}^3$, which is a better result than the one given by the previous alternating strategy. The optimal bolt is at the point $\mathbf{x}_0 = (-10.1, 32.0, 33.2)$, which is quite close to the optimal location given by the previous alternating strategy. Then, the optimal location is almost the same but the weight reduction is better with a strategy of 1 iteration of structure advection and 1 iteration of parametric gradient for this test case.

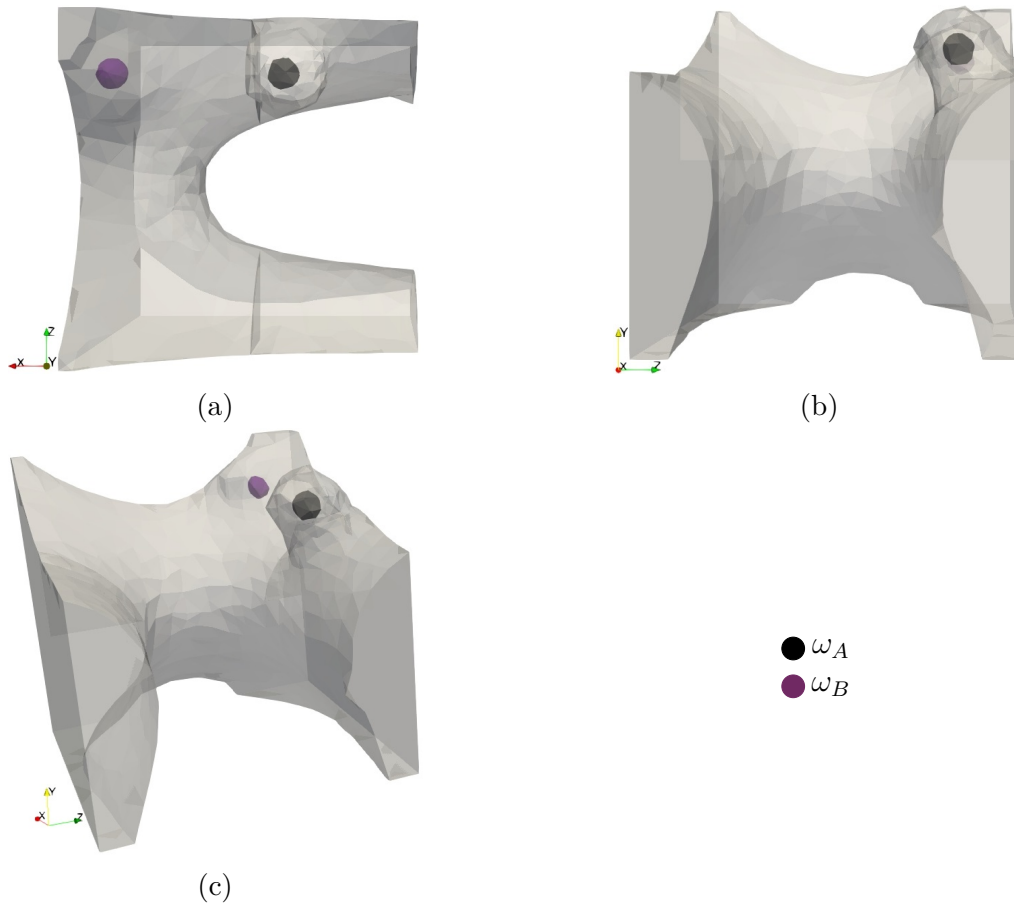


Figure 8.28: Optimal structure and bolt location for the problem of volume minimization under a compliance constraint and Von Mises criterion at the rim of the bolt root with an alternating strategy of 1 iteration of structure advection and 1 iteration of parametric gradient for bolt location

The history of convergence is given in Fig. 8.29. We still display deliberately all iterations, even those which have been rejected. A brutal decrease of the volume provokes an important increase of the compliance and the Von Mises constraint. The coupling proves its effectiveness by bringing each constraint back in the admissible domain : the structure advection acts for the compliance and the parametric gradient acts mainly for the Von Mises criterion.

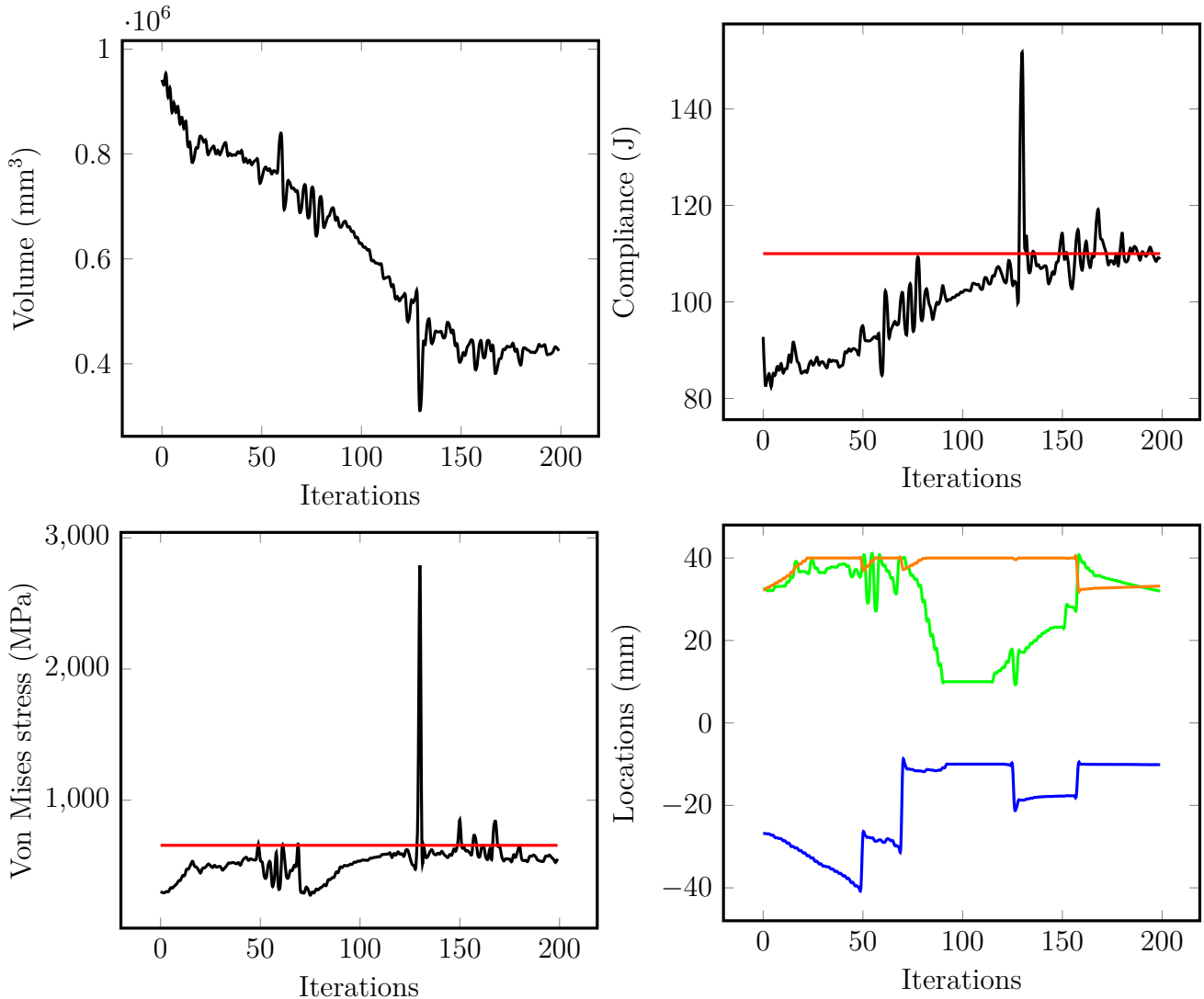


Figure 8.29: History of convergence of the problem of volume minimization under a compliance constraint and Von Mises criterion at the rim of the bolt root with an alternating strategy of 1 iteration of structure advection and 1 iteration of parametric gradient for bolt location (X in blue, Y in green and Z in orange)

Fatigue constraint on the bolt root

Fig. 8.30 gives different views of the optimal structure and bolt location for the problem of volume minimization under a compliance constraint and a fatigue constraint on the bolt root. We recall that the fatigue constraint was too difficult to be respected with the initial structure with holes for a structure optimization with fixed bolt. Then, the constraint had to be activated on a pre-optimized structure and led to a final volume of $V(\Omega) = 674\,574\text{ mm}^3$. The coupling proves its effectiveness by beginning with the structure with holes (see Fig. 8.18) and by ending with the structure displayed in Fig. 8.30. The final volume is $V(\Omega) = 434\,497\text{ mm}^3$ and the bolt optimal location is $\mathbf{x}_0 = (-10, 30.5, 20.4)$.

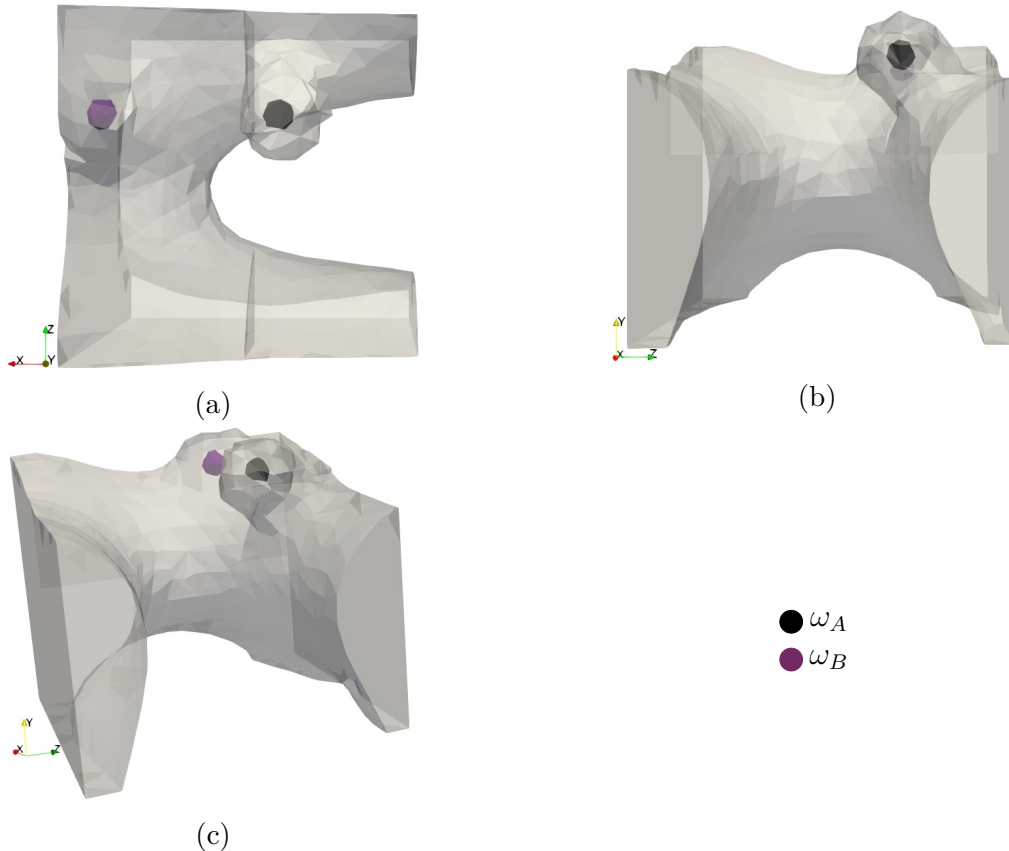


Figure 8.30: Optimal structure and bolt location for the problem of volume minimization under a compliance constraint and fatigue constraint on the bolt root with an alternating strategy of 3 iterations of structure advection and 1 iteration of parametric gradient for bolt location

8.3.5 Summary

The 6 DOFs bolt is initially placed by the topological derivative at the point $\mathbf{x}_0 = (-26.8, 32.5, 32.4)$ to decrease the compliance (see Fig. 8.16). Let us denote the constraints by their initial letters

- (C) : Compliance
- (VMC) : Von Mises at the Center
- (VMR) : Von Mises at the Rim
- (F) : Fatigue

Fig. 8.31 sums up the ramifications of structure and coupled structure/location optimization for this 3d use case. It gives the type of the optimization process, the constraint(s) taken into account and the final volume converted into liter (L) to be shorter. For coupled structure and location optimizations, we also give the alternating strategy between structure and location. For example, we denote "strategy 3-1" for 3 iterations of structure advection and 1 iteration of parametric gradient for the bolt location, and so on until convergence.

The optimal topology is always the same, whatever the optimization constraints. Differences lie on material distribution around the bolt. Depending on the choice of the alternating strategy between structure and location optimization, the coupling provides better results than structure optimization with fixed bolt.

Remark 76. *All shapes could be smoothed by using a refined mesh. We chose to use a coarse mesh and refine only around the spheres to save time computation.*

Simplified industrial use case

Contents

9.1 Rigid supports	269
9.1.1 Setting of the problem	269
9.1.2 A coupled optimization method	273
9.1.3 Results	276
9.2 Idealized bolt connections	279
9.2.1 Setting of the problem	279
9.2.2 The optimization problem	281
9.2.3 Reference optimization : structure only	282
9.2.4 Coupled optimization	288

This chapter deals with the simplified industrial use case of a bracket and accessories assembly. The first section models connections between the bracket and the crankcase by rigid supports. We show that the optimization of both structure and connections locations brings substantial gain on a simplified industrial use case, even if the connection model is basic. The second section investigates a coupled optimization of the structure and the locations and number of connections. It gathers all key points developed in this thesis, namely: the 6 degrees of freedom idealized bolt model complemented by specific mechanical constraints, the topological derivative to place new bolts, the parametric gradient-based algorithm to optimize bolts locations, and the level-set method to optimize the structure of the bracket.

9.1 Rigid supports

This section focuses on a coupled optimization of the topology of a part of an assembly and the locations of its rigid supports. It has been published in the article [96]:

L Rakotondrainibe, G Allaire, P Orval, Topology optimization of connections in mechanical systems. *Structural and Multidisciplinary Optimization*, 61:2253-2269, 2020.

The simplification procedure of this industrial use case is given in Appendix A.

9.1.1 Setting of the problem

Scope of the study

This section is devoted to a simplified model of an accessories and bracket assembly taken from a diesel engine (cf. Fig. 9.1). This simplified model has the characteristic dimensions of a reference model given by Renault (cf. Fig. 9.2). In the following test case, accessories are an alternator, a belt tensioning roller and an air conditioning (AC) compressor. Perfect bonding is assumed between the accessories and the bracket. The union of all accessories and of the bracket is what is called assembly. The accessories bracket insures their positioning and their fastening to the crankcase. The alternator supplies electricity to the vehicle. The belt tensioning roller regulates the belt tension. The AC compressor insures the flow and compression of the air conditioning fluid. In the sequel, the accessories are not optimized.

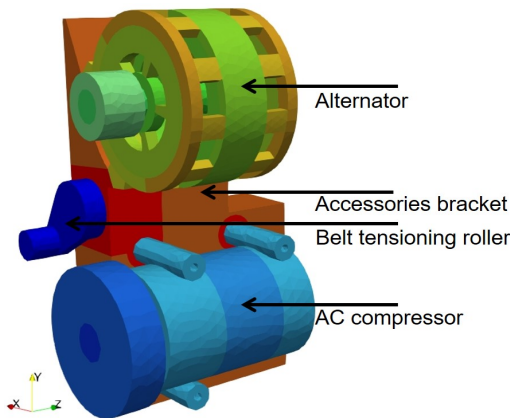


Figure 9.1: Simplified accessories and bracket where only the accessories bracket (in brown) is to be optimized



Figure 9.2: Reference engine (belt, accessories and bracket are in the lower left-hand corner)

In this test case, connections are rigid supports. They correspond to seven clamped zones of the bracket to the crankcase which is not represented in this study. For the sake of simplicity, they are represented by discs on the surface of the bracket. We choose this ideal shape in order to be functional and user-friendly.

The elasticity problem

Let \mathcal{D} be the working domain containing the accessories and bracket assembly. This assembly $\Omega_{ASB} \subset \mathcal{D}$ is made of disjoint parts

$$\Omega_{ASB} = \Omega \cup \Omega_{NDS} \cup \Omega_{ACC},$$

namely the design-space Ω (in brown in Fig. 9.1) and the non design-space Ω_{NDS} of the bracket and the accessories Ω_{ACC} (alternator, belt tensioning roller and AC compressor). Its boundaries is likewise divided into disjoint parts

$$\partial\Omega_{ASB} = \Gamma_{TF} \cup \Gamma_D \cup \Gamma_N,$$

where Γ_{TF} is the traction-free boundary, Γ_D corresponds to clamped zones and loads are applied on accessories pulleys Γ_N (Neumann boundary conditions). Since the accessories are not optimized, it is better to distinguish the traction-free boundary of the design-space of the bracket, denoted Γ , from the traction-free boundaries of accessories, that is $\Gamma_{TF} \setminus \Gamma$. These boundaries are displayed in Fig. 9.3 for further clarity. The orange part is the boundary to be optimized. We denote by \mathbf{n} the outer unit normal to $\partial\Omega_{ASB}$.

The assembly Ω_{ASB} is made of linear isotropic elastic materials. Typically, the bracket is aluminium and accessories are mostly aluminium or steel. For a displacement field $\mathbf{u} : \Omega_{ASB} \rightarrow \mathbb{R}^3$, the strain tensor is then defined by

$$\varepsilon(\mathbf{u}) = \frac{1}{2}(\nabla\mathbf{u} + \nabla^T\mathbf{u}).$$

The stress tensor is given by the Hooke's law

$$\mathbf{A}\varepsilon(\mathbf{u}) = 2\mu\varepsilon(\mathbf{u}) + \lambda\text{tr}(\varepsilon(\mathbf{u}))I,$$

with μ and λ the Lamé coefficients of the material. Surface loads on the accessories pulley are applied simultaneously on 3 different parts of Γ_N . Loads \mathbf{g} are then split into \mathbf{g}_{ALT} , \mathbf{g}_{BTR} and \mathbf{g}_{COMP} as displayed in Fig. 9.4. They correspond to integrated contact force of the tensioned belt on each pulley given in Table 9.1. These are values of the tension forces applied in the reference model. The mechanical analysis problem is then a single and static load case.

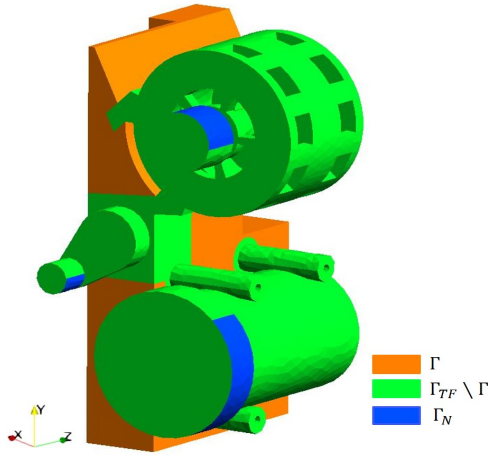


Figure 9.3: Boundaries of the sub-parts

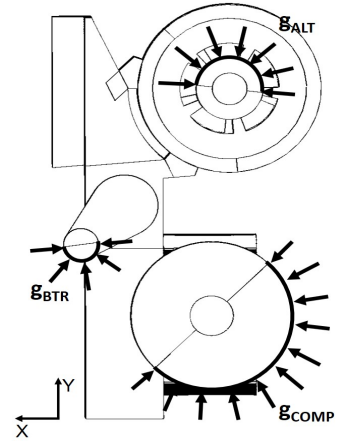


Figure 9.4: Load case

In the sequel, there are seven rigid supports, which are discs, centered at points \mathbf{x}_i , $1 \leq i \leq 7$ (cf. Fig. 9.6). Mathematically speaking, rigid supports correspond to zero displacement on the clamped zones Γ_D (Dirichlet boundary condition). However, the transition between Dirichlet and Neumann boundary conditions leads to singularity of the elastic displacement, which is a delicate issue for computing the shape derivative (see [50, 43] and Remark 77 for more details). To avoid mathematical technicalities, we rather use a penalization and regularization technique

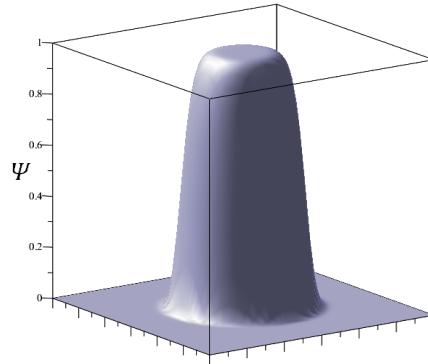
Table 9.1: Tension force values

Accessory	Tension force (N)
Alternator	2 020
Belt tensioning roller	1 554
AC compressor	2 742

to enforce the Dirichlet boundary condition. More precisely, the Dirichlet condition $\mathbf{u} = 0$ on Γ_D is replaced by the following Robin or Fourier condition

$$\mathbf{A}\varepsilon(\mathbf{u})\mathbf{n} = -\frac{1}{\epsilon}\mathbf{u}\Psi(\mathbf{x} - \mathbf{x}_i) \quad (9.1)$$

for each rigid support $1 \leq i \leq 7$. The penalization coefficient $\epsilon > 0$ is a very small value and Ψ is a regularization of the characteristic function of the rigid support i centred at \mathbf{x}_i . To avoid discontinuous boundary condition on Γ_{BRDS} , the smooth function Ψ is equal to 1 inside the disc of center \mathbf{x}_i , then decrease to 0 in the vicinity of that disc and is equal to 0 otherwise (cf. Fig. 9.5). Furthermore, this penalization technique avoids remeshing the rigid supports zones while optimizing their location. The center \mathbf{x}_i of the smoothed characteristic function is the only parameter that varies. They are restricted such that functions $\Psi(\mathbf{x} - \mathbf{x}_i)$ have disjointed support.

Figure 9.5: Regularized characteristic function Ψ of a given rigid support

Assuming that surface loads are smooth enough, the displacement field \mathbf{u} of the assembly is then the unique solution of the linear elasticity problem

$$\left\{ \begin{array}{l} -\mathbf{div}(\mathbf{A}\varepsilon(\mathbf{u})) = \mathbf{0} \text{ in } \Omega_{ASB} \\ \mathbf{A}\varepsilon(\mathbf{u})\mathbf{n} = \mathbf{g} \text{ on } \Gamma_N \\ \mathbf{A}\varepsilon(\mathbf{u})\mathbf{n} = \mathbf{0} \text{ on } \Gamma_{TF} \setminus \Gamma \\ \mathbf{A}\varepsilon(\mathbf{u})\mathbf{n} = -\frac{1}{\epsilon}\mathbf{u} \sum_{i=1}^7 \Psi(\mathbf{x} - \mathbf{x}_i) \text{ on } \Gamma \end{array} \right. \quad (9.2)$$

Note that, since Ψ is a smooth compactly supported function, the solution \mathbf{u} of the above system is smooth and its shape derivative can easily be computed, in particular when moving the positions \mathbf{x}_i of the rigid supports.

The optimization problem

An industrial goal is to minimize the weight of the bracket. Since the material density is constant, the weight minimization is equivalent to a volume minimization. We consider the volume of the optimizable part of the bracket, in other words, the design space of the bracket

$$V(\Omega) = \int_{\Omega} dV. \quad (9.3)$$

The volume reduction implies a loss of the assembly stiffness which is controlled by the increase of the work done by the loads, that is to say the compliance of the assembly, which reads

$$C(\Omega, \mathbf{x}_i) = \int_{\Gamma_N} \mathbf{g} \cdot \mathbf{u} dS. \quad (9.4)$$

The initial compliance, denoted C_0 , is the work done by loads with the full bracket before the optimization process. In this test case, an increase of a given rate η of the initial compliance is allowed.

Design variables are the structure of the bracket (denoted by Ω) and the rigid supports locations \mathbf{x}_i . The main purpose is then to find simultaneously the best compromise between the topology of the bracket and the locations of rigid supports. As there are two types of design variables, there should be two types of design-spaces (cf. Fig. 9.6). Each support is allowed to translate in the plane (\mathbf{Y}, \mathbf{Z}) representing the crankcase face, within a specific allocated area to avoid collision of supports. One can choose an other division. The design space of the structure is naturally the entire bracket.

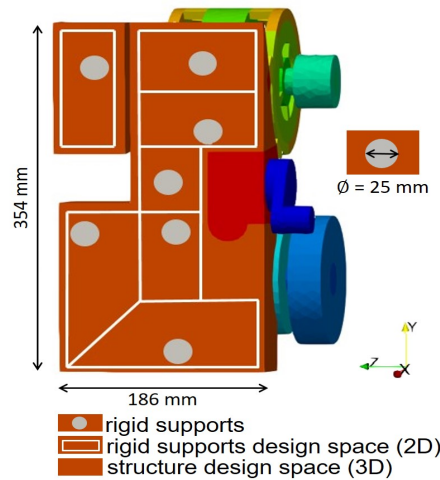


Figure 9.6: Rigid supports and structure design spaces

The optimization problem is then to minimize the volume of the bracket (9.3) under a constraint on the maximal compliance of the assembly (9.4). A typical formulation of this problem is

$$\begin{aligned} \min_{(\Omega, \mathbf{x}_i) \in \mathcal{U}_{ad}} \quad & V(\Omega), \\ \text{s.t.} \quad & C(\Omega, \mathbf{x}_i) \leq (1+\eta)C_0 \end{aligned} \quad (9.5)$$

where \mathcal{U}_{ad} is the set of admissible shapes of the structure and admissible locations of rigid supports. Note that the volume $V(\Omega)$ does not depend on the rigid supports locations \mathbf{x}_i . The

problem (9.5) is rewritten using the augmented Lagrangian functional, $J(\Omega, \mathbf{x}_i)$, that reads

$$\min_{(\Omega, \mathbf{x}_i) \in \mathcal{U}_{ad}} \max_{\alpha \geq 0} \left\{ J(\Omega, \mathbf{x}_i) = V(\Omega) + \alpha(C(\Omega, \mathbf{x}_i) - (1 + \eta)C_0) + \frac{\beta}{2}(C(\Omega, \mathbf{x}_i) - (1 + \eta)C_0)^2 \right\}, \quad (9.6)$$

where α and β are respectively Lagrange multiplier and penalty parameter for the compliance constraint. The value of α is optimized and that of β is updated during the optimization process (see Subsection 9.1.2 for details). Readers are referred to [70] and [84] for more informations about augmented Lagrangian methods.

9.1.2 A coupled optimization method

We propose here a coupled method for the optimization of both the structure of the bracket and the locations of rigid supports. An important distinction should be made between connections and structure. Although both are optimized using a gradient-based method, this distinction comes from their different representation. Rigid supports have simple and fixed shapes: their centers are the only design variables. By contrast, the shape of the structure is geometrically more complex. Its boundary is optimized by using the level-set method. As there are two types of design-variables, there are two associate design-spaces. In the following, to compute gradients (more precisely, partial derivatives) with respect to one type of design variables, the other type of design variables is kept fixed. Thus, support locations are fixed when the structure is optimized and vice versa.

Parametrization of the rigid supports

The rigid supports have fixed shapes and sizes and only their centers are design variables. Their optimization is thus performed with a parametric gradient-based algorithm

$$\mathbf{x}_i^{k+1} = \mathbf{x}_i^k - \delta^k \frac{\partial J}{\partial \mathbf{x}_i}(\Omega, \mathbf{x}_i^k), \quad (9.7)$$

where \mathbf{x}_i^k is the center of the rigid support i at iteration k , δ^k is the descent step and $\frac{\partial J}{\partial \mathbf{x}_i}(\Omega, \mathbf{x}_i)$ is the partial derivative of (9.6). Because of our choice of a penalized and regularized formulation of the rigid supports, they don't need to be exactly meshed and there is no remeshing during the optimization process. This approach is then numerically cost-effective.

Derivative of the objective function with respect to support locations

Consider the rigid support i centered at point \mathbf{x}_i . The descent direction of (9.7) is obtained by differentiating J with respect to the point \mathbf{x}_i . This Lagrangian functional J , defined by (9.6), depends on \mathbf{x}_i through the compliance but it is not clearly explicit in its expression (9.6). To bring to light this dependence, let us consider for simplicity the compliance C , defined by (9.4), instead of J (which depends polynomially on C) and define another Lagrangian function

$$\begin{aligned} \mathcal{L}(\Omega, \mathbf{v}, \mathbf{q}, \mathbf{x}_i) &= \int_{\Gamma_N} \mathbf{g} \cdot \mathbf{v} dS + \int_{\Omega_{ASB}} \mathbf{A}\varepsilon(\mathbf{v}) : \varepsilon(\mathbf{q}) dV - \int_{\Gamma_N} \mathbf{g} \cdot \mathbf{q} dS \\ &+ \frac{1}{\epsilon} \sum_{i=1}^7 \int_{\Gamma} \mathbf{v} \cdot \mathbf{q} \Psi(\mathbf{x} - \mathbf{x}_i) dS, \end{aligned} \quad (9.8)$$

where $\mathbf{v}, \mathbf{q} \in H^1(\mathbb{R}^3)^3$ and $\Omega \subset \Omega_{ASB}$ are independent variables. As usual, one can check that the system is self-adjoint, *i.e.*, the adjoint state \mathbf{p} is simply $\mathbf{p} = -\mathbf{u}$. Introduce the coordinates of the vector $\mathbf{x}_i = (x_i, y_i, z_i)$. Recalling that rigid supports are allowed to translate in the plane (\mathbf{Y}, \mathbf{Z}) , the partial derivative of \mathcal{L} with respect to x_i is zero. The descent directions along \mathbf{Y} and \mathbf{Z} are respectively obtained by first differentiating the Lagrangian (9.8) at y_i and z_i for fixed (\mathbf{v}, \mathbf{q}) and, second, evaluating the derivative at $(\mathbf{v}, \mathbf{q}) = (\mathbf{u}, -\mathbf{u})$. We obtain

$$\begin{aligned} \frac{\partial \mathcal{L}}{\partial y_i}(\Omega, \mathbf{u}, -\mathbf{u}, \mathbf{x}_i) &= \frac{1}{\epsilon} \int_{\Gamma} |\mathbf{u}|^2 \frac{\partial \Psi}{\partial y_i}(\mathbf{x} - \mathbf{x}_i) dS, \\ \frac{\partial \mathcal{L}}{\partial z_i}(\Omega, \mathbf{u}, -\mathbf{u}, \mathbf{x}_i) &= \frac{1}{\epsilon} \int_{\Gamma} |\mathbf{u}|^2 \frac{\partial \Psi}{\partial z_i}(\mathbf{x} - \mathbf{x}_i) dS. \end{aligned} \quad (9.9)$$

The adjoint state is defined such that the partial derivative of the Lagrangian is equal to the partial derivative of the compliance. We have then

$$\frac{\partial \mathcal{L}}{\partial \mathbf{x}_i}(\Omega, \mathbf{u}, -\mathbf{u}, \mathbf{x}_i) = \frac{\partial C}{\partial \mathbf{x}_i}(\Omega, \mathbf{u}, -\mathbf{u}, \mathbf{x}_i). \quad (9.10)$$

The partial derivative of J , defined by (9.6), is now easy to calculate and it is left to the readers.

Remark 77. *If the Dirichlet boundary conditions on the supports $\Gamma_{BR_{DS}}$ were not penalized and regularized, the computation of the derivative (9.9) would be much more involved. Although the computation of shape derivatives for Dirichlet boundary conditions is well known (see e.g. [5, 7]), the difficulty is that the elastic displacement \mathbf{u} is not smooth on the line which is the transition between Dirichlet boundary conditions and Neumann boundary conditions and therefore most classical formulas of shape derivatives do not hold true. For more details, the reader is referred to [50, 43]. This lack of regularity of \mathbf{u} at the interface on the boundary between a Dirichlet zone and a Neumann zone is overcome by the penalization or Robin boundary condition (9.1), as well as the smoothness of the regularization Ψ of the characteristic function of the support (see Fig. 9.5). In such a case, the resulting displacement \mathbf{u} is smooth and the problem is suitable for the classical formulas of shape derivatives with Hadamard's method. This difficulty appears also in the case of an interface optimization and it can be cured also by a regularization process as explained in [6].*

Level-set method for the structure

Let $\mathcal{D} \in \mathbb{R}^3$ be a working domain containing all admissible shapes. The structure Ω is described by a function φ defined on \mathcal{D} by

$$\begin{cases} \varphi < 0 & \text{in } \Omega \\ \varphi = 0 & \text{on } \partial\Omega \cap \overline{\mathcal{D}}. \\ \varphi > 0 & \text{on } \mathcal{D} \setminus \overline{\Omega} \end{cases} \quad (9.11)$$

The level-set method captures a given shape on a fixed mesh and it does not require remeshing. The shape is optimized using a gradient-based algorithm. The shape, initially defined by $\varphi_0(\mathbf{x})$, is updated to a new shape defined by $\varphi(t, \mathbf{x})$, by solving the following advection Hamilton-Jacobi equation

$$\begin{cases} \frac{\partial \varphi}{\partial t}(t, \mathbf{x}) + V(t, \mathbf{x}) |\nabla \varphi(t, \mathbf{x})| = 0, \\ \varphi(0, \mathbf{x}) = \varphi_0(\mathbf{x}) \end{cases}, \quad (9.12)$$

where $V(t, \mathbf{x})$ is a scalar advection velocity given by the shape derivative of the Lagrangian functional (9.6).

Shape derivative for the structure

The advection velocity of (9.12) is obtained by Hadamard's method of shape differentiation. The dependence on \mathbf{x}_i is left out to ease the notations. For a bounded smooth domain Ω in \mathbb{R}^3 , we consider variations of the form $\Omega_\theta = (Id + \boldsymbol{\theta})(\Omega)$, where $\boldsymbol{\theta} \in \mathcal{C}^1(\mathbb{R}^3)^3$ is a small vector field. In other words, $\boldsymbol{\theta}$ is the displacement field defining the transport of the initial domain Ω to the new one Ω_θ . Following [81, 94, 105, 109] the shape derivative of a function J at Ω is defined as the Fréchet differential at 0 of the map $\boldsymbol{\theta} \mapsto J((Id + \boldsymbol{\theta})(\Omega))$,

$$J((Id + \boldsymbol{\theta})(\Omega)) = J(\Omega) + J'(\Omega)(\boldsymbol{\theta}) + o(\boldsymbol{\theta}) \text{ with } \lim_{\boldsymbol{\theta} \rightarrow 0} \frac{|o(\boldsymbol{\theta})|}{\|\boldsymbol{\theta}\|} = 0, \quad (9.13)$$

where $\boldsymbol{\theta} \mapsto J'(\Omega)(\boldsymbol{\theta})$ is a continuous linear map on $\mathcal{C}^1(\mathbb{R}^3)^3$. The shape derivative of the volume is well-known

$$V'(\Omega)(\boldsymbol{\theta}) = \int_{\Gamma} \boldsymbol{\theta} \cdot \mathbf{n} dS.$$

As in [7], the shape derivative of the compliance is obtained by differentiating the Lagrangian (9.8) at Ω for fixed (\mathbf{v}, \mathbf{q}) . Recall that the inhomogeneous Neumann boundaries (where the loads are applied) are fixed. It means that $\boldsymbol{\theta} \equiv 0$ on Γ_N . Again, since the Lagrangian (9.8) features the compliance, the problem is self-adjoint and the adjoint state is simply $\mathbf{p} = -\mathbf{u}$. Differentiating $\mathcal{L}(\Omega, \mathbf{v}, \mathbf{q})$ with respect to the shape and evaluating the derivative at $(\mathbf{v}, \mathbf{q}) = (\mathbf{u}, -\mathbf{u})$ yields

$$\frac{\partial \mathcal{L}}{\partial \Omega}(\Omega, \mathbf{u}, -\mathbf{u})(\boldsymbol{\theta}) = - \int_{\Gamma} \boldsymbol{\theta} \cdot \mathbf{n} \left(\mathbf{A}\boldsymbol{\varepsilon}(\mathbf{u}) : \boldsymbol{\varepsilon}(\mathbf{u}) + \frac{1}{\epsilon} \sum_{i=1}^7 \left(\frac{\partial |\mathbf{u}|^2}{\partial \mathbf{n}} + H|\mathbf{u}|^2 \right) \Psi(\mathbf{x} - \mathbf{x}_i) \right) dS,$$

where $H = \text{div}(\mathbf{n})$ is the mean curvature. However, rigid supports locations are fixed during the optimization of the structure. They are excluded from the design-space of the structure. Therefore, the vector $\boldsymbol{\theta}$ vanishes on each rigid support. The shape derivative of the Lagrangian thus reads

$$\frac{\partial \mathcal{L}}{\partial \Omega}(\Omega, \mathbf{u}, -\mathbf{u})(\boldsymbol{\theta}) = - \int_{\Gamma} \boldsymbol{\theta} \cdot \mathbf{n} \mathbf{A}\boldsymbol{\varepsilon}(\mathbf{u}) : \boldsymbol{\varepsilon}(\mathbf{u}) dS. \quad (9.14)$$

As previously, the shape derivative of the Lagrangian is equal to the shape derivative of the compliance. All the elements are here to calculate the shape derivative of the Lagrangian function (9.6) and it is left to the readers.

Interactions between rigid supports and structure

From a technological point of view, the bolt threads need some minimal surrounding of material so that diffusion of efforts into the structure is appropriate (cf. Fig. 9.7). This minimal volume of material has a fixed geometry that is deduced from the characteristic shape and size of the rigid support. In numerical practice during the optimization process, this minimal volume follows the rigid support location. Imposing a negative level set function inside this non-design domain ensures an appropriate interaction with the design space of the structure being optimized.

We recall that in the following, for the sake of simplicity, two rigid supports cannot merge nor collapse. This is ensured by assigning disjointed design space for each rigid support (see Fig. 9.6).

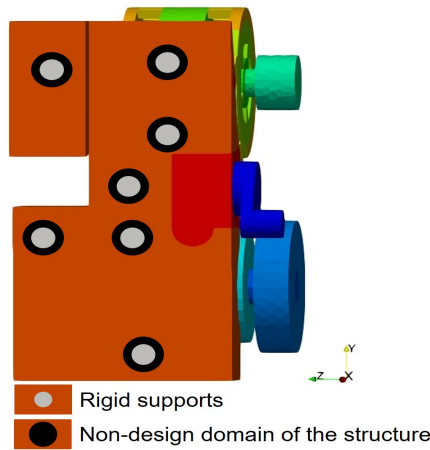


Figure 9.7: Rigid supports surrounded by non-design domain of the structure

Algorithm

The level-set of the structure is initialized as the completely filled bracket design space. The number of connections is fixed to 7. Their initial location corresponds approximately to the reference model (see Fig. 9.6). The structure and the support locations are alternatively optimized. Inside the optimization loop, two iterations of structure optimization are performed, followed by one iteration for the support locations, until convergence. This alternate scheme handles easily the different order of sensibilities magnitude of respectively the structure and the supports. The Lagrange multiplier for the constraint on the compliance defined at (9.6) is optimized according to the optimality condition at each iteration by

$$\alpha^{k+1} = \alpha^k + \beta(C(\Omega^k, \mathbf{x}_i^k) - (1 + \eta)C_0), \quad (9.15)$$

The penalty parameter β is multiplied by a factor 1.1 every 10 iterations. They are initialized to $\alpha = 1$ and $\beta = 0.01$. Concerning the rigid supports, which are not meshed and move according to their center \mathbf{x}_i , they are updated by (9.7) where the descent step δ^k is initialized to move them by at most one or two lengthscales of the mesh. The Hamilton-Jacobi equation (9.12) is advected with a standard scheme [7].

This work relies on two types of continuous gradients (the shape derivative for the structure and a family of partial derivatives for rigid supports). An elementary stopping criterion would be to check if the norm of each gradient tends toward zero. However, numerical discretization errors of these derivatives, due to the present differentiate-then-discretize method, imply that their norm will never go to zero. One could implement a stopping criterion by checking if the gradient norm is small enough, which requires a calibration of the numerical errors. For simplicity, we did not use any stopping criterion and rather the number of iterations was fixed at the beginning. The algorithm can be restarted with the last shape and locations as initial guess if the number of iterations is not satisfactory.

9.1.3 Results

The test case uses a tetrahedral mesh with 109 360 elements. We recall that the optimization problem is to minimize the volume of the bracket under a compliance constraint (see (9.5)). An increase of $\eta = 2\%$ of the compliance is allowed. Figs. 9.8 and 9.9 compare the optimal bracket obtained respectively by a classical structure optimization (without moving rigid supports) and by a coupled optimization of both structure and support locations. The bracket topology is

significantly different since it is a single block in the first case whereas it is divided into two parts in the coupling case. Extremal changes in support locations range from 12 to 28 mm. The support optimization has been able to identify one useless connection. It is still displayed on Fig. 9.9 because of the settings of the non-design domain of the structure around the rigid support. However, this support, disconnected from the structure, is not necessary to respect the compliance constraint. It is noteworthy that the same support is needed by the optimized design on Fig. 9.8 in order to respect the compliance constraint. Therefore, the coupled optimization, not only can improve the final design, but can also indirectly optimize the number of connections. Of course, it only leads to a reduction of that number, not an increase. Finally, this use case reveals about 1.50kg of lightening of the bracket compared to a classical optimization of its structure (corresponding to an additional 35% improvement).

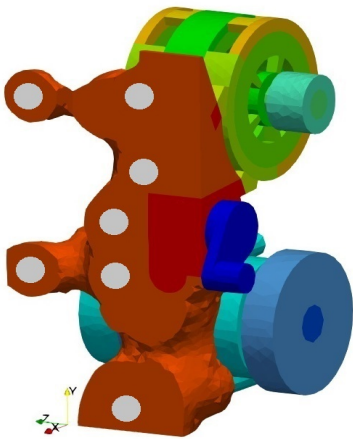


Figure 9.8: Classic structure optimization for fixed support locations

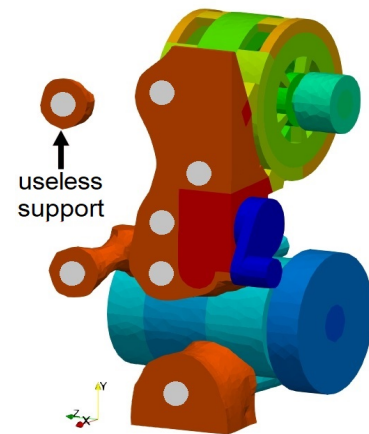


Figure 9.9: Coupled support locations and structure optimization

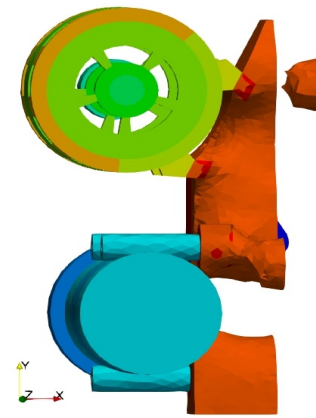
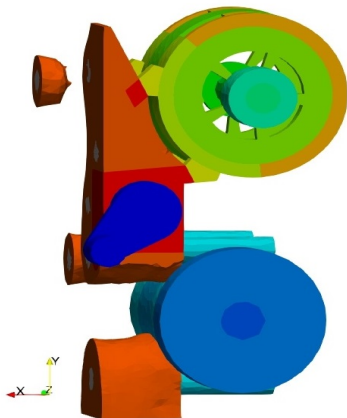


Figure 9.10: Lateral views of result in Fig. 9.9 : Coupled support locations and structure optimization

Figs. 9.11 and 9.12 give the history of convergence of the volume and the compliance for the classical structure optimization and for the coupled optimization. One can notice oscillations of the compliance in the case of the coupling. Those oscillations are typical of augmented Lagrangian algorithm where the value of the constraint converge non-monotonically to the target value. Actually, the optimization of support locations decreases the compliance. It

counterbalances the increase due to the volume minimization. Results are gathered in the Table 9.2.

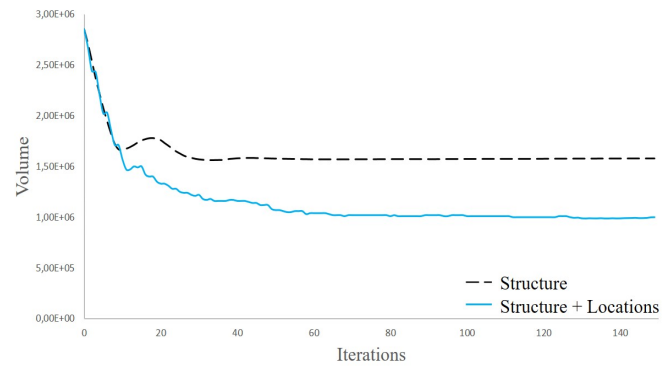


Figure 9.11: History of volume convergence for classical and coupled optimization

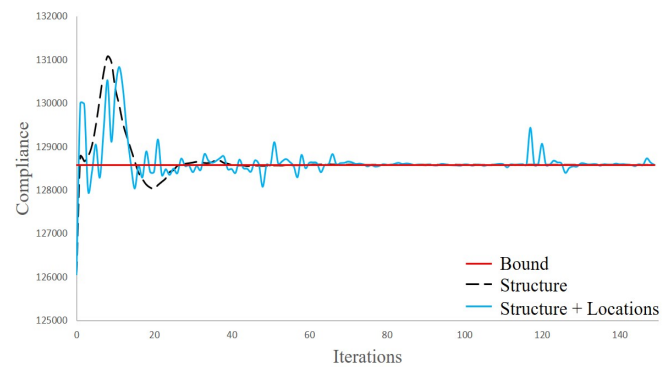


Figure 9.12: History of compliance convergence for classical and coupled optimization

Table 9.2: Comparison of classical and coupled optimization results

Design variables	Weight (kg)	Volume (mm ³)	Compliance (μ J)
Structure	4.22	1.56E+06	128 581
Supports + Structure	2.71	1.00E+06	128 581

9.2 Idealized bolt connections

9.2.1 Setting of the problem

The simplified model is revisited for the use of idealized bolts. The upper portion of the bracket is removed and the crankcase is added with an idealized geometry as two disjoint parts on the assembly (in gray in Fig. 9.13). Then the assembly Ω_{ASB} is made of disjoint parts

$$\Omega_{ASB} = \Omega \cup \Omega_{NDS} \cup \Omega_{ACC} \cup \Omega_{CKC}$$

namely the design-space Ω (in brown in Fig. 9.13) and the non design-space Ω_{NDS} of the bracket, the accessories Ω_{ACC} and the crankcase Ω_{CKC} . Boundaries are defined by

$$\partial\Omega_{ASB} = \Gamma_{TF} \cup \Gamma_D \cup \Gamma_N$$

where Γ_{TF} is the traction-free boundary, Γ_D corresponds to clamped zones and loads are applied on accessories pulleys Γ_N as displayed in Fig. 9.14. Since the accessories are not optimized, it is better to distinguish the traction-free boundary of the design-space of the bracket, denoted Γ , from the traction-free boundaries of accessories, that is $\Gamma_{TF} \setminus \Gamma$. The crankcase is not tied to the bracket. A penalized and regularized sliding contact condition is imposed between them (see [74] for the description and [39] and [46] for convergence proofs). The contact model in the framework of shape optimization is studied in [44]. The load case remains the same (see Fig. 9.4 and Table 9.1). It corresponds to surface loads \mathbf{g} on the accessories pulley.

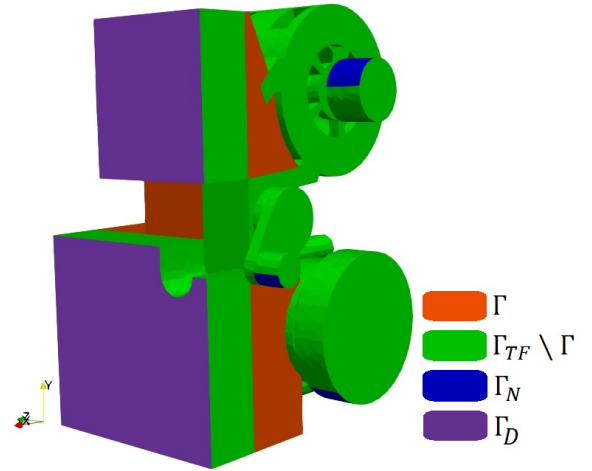
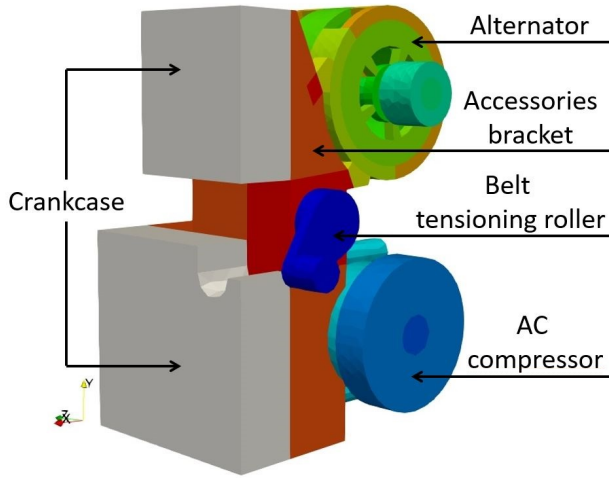


Figure 9.13: Simplified accessories and bracket assembly used with the idealized bolt model

Figure 9.14: Boundaries of the assembly

Connections are modeled by 6 DOFs idealized bolts according to the model described in Chapter 2. We consider n identical idealized bolts with the following properties, corresponding to M10×1.5 standard bolt :

- radius $r_b = 4.3$ mm
- length $\ell = 50$ mm
- Young's modulus $E = 200$ GPa
- Poisson's coefficient $\nu = 0.3$

- Pre-tension force $\Phi = 20\,000$ N
- Minimal yield stress of the root $Re_{min} = 900$ MPa

Then, the bolts are described by the same rigidity matrix \mathbf{K} (see (2.1)) with a traction/torsion and a shear/flexion parts respectively denoted $\bar{\mathbf{K}}$ and $\tilde{\mathbf{K}}$. Denote ω_{A_i} and ω_{B_i} the head and the threads of the bolt i with $1 \leq i \leq n$. Bolts extremities are rigid spheres in order to provide an appropriate representation of the Euler-Bernoulli condition for long beam (see Section 2.3). Therefore, the space of admissible displacements corresponds to zero displacement on Γ_D and rigid body motions in bolts extremities

$$\mathcal{W}_{RB} = \left\{ \begin{array}{l} \mathbf{w} = \mathbf{0} \text{ on } \Gamma_D, \\ \mathbf{w} \in (H^1(\Omega_{ASB}))^3, \mathbf{w}(\mathbf{x}) = \mathbf{C}_a^i + \mathbf{R}_a^i \mathbf{x} \text{ in } \omega_{A_i}, \forall i \in \llbracket 1, n \rrbracket, \\ \mathbf{w}(\mathbf{x}) = \mathbf{C}_b^i + \mathbf{R}_b^i \mathbf{x} \text{ in } \omega_{B_i}, \forall i \in \llbracket 1, n \rrbracket, \end{array} \right\}. \quad (9.16)$$

We recall the notation of the average degrees of freedom on ω_A of the displacement field for the average degrees of freedom on ω_A of an arbitrary displacement field \mathbf{w}

$$\mathbf{w}^A = \left(\begin{array}{c} \int_{\omega_A} \mathbf{w} dV \\ \frac{1}{2} \int_{\omega_A} \text{curl}(\mathbf{w}) dV \end{array} \right) = \left(\begin{array}{c} \frac{1}{|\omega_A|} \int_{\omega_A} \mathbf{w} dV \\ \frac{1}{2|\omega_A|} \int_{\omega_A} \text{curl}(\mathbf{w}) dV \end{array} \right).$$

The pre-stressed state, or Step 1, is described by a displacement field \mathbf{u}_{S1} , solution of the variational problem :

$$\begin{aligned} \text{Find } \mathbf{u}_{S1} \in \mathcal{W}_{RB} \text{ s.t. } \forall \mathbf{w} \in \mathcal{W}_{RB}, \quad & \int_{\Omega_{ASB} \setminus \bigcup_{i=1}^n (\omega_{A_i} \cup \omega_{B_i})} \mathbf{A} \varepsilon(\mathbf{u}_{S1}) : \varepsilon(\mathbf{w}) dV \\ & + \sum_{i=1}^n (\mathbf{U}_{S1}^{B_i} - \mathbf{U}_{S1}^{A_i})^T \tilde{\mathbf{K}} (\mathbf{W}^{B_i} - \mathbf{W}^{A_i}) + \sum_{i=1}^n \Phi \left(\int_{\omega_{B_i}} \mathbf{w} \cdot \mathbf{e} dV - \int_{\omega_{A_i}} \mathbf{w} \cdot \mathbf{e} dV \right) = 0. \end{aligned} \quad (9.17)$$

The in-service state, or Step2, is described by a displacement field \mathbf{u}_{S2} , solution of the variational problem :

$$\begin{aligned} \text{Find } \mathbf{u}_{S2} \in \mathcal{W}_{RB} \text{ s.t. } \forall \mathbf{w} \in \mathcal{W}_{RB}, \quad & \int_{\Omega_{ASB} \setminus \bigcup_{i=1}^n (\omega_{A_i} \cup \omega_{B_i})} \mathbf{A} \varepsilon(\mathbf{u}_{S2}) : \varepsilon(\mathbf{w}) dV - \int_{\Gamma_N} \mathbf{g} \cdot \mathbf{w} dS \\ & + \sum_{i=1}^n (\mathbf{U}_{S2}^{B_i} - \mathbf{U}_{S2}^{A_i})^T \mathbf{K} (\mathbf{W}^{B_i} - \mathbf{W}^{A_i}) - \sum_{i=1}^n (\mathbf{U}_{S1}^{B_i} - \mathbf{U}_{S1}^{A_i})^T \bar{\mathbf{K}} (\mathbf{W}^{B_i} - \mathbf{W}^{A_i}) \\ & + \sum_{i=1}^n \Phi \left(\int_{\omega_{B_i}} \mathbf{w} \cdot \mathbf{e} dV - \int_{\omega_{A_i}} \mathbf{w} \cdot \mathbf{e} dV \right) = 0. \end{aligned} \quad (9.18)$$

9.2.2 The optimization problem

The problem is to minimize the volume of the bracket $V(\Omega) = \int_{\Omega} dV$ under a constraint on the compliance of the assembly $C(\Omega) = \int_{\Gamma_N} \mathbf{g} \cdot \mathbf{u}_{S2} dS$. Mechanical constraints, specific to the bolt, are added for physical representativeness of the model. There are defined in Section 2.4. Von Mises constraints, evaluated at the end of Step 2, and fatigue constraint are implemented on each bolts. For the sake of simplicity, we consider for fatigue cycle that belt tension undergoes variations of full amplitude \mathbf{g} , which is not the case in real in-service conditions. We recall their expression

- Von Mises constraint at the rim for the bolt i , $1 \leq i \leq n$

$$VMR_i(\Omega, \mathbf{x}_i) = \left(\frac{\sqrt{(F_i^1(\mathbf{u}_{S2}))^2}}{\pi r_b^2} + \frac{\sqrt{(M_i^2(\mathbf{u}_{S2}) - \ell_0 F_i^3(\mathbf{u}_{S2}))^2 + (M_i^3(\mathbf{u}_{S2}) + \ell_0 F_i^2(\mathbf{u}_{S2}))^2}}{\frac{\pi}{4} r_b^3} \right)^2 + 3 \left(\frac{M_i^1(\mathbf{u}_{S2})}{\frac{\pi}{2} r_b^3} \right)^2$$

- Von Mises constraint at the center for the bolt i , $1 \leq i \leq n$

$$VMC_i(\Omega, \mathbf{x}_i) = \left(\frac{F_i^1(\mathbf{u}_{S2})}{\pi r_b^2} \right)^2 + 3 \left(\frac{4 \sqrt{(F_i^2(\mathbf{u}_{S2}))^2 + (F_i^3(\mathbf{u}_{S2}))^2}}{3 \pi r_b^2} \right)^2$$

- Fatigue constraint for the bolt i , $1 \leq i \leq n$

$$F_i(\Omega, \mathbf{x}_i) = \left(\frac{\sqrt{(\Delta F_i^1)^2}}{\pi r_b^2} + \frac{\sqrt{(\Delta M_i^2 - \ell_0 \Delta F_i^3)^2 + (\Delta M_i^3 + \ell_0 \Delta F_i^2)^2}}{\frac{\pi}{4} r_b^3} \right)^2$$

Remark 78. We use the unit system of (N, kPa, mm). We recall that all Von Mises and fatigue constraints and so their corresponding bound are squared. Therefore, they are given in kPa^2 .

Denote $\mathbf{X} = (\mathbf{x}_1, \dots, \mathbf{x}_n)$ where \mathbf{x}_i , $1 \leq i \leq n$, is the center of the head of the bolt i . The coupled optimization of both the structure of the bracket and the bolts location reads

$$\begin{aligned} & \min_{(\Omega, \mathbf{X}) \in \mathcal{U}_{ad}} V(\Omega), \\ \text{s.t.} & \begin{cases} C(\Omega, \mathbf{X}) \leq C_0 \\ VMR_i(\Omega, \mathbf{x}_i) \leq VM_0, \forall i \in \llbracket 1, n \rrbracket \\ VMC_i(\Omega, \mathbf{x}_i) \leq VM_0, \forall i \in \llbracket 1, n \rrbracket \\ F_i(\Omega, \mathbf{x}_i) \leq F_0, \forall i \in \llbracket 1, n \rrbracket \end{cases} \end{aligned} \quad (9.19)$$

where constraints bounds are

- Compliance : $C_0 = 325000 \mu\text{Pa}$,

- Von Mises : $VM_0 = 6.56 \times 10^{11}$ kPa²,
- Fatigue : $F_0 = 3.5 \times 10^{10}$ kPa².

Remark 79. *The Von Mises bound VM_0 is equal to $(0.9Re_{min})^2$ while the fatigue bound F_0 has to be suited to the simplified model.*

The optimization problem (9.19) is computed with the Augmented Lagrangian method. It is thus rewritten as

$$\begin{aligned}
& \min_{(\Omega, \mathbf{X}) \in \mathcal{U}_{ad}} \max_{\alpha \in \mathbb{R}^{3n+1}} \left\{ \mathcal{L}(\Omega, \mathbf{X}) = V(\Omega) + \alpha_C \max \left(C(\Omega, \mathbf{X}) - C_0, -\frac{\alpha_C}{\beta_C} \right) + \frac{\beta_C}{2} \max \left(C(\Omega, \mathbf{X}) - C_0, -\frac{\alpha_C}{\beta_C} \right)^2 \right. \\
& + \sum_{i=1}^n \alpha_{VMR,i} \max \left(VMR_i(\Omega, \mathbf{x}_i) - VM_0, -\frac{\alpha_{VMR,i}}{\beta_{VMR,i}} \right) + \frac{\beta_{VMR,i}}{2} \max \left(VMR_i(\Omega, \mathbf{x}_i) - VM_0, -\frac{\alpha_{VMR,i}}{\beta_{VMR,i}} \right)^2 \\
& + \sum_{i=1}^n \alpha_{VMC,i} \max \left(VMC_i(\Omega, \mathbf{x}_i) - VM_0, -\frac{\alpha_{VMC,i}}{\beta_{VMC,i}} \right) + \frac{\beta_{VMC,i}}{2} \max \left(VMC_i(\Omega, \mathbf{x}_i) - VM_0, -\frac{\alpha_{VMC,i}}{\beta_{VMC,i}} \right)^2 \\
& \left. + \sum_{i=1}^n \alpha_{F,i} \max \left(F_i(\Omega, \mathbf{x}_i) - F_0, -\frac{\alpha_{F,i}}{\beta_{F,i}} \right) + \frac{\beta_{F,i}}{2} \max \left(F_i(\Omega, \mathbf{x}_i) - F_0, -\frac{\alpha_{F,i}}{\beta_{F,i}} \right)^2 \right\}
\end{aligned} \tag{9.20}$$

where $\alpha = (\alpha_C, \alpha_{VMR,1}, \dots, \alpha_{VMR,n}, \alpha_{VMC,1}, \dots, \alpha_{VMC,n}, \alpha_{F,1}, \dots, \alpha_{F,n})$ are Lagrange multipliers and $\beta = (\beta_C, \beta_{VMR,1}, \dots, \beta_{VMR,n}, \beta_{VMC,1}, \dots, \beta_{VMC,n}, \beta_{F,1}, \dots, \beta_{F,n})$ are penalty parameters.

The coupled optimization involves two design-variables and thus requires two design spaces as pictured in Fig. 9.15. The design space of the structure is naturally the entire bracket. In the sequel, the structure is always initialized to the completely filled bracket design space. Bolts translate inside the area delimited by the white lines in Fig. 9.15 without non-overlapping condition. We alternate 1 iteration of structure and 1 iteration of locations optimization.

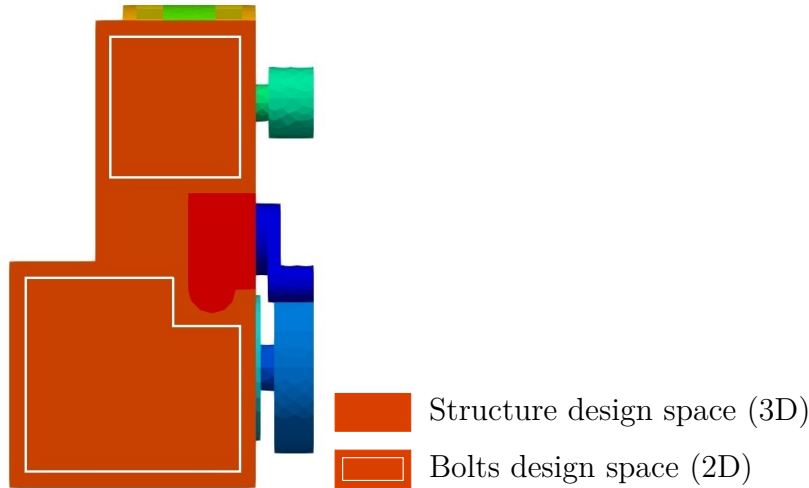


Figure 9.15: Structure and bolts design spaces

9.2.3 Reference optimization : structure only

Seven bolts are initially placed according to an user's proposition. Their distribution and numbering are displayed in Fig. 9.16. Reference results are computed with these invariant bolts.

Their orientation is fixed to respect industrial design constraints. Their locations are unchanged here and the only design variable is the structure of the bracket, which is initialized as the completely filled bracket design space.

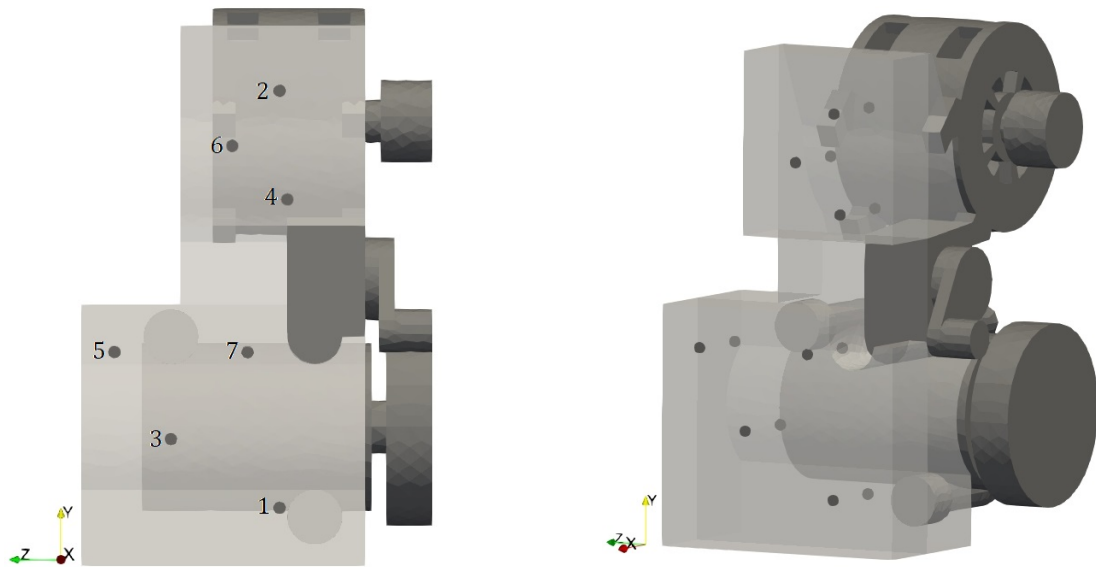


Figure 9.16: Proposition of the user of the distribution of 7 idealized bolts (in black)

We perform, as a comparative basis, a topology optimization of the bracket to minimize its volume under a compliance constraint. Bolts mechanical constraints are inactive here. Final shape of the bracket is given in Fig. 9.17. The bracket has a final volume of $V(\Omega) = 1.00 \times 10^6 \text{ mm}^3$. The compliance bound is reached. The bracket is massive on the upper part. Material reserve around two bolts are visible on the lower part. Even if bolts mechanical constraints are not activated in this optimization problem, Von Mises stresses and fatigue are monitored. Their final values are given in Table 9.3. Then, we notice that Von Mises stresses are always under the threshold. Fatigue of bolt 1 is higher than the bound while bolts 2 and 4 are lower but close to the bound.

A second reference optimization is run where bolts mechanical constraints are activated to highlight their importance and impact on the structure. Final shape of the bracket is given in Fig. 9.18. The bracket has a final volume of $V(\Omega) = 1.13 \times 10^6 \text{ mm}^3$. The compliance bound is not reached. Then, the assembly is stiffer and slightly heavier when bolt mechanical constraints are activated. Moreover, material is more regularly distributed between the upper and the lower parts. The thickness is much more consistent from top to bottom. The bracket structure is smoother and thus appears more convenient for manufacture. Final Von Mises stresses and fatigue and given in Table 9.4. We recall that Von Mises optimization constraints are implemented at the end of Step 2. Nevertheless, we monitor the value of Von Mises stresses at the end of Step 1 to get more information about bolts behavior. All Von Mises constraints are significantly far from the bound. It would be higher if the pre-tension force was larger. All optimization constraints are respected. The only saturated one is the fatigue of bolt 4.

Fig. 9.19 compares the history of convergence of the volume, the compliance and the fatigue of bolts 1, 2 and 4 for the problem under compliance constraint and the problem under compliance and bolts mechanical constraints. These bolts have the highest fatigue state when mechanical constraints are inactive. Their activation changes the shape of the bracket and

changes consequently the stress states of these bolts.

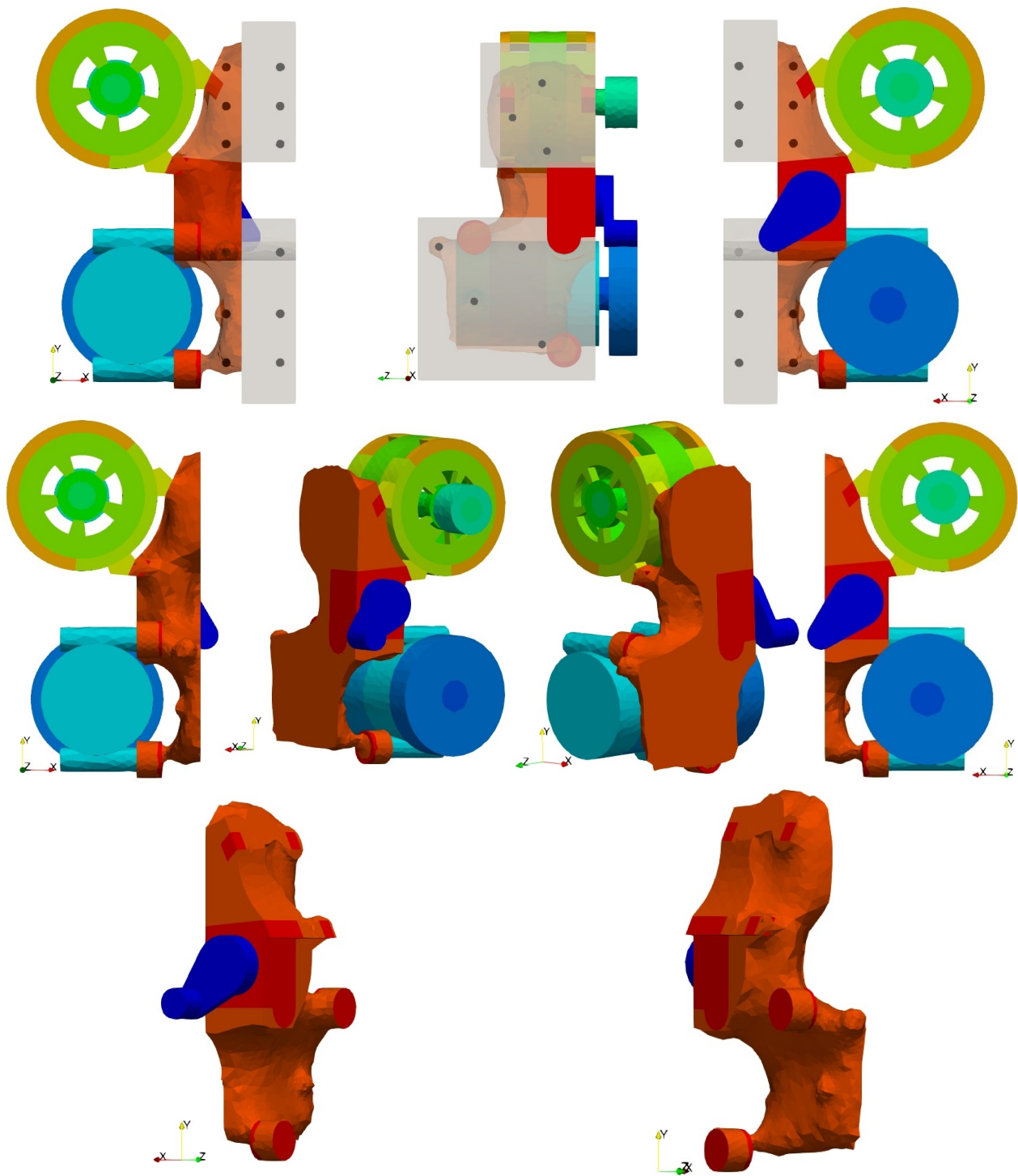


Figure 9.17: Final assembly for volume minimization of the bracket under compliance constraint with seven bolts

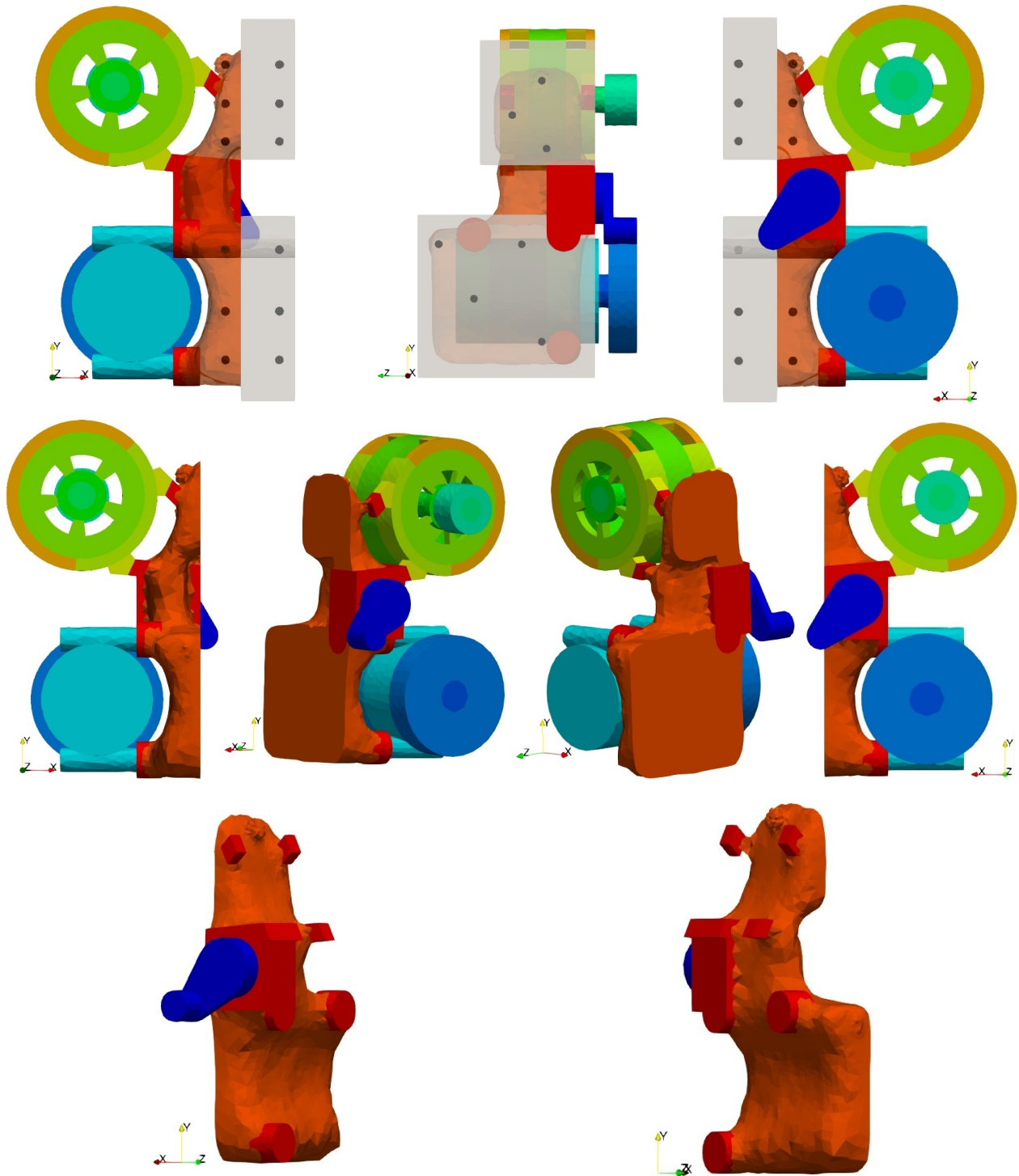


Figure 9.18: Final assembly for volume minimization of the bracket under compliance and bolts mechanical constraints with seven bolts

	<i>VMR</i> Step 1	<i>VMR</i> Step 2	<i>VMC</i> Step 1	<i>VMC</i> Step 2	F
Bolt 1	2.69×10^{11}	3.67×10^{11}	1.19×10^{11}	1.42×10^{11}	3.66×10^{10}
Bolt 2	2.63×10^{11}	3.66×10^{11}	1.19×10^{11}	1.46×10^{11}	3.41×10^{10}
Bolt 3	2.11×10^{11}	2.51×10^{11}	1.19×10^{11}	1.40×10^{11}	8.27×10^{09}
Bolt 4	1.85×10^{11}	2.98×10^{11}	1.19×10^{11}	1.36×10^{11}	3.26×10^{10}
Bolt 5	1.40×10^{11}	2.23×10^{11}	1.19×10^{11}	1.87×10^{11}	1.28×10^{10}
Bolt 6	2.20×10^{11}	2.96×10^{11}	1.19×10^{11}	1.43×10^{11}	2.08×10^{10}
Bolt 7	1.49×10^{11}	2.48×10^{11}	1.19×10^{11}	1.36×10^{11}	2.20×10^{10}

Table 9.3: Summary of final bolts stresses (in kPa^2) for volume minimization of the bracket under compliance constraint

	<i>VMR</i> Step 1	<i>VMR</i> Step 2	<i>VMC</i> Step 1	<i>VMC</i> Step 2	F
Bolt 1	2.70×10^{11}	3.63×10^{11}	1.19×10^{11}	1.38×10^{11}	3.28×10^{10}
Bolt 2	2.60×10^{11}	3.71×10^{11}	1.19×10^{11}	1.51×10^{11}	3.19×10^{10}
Bolt 3	2.11×10^{11}	2.51×10^{11}	1.19×10^{11}	1.39×10^{11}	7.57×10^{09}
Bolt 4	1.88×10^{11}	3.03×10^{11}	1.19×10^{11}	1.38×10^{11}	3.50×10^{10}
Bolt 5	1.46×10^{11}	1.77×10^{11}	1.19×10^{11}	1.45×10^{11}	1.73×10^{09}
Bolt 6	2.22×10^{11}	3.01×10^{11}	1.19×10^{11}	1.45×10^{11}	2.17×10^{10}
Bolt 7	1.47×10^{11}	2.46×10^{11}	1.19×10^{11}	1.35×10^{11}	2.17×10^{10}

Table 9.4: Summary of final bolts stresses (in kPa^2) for volume minimization of the bracket under compliance and bolts mechanical constraints

Remark 80. All Von Mises stresses at the center of the root evaluated at the end of Step 1 seem to have the same value, namely $1.19 \times 10^{11} \text{ kPa}^2$. They differ from each other after the third displayed number.

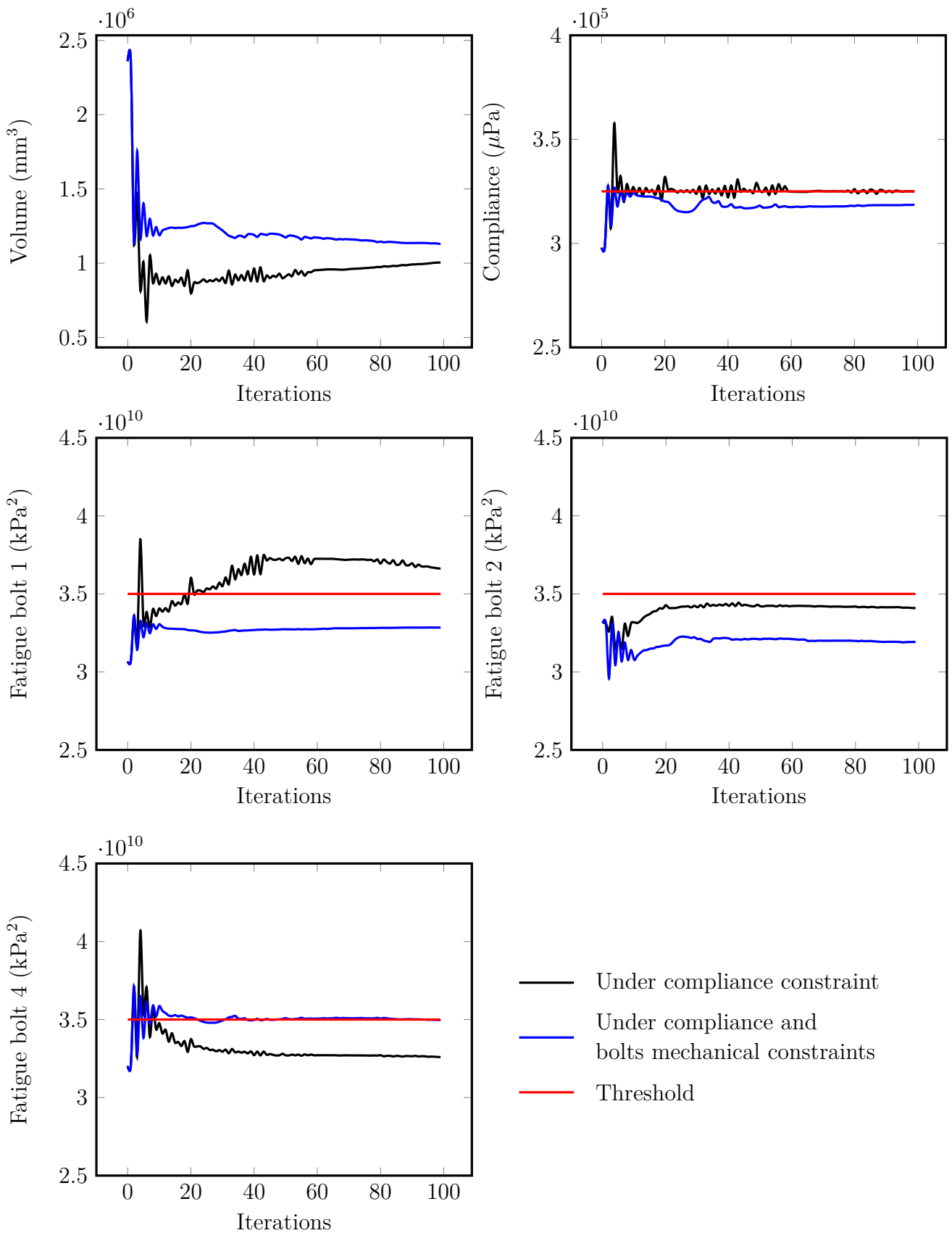


Figure 9.19: History of convergence the volume, the compliance and the fatigue of bolts 1, 2 and 4 for the problem under compliance constraint and the problem under compliance and bolts mechanical constraints

9.2.4 Coupled optimization

Use of three idealized bolts

Let us start with bolts 2, 3 and 4 from the proposition of the user (see Fig. 9.16) and renumber them as displayed in Fig. 9.20. The problem is to optimize both the structure of the bracket and the bolts location to solve (9.19).

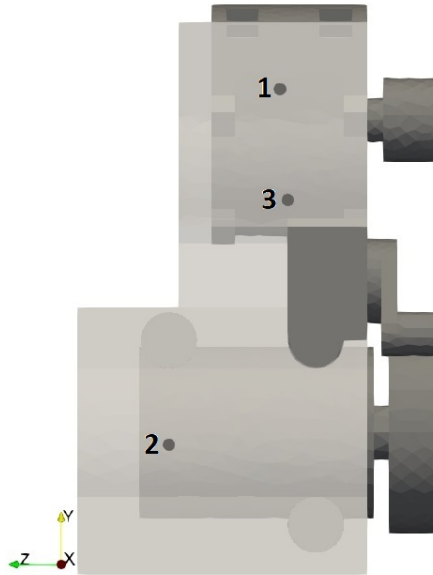


Figure 9.20: Initialization with three bolts

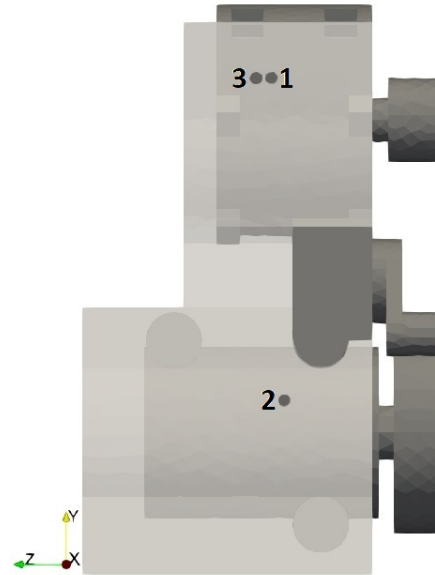


Figure 9.21: Result with three bolts

This problem is quite ill-posed because the constraints of compliance and fatigue of bolts 1 and 3 are violated from the beginning. The structural optimization is not conclusive since the volume is unchanged. However, the locations optimization decreases the compliance and improves substantially the fatigue state of bolts 1 and 3 as shown in Fig. 9.22. Unfortunately, these improvements are not enough to go back to the feasible design. Moreover, the fatigue of bolt 1 is well above the threshold, which concludes that this problem is infeasible with only three bolts.

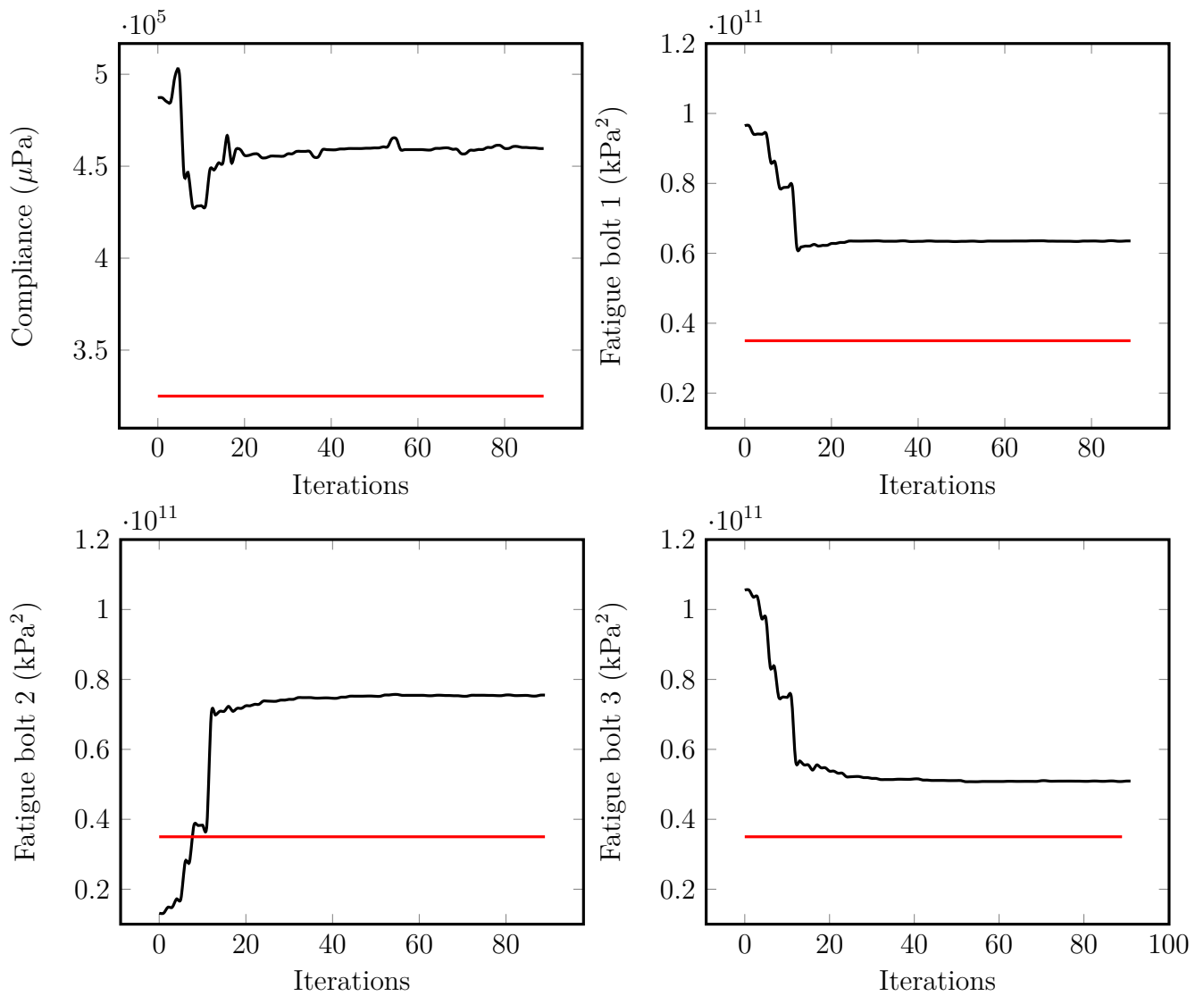


Figure 9.22: History of convergence the compliance and the fatigue of bolts 1, 2 and 3 for the problem under compliance constraint and the problem under compliance and bolts mechanical constraints with three bolts

Use of four idealized bolts

Let us start with bolts 1, 2, 3 and 4 from the proposition of the user (see Fig. 9.16). The compliance, with these four bolts, is $C(\Omega) = 348753 \mu\text{J}$, which violates the bound. Moreover, the fatigue of three bolts are violated. Thus, we foreseen that the problem will not be feasible with only four bolts.

Use of five idealized bolts

Starting again with bolts 1, 2, 3 and 4 from the proposition of the user (see Fig. 9.16), we add a fifth bolt by applying the topological derivative to decrease the compliance of the assembly. The additional bolt is on the same plane parallel to (\mathbf{Y}, \mathbf{Z}) and with the same orientation along \mathbf{X} as the existing bolts. Negative iso-values of the topological derivative are given in Fig. 9.23. The most interesting area (in blue), places the fifth bolt at the left hand-side of the bracket. Then, the fifth bolt is placed in the upper left corner of the bracket (see Fig. 9.24). The new compliance (with five bolts) is $C(\Omega) = 304971 \mu\text{J}$, which is under the bound. The fifth bolt softens fatigue of all existing bolts. Therefore all constraints are in the feasible design. The problem (9.19) is feasible with five bolts.

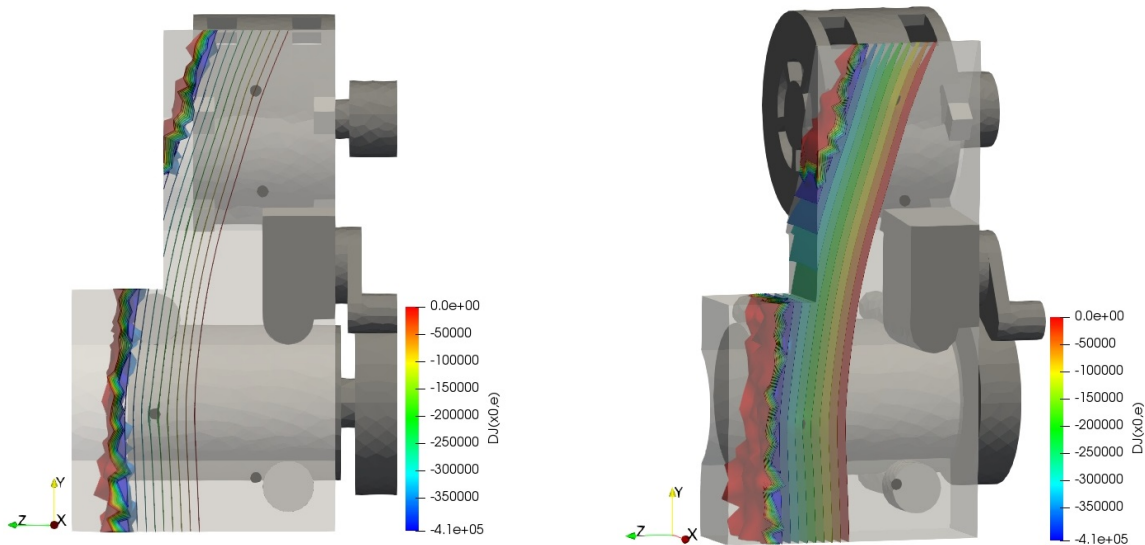


Figure 9.23: Iso-values of the topological derivative on the assembly with four bolts

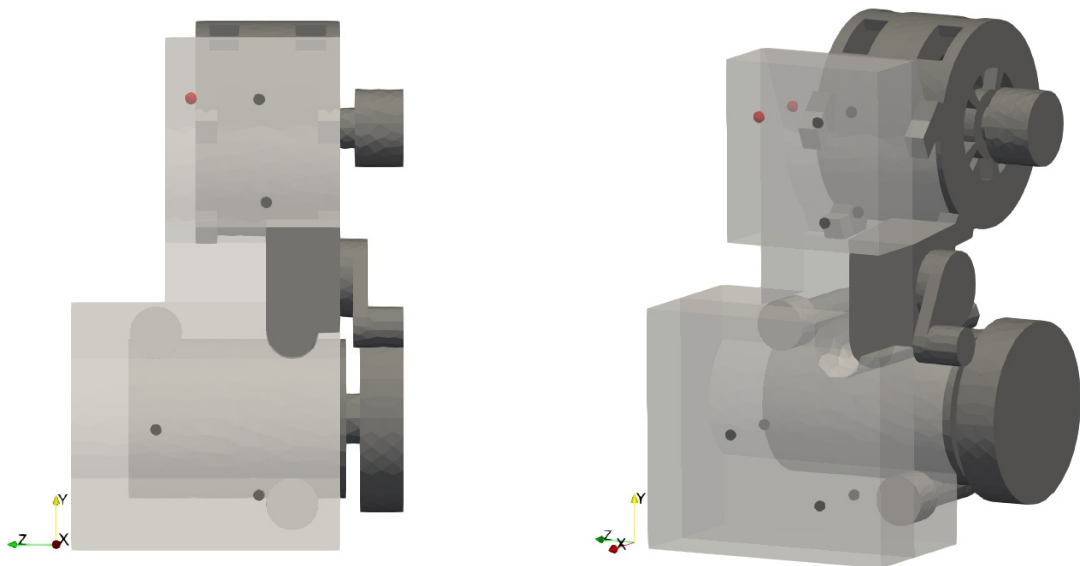


Figure 9.24: Fifth bolt (in red) placed by the topological derivative

Consider the assembly with five bolts (see Fig. 9.25). Bolts 1 to 4 are taken from the proposition of the user and bolt 5 is placed by the topological derivative. The problem is to optimize both the structure of the bracket and the bolts location to solve (9.19).

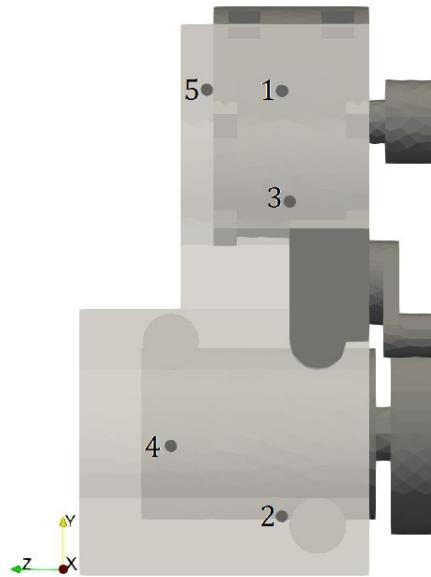


Figure 9.25: Initialization with five bolts

Final shape and bolts location are given in Fig. 9.26. The compliance threshold is reached and all bolts mechanical constraints are respected. Bolts location changed with respectively a minimum and a maximum displacement amplitude of 0.09 mm for bolt 3 and 5.24 mm for bolt 2. The bracket is smooth with a rather regular material distribution between the upper and the lower parts. Finally, the bracket has a final volume of $V(\Omega) = 9.56 \times 10^5 \text{ mm}^3$. It represents a weight reduction of about 15.5% compared to the reference result with bolts mechanical constraints for which the volume is $V(\Omega) = 1.13 \times 10^6 \text{ mm}^3$. As a conclusion, the coupled optimization provides a lighter structure with five bolts than the classic shape optimization with seven invariant bolts for equivalent mechanical performances.

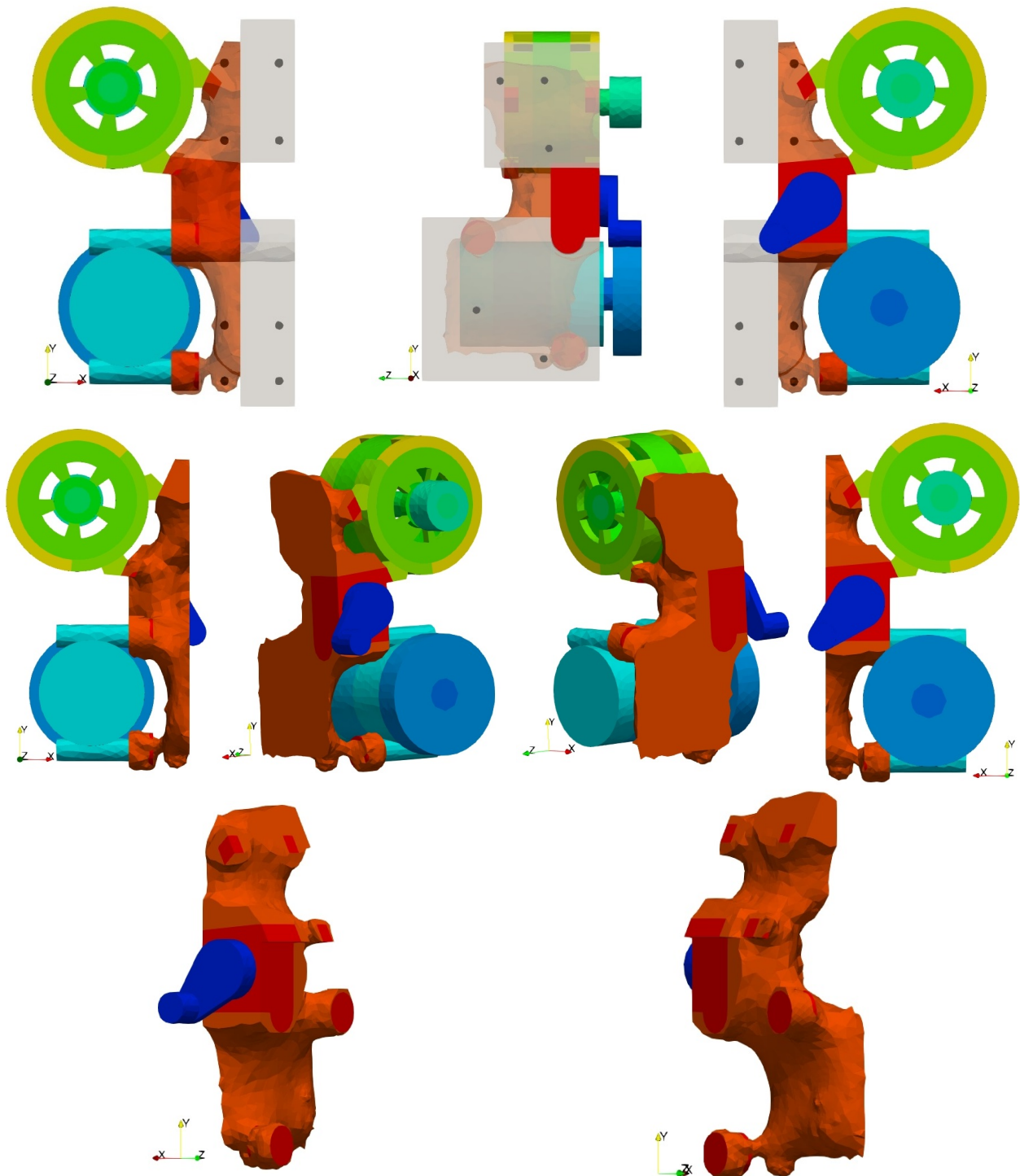


Figure 9.26: Final assembly for volume minimization of the bracket under compliance and bolts mechanical constraints with five bolts

Use of six idealized bolts

The assembly with the optimal bracket with five bolts (see Fig. 9.26) reaches the compliance threshold $C_0(\Omega) = 325000 \mu\text{J}$. Then, we apply again the topological derivative on that optimal assembly to place a sixth both in order to decrease the compliance. Negative iso-values of the topological derivative are given in Fig. 9.27. The sixth bolt is then placed in the lower left corner of the bracket (see Fig. 9.28). The new compliance is $C(\Omega) = 313991 \mu\text{J}$. All bolts mechanical constraints are in the feasible design.

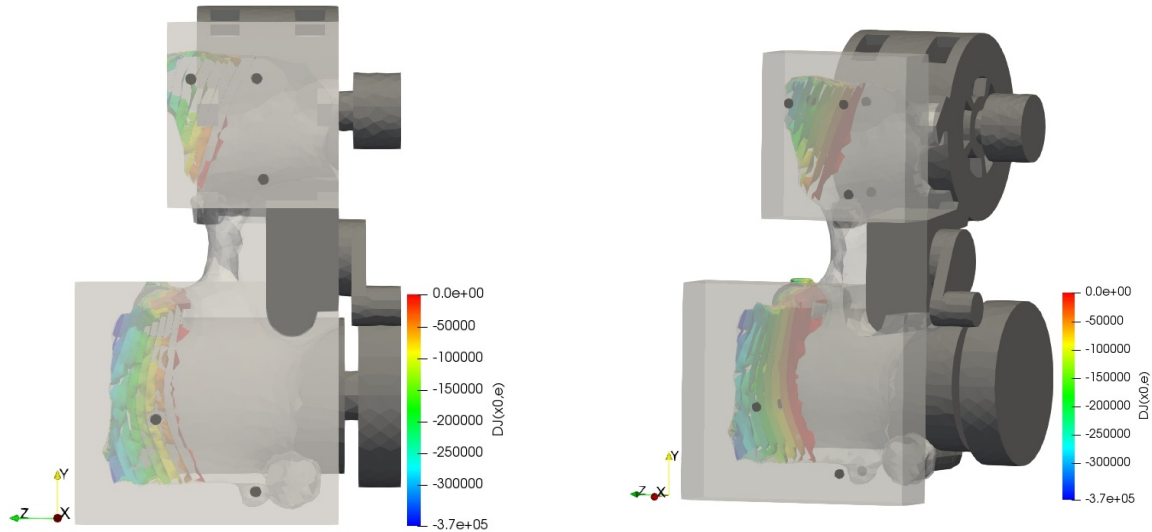


Figure 9.27: Iso-values of the topological derivative on the assembly with the optimal bracket for five bolts

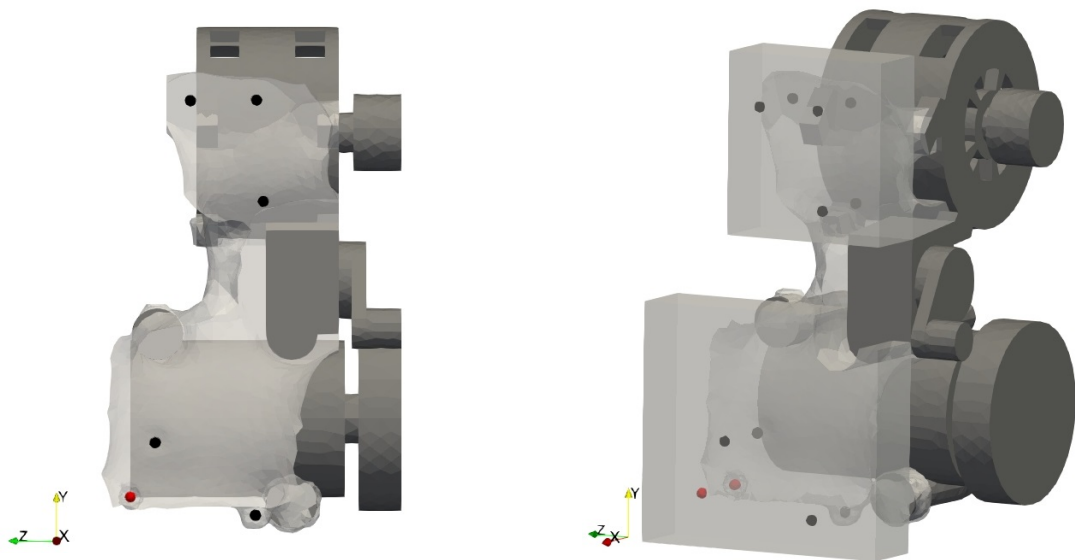


Figure 9.28: Sixth bolt (in red) placed by the topological derivative

We solve the problem (9.19) to optimize the structure of the bracket and the locations of six bolts. Final structure and bolts location are given in Fig. 9.29. Once again, the compliance threshold is reached and all bolts mechanical constraints are respected. Bolts location barely changed with respectively a minimum and a maximum displacement amplitude of 0.04 mm for bolt 2 and 0.72 mm for bolt 1. The shape of the bracket does not change a lot. The add of the sixth bolt smoothes curves and corners. The bracket has a final volume of $V(\Omega) = 8.57 \times 10^5 \text{ mm}^3$, which represents a reduction of 24.14% compared to the reference result with seven fixed bolts for which the volume is $V(\Omega) = 1.13 \times 10^6 \text{ mm}^3$.

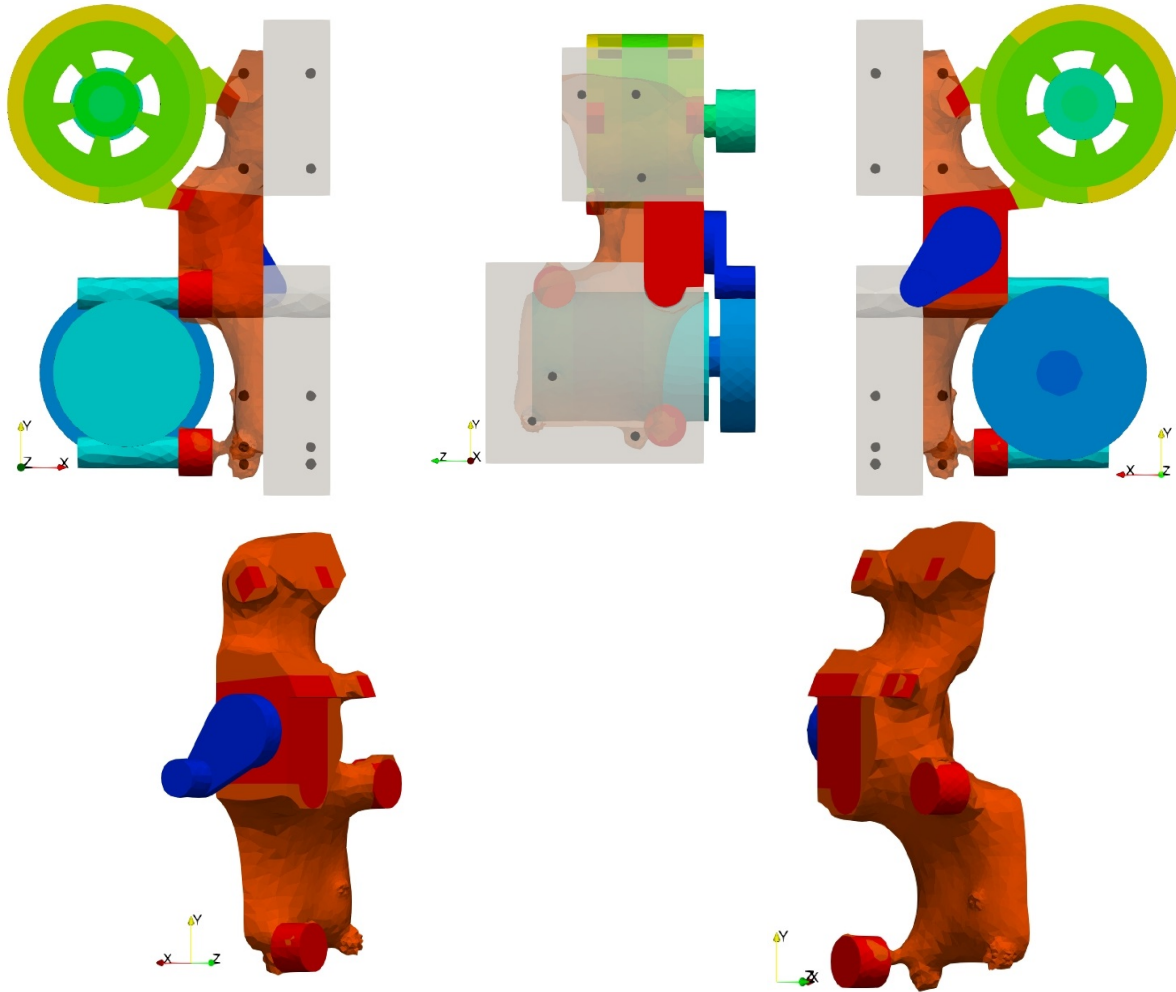


Figure 9.29: Final assembly for volume minimization of the bracket under compliance and bolts mechanical constraints with six bolts

This simplified but representative industrial use case concludes that the placement with the topological derivative followed by the coupled optimization of structure and bolts locations provides lighter structure with fewer bolts and equivalent mechanical performances than a classic structural optimization with fixed bolts. Fig. 9.30 summarizes volumes of the bracket according to the number of bolts and the type of optimization.

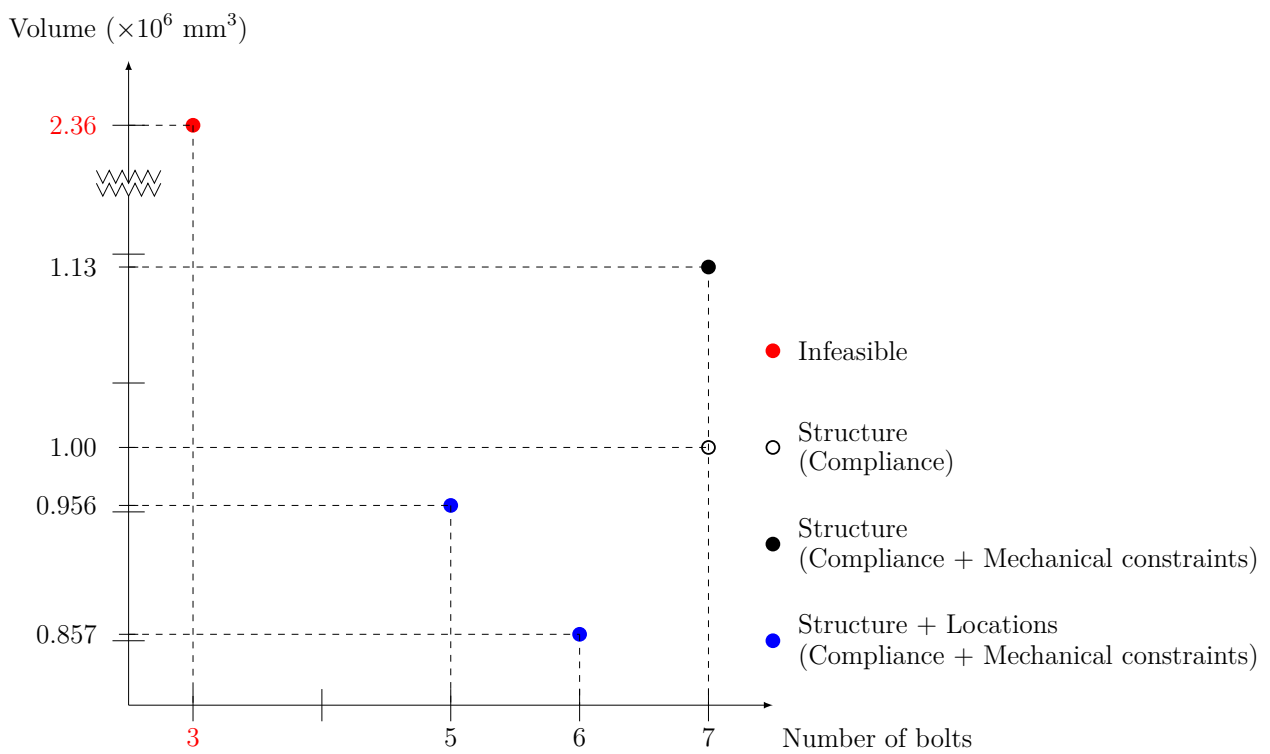


Figure 9.30: Summary of volumes according to the number of bolts and the type of optimization

Conclusion and perspectives

This thesis presented a method to optimize concurrently the shape and the topology of a part, on the one hand, and the locations and the number of its mechanical connections, on the other hand. An idealized model of long bolt connection, with its specific mechanical constraints, has been established for the use of topology optimization and topological derivative developments. The idealized bolt has been embodied by two spheres linked by an Euler-Bernoulli beam. Two variant formulations were proposed. For the sake of simplicity, the first one, with elastic spheres, was used to carry out topological sensitivity analysis. The second one, with rigid spheres, was considered for complying with idealized bolt model and is used in the simplified industrial use case. It has been checked that the topological derivative has the same analytical behavior whatever the spheres are elastic or rigid.

The coupled optimization of both structure and connections involved four tools

- Level-set method to optimize the structure
- Topological derivative to place and orient one new small connection
- Parametric gradient to optimize the connections location
- Coupling level-set method and parametric gradient to optimize both the structure and the connections location.

Numerical academic and industrial applications of this coupling proved its effectiveness for a problem of volume minimization under mechanical or geometrical constraints. It provides better results than a topology optimization with pre-defined and fixed connections. However, it required a shrewd strategy for even better results that depends on the use case that is considered. It raises the question of a learning process for the automation of this coupling in a software. It might be suggested, for example, to place and orient successively as many connections as required with the topological derivative. Then, optimize simultaneously all connections locations with the parametric gradient. Finally, launch the optimization of the structure.

This coupled optimization could be enriched according to various research avenues. A parametric gradient-based algorithm could be derived to optimize the implementation length ℓ or the direction \mathbf{e} of the bolt. The bolt is nucleated with a small size in the framework of topological derivative. Once this small bolt is created, we could propose to optimize its size with an adequate penalization parameter to get a standard size. Moreover, the fastener hole should be added to the topological sensitivity analysis with respect to an idealized bolt. This hole models the free space for the passage of bolt. Other objective functions and optimization constraints can, in principle, easily be implemented, such as displacement target or contact pressure. Also, a more efficient method than the Augmented Lagrangian (see e.g. [48]) could be used to handle numerous optimization constraints. Finally, this work could be extended

to dynamic analysis. The same tools (level-set method, parametric gradient and topological derivative) are reusable to optimize eigen frequencies problem for example. This work opens up the perspective of the optimization of assembled systems with gradient-based algorithms for industrial purposes.

Appendices

Simplified industrial use case

The goal of this appendix is to establish the simplified model of an accessories and bracket assembly used in Section 9.1. The simplified model is based on a real assembly provided by Renault. It has to be representative enough for static and dynamic analysis.

A.1 General information

A.1.1 Description of an accessories and bracket assembly

The accessories and bracket assembly is part of the powertrain. It is made of a bracket and different accessories such as an alternator, an air conditioning compressor, a water pump and a belt tensioning roller. All the accessories are driven by a belt.

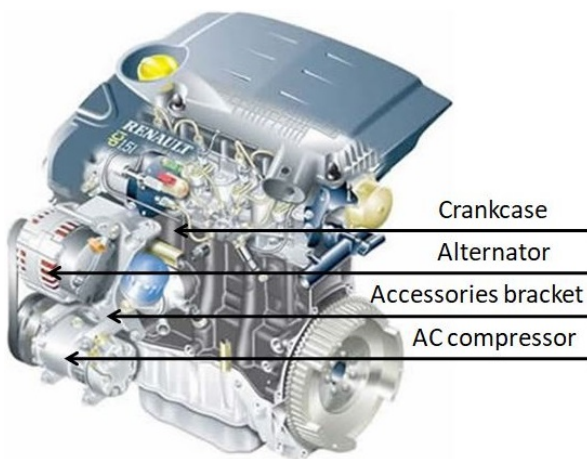


Figure A.1: Reference engine (belt, accessories and bracket are in the lower left-hand corner)

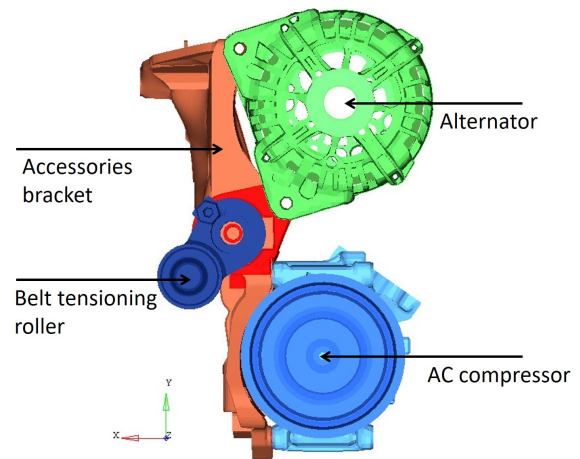


Figure A.2: Accessories and bracket assembly of the K9K gen6 engine

The present work focuses on the accessories and bracket assembly taken from the K9K gen6 engine of Renault (see Figs. A.1 and A.2). Accessories are an alternator, a belt tensioning roller

(BTR) and an air conditioning (AC) compressor. The bracket insures their positioning and their fastening to the crankcase. Thus, the bracket makes the accessories respect the belt course. The bracket also insures the advantageous cubic shape of the crankcase. Moreover, it allows a large variety of accessories. The alternator supplies electricity to the vehicle. The AC compressor insures the flow and compression of the air conditioning fluid. The belt tensioning roller guides the belt and regulates its tension.

A.1.2 Design rules

Design rules of the accessories and bracket assembly K9K gen6 are defined by technical policies of the accessories bracket and the belt drive system of the accessories of Renault. The belt drives the accessories by transmitting the rotational movement of the crankshaft to their pulley. The axis of each accessory pulley is parallel to the axis of the crankshaft (see Fig. A.3).

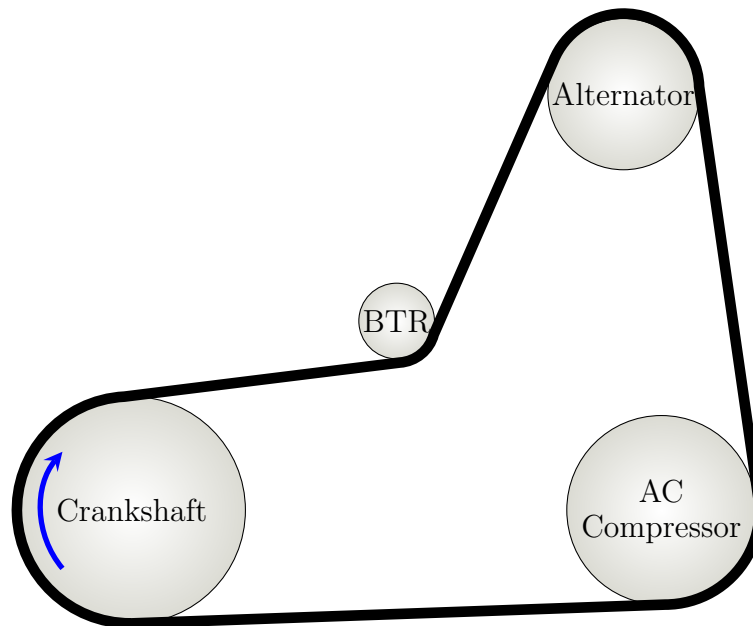


Figure A.3: Diagram of the belt course

A.1.3 Fastening of accessories

The fastening of accessories to the bracket is defined by technical policies of the accessories bracket and the belt drive system of the accessories. A small column on the bracket and two clevis¹ on the alternator ensure the alternator fastening. The AC compressor is fixed by three small columns and bolts. The belt tensioning roller is fastened with two bolts and indexed by a double-flat spot. Fixing bosses of the crankcase are numerically represented by stiffness linked to the supporting frame.

A.2 Mechanical and geometric simplification

The mechanical behaviour and the geometry of the reference model is simplified to reduce the number of elements and to homogenize the mesh. In fact, the reference mesh is made of tetrahedrons, pentahedrons and hexahedrons. It also contains Nastran elements such as PBEAM, PBUSH, RBE2, etc. The reference model has then 499 076 elements. This number is reduced to shorten the computing time and lighten the model.

This simplified model has the characteristic dimensions of a reference model. Its mesh is entirely tetrahedral. Details are removed. The mechanical behaviour of the assembly is kept at first order. Material properties and accessories geometry are respectively adapted and simplified with classic principles of the strength of materials.

The optimization process concerns the bracket and its connections to the crankcase. Therefore, the accessories are coarsely meshed.

A.2.1 Simplification of the alternator

The alternator of the reference model is shown in Figure A.4. Its characteristic dimensions are kept in the simplified model (see Fig. A.5). The reference rotor and pulley axis are not meshed in the reference model. They are modeled by PBEAM, PBAR and PBUSH elements. However, the rotor represents a huge part of the alternator inertia. The axis of the pulley is required to compute its deflection. Both, the rotor and the axis, are represented by cylinders. This adds an important number of elements. The hollow structure of the alternator cage is kept. Blades details are mechanically irrelevant. The simplified model keeps half of the blades. Moreover, the small size of reference blades generates a refined mesh that extends the computing time. Blades size is doubled in the simplified model. Their mesh can then be coarser.

A.2.2 Simplification of the belt tensioning roller

The belt tensioning roller has an inconsequential mechanical impact on the analysis at first order. Details of the reference roller (see Fig. A.6) are ignored. As a consequence, its simplified geometry is basically made of cylinders with the characteristic dimensions of the reference model as displayed in Figure A.7. Nevertheless, the hole is kept and sealed by a plate connecting the cylinders. The mesh of the simplified roller is coarse.

A.2.3 Simplification of the compressor

The reference AC compressor is made of filled parts and contains many irrelevant details for the goal of this study (see Fig. A.8). They are ignored in the simplified model. The main

¹U shaped fastener

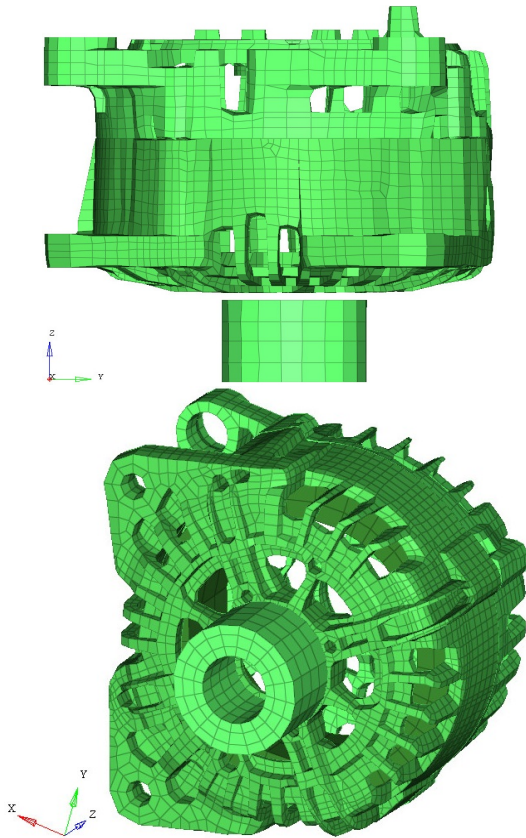


Figure A.4: Reference alternator

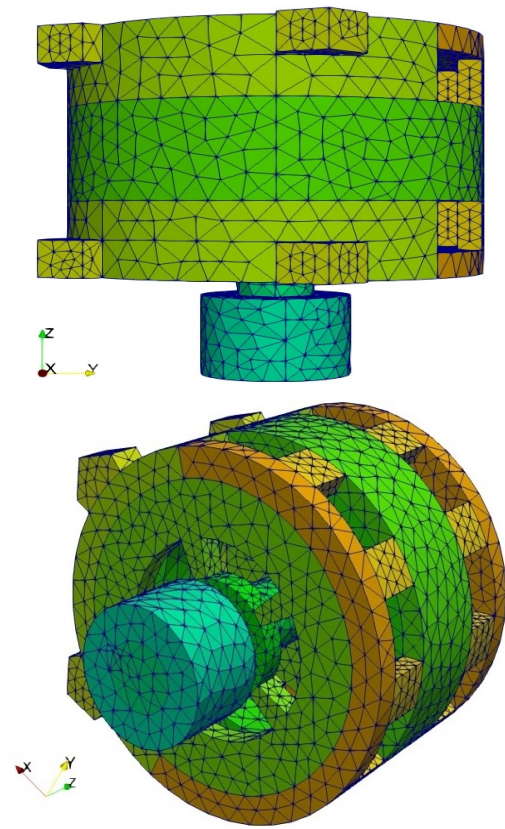


Figure A.5: Simplified alternator

body of the compressor, the fixing columns, the cap and the pulley are all simply embodied by cylinders (see Fig. A.9). Changes of the geometry imply naturally some changes of the mechanical behavior. Therefore, equivalent material properties are established to keep the physical representativeness of the simplified model.

The reference model was analyzed under static and vibratory solicitations in order to determine the configurations that lead to important deformations of the assembly. Fig. A.10 displays the strain energy of the assembly for flexion solicitation of the compressor. This loading mode implies an important work of the alternator. It is then necessary to preserve this flexion behavior of the compressor.

The main body of the compressor is hollowed out between the fixing columns to reduce the number of elements. In order to preserve its flexion / torsion / compression behavior, equivalent material properties are established for the hollow cylinder. They are parameterized by the ratio of bulk density and of Young modulus between the reference and simplified model. They are also parameterized with the ratio between the external and internal diameter of the hollow cylinder.

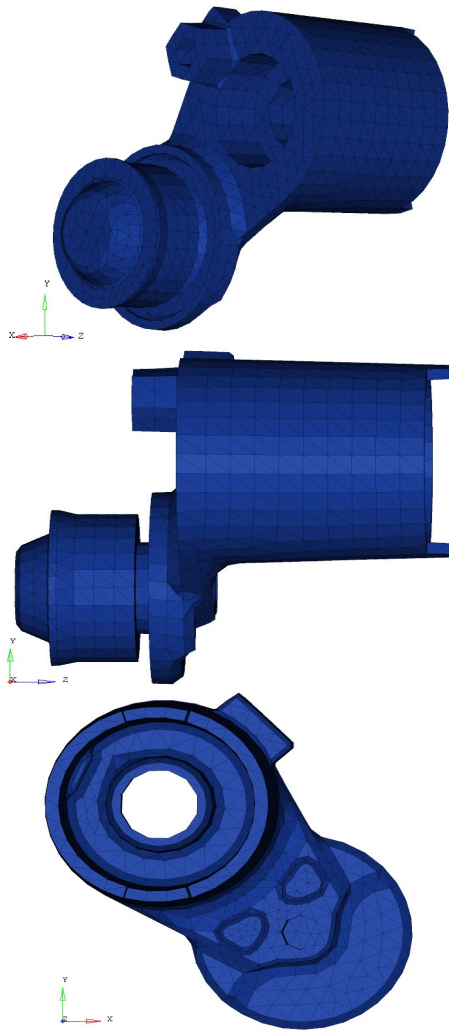


Figure A.6: Reference belt tensioning roller

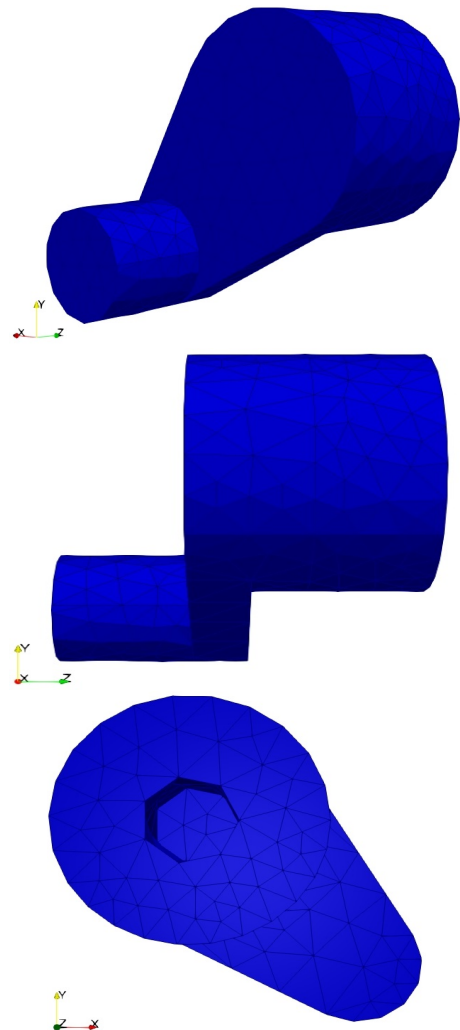


Figure A.7: Simplified belt tensioning roller

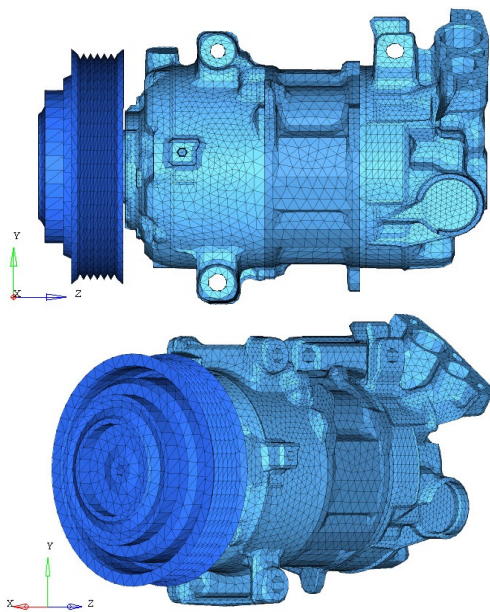


Figure A.8: Reference AC compressor

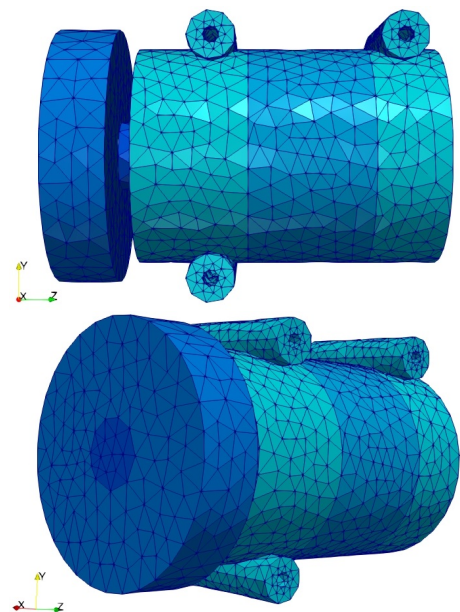


Figure A.9: Simplified AC compressor

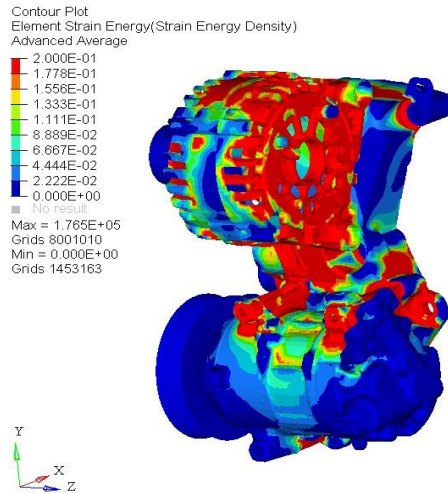


Figure A.10: Strain energy for a flexion solicitation of the compressor

A.2.4 Simplification of the accessories bracket

The bracket is made of aluminium alloy. For the purpose of topology optimization, the mesh is thinner than the one of the accessories. The initial model has a complex geometry (see Fig. A.11). Mounting holes to the crankcase are removed from the simplified model. They are represented by level-set functions. Moreover, the simplified model is made with basic geometry which make it larger than the reference model (see Fig. A.12). It provides a greater domain of admissible shapes.

A.3 Summary of the simplified model

The simplified accessories and bracket assembly keeps the physically representative at first order. It mostly respects the conservation of inertia and stiffness in loading modes at first order. Even if the alternator requires more elements for practical reasons, the size of the model has been divided by a factor 5 (cf. Table A.1).

	Reference model	Simplified model
Alternator	8 376	14 704
Belt tensioning roller	9 213	1 406
AC Compressor	88 565	8 957
Bracket	391 334	84 291
Total	499 076	109 358

Table A.1: Comparison of the number of elements for the reference and the simplified models

The only lack of this model concerns the overrated stiffness of the fastenings of the accessories to the bracket. In fact, these fastenings are modeled by RBE2 and PBEAM elements in the reference model while the simplified model embeds the accessories to the bracket.

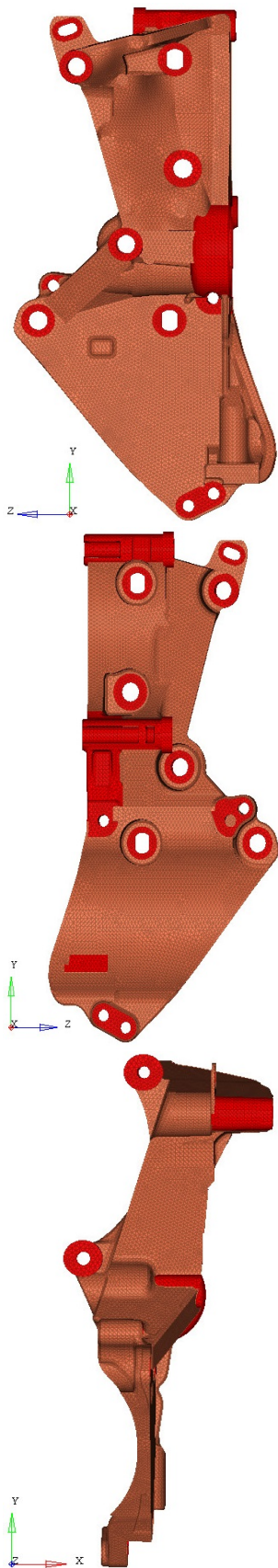


Figure A.11: Reference bracket

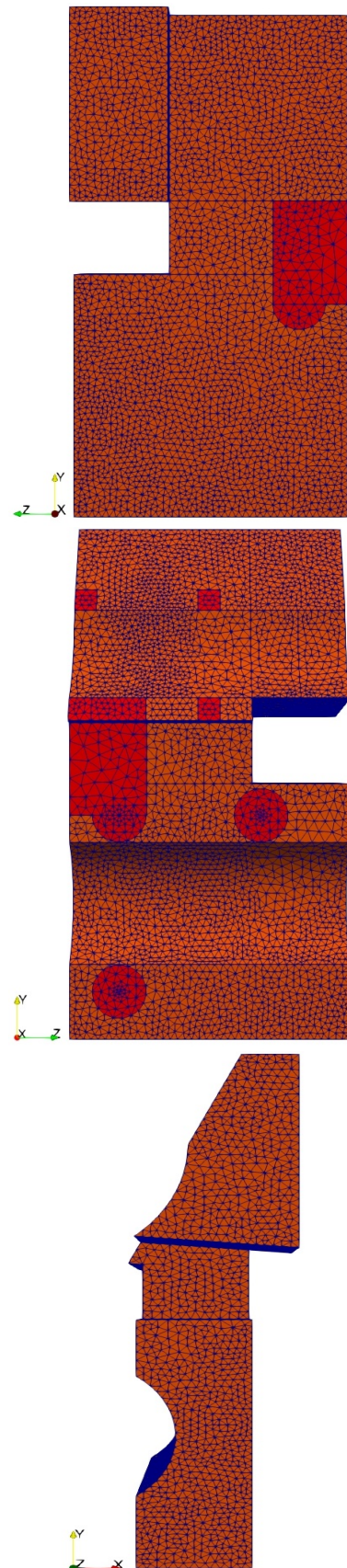


Figure A.12: Simplified bracket

Bibliography

- [1] *NX Nastran User's Guide*. Siemens PLM Software, United States, 2014.
- [2] M Abid, A Khan, D H Nash, M Hussain, and H A Wajid. Simulation of optimized bolt tightening strategies for gasketed flanged pipe joints. *14th International Conference on Pressure Vessel Technology*, 130:201–213, 2015.
- [3] B Åakeson and N Olhoff. Minimum stiffness of optimally located supports for maximum value of beam eigen frequencies. *Journal of Sound and Vibration*, 120(3):457–463, 1988.
- [4] G Allaire. *Shape optimization by the homogenization method*. Springer-Verlag, Applied Mathematical Sciences 146, 2002.
- [5] G Allaire. *Conception optimale de structures*. Springer-Verlag, Berlin, Mathématiques et Applications 58, 2007.
- [6] G. Allaire, C. Dapogny, G. Delgado, and G. Michailidis. Multi-phase structural optimization via a level set method. *ESAIM Control Optim. Calc. Var.*, 20(2):576–611, 2014.
- [7] G Allaire, F Jouve, and A M Toader. Structural optimization using sensitivity analysis and a level-set method. *J. Comp. Phys.*, 194(1):363–393, 2004.
- [8] G Allaire, F Jouve, and N Van Goethem. Damage evolution in brittle materials by shape and topological sensitivity analysis. *J. Comp. Phys.*, 203:5010–5044, 2011.
- [9] G Allaire and O Pantz. Structural optimization with Freefem++. *Structural and Multi-disciplinary Optimization*, 32:173–181, 2006.
- [10] L Ambrosio and G Buttazzo. An optimal design problem with perimeter penalization. *Calc. Var.*, 1:55–69, 1993.
- [11] H Ammari and H Kang. *Reconstruction of small inhomogeneities from boundary measurements*. Springer, Berlin, 2004.
- [12] S Amstutz. The topological asymptotic for the navier-stokes equations. *ESAIM: Control, Optimisation and Calculus of Variations*, 11:401–425, 2005.
- [13] S Amstutz, I Horchani, and M Masmoudi. Crack detection by the topological gradient method. *Control and Cybernetics*, 34(1):81–101, 2005.
- [14] D Auroux and M Masmoudi. Image processing by topological asymptotic expansion. *J. Math. Imaging Vis.*, 33:22–134, 2009.

- [15] D Auroux, M Masmoudi, and L Belaid. Image restoration and classification by topological asymptotic expansion. *Variational formulations in mechanics : theory and applications*, pages 23–42, 2006.
- [16] E Aydin, M Dutkiewicz, B Öztürk, and M Sonmez. optimization of elastic spring supports for cantilever beams. *Structural and Multidisciplinary Optimization*, 62:55–81, 2020.
- [17] N Aziz, H Jalalifar, A Remennikov, S Sinclair, and A Green. Optimisation of the bolt profile configuration for load transfer enhancement. *Coal Operators' Conference, University of Wollongong & the Australasian Institute of Mining and Metallurgy*, pages 125–131, 2008.
- [18] M P Bendsøe. Optimal shape design as a material distribution problem. *Structural and multidisciplinary optimization*, 1(4):193–202, 1989.
- [19] M P Bendsøe and N Kikuchi. Generating optimal topologies in structural design using a homogenization method. *Comp. Meth. Appl. Mech. Eng.*, 71:197–224, 1988.
- [20] M P Bendsøe and O Sigmund. *Topology optimization: theory, methods and applications*. Springer, Berlin, 2003.
- [21] M Berot. *Modélisation simplifiée d'assemblages par éléments équivalents*. PhD thesis, École Nationale Supérieure des Mines de Paris, 2009.
- [22] G Bianchi, G Aglietti, and G Richardson. Optimization of bolted joints connecting honeycomb panels. *Proceedings of the 1st CEAS, 10th European Conference on Spacecraft Structures, Materials and Mechanical Testing*, 2007.
- [23] J Bickford. *An introduction to the design and behavior of bolted joints*, volume 97 of *Mechanical Engineering*. Marcel Dekker, New York, 3 edition, 1995.
- [24] D Bojczuk. Optimization of buckling load and natural frequency for bar structures with variable support conditions. *Proceedings of the 17th International Conference on Computer Methods in Mechanics*, 2007.
- [25] D Bojczuk and Z Mroz. On optimal design of supports in beam and frame structures. *Struct. Optim.*, 16:47–57, 1998.
- [26] D Bojczuk and A Rebosz-Kurdek. Optimal design of bar structures with their supports in problems of stability and free vibrations. *Journal of theoretical and applied mechanics*, 52(2):533–546, 2014.
- [27] J F Bonnans, J C Gilbert, C Lemaréchal, and Sagastizábal. *Numerical optimization : theoretical and practical aspects*. Springer Science & Business Media, Optimization, 2006.
- [28] M Bonnet and F Carkoni. Analysis of topological derivative as a tool for qualitative identification. *Inverse Problems*, 35(104007), 2019.
- [29] B Bourdin and A Chambolle. Design-dependent loads in topology optimization. *ESAIM: Control, Optimisation and Calculus of Variations*, 9:19–48, 2003.
- [30] T E Bruns. A reevaluation of the simp method with filtering and an alternative formulation for solid-void topology optimization. *Structural and Multidisciplinary Optimization*, 30(6):428–436, 2005.

- [31] H Brézis. *Functional analysis, Sobolev spaces and partial differential equations*. Springer Science & Business Media, 2010.
- [32] T Buhl. Simultaneous topology optimization of structure and supports. *Struct. Multidiscip. Optim.*, 23:336–346, 2002.
- [33] M Burger and R Stainko. Phase-field relaxation of topology optimization with local stress constraints. *SIAM Journal on Control and Optimization*, 45(4):1447–1466, 2006.
- [34] W Cai, J Yuan, S J Hu, L Infante, and C Clemens. Optimal fixture design for sheet metal holding. *IBEC/94 Body Assembly & Manufacturing*, pages 123–128, 1994.
- [35] C Cao. *Bolt profile configuration and load transfer capacity optimization*. PhD thesis, School of Civil, Mining and Environmental Engineering, University of Wollongong, 2012.
- [36] J C ea, S Garreau, P Guillaume, and M Masmoudi. The shape and topological optimizations connection. *Comput. Methods Appl. Mech. Engrg.*, 188:713–726, 2000.
- [37] S Chen, B Merriman, Osher S J, and P Smereka. A simple level set method for solving stefan problems. *J. Comput. Phys.*, 135:8–29, 1997.
- [38] D Chenais. On the existence of a solution in a domain identification problem. *J. Math. Anal. Appl.*, 52:189–289, 1975.
- [39] F Chouly and P Hild. On the convergence of the penalty method for unilateral contact problems. *Applied Numerical Mathematics*, 65:27–40, 2013.
- [40] G Cohen. Convexit  et optimisation. Engineering school, 1999-2001 Ecole Nationale des Ponts et Chauss ees, 2000, pp.139. cel-00356686.
- [41] J A Collins, H R Busby, and G H Staab. *Mechanical Design of Machine Elements and Machines*. Wiley, 2009.
- [42] I Coria Mart nez, I Mart n, H Bouzid, and J Aguirrebeitia. Optimized bolt tightening sequences in bolted joints using superelement fe modeling technique. *37th International Conference on Ocean, Offshore and Artic Engineering*, 2018.
- [43] C Dapogny, N Lebbe, and E Oudet. Optimization of the shape of regions supporting boundary conditions. *Numer. Math.*, 146:51–104, 2020.
- [44] J Desai. *Topology optimization in contact, plasticity and fracture mechanics using a level-set method*. PhD thesis, Universit  de Paris, 2021. in preparation.
- [45] C Dobrzynski and P Frey. Anisotropic Delaunay mesh adaptation for unsteady simulations. *Proc. 17th Int. Meshing Roundtable, Pittsburg*, 2008.
- [46] S Drabla, M Sofonea, and B Teniou. Analysis of a frictionless contact problem for elastic bodies. *Annales Polonici Mathematici*, 69(1):75–88, 1998.
- [47] H A Eschenauer, V V Kobelev, and A Schumacher. Bubble method for topology ans shape optimization of structures. *Structural Optimization*, 8(1):42–51, 1994.
- [48] F Feppon, G Allaire, and C Dapogny. Null space gradient flows for constrained optimization with applications to shape optimization. *to appear in COCV*, January 2019. HAL preprint: hal-01972915.

- [49] R Fletcher. *Practical methods of optimization*. John Wiley & Sons, 2013.
- [50] G Fremiot and J Sokołowski. Shape sensitivity analysis of problems with singularities. *Lecture notes in pure and applied mathematics*, 216:255–276, 2001.
- [51] S Garreau, P Guillaume, and M Masmoudi. The topological asymptotic for pde systems : The elasticity case. *SIAM Journal on Control and Optimization*, 39(6):1756–1778, 2001.
- [52] S M Giusti, A Ferrer, and J Oliver. Topological sensitivity analysis in heterogeneous anisotropic elasticity problem. theoretical and computational aspects. *Comput. Methods Appl. Mech. Engrg.*, 311:134–150, 2016.
- [53] S M Giusti, J Sokołowski, and J Stebel. On topological derivatives for contact problems in elasticity. *J Optim Theory Appl*, 165:279–294, 2015.
- [54] N Govindu, T Jayanand Kumar, and S Venkatesh. Design and optimization of screwed fasteners to reduce stress concentration factor. *Journal of Applied Mechanical Engineering*, 4(4), 2015.
- [55] R Grzejda. Modelling bolted joints using a simplified model. *Journal of Mechanical and Transport Engineering*, 69(1):23–37, 2017.
- [56] P Guillaume and K Sid Idris. The topological asymptotic expansion for the dirichlet problem. *SIAM Journal on Control and Optimization*, 41(4):1042–1072, 2002.
- [57] J Guillot. Assemblages par éléments filetés. Technical report, Techniques de l’Ingénieur, 1989. B 5560.
- [58] J Guillot. Modélisation et calcul des assemblages visées. généralités. Technical report, Techniques de l’Ingénieur, 1989. BM 5560.
- [59] J Hadamard. *Mémoire sur le problème d’analyse relatif à l’équilibre des plaques élastiques encastrées*. Bull. Soc. Math., France, 1907.
- [60] F Hecht. New development in FreeFem++. *J. Numer. Math.*, 20(3-4):251–265, 2012.
- [61] J Hou, J Zhu, J Wang, and W Zhang. Topology optimization of multi-fasteners jointed structure considering fatigue constrains. *Int. J. Simul. Multidisci. Des. Optim.*, 9, A4, 2018.
- [62] X Huang and Y Xie. Convergent and mesh-independent solutions for the bi-directional evolutionary structural optimization method. *Finite Elements in Analysis and Design*, 43(14):1039–1049, 2007.
- [63] T Jiang and M Chirehdast. A systems approach to structural topology optimization: Designing optimal connections. *ASME. J. Mech.- Des.*, 119(1):40–47, 1997.
- [64] T Jiang and P Y Papalambros. A first order method of moving asymptotes for structural optimization. *WIT Transactions on the Built Environment*, 14, 1995.
- [65] R P Johanson. *Topology optimization of multicomponent structures*. PhD thesis, The University of Michigan, Ann Arbor, 1996.

- [66] M Kerguignas and G Caignaert. *Résistance des matériaux*. DUNOD Université, 4ème ed., Paris, 1977.
- [67] R V Kohn and G Strang. Optimal design and relaxation of variational problems. i. *Comm. Pure Appl. Math.*, 39(1):113–137, 1986.
- [68] Q Li, G P Steven, and Y M Xie. Evolutionary structural optimization for connection topology design of multi-component systems. *Engineering Computations*, 18(3/4):460–479, 2001.
- [69] P Liu and Z Kang. Integrated topology optimization of multi-component structures considering connecting interface behavior. *Computer Methods in Applied Mechanics and Engineering*, 341:851–887, 2018.
- [70] D G Luenberger and Y Ye. *Linear and Nonlinear Programming*. Springer, New York, 2008. 3rd Edition.
- [71] K A Lurie, A V Cherkaev, and A V Fedorov. Regularization of optimal design problems for bars and plates. i, ii. *J. Optim. Theory Appl.*, 37(4):499–522, 523–543, 1982.
- [72] J Mackerle. Finite element analysis of fastening and joining: A bibliography (1990–2002). *International Journal of Pressure Vessels and Piping*, 80(4):253–271, 2003.
- [73] M Malladi, J A Sethian, and B C Vemuri. A fast level set based algorithm for topology independent shape modeling. *J. Math. Imaging and Vision*, 6(2):269–290, 1996.
- [74] A Maury. *Shape optimization for contact and plasticity problems thanks to the level set method*. PhD thesis, Université Pierre et Marie Curie - Paris VI, 2016.
- [75] R J Menassa and W R DeVries. Optimization methods applied to selecting support positions in fixture design. *ASME Journal of engineering for industry*, 113:412–418, 1991.
- [76] J Montgomery. Methods for modeling bolts in the bolted joint. *ANSYS World Users Conference*, 2002.
- [77] J-M Monville. Optimal tightening process of bolted joints. *Int. J. Simul. Multisci. Des. Optim.*, 7(A4), 2006.
- [78] Z Mroz and G I N Rozvany. Optimal design of structures with variable support conditions. *J. Optim. Theory Appl*, 15:85–101, 1975.
- [79] W Mulder, S Osher, and J A Sethian. Computing interface motion in compressible gas dynamics. *J. Comput. Phys.*, 100:209–228, 1992.
- [80] F Murat and J Simon. Etudes de problèmes d’optimal design. *Lecture Notes in Computer Science*, 41:54–62, 1976.
- [81] F Murat and J Simon. Sur le contrôle par un domaine géométrique, 1976. Internal Report No 76 015, univ, Paris VI.
- [82] F Murat and L Tartar. Calcul des variations et homogénéisation. *Les Méthodes de l’Homogénéisation Théorie et Applications en Physique, Coll. Dir. Etudes et Recherches EDF, Eyrolles*, pages 319–369, 1985.

- [83] F Murat and L Tartar. Optimality conditions and homogenization. *Nonlinear Variational Problems*, A. Marino et al. eds., pages 1–8, 1985.
- [84] J Nocedal and S J Wright. *Numerical Optimization*. Springer, New York, 2006.
- [85] A A Novotny, R A Feijoo, E Taroco, and C Padra. Topological sensitivity analysis for three-dimensional linear elasticity problem. *Computer Methods in Applied Mechanics and Engineering*, 196(41-44):454–4364, 2007.
- [86] A A Novotny and J Sokołowski. *Topological derivatives in shape optimization*. Springer, Heidelberg, 2013.
- [87] A Oinonen, P Tanskanen, T Björk, and G Marquis. Pattern optimization of eccentrically loaded multi-fastener joints. *Struct Multidisc Optim*, 40:597–609, 2010.
- [88] N Olhoff and B Åakeson. Minimum stiffness of optimally located supports for maximum value of column buckling loads. *Structural Optimization*, 3:163–175, 1991.
- [89] N Olhoff and JE Taylor. Designing continuous columns for minimum total cost of material and interior supports. *J. Struct. Mech.*, 6:367–382, 1978.
- [90] S J Osher and R Fedkiw. *Level set methods and dynamic implicit surfaces*, volume 153. Springer Science & Business Media, Applied Mathematical Sciences, 2006.
- [91] S J Osher and J A Sethian. Fronts propagating with curvature-dependent speed: Algorithms based on Hamilton-Jacobi formulations. *J. Comput. Phys.*, 79:12–49, 1988.
- [92] N L Pedersen. Optimization of bolt thread stress concentrations. *Arch Appl Mech*, 83:1–14, 2013.
- [93] P Pedersen. Topology optimization of 3d trusses with cost of supports. *Advances in Design Automation*, 65:761–768, 1993.
- [94] O Pironneau. *Optimal shape design for elliptic systems*. Springer-Verlag, New-York, 1984.
- [95] O Querin, V Young, G Steven, and Y Xie. Computational efficiency and validation of bi-directional evolutionary structural optimization. *Computer Methods in Applied Mechanics and Engineering*, 189(2):559–573, 2000.
- [96] L Rakotondrainibe, G Allaire, and P Orval. Topology optimization of connections in mechanical systems. *Structural and Multidisciplinary Optimization*, 61:2253–2269, 2020.
- [97] G I N Rozvany. Aims, scope, methods, history and unified terminology of computer-aided topology optimization in structural mechanics. *Structural and Multidisciplinary Optimization*, 21(2):90–108, 2001.
- [98] G I N Rozvany. A critical review of established methods of structural topology optimization. *Structural and Multidisciplinary Optimization*, 37(3):217–237, 2009.
- [99] L I Rudin and S J Osher. Total variation based image restoration with free local constraints. *ICIP 1, IEEE*, pages 1–35, 1994.
- [100] B Samet, S Amstutz, and M Masmoudi. The topological asymptotic for the helmholtz equation. *SIAM J. Control Optim.*, 42(5):1523–1544, 2003.

- [101] M Schneider and H Andra. The topological gradient in anisotropic elasticity with an eye towards lightweight design. *Mathematical Methods in the Applied Sciences*, 2013.
- [102] A Schumacher. *Topologieoptimierung von Bauteilstrukturen unter Verwendung von Lochpositionierungskriterien*. PhD thesis, Universität-Gesamthochschule-Siegen, 1995. PhD thesis.
- [103] J A Sethian. *Level set methods and fast marching methods: evolving interfaces in computational geometry, fluid mechanics, computer vision, and materials science*, volume 3. Cambridge university press, 1999.
- [104] A Sharma. Level set method for computational multi-fluid dynamics : A review on developments, applications and analysis. *Indian Academy of Sciences*, 40(3):627–652, 2015.
- [105] J Simon. Differentiation with respect to the domain in boundary value problems. *Num. Funct. Anal. Optimiz.*, 2:649–687, 1980.
- [106] M Smith. *ABAQUS/Standard User's Manual, Version 6.9*. Dassault Systèmes Simulia Corp, United States, 2009.
- [107] J Sokołowski and A Żochowski. On the topological derivative in shape optimization. *SIAM Journal on Control and Optimization*, 37:1251–1272, 1999.
- [108] J Sokołowski and A Żochowski. Topological derivatives of shape functionals for elasticity systems. *Mechanics of Structures and Machines*, 29:333–351, 2001.
- [109] J Sokołowski and J P Zolesio. *Introduction to shape optimization*. Springer-Verlag, Berlin, 1992.
- [110] J H Son and B M Kwak. Optimization of boundary conditions for maximum fundamental frequency of vibrating structures. *AIAA journal*, 31(12):2351–2357, 1993.
- [111] D C Sorensen. Newton's method with a model trust region modification. *SIAM J. Numer. Anal.*, 19(2):409–426, 1982.
- [112] A Sorrentino, D Castagnetti, A Spaggiari, and E Dragoni. Shape optimization of the fillet under a bolt's head. *The Journal of Strain Analysis for Engineering Design*, 54(4):247–253, 2019.
- [113] G G Stokes. On the effect of the internal friction of fluids on the motion of pendulums. *Trans. Camb. Phil. Soc.*, 9(II):8–106, 1851.
- [114] M Stolpe and K Svanberg. An alternative interpolation scheme for minimum compliance topology optimization. *Structural and Multidisciplinary Optimization*, 22(2):116–124, 2001.
- [115] K Svanberg. The method of moving asymptotes - a new method for structural optimization. *International Journal for Numerical Methods in Engineering*, 24:359–373, 1987.
- [116] D Szelag and Z Mroz. Optimal design of elastic beams with unspecified support conditions. *ZAMM J. Appl. Math. Mech.*, 58:501–510, 1978.

- [117] A Takezawa, S Nishiwaki, and M Kitamura. Shape and topology optimization based on the phase field method and sensitivity analysis. *Journal of Computational Physics*, 229(7):2697–2718, 2010.
- [118] Z Tan and R D Reitz. An ignition and combustion model based on the level-set method for spark ignition engine multidimensional modeling. *Combustion and Flame*, 145(1-2):1–15, 2006.
- [119] G N Vanderplaats and F Moses. Structural optimization by methods of feasible directions. *Computers & Structures*, 3:739–755, 1973.
- [120] BP Wang and JL Chen. Application of genetic algorithm for the support location optimization of beams. *Comput. Struct*, 58:797–800, 1996.
- [121] D Wang. *Structural optimization with evolutionary shift method*. PhD thesis, Department of Aircraft Manufacturing Engineering, Northwestern Polytechnical University, 2003. PhD thesis.
- [122] D Wang, JS Jiang, and WH Zhang. Optimization of support positions to maximize the fundamental frequency of structures. *Int. J. Numer. Methods Eng.*, 61, 2004.
- [123] M Y Wang, X Wang, and D Guo. A level set method for structural topology optimization. *Comput. Methods Appl. Mech. Engrg.*, 192:227–246, 2003.
- [124] M Y Wang and S Zhou. Phase field: a variational method for structural topology optimization. *Comput Model Eng Sci*, 6(6):547–566, 2004.
- [125] C Woischwill and I Y Kim. Multimaterial multijoint topology optimization. *International Journal for Numerical Methods in Engineering*, 115(13):1552–1579, 2018.
- [126] Q Xia, M Y Wang, and T Shi. A level set method for shape and topology optimization of both structure and support of continuum structures. *Comput. Methods Appl. Mech. Engrg.*, 272:340–353, 2014.
- [127] Y M Xie and X Huang. Recent developments in evolutionary structural optimization (eso) for continuum structures. *IOP Conference Series: Materials Science and Engineering*, 2010.
- [128] Y M Xie and G P Steven. A simple evolutionary procedure for structural optimization. *Computers & Structures*, 49(5):885–896, 1993.
- [129] B Żylinski and R Buczkowski. Analysis of bolt joint using the finite element method. *Archive of Mechanical Engineering*, 57(3):275–292, 2010.
- [130] E Zahavi. *The Finite Element Method in Machine Design*. Prentice-Hall, 1992.
- [131] M Zhou and G Rozvany. On the validity of ESO type methods in topology optimization. *Structural and Multidisciplinary Optimization*, 21(1):80–83, 2001.
- [132] Y Zhou and K Saitou. Gradient-based multi-component topology optimization for stamped sheet metal assemblies (MTO-S). *Structural and Multidisciplinary Optimization*, 58(1):83–94, 2018.

-
- [133] J Zhu and Sethian J A. Projection methods coupled to level set interface techniques. *J. Comput. Phys.*, 102:128–138, 1992.
- [134] J H Zhu, H H Gao, Zhang W H, and Y Zhou. A multi-point constraints based integrated layout and topology optimization design of multi-component systems. *Structural and Multidisciplinary Optimization*, 51(2):397–407, 2015.
- [135] J H Zhu, W J Guo, W H Zhang, and T Liu. Integrated layout and topology optimization design of multi-frame and multi-component fuselage structure systems. *Structural and Multidisciplinary Optimization*, 56(1):21–45, 2017.
- [136] J H Zhu, J Hou, W H Zhang, and Y Li. Structural topology optimization with constraints on multi-fasteners joint loads. *Structural and Multidisciplinary Optimization*, 50:561–571, 2014.
- [137] J H Zhu and W H Zhang. Maximization of structure natural frequency with optimal support layout. *Structural and Multidisciplinary Optimization*, 31:462–469, 2006.
- [138] J H Zhu and W H Zhang. Integrated layout design of supports and structures. *Computer Methods in Applied Mechanics and Engineering*, 199(9-12):557–569, 2010.
- [139] G Zoutendijk. *Methods of feasible directions: A study in linear and non-linear programming*. Elsevier Publishing Co., Amsterdam-London- New York-Princeton, N. J., 1960.

Titre : Optimisation topologique des liaisons dans les systèmes mécaniques

Mots clés : Optimisation topologique, Système assemblé, Liaisons mécaniques, Vis, Gradient topologique, Méthode des lignes de niveaux

Résumé : L'optimisation topologique est communément appliquée aux pièces mécaniques. En général, elle n'implique qu'une seule pièce dont les liaisons mécaniques sont supposées fixes. Cette thèse propose une autre approche de l'optimisation topologique où les liaisons sont des variables de conception, au même titre que la géométrie et la topologie de la forme de la pièce. On s'intéresse aux vis longues normalisées avec précontrainte de serrage. Le modèle de la vis est idéalisé, le but étant d'obtenir une représentation fonctionnelle, mais réaliste et peu coûteuse en termes de temps de calcul. Le modèle idéalisé est complété par des contraintes mécaniques spécifiques à la vis.

Le problème consiste à optimiser simultanément la structure d'une pièce, d'une part, et les positions et

le nombre de vis, d'autre part. La structure élastique est représentée par une fonction ligne de niveaux et elle est optimisée avec la méthode de variations de frontière d'Hadamard. Les positions sont optimisées avec un algorithme de descente de gradient paramétrique. Le concept de gradient topologique est adapté pour ajouter une petite vis idéalisée au meilleur emplacement avec une orientation optimale pour optimiser le nombre de vis. Cette optimisation couplée (structure et liaisons) est illustrée par des cas tests académiques 2d et 3d. Elle est ensuite appliquée à un cas test industriel simplifié. Le couplage fournit une pièce plus performante que l'optimisation de forme à liaisons fixées. Cette approche tend par conséquent à optimiser les systèmes assemblés.

Title : Topology optimization of connections in mechanical systems

Keywords : Topology optimization, Assembled system, Mechanical connections, Bolt, Topological derivative, Level-set method

Abstract : Topology optimization is commonly used for mechanical parts. It usually involves a single part and connections to other parts are assumed to be fixed. This thesis proposes an other approach of topology optimization in which connections are design variables, as well as the structure. We focus on standard long bolt with prestressed state. This connection model is idealized to be enough representative but computationally cheap. The idealized model is complemented with mechanical constraints specific to the bolt.

The problem is to optimize concurrently the topology and the geometry of a structure, on the one hand, and the locations and the number of bolts, on the other hand. The elastic structure is represented by a

level-set function and is optimized with Hadamard's boundary variation method. The locations are optimized using a parametric gradient-based algorithm. The concept of topological derivative is adapted to add a small idealized bolt at the best location with the optimal orientation, and thus optimizes the number of bolts. This coupled topology optimization (shape and connections) is illustrated with 2d and 3d academic test cases. It is then applied on a simplified industrial test case. The coupling provides more satisfactory performance of a part than shape optimization with fixed connections. The approach presented in this work is therefore one step closer to the optimization of assembled systems.

